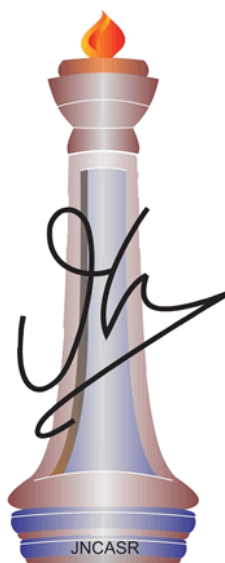

**Synthesis and Characterization of Versatile
Low Molecular Weight Gelators towards
Functional Metal-organic Soft-materials**

A Thesis Submitted for the Degree of

Doctor of Philosophy

By

Papri Sutar



**Chemistry & Physics of Materials Unit (CMPU)
Jawaharlal Nehru Centre for Advanced Scientific Research**

(A Deemed University)

Bangalore-560064

April, 2018

Dedicated to My Family

DECLARATION

I hereby declare that the matter embodied in the thesis entitled “**Synthesis and Characterization of Versatile Low Molecular Weight Gelators towards Functional Metal-organic Soft-materials**” is the resultant of the investigations carried out by me at the Molecular Materials Laboratory, Chemistry and Physics of Materials Unit (CPMU), Jawaharlal Nehru Centre for Advanced Scientific Research (JNCASR), Bangalore, India under the supervision of **Prof. Tapas Kumar Maji** and that it has not been submitted elsewhere for the award of any degree or diploma.

In keeping with the general practice in reporting the scientific observations, due acknowledgement has been made whenever the work described is based on the findings of other investigators. Any omission that might have occurred due to oversight or error in judgement is regretted.

.....
Papri Sutar

Date:

Place:

CERTIFICATE

I hereby certify that the work described in this thesis entitled “**Synthesis and Characterization of Versatile Low Molecular Weight Gelators towards Functional Metal-organic Soft-materials**” has been carried out by **Ms. Papri Sutar** under my supervision at the Molecular Materials Laboratory, Chemistry and Physics of Materials Unit (CPMU), Jawaharlal Nehru Centre for Advanced Scientific Research (JNCASR), Bangalore, India and that it has not been submitted elsewhere for the award of any degree or diploma.

.....

Prof. Tapas Kumar Maji
(Research Supervisor)

Date:

Place:

ACKNOWLEDGEMENTS

Firstly, I would like to express my sincere gratitude to my research supervisor Prof. Tapas Kumar Maji for his kind support, valuable guidance and constant encouragement which he has provided me throughout the course of investigation. His sincerity, enthusiasm, dedication and discipline for research have always motivated me to grow as a researcher. I will always be grateful to him for giving me enough freedom to pursue research on my area of interest. I am thankful to him for never letting me quit and constantly pushing me beyond my pre-set boundaries.

I would like to thank Prof. C. N. R. Rao for being a constant source of inspiration to me. His motivational talk has always influenced me to do better in research as well as in life.

I would like to thank the past and present CPMU chairman Prof. G. U. Kulkarni, Prof. S. Balasubramanian, and Prof. N. Chandrabhas for allowing me to use the various facilities of the centre.

I would like to thank Prof. S. Balasubramanian, Prof. A. Sundaresan, Prof. S. Rajaram from JNCASR and Prof. T. N. Guru Row from IISc, for their informative courses that have been extremely helpful to me.

I would like to specially thank Prof. Subi J. George and Mr. Suman Kuila for helping me in lifetime measurements, Prof. Rajesh Ganapathy for rheology measurements, Prof. K. S. Narayan and Mr. Anaranya Gorai for quantum yield measurements.

I am thankful to Prof. Aninda J. Bhattacharyya and Dr. D. Dutta for valuable discussions and initial assistance on proton conductivity measurements. Special thanks go to Dr. Sunita Dey, Mr. Anand Roy, Dr. K Gopalakrishnan and Mr. Sreedhara M B for helping me in various stages of preparing photocatalysis setup and in electrode preparation.

I am lucky to have wonderful labmates who have always maintained healthy and friendly lab-environments. I am grateful to all my past labmates, Dr. Prakash Kanoo, Dr. Sudip Mohapatra, Dr. Jayaramulu. K., Dr. Ritesh Haldar, Dr. Arpan Hazra, Dr. V. Suresh, Dr. Anindita Chakraborty, Dr. Nivedita Sikdar, Ms. Komal, who have been extremely

helpful to me. I would like to specially thank Dr. Anindita Chakraborty and Dr. V. Suresh who had helped me in innumerable ways during my early Ph.D. days and are still guiding me in different ways. I am thankful to my present labmates Syamantak da, Sohini, Subhajit, Parul, Sanchita, Mrinal, Tarandeep, Pramod, Dr. Debabrata Samanta, Dr. Ashish Singh, Dr. Subarna Dey, Dr. Darsi Rambabu, Dr. Chayanika Das.

I am grateful to all SRFs and POCEs, Abhinav, Paromita, Vamakshi, Subhadip for helping me in different research projects. I would like to specially thank visiting scientist, Dr. Meenakshi Ghosh not only for helping me in one of my research problem, but also for a wonderful two month's memories that I will cherish forever.

I am thankful to all the technical staffs of JNCASR, Ms. Selvi (FESEM), Mrs. Usha (TEM), Mr. Basavaraj (AFM), Mr. Mahesh (NMR), Mr. Vasu (UV/PL/IR), Mr. Anil (PXRD), Shivakumar (HRMS), for their help with the various characterization techniques. This thesis would not be possible without their generous help.

I am thankful to all my batchmates, Swathi, Dheeraj, Sreedhara, Sanjay, Shisir. I have few good friends who have always been with me during the roller-coaster ride of Ph.D. I would like to thank Debosree, Sutanuka, Srimayee, Anindita di, Sunita di, Abhishek and Mitali. This thesis would be incomplete without their emotional support.

My heartfelt thanks go to Mrs. Supriti Maji, Sonai and Neel for their love and hospitality.

I thank Administrative Staff, Hostel Staff, Mess Workers, House Keeping Staff and Security for providing and maintaining the various facilities that have been helped me immensely.

I am thankful to all of my school and college teachers who have impacted my life in various ways.

There is no perfect word that could express the gratitude to my family. I am thankful to Maa, Baba, Bunu (my younger sister), Baromaa (Aunt), Jethumoni (Uncle) and Didon (Grandmother) for showering me with their unconditional love and blessings. Without their support I would never be able to finish my Ph.D. I am also thankful to my husband, Deepjay for being with me through thick and thin and serving as a constant source of motivation. This thesis is dedicated to my loving family.

PREFACE

This thesis is organized into six chapters. First five chapters describe the self-assembly of various low molecular weight gelators (LMWGs) to hydrogel, organogel, coordination polymer gels (CPGs), their photophysical properties and versatile applications related to energy and environment. The last chapter describes the metal-organic cube (MOC)-based hydrogels and their applications.

Chapter 1 gives brief overview of LMWGs, CPGs, metal-organic cages and cage derived gels, discusses their importance, properties and potential applications.

Chapter 2 reports rational design and synthesis of a blue emitting LMWG having 9,10-diphenylanthracene core and terminal terpyridine groups. Self-assembly of the LMWG in organic solvent results in organogel which exhibits nanofiber morphology. Coordination of Tb^{III} and Eu^{III} ion to LMWG results in green and pink emissive CPGs, respectively. The CPGs show coiled nanofiber morphology. Moreover, coordination of both Tb^{III} and Eu^{III} to LMWG yields bimetallic CPGs in which precise stoichiometric control over LMWG: Eu^{III}:Tb^{III} leads to tunable yellow and white emitting bimetallic CPGs. High processability of CPGs is utilized for large area coating applications. Moreover, a white-light emitting LED has been fabricated through mere coating of white-light emitting CPG over a commercial blue LED.

Chapter 3 comprises of two parts: **Part 3A** reports synthesis of a flexible, amphiphilic LMWG having 4,4',4''-[1,3,5-phenyl-tri(methoxy)]-tris-benzene core and three terminal 2,2':6',2''-terpyridyl moieties which are connected by alkylamide chain. The LMWG exhibits bimodal self-assembly in aqueous and organic solvents and results in hydrogel and organogel, respectively. The donor-acceptor π -stacking results in CT emission in hydrogel and donor-donor π -stacking results in normal LMWG-based emission in organogel. Also, different spatial disposition of π -chromophores lead to the formation of nanospheres and nanofibers in hydrogel and organogel, respectively. Moreover, the hydrogel-nanospheres having surface-exposed amide groups, are exploited as soft nano-catalyst for Knoevenagel condensation reaction. Hydrogel-nanocatalysts show high recyclability without change in morphologies. The enhanced catalytic activity is correlated to the high surface-to-volume ratio of the nanospheres of hydrogel which facilitate easy contact between the substrates and catalytic surface. **Part 3B** reports self-assembly of the same LMWG with different metal ions which results in CPGs that show controllable nanomorphologies, tunable emission and stimuli-responsive behaviours. The

LMWG also act as a selective chemosensor for Zn^{II} with very low limit of detection (0.18 ppm) in aqueous medium. Self-assembly of the LMWG with Zn^{II} in $\text{H}_2\text{O}/\text{MeOH}$ solvent mixture results in a CPG which exhibits sheet-like morphology and charge-transfer emission. On the other hand, coordination of LMWG with Tb^{III} and Eu^{III} in CHCl_3/THF solvent mixture results in green and red emissive CPGs, respectively with nanotubular morphology. Moreover, precise stoichiometric control of LMWG: Eu^{III} : Tb^{III} ratio leads to the formation of bimetallic CPGs which show tunable emissions, including white-light-emission. We also explore the multi-stimuli responsive properties of the white-light-emitting CPG by exploiting the dynamics of Ln^{III} -tpy coordination.

Chapter 4 reports synthesis and self-assembly of two LMWGs having pyrene derivatives as core and 2,2':6',2''-terpyridyl groups as metal binding sites. Self-assembly of the LMWGs results in organogels which shows nanofiber morphologies. The coordination driven self-assembly of LMWGs with ruthenium ions (Ru^{II}) results in CPGs that exhibit broad visible-light absorption due to metal-to-ligand charge transfer (MLCT) transition and π - π^* transition of pyrene centres. The CPGs show visible-light driven hydrogen evolution and good recyclability. Moreover, their photocatalytic activities are improved by many folds after doping with a transition metal co-catalyst which has structural resemblance with the naturally occurring [FeFe] hydrogenase.

Chapter 5 reports synthesis of two photo-responsive LMWG, containing stilbene and azobenzene core which are connected to 2,2':6',2''-terpyridyl moieties by flexible alkylamide chains. Self-assembly of the stilbene containing LMWG is driven by π - π stacking and H-bonding interactions and results in organogel which shows nanofiber morphology. Interestingly, the azobenzene core based LMWG does not form gel in the same condition. Coordination driven self-assembly of the LMWG with Zn^{2+} results in CPG which also exhibits nanofiber morphology. Both organogel and CPG show blue emission which quenched significantly after irradiation with UV light ($\lambda=365$ nm) indicating photochemical change of gelators in both. $^1\text{H-NMR}$ study confirms that the gelator molecules undergo [2+2] cyclo-addition and form tetraphenyl cyclobutane in gel-state after photo-irradiation. Such photo-cyclization also affects the nano-morphology of the photo-irradiated gels which show nanotape morphology.

Chapter 6 comprises of two parts: **Part 6A** reports synthesis of a water soluble anionic MOC $\{[\text{Ga}_8(\text{ImDC})_{12}]^{12-}\}$ and its self-assembly to hydrogels in presence of different molecular binders. The charge-assisted H-bonding interactions between the anionic MOCs and cationic molecular binders such as, ammonium ion (NH_4^+), N-(2-

aminoethyl)-1,3-propanediamine, guanidine hydrochloride, and β -alanine, drive the self-assembly. Depending upon the structure and geometry of the molecular binders, the hydrogels show different morphologies. The hydrogel, formed with ammonium cations exhibits nanotubular morphology with negatively charged surface. This hydrogel is explored for gel-chromatographic separation of cationic species from anionic counterparts. The hydrogels also exhibit pH-responsive behaviours. **Part 6B** reports the proton conductivities of a MOC-based supramolecular porous framework and MOC-based hydrogels. The proton conductivity of all the materials increases with increasing humidity at a particular temperature and follow the Grotthuss mechanism. The highest value of proton conductivity of the porous framework is $1.4 \times 10^{-3} \text{ Scm}^{-1}$ at 98% RH and 25 °C. The proton conductivity drops drastically under anhydrous condition which indicates that the H-bonded guest water molecules present throughout the network play important role in facilitating the proton conductivity. Proton conductivity of two MOC-based hydrogels, MOC-G1 and MOC-G2, prepared by using ammonium cations and guanidium cations as molecular binders, are also studied. Among them, the MOC-G1 having nanotubular morphology exhibits highest proton conductivity ($1.8 \times 10^{-2} \text{ Scm}^{-1}$ at 98% RH and 25 °C) which is comparable with the other highest reported values in literature. **Part 6C** reports capacitive behaviour of a hydrogel formed by supramolecular self-assembly of MOC and graphene oxide (GO). Self-assembly of anionic MOC and GO is driven by H-bonding interaction between the carboxylate groups of MOC and hydroxyl or epoxy groups of GO, present on the basal plane and results in **MOC+GO** hydrogel which show layered nanostructure. The MOCs are intercalated between the GO sheets. The hydrogel exhibits capacitive behaviour and its specific capacitance ($C_{\text{sp}} = 10 \text{ F/g}$) is higher than the C_{sp} of as-synthesized GO (0.68 F/g).

Table of Contents

Chapter 1	1
<i>Introduction</i>	1
1.1 Gel materials.....	3
1.2 Different types of supramolecular gels.....	3
1.3 Hydrogels and its applications.....	7
1.3.1 Hydrophobic interaction.....	8
1.3.2 Hydrogen bonding.....	9
1.3.3 Electrostatic Interaction.....	10
1.3.4 Host-guest interaction.....	12
1.4 Organogels and its applications.....	14
1.5 Metal containing supramolecular gels.....	16
1.5.1 Coordination polymer gels (CPGs).....	17
1.5.2 Applications of CPGs.....	18
1.5.2.1 CPGs for Drug delivery.....	18
1.5.2.2 CPG for Self-healing.....	19
1.5.2.3 CPGs for chemosensing.....	20
1.5.2.4 CPGs for catalysis.....	22
1.5.2.5 CPGs for optoelectronics.....	23
1.6 Metal-organic cage.....	26
1.6.1 Design principles of metal-organic cage.....	28
1.6.2 Synthesis and applications of metal-organic cage.....	31
1.6.2.1 Ion transport.....	31
1.6.2.2 Proton conductivity.....	32
1.6.2.3 Molecular recognition and imaging.....	34
1.6.2.4 Drug delivery.....	35
1.7 Metal-organic cage based gels.....	37
1.9 Scope of the work.....	40
1.10 Outlook.....	41
1.11 Reference.....	43

Chapter 2	53
<i>Tunable Emission in Lanthanide Coordination Polymer Gels Based on a Rationally Designed Blue Emissive Gelator</i>	53
2.1 Introduction.....	57
2.2 Experimental section.....	58
2.2.1 Materials.....	58
2.2.2 Physical measurements.....	58
2.2.3 Synthesis.....	59
2.3 Results and discussion.....	62
2.3.1 Photophysical properties of L.....	62
2.3.2 Titration of L with Tb ^{III} and Eu ^{III} ions.....	64
2.3.3 Characterization of organogel (OG).....	65
2.3.4 Characterization of TbL and EuL gels.....	67
2.3.5 Tunable emission of coordination polymer gels.....	70
2.4 Summary.....	73
2.5 References.....	73
Chapter 3A	77
<i>Bimodal Self-assembly of an Amphiphilic Gelator to Hydrogel-nanocatalyst and Organogel of Different Morphologies and Photophysical Properties</i>	77
3A.1 Introduction.....	81
3A.2 Experimental section.....	82
3A.2.1 Materials.....	82
3A.2.2 Physical measurements.....	82
3A.2.3 Synthesis.....	83
3A.3 Results and discussion.....	85
3A.3.1 Characterization of L.....	85
3A.3.2 Characterization of hydrogel (HG).....	86
3A.3.3 Characterization of organogel (OG).....	90
3A.3.4 Catalytic activity of the hydrogel nanospheres.....	93
3A.4 Summary.....	99
3A.5 References.....	99

Chapter 3B	103
<i>Coordination Polymer Gels with Modular Nano-morphologies, Tunable Emissions and Stimuli-responsive Behaviour Based on an Amphiphilic Tripodal Gelator</i>	103
3B.1 Introduction.....	107
3B.2 Experimental section.....	109
3B.2.1 Materials.....	109
3B.2.2 Physical measurements.....	109
3B.2.3 Synthesis.....	110
3B.3 Results and discussion.....	111
3B.3.1 Metal ion sensing.....	111
3B.3.2 Synthesis and characterization of charge transfer CPG.....	114
3B.3.3 Synthesis, characterization of TbL and EuL organogel.....	117
3B.3.4 Stimuli-responsive behaviours of white-light-emitting CPGs.....	224
3B.4 Summary.....	126
3B.5 References.....	127
Chapter 4	131
<i>Ruthenium Based Coordination Polymer Gels as a Photosensitizer for Biomimetic Hydrogen Evolution</i>	131
4.1 Introduction.....	135
4.2 Experimental section.....	136
4.2.1 Materials.....	136
4.2.2 Physical measurements.....	137
4.2.3 Synthesis.....	137
4.2.4 Photocatalytic hydrogen evolution experiment.....	141
4.3 Results and discussion.....	142
4.3.1 Characterization of [FeFe](cbdt)(CO) ₆	142
4.3.2 Characterization of G1 and G2.....	142
4.3.3 Characterization of organogels.....	144
4.3.4 Characterization of CPGs.....	146
4.3.5 Photocatalytic hydrogen evolution.....	149
4.3.6 DFT calculation.....	152

4.4 Summary.....	154
4.5 References.....	154

Chapter 5.....157

Photo-responsive Gel: Tuning of Morphology and Optical Property by [2+2] Cyclo-addition Reaction.....157

5.1 Introduction.....	161
5.2 Experimental section.....	163
5.2.1 Materials.....	163
5.2.2 Physical measurements.....	163
5.2.3 Synthesis.....	164
5.3 Results and discussion.....	167
5.3.1 Characterization of L1 and L2.....	167
5.3.2 Photophysical properties of L1 and L2.....	168
5.3.3 Titration of L1 and L2 with Zn ^{II}	170
5.3.4 Characterization of OG1 organogel.....	171
5.3.5 Characterization of ZnL1 coordination polymer gel.....	175
5.4 Summary.....	178
5.5 References.....	178

Chapter 6A.....183

Binder Driven Self-assembly of Metal-Organic Cubes towards Functional Hydrogels..... 183

6A.1 Introduction.....	185
6A.2 Experimental section.....	189
6A.2.1 Materials.....	189
6A.2.2 Physical measurements.....	189
6A.2.3 Adsorption measurements.....	190
6A.2.4 Single-crystal X-ray diffraction.....	190
6A.2.5 Synthesis.....	190
6A.3 Results and discussion.....	194
6A.3.1 Characterization of {(Me ₂ NH ₂) ₁₂ [Ga ₈ (ImDC) ₁₂]·DMF·29H ₂ O} (1).....	194
6A.3.2 Characterization of MOC-G1 hydrogel.....	197

6A.3.3 Characterization of other hydrogels.....	200
6A.3.4 Gel-column chromatographic separation.....	203
6A.3.5 pH responsive behaviour.....	208
6A.4 Summary.....	209
6A.5 References.....	210

Chapter 6B.....213

Proton Conductivity in Metal-Organic Cube Based Framework and derived Hydrogels.....213

6B.1 Introduction.....	217
6B.2 Experimental section.....	219
6B.2.1 Materials.....	219
6B.2.2 Physical measurements.....	219
6B.2.3 Proton conductivity measurement.....	219
6B.3 Results and discussion.....	220
6B.3.1 Synthesis and structure description	220
6B.3.2 Characterization of MOC-G1 hydrogels.....	222
6B.3.3 Characterization of MOC-G2 hydrogels.....	223
6B.3.4 Proton conductivity of 1.....	224
6B.3.5 Proton conductivity of MOC-G1.....	228
6B.3.6 Proton conductivity of MOC-G2.....	232
6B.4 Summary.....	234
6B.5 References.....	234

Chapter 6C.....237

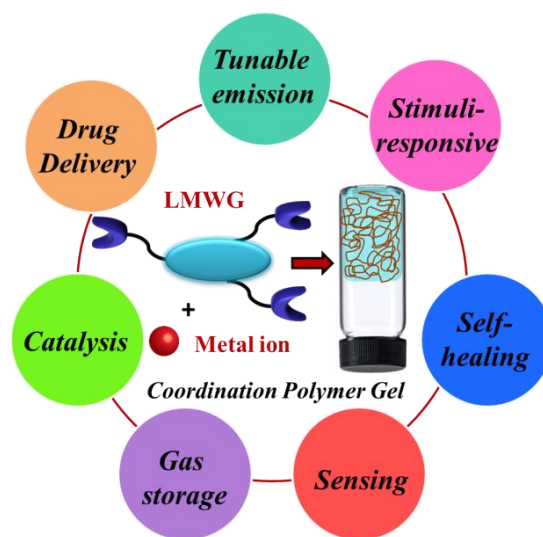
Layered Heterostructure Hydrogels Based on Metal-Organic Cube and GO/MoS₂ as Capacitive Materials.....237

6C.1 Introduction.....	241
6C.2 Experimental section.....	243
6C.2.1 Materials.....	234
6C.2.2 Physical measurements.....	243
6C.2.3 Electrochemical measurement.....	244
6C.2.4 Synthesis.....	245

6C.2.5 Preparation of electrode.....	246
6C.3 Results and discussion.....	247
6C.3.1 Characterization of GO and 1T/2H-MoS ₂	247
6C.3.2 Characterization of hydrogels.....	248
6C.3.3 Electrochemical studies of hydrogels.....	257
6C.4 Summary.....	262
6C.5 References.....	263
Chapter 7.....	267
<i>Thesis Summary.....</i>	<i>268</i>

Chapter 1

Introduction



1.1 Gel materials

Over the past few decades, enormous research interest has been directed towards the development of functional gel materials due to their widespread applications in biomedicine, optoelectronics, cosmetics, and in food industry.¹ Gels are soft materials which are easily recognized by “inversion test” method, which means if a pot of gel is turned upside down it remains stable under gravitational force.² Daily-life examples of gel include shower gel, shampoo, toothpaste, hair gel, soft contact lenses, etc. which are basically multi-component gels. In general, gels are viscoelastic solid-like materials which comprise of two coexisting phases; a large amount of liquid phase and a solid network which immobilises the flow of solvents. Depending upon the nature of solid phase gels are broadly divided into two categories: i) polymeric gels and ii) supramolecular gels (Chart 1). Among these two types, polymeric gels have been known for centuries. They consist of cross-linked polymer networks and the interstitial spaces of the network are filled with fluid. Polymer gels have ability to undergo substantial swelling and collapsing depending upon the environment. Because of such remarkable properties polymer gels have been well-explored for diverse applications in the fields of food, medicine, materials science, cosmetics, pharmacology and sanitation.^{1,3} Poly vinyl alcohol (PVA), poly acrylic acid (PAA) and poly acrylonitrile (PAN) are the commonly used in industry to prepare polymer gels. The major drawback of polymeric gel is that they cannot undergo reversible gel-sol transition and therefore have low processability. Recently, a new type of gel, known as supramolecular gel, derived from self-assembly of low-molecular weight gelators (LMWGs) have been developed (Chart 1).⁴ Supramolecular gels have attracted increasing attention due to easy synthesis, high solution processability and dynamic sol-gel reversibility which are useful for versatile applications.

1.2 Different types of supramolecular gels

Supramolecular gels which are also viscoelastic materials contain two phases; the solid network and the solvent phase. Here the solid networks are made of supramolecular nano/meso-structures. Depending upon the nature of the liquid phase, supramolecular gels are broadly classified into two categories: hydrogels and organogels. As the name indicates, in hydrogels water is immobilized in a solid network, whereas in organogels organic solvents are immobilized in a solid network. The solid networks of

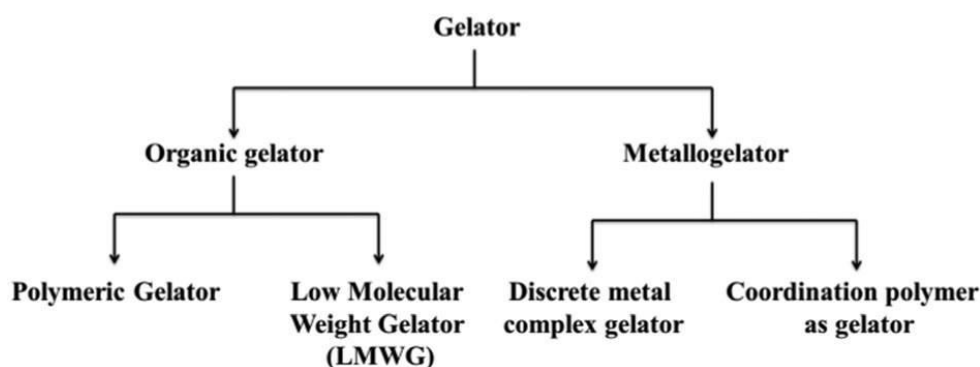


Chart 1. Classification of gelators. Figure reproduced from ref. 6f with permission.

supramolecular gels consist of a small amount (usually less than 5% by weight) of LMWGs.⁵ The LMWGs self-assemble in organic solvents or water through various non-covalent interactions, such as H-bonding, hydrophobic interactions, dipolar interactions, electrostatic interactions and π - π stacking, which facilitate their one dimensional growth to fibrils. These fibrils are further assembled through van der Waals interactions and form fibers. Three-dimensional entanglements of fibers result in a typical fibrous network of gel (Figure 1).⁶ However, instead of the conventional fibrous network, self-assembly of LMWGs could also result in other nanostructures, such as ribbons, platelets, spheres, tubular structures or cylinders, which further entangle to form three-dimensional networks that encapsulate the solvent molecules and prevent their flow.^{5b} Gelator molecules can be classified into two categories according to their mode of molecular aggregation: hydrogen-bond based gelators^{5c} and non-hydrogenbond based gelators

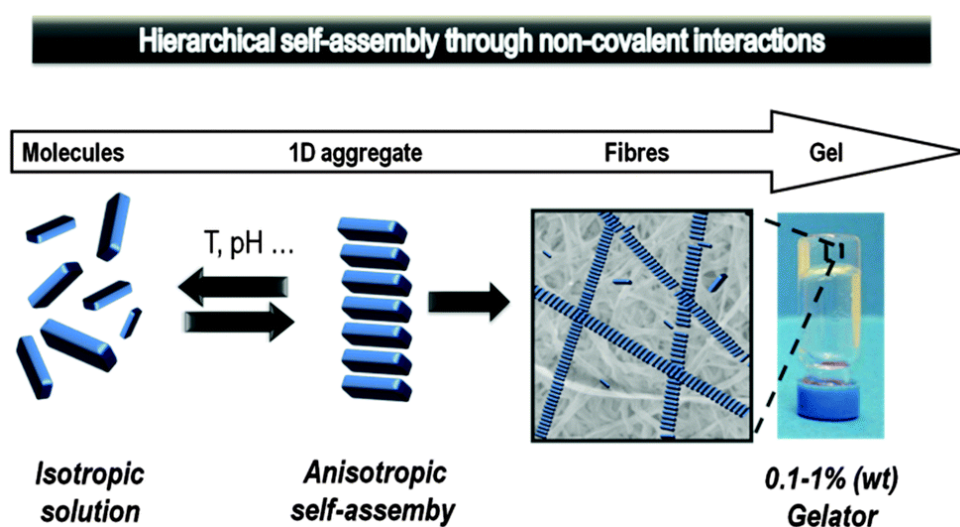


Figure 1. Bottom-up self-assembly of a supramolecular gel from LMWG. Figure reproduced from ref. 6e with permission.

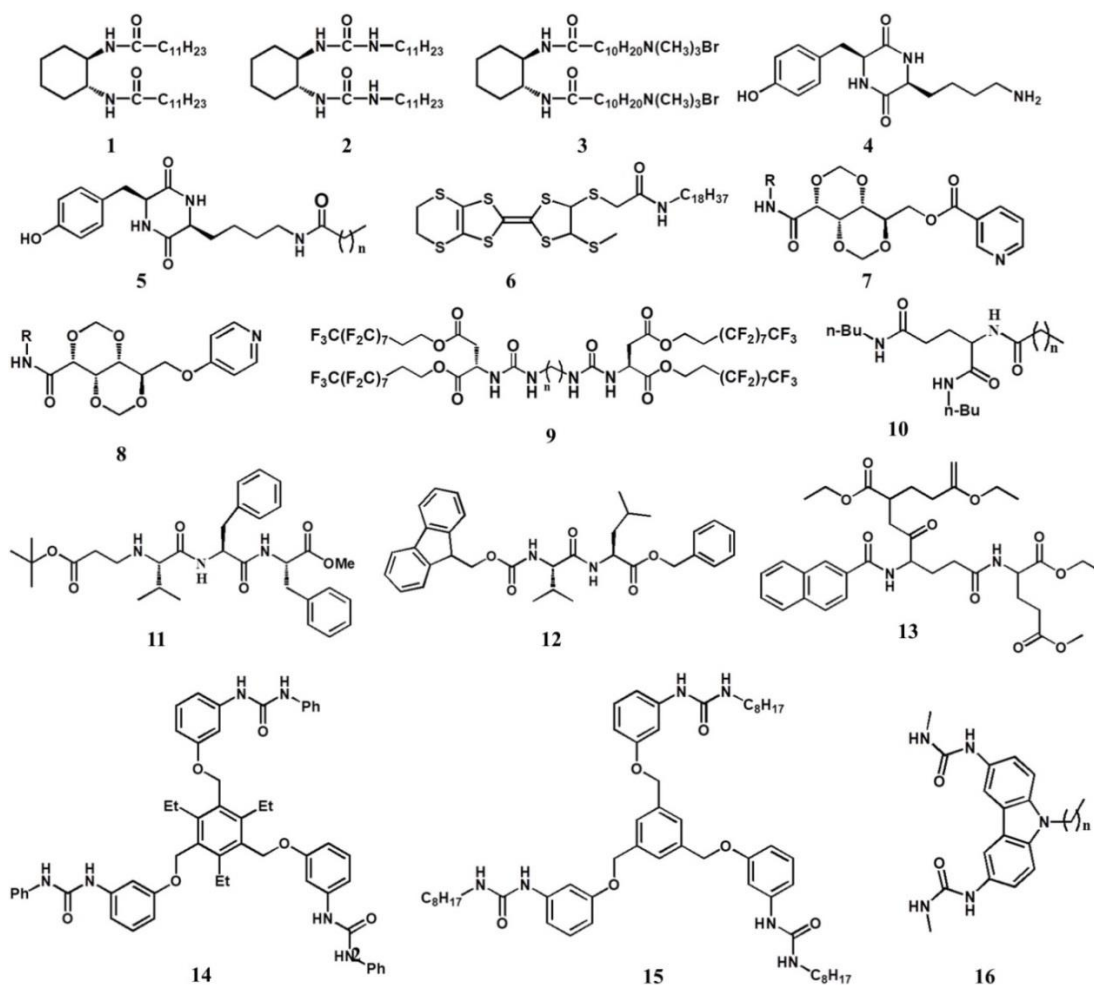


Figure 2. List of hydrogen bond-based gelators (1-16).

(Figure 2, 3).^{5d} Examples of hydrogen-bond based gelators include aliphatic amide, urea, peptide, amino acid and sugar derivatives, which have both H-bond donating and accepting sites (Figure 2).⁷ Non-hydrogen-bond based gelators include cholesterol derivatives, dendrimers, porphyrins and molecules having extended π -cores which aggregate through π - π stacking, van der Waals forces and/or solvophobic interactions (Figure 3).⁸ There another kind of gelators, known as amphiphilic gelators which have both H-bonding sites and π -core. The amphiphilic gelators self-assembled by H-bonding and hydrophobic interactions (Figure 4). Usually, the bottom-up approach to self-assembly is utilized to construct supramolecular structures of gels. In a typical synthetic procedure, the gelator molecules are heated in a particular solvent or mixture of solvents until they completely dissolved to form clear solution (sol form). Upon cooling the sol, the gelator molecules undergo supramolecular assembly to form three-dimensional nano- or microstructures which immobilize solvent molecules and form stable gel. The sol-gel

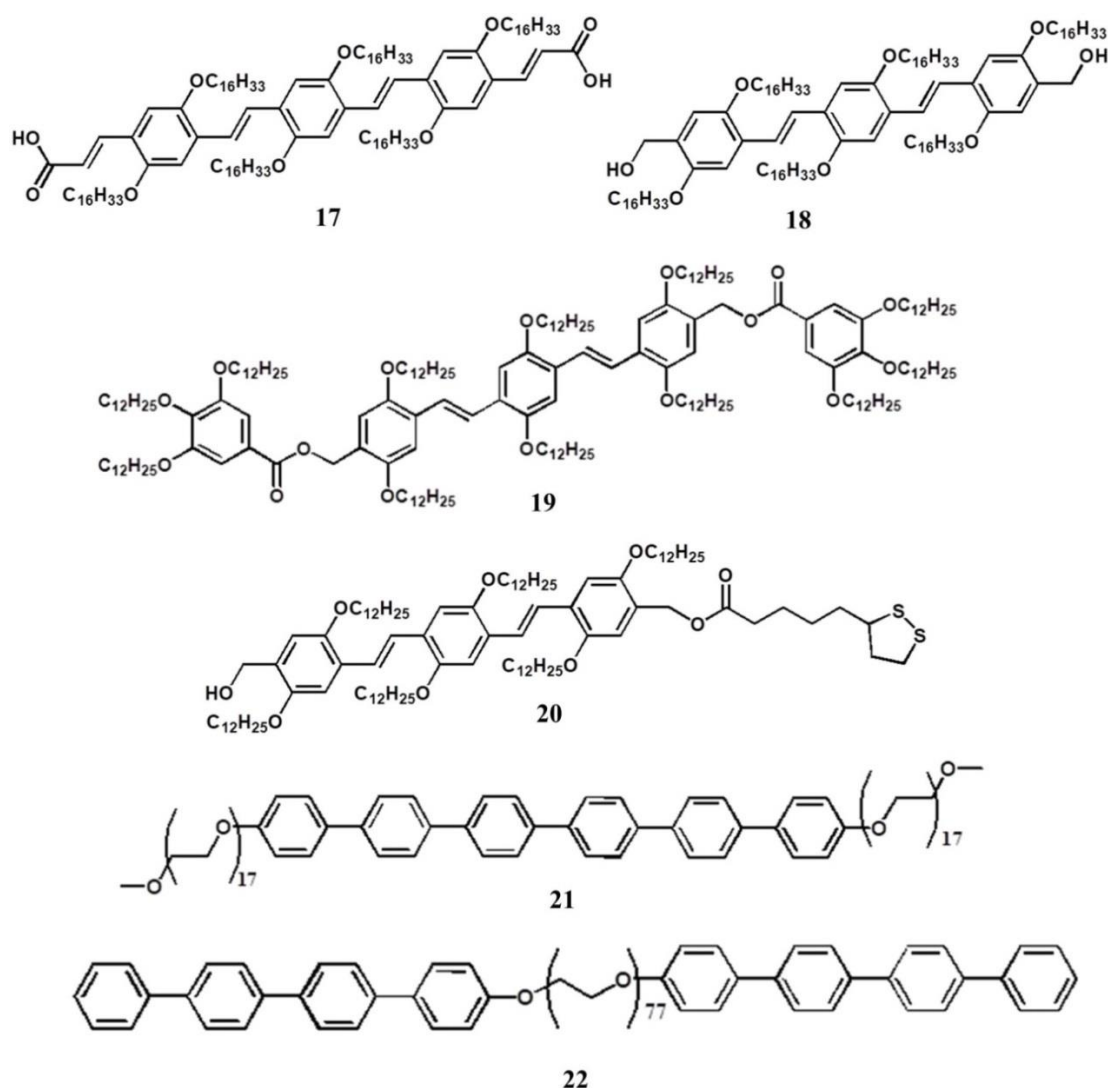


Figure 3. List of non-hydrogen bond based gelators (17-22).

phase transition process is usually thermoreversible for many times without significant change in gel-nanostructure. Gels could also be prepared by sonicating the solution of gelator molecules. The supramolecular organogels and hydrogels exhibit a wide range of applications which have been nicely summarized by Smith *et al.*⁹ Despite the great development in hydrogel and organogel chemistry, recently there has been increasing interest in the investigation of supramolecular metallogels (Chart 1).¹⁰ A metallogel is defined as a gel which contains both LMWGs and metal ions. The coordination of metal ions to LMWG directly or indirectly participates in the formation of metallogel network. Again, metallogelators could be classified into two categories: i) discrete metal complex as gelator and ii) coordination polymer as gelator. The synergistic combination of metal ion and LMWG results in many novel functionalities in metallogels. The properties and

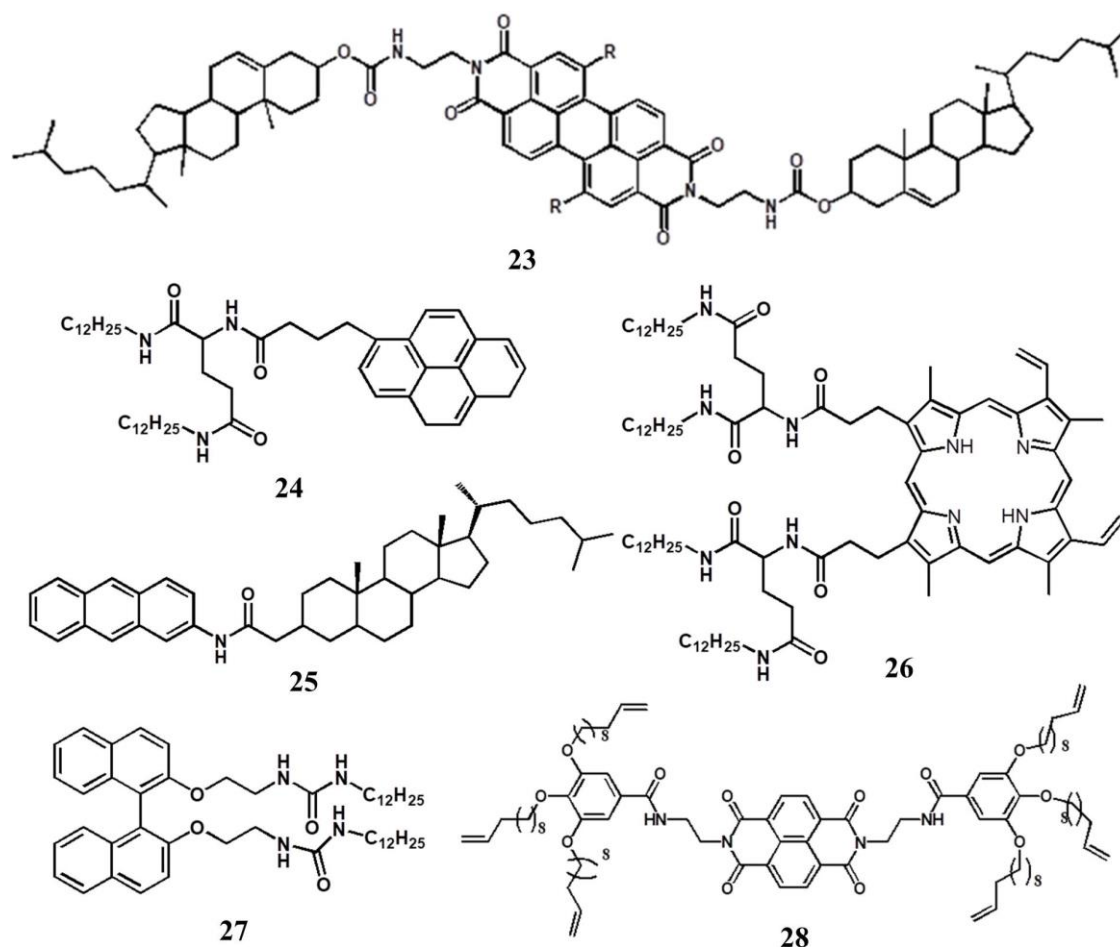


Figure 4. List of amphiphilic gelators that aggregate through both H-bonding and π - π stacking or hydrophobic interactions (23-28).

applications of all the different types of supramolecular gels are discussed systematically in the following sections.

1.3 Hydrogels and its applications

As discussed earlier, the supramolecular gels are mainly divided into two groups, namely supramolecular hydrogel and organogel. Among them, hydrogel is a swollen network containing water, and supramolecular nanostructures which consist of self-assembled gelators. To date, a wide variety of gelators have been explored for preparing hydrogels. Majority of these gelators are based on natural products, such as amino acids, saccharides, nucleosides, nucleotides or bile acids.⁹ Despite this variety, there are other type of gelators which contain both hydrophilic and hydrophobic units, also known as amphiphilic gelators. The supramolecular interactions, involved in the physical crosslinking of gelator molecules in hydrogels are mainly hydrophobic interaction,

hydrogen bonding, electrostatic interaction and host-guest interaction. Next sections are the discussions about these interactions.

1.3.1 Hydrophobic interaction

Hydrophobic interactions play a dominant role in the formation of large biological systems. These interactions are also useful for preparing hydrogels. Among different kind of supramolecular interactions, hydrophobic interaction is especially suitable to the formation of hydrogels. Water-soluble gelators having hydrophobic core, end groups or side chains prefer to get self-assembled by hydrophobic cross-linking. Such gelators usually form micelles at lower concentrations, because they are essentially amphiphilic molecules and therefore can act as surfactants. At low concentrations the hydrophilic parts of the gelator form loops, thereby allowing all hydrophobic groups to be accommodated in the micellar core. However, at higher concentration the pre-formed micelles aggregates and results in a network (Figure 5).^{11a,b,l} The concentration, at which the aggregation happens, is dependent on the nature and ratio of the hydrophilic and hydrophobic groups present in the gelator. It also depends upon additional components present in water, such as salt or surfactants. The hydrogels formed by hydrophobic association exhibit a high degree of toughness due to the mobility of the junction zones within the gel network, which contributes to the dissipation of the crack energy along the

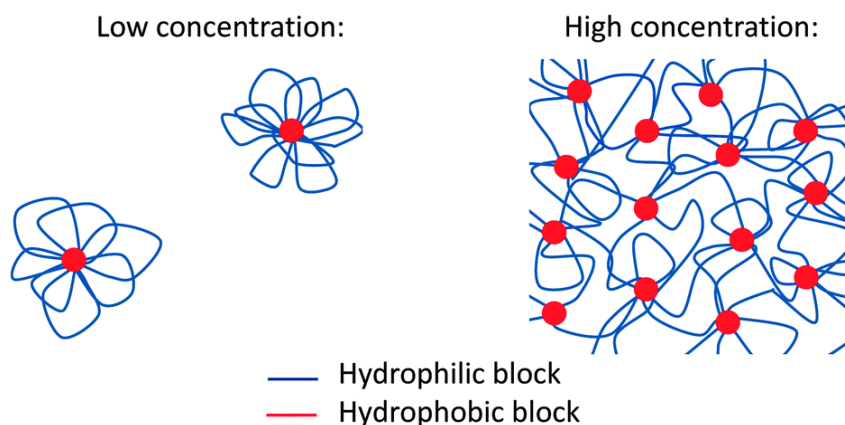


Figure 5. Behavior of ABA-triblock copolymers with a hydrophobic–hydrophilic–hydrophobic structure in water at different concentrations. This figure has been reproduced with permission from reference no. 111

hydrogel sample. Therefore, such hydrogels usually exhibit good self-healing properties. Several reports are there on hydrophobically associated hydrogels. However, most of them are made of polymeric gelators.^{11c-g} Some of the earliest examples were reported by

Tsitsilianis *et al.*, who showed the formation of hydrogels from polystyrene-*b*-poly(sodium acrylate)-*b*-polystyrene (PSt-*b*-PNaA-*b*-PSt) triblock copolymers. In their example micelles were formed below 0.2% concentration, while weak gels were formed above 0.4% concentration.^{11h,i} Other hydrogels prepared from triblock copolymers with a hydrophobic–hydrophilic–hydrophobic structure, in which the hydrophilic block was formed by poly(sodium methacrylate) and the hydrophobic blocks by polybutadiene (10 wt%), were reported by Vlassopoulos *et al.*^{11j} The effect of cationic and anionic surfactants was also studied, and it was found that the addition of surfactants induces gel formation by promoting bridge formation between micelles at a low polymer concentration. Weiss *et al.* reported physically crosslinked hydrogels made from the ABA-triblock copolymer with hydrophobic poly(2-(N-ethylperfluorooctanesulfonamido)ethylmethyl acrylate) as outer blocks and hydrophilic poly(N,N'-dimethylacrylamide) (PDMAM) as middle block.^{11k} Few examples of LMWG that possess an amphiphilic structure and self-assembled by hydrophobic interaction are represented in Figure 4. All these amphiphilic LMWG either has flexible long hydrocarbon chains or a hydrophobic, rigid tetracyclic steroid unit.

1.3.2 Hydrogen bonding

Hydrogen bond is a type of non-covalent interaction (X-H...Y) that plays an important role in the structure-property correlation of bio-macromolecules and in various biological molecular recognition processes.^{12a-d} Hydrogen bond is also widely employed in the construction of discrete organic cages, extended crystalline metal-organic architectures and soft supramolecular gels.^{12e,h} The reason behind such versatility of hydrogen bond is essentially the short and directional electronic interaction between donors and acceptors that result in wide range of materials with an array of exciting and complementary properties.¹²ⁱ Interestingly, the hydrogen bonds are well-known to be dynamic, *i.e* constantly breaking and reforming when triggered by external stimuli. This promising feature makes the hydrogen bond one of the most commonly employed supramolecular interactions in the preparation of hydrogels. There are several examples of hydrogen-bonding gelators as shown in Figure 2. All of them contain multiple hydrogen bonds sites, such as in ureidopyrimidinone (UPy), urea, peptide, amino acid and sugar derivatives. In addition, they often contain water shielding hydrophobic groups which are required to form a strong network of hydrogel. In the case of biopolymers such as peptides or agarose, hydrogen bonding stabilizes the secondary structure and induces

the hydrogel formation by self-assembling into fibrils or fibers (Figure 6).^{11b} Most of the hydrogen bonding gelators follow similar mechanism to form hydrogel networks.

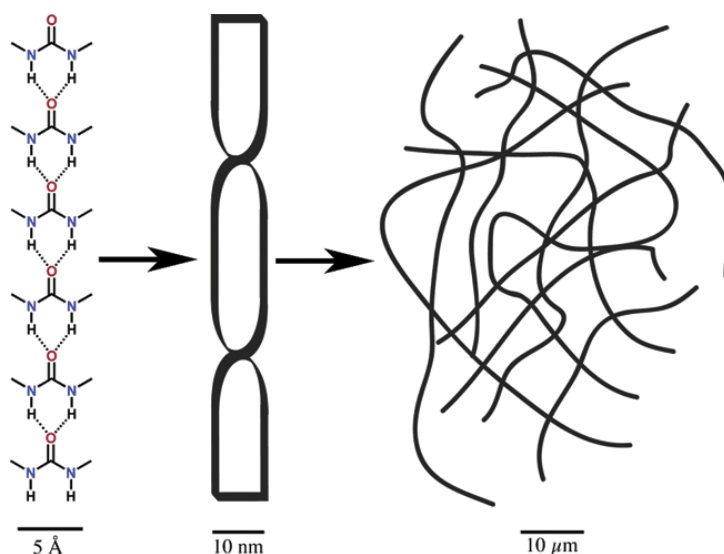


Figure 6. The primary, secondary, and tertiary structure of a self-assembled gel formed by H-bonding interaction. Figure reproduced from ref. 11b with permission.

1.3.3 Electrostatic Interaction

As charged groups are easily water-soluble, the strong electrostatic interaction between oppositely charged species is another common example of supramolecular interaction utilized for preparing hydrogels. This can be done by using for example blocks of ionic monomers, which can form complex clusters that will act as supramolecular crosslinks, together with nonionic water-soluble blocks. Mixtures of homopolymers of certain weak polyions can also form hydrogels, as the ionic groups will only participate in crosslinking while others will remain in solution.^{ref} As the solubility of ionic groups is low in most organic solvents, examples of organogels formed by electrostatic interaction are very rare. However, weak electrostatic interaction can sometime play role in the formation of organogel. In a recent review, Yoon *et al.* have discussed about supramolecular materials based on electrostatic interactions for biomedical applications.^{13a} In an early example, Aida *et al.* reported a series of dendritic molecular binders (Gn-binder) which contain multiple guanidinium ions at the end (Figure 7). The electrostatic interaction in combination with H-bonding interaction, between anionic clay nanosheets and dendritic molecular binders facilitated the cross-linking of the clay nanosheets and formed hydrogels (Figure 8).^{13c} Another example of a hydrogel formed by electrostatic interaction was shown by Hennink *et al.*^{13b} Oppositely charged dextran

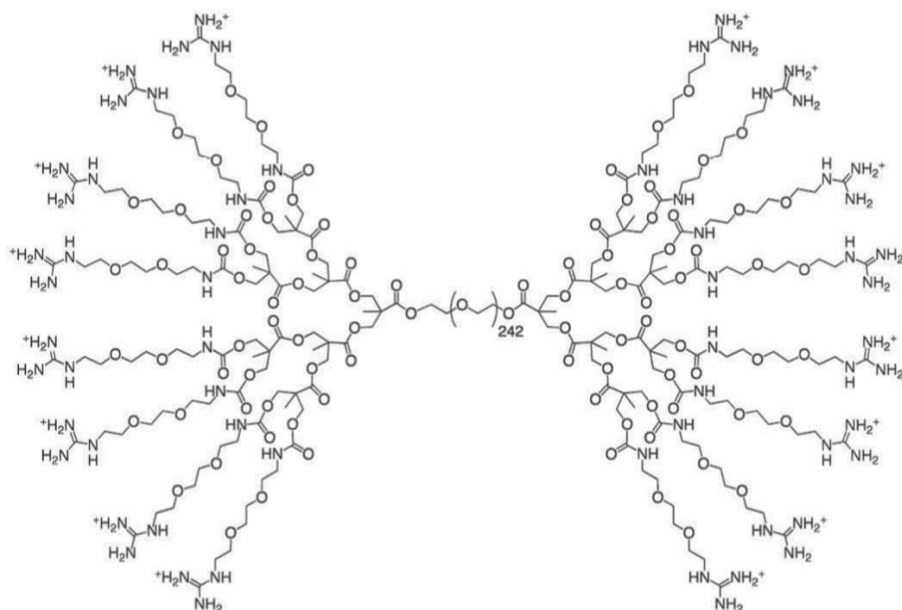


Figure 7. The structure of molecular binder which participate in electrostatic interaction with clay nanosheets. Figure reproduced from ref. 13c with permission.

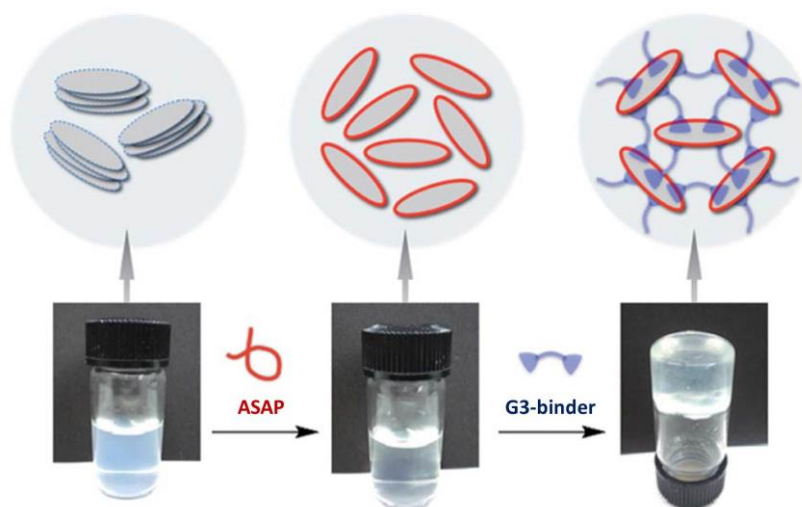


Figure 8. The mechanism for hydrogelation by the electrostatic interaction between G3-binder and exfoliated clay nanosheet. Figure reproduced from ref. 13c with permission.

microspheres were formed by copolymerization of hydroxyethyl methacrylate-functionalized dextran with either methacrylic acid or DMAEMA. Gelation occurred when equal volumes of positively and negatively charged microspheres were mixed together at pH 7. The hydrogel network showed so-called shear thinning behaviour, *i.e.* the physical network was broken at high stress and reformed when the stress was removed.

1.3.4 Host-guest interaction

Another important supramolecular interaction commonly employed for gel formation is host-guest interaction which is nothing but a resultant of combined hydrogen bonding and electrostatic interaction.^{14a-c} Supramolecular gels formed by host-guest interactions have several important characteristics, such as strong binding affinity, fixed geometry and directionality. Moreover, the host-guest gels are often found to be responsiveness to pH or other external stimuli which make them very appealing for biomedical applications such as drug delivery. Cyclodextrins (CD) are the most common example of host molecules. They are hydrophilic on the outside and relatively hydrophobic on the inside cavity where different guest components (e.g. aliphatic molecules, adamantane and ferrocene) can be accommodated.^{14h} In addition, they are commercially available and can be modified relatively easily. Other examples of host that

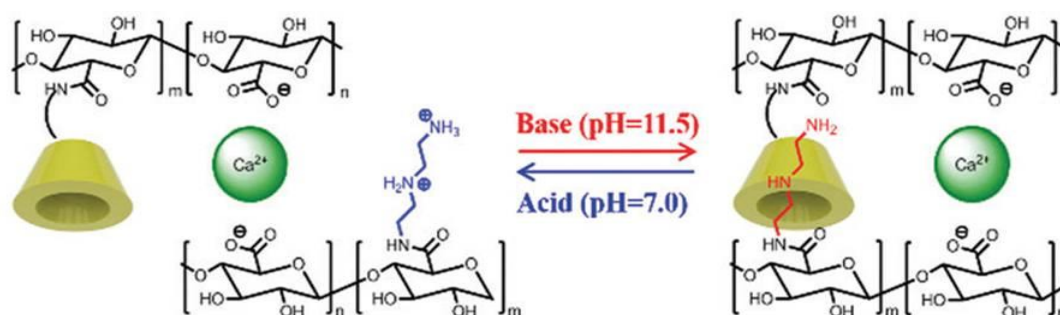


Figure 9. A supramolecular hydrogel formed of Ca^{II} -crosslinked β -CD modified alginate and DETA-modified alginate, which takes advantage of pH-sensitive β -CD-DETA host-guest interactions to achieve the shape memory behaviour. Figure reproduced from ref. 14j with permission.

have been used for supramolecular gel formation are cucurbituril, crown ether^{14d-f} and pillarene^{14g,h}. Host-guest interaction is one important driving force for fabricating supramolecular shape memory hydrogels (SSMHs).¹⁴ⁱ A typical example of host-guest interaction is the pH-sensitive complexation of β -CD and diethylenetriamine (DETA), which is formed in basic medium but dissociated in neutral medium. Han *et al.* fabricated a pH-responsive shape memory hydrogel by crosslinking the β -CD modified alginate and (DETA)-modified alginate with Ca^{II} at room temperature (Figure 9).^{14j} Due to pH-responsive nature of the β -CD-DETA interactions, the hydrogel could be deformed into many different shapes in the basic medium and recovered to the original state in the neutral medium. The fixity and recovery ratio of this hydrogel were found to be 95% and

96%, respectively. Such pH-triggered SSMHs have promising medical applications. Apart from pH-response, supramolecular host-guest hydrogels are known to show photo-responsive behaviour. Tamesue *et al.* first showed photo-switchable supramolecular hydrogels prepared from CD-functionalized glucan as the host and azobenzene

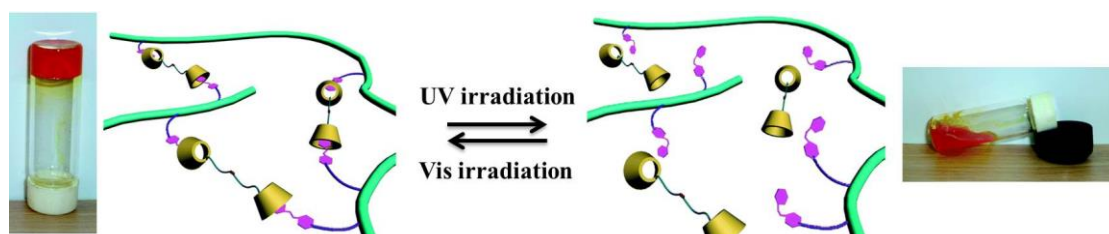


Figure 10. Light-responsive sol-gel transition of host-guest supramolecular hydrogels. Figure reproduced from ref. 14l with permission.

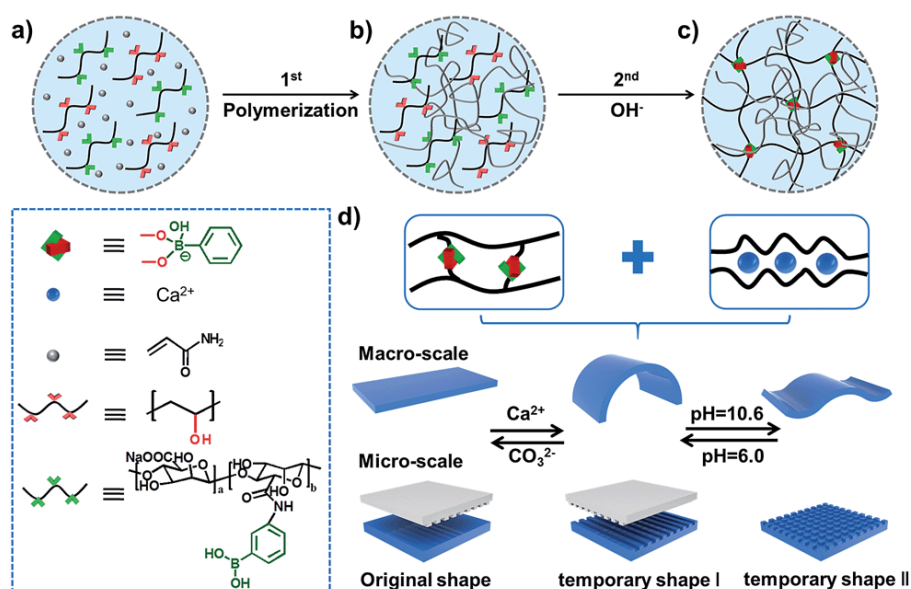


Figure 11. Schematic illustration of stretchable supramolecular hydrogels with a triple shape memory effect, (a–c) Acrylamide is polymerized in the presence of Alg-PBA and PVA, then the supramolecular network is formed via immersion into alkaline solution to generate dynamic PBA–diol ester bonds, (d) The reversible PBA–diol ester bonds and the chelation of Alg/ Ca^{II} endow the hydrogel with triple shape memory behavior at both the macro-scale and micro-scale. Figure reproduced from ref. 17m with permission.

functionalized polymer as the guest.^{14k} Guan *et al.* reported a photo-responsive hydrogel formed by host-guest interaction of poly(N-isopropylacrylamide) (PNIPAM) containing azobenzene groups and cyclodextrin dimers. Upon UV-light irradiation the azobenzene

groups undergo *trans* to *cis* isomerization which hampers the host-guest interactions and therefore the hydrogel converts to sol (Figure 10).^{14l} Chen *et al.* reported a mechanical stretchable supramolecular hydrogel with a triple shape memory effect at the macro/micro scale. The introduction of a double network concept into supramolecular shape memory hydrogels endows them with excellent mechanical properties.^{14m} The design of two non-interfering supramolecular interaction systems of both dynamic phenylboronic (PBA)–diol ester bonds and the chelation of alginate with Ca^{II} endues the hydrogel with outstanding triple shape memory functionalities (Figure 11)

1.4 Organogels and its applications

Usually, organogels are formed by dissolving a small amount of the gelator in hot organic solvent followed by cooling below the gel transition temperature (T_{gel}). Organogels are characterized by using a variety of analytical tools, particularly spectroscopic and microscopic techniques. Organogels exhibit diverse supramolecular architectures with wide range of properties. The diversity of nanostructures and properties of the organogels make them promising candidates for several potential applications in different fields, such as food, cosmetics, medicine, tissue engineering, biomineralization, catalysis, controlled release etc.^{15a-f} In recent years, organogels based on functional chromophoric-gelators and dyes have attracted immense interest as novel functional materials for optoelectronic applications, especially energy transfer and light harvesting applications.^{15d,g} Supramolecular alignment of chromophoric assemblies achieved through gelation provides functional materials with tunable optoelectronic properties which have potential applications in molecular and supramolecular electronic devices. For example, chromophore based organogels are excellent model systems for the active layers in plastic electronic devices.^{15d,h,i} Therefore, a large variety of chromophore based organogelators have been synthesized and studied which include chromophores such as phthalocyanines, porphyrins, [n]acenes, pyrene, cyanine, squaraine, fluorene, tetrathiafulvene, phenanthroline, azobenzene, stilbene, butadiene, hexabenzocoronene, thiophene, phenylene, phenylacetylene, phenylenevinylene etc.^{15d,g} Among these, naphthalene, anthracene, pyrene, perylenes, phenylenevinylenes etc. are useful chromophore systems for energy transfer processes. In recent years, a large number of reports have appeared on organogelators based on these chromophores as scaffolds for energy transfer and light harvesting applications.

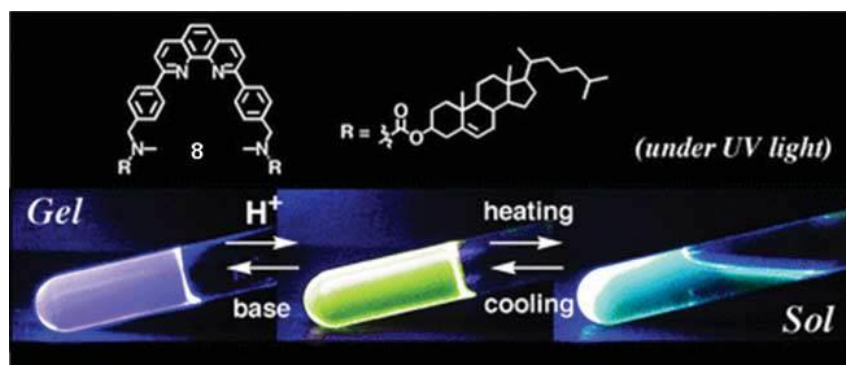


Figure 12. Emission changes in the cholesterol appended phenanthroline based gelator upon protonation with TFA. Figure reproduced from ref. 15k with permission.

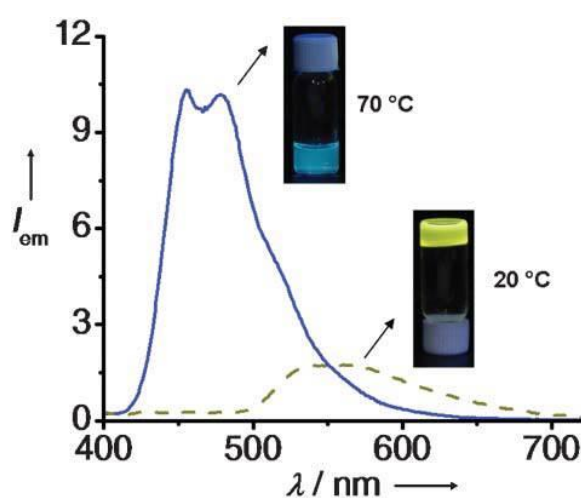


Figure 13. Emission spectra of an OPV based gel in cyclohexane at 20 °C and 70 °C and corresponding colour change. Figure reproduced from ref. 4d with permission.

One of the early examples of energy transfer in a gel medium is reported by Sagawa *et al.*^{15j} Pyrene and porphyrin functionalized L-glutamate derivatives were used for this purpose. Detailed gelation studies revealed that the pyrene derivative forms physical gels in benzene and cyclohexane. However, the porphyrin derivative failed to form gel in any solvents. Spectroscopic studies suggest that amide hydrogen bonding leads these molecules to form ordered co-facial chiral aggregates even in the solution state. Energy transfer studies in the mixed assemblies of pyrene and porphyrin derivatives revealed singlet–singlet energy migration from pyrene excimers to the free base porphyrin. In another example a cholesterol appended 1,10-phenanthroline based gelator showed proton sensitive energy transfer phenomena.^{15k} In the presence of two equivalents of trifluoroacetic acid (TFA), the purple emission (360 nm) of the gel was quenched completely, with the appearance of the yellow emission (530 nm) corresponding to the

protonated form of the gelator due to energy transfer from the neutral to the protonated form (Figure 12). Electron and energy transport properties of π -conjugated molecules are strongly influenced by the orientation of the chromophores within the self-assembly. A viable approach towards this end is the design of conjugated building blocks that form organogels in appropriate solvents through noncovalent interactions leading to entangled fibrous assemblies.^{15d,g} Oligo(p-phenylenevinylene) (OPV) derived gelators are most suitable for this purpose. The photophysical and morphological properties of the OPV based organogels could be modified by simply modifying the structures and the non-covalent interactions. The most striking feature of the gelation of OPVs is the modulation in optical properties. Upon gelation, OPVs exhibit a large shift in the emission towards the long wavelength region (Figure 13).^{15l-n}

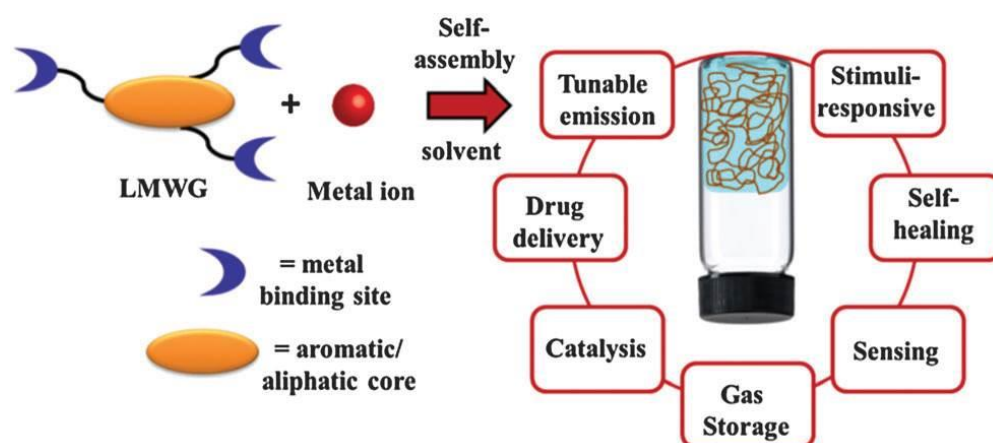
1.5 Metal containing supramolecular gels

In this type of supramolecular gel, the coordination of metal ions is directly or indirectly involved in the formation of gels and they are usually known as metallogels. The metallogel contains both LMWGs and metal ions.^{2a,16} Metallogels are broadly divided into two categories (Chart 1). In one case, discrete metal complexes are self-assembled through various non-covalent interactions, exerted by ligand or metal ions, and result in a fibrous network.¹⁰ Here, metal ions are integral parts of gelator molecules which assemble into primary, secondary, and tertiary structures. However, metal ions are not directly involved in the organization of the fibrous network.¹⁷ These systems usually contain substitutionally inert metal ions which are held by multidentate or macrocyclic ligands. In 1996, Terech *et al.* first reported the fibrillar aggregates of Zn^{II}-metalloporphyrinates in organic solvent.^{17j} In later years, a great deal of work on porphyrin-based metallogels was carried out by Shinkai *et al.*, who explored a wide variety of substituents to the porphyrin core.¹⁸ Later on, Abe *et al.* developed redox active metallocene-based metallogelators.^{19a} Platinum(II) containing metallogelators with luminescence properties were developed by Nolte *et al.* and Yam *et al.*^{19b, 19c} Recently, a new kind of metallogel has emerged in which metal ions act as nodes and LMWGs act as linkers. Therefore, the combination of a metal ion and a LMWG results in a coordination polymer, which immobilizes the large amount of solvent within it. This type of gel is called the coordination polymer gel (CPG).^{6b,f} In the case of CPG, gelation is induced by metal–ligand coordination and metal ions actively participate in the formation of the gel network. Early research on CPGs was started by Xu *et al.* who reported a series of

pyridine-based LMWGs which upon coordination with Pd^{II} resulted in catalytically active CPGs.^{20a} Weiss *et al.* reported CPGs of bisphosphonate esters, phosphonic acids, monophosphonate esters, and phosphoric acid esters by the self-assembly with different metal ions.^{20b} Later on, James *et al.* and McGrail *et al.* showed that linkers which are utilized for synthesizing crystalline coordination polymers could also be used for synthesizing CPGs.^{20c, 20d} By following their novel examples, different research groups started to rationally design a large variety of LMWGs, which upon coordination with metal ions result in CPGs. The reason behind the growth of interest stems from the fact that the presence of metal ions provides an additional scope for tuning the properties of the gel materials. Indeed, the unique redox, optical, electronic and magnetic properties of metal ions could be easily introduced in soft organic–inorganic hybrids which hold great promise for applications in diverse fields, including biomedicine, catalysis and optoelectronics.²⁰ The next sections focus on CPGs.

1.5.1 Coordination polymer gels (CPGs)

The use of metal–ligand coordination chemistry to direct the assembly of LMWGs has opened up a new platform at the frontiers of supramolecular chemistry and coordination chemistry. The reason for the utilization of metal–ligand interactions as a tool to construct higher dimensional structures is due to their dynamic nature, which allows the formation of controllable and extended structures. Metal–organic frameworks (MOFs) are well-known examples where extended metal–organic linker interactions are utilized to construct infinite, long-range ordered one-, two-, or three-dimensional structures.²¹ Usually, MOF are highly crystalline and their structure can be easily determined by single crystal X-ray crystallography. MOFs showed promising applications in gas storage, separation, catalysis and optoelectronics.²² However, low solution processability of crystalline bulk MOFs greatly limits their application in device fabrication and biological sciences. In this regard, coordination polymer gels or MOF-gels are superior as reversible sol–gel behaviour and different nano-morphologies, enhances their processability and facilitates the easy fabrication of large-area and flexible displays and portable sensing-kits. Moreover, the stimuli-responsive behaviour of CPGs could be utilized for targeted drug delivery.²³ The first step to synthesize a CPG is to rationally design a LMWG containing, at least, two metal ion binding sites. Binding of



Scheme 4. General synthetic procedure of coordination polymer gels and their application in various fields. Figure reproduced from ref. 6f with permission.

metal ions to such gelators induces the self-assembly to form 1D/2D/3D coordination polymers which further assemble to form the fibrous architecture of CPGs. The LMWGs act as linkers and metal ions act as nodes. The structure of the coordination polymer network is strongly dependent on the geometry of metal ions, the conformation and binding sites of LMWGs.^{23c} It is known that, depending on the metal ions, coordination geometry and structures of LMWGs, CPGs show different properties, such as intriguing spectroscopic, catalytic and redox properties (Scheme 4).^{6b} In summary, selection of metal ions, molecular designing of LMWGs and fine tuning of the gelation conditions are crucial steps that control the self-assembly process to generate various nanostructures and properties of the resulting CPGs.

1.5.2 Applications of CPGs

1.5.2.1 CPGs for Drug delivery

CPGs have emerged as an alternative to current polymeric gels for controlled drug delivery. Several coordination polymer hydrogels have been widely employed as intelligent carriers for controlled drug-delivery.²⁴ Since CPGs are essentially formed by coordination-driven self-assembly of LMWGs, controlling the reversible formation and breakage of coordination bonds is an essential step to exploit the CPGs for drug delivery application. Perturbation of coordination bond in CPGs is normally achieved by chemical or physical stimuli. Stimuli-responsive CPGs as a drug delivery system are successfully demonstrated for regenerative medicine by several groups.^{24a, b} Jung *et al.* reported a coordination polymer hydrogel, formed by the coordination driven self-assembly of a

pyridine-based LMWG and Cu^{II} and its efficiency as a delivery system for curcumin (Figure 14).^{24c}

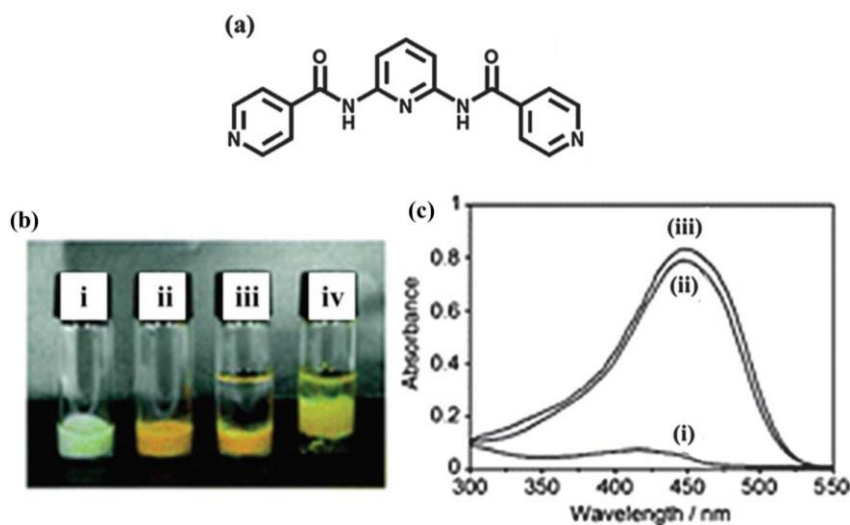


Figure 14. (a) Molecular structure of pyridine-based gelator, (b) Photographs of (i) the coordination polymer hydrogel (ii) CPG with curcumin (iii) CPG with curcumin + aqueous solution after 10 min and (iv) after 80 min, (c) UV-Vis spectra of the supernatant aqueous solution after (i) 10 min and (ii) 80 min and (iii) the stock solution of curcumin. Figure reproduced from ref. 24c with permission.

1.5.2.2 CPG for Self-healing

The ability to automatically heal or restore a damage made by any external force is one of the most fascinating and important properties found in living organisms.^{25a} Over the past few decades, scientists have been trying to develop self-healable synthetic soft-materials for bio-medical applications.^{25b-e} Significant progress has been made in the construction of self-healing materials based on covalently cross-linked polymers or supramolecular gels with polymers. However, the preparation of macroscopic self-healing materials by coordination interactions continues to be a challenge. On the other hand, there is increasing evidence that metal–ligand coordination plays an important role in many dynamic biological processes.^{25f-h} From this perspective, supramolecular CPGs are envisioned as suitable self-healing candidates. Yan *et al.* studied the self-healing properties of homo- and hetero-metallic CPGs prepared from tetrazole-based LMWG and Co^{II} and Ni^{II} ions (Figure 15).²⁵ⁱ The homometallic CPGs, Co-CPG and Ni-CPG did not show self-healing behaviour due to the brittleness and instability in air (Figure 15b, d and e). However, the heterometallic CPGs, Co-Ni-CPGs exhibited excellent self-healing behaviour (Figure 15c). In another work, Yan *et al.* reported a self-healing and moldable

supramolecular Pd-CPG synthesized from ditetrazole-based LMWG and Pd(OAc)₂ (Figure 16a-c).^{25j} This CPG not only exhibited self-healing property, but also showed deformation recovery and bottom-up load-bearing properties (Figure 16d, e).

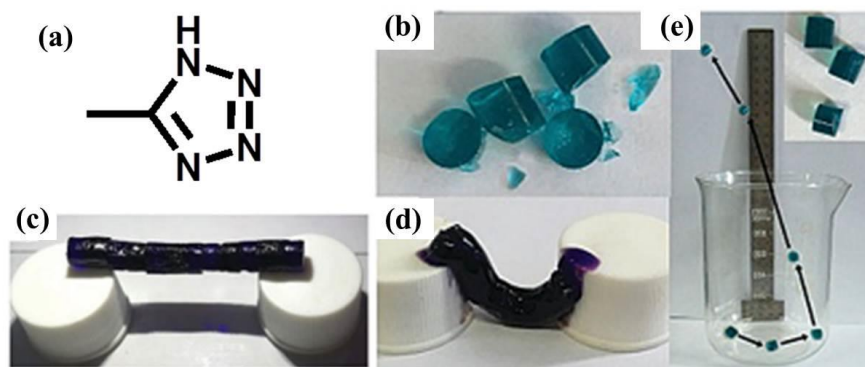


Figure 15. (a) Molecular structure of tetrazole-based gelator, (b) Picture of brittle Ni-CPG blocks, (c) Self-healing bridge made of heterometallic Co–Ni-CPG, (d) Fragile bridge made of Co-CPG, (e) Bouncing trajectory of the gel block Ni-CPG after rebounding from the bottom of the beaker (beaker wall is 16 cm). Figure reproduced from ref. 25i with permission.

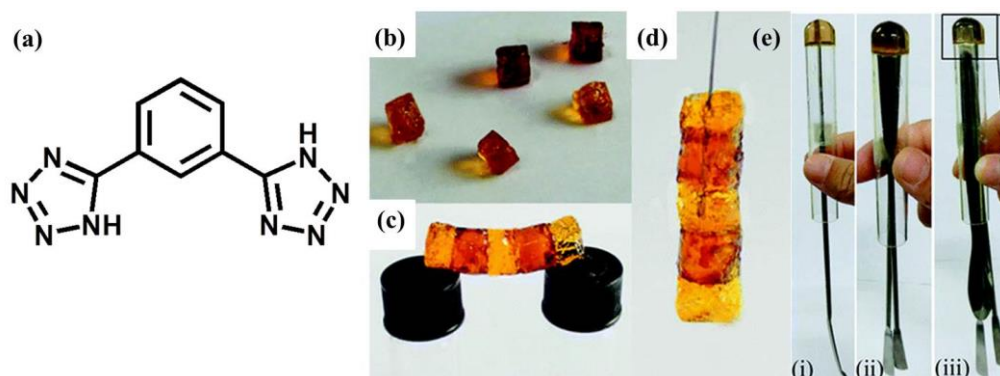


Figure 16. (a) Molecular structure of ditetrazole-based LMWG, (b) Blocks of freshly prepared Pd-CPG, (c) Blocks of Pd-CPG connected horizontally, (d) Blocks of Pd-CPG connected vertically, can withstand its own weight, (e) Bottom-up load-bearing ability of Pd-CPG. Figure reproduced from ref. 25j with permission.

1.5.2.3 CPGs for chemosensing

The chemosensing applications of the CPG are of particular interest as gel networks and other functional groups present in gel systems can respond to the introduction of external species by altering the conformation of the coordination complex. Such changes in CPGs, can be visualized by the naked eye and provide specific information for the

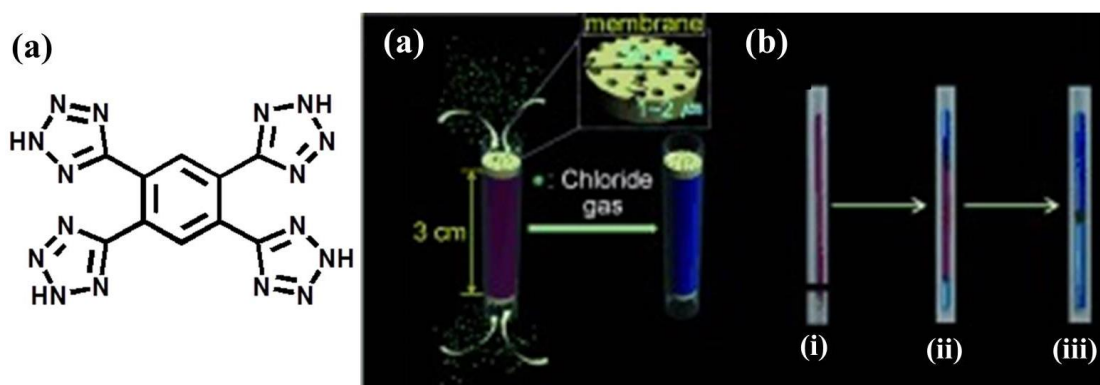


Figure 17. (a) Molecular structure of 1,2,4,5-tetra(2H-tetrazole-5-yl)-benzene, (b) Representation of a Co-CPG coated capillary as a portable chemosensor, (b) Photographs of the Co-CPG coated (20 mm) capillary (i) at the initial stage, (ii) after 10 s and (iii) after 30 s of exposure to chloride gas. Figure reproduced from ref. 26a with permission.

externally added contaminants. Moreover, the “soft” nature of the CPGs makes them excellent candidates for qualitative and quantitative detection of toxic gases or dangerous chemicals. Shinkai *et al.* reported a Co-CPG prepared from 1,2,4,5-tetra(2H-tetrazole-5-yl)-benzene and CoBr_2 which acted as a chemosensor for chloride containing molecules, such as HCl , SOCl_2 , $(\text{COCl})_2$, and COCl_2 (Figure 17a).^{26a} They also prepared a portable chemosensor kit by filling a capillary with Co-CPG and closing the ends of capillary with membrane filters (Figure 17b). After phosgene gas was passed through the capillary, the colour of the capillary coated with the Co-CPG changed from red to blue (Figure 17b). Berke *et al.* reported a Al-CPG prepared from 1,4,5,8-triptycenetetracarboxylic

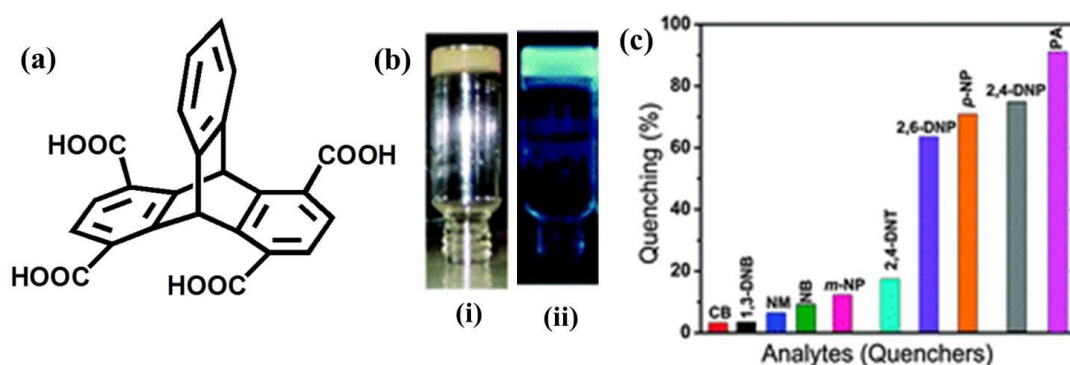


Figure 18. (a) Molecular structure of 1,4,5,8-triptycenetetracarboxylic acid, (b) Picture of Al-CPG under (i) daylight and (ii) UV light, (c) Percentage (%) quenching of fluorescence of the Al-CPG dispersed in ethanol by the addition of different analytes (quenchers) at room temperature. Figure reproduced from ref. 26b with permission.

acid (Figure 18a-b). The Al-CPG exhibited detection of nitroaromatic compounds, particularly picric acid (Figure 18c).^{26b}

1.5.2.4 CPGs for catalysis

Functional nanoscale CPGs, prepared from metal ions and LMWGs, have received immense interest in catalysis. The CPG nanofibers have been proven to be efficient and promising catalysts, because they are self-supported and recycled, and result in enhanced efficiency because of their well-ordered arrangement of catalytically active sites.²⁷ Jung and co-workers reported the formation of silver nanoparticles within a CPG, prepared from a tetrazole-based LMWG and Ag^{I} ions.^{27a} They also showed the catalytic activity of silver nanoparticles for reduction of 4-nitrophenol. Xu *et al.* reported the design and synthesis of a number of CPGs prepared from a series of pyridine-based ligands and Pd^{II} and studied their catalytic activity towards the oxidation of benzyl alcohol to benzaldehyde (Figure 19).^{20a} Banerjee *et al.* documented the synthesis, structure, gas adsorption and catalytic properties of a crystalline porous coordination polymer (Ca-MOF) as well as a stable CPG (Ca-CPG) both prepared from 5-(1,2,4-triazolyl) isophthalic acid and Ca^{II} ions (Figure 20a).^{27b} The gel showed good catalytic activity for the hydrosilylation of benzaldehyde with diphenylsilane (Figure 20b). The

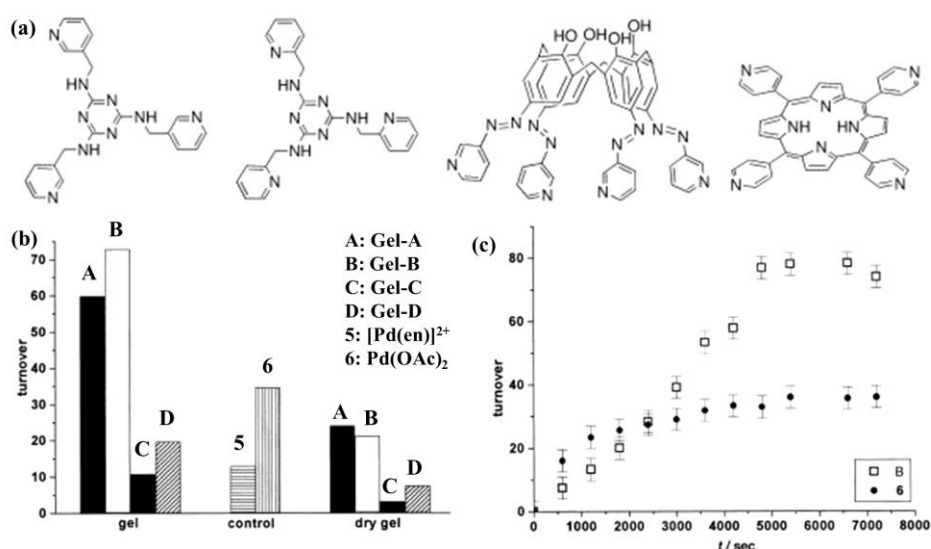


Figure 19. (a) Molecular structures of different pyridine-based gelators, (b) The catalytic turnovers (cumulative) for the oxidation of benzyl alcohol by air (1 atm) by using gels, their corresponding dry gels (formed by precipitating coordination polymers in acetone) and $[\text{Pd}(\text{en})]^{2+}$ and $\text{Pd}(\text{OAc})_2$ as catalysts, and (c) the catalytic turnover versus time curve of Gel-B and the compound $\text{Pd}(\text{OAc})_2$. Figure reproduced from ref. 20a with permission

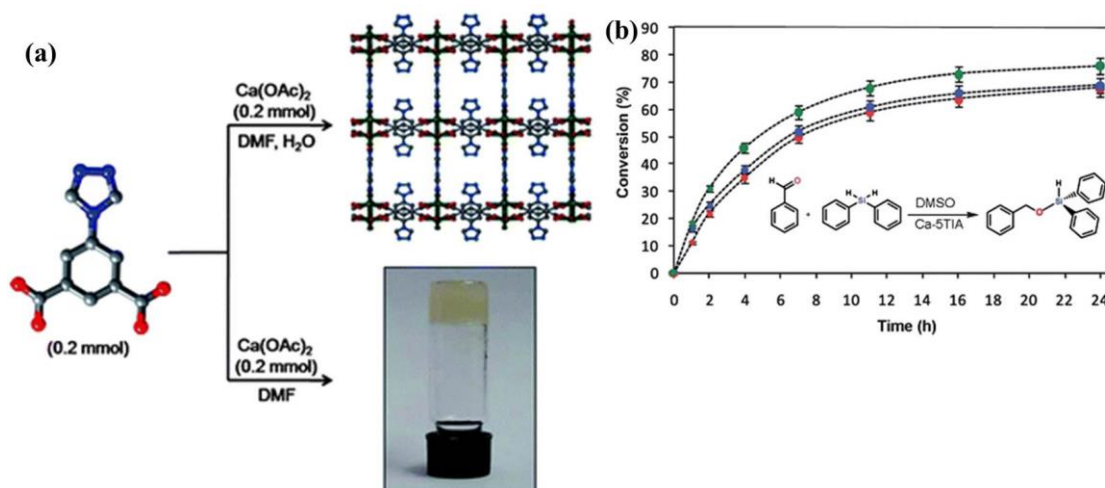


Figure 20. (a) Schematic diagram showing the synthesis of Ca-MOF (top) and Ca-CPG (bottom) under different conditions, (b) The kinetic profiles for the hydrosilylation of benzaldehyde catalysed by Ca-MOF (red), Ca-CPG xerogel (blue) and Ca-CPG in gel state (green). Figure reproduced from ref. 27b with permission

key factors responsible for catalytic activity were: (i) a low restriction in mass transport due to porosity and (ii) the Lewis acid character of Ca^{II} .

1.5.2.5 CPGs for optoelectronics

Since CPGs are formed by the assembly of LMWGs and metal ions, a wide range of emission phenomena can be explored from these soft organic–inorganic hybrids. The emission properties of CPGs stemmed from either chromophoric linkers or metal ions (particularly lanthanide ions).²⁸ Apart from this, metal to ligand charge transfer (MLCT) emission or ligand to metal charge transfer (LMCT) emission, guest-responsive emission properties could also be observed in CPGs. However, examples of latter cases are very rare. The below sections discussed about the emission properties of CPGs; (i) luminescent CPGs based on chromophoric LMWGs and (ii) luminescent CPGs based on metal ions.

Chromophoric LMWG based emission: The rational design of highly π -conjugated chromophoric LMWGs containing suitable metal binding sites has emerged as a potential strategy to prepare luminescent CPGs.²⁸ In an early example, Vittal *et al.* reported a luminescent CPG prepared from N-(7-hydroxyl-4-methyl-8-coumarinyl)-glycine and Zn^{II} in basic aqueous solution (Figure 21a).^{28a} The CPG showed strong blue emission and pH-responsive change in emission. It exhibited typical fibrous gel networks. Recently, Maji *et al.* reported an aggregation induced emission (AIE) active

tetraphenylethene (TPE)-based LMWG which formed organogel and CPG in presence of Eu^{III} (Figure 22a). The Eu-CPG showed AIE and MCIE (matrix coordination induced emission) phenomena and coordination induced change in nano-morphology (Figure 22b, f).^{28b} The Eu-CPG was highly processable and could easily be cast on a quartz substrate which upon air drying resulted in a transparent film (Figure 22c-e).

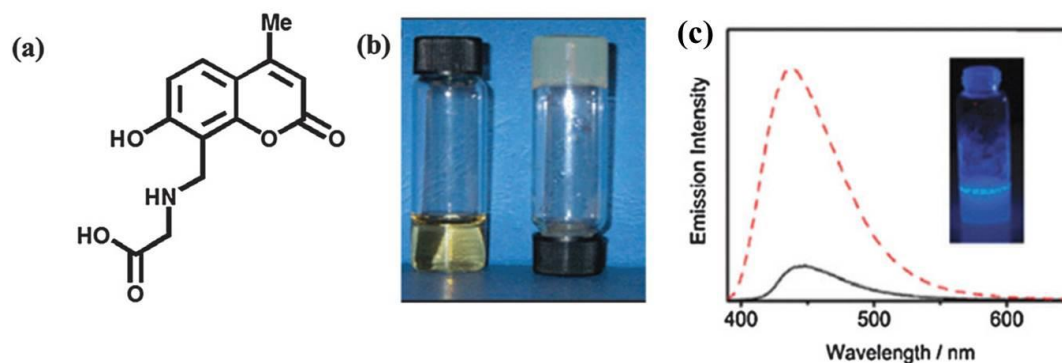


Figure 21. (a) Molecular structure of N-(7-hydroxyl-4-methyl-8-coumarinyl)-glycine, (b) Photographs of the LMWG solution (left) and coordination polymer hydrogel (right), (c) Emission spectra of the gelator in H_2O (solid line) and CPG (dashed line) upon excitation 340 nm, inset showing the picture of CPG under UV light. Figure reproduced from ref. 28a with permission

Metal centres based emission: Recently, Gunnlaugsson *et al.* reported a luminescent CPG prepared by Eu^{III} directed self-assembly of a tripodal terpyridine-based LMWG which showed fibrous gel structure.^{28c} The same group demonstrated the lanthanide ion ($\text{Ln}^{3+} = \text{Eu}^{3+}, \text{Tb}^{3+}$) directed self-assembly of another pyridine-based LMWG which resulted in luminescent CPGs (Figure 23a, b). This CPG not only showed strong Ln^{3+} -centred emission but also exhibited self-healing properties (Figure 23c-h).^{28d} Recently, Andersen *et al.* designed terpyridyl (tpy)-end capped four-arm poly(ethyleneglycol) polymer which on coordination with lanthanide ions ($\text{Ln}^{\text{III}} = \text{Tb}^{\text{III}}$ and Eu^{III}) resulted in luminescent CPGs (Figure 24a).^{28e} The optical properties of these highly luminescent polymer networks were readily modulated by the stoichiometry of Ln^{III} ions and a white-light-emitting gel was prepared (Figure 24b). Moreover, the dynamic nature of the $\text{Ln}-\text{N}_{\text{tpy}}$ coordination bond in white-light-emitting gel was also exploited for reversible stimuli-responsive changes in the sol-gel transition and optical properties.

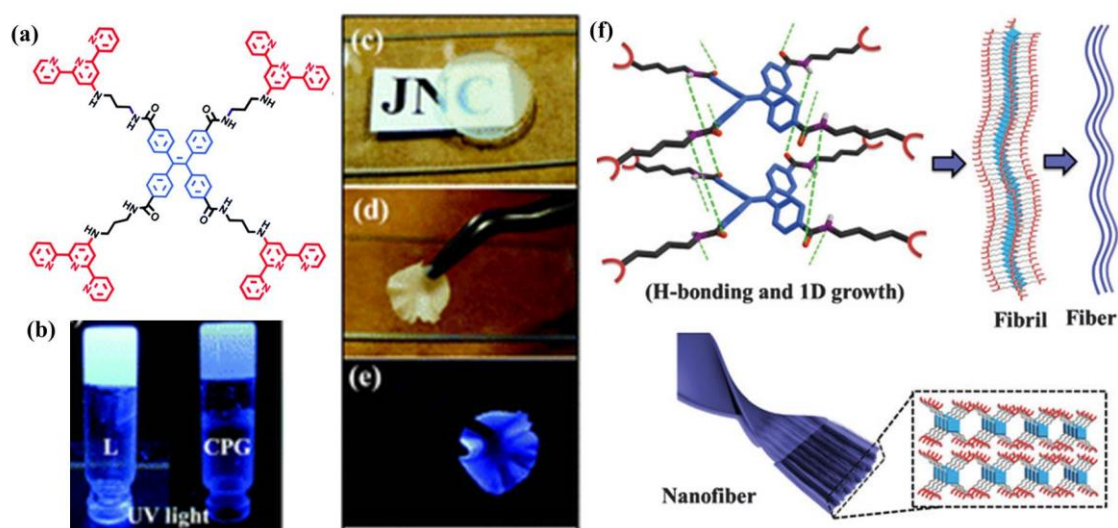


Figure 22. (a) Molecular structure of TPE-based LMWG, (b) Images of the organogel and Eu-CPG under UV light, (c)-(e) Formation of transparent and stable films of the Eu-CPG showing its easy processability and stability, (f) Schematic representation of self-assembly of TPE-based LMWG through H-bonding between amide groups and formation of 1D nanostructures. Figure reproduced from ref. 28b with permission

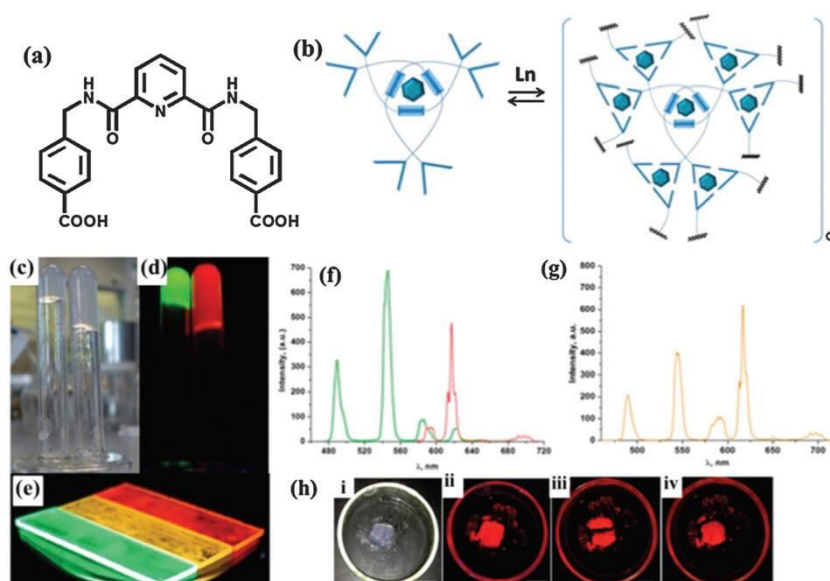


Figure 23. (a) Molecular structure of pyridine-based LMWG, (b) Schematic of the formation of higher order self-assembly, (c) Picture of Tb-CPG and Eu-CPG under day light and (d) under UV-light, (e) Luminescence of Eu-CPG, Tb-CPG and mixed CPG on quartz plates, (f) Emission spectra of Tb-CPG (green), Eu-CPG (red), (g) Emission spectra of mixed CPG, (h) Self-healing experiment of Eu-CPG where (i) is the Eu-CPG in the day light, (ii) the same gel under UV light, (iii) gel after being cut into halves and (iv) self-healing of the gel. Figure reproduced from ref. 28d with permission

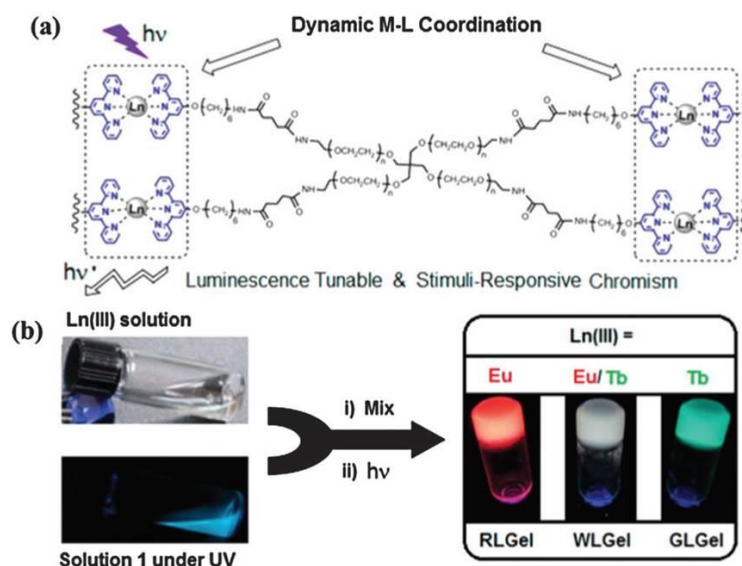


Figure 24. (a) Structure of terpyridine capped poly(ethylene glycol) polymer which was cross-linked via Ln–tpy coordination, (b) Schematic preparation of red, green and white emitting CPGs and their pictures obtained under UV light. Figure reproduced from ref. 28e with permission

1.6 Metal-organic cage

Over past few decades, researchers have witnessed the fast growth of fascinating metal–organic materials (MOMs), e.g., polygons, discrete polyhedral cage systems, and coordination polymers.^{29a} The structural motif in these materials includes metal moieties (ions or clusters) coordinated by the polydentate organic linkers. Based on the connectivity and geometry of the building components, different geometry of MOMs

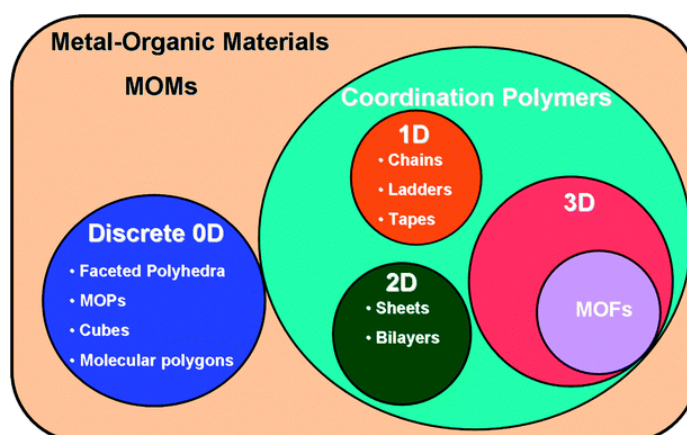


Figure 25. Different types of Metal–organic materials encompassing discrete and extended structures with one, two, or three dimensionality. Figure reproduced from ref. 29a with permission

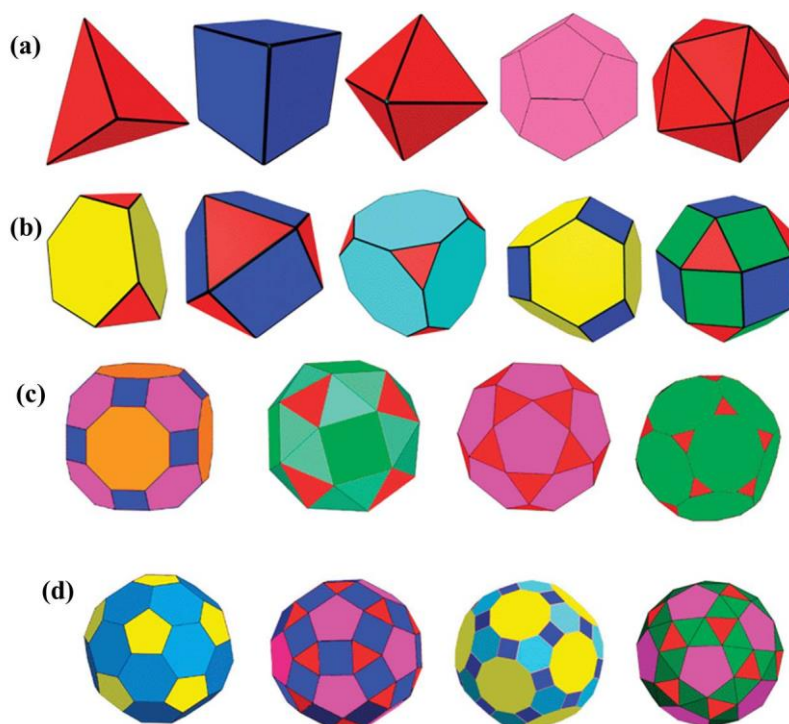


Figure 26. (a) (left to right): tetrahedron, hexahedron (cube), octahedron, dodecahedron, and icosahedron, (b) Truncated tetrahedron, cuboctahedron, truncated cube, truncated octahedron, and rhombicuboctahedron, (c) Truncated cuboctahedron, snub cube, icosidodecahedron, and truncated dodecahedron, (d) Truncated icosahedron, rhombicosidodecahedron, truncated icosidodecahedron, and snub dodecahedron. Figure reproduced from ref. 29b with permission

such as, 0D (polygons and discrete polyhedra), 1D (chains and ladders), 2D (sheets and bilayers), and 3D (extended networks) could be achieved (Figure 25).^{29a,b} Metal–organic cages or metal-organic polyhedral (MOPs) are one important class of MOM. Unlike MOFs, they are discrete, 0D metal-organic moieties having well-defined structures and confined cavities. MOPs are constructed from metal ions and suitable organic linkers which occupy the edges and vertices of a particular polygon, respectively. MOPs could exist in different polyhedral forms such as, platonic, Archimedean, faceted, and stellated and therefore have established themselves as fascinating class of MOMs.^{29b} Different examples of platonic and archimedean MOPs are shown in Figure 26. Moreover, the presence of several point of extensions around the discrete MOPs allow further growth via metallic nodes (vertices) with higher connectivity and/or polytopic organic spacers (faces). Hence, MOPs could act as secondary building blocks (SBBs). Recent examples showed how MOPs as SBBs could be exploited for generation of an extended network

structures.^{29d-g} Another important property of MOP is their high solubility in organic and aqueous medium.^h Such soluble nature of MOPs makes them useful materials for certain applications in the homogeneous media in contrast to MOFs which mostly exist as insoluble crystalline solids. Further the advantage of robustness and chemical stability make MOPs important materials for various applications.

1.6.1 Design principles of metal-organic cage

Several strategies are used to design the discrete metal–organic self-assemblies. These include directional bonding, symmetry interaction, molecular paneling, and reticular chemistry etc.^{29b, 30a-d} The important parameters to design the geometry, size and function of the molecular cages are; i) the coordination geometry of the metal center, and ii) the type and shape of the organic bridging linker. On account of these factors, different spherical or polyhedral cages can be synthesized. Transition metal ions are commonly employed to construct the MOPs cages. The metal ions which occupy the vertices, play an important role in achieving the required properties and shape. To date, various transition metal ions, like Fe^{II}, Co^{II}, Ni^{II}, Cu^{II}, Zn^{II}, Mo^{II}, Ru^{II}, Rh^{II}, Pd^{II}, and lanthanides etc. have been used to construct metal-organic cages. Another important component of

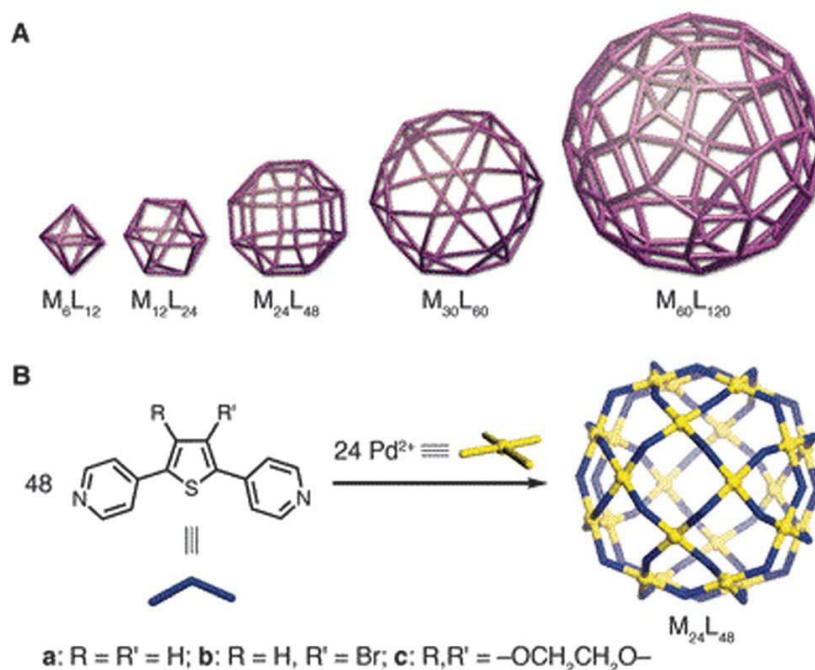


Figure 27. (A) The family of M_nL_{2n} polyhedral cages (metals (M) and bridging ligands (L) are mapped onto the vertices and edges, respectively). (B) Selfassemblies of the $M_{24}L_{48}$ rhombicuboctahedron. Figure reproduced from ref. 29g with permission

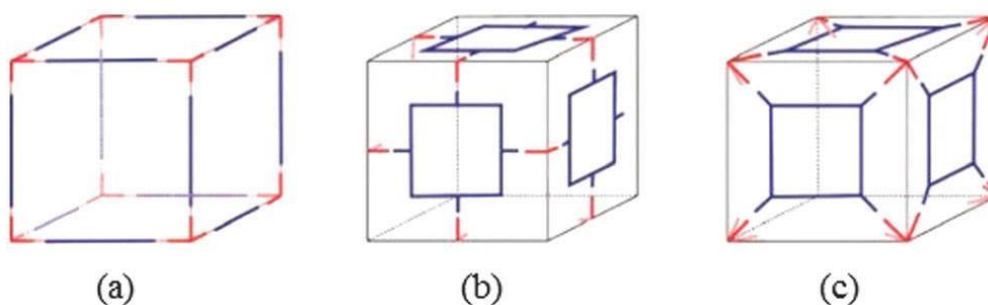


Figure 28. (a) Linear ditopic edge components connected with C_3 symmetric corner components, (b) C_4 symmetric facial components connected with the bent ditopic edge components and (c) C_4 symmetric facial components connected with C_3 symmetric corner components. Figure reproduced from ref. 4d with permission

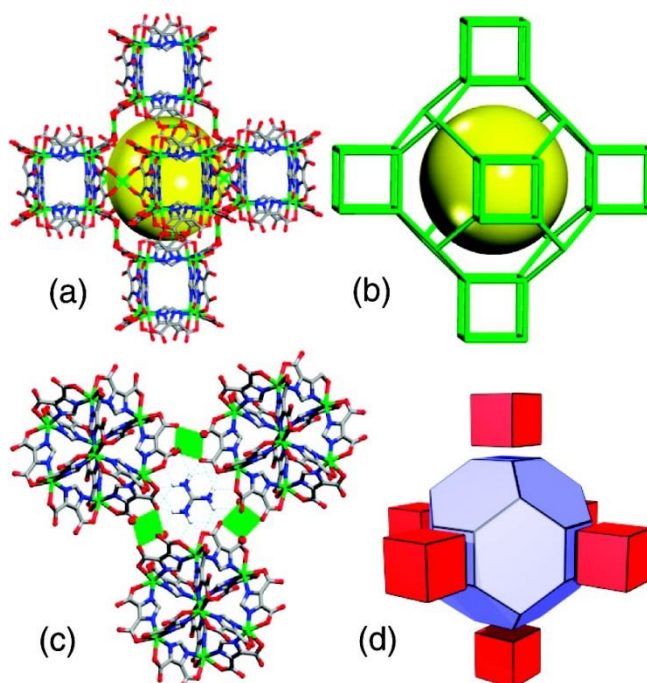


Figure 29. Cage connected by corner sharing. Figure reproduced from ref. 31c with permission

cage is the bridging linkers. Many multidentate ligands bearing different types of functionalities, e.g., carboxylic, hydroxyl, nitrogen and/or Schiff base groups, etc., have been utilized to bridge the geometrically pre-fixed metal nodes. The type and shape of the ligand, and its combination with metal ions basically decide the exact geometry of the cage (Figure 27).^{29g,30a, e, f}

To date, a wide variety of cage structures have been designed by the suitable combination of the building components (ligands and metal ions/clusters) possessing

different connectivity. To overview the general design blueprints for the MOP synthesis, two main approaches are considered: edge-directed and face-directed (Figure 28).^{29f} An important requisite for synthesizing a polyhedral structure is, at least one component of the systems must show a bent ($\theta < 180^\circ$) geometry. This provides the needed curvature for the formation of a finite symmetry. The edge-directed approach involves the connection of ditopic edge components with the multitopic components at the vertices of the polyhedron (Figure 28). However, in the case of face-directed methodology, polytopic facial components are linked with the ditopic components or tritopic components at the edges (Figure 28b) or corners (Figure 28c), respectively. The size and geometry of the MOPs can be modulated accordingly with the control over building components. Various combinations of the C_2 , C_3 , C_4 , and C_5 symmetric components such as edges, faces and corners can result in interesting MOP's symmetries. For the cubic symmetry, a C_3 symmetric component plays a key role.³¹ Thus, metal–organic cubical cages with T, O, and I symmetries result from the combinations of a C_3 symmetric building component with a component of C_2 , C_4 , and C_5 symmetry, respectively. For example, Eddaoudi and co-workers reported a series of metal-organic cube which act as a building block for extended framework which showed zeolite-like topologies (Figure 29).^{31c} Similarly, these

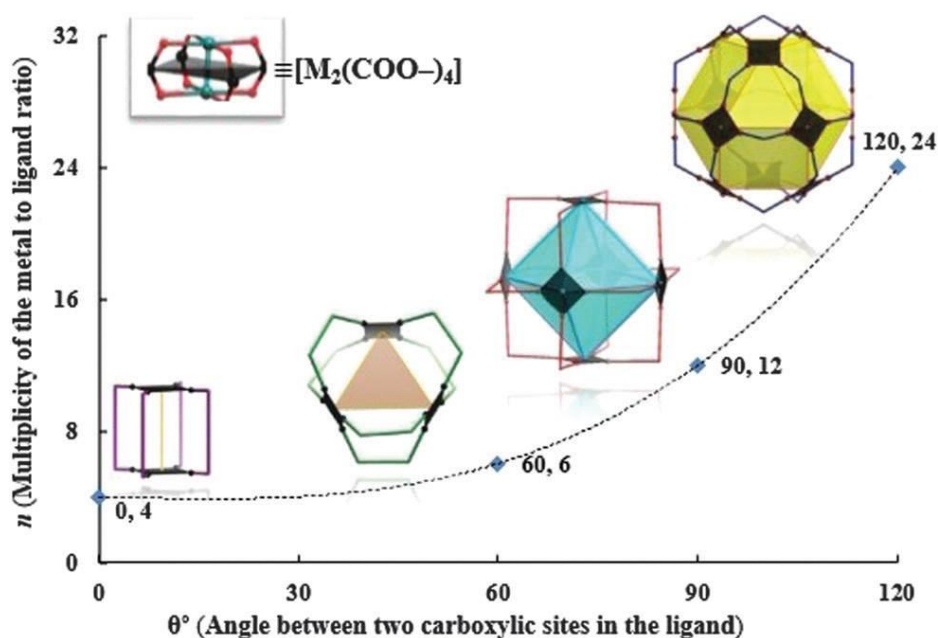


Figure 30. The modular family of metal–carboxylate self-assembled cages built from dinuclear paddlewheel (PW) cluster $[M_2(COO^-)_4]$, where metals (M) and angular ditopic bridging ligands (colored lines) are mapped onto the vertices and edges, respectively. Figure reproduced from ref. 30d with permission

approaches have been used to design a wide range of polyhedral cages having platonic dimensions and significantly larger structures like a cuboctahedron (Archimedean) and so on. The MOP augmentation can be obtained when SBUs are used as the building components of the MOPs as compared to primary building units. The paddlewheel cluster, $[M_2(COO^-)_4]$, serves as a square planar tetratopic SBU in the MOPs (Figure 30).^{30d}

1.6.2 Synthesis and applications of metal-organic cage

Synthesis of metal-organic polyhedral or cage is achieved by coordinating metal ions with organic linkers under the given conditions of a suitable solvent system, temperature, and pressure. The general synthetic protocols involve solvothermal, reflux and stirring at ambient conditions. Usually, the spontaneous reaction of metallic and ligand precursors have low activation energy barrier, which can be easily crossed at room temperature. This has been observed in the case of transition metal cages of carboxylic, Schiff-base, and/or pyridine based ligands. Sometimes, simple heating over room temperature is required. For example, Pd^{II}-bispyridyl based cages are synthesized and characterized in dimethylsulfoxide at 70 °C for a given time scale, ranging from 0.5 to 24 h.^{29g} Fe-cages are prepared by mixing Fe^{II} salt and respective amines and aldehydes in acetonitrile for 24 h at 50 °C following the addition of diisopropyl ether.^{32a,b} However, choosing the suitable solvent system is the most sophisticated step for self-assembly followed by the crystallization process. Criteria for the proper solvent system are to fulfil the solubility of starting materials and maintain the reasonable rate of evaporation. However, the synthesis under the room temperature conditions takes several days to obtain crystals. Hence, to speed up the process, the solvothermal method is also a reasonable approach. While in this case along with solvent parameters, reaction temperature, holding time and the chemical reactivity vs. pressure are crucial for the product morphology and crystallinity.^{32c, d}

1.6.2.1 Ion transport

In living cell the flow of Na^I and K^I is regulated by ion channels. To understand the mechanism and operational details of biological ion channel, artificial ion channels are designed recently.^{33a-d} The ion transport behaviour of metal-organic cage is of great interest. Furukawa *et al.* first synthesized a charge-neutral MOP-18 with overall size of 5 nm having a hydrophilic cuboctahedral cavity (diameter of 13.8 Å) (Figure 31a).^{33e} Later,

Kim and co-workers reported a synthetic ion channel formed with MOP-18 that transports proton and alkali metal ions across lipid membranes (Figure 31b).^{33g} Similar to MOP-18, the rhodium–organic cuboctahedron ($C_{14}RhMOP$) having nanopores of 0.6 nm, obtained from $Rh_2(OAc)_4(MeOH)_2$ and 5-dodecyloxy-1,3-BDC embedded into a bilayer of the lipid membrane, has been studied for ion-transport.^{30f} Similar to cationic transport, anionic transport is also possible using the metal–organic self-assemblies. In this regard Nitschke *et al.* have established various cationic M^{II} -cages which offer differential binding affinities for a set of anions through host-guest mechanism.^{32a,b}

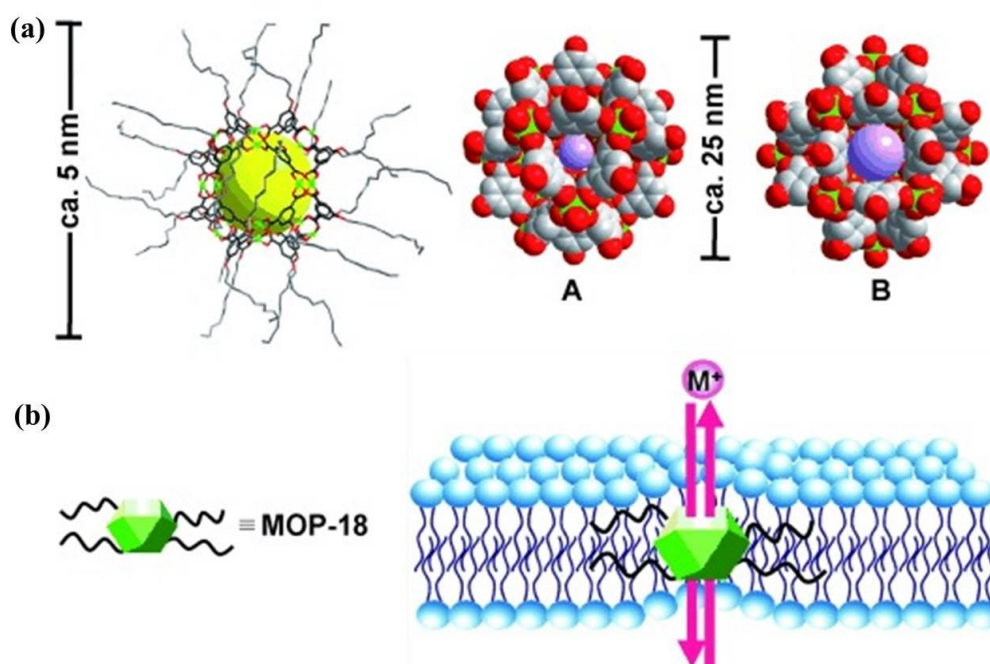


Figure 31. (a) MOP-18 with a framework formula $Cu_{24}(5-OC_{12}H_{25}-mBDC)_{24}$ has a large cavity (yellow sphere, diameter 13.8 Å). Triangular and square windows are shown as spheres (purple) that fit into the windows (diameter 3.8 Å, for A and 6.6 Å, for B). (b) A schematic diagram for a synthetic ion channel formed by MOP-18 in lipid bilayers. Figure reproduced from ref. 33g with permission

1.6.2.2 Proton conductivity

The proton conducting materials are essential in many applications, especially hydrogen fuel cells. Over the years, researchers have developed many organic and inorganic materials, such as sulfonated polyether ketone, oxo acid, ceramic oxides hydroxides, apatites etc. as promising candidates for proton conduction.^{34a-i} However, low mechanical strength and chemical stability at high temperature limits wide-spread

application of these materials in proton exchange membrane fuel cell (PEMFC). The commercially used proton exchange membrane, Nafion shows appreciable proton conductivity at low temperature and high humidity.^{34j-k} However, the conductivity decreases drastically with increasing temperature and decreasing humidity. Therefore, developing new proton conducting materials which operates at wide temperature and humidity range, without compromising the chemical stability and mechanical strength, is of utmost importance. Recently, porous materials such as, coordination polymers (CPs) or metal–organic frameworks (MOFs) and porous organic materials (POM) have emerged as a promising proton conducting materials.³⁵ The high crystallinity, open framework architecture and high structural stability make them better candidates for studying proton conductivity and understanding its mechanisms. For MOF materials, most common strategies for enhancing the proton conductivity involve the enhancement of proton carrier concentration by controlling framework or extra-framework compositions. In another strategy, the proton mobility is improved by constructing materials with desired

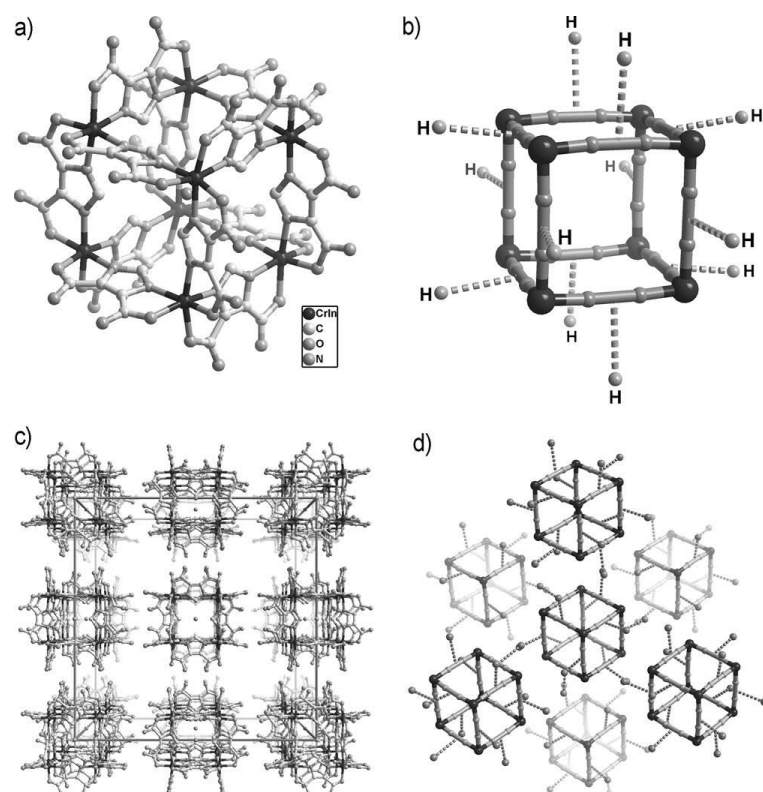


Figure 32. a) Structure of the $[\text{Cr}_4\text{In}_4(\text{Himdc})_{12}]\cdot\text{H}_2\text{O}$ cube. b) The distribution of 12 H-atoms on the surface of each cube. c) 3D supramolecular packing of the cubes. d) The orientation of each cube and six neighboring cubes. Figure reproduced from ref. 35m with permission

H-bonded networks. For example, Kitagawa and co-workers reported highly proton-conductive zinc oxalate MOFs by maximizing the proton carriers with the simultaneous introduction of adipic acid molecules on the framework and the counter cation (NH_4^+) in the void space.^{35k} Shimizu *et al.* reported proton conductivity in PCMOF21 which have combined trisulfonate and triphosphonate groups.^{35l} However, synthesis of these materials usually requires greater degree of ligand deprotonation which sometimes reduces the concentration of proton carriers. For this reason, researchers have recently showed that discrete metal–organic cages which are formed through partial deprotonation of ligands, represent a superior materials for improved proton conductivity. The finite structures of metal-organic cages provide an opportunity to decorate their external surface with free functional groups (such as, carboxylate, imidazolate etc.) which eventually helps in fast mobility of proton carriers. Moreover, the extensive hydrogen bonding between the cage and the surrounding guest molecules also offer an efficient pathway for proton conduction. Zhai *et al.* reported two mixed-metal metal-organic cubes that showed high proton conductivity due to the presence of free carboxylic acid groups on the surface of each cube which participates in H-bonding with the guest water molecules (Figure 32).^{35m} The proton conductivity of the cubes was found to be in the order of 10^{-2} Scm^{-1} at 23 °C and 98 % relative humidity.

1.6.2.3 Molecular recognition and imaging

The molecular recognition refers to a specific interaction between two or more molecules through non-covalent interactions such as hydrogen bonding, metal coordination, hydrophobic forces, Van der Waals forces, π – π interactions, halogen bonding, and electrostatic effect. In addition to these direct interactions as well the solvent can play a dominant indirect role in driving molecular recognition in solution. Molecular recognition plays an important role in biological systems. Recently, researchers have shown that specially designed artificial supramolecular systems can exhibit molecular recognition. Functional moieties in the ligands impart certain desirable properties like photophysical properties for the given biochemical protocols. More specifically, special functional groups in MOPs are selected to match with particular molecular species present in the targeted systems which may be in vivo or in vitro. Luminescent cages can be used for molecular detection and to better understand the physiological processes for trapped compounds. Besides this, symmetry, stability, biocompatibility and biodegradability of MOPs make the task more attractive. Therefore, MOPs have great

potential in biochemistry owing to solution stability and properties under specific experimental conditions and chemical environments like acidic, basic, sensing species, and temperature etc.



Figure 33. Structure of the Ce-H2TTS functional tetrahedron showing the sequence of fluorescent variation of the tetrahedron upon the addition of PTIO and NO. Figure reproduced from ref. 36a with permission

Well-confined MOP self-assemblies including adjustable lipophilic features exhibiting biocompatibility and cell permeability are handy for the application to biomolecular imaging and detection. MOP functionalization with amide groups, the characteristic structural motif of a protein, could be a useful attempt to achieve functional metal–organic polyhedra with suitable hydrophilic/lipophilic characteristics. A robust neutral cerium-based tetrahedron Ce₄-H2TTS incorporates a triphenylamine moiety with three amide groups (H6TTS), often used as a bright blue emitter, is emphasized as a luminescent detector of 2-phenyl-4,4,5,5-tetra-methylimidazoline-3-oxide (PTIO) which is a specific spin-labeling nitric oxide (NO) trapper.^{36a} Interestingly, the molecular cage Ce-H2TTS also demonstrated a high selectivity and sensitivity towards quantificational detection of tryptophan (Trp) over all other natural amino acids and Trp-containing peptides (*in vitro*) (Figure 33).

1.6.2.4 Drug delivery

Drug delivery to specific locations within the human body using material-based systems occupied the forefront of biomedical research for the past few decades. Development of new materials for the well-controlled drug delivery systems remains a challenging task. Recently, metal–organic cages with proper functionalities and appealing drug hosting and release potential are a new input to the field.^{36b} Analogous to enzymes

and other large biomolecular systems for encapsulating guest in a confined environment, it is advantageous to use the MOP self-assemblies which offer storage, carriers and then controlled release.^{32d} Precise surface decoration and hence functionalization with a long aliphatic hydrocarbon chain to get amphiphilic and biocompatible supramolecular self-assemblies could achieve an anticipated environment for drug loading and release. Moreover, metal–organic cages have the potential to selectively encapsulate the molecules based on the size of the cage cavity. For the drug delivery studies, it is important to load the drug into a third party carrier agent and then get the release as required. The release of encapsulated guest molecules from the cage cavity is the working mechanism for the drug delivery. Therefore, in light of this it is very attractive that self-assembled cages have the immense potential to be used in pharmaceuticals as drug vectors and delivery agents. The release profile of Caffeine, a widely used stimulant drug, from a cuboctahedral MOP was investigated by Mallick *et al.*^{32d} The hydrolytic conversion of MOP to the extended framework, occurring via a potential unfolding process, facilitated the drug release. The release plot patterned like sustained delivery of cavity-trapped caffeine;

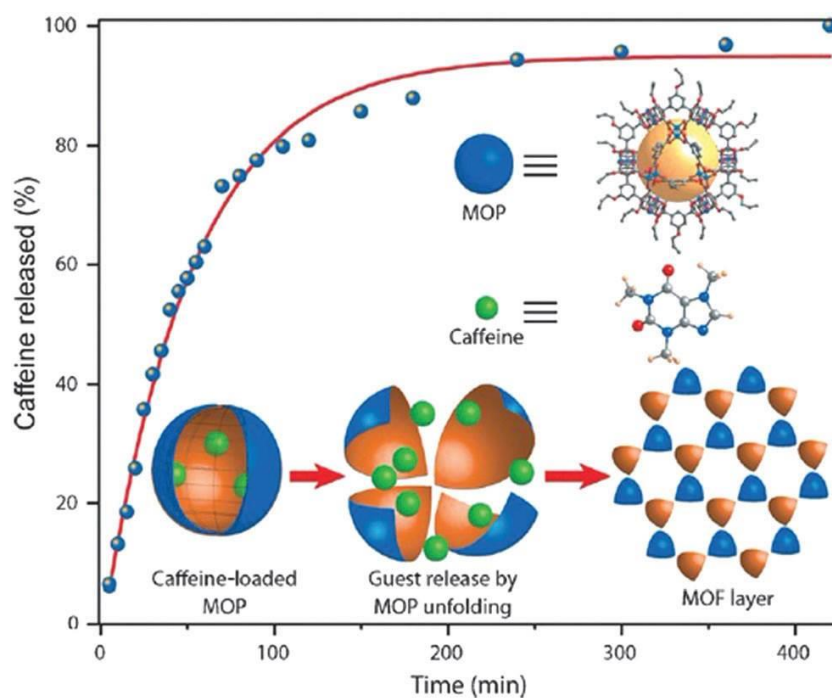


Figure 34. Release profile of encapsulated caffeine molecules from the selfassembly derived from Cu^{2+} paddlewheels and 5-(prop-2-ynyloxy)isophthalic acid. A schematic representation of the release driven by the unfolding event is also shown. Figure reproduced from ref. 32d with permission

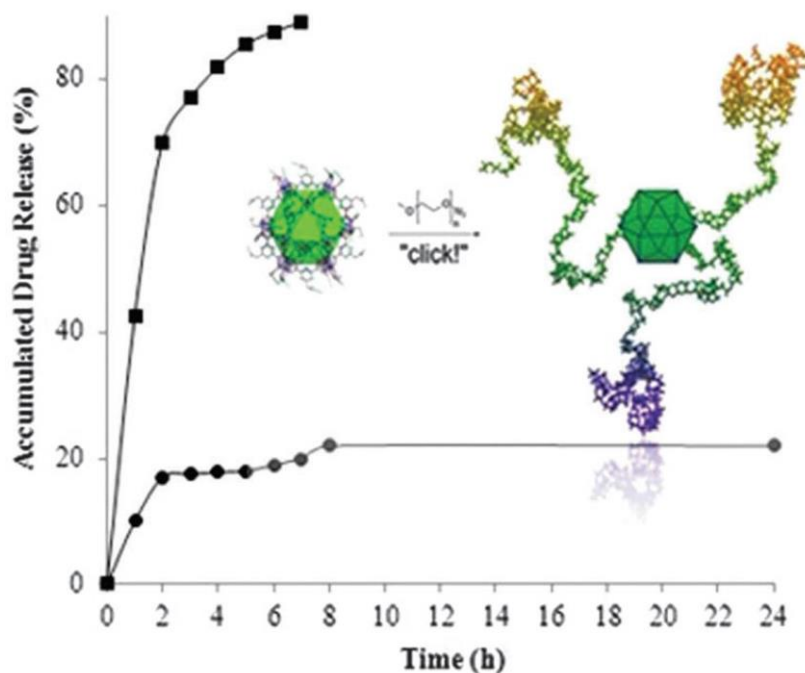


Figure 35. Drug release profiles of 5-fluorouracil (5-FU) from; (a) surface functionalized Cu-cage (circle) and control (square). Figure reproduced from ref. 36b with permission

this outcome is based on gradual departure of the loaded drug from the pores to the aqueous media (Figure 34). In another work, Zhao *et al.* reported a porous coordination nanocage containing surface-exposed alkyne groups which was functionalized through click reaction with azide terminated polyethylene glycol.^{36b} The surface functionalized cage was successfully applied as a drug delivery agent for an anticancer drug, 5-Fluorouracil (5-FU) in aqueous medium. The surface functionalized MOP showed a slow release profile due to the strong interaction between the Lewis acid site of MOP and basic sites of 5-FU (Figure 35).

1.7 Metal-organic cage based gels

Recently, a new class of gel has emerged where soluble polymers containing appropriate cage forming functional groups react with metal ions to form gels. This multi-metal–ligand based supramolecular polymerization approach yields cage-cross-linked polymer gels, also known as polyMOC gels.³⁷ In polyMOC gels the metal–organic cages act as the junction points between cross-linked polymers (Figure 36).^{37a} In the conventional CPGs, the single metal ion which is typically bound to maximum 2–3 ligands, act as the junction between gelators. Therefore, the ability to tune the average number of bridges that connects network junction is limited in conventional CPGs.

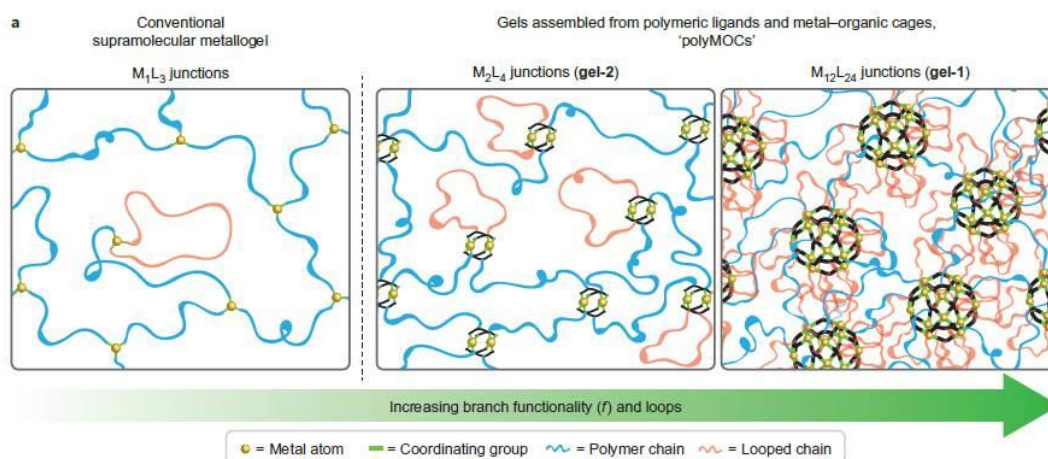


Figure 36. Schematic representations of traditional supramolecular metallogels compared with the polyMOCs with M_2L_4 and $M_{12}L_{24}$ junctions. Figure reproduced from ref. 37a with permission

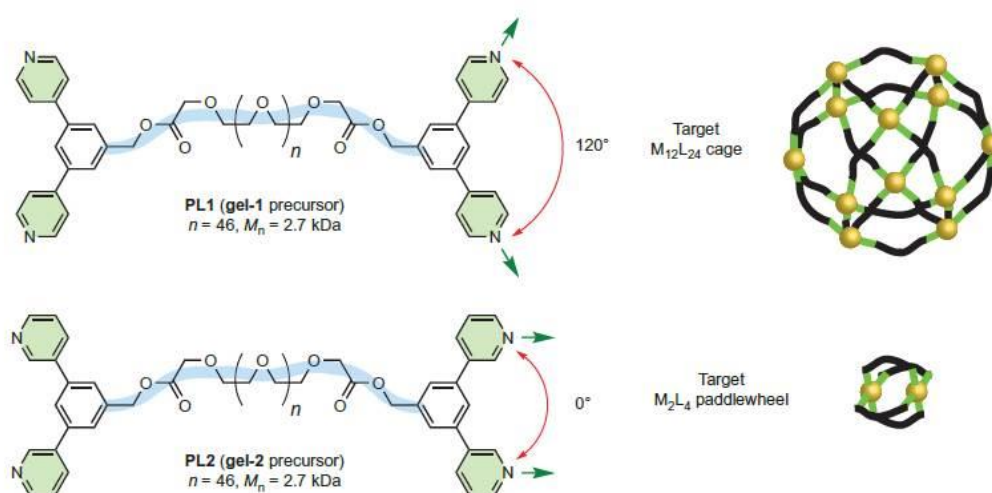


Figure 37. b, Chemical structure of bis-para-pyridine-terminated PEG PL1 and a schematic of the $M_{12}L_{24}$ cage that is expected to arise from the assembly of 24 bis-para-pyridine ligands and 12 Pd^{2+} atoms. c, Chemical structure of bis-meta-pyridine-terminated PEG PL2 and a schematic of the M_2L_4 paddlewheel that is expected to arise from the assembly of four bis-meta-pyridine ligands and two Pd^{2+} atoms. Figure reproduced from ref. 37a with permission

However, this is not true in case of polyMOC gels. Since metal–organic cages have multiple network propagating points, the number of bridges connected to network junction could be tuned by tuning the size of the cage. Therefore, the polyMOC gels show enhanced mechanical properties and porosity.

Recently, Johnson and co-workers described the synthesis of polyMOC gels via the self-assembly of Pd^{II} ions and *para*-bispyridine or *meta*-bispyridine functionalized polyethylene glycol (PEG) chains (Figure 37).^{37a} The difference in the average size of the junction cage and the corresponding number of polymer chains connected to each cage determined the network branch functionality (f) of the gel. An increase in f leads to a direct increase in the elastic modulus of the resultant gel. They also showed that polyMOC gels containing a large MOC junction and a high number of loop defects, it is possible to replace the defects selectively with pyrene-based fluorescent free ligands. The resultant pyrene modified polyMOC gel showed high fluorescence without compromising the mechanical integrity. The synthesis of cage-cross-linked polymer gels (polyMOC gels) has offered a new approach to incorporate different organic or metal–organic cages with a wide range of internal cavities inside mesoscopic pores of polymeric supramolecular gels. They can be explored for controlled and stimuli-responsive release of drug molecules, fragrances or pesticides. Johnson and co-workers also reported a stepwise assembly for the integration of metal–organic cages into block copolymers (BCPs).^{37d} This approach creates “block co-polyMOC” (BCPMOC) materials whose microscopic structures and mechanical properties are readily tunable by adjusting the size and geometry of the metal-organic cage and the composition of the BCPs. The same group also reported star polymer metal–organic cage (poly-MOC) materials whose structures, mechanical properties, functionalities, and dynamics can all be precisely tailored through a simple three-component assembly strategy.^{37b} The star polyMOC network is composed of tetra-arm star polymers functionalized with ligands on the chain ends, small molecule ligands, and palladium ions; polyMOCs are formed via metal–ligand coordination and thermal annealing. The ratio of small molecule ligands to polymer-bound ligands determines the connectivity of the MOC junctions and the network structure.

Nitschke *et al.* reported the first polyMOC gel prepared by metal-templated condensation of a 2-formylpyridine functionalized water-soluble polymer, 4,4'-diaminobiphenyl-2,2'-disulfonic acid and iron(II) sulphate heptahydrate (Figure 38).^{37e} The as-prepared MOC-cross-linked hydrogel contained two distinct kinds of spaces within it (i) mesoscopic pores of polymeric supramolecular gels and (ii) the well-defined inner pore of the cages. The gel showed selective encapsulation of guest molecules. Moreover, the hydrogel allowed controlled release of closely related small molecules at different rates in response to competing guests, depending upon whether they were

selectively encapsulated within the inner pore of the cages. Also, multi-stimuli responsive nature of the hydrogel allowed triggered release of the macromolecular cargo.

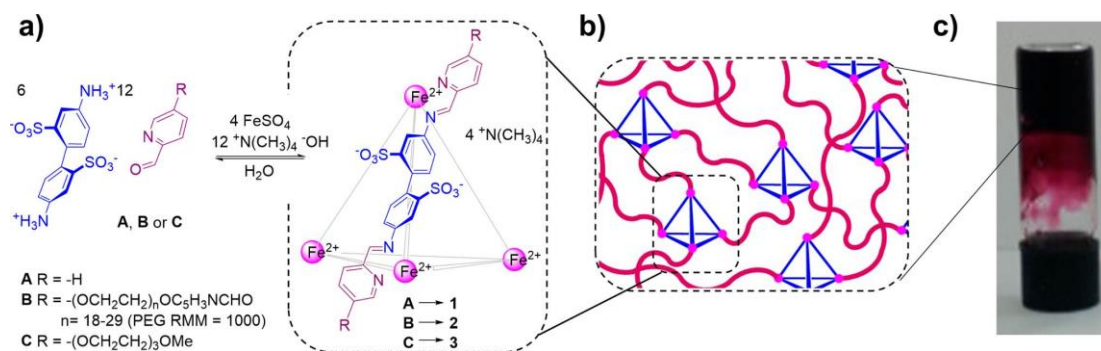


Figure 38. Metal-organic cage cross-linked hydrogel formation: (a) synthesis of cages 1–3 using aldehydes A–C, and (b) a schematic view of the structure of the cage-cross-linked gel. (c) A photograph showing an inverted vial containing a 15 wt % hydrogel formed by cage. Figure reproduced from ref. 37e with permission

1.9 Scope of the work

The last few decades have witnessed a rapid growth in the development of functional hydrogels and organogels which are formed by the self-assembly of LMWGs. The dynamic nature and high processability of such supramolecular gels have been exploited for the applications in diverse fields, including tissue engineering, bio-medicine, and opto-electronics. More recently, the CPGs, formed by the self-assembly of suitable metal ions and LMWGs, have attracted enormous research attention. CPGs are highly promising soft-hybrid materials, as the presence of metal ions endows them with unique redox, optical, electronic, and catalytic properties. To date, various elegant design principals have been adopted to construct a large number of LMWGs. However, little attentions have been given to develop both hydrogel/organogel and CPGs from the same LMWG and systematic study on the influence of metal coordination to the morphology and photophysical properties of the gels. This thesis reports research work in this direction (Figure 40). The design principle adapted to construct a series of LMWGs, reported in this thesis involves: i) the presence of π -chromophores (C_2 , C_3 and C_4 symmetric) as the core, ii) terminal terpyridine groups as metal ion binding sites, iii) the core and terpyridines are connected via flexible alkylamide chain.

The RGB approach is the most widely adopted technique for tunable emission, including white-light-emission in supramolecular organic hybrid and crystalline Ln^{III}-

MOF. However, low processability of bulk Ln^{III} -MOF and fluorescence quenching caused by the aggregation of chromophores in organic hybrids are the major drawbacks which inhibit their practical applications. Moreover, only handfuls of white-light-emitting materials, suitable for solid-state-lighting applications have been reported to date. Nevertheless, realizing white-light-emission in Ln^{III} -CPGs is still an unexplored area of research. In this thesis different possible applications of Ln^{III} -CPGs have been exploited. The tunable emissions of the Ln^{III} -CPGs have not only been utilized for solid-state-lighting, but also explored for multi-stimuli responsive sensing applications exploiting the dynamic nature of Ln^{III} -terpyridine coordination bonds. Though ample reports of LMWGs are there in literature, it is still a daunting task to design *a priori* a LMWG which can self-assemble to both hydrogel and organogel with different properties. Herein, this problem has been addressed by designing amphiphilic LMWG which self-assembled to hydrogel and organogel with distinctly different morphology and photo-physical properties. Moreover, the hydrogel are exploited as efficient nano-catalyst for facilitating the reactions of industrial importance. Photo-responsive change in structure and

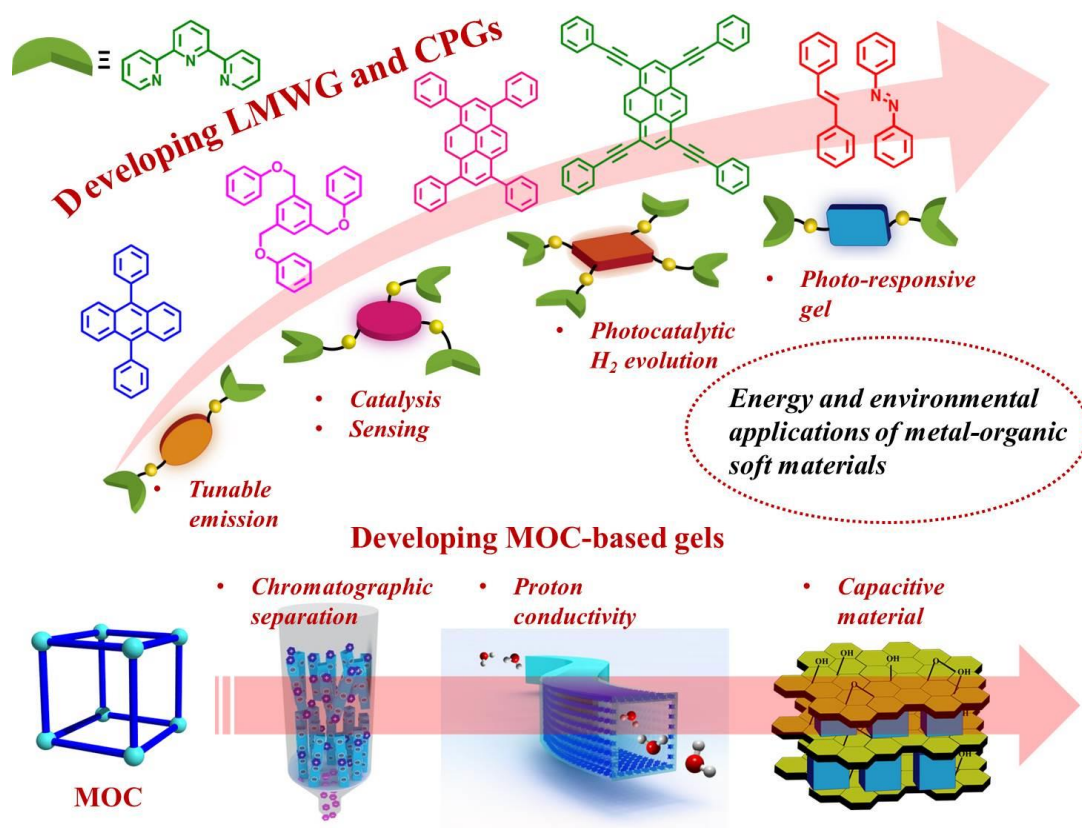


Figure 39: Scheme showing systematic development of various LMWG, CPGs and MOC-based hydrogels which show different energy and environmental applications.

properties of bulk MOFs have recently been reported by exploiting well-known photo-chemical reactions: a) *trans-cis* isomerization of azobenzene, and b) [2+2] cyclo-addition of stilbene. However, effect of such photo-chemical changes on the properties and nano-morphologies of CPGs are not yet reported. This thesis partially deals with such problem. Visible-light-driven water splitting for hydrogen evolution is the foremost important topic of research now-a-days. Various organic polymers, inorganic solid-state materials, and metal-organic frameworks are exploited as efficient photo-catalysts in literature. Recently, π -conjugated hydrogels containing suitable co-catalysts have emerged as new type soft photo-catalyst for water-splitting. However, designing CPG as an efficient photo-catalyst is an obvious gap in this field. This thesis has attempted to fill this gap by synthesizing Ru^{II}-CPGs which exhibited excellent photo-catalytic activity in presence of an earth-abundant co-catalyst.

Metal-organic cage is an important supramolecular building block for preparing supramolecular porous framework. Recently, they are employed as building blocks for preparing polymeric gels (PolyMOC gels) where cages are formed at the junction of organic polymer, *in-situ* during gelation. However, supramolecular self-assembly of preformed, discrete metal-organic cages to hydrogel is not explored yet. One major part of this thesis dealt with supramolecular self-assembly of water soluble metal-organic cubes (MOCs) to hydrogels in presence of different molecular binders and their versatile applications. Introduction of different kind of molecular binders tuned the nano-morphology and the properties of the hydrogels which showed gel-chromatographic separation of charged species and excellent proton conductivity at ambient condition. Moreover, the MOC-based hydrogels were employed for preparing mixed dimensional heterostructures that exhibited capacitive behaviour.

1.10 Outlook

In general, CPGs have been proven as an important class of multi-functional soft-hybrid materials. The presence of coordinated metal ions endows the CPGs with unique redox, optical, electronic, catalytic properties and also enhances their mechanical properties compared to organic gelator-based soft materials. Easy solution processability and the dynamic nature of CPGs hold great promise for application in different fields, including nanoelectronics, biomedicine, catalysis, etc. Among various CPGs reported to date, the luminescent CPGs are employed extensively for the easy fabrication of large-area displays, white-light-emitting LEDs (WLED), etc. Additionally, the stimuli-

responsive luminescent CPGs are exploited for fabricating portable sensing kits. The reversible sol–gel behaviour of stimuli-responsive CPGs is utilized for targeted drug delivery. On the other hand, many CPGs showed good catalytic activity due to the presence of microporosity that allows solvent-assisted easy diffusion of starting materials and fast removal of the product from the catalytic sites. Despite such overwhelming applications, the characterization and structure–property correlation of CPGs are the challenging issues that still need to be addressed. As single-crystal structure determination is not possible here, scientists have to rely on powder X-ray diffraction or fiber X-ray diffraction, various spectroscopic and electron microscopic techniques. The development of new characterization techniques will greatly help us to study the structure–property correlation in CPGs. Despite many challenges, a limitless combination of metal ions and organic ligands would provide scientists a vast platform for preparing a large variety of functional CPGs. It should be noted that CPGs are still in the stage of exploration and will flourish more in the near future. So far, few CPGs have been explored for limited applications; however, the full potential of CPGs is yet to be established. On the other hand, the MOC-based gels have huge unexplored potential as its property could easily be tuned by designing appropriate molecular binders. It should be mentioned that the development MOC-based gels is still in budding stage and in future many different applications of MOC-based gels could be explored.

1.11 Reference

1. (a) Y. Osada and K. Kajiwara, in (*translator*) *Gels hand book*, ed. T. Fushimi, O. Hirasa, Y. Hirokawa, T. Matsunaga, T. Shimomura and L. Wang, assoc. ed. H. Ishida, Academic Press, San Diego, 2001, vol. 1–3; (b)
2. (a) M.-O. M. Piepenbrock, G. O. Lloyd, N. Clarke and J. W. Steed, *Chem. Rev.*, 2010, **110**, 1960–2004;
3. (a) J. Jagur-Grodzinski, *Polym. Adv. Technol.*, 2010, **21** 27–47; (b) S. Chaterji, K. Kwon, and K. Park, *Prog Polym Sci.*, 2007, **32**, 1083–1122; (c) Y. Osada and J. Gong, *Prog. Polym. Sc.*, 1993, **18**, 187–226.
4. (a) X. Yu, L. Chen, M. Zhang and T. Yi, *Chem. Soc. Rev.*, 2014, **43**, 5346–5371; (b) N. M. Sangeetha and U. Maitra, *Chem. Soc. Rev.*, 2005, **34**, 821–836; (c) D. Diaz Diaz, D. Kuhbeck and R. J. Koopmans, *Chem. Soc. Rev.*, 2011, **40**, 427–448; (d) T. Vermonden, R. Censi and W. E. Hennink, *Chem. Rev.*, 2012, **112**, 2853–2888; (e) S. Zhang, M. A.

Greenfield, A. Mata, L. C. Palmer, R. Bitton, J. R. Mantei, C. Aparicio, M. O. de la Cruz and S. I. Stupp, *Nat. Mater.*, 2010, **9**, 594–601.

5. (a) T. Yi, K. Sada, K. Sugiyasu, T. Hatano and S. Shinkai, *Chem. Commun.*, 2003, 344; (b) J. H. Jung, Y. Ono and S. Shinkai, *Angew. Chem., Int. Ed.*, 2000, **39**, 1862; (c) C. Shi, Z. Hung, S. Kilic, J. Xu, R. M. Enick, E. J. Beckman, A. J. Carr, R. E. Melendez and A. D. Hamilton, *Science*, 1999, **286**, 1540; (d) R. Wang, C. Geiger, L. Chen, B. Awanson and D. G. Whitten, *J. Am. Chem. Soc.*, 2000, **122**, 2399.

6. (a) P. Terech and R. G. Weiss, *Chem. Rev.*, 1997, **97**, 3133; (b) J. H. Jung, J. H. Lee, J. R. Silverman and G. John, *Chem. Soc. Rev.*, 2013, **42**, 924; (c) M. D. Segarra-Maset, V. J. Nebot, J. F. Miravet and B. Escuder, *Chem. Soc. Rev.*, 2013, **42**, 7086; (d) M. Moniruzzaman, A. Sahin and K. I. Winey, *Carbon*, 2009, **47**, 645; (e) *Functional Molecular Gels*, ed. B. Escuder and J. F. Miravet, RSC, Cambridge, 2014; (f) P. Sutar and T. K Maji, *Chem. Commun.*, 2016, 52, 8055–8074

7. (a) L. Frkanec and M. Z'inic', *Chem. Commun.*, 2010, **46**, 522; (b) J. Brinksma, B. L. Feringa, R. M. Kellogg, R. Vreeker and J. v. Esch, *Langmuir*, 2000, **16**, 9249; (c) Y.-C. Lin, P.-I. Wang and S.-W. Kuo, *Soft Matter.*, 2012, **8**, 9676; (d) S. R. Jadhav, P. K. Vemula, R. Kumar, S. R. Raghavan and G. John, *Angew. Chem., Int. Ed.*, 2010, **49**, 7695; (e) N. N. Adarsh, D. K. Kumar and P. Dastidar, *Tetrahedron*, 2007, **63**, 7386; (f) A. R. Hirst and D. K. Smith, *Langmuir*, 2004, **20**, 10851.

8. A. A. Sobczuk, S.-i. Tamaru and S. Shinkai, *Chem. Commun.*, 2011, **47**, 3093.

9. A. R. Hirst, B. Escuder, J. F. Miravet and D. K. Smith, *Angew. Chem., Int. Ed.*, 2008, **47**, 8002.

10. (a) Anthony Yiu-Yan Tam and Vivian Wing-Wah Yam, *Chem. Soc. Rev.*, 2013, **42**, 1540–1567.

11. (a) T. Annable, R. Buscall, R. Ettelaie and D. Whittlestone, *J. Rheol.*, 1993, **37**, 695–726; (b) L. A. Estroff and A. D. Hamilton, *Chem. Rev.*, 2004, **104**, 1201–1218; (c) V. Tirtaatmadja, K. C. Tam and R. D. Jenkins, *Macromolecules*, 1997, **30**, 3271–3282; (d) R. D. Jenkins, C. A. Silebi and M. S. El-Aasser, *Polymers as Rheology Modifiers*, American Chemical Society, 1991, vol. 462, pp. 222–233 (e) J. Sprakel, E. Spruijt, M. A. Cohen Stuart, N. A. M. Besseling, M. P. Lettinga and J. van der Gucht, *Soft Matter*, 2008, **4**, 1696–1705; (f) L. E. Bromberg and D. P. Barr, *Macromolecules*, 1999, **32**, 3649–3657; (g) A. C. Lara-Ceniceros, C. Rivera-Vallejo and E. J. Jimenez-Regalado, *Polym. Bull.*, 2007, **58**, 425–433; (h) C. Tsitsilianis, I. Iliopoulos and G. Ducouret, *Macromolecules*, 2000, **33**, 2936–2943; (i) C. Tsitsilianis and I. Iliopoulos, *Macromolecules*, 2002, **35**,

3662–3667; (j) S. Pispas, D. Vlassopoulos, G. Fytas, B. Loppinet and N. Hadjichristidis, *Polymer*, 2006, **47**, 7302–7311; (k) H. Niu, F. Wang and R. A. Weiss, *Macromolecules*, 2015, **48**, 645–654; (l) L. Voorhaar and R. Hoogenboom, *Chem. Soc. Rev.*, 2016, **45**, 4013–4031

12. (a) Jeffrey, G. A., Saenger, W., *Hydrogen Bonding in Biological Structures*. Springer-Verlag: New York, 1991; (b) Saenger, W., *Principles of Nucleic Acid Structure*. Springer-Verlag: New York, 1984; (c) Schulz, G. E., Schirmer, R. H., *Principles of Protein Structure*. Springer-Verlag: New York, 1979; (d) Redinha, J. S., Lopes Jesus, A. J., *Molecular Recognition and Crystal Growth*. In *Molecular Recognition: Biotechnology, Chemical Engineering and Materials Applications*. Mcevoy, J. A., Ed.; Nova Publishers: New York, 2011; (e) Mottillo, C. and Friscic, T., *Supramolecular imidazolium frameworks: direct analogues of metal azolate frameworks with charge-inverted node-and-linker structure*. *Chem. Commun.* **51**, 8924–8927 (2015); (f) Hazra, A., Gurunatha, K. L., and Maji, T. K., *Charge-Assisted Soft Supramolecular Porous Frameworks: Effect of External Stimuli on Structural Transformation and Adsorption Properties*. *Cryst. Growth Des.* **13**, 4824–4836 (2013); (h) Dastidar, P., Das, U. K., Adalder, T. K., Majumder, J., and Roy, R., in *Hydrogen Bonded Supramolecular Materials*, edited by Zhan-Ting Li and Li-Zhu Wu (Springer Berlin Heidelberg, Berlin, Heidelberg, 2015), pp. 101–131; (i) Desiraju, G. R., *Hydrogen Bridges in Crystal Engineering: Interactions without Borders*. *Acc. Chem. Res.* **35**, 565–573 (2002).

13. (a) H. Yoon, E. J. Dell, J. Freyer, L. M. Campos and W.-D. Jang, *Polymer*, 2014, **55**, 453–464; (b) S. R. Van Tomme, M. J. van Steenbergen, S. C. De Smedt, C. F. van Nostrum and W. E. Hennink, *Biomaterials*, 2005, **26**, 2129–2135; (c) Q. Wang, J. L. Mynar, M. Yoshida, E. Lee, M. Lee, K. Okuro, K. Kinbara and T. Aida, *Nature*. **463**, 339–343 (2010).

14. (a) H. Frisch and P. Besenius, *Macromol. Rapid Commun.*, 2015, **36**, 346–363; (b) X. Ma and H. Tian, *Acc. Chem. Res.*, 2014, **47**, 1971–1981; (c) Z. Qi and C. A. Schalley, *Acc. Chem. Res.*, 2014, **47**, 2222–2233; (d) M. Zhang, D. Xu, X. Yan, J. Chen, S. Dong, B. Zheng and F. Huang, *Angew. Chem., Int. Ed.*, 2012, **51**, 7011–7015; (e) S. Li, H.-Y. Lu, Y. Shen and C.-F. Chen, *Macromol. Chem. Phys.*, 2013, **214**, 1596–1601; (f) D. Liu, D. Wang, M. Wang, Y. Zheng, K. Koynov, G. K. Auernhammer, H.-J. Butt and T. Ikeda, *Macromolecules*, 2013, **46**, 4617–4625; (g) W. Xia, M. Ni, C. Yao, X. Wang, D. Chen, C. Lin, X.-Y. Hu and L. Wang, *Macromolecules*, 2015, **48**, 4403–4409; (h) A. Harada, Y. Takashima and M. Nakahata, *Acc. Chem. Res.*, 2014, **47**, 2128–2140; (i) W. Lu, X. Le, J.

Zhang, Y. Huang and T. Chen, *Chem. Soc. Rev.*, 2017, **46**, 1284-1294; (j) X. J. Han, Z. Q. Dong, M. M. Fan, Y. Liu, J. H. Li, Y. F. Wang, Q. J. Yuan, B. J. Li and S. Zhang, *Macromol. Rapid Commun.*, 2012, **33**, 1055–1060; (k) S. Tamesue, Y. Takashima, H. Yamaguchi, S. Shinkai and A. Harada, *Angew. Chem. Int. Ed.*, 2010, **49**, 7461–7464; (l) Y. Guan, H.-B. Zhao, L. -X. Yu, S. -C. Chen and Y. -Z. Wang, *RSC Adv.*, 2014, **4**, 4955–4959; (m) X. Le, W. Lu, J. Zheng, D. Tong, N. Zhao, C. Ma, H. Xiao, J. Zhang, Y. Huang and T. Chen, *Chem. Sci.*, 2016, **7**, 6715-6720.

15. (a) Molecular Gels, Materials with Self-Assembled Fibrillar Networks, ed. R. G. Weiss and P. Terech, Kluwer Press, Dordrecht, 2005; (b) L. A. Estroff and A. D. Hamilton, *Chem. Rev.*, 2004, **104**, 1201; (c) N. M. Sangeetha and U. Maitra, *Chem. Soc. Rev.*, 2005, **34**, 821; (d) T. Ishi-i and S. Shinkai, *Top. Curr. Chem.*, 2005, **258**, 119; (e) Z. Yang and B. Xu, *J. Mater. Chem.*, 2007, **17**, 2385; (f) K. J. C. van Bommel, A. Friggeri and S. Shinkai, *Angew. Chem., Int. Ed.*, 2003, **42**, 980; (g) A. Ajayaghosh, S. J. George and A. P. H. J. Schenning, *Top. Curr. Chem.*, 2005, **258**, 83; (h) J. Puigmartí-Luis, V. Laukhin, A. P. del Pino, J. Vidal-Gancedo, C. Rovira, E. Laukhina and D. B. Amabilino, *Angew. Chem., Int. Ed.*, 2007, **46**, 238; (i) Y. Yamamoto, T. Fukushima, Y. Suna, N. Ishii, A. Saeki, S. Seki, S. Tagawa, M. Taniguchi, T. Kawai and T. Aida, *Science*, 2006, **314**, 1761; (j) T. Sagawa, S. Fukugawa, T. Yamada and H. Ihara, *Langmuir*, 2002, **18**, 7223; (k) K. Sugiyasu, N. Fujita, M. Takeuchi, S. Yamada and S. Shinkai, *Org. Biomol. Chem.*, 2003, **1**, 895; (l) A. Ajayaghosh and S. J. George, *J. Am. Chem. Soc.*, 2001, **123**, 5148; (m) S. J. George and A. Ajayaghosh, *Chem.–Eur. J.*, 2005, **11**, 3217; (n) V. K. Praveen, S. J. George and A. Ajayaghosh, *Macromol. Symp.*, 2006, **241**, 1.

16. (a) K. Murata, M. Aoki, T. Nishi, A. Ikeda and S. Shinkai, *Chem. Commun.*, 1991, 1715; (b) K. Murata, M. Aoki, T. Suzuki, T. Harada, H. Kawabata, T. Komori, F. Ohseto, K. Ueda and S. Shinkai, *J. Am. Chem. Soc.*, 1994, **116**, 6664.

17. (a) H. B. Aiyappa, S. Saha, P. Wadge, R. Banerjee and S. Kurungot, *Chem. Sci.*, 2015, **6**, 603; (b) S. Saha, G. Das, J. Thote and R. Banerjee, *J. Am. Chem. Soc.*, 2014, **136**, 14845; (c) H. B. Aiyappa, S. Saha, B. Garai, J. Thote, S. Kurungot and R. Banerjee, *Cryst. Growth Des.*, 2014, **14**, 3434; (d) S. Saha, J. Bachl, T. Kundu, D. Díaz Díaz and R. Banerjee, *Chem. Commun.*, 2014, **50**, 7032; (e) S. Saha, J. Bachl, T. Kundu, D. Díaz Díaz and R. Banerjee, *Chem. Commun.*, 2014, **50**, 3004; (f) S. Saha, E.-M. Schön, C. Cattivola, D. Díaz Díaz and R. Banerjee, *Chem. – Eur. J.*, 2013, **19**, 9562; (g) R. J. H. Hafkamp, B. P. A. Kokke, I. M. Danke, H. P. M. Geurts, A. E. Rowan, M. C. Feiters and R. J. M. Nolte, *Chem. Commun.*, 1997, 545; (h) N. Fujita, Y. Sakamoto, M. Shirakawa, M. Ojima,

A. Fujii, M. Ozaki and S. Shinkai, *J. Am. Chem. Soc.*, 2007, **129**, 4134; (i) M. Shirakawa, N. Fujita, T. Tani, K. Kaneko and S. Shinkai, *Chem. Commun.*, 2005, 4149; (j) P. Terech, G. Gebel and R. Ramasseul, *Langmuir*, 1996, **12**, 4321.

18. (a) T. Kishida, N. Fujita, K. Sada and S. Shinkai, *Langmuir*, 2005, **21**, 9432; (b) T. Kishida, N. Fujita, K. Sada and S. Shinkai, *J. Am. Chem. Soc.*, 2005, **127**, 7298; (c) M. Shirakawa, S. Kawano, N. Fujita, K. Sada and S. Shinkai, *J. Org. Chem.*, 2003, **68**, 5037.

19. (a) K. Tsuchiya, Y. Orihara, Y. Kondo, N. Yoshino, T. Ohkubo, H. Sakai and M. Abe, *J. Am. Chem. Soc.*, 2004, 126, 12282, DOI: 10.1021/ja0467162; (b) R. J. H. Hafkamp, B. P. A. Kokke, I. M. Danke, H. P. M. Geurts, A. E. Rowan, M. C. Feiters and R. J. M. Nolte, *Chem. Commun.*, 1997, 545; (b) A. Y. Y. Tam, K. M. C. Wong, G. X. Wang and V. W. W. Yam, *Chem. Commun.*, 2007, 2028.

20. (a) B. Xing, M.-F. Choi and B. Xu, *Chem. – Eur. J.*, 2002, **8**, 5028; (b) M. George, G. P. Funkhouser, P. Terech and R. G. Weiss, *Langmuir*, 2006, **22**, 7885; (c) Q. Wei and S. L. James, *Chem. Commun.*, 2005, 1555; (d) S. K. Nune, P. K. Thallapally and B. P. McGrail, *J. Mater. Chem.*, 2010, **20**, 7623; (e) T. Tu, W. Fang, X. Bao, X. Li and K. H. Dötz, *Angew. Chem., Int. Ed.*, 2011, **50**, 6601; (f) C. Po, Z. Ke, A. Y.-Y. Tam, H.-F. Chow and V. W.-W. Yam, *Chem. – Eur. J.*, 2013, **19**, 15735; (g) S. Sarkar, S. Dutta, S. Chakrabarti, P. Bairi and T. Pal, *ACS Appl. Mater. Interfaces*, 2014, **6**, 6308.

21. (a) R. Haldar and T. K. Maji, *CrystEngComm*, 2013, 15, 9276; (b) Themed Issue: Metal–organic Frameworks, *Chem. Rev.*, 2012, **112**, 673; (c) R. Haldar, K. Prasad, P. Samanta, S. K. Pati and T. K. Maji, *Cryst. Growth Des.*, 2016, **16**, 82.

22. (a) S. Roy, V. M. Suresh and T. K. Maji, *Chem. Sci.*, 2016, **7**, 2251; (b) A. Chakraborty, S. Bhattacharyya, A. Hazra, A. C. Ghosh and T. K. Maji, *Chem. Commun.*, 2016, **52**, 2831; (c) S. Bhattacharyya, A. Chakraborty, K. Jayaramulu, A. Hazra and T. K. Maji, *Chem. Commun.*, 2014, **50**, 13567; (d) R. Haldar, R. Matsuda, S. Kitagawa, S. J. George and T. K. Maji, *Angew. Chem., Int. Ed.*, 2014, **126**, 11966; (e) N. Sikdar, K. Jayaramulu, V. Kiran, K. V. Rao, S. Sampath, S. J. George and T. K. Maji, *Chem. – Eur. J.*, 2015, **21**, 11701; (f) A. Hazra, K. L. Gurunatha and T. K. Maji, *Cryst. Growth Des.*, 2013, **13**, 4824.

23. (a) M. Maity and U. Maitra, *J. Mater. Chem. A*, 2014, **2**, 18952; (b) W. Fang, C. Liu, Z. Lu, Z. Sun and T. Tu, *Chem. Commun.*, 2014, **50**, 10118; (c) S. Bhattacharjee and S. Bhattacharya, *Chem. Commun.*, 2014, **50**, 11690; (d) I. U. Arachchige and S. L. Brock, *J. Am. Chem. Soc.*, 2007, **129**, 1840; (e) W. J. Peveler, J. C. Bear, P. Southern and I. P.

Parkin, *Chem. Commun.*, 2014, **50**, 14418; (f) Z. Xie, F. Wang and C.-y. Liu, *Adv. Mater.*, 2012, **24**, 1716.

24. (a) Z. Yang, G. Liang, L. Wang and B. Xu, *J. Am. Chem. Soc.*, 2006, **128**, 3038; (b) B. Joddar and Y. Ito, *J. Mater. Chem.*, 2011, **21**, 13737; (c) H. Lee, J. H. Lee, S. Kang, J. Y. Lee, G. John and J. H. Jung, *Chem. Commun.*, 2011, **47**, 2937.

25. (a) *Self-healing Materials: An Alternative Approach to 20 Centuries of Materials Science*, ed. S. Van der Zwaag, Springer, Dordrecht, 2007; (b) J. M. Lehn, *Prog. Polym. Sci.*, 2005, **30**, 814; (c) A. Phadke, C. Zhang, B. Arman, C.-C. Hsu, R. A. Mashelkar, A. K. Lele, M. J. Tauber, G. Arya and S. Varghese, *Proc. Natl. Acad. Sci. U. S. A.*, 2012, **109**, 4383; (d) N. H. Andersen, M. J. Harrington, H. Birkedal, B. P. Lee, P. B. Messersmith, K. Y. C. Lee and J. H. Waite, *Proc. Natl. Acad. Sci. U. S. A.*, 2011, **108**, 2651; (e) M. Krogsgaard, M. A. Behrens, J. S. Pedersen and H. Birkedal, 2013, **14**, 297; (f) W. Maret, K. S. Larsen and B. L. Vallee, *Proc. Natl. Acad. Sci. U. S. A.*, 1997, **94**, 2233; (g) W. Maret and Y. Li, *Chem. Rev.*, 2009, **109**, 4682; (h) D. H. Busch, *Acc. Chem. Res.*, 1978, **11**, 392; (i) L. Yan, L. Shen, M. Lv, W. Yu, J. Chen, S. Wang, X. Fu and Z. Ye, *Chem. Commun.*, 2015, **51**, 17627; (j) L. Yan, S. Gou, Z. Ye, S. Zhang and L. Ma, *Chem. Commun.*, 2014, **50**, 12847-12850.

26. (a) H. Lee, S. H. Jung, W. S. Han, J. H. Moon, S. Kang, J. Y. Lee, J. H. Jung and S. Shinkai, *Chem. – Eur. J.*, 2011, **17**, 2823; (b) S. Barman, J. A. Garg, O. Blacque, K. Venkatesan and H. Berke, *Chem. Commun.*, 2012, **48**, 11127.

27. (a) J. H. Lee, S. Kang, J. Y. Lee and J. H. Jung, *Soft Matter*, 2012, **8**, 6557; (b) A. Mallick, E.-M. Schön, T. Panda, K. Sreenivas, D. Di'az Di'az and R. Banerjee, *J. Mater. Chem.*, 2012, **22**, 14951; (c) Yamada, Y. M. A.; Maeda, Y.; Uozumi, Y. *Org. Lett.* 2006, **8**, 4259–4262. (d) Tu, T.; Assenmacher, W.; Peterli, K. H.; Weisbarth, R.; Nieger, M.; Do'tz, K. H. *Angew. Chem., Int. Ed.* 2007, **46**, 6368–6371. (e) Tu, T.; Assenmacher, W.; Peterlik, H.; Schnakenburg, G.; Do'tz, K. H. *Angew. Chem., Int. Ed.* 2008, **47**, 7127–7131. (f) Xing, B.; Choi, M.-F.; Xu, B. *Chem. Eur. J.* 2002, **8**, 5028–5032. (g) Miravet, J. F.; Escuder, B. *Chem. Commun.* 2005, 5796–5798; (h) Rodríguez-Llansola, F.; Escuder, B.; Miravet, J. F. *J. Am. Chem. Soc.* 2009, **131**, 11478–11484.

28. (a) W. L. Leong, A. Y.-Y. Tam, S. K. Batabyal, L. W. Koh, S. Kasapis, V. W.-W. Yam and J. J. Vittal, *Chem. Commun.*, 2008, 3628; (b) V. M. Suresh, A. De and T. K. Maj, *Chem. Commun.*, 2015, **51**, 14678; (c) O. Kotova, R. Daly, C. M. G. dos Santos, M. Boese, P. E. Kruger, J. J. Boland and T. Gunnlaugsson, *Angew. Chem., Int. Ed.*, 2012, **51**, 7208. (d) M. M. Calvo, O. Kotova, M. E. Mobius, A. P. Bell, T. McCabe, J. J. Boland and

T. Gunnlaugsson, *J. Am. Chem. Soc.*, 2015, **137**, 1983; (e) P. Chen, Q. Li, S. Grindy and N. H. Andersen, *J. Am. Chem. Soc.*, 2015, **137**, 11590; (f) P. Sutar, V. M. Suresh and T. K. Maji, *Chem. Commun.*, 2015, **51**, 9876.

29. (a) J. J. Perry Iv, J. A. Perman and M. J. Zaworotko, *Chem. Soc. Rev.*, 2009, **38**, 1400–1417; (b) T. R. Cook, Y.-R. Zheng and P. J. Stang, *Chem. Rev.*, 2012, **113**, 734–777; (c) C. M. Vetromile, A. Lozano, S. Feola and R. W. Larsen, *Inorg. Chim. Acta*, 2011, **378**, 36–41; (d) T. Kikuchi, S. Sato and M. Fujita, *J. Am. Chem. Soc.*, 2010, **132**, 15930–15932; (e) C. He, Z. Lin, Z. He, C. Duan, C. Xu, Z. Wang and C. Yan, *Angew. Chem., Int. Ed.*, 2008, **47**, 877–881; (f) M. J. Prakash and M. S. Lah, *Chem. Commun.*, 2009, 3326–3341; (g) Q.-F. Sun, J. Iwasa, D. Ogawa, Y. Ishido, S. Sato, T. Ozeki, Y. Sei, K. Yamaguchi and M. Fujita, *Science*, 2010, **328**, 1144–1147; (h) M. H. Alkordi, J. L. Belof, E. Rivera, L. Wojtas and M. Eddaoudi, *Chem. Sci.*, 2011, **2**, 1695–1705.

30. (a) D. J. Tranchemontagne, Z. Ni, M. O’Keeffe and O. M. Yaghi, *Angew. Chem., Int. Ed.*, 2008, **47**, 5136–5147; (b) K. Harris, D. Fujita and M. Fujita, *Chem. Commun.*, 2013, **49**, 6703–6712; (c) M. M. Smulders, I. A. Riddell, C. Browne and J. R. Nitschke, *Chem. Soc. Rev.*, 2013, **42**, 1728–1754; (d) N. Ahmad, A. H. Chughtai, H. A. Younus and F. Verpoort, *Coord. Chem. Rev.*, 2014, **280**, 1–27; (e) M. Liu, W. Liao, C. Hu, S. Du, and H. Zhang, *Angew. Chem. Int. Ed.*, 2012, **51**, 1585–1588; (f) S. –T. Zheng, T. Wu, B. Irfanoglu, F. Zuo, P. Feng, and X. Bu, *Angew. Chem. Int. Ed.*, 2011, **50**, 8034–8037

31. (a) D. F. Sava, V. C. Kravtsov, J. Eckert, J. F. Eubank, F. Nouar, and M. Eddaoudi, *J. Am. Chem. Soc.*, 2009, **131**, 10394–10396; (b) Y. Liu, V. Kravtsov, R. D. Walsh, P. Poddar, H. Srikanthc and M. Eddaoudi, *Chem. Commun.*, 2004, 2806–2807; (c) M. H. Alkordi, J. A. Brant, L. Wojtas, V. C. Kravtsov, A. J. Cairns, and M. Eddaoudi, *J. Am. Chem. Soc.* 2009, **131**, 17753–17755; (d) S. –T. Zheng, J. Zhang, X. –X. Li, W. –H. Fang, and G. –Y. Yang, *J. Am. Chem. Soc.*, 2010, **132**, 15102–15103.

32. (a) Y. R. Hristova, M. M. J. Smulders, J. K. Clegg, B. Breiner and J. R. Nitschke, *Chem. Sci.*, 2011, **2**, 638–641; (b) S. Ma, M. M. Smulders, Y. R. Hristova, J. K. Clegg, T. K. Ronson, S. Zarra and J. R. Nitschke, *J. Am. Chem. Soc.*, 2013, **135**, 5678–5684; (c) I. A. Riddell, M. M. Smulders, J. K. Clegg, Y. R. Hristova, B. Breiner, J. D. Thoburn and J. R. Nitschke, *Nat. Chem.*, 2012, **4**, 751–756; (d) A. Mallick, B. Garai, D. D. Díaz and R. Banerjee, *Angew. Chem., Int. Ed.*, 2013, **52**, 13755–13759.

33. (a) T. M. Fyles, *Chem. Soc. Rev.*, 2007, **36**, 335–347; (b) M. R. Ghadiri, J. R. Granja and L. K. Buehler, *Nature*, 1994, **369**, 301–304; (c) G.W. Gokel and S. Negin, *Acc. Chem. Res.*, 2013, **46**, 2824–2833; (d) N. Sakai and S. Matile, *Angew. Chem., Int. Ed.*,

- 2008, **47**, 9603–9607; (e) H. Furukawa, J. Kim, K. E. Plass and O. M. Yaghi, *J. Am. Chem. Soc.*, 2006, **128**, 8398–8399; (f) R. Kawano, S. Furukawa, D. Kiriya, T. Osaki, K. Kamiya, S. Kitagawa and S. Takeuchi, Synthetic nanocage formed by rhodium-organic cuboctahedra: For single molecule detection in lipid bilayer, *Solid-State Sensors, Actuators and Microsystems (TRANSDUCERS & EUROSENSORS XXVII)*, 2013 *Transducers & Eurosensors XXVII* The 17th International Conference, IEEE, Barcelona, Spain, 16–20 June 2013*, pp. 854–855, DOI: 10.1109/Transducers.2013.6626901; (g) M. Jung, H. Kim, K. Baek, and K. Kim, *Angew. Chem. Int. Ed.*, 2008, **47**, 5755–5757.
34. (a) J. A. Asensio, E. M. Sánchez and P. Gómez-Romero, *Chem. Soc. Rev.*, 2010, **39**, 3210–3239; (b) S. R. Narayanan, S. –P. Yen, L. Liu, and S. G. Greenbaum, *Phys. Chem. B*, 2006, **110**, 3942–3948; (c) “*Proton Conductors: Solids, Membranes and Gels-Materials and Devices*”: P. Colomban in *Chemistry of Solid State Materials*, Vol. 2, Cambridge University Press, Cambridge, 1992; (d) K. D. Kreuer, *Chem. Mater.*, 1996, **8**, 610–641; (e) K. D. Kreuer, S. J. Paddison, E. Spohr and M. Schuster, *Chem. Rev.* 2004, **104**, 4637–4678; (f) S. H. Kim, A. Mehmood, Y. Ahn, H.-S. Kim, H. Y. Ha, D. Kim and O. H. Han, *J. Electroanal. Chem.*, 2016, **782**, 32–35; (g) C. H. Lee, H. B. Park, Y. M. Lee and R. D. Lee, *Ind. Eng. Chem. Res.*, 2005, **44**, 7617–7626; (h) Y. –L. Liu, *Polym. Chem.*, 2012, **3**, 1373–1383; (i) S. P. Jiang, *J. Mater. Chem. A*, 2014, **2**, 7637–7655; (j) R. He, Q. Li, G. Xiao and N. J. Bjerrum, *J. Membr. Sci.*, 2003, **226**, 169–184; (k) S. J. Paddison, *Annu. Rev. Mater. Res.*, 2003, **33**, 289 – 319; (l) S. J. Peighambardoust, S. Rowshanzamir, M. Amjadi, *Int. J. Hydrogen Energy.*, 2010, **35**, 9349 – 9384.
35. (a) M. Yoon, K. Suh, S. Natarajan and K. Kim, *Angew. Chem. Int. Ed.*, 2013, **52**, 2688 – 2700; (b) S. S. Nagarkar, S. M. Unni, A. Sharma, S. Kurungot, and S. K. Ghosh, *Angew. Chem. Int. Ed.* 2014, **53**, 2638 –2642; (c) P. Ramaswamy, R. Matsuda, W. Kosaka, G. Akiyama, H. J. Jeona and S. Kitagawa, *Chem. Commun.*, 2014, **50**, 1144–1146; (d) P. Ramaswamy, N. E. Wong and G. K. H. Shimizu, *Chem. Soc. Rev.*, 2014, **43**, 5913–5932; (e) V. G. Ponomareva, K. A. Kovalenko, A. P. Chupakhin, D. N. Dybtsev, E. S. Shutova and V. P. Fedin, *J. Am. Chem. Soc.*, 2012, **134**, 15640–15643; (f) D. B. Shinde, H. B. Aiyappa, M. Bhadra, B. P. Biswal, P. Wadge, S. Kandambeth, B. Garai, T. Kundu, S. Kurungot and R. Banerjee, *J. Mater. Chem. A.*, 2016, **4**, 2682–2690; (g) H. Xu, S. Tao and D. Jiang, *Nature Mater.*, 2016, **15**, 722–726; (h) H. Ma, B. Liu, B. Li, L. Zhang, Y.-G. Li, H.-Q. Tan, H.-Y. Zang and G. Zhu, *J. Am. Chem. Soc.*, 2016, **138**, 5897–5903; (i) S. Chandra, T. Kundu, K. Dey, M. Addicoat, T. Heine and R. Banerjee,

Chem. Mater., 2016, **28**, 1489–1494; (j) A. Karmakar, R. Illathvalappil, B. Anothumakkool, A. Sen, P. Samanta, A. V. Desai, S. Kurungot, S. K. Ghosh, *Angew. Chem. Int. Ed.*, 2016, **55**, 10667–10671; (k) M. Sadakiyo, T. Yamada and H. Kitagawa, *J. Am. Chem. Soc.*, 2009, **131**, 9906–9907; (l) S. Kim, K. W. Dawson, B. S. Gelfand, J. M. Taylor, G. K. H. Shimizu, *J. Am. Chem. Soc.* 2013, **135**, 963 – 966; (m) Q.-G. Zhai, C. Mao, X. Zhao, Q. Lin, F. Bu, X. Chen, X. Bu, and P. Feng, *Angew. Chem. Int. Ed.*, 2015, **54**, 7886–789.

36. (a) J. Wang, C. He, P. Wu, J. Wang and C. Duan, *J. Am. Chem. Soc.*, 2011, **133**, 12402–12405; (b) D. Zhao, S. Tan, D. Yuan, W. Lu, Y. H. Rezenom, H. Jiang, L. –Q. Wang, and H. –C. Zhou, *Adv. Mater.* 2011, **23**, 90–93.

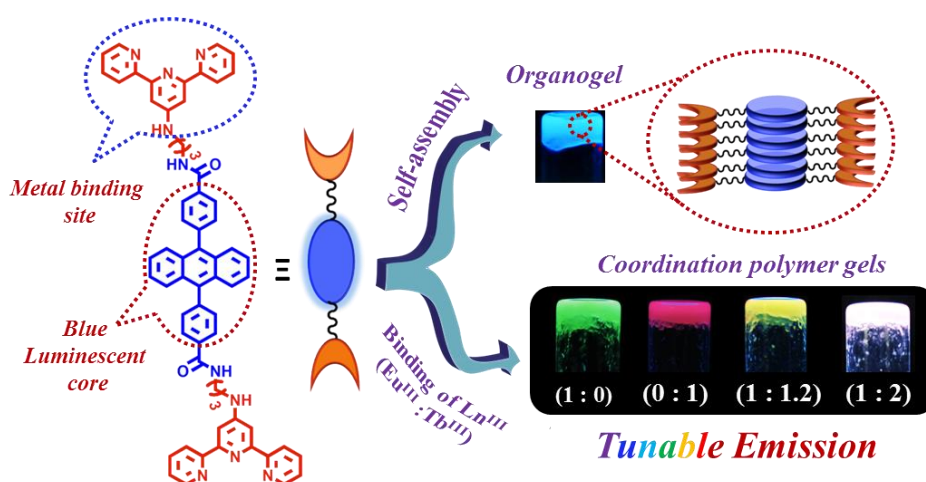
37. (a) A. V. Zhukhovitskiy, M. Zhong, E. G. Keeler, V. K. Michaelis, J. E. P. Sun, M. J. A. Hore, D. J. Pochan, R. G. Griffin, A. P. Willard and J. A. Johnson, *Nat. Chem.*, 2016, **8**, 33–41; (b) Y. Wang, Y. Gu, E. G. Keeler, J. V. Park, R. G. Griffin, and J. A. Johnson, *Angew. Chem. Int. Ed.*, 2017, **56**, 188 –192; (c) A. V. Zhukhovitskiy, J. Zhao, M. Zhong, E. G. Keeler, Eric A. Alt, P. Teichen, R. G. Griffin, M. J. A. Hore, A. P. Willard, and J. A. Johnson, *Macromolecules* 2016, **49**, 6896–6902; (d) Y. Wang, M. Zhong, J. V. Park, A. V. Zhukhovitskiy, W. Shi, and J. A. Johnson, *J. Am. Chem. Soc.* 2016, **138**, 10708–10715; (e) J. A. Foster, R. M. Parker, A. M. Belenguer, N. Kishi, S. Sutton, C. Abell, and J. R. Nitschke, *J. Am. Chem. Soc.* 2015, **137**, 9722–9729.

Chapter 2

Tunable Emission in Lanthanide Coordination Polymer Gels Based on a Rationally Designed Blue Emissive Gelator

Abstract

This chapter reports rational design and synthesis of a blue emitting LMWG (**L**) having 9,10-diphenylanthracene core and terminal terpyridine groups. Self-assembly of **L** in organic solvents results in organogel which exhibits nanofiber morphology. Coordination of Tb^{III} and Eu^{III} ion to LMWG leads to the formation of green and pink emissive coordination polymer gels (CPGs), respectively which show coiled nanofiber morphology. Moreover, coordination of both Tb^{III} and Eu^{III} to LMWG yields bimetallic CPGs in which precise stoichiometric control over LMWG: Eu^{III}: Tb^{III} leads to tunable yellow and white emitting bimetallic CPGs. High processability of CPGs is utilized for large area coating applications. Moreover, a white-light emitting LED has been fabricated through mere coating of white-light emitting CPG over a commercial blue LED.



Paper published based on this work:

P. Sutar, V. M. Suresh and T. K. Maji, *Chem. Commun.*, **2015**, 51, 9876-9879.

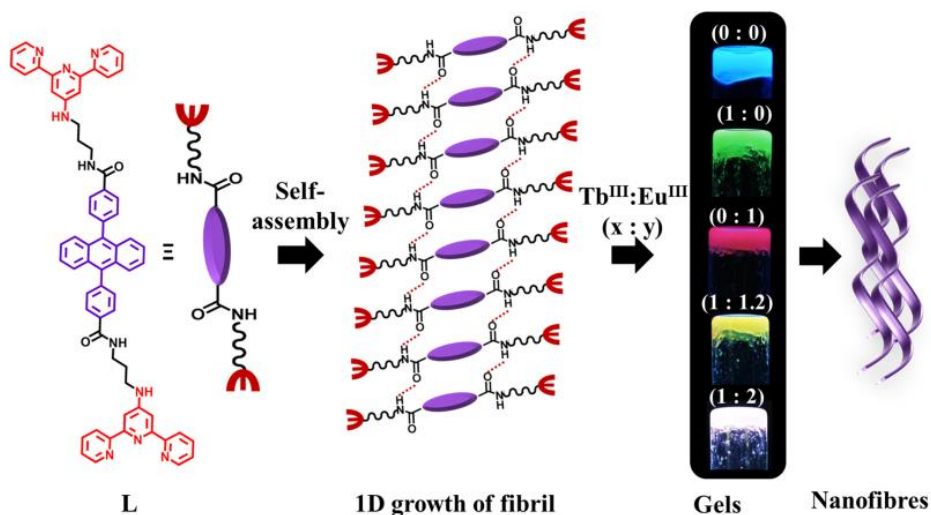
2.1 INTRODUCTION

Over past few decades, enormous research interest has been directed towards the development of new functional supramolecular gels from low molecular weight gelators (LMWGs).¹ Easy solution processability and dynamic nature of such soft materials hold great promise for applications in diverse fields, including biomedicine, nanoelectronics and catalysis.² Recently, the concept of coordination polymer gels (CPGs) has been emerged where coordination of metal ions to a suitably designed LMWG results in supramolecular self-assembled networks.³ Such soft organic-inorganic hybrids are highly promising since the incorporation of metal ions renders an opportunity to emulate its unique redox, optical, electronic and magnetic properties in supramolecular gels.^{3a, 4} Particularly, metallo gels of lanthanide ions (Ln^{III}) are of specific interest as they show narrow band emissions (red: Eu^{III} , Pr^{III} , Sm^{III} ; green: Tb^{III} , Er^{III} ; blue: Tm^{III} , Ce^{III}) with high quantum yields when binded to suitable π -chromophoric linkers.⁵ Such unique emission properties of Ln^{III} ions, stemming from sensitized f-f electronic transition have been investigated in bulk crystalline coordination polymers and exploited for solid state lighting and sensing applications.⁶ However, low solution processability greatly limits their application in device fabrication and biological sciences. In this regard, lanthanide coordination polymer gels (Ln^{III} CPGs) are superior as reversible sol-gel behaviour with enhanced processability would facilitate easy fabrication of large-area and flexible displays, portable sensing kits.

Recently, white-light-emitting materials have merited immense research interest due to their potential application in solid state lighting.⁷ White-light-emitting materials can be trichromatic in which blue, green and red light emitting components are introduced to cover the entire visible spectral window. Such materials are superior compared to the monochromatic (that emits entire visible regions) and dichromatic (that emit in blue and yellow regions) materials due to the finer colour rendering properties and high quantum efficiencies.⁸ To date a handful of trichromatic white light emitting materials, suitable for solid state lighting applications have been reported.⁷ However, realization of white-light-emission based on CPG is yet to be accounted.

In this chapter, the rational design of a new LMWG, 9,10-(4-carboxyphenyl)anthracenedi- $\{[3-([2,2':6',2'']\text{terpyridin-4'ylamino})\text{-propyl}]\text{-amide}$ (**L**) having a blue emitting 9,10-diphenylanthracene core and terminal terpyridine groups and its gelation properties have been reported. Coordination of **L** through terpyridine with

Tb^{III} and Eu^{III} resulted in CPGs (**TbL** and **EuL**) which showed green and pink emission respectively. Moreover, coordination of both Tb^{III} and Eu^{III} to **L** yielded bimetallic CPGs (**TbEu1**, **TbEu2**) in which precise stoichiometric control over **L**: Eu^{III}: Tb^{III} ratio led to tunable yellow and white emissions (Scheme 1).



Scheme 1. Schematic showing self-assembly of **L** through H-bonding and π - π stacking interactions and its coordination to Ln^{III} forming luminescent CPGs.

2.2 EXPERIMENTAL SECTION

2.2.1 Materials

9,10-dibromoanthracene, 4-carboxyphenyl boronic acid, 1,3-diaminopropane, 4'-chloro-2,2':6',2''-terpyridine, trichloroisocyanuric acid (TCIC) and triphenylphosphine (PPh₃) were purchased from Sigma-Aldrich chemical Co. Ltd. Solvents were pre-dried using standard procedures before using. For UV-Vis experiments, spectroscopic grade solvents were purchased from Spectrochem.

2.2.2 Physical measurements

¹H-NMR was recorded on a Bruker AV-400 spectrometer with chemical shifts recorded as ppm and all spectra were calibrated against TMS. High resolution mass spectra (HRMS) was recorded on Agilent 6538 Ultra High Definition (UHD) Accurate-Mass Q-TOF-LC/MS system using electrospray ionization (ESI) modes. Elemental analysis was performed on a Thermo Fisher Flash 2000 Elemental Analyser. UV-Vis spectra were recorded in a Perkin-Elmer lambda 900 spectrometer. Fluorescence studies were accomplished using Perkin Elmer Ls 55 luminescence spectrometer. Fourier

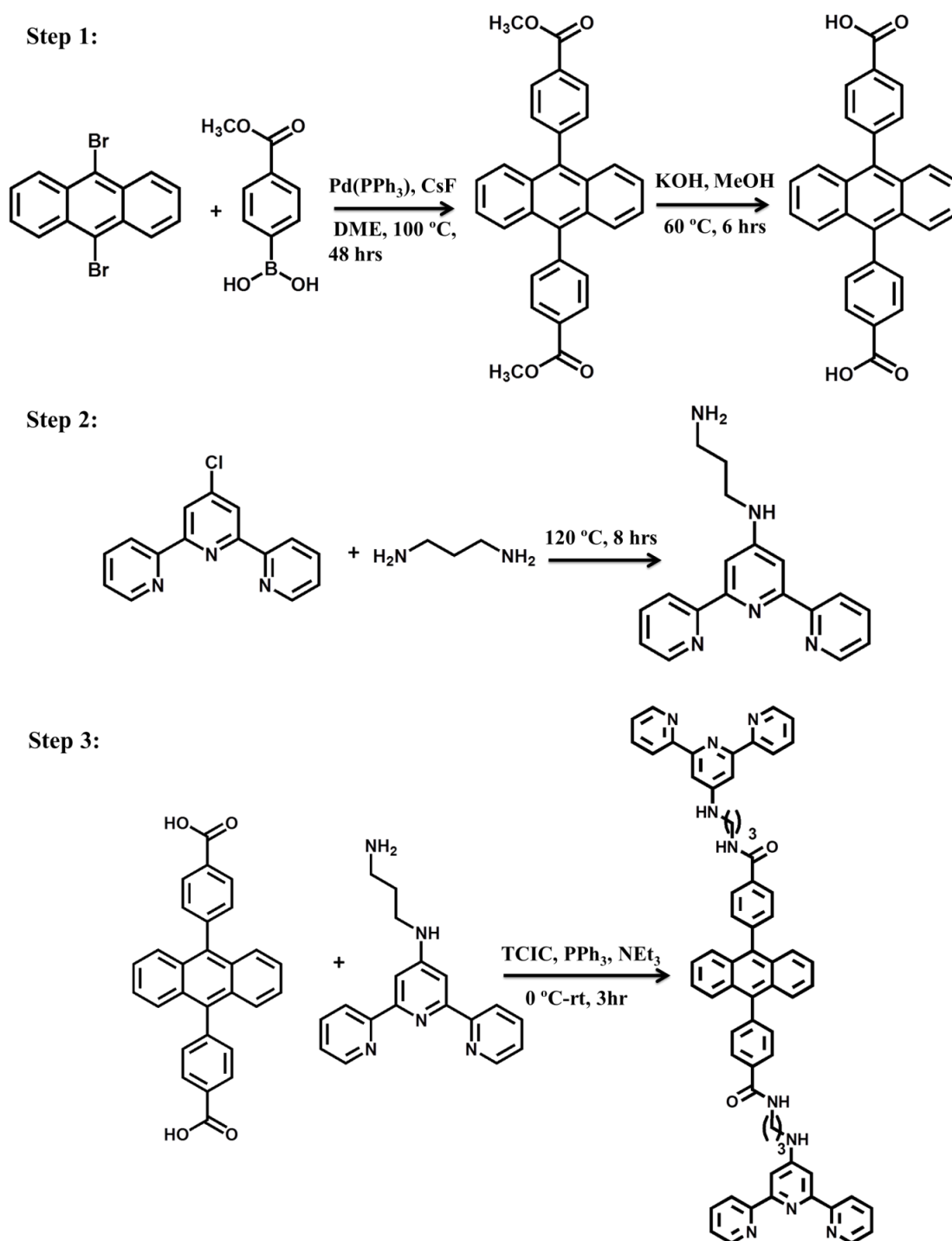
transform infrared spectra (FTIR) analyses were carried out by making samples with KBr pellets using Bruker FTIR spectrometer. Powder X-ray diffraction (PXRD) studies were recorded on a Bruker D8 discover instrument using Cu-K α radiation. The elemental analyses were carried out using a Thermo Scientific Flash 2000 CHN analyzer. Morphology studies were carried out using Lica-S440I field emission scanning electron microscopy (FESEM) by placing samples on silicon wafer under vacuum with accelerating voltage of 10 kV. Energy dispersive X-ray spectroscopy (EDXS) analysis was performed with an EDAX genesis instrument attached to the FESEM column. Transmission electron microscopy (TEM) analyses were performed using JEOL JEM-3010 with accelerating voltage of 300 kV. For this analysis the xerogels were dispersed in ethanol and then drop casted on a carbon coated copper grid.

2.2.3 Synthesis

Synthesis of 9,10-(4-carboxyphenyl)anthracene: 9,10-dibromoanthracene (740 mg, 2.2 mmol), methyl-4-carboxyphenyl boronic acid (1 g, 5.5 mmol), CsF (4 g, 2.7 mmol) and Pd(PPh₃)₄ (200 mg, 0.17 mmol) were suspended in 1,2-dimethoxyethane (30 ml). The reaction mixture was refluxed at 100 °C for 48 hours maintaining the inert condition. After that, the reaction mixture was cooled to room temperature and 100 ml H₂O was added to dissolve the excess CsF, and the organic product was extracted by CHCl₃. Pure 9,10-(methyl-4-carboxyphenyl)anthracene was obtained after running the crude product through column using CHCl₃/hexane as eluent. Yield: 96%. The as-prepared 9,10-(methyl-4-carboxyphenyl) anthracene (563 mg, 1.26 mmol) was suspended in 30 ml MeOH containing KOH (425 mg, 7.56 mmol) and the reaction mixture was refluxed at 60° C for 6 hours. After cooling to room temperature 6 N HCl was added drop-wise into the reaction mixture. The white precipitate formed was filtered and washed repeatedly by cold water and dried under vacuum. Yield: 96 %. ¹H-NMR (400 MHz, CDCl₃) δ : 8.23 (d, 4H, ArH), 7.62 (m, 4H, ArH), 7.55 (m, 4H, ArH), 7.46 (m, 4H, ArH), 13.11 (br, 2H, COOH). Selected FTIR data (KBr, cm⁻¹): 2986 (b), 2667 (m), 2547 (m), 1688 (s, sh), 1608 (s), 1425 (m), 1291 (m), 769 (m). CHN analysis for C₂₈H₁₈O₄: Calc. C, 80.38; H, 4.30%. Expt.: C, 80.85; H, 4.12%.

Synthesis of 2,2':6',2''-terpyridin-4'-yl-propane-1,3-diamine: 4'-chloro-2,2':6',2''-terpyridine, (300 mg, 1.12 mmol) was suspended in 1,3-diamino propane (2.16 ml). The reaction mixture was then refluxed at 120 °C for overnight. After cooling to room temperature, H₂O (25 mL) was added. The white precipitate formed was filtered

and further washed with H₂O. The solid was dissolved in dichloromethane and extracted twice with H₂O. The organic layers were combined and dried over Na₂SO₄, filtered and the solvent was removed under reduced pressure to yield a white solid product. Yield: 82%. ¹H-NMR (400 MHz, CDCl₃) δ: 8.53 (d, 2H, ArH), 8.52 (d, 2H, ArH), 7.76 (t, 2H,



Scheme 2. Synthetic scheme for 9,10-(4-carboxyphenyl)anthracene-di-{{3-([2,2':6',2'']-terpyridin-4'-ylamino)-propyl}-amide} (**L**).

ArH), 7.60 (s, 2H, ArH), 7.25 (t, 2H, ArH), 5.16 (t, 1H, NH), 3.41 (m, 2H, NHCH₂), 2.84 (m, 2H, CH₂), 1.77 (m, 2H, NH₂CH₂). Selected FTIR data (KBr, cm⁻¹): 3340 (b), 2965 (m), 1610-1560 (s), 1464 (m), 1402 (m), 1261 (m), 1094-981 (s), 791 (s). CHN analysis for C₁₈H₁₉N₅ Calc.: C, 70.81; H, 6.22; N, 22.95%. Expt.: C, 70.90; H, 6.11; N, 22.83%.

Synthesis of 9,10-(4-carboxyphenyl)anthracene-di-[[3-([2,2':6',2'']-terpyridin-4'-ylamino)-propyl]-amide} (L) : 9,10-(4-carboxyphenyl)anthracene (200 mg, 0.478 mmol) was dissolved in anhydrous THF (20 mL). TCIC (244 mg, 1.05 mmol) and PPh₃ (275 mg, 1.05 mmol) were added into the reaction mixture and stirred at 0 °C for 40 min under inert condition. 2,2':6',2''-terpyridin-4'-yl-propane-1,3-diamine (320 mg, 1.05 mmol) was dissolved into anhydrous THF and Et₃N (293 μl, 2.1 mmol) was added into it. This reaction mixture was drop-wise added into 9,10-(4-carboxyphenyl)anthracene/TCIC/PPh₃ solution at 0° C and stirred for 45 minutes. After that the reaction mixture was stirred at room temperature for 3 hrs. Precipitate was collected by filtration and washed several times with CHCl₃ and dried under vacuum. Yield: 88%. ¹H-NMR (400 MHz, CDCl₃) δ: 8.87 (s, 3H, ArH), 8.74 (d, 1H, ArH), 8.30 (m, 1H, ArH), 8.26 (m, 3H, ArH), 8.15 (m, 5H, ArH), 7.79 (s, 3H, ArH), 7.69 (m, 2H, ArH), 2.98 (m, 4H, NHCH₂), 1.99 (m, 2H, CH₂). Selected FTIR data (KBr, cm⁻¹): 3436 (m), 3239 (m), 2980- 2888 (m), 2740 (m), 2674 (s), 2493 (m), 1645 (s), 1583 (m), 1472 (m), 1396 (s), 1166 (s), 1135(s), 790 (s). CHN analysis for C₆₄H₅₂N₁₀O₂ Calc.: C, 77.41; H, 5.24; N, 14.11%. Expt.: C, 77.53; H, 5.33; N, 14.20%. HRMS (+ESI): *m/z* calculated for C₆₄H₅₂N₁₀O₂: 992.4275, found: 993.3209 [M+H]⁺.

Synthesis of organogel (OG): 1×10⁻³ M solution of **L** in 1:1 CHCl₃/THF mixture was heated at 90 °C for few minutes to form a viscous liquid which on cooling resulted in opaque gel (**OG**). The formation of gel was confirmed by inversion of test tube method. Selected FTIR data (KBr, cm⁻¹): 3424 (m), 3233 (s), 2968- 2831 (s), 2722 (s), 1638 (s), 1583 (s), 1461 (s), 1376 (s), 1166 (m), 973 (m), 841 (s), 792 (s).

Synthesis of coordination polymer gels (TbL and EuL): Solution of **L** (1×10⁻³ M) in CHCl₃/ THF (1:1) was mixed with solution of Tb(NO₃)₃.6H₂O or Eu(NO₃)₃.6H₂O (1×10⁻³ M, in THF) in 1:1 volumetric ratio. The mixture was heated at 90 °C for 3 minutes to prepare a viscous solution which eventually resulted in stable opaque gel upon cooling. Selected FTIR data (KBr, cm⁻¹): For **TbL** xerogel : 3400 (b), 2964- 2916 (m), 1624 (s), 1479 (s), 1383 (s), 1263 (s), 1103- 1019 (s), 804 (s). For **EuL** xerogel: 3400 (b), 2976- 2836 (m), 1630 (m), 1464 (m), 1166 (m), 972 (m), 839 (m). CHN analysis:

Calculated values for **TbL**: C, 58.33; H, 4.59; N, 12.28%. Found: C, 58.42; H, 4.61; N, 12.26%. Predicted formula: [Tb(L)(NO₃)₃.2THF]. Calculated values for **EuL**: C, 58.57; H, 4.61; N, 12.33%. Found: C, 58.62; H, 4.65; N, 12.38%. Predicted formula: [Eu(L)(NO₃)₃.2THF].

Synthesis of TbEu1 and TbEu2: First (1×10^{-3} M) and (1.2×10^{-3} M) solutions of Tb(NO₃)₃.6H₂O and Eu(NO₃)₃.6H₂O respectively were prepared by dissolving the metal salts in THF. After that 250 μ l solution of Tb(NO₃)₃.6H₂O and 250 μ l solution of Eu(NO₃)₃.6H₂O were added into 500 μ l solution of **L** (1×10^{-3} M). The mixture was heated at 90 °C for few minutes to form viscous solution which eventually converted to stable gel (**TbEu1**) after cooling. **TbEu2** was prepared in a similar way. First (1×10^{-3} M) and (2×10^{-3} M) solution of Tb(NO₃)₃.6H₂O and Eu(NO₃)₃.6H₂O respectively were prepared in THF. After that 250 μ l solution of Tb(NO₃)₃.6H₂O and 250 μ l solution of Eu(NO₃)₃.6H₂O were added into 500 μ l solution of **L** (1×10^{-3} M) and the mixture was heated at 90 °C for few minutes. The viscous solution formed was cooled and formed **TbEu2** coordination polymer gel. Selected FTIR data for **TbEu2** (KBr, cm⁻¹): 3421 (b), 2948- 2829 (m), 1628 (s), 1460 (m), 1161 (m), 974-838 (m), 735 (m).

2.3 RESULTS AND DISCUSSION

2.3.1 Photophysical properties of L

The anthracene based LMWG (**L**) was synthesized by amine coupling between 9,10-(4-carboxyphenyl)anthracene and 2,2':6',2''-terpyridin-4'-yl-propane-1,3-diamine (Scheme 2). The product was characterized using ¹H-NMR and HRMS. Methanolic solution of **L** (10^{-4} M) showed a broad absorption in the range 280-310 nm which was assigned to the π - π^* transition of 9,10-diphenylanthracene (ant) core and terminal

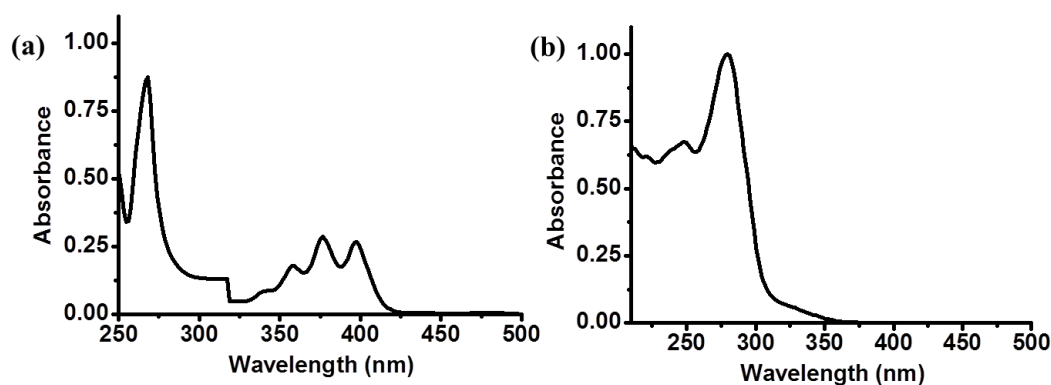


Figure 1. (a) Absorption spectra of 9,10-(4-carboxyphenyl)anthracene in DMSO, (b) absorption spectra of 2,2':6',2''-terpyridin-4'-yl-propane-1,3-diamine in MeOH.

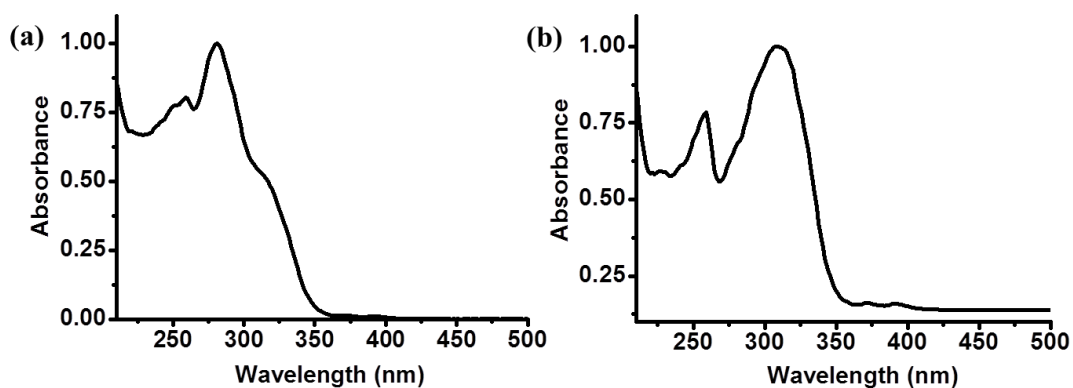


Figure 2. (a) Absorption spectra of **L** in MeOH , (b) Absorption spectra of **L** after subtracting the absorption spectra of 2,2':6',2''-terpyridin-4'-yl-propane-1,3-diamine which shows peak at 310 nm indicating π - π^* transition of ant core.

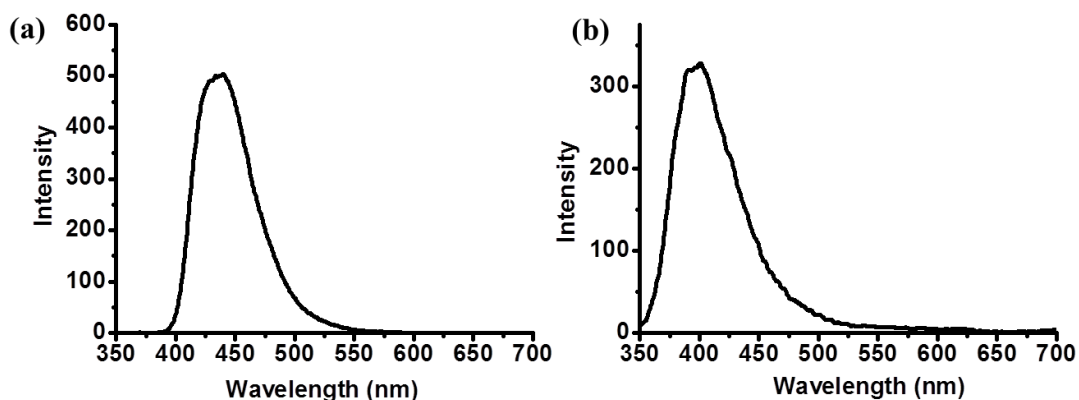


Figure 3. (a) Emission spectra of 9,10-(4-carboxyphenyl)anthracene in DMSO (10^{-4} M), (b) 2,2':6',2''-terpyridin-4'-yl-propane-1,3-diamine in MeOH (10^{-4} M).

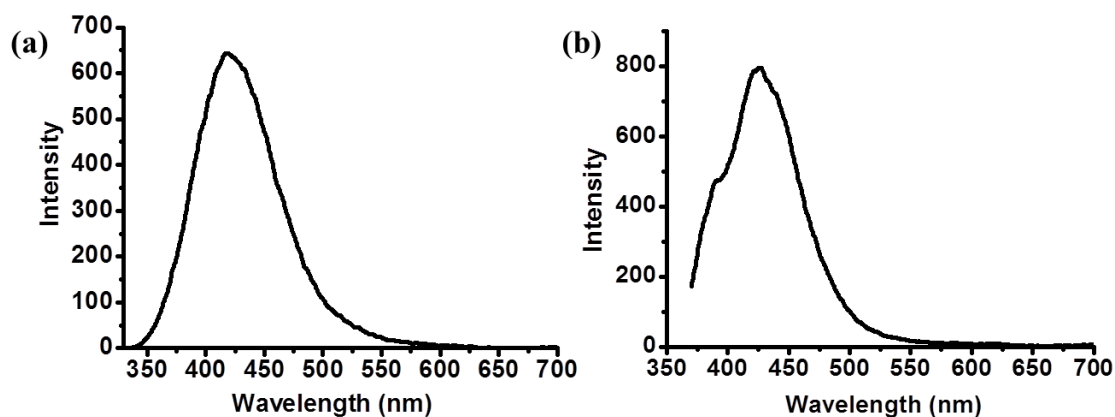


Figure 4. (a) Emission spectra of **L** in MeOH (10^{-4} M), (b) Combined emission spectra of 9,10-(4-carboxyphenyl)anthracene and 2,2':6',2''-terpyridin-4'-yl-propane-1,3-diamine . This indicates emission is originating from both ant and tpy.

terpyridine (tpy) groups (Figure 1 and Figure 2a). Absorption spectrum of **L** after subtracting the absorption spectra of 2,2':6',2''-terpyridin-4'-yl-propane-1,3-diamine showed clear presence of π - π^* transition of ant core (Figure 2b). Excitation at 280 nm resulted in strong blue emission with maxima at 428 nm which could be considered as combined emission from ant and tpy parts of **L** (Figure 3 and Figure 4).

2.3.2 Titration of **L** with Tb^{III} and Eu^{III} ions

Interaction of **L** with Tb^{III} ions was studied in methanol solution by gradually adding Tb^{III} (10^{-4} M) to solution of **L** (10^{-4} M) (Figure 5a). With incremental addition of Tb^{III}, absorption spectrum showed a significant bathochromic shift at 280 nm with appearance of a broad shoulder at 327 nm, suggesting complexation of Tb^{III} to the tpy groups of **L**.¹⁰ The corresponding emission spectra of the solution ($\lambda_{\text{ex}} = 280$ nm) showed a decrease in intensity at 428 nm with concomitant appearance of sharp peaks at 490 nm, 546 nm, 587 nm and 623 nm which could be attributed to $^5\text{D}_4$ - $^7\text{F}_J$ (J= 6-3) transitions of

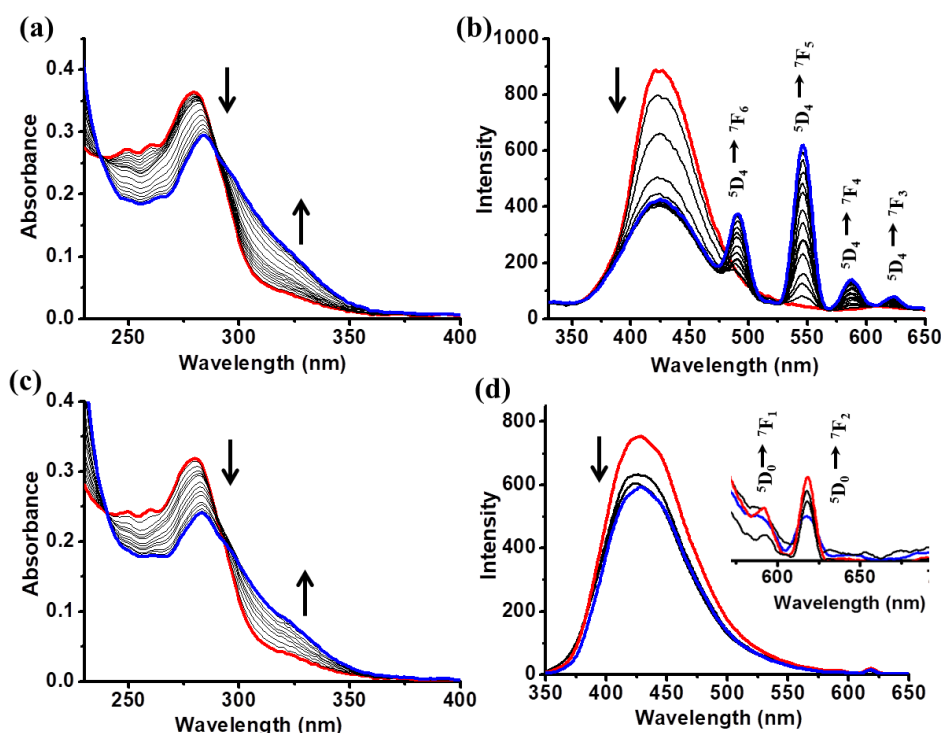


Figure 5. Spectral changes in (a) and (c) absorption and (b) and (d) emission spectra of **L** upon incremental addition of methanolic solution of Tb^{III} and Eu^{III}, respectively. Arrows indicate observed changes.

Tb^{III} (Figure 5b). This sensitized emission further confirmed the binding of Tb^{III} to the tpy groups of **L**.¹¹ Interestingly, emission of **L** at 428 nm was not suppressed completely even after

addition of 2 eq of Tb^{III} ions. This residual emission was attributed to the central ant core which probably did not involve in sensitization of Tb^{III} due to large spatial distance between ant core and Tb^{III} ion. Similar changes in absorption spectra were also observed in case of Eu^{III} ion (Figure 5c). However, the emission spectra exhibited weak bands at 592 nm and 618 nm, assigned to the $^5\text{D}_0\text{-}^7\text{F}_1$ and $^5\text{D}_0\text{-}^7\text{F}_2$ transition of Eu^{III} . A feeble decrease in emission at 428 nm was also observed (Figure 5d). This result indicated weak energy transfer from tpy to Eu^{III} .

2.3.3 Characterization of organogel (OG)

Heating solution of **L** (10^{-3} M) in CHCl_3/THF (2: 1), followed by cooling at room temperature resulted in an opaque gel (**OG**) that remained stable upon inversion (Figure 6a). FESEM images of **OG** xerogel revealed the fibrous morphology (Figure 6b-c). Nanofibers were several micrometer long with approximate diameter of 40-50 nm. Interestingly, presence of nanorings was also observed which were formed via coiling of nanofibers (Figure 6c). TEM images also supported the existence of nanofibers and nanorings (Figure 7a-c). Formation of nanofibers could be explained based on the self-assembly of **L** as shown in the Scheme 1. In binary mixture of solvents like CHCl_3/THF , **L** assembled through the H-bonding between amide groups and $\pi\text{-}\pi$ stacking between ant cores of neighbouring **L** and formed fibrils. These fibrils on aggregation formed fibers which further entangled to form typical fibrous gel architecture. The presence of H-bonding and $\pi\text{-}\pi$ stacking in gel were supported by PXRD and FTIR analysis. PXRD of the **OG** xerogel showed broad peak at $2\theta = 21.8^\circ$, corresponding to the d -spacing value of 4.0 Å which supported the presence of $\pi\text{-}\pi$ stacking in gel (Figure 8). Moreover, FTIR spectrum of **OG** xerogel on comparison with **L** exhibited a decrease in -N-H and -C=O stretching frequency from 3436 cm^{-1} to 3424 cm^{-1} and from 1645 cm^{-1} to 1638 cm^{-1} ,

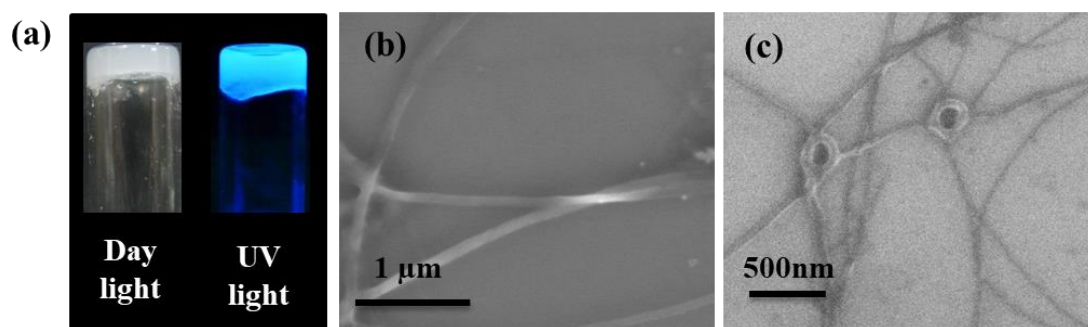


Figure 6. (a) Photographs of the **OG** gel under day and UV light, (b), (c) FESEM images of **OG** xerogel.

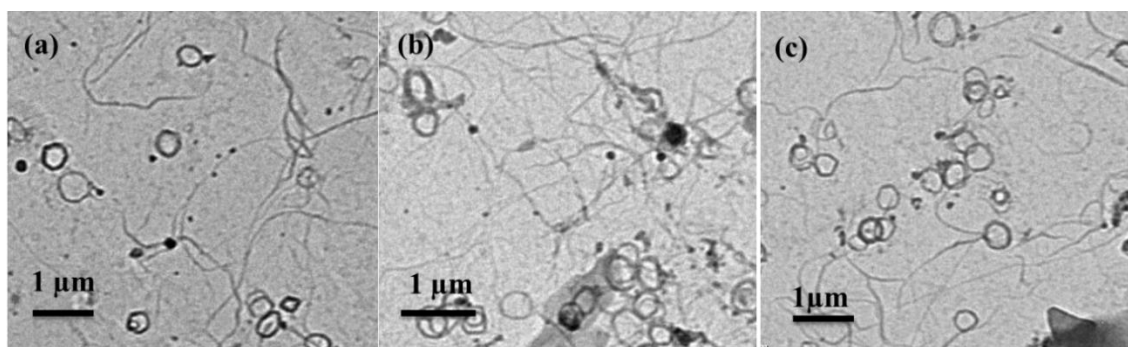


Figure 7. (a), (b), (c) TEM images the **OG** xerogel.

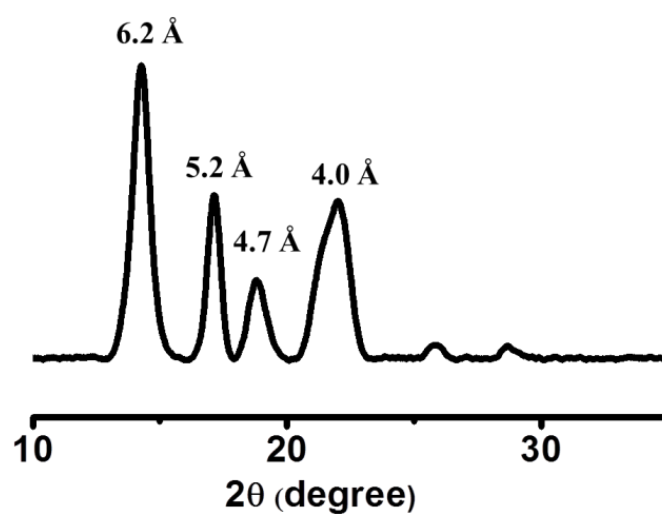


Figure 8. PXRD pattern of **OG** xerogel with corresponding *d*- spacing values.

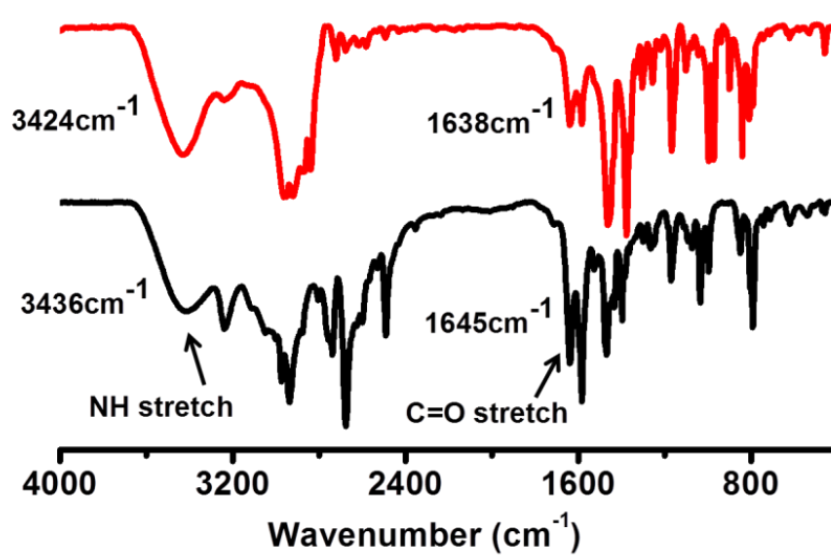


Figure 9. Comparison of FTIR of **L** (black) and **OG** xerogel (red).

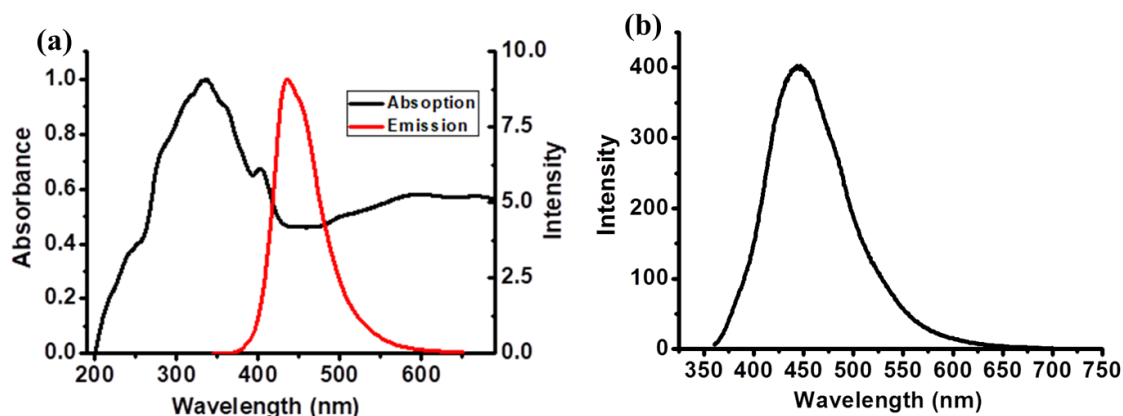


Figure 10. (a) Solid state absorption (black) and emission (red) spectra of **OG** xerogel, (b) Emission spectra of **OG** coated quartz substrate.

respectively, indicating the presence of intermolecular H-bonding in this assembly (Figure 9). The absorption spectrum of **OG** xerogel showed maxima around 350 nm (Figure 10a). Upon exciting at 350 nm it showed intense blue emission with maxima at 435 nm, originating from both ant core and tpy (Figure 10a). Emission spectra of organogel film prepared on quartz substrate was also recorded and it showed similar emission behaviour with a maximum at 435 nm (Figure 10b).

2.3.4 Characterization of **TbL** and **EuL** gels

Heating the mixture of **L** and $\text{Tb}(\text{NO}_3)_3 \cdot 6\text{H}_2\text{O}$ (molar ratio= 1: 1) in the aforementioned CHCl_3/THF (1: 1) solvent mixture followed by cooling resulted in a stable CPG (**TbL**) (Figure 11a). Likewise, **EuL** was also prepared by using 1:1 molar ratio of **L** and $\text{Eu}(\text{NO}_3)_3 \cdot 6\text{H}_2\text{O}$ (Figure 11b). The formation of gels was confirmed by

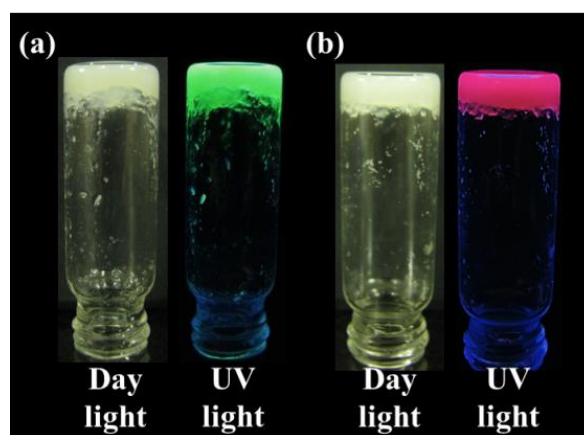


Figure 11. (a) Photograph of **TbL** under day and UV light, (b) Photograph of **EuL** under day and UV light.

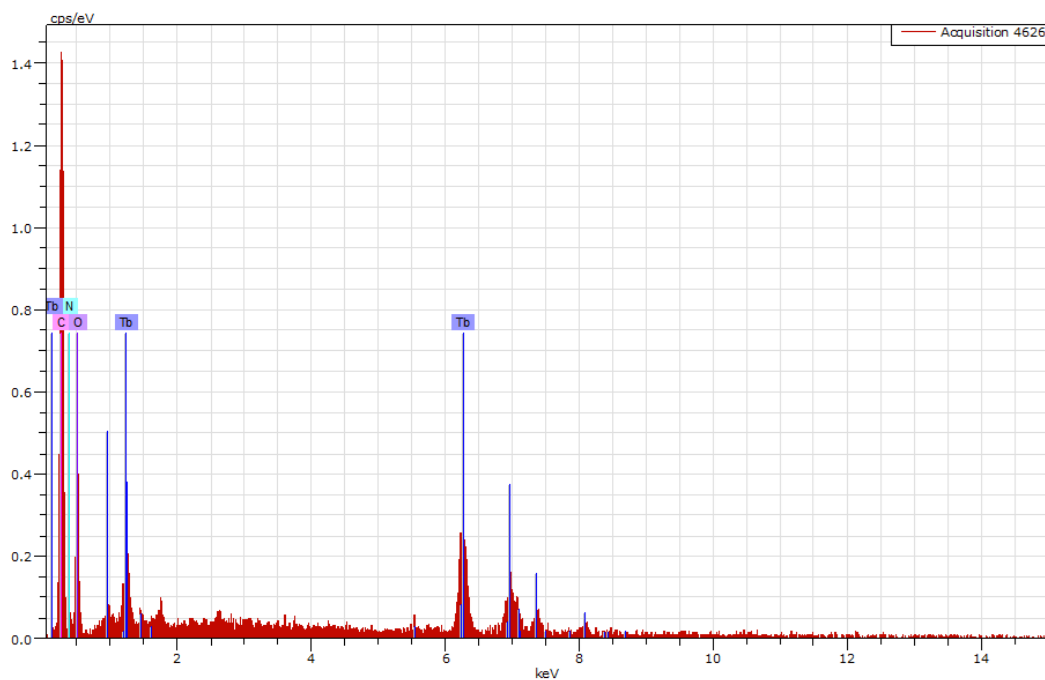


Figure 12. EDXS of **TbL** showing the presence of Tb^{III} .

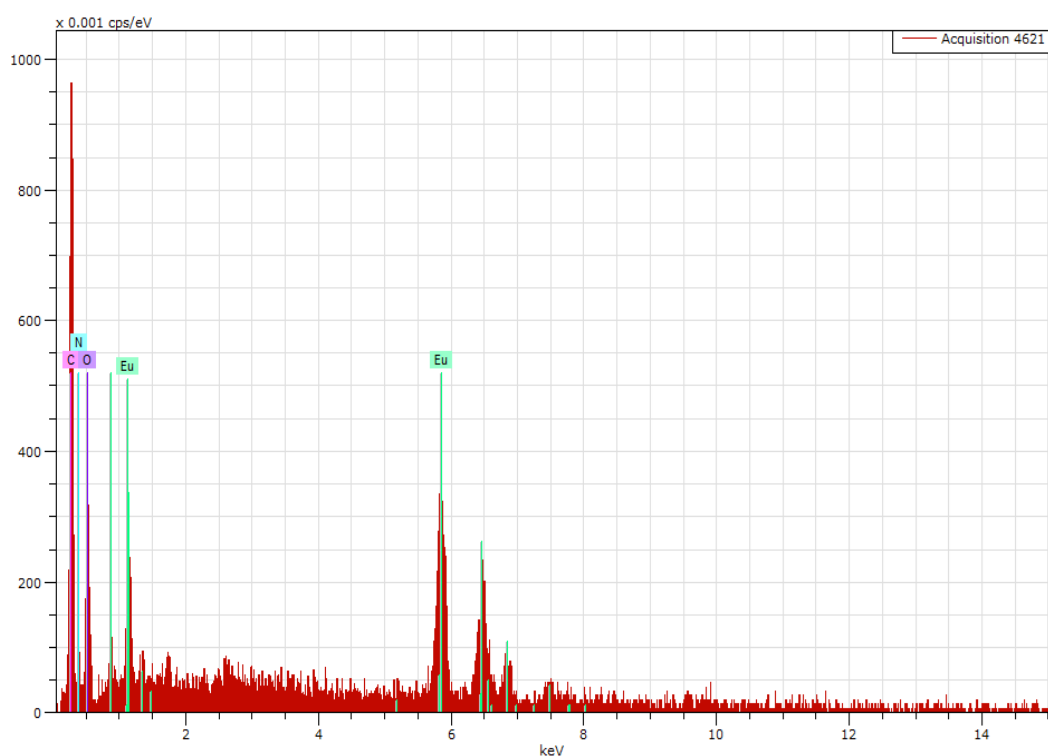


Figure 13. EDXS of **EuL** showing the presence of Eu^{III} .

inversion test method. The presence of coordinated Tb^{III} and Eu^{III} in respective **TbL** and **EuL** xerogels were confirmed by EDXS analysis (Figure 12 and Figure 13). CHN analysis of **TbL** and **EuL** xerogels indicated the probable formula as $[\text{Tb}(\text{L})(\text{NO}_3)_3 \cdot 2\text{THF}]$ and $[\text{Eu}(\text{L})(\text{NO}_3)_3 \cdot 2\text{THF}]$, respectively. To get insight into the

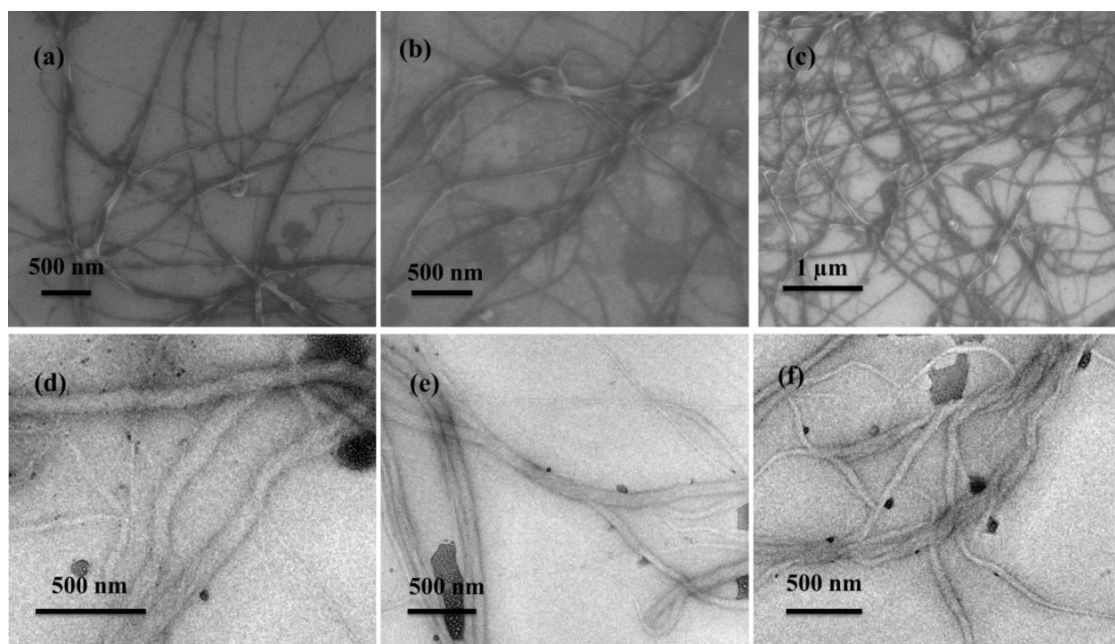


Figure 14. (a), (b), (c) FESEM images of **TbL** xerogel, (d), (e), (f) TEM images of **TbL** xerogel showing the presence of coiled-nanofiber morphology.

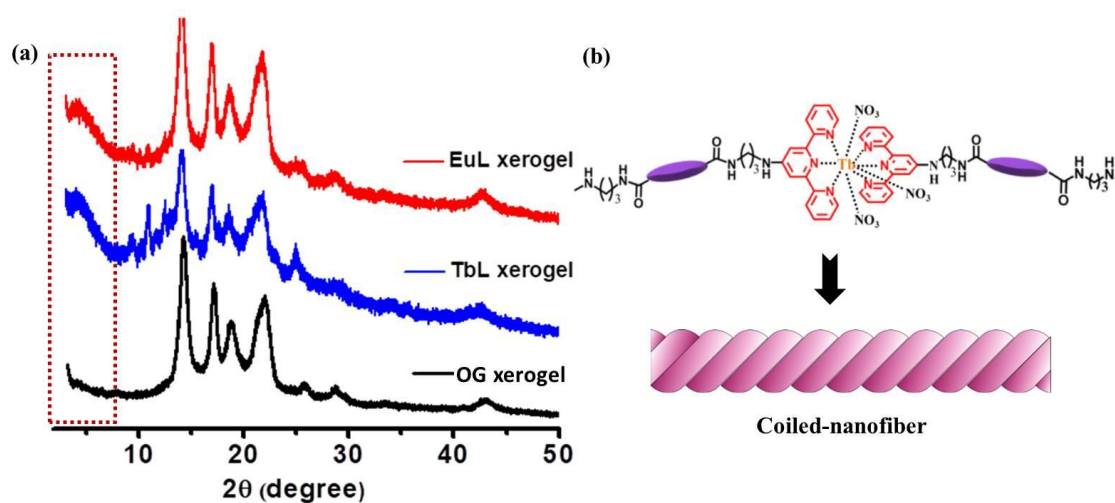


Figure 15. (a) Comparison of PXRD of **OG** (black), **TbL** (blue) and **EuL** (red) xerogels (a low angle peak in **TbL** and **EuL** xerogels is highlighted in the box), (b) Probable coordination environment around Tb^{III} in **TbL** leads to the formation of coiled-nanofiber morphology.

mode of packing in CPG, **TbL** xerogel was analysed by TEM and FESEM images (Figure 14). The **TbL** xerogel exhibited uniformly distributed coiled-nanofiber morphology with diameter of 80-50 nm which was higher than that of **OG** nanofibers (40-50 nm) (Figure 14). It was expected that the 1D self-assembled primary structure of

LMWG with pendent tpy groups on the outer surface would form higher ordered structures through coordination-driven interaction with Ln^{III} ions. This phenomenon has also been affirmed by PXRD analysis. **OG** xerogel and metallogels (**TbL** and **EuL**) showed similar PXRD pattern with peaks at $2\theta = 14.1^\circ$, 16.9° , 18.6° and 21.8° , corresponding to d -spacing values of 6.2 Å, 5.2 Å, 4.7 Å, and 4.0 Å respectively (Figure 15a). The similarities in PXRD pattern suggested that the primary assembly of **L** was retained in CPGs. However, **TbL** and **EuL** showed an additional low angle peak at 4.3° , (d -spacing value of 20.4 Å) which indicated formation of higher-ordered self-assembled structures in CPGs upon metal coordination to tpy moieties (Figure 15b).

2.3.5 Tunable emission of coordination polymer gels

Absorption spectra of **TbL** and **EuL** exhibited broad band around 390 nm and 350 nm, respectively (Figure 16a-b). Emission spectrum of **TbL** xerogel displayed characteristic peaks for Tb^{III} ($\lambda_{\text{ex}} = 280$ nm) at 486 nm, 540 nm, 580 nm, 618 nm and **L** centred peak at 435 nm (Figure 16c). Nevertheless, emission spectrum of **EuL** xerogel ($\lambda_{\text{ex}} = 280$ nm), showed well preserved **L** centred peak at 435 nm along with sharp peaks for Eu^{III} at 590 nm, 615 nm (Figure 16d). **TbL** and **EuL** gels showed intense green and

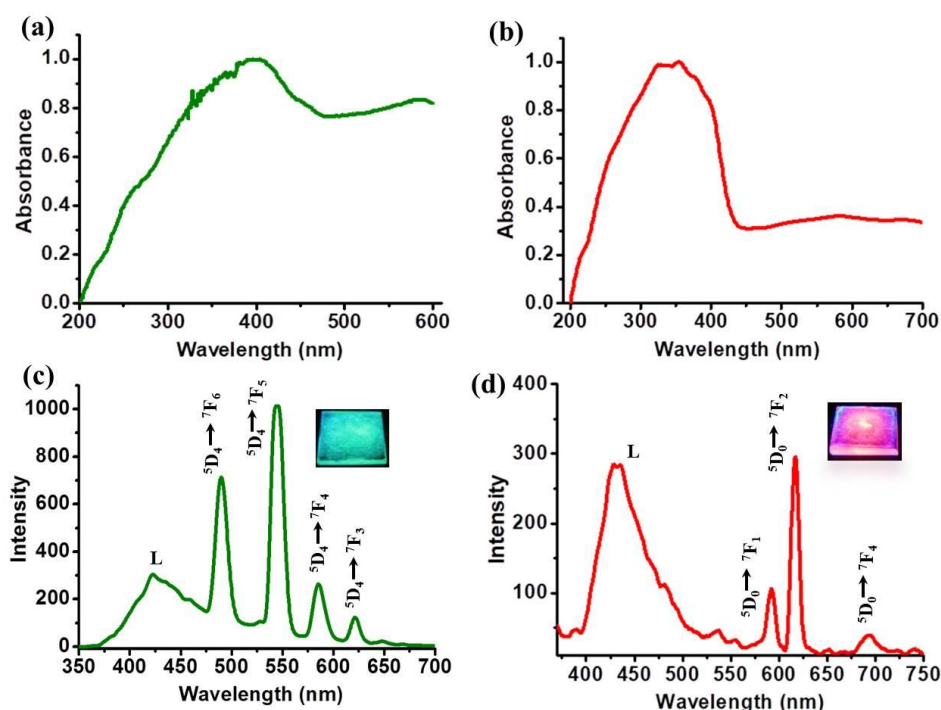


Figure 16. (a), (b) Solid state absorption spectra of **TbL** and **EuL** xerogels, respectively, (c), (d), Emission spectrum of **TbL** and **EuL** xerogels, respectively. Inset showing picture of **TbL** and **EuL** gels coated on quartz substrates.

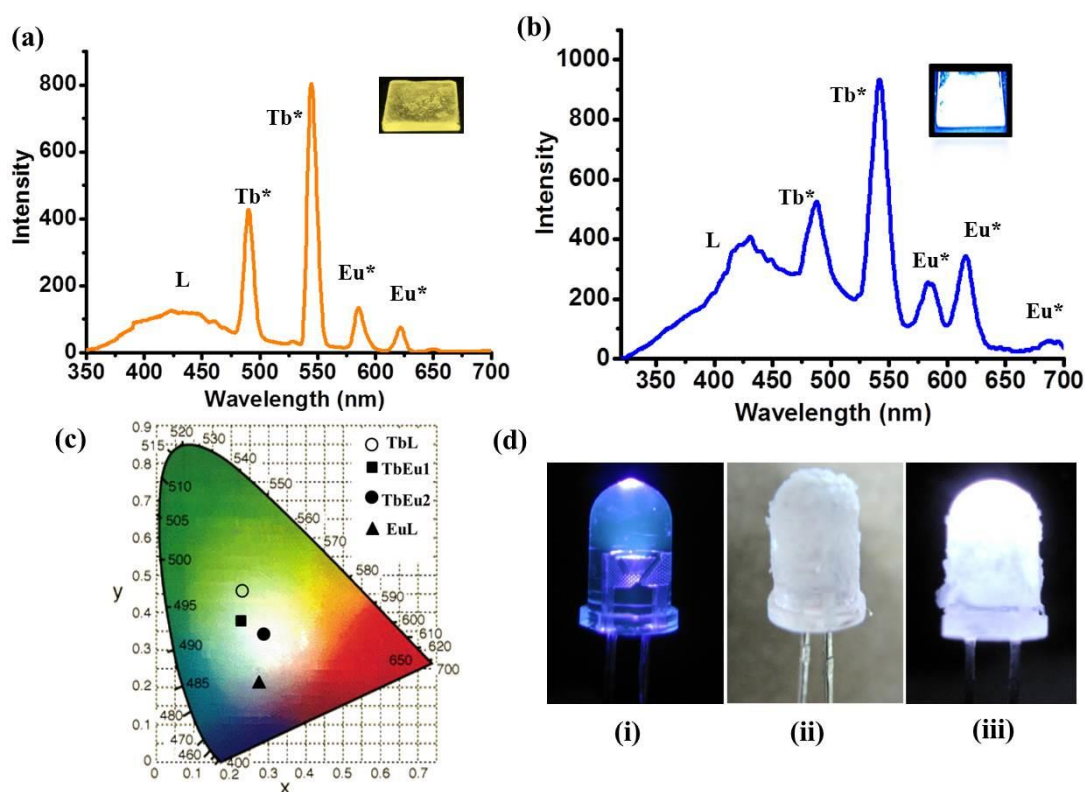


Figure 17. (a), (b) Emission spectra of **TbEu1** and **TbEu2** xerogels, respectively. Inset shows the yellow and white-light-emission from the quartz plates coated with **TbEu1** and **TbEu2**, respectively), (c) CIE chromatography of **TbL** (circle), **EuL** (triangle), **TbEu1** (square) and **TbEu2** (solid circle), (d) Photograph of an illuminating ultraviolet LED (i), same LED coated with **TbEu2** gel under day light (ii) and LED showing bright white light after switching on the LED (iii).

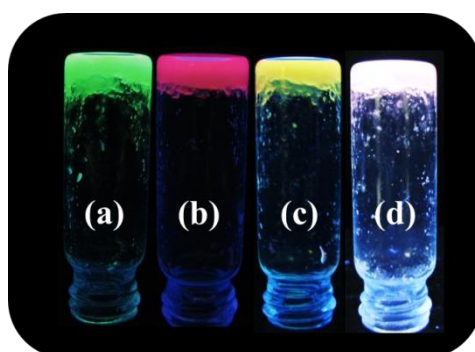


Figure 18. Photograph of (a) **TbL**, (b) **EuL**, (c) **TbEu1** and (d) **TbEu2** gels under UV light showing green, pink, yellow and white emission, respectively.

pink emissions, respectively under UV light. Respective CIE (Commission International de L'Eclairage) coordinates of **TbL** and **EuL** emission were calculated to be (0.25, 0.43)

and (0.26, 0.23), respectively (Figure 17c). The absolute quantum yield (QY) upon excitation at 340 nm was 4.2% for **TbL** and 12.4% for **EuL** and these values are comparable with other reported values of $\text{Tb}^{\text{III}}/\text{Eu}^{\text{III}}$ based metallogel and coordination polymers.^{5c, 8b, 8c} As seen in Figure 16c, emission spectrum of **TbL** extended from 400 nm to 600 nm in which blue (from **L**) and green (from Tb^{III}) parts were major components. Therefore, by further introducing a red component (from Eu^{III}) into **TbL**, the entire visible spectrum (400-800 nm) could be covered via RGB approach. To validate this hypothesis, bimetallic CPGs were prepared. Tb^{III} and Eu^{III} metal ions of different ratios were simultaneously added into **L** solution during gelation. A bimetallic CPG, **TbEu1** with $\text{Tb}^{\text{III}}:\text{Eu}^{\text{III}} = 1:1.2$ was prepared which showed strong greenish yellow emission under UV light (Figure 17a and Figure 18). The corresponding emission spectrum displayed bands characteristic of **L**, Tb^{III} and Eu^{III} -centred peaks. The emission intensity from Tb^{III} at 545nm (green) predominated over Eu^{III} peaks at 590 nm and 615 nm (red) (Figure 17a). The CIE coordinate of **TbEu1** was calculated to be (0.24, 0.38) (Figure 17c). It was envisioned that by further increasing Eu^{III} concentration, the emission feature of bimetallic CPG could be tuned towards white light. Indeed, by changing the ($\text{Tb}^{\text{III}}:\text{Eu}^{\text{III}}$) ratio to 1:2, a bimetallic CPG (**TbEu2**) was prepared which showed near white light emission (Figure 17b). The CIE coordinate of **TbEu2** was calculated to be (0.28, 0.34)

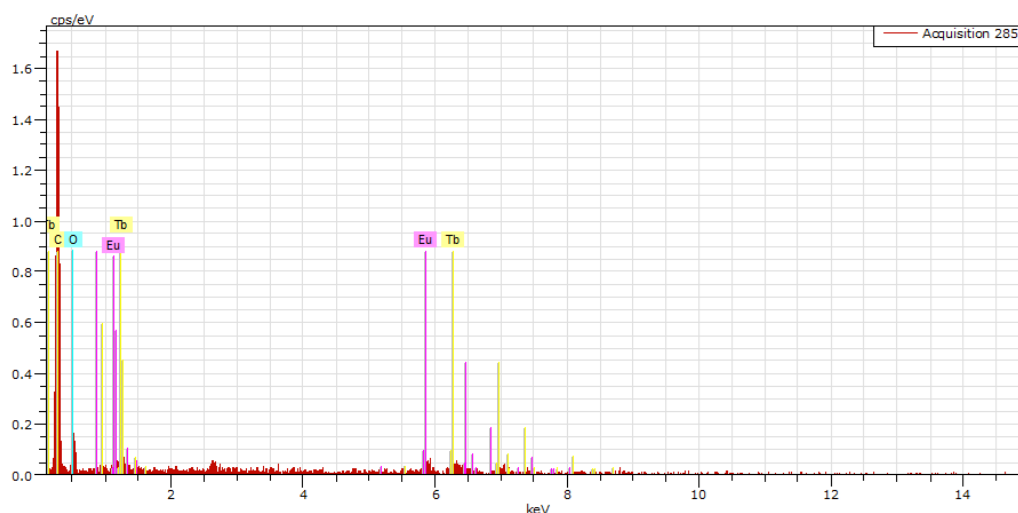


Figure 19. EDXS of **TbEu2** showing the presence of both Tb^{III} and Eu^{III} in xerogel.

(Figure 17c).¹² Upon excitation at 340 nm the absolute QY of **TbEu2** was found to be 5.0%. The presence of both Tb^{III} and Eu^{III} in **TbEu2** xerogel was confirmed by EDAX (Figure 19). Excellent processability and colour tunability of these “soft hybrids” was

exploited for coating on various substrates. All the CPGs and the quartz substrates coated with corresponding CPGs showed strong red, green, yellow and white-light-emissions (Figure 16c-d, Figure 17a-b and Figure 18). The white light emitting gel has also been used to fabricate white-light-emitting-diode (WLED) by simply coating a commercial ultraviolet LED with **TbEu2**. Upon turning on the LED, it displayed bright white light (Figure 17d).

2.4 SUMMARY

In summary, the preceding results demonstrated a rational design of a LMWG having blue luminescent core and a metal chelator type which could also act as a sensitizer for lanthanide ions. Coordination driven self-assembly of LMWG with Ln^{III} ($\text{Tb}^{\text{III}}/\text{Eu}^{\text{III}}$) resulted in bright green/pink luminescent CPGs. While, self-assembly of **L** with mixed metal ions with controlled stoichiometry of **L**: Tb^{III} : Eu^{III} yielded bimetallic CPGs with tunable emission including yellow and near white light. These soft coordination polymer nanostructures were highly processable. Gentle heating of gels formed viscous liquids which were easily transferred to solid substrate without any loss in emission intensity. Based on this approach a bright white-light-emitting LED has been fabricated. Such trichromatic approach of colour tunability in coordination polymer gels would provide new perspective for developing robust and easily processable light emitting materials for potential applications in optoelectronics and sensing.

2.5 REFERENCES

1. (a) N. M. Sangeetha and U. Maitra, *Chem. Soc. Rev.*, 2005, **34**, 821-836; (b) M. D. Segarra-Maset, V. J. Nebot, J. F. Miravet and B. Escuder, *Chem. Soc. Rev.*, 2013, **42**, 7086-7098; (c) C. Tomasini and N. Castellucci, *Chem. Soc. Rev.*, 2013, **42**, 156-172; (d) M.-O. M. Piepenbrock, N. Clarke, J. A. Foster and J. W. Steed, *Chem. Commun.*, 2011, **47**, 2095-2097; (e) J. W. Steed, *Chem. Soc. Rev.*, 2010, **39**, 3686-3699.
2. (a) D. Diaz Diaz, D. Kuhbeck and R. J. Koopmans, *Chem. Soc. Rev.*, 2011, **40**, 427-448; (b) T. Vermonden, R. Censi and W. E. Hennink, *Chem. Rev.*, 2012, **112**, 2853-2888; (c) S. Zhang, M. A. Greenfield, A. Mata, L. C. Palmer, R. Bitton, J. R. Mantei, C. Aparicio, M. O. de la Cruz and S. I. Stupp, *Nat Mater*, 2010, **9**, 594-601.
3. (a) J. H. Jung, J. H. Lee, J. R. Silverman and G. John, *Chem. Soc. Rev.*, 2013, **42**, 924-936; (b) M.-O. M. Piepenbrock, G. O. Lloyd, N. Clarke and J. W. Steed, *Chem. Rev.*, 2009, **110**, 1960-2004; (c) A. Y.-Y. Tam and V. W.-W. Yam, *Chem. Soc. Rev.*, 2013, **42**,

1540-1567; (d) X. Yan, T. R. Cook, J. B. Pollock, P. Wei, Y. Zhang, Y. Yu, F. Huang and P. J. Stang, *J. Am. Chem. Soc.*, 2014, **136**, 4460-4463; (e) G. M. Peters, L. P. Skala, T. N. Plank, B. J. Hyman, G. N. Manjunatha Reddy, A. Marsh, S. P. Brown and J. T. Davis, *J. Am. Chem. Soc.*, 2014, **136**, 12596-12599.

4. (a) T. Tu, W. Fang, X. Bao, X. Li and K. H. Dötz, *Angew. Chem. Int. Ed.*, 2011, **50**, 6601-6605; (b) C. Po, Z. Ke, A. Y.-Y. Tam, H.-F. Chow and V. W.-W. Yam, *Chem. Eur. J.*, 2013, **19**, 15735-15744; (c) S. Sarkar, S. Dutta, S. Chakrabarti, P. Bairi and T. Pal, *ACS Appl. Mater. Interfaces.*, 2014, **6**, 6308-6316; (d) M. Maity and U. Maitra, *J. Mater. Chem. A.*, 2014, **2**, 18952-18958; (e) W. Fang, C. Liu, Z. Lu, Z. Sun and T. Tu, *Chem. Commun.*, 2014, **50**, 10118-10121; (f) S. Bhattacharjee and S. Bhattacharya, *Chem. Commun.*, 2014, **50**, 11690-11693.

5. (a) H. Kim and J. Young Chang, *RSC Advances*, 2013, **3**, 1774-1780; (b) O. Kotova, R. Daly, C. M. G. dos Santos, M. Boese, P. E. Kruger, J. J. Boland and T. Gunnlaugsson, *Angew. Chem. Int. Ed.*, 2012, **51**, 7208-7212; (c) M. Martínez-Calvo, O. Kotova, M. E. Möbius, A. P. Bell, T. McCabe, J. J. Boland and T. Gunnlaugsson, *J. Am. Chem. Soc.*, 2015, **137**, 1983-1992; (d) S. Bhowmik, S. Banerjee and U. Maitra, *Chem. Commun.*, 2010, **46**, 8642-8644.

6. (a) S. Bhattacharyya, A. Chakraborty, K. Jayaramulu, A. Hazra and T. K. Maji, *Chem. Commun.*, 2014, **50**, 13567-13570; (b) Y. Liu, D. Tu, H. Zhu and X. Chen, *Chem. Soc. Rev.*, 2013, **42**, 6924-6958; (c) S. Roy, A. Chakraborty and T. K. Maji, *Coord. Chem. Rev.*, 2014, **273-274**, 139-164; (d) L. D. Carlos, R. A. S. Ferreira, V. de Zea Bermudez, B. Julian-Lopez and P. Escribano, *Chem. Soc. Rev.*, 2011, **40**, 536-549; (e) S. Mohapatra, S. Adhikari, H. Rijju and T. K. Maji, *Inorg. Chem.*, 2012, **51**, 4891-4893.

7. (a) G. M. Farinola and R. Ragni, *Chem. Soc. Rev.*, 2011, **40**, 3467-3482; (b) M. Shang, C. Li and J. Lin, *Chem. Soc. Rev.*, 2014, **43**, 1372-1386; (c) C.-Y. Sun, X.-L. Wang, X. Zhang, C. Qin, P. Li, Z.-M. Su, D.-X. Zhu, G.-G. Shan, K.-Z. Shao, H. Wu and J. Li, *Nat Commun.*, 2013, **4**.

8. (a) C. Fan and C. Yang, *Chem. Soc. Rev.*, 2014, **43**, 6439-6469; (b) X. Rao, Q. Huang, X. Yang, Y. Cui, Y. Yang, C. Wu, B. Chen and G. Qian, *J. Mater. Chem.*, 2012, **22**, 3210-3214; (c) Y. Lu and B. Yan, *J. Mater. Chem. C.*, 2014, **2**, 5526-5532; (d) D. K. Maiti, S. Roy, A. Baral and A. Banerjee, *J. Mater. Chem. C.*, 2014, **2**, 6574-6581.

9. R. d. C. Rodrigues, I. M. A. Barros and E. L. S. Lima, *Tetrahedron Lett.*, 2005, **46**, 5945-5947.

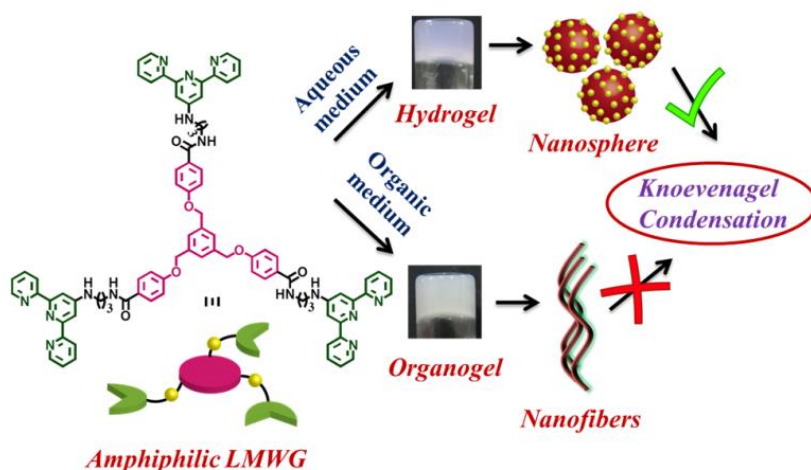
10. (a) E. S. Andreiadis, R. Demadrille, D. Imbert, J. Pécaut and M. Mazzanti, *Chem. Eur. J.*, 2009, **15**, 9458-9476; (b) L. J. Charbonniere, S. Mameri, D. Flot, F. Waltz, C. Zandanel and R. F. Ziessel, *Dalton Trans.*, 2007, 2245-2253.
11. A. Wild, A. Winter, F. Schlutter and U. S. Schubert, *Chem. Soc. Rev.*, 2011, **40**, 1459-1511.
12. (a) C. Vijayakumar, V. K. Praveen and A. Ajayaghosh, *Adv. Mater.*, 2009, **21**, 2059-2063; (b) S. Saha, G. Das, J. Thote and R. Banerjee, *J. Am. Chem. Soc.*, 2014, **136**, 14845-14851.

Chapter 3A

**Bimodal Self-assembly of an Amphiphilic
Gelator to Hydrogel-nanocatalyst and
Organogel of Different Morphologies and
Photophysical Properties**

Abstract

This chapter reports the rational design and synthesis of a flexible, amphiphilic LMWG (**L**) having 4,4',4''-[1,3,5-phenyl-tri(methoxy)]-tris-benzene core (π -donor) and three terminal 2,2':6',2''-terpyridyl moieties (π -acceptor) connected by alkylamide chain. **L** exhibits bimodal self-assembly in aqueous and organic solvents and results in hydrogel and organogel, respectively. The donor-acceptor π -stacking results in CT emission in hydrogel and donor-donor π -stacking results in normal LMWG-based emission in organogel. Also, different spatial disposition of π -chromophores lead to the formation of nanospheres and nanofibers in hydrogel and organogel, respectively. Since the exterior of the hydrogel-nanosphere is decorated with free amide groups, it has been exploited as soft nano-catalyst for Knoevenagel condensation reaction. The application of LMWG-derived hydrogel as heterogeneous nanocatalyst is underexplored and catalyzing Knoevenagel condensation reaction is yet to be reported. Hydrogel-nanocatalysts show high recyclability without change in morphologies. The enhanced catalytic activity is correlated to the high surface-to-volume ratio of the nanospheres of hydrogel which facilitate easy contact between the substrates and catalytic surface. Moreover, hydrogel-nanocatalysts are eco-friendly as they are metal-free and contain huge amount of water.



Paper published based on this work:

P. Sutar, and T. K. Maji, *Chem. Commun.* 2016, **52**, 13136–13139.

3A.1 INTRODUCTION

Over a past few decades, there has been a growing interest in the development of hydrogels or organogels from the self-assembly of low molecular weight gelators (LMWGs).¹ Owing to the dynamic behaviour and high processability, such supramolecular gels exhibit impending applications in diverse fields, including tissue engineering, bio-medicine, opto-electronics.² Although many elegant design strategies have been implemented to construct a number of LMWGs, it is still a daunting task to design a priori a LMWG which can act as both organogelator and hydrogelator.³ This is because a critical balance between hydrophobicity and hydrophilicity is required to design such LMWG. In this regard, a novel strategy would be to design an amphiphilic LMWG with donor and acceptor π -chromophores, connected by flexible alkylamide chain. Self-assembly of such LMWG not only advances the possibility to form CT gel, but also could result in different nanostructures of hydrogel and organogel depending upon polarity of the solvent medium.⁴ By considering the extensive opto-electronic applications of supramolecular CT nanostructures, it is worth to design such LMWGs which can pave the way towards adaptive soft-material.⁵

Knoevenagel condensation is an important base-catalyzed reaction in research and industry.⁶ Till date, many amide functionalized metal-organic frameworks (MOFs) or microporous organic polymers (MOPs) are utilized as heterogeneous Knoevenagel catalysts because amide is a well-explored base-type catalytic site.⁷ However, inaccessibility of catalytic sites due to small pore size or pore blocking often limit their activity. In this respect hydrogels of amide-functionalized LMGWs are superior as wide pores of gel-network facilitate easy diffusion of reactive species towards the catalytic sites.⁸ Since hydrogels are metal-free and contain huge amount of water within, they are environmentally more benign compared to MOFs. Moreover, hydrogel-nanocatalysts could host different hydrophilic substrates on their outer surface and their high surface-to-volume ratio could facilitate contact with catalytic sites. However, use of LMWG-derived hydrogel as heterogeneous catalyst for Knoevenagel condensation is yet to be accounted.

This chapter reports a new C_3 -symmetric LMWG (**L**) with a 4,4',4''-[1,3,5-phenyl-tri(methoxy)]-tris-benzene (tmb) as core, connected to three 2,2':6',2''-terpyridyl (tpy) moieties through flexible alkylamide chain (Scheme 1). The self-assembly of **L** in aqueous and organic solvent mediums resulted in hydrogel (**HG**) and organogel (**OG**) with nanosphere and nanofiber morphologies, respectively. The **HG** exhibited CT

emission, whereas the **OG** showed normal LMWG-based emission. Due to the presence of surface-exposed amide groups, **HG** was exploited as heterogeneous nanocatalyst for Knoevenagel condensation reaction.



Scheme 1. Schematic showing the self-assembly of **L** to hydrogel and organogel and their catalytic activity.

3A.2 EXPERIMENTAL SECTION

3A.2.1 Materials

1,3,5-tris(bromomethyl)benzene, methyl-4-hydroxybenzoate, 4'-chloro-2,2':6',2''-terpyridine, 1,3-diaminopropane, triphenylphosphine (PPh₃), trichloroisocyanuric acid (TCIC) were purchased from Sigma-Aldrich chemical Co. Ltd. Potassium carbonate, potassium iodide, malononitrile and all solvents were purchased from Spectrochem. For doing catalysis all substrates, benzaldehyde, 4-nitrobenzaldehyde, 4-chlorobenzaldehyde, *para*-tolualdehyde and *para*-anisaldehyde, were purchased from Sigma-Aldrich chemical Co. Ltd. All solvents were pre-dried using standard procedures before using. For UV-Vis experiments spectroscopic grade solvents were purchased from Spectrochem.

3A.2.2 Physical measurements

¹H-NMR was recorded on a Bruker AV-400 spectrometer with chemical shifts recorded as ppm and all spectra were calibrated against TMS. UV-Vis spectra were

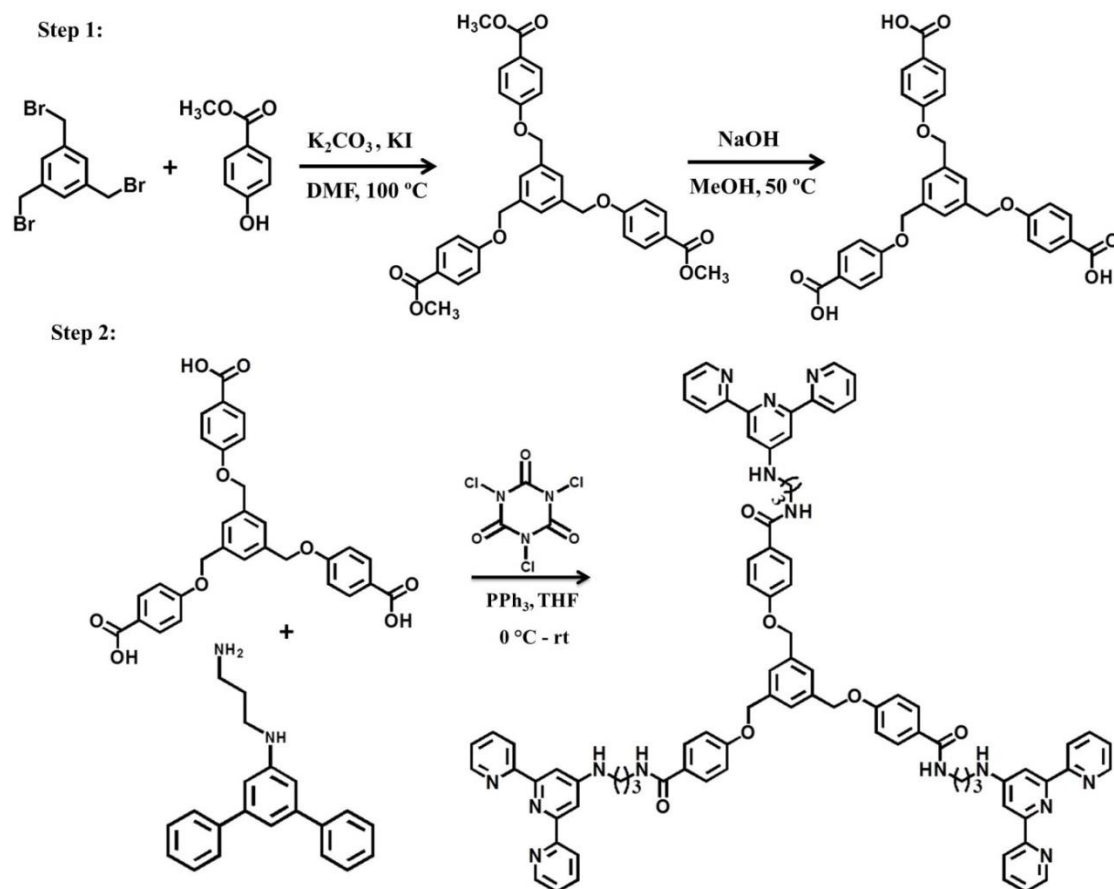
recorded in a Perkin-Elmer lamda 900 spectrometer. Fluorescence studies were accomplished using Perkin Elmer Ls 55 Lumeniscence spectrometer. Fourier transform infrared (FTIR) spectral studies were carried out by making samples with KBr pellets using Bruker FTIR spectrometer. Powder X-ray diffraction (PXRD) studies were recorded on a Bruker D8 discover instrument using Cu-K α radiation. Morphology studies were carried out using Lica-S440I field emission scanning electron microscopy (FESEM) by placing samples on silicon wafer under vacuum with accelerating voltage of 10 kV. Transmission electron microscopy (TEM) analysis was performed using JEOL JEM-3010 with accelerating voltage of 300 kV. For this analysis the xerogels were dispersed in ethanol and then drop casted on a carbon coated copper grid.

3A.2.3 Synthesis

Synthesis of 4,4',4''-[1,3,5-phenyl-tri(methoxy)]-tris-benzoic acid: methyl-4-hydroxybenzoate (1.065 g, 7 mmol), potassium carbonate (2.89 g, 21 mmol), potassium iodide (85 mg, 0.518 mmol) were suspended in dry N,N-dimethylformamide (DMF). The reaction mixture was refluxed at 100 °C for 2 hours maintaining the inert condition. 1,3,5-tris(bromomethyl)benzene (500 mg, 1.4 mmol) was dissolved in 20 ml dry DMF and was drop-wise added to the above heated reaction mixture. The mixture was subsequently stirred and heated at 100 °C for 4 hours. After cooling the reaction mixture to room temperature, 100 ml distilled water was added and the precipitate formed was collected by filtration. The precipitate was washed several times with cold water and air dried. The product obtained was white solid. Yield= 85%. $^1\text{H-NMR}$ (400 MHz, DMSO- d^6) δ : 7.92 (d, 6H, ArH), 7.54 (s, 3H, ArH), 7.14 (d, 6H, ArH), 5.29 (s, 6H, -CH $_2$ -), 3.82 (s, 9H, -OCH $_3$). The product was taken in a round bottom flux. 40 ml methanol and 6 g of NaOH in 20 ml of distilled water were added into it. The reaction mixture was refluxed at 50 °C for 12 hours. After cooling to room temperature, the solution was placed in an ice bath and acidified to pH =2 with 3N HCl. The precipitate was then collected, washed several times with distilled water and air dried. A brownish solid was obtained. Yield = 98%. $^1\text{H-NMR}$ (400 MHz, DMSO- d^6) δ : 7.89 (d, 6H, ArH), 7.53 (s, 3H, ArH), 7.11 (d, 6H, ArH), 5.22 (s, 6H, -CH $_2$ -). Selected FTIR data (KBr, cm $^{-1}$): 3451 (b), 3078-2879 (s), 2673 (s), 2550 (s), 1680 (sh), 1603 (sh), 1510 (m), 1428 (m), 1248 (sh), 1169 (sh), 1009 (m), 940 (s), 846 (m), 771 (m), 695 (s), 648 (s), 609 (s), 564 (s), 504 (s).

Synthesis of 2,2':6',2''-terpyridin-4'-yl-propane-1,3-diamine: The detail synthetic procedure of 2,2':6',2''-terpyridin-4'-yl-propane-1,3-diamine was discussed in

Chapter 2. The $^1\text{H-NMR}$, FTIR and CHN analysis of 2,2':6',2''-terpyridin-4'-yl-propane-1,3-diamine were also discussed in Chapter 2.



Scheme 2. Synthetic scheme for 4,4',4''-[1,3,5-phenyl-tri(methoxy)]-tris-benzene{[3-([2,2':6',2''-terpyridin-4'-ylamino)-propyl]-amide} (**L**).

Synthesis of 4,4',4''-[1,3,5-phenyl-tri(methoxy)]-tris-benzene{[3-([2,2':6',2''-terpyridin-4'-ylamino)-propyl]-amide} (L**):** 4,4',4''-[1,3,5-phenyl-tri(methoxy)]-tris-benzoic acid (280 mg, 0.529 mmol) was dissolved in anhydrous THF (30 mL). TCIC (406 mg, 1.748 mmol) and PPh_3 (458 mg, 1.748 mmol) were added into the reaction mixture and stirred at 0 °C for 40 min under inert condition. 2,2':6',2''-terpyridin-4'-yl-propane-1,3-diamine (532 mg, 1.748 mmol) was dissolved in anhydrous THF (20 mL) and Et_3N (484 μL , 3.496 mmol) was added into it. This reaction mixture was drop-wise added into 4,4',4''-[1,3,5-phenyl-tri(methoxy)]-tris-benzoic acid / TCIC / PPh_3 solution at 0 °C and stirred for 45 minutes. After that the reaction mixture was stirred at room temperature for 3 hrs. Precipitate was collected by filtration and washed several times with CHCl_3 and dried under vacuum. Yield: 88%. Melting point (m.p) of **L** = $\sim 300^\circ\text{C}$. $^1\text{H-NMR}$ (400 MHz, $\text{DMSO-}d^6$) δ : 8.65

(d, 2H, ArH), 8.89 (d, 2H, ArH), 8.23 (m, 2H, ArH), 7.90 (s, 2H, ArH), 7.78 (m, 2H, ArH), 7.73 (m, 2H, ArH), 7.53 (s, 1H, ArH), 7.05 (d, 2H, ArH), 5.21 (s, 2H, ArCH₂OAr), 3.72 (m, 2H, CONHCH₂), 3.02 (m, 2H, CH₂), 2.04 (m, 2H, CH₂NH). Selected FTIR data (KBr, cm⁻¹): 3436 (b), 3039 (b), 2779 (s), 2676 (s), 2493 (s), 1721 (sh), 1695(sh), 1600 (m), 1470 (m), 1399 (m), 1249 (s), 1167 (s), 850 (s), 790 (m), 534 (m). HRMS (ESI, *m/z*): [M+H]⁺ calculated for C₈₄H₇₅N₁₆O₆, 1391.4252; found: 1391.4254. Anal. calcd for C₈₄H₇₅N₁₅O₆ Calc.: C, 72.53; H, 5.43; N, 15.11%; Expt.: C, 72.61; H, 5.53; N, 15.05%.

Synthesis of the hydrogel of L (HG): 9 mg **L** was dissolved in 600 µl MeOH and 400 µl water was added into the solution during sonication. The mixture was kept at room temperature. After 5-6 min opaque gel was formed. The formation of gel was confirmed by inversion-test method. The **HG** xerogel was prepared by drying the hydrogel in air. Selected FTIR data of **HG** xerogel (KBr, cm⁻¹): 3436 (b), 3040 (b), 2781 (s), 2679 (s), 2493 (s), 1722 (sh), 1693 (sh), 1594 (m), 1469 (m), 1398 (m), 1248 (s), 1055 (s), 851 (s), 788 (m), 537 (m).

Synthesis of the organogel of L (OG): 8 mg of **L** was dissolved in 800 µl CHCl₃/THF (v:v= 1:1) solvent mixture. The resulting mixture was heated at 90 °C for few minutes to form a viscous liquid which on cooling resulted in opaque gel. The formation of gel was confirmed by inversion test method. **OG** xerogel was prepared by drying the organogel in air. Selected FTIR data of **OG** xerogel (KBr, cm⁻¹): 3420 (b), 3053 (b), 2778 (m), 1716 (sh), 1688(sh), 1465 (m), 1396 (sh), 1052 (m), 771 (s), 534 (sh).

General procedure for the catalytic reactions: Various benzaldehyde derivatives (1 mmol) and melanonitrile (1 mmol) were taken in a Schlenk tube and 15 ml dry THF was added into it under inert atmosphere. The reaction mixture was stirred at room temperature for 5 minutes and **HG** xerogel (1 mol %) was added into it. After that the reaction mixture was refluxed at 40 °C under nitrogen atmosphere. The reaction mixture was cooled down to room temperature and filtered to recover the catalyst. The filtrate was concentrated and analysed using GC-MS analyser and ¹H-NMR spectroscopy.

3A.3 RESULTS AND DISCUSSION

3A.3.1 Characterization of L

The synthesis of **L** was carried out in multi-steps from commercially available 1,3,5-tris(bromomethyl)benzene, methyl 4-hydroxybenzoate and 4-chloro-2,2':6',2"-terpyridine (Scheme 2).^{2c} Reaction of 1,3,5-tris(bromomethyl)benzene with methyl 4-hydroxybenzoate first resulted in methyl 4,4',4"-[1,3,5-phenyl-tri(methoxy)]-tris-benzoate

which was subsequently hydrolysed to corresponding acid. The resulting acid was further coupled with 2,2':6',2''-terpyridin-4-yl-propane-1,3-diamine in 1:3 stoichiometry to get the targeted **L** in approximately 88% yield. The formation of **L** was confirmed by $^1\text{H-NMR}$, HRMS and FTIR spectra. The HRMS showed peak at $m/z = 1391.423$ corresponding to the $[\text{L} + \text{H}]^+$ species. The FTIR spectrum of **L** exhibited bands at 3436 cm^{-1} and 1695 cm^{-1} corresponding to N-H and C=O stretching frequency of amide, respectively. The elemental analysis of **L** also confirmed its purity. The melting point of **L** was found to be $\sim 300\text{ }^\circ\text{C}$. Methanolic solution of **L** (10^{-5} M) showed a broad absorption band at 250-320 nm which could be assigned to the $\pi\text{-}\pi^*$ transition of the tmb core and terminal tpy moieties (Figure 1a). Upon excitation at 280 nm, the same solution exhibited blue emission with maxima at 420 nm which could be considered as combined emission from tmb and tpy groups of **L** (Figure 1b).

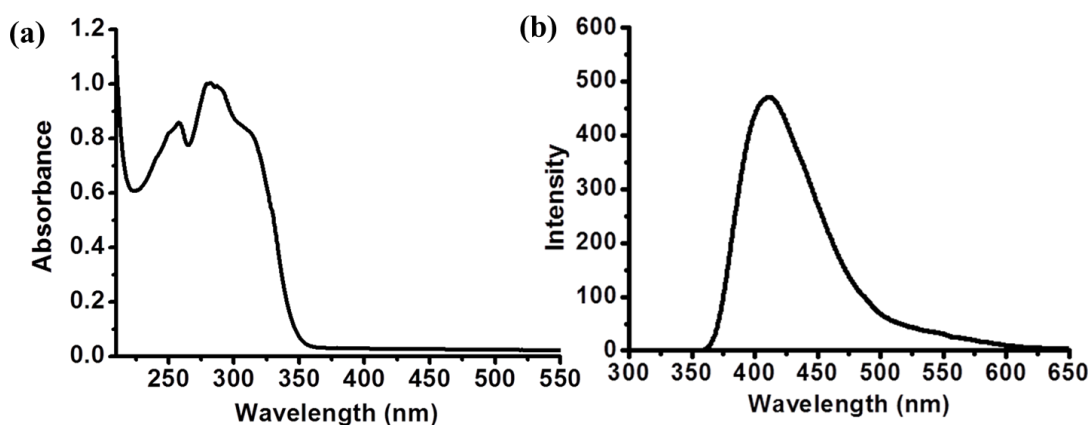


Figure 1. (a) Absorption spectra of **L** ($1 \times 10^{-4}\text{ M}$) in MeOH, (b) emission spectra of **L** ($1 \times 10^{-4}\text{ M}$) in MeOH.

3A.3.2 Characterization of hydrogel (HG)

Gelation propensity of **L** was thoroughly checked in various solvents. The solution of **L** (9 mg/ml) in $\text{H}_2\text{O}/\text{MeOH}$ mixture formed the translucent hydrogel (**HG**) at room temperature (Figure 2a). Upon shaking, **HG** was transformed into a sol, which again converted back to a gel on resting, thereby confirming its thixotropic nature. Insight into the morphology of **HG** was obtained by recording FESEM and TEM images of corresponding xerogel. FESEM and TEM images of **HG** xerogel revealed the presence of nanospheres with the diameter in 600- 700 nm range (Figure 2b-h). High resolution TEM image showed that surface of the nanospheres consisted of layered sheets (Figure 2h). Formation of the nanosphere occurred through a two-step hierarchical self-assembly

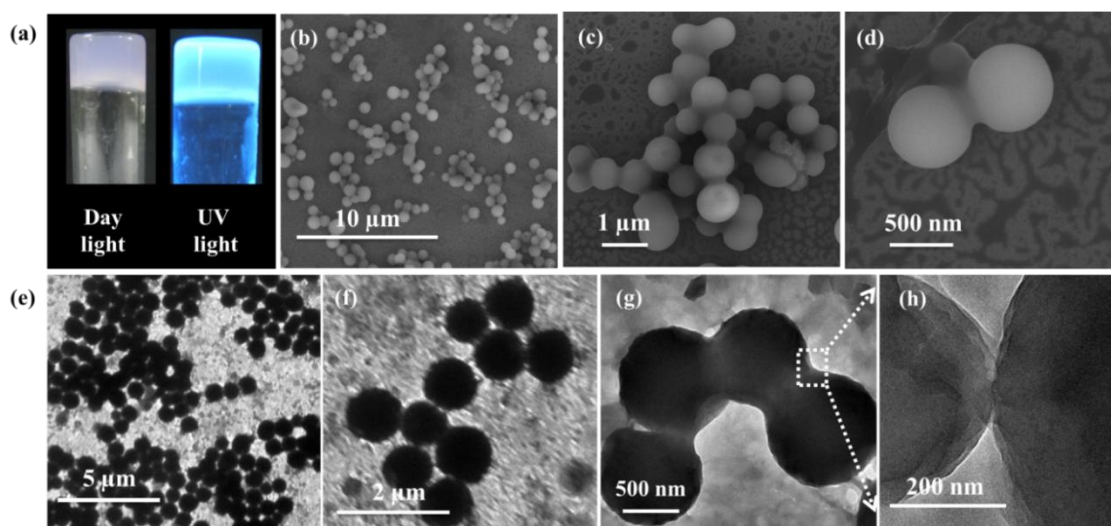
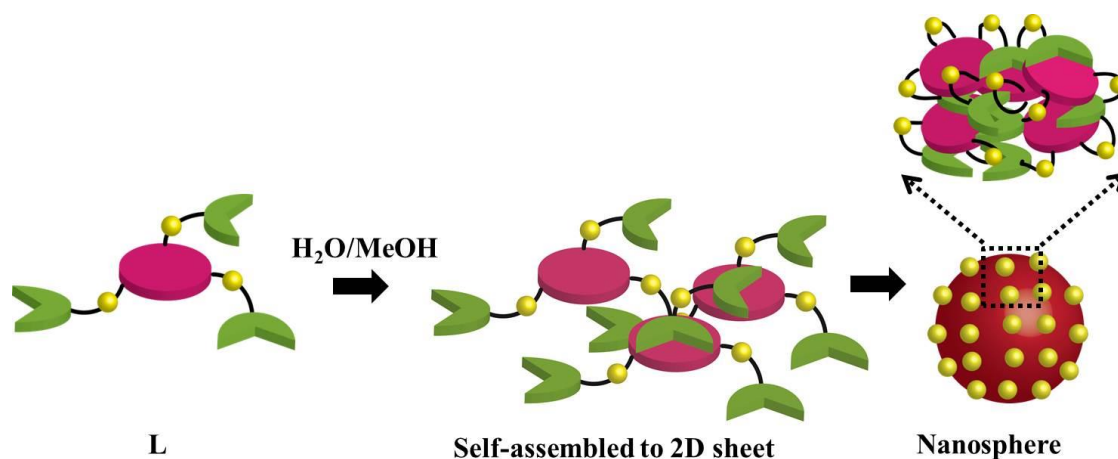


Figure 2. (a) Photograph of **HG** hydrogel under day light and UV-light, (b), (c) and (d) FESEM images of **HG** xerogel, showing of the formation of nanosphere, (e), (f), (g) TEM images of **HG** xerogel, (h) High resolution TEM image of **HG** xerogel.



Scheme 3. Schematic showing mechanism of self-assembly of **L** to nanospheres of **HG**.

process as shown in Scheme 3.⁹ First, in polar solvent the molecules were assembled through inter molecular π - π stacking between the tmb and tpy moieties and resulted in extended 2D sheets. As time proceeds, the π -stacked tmb and tpy tried to minimize their contact with $\text{H}_2\text{O/MeOH}$ due to hydrophobic effect, whereas amide groups present on the sheets tried to be exposed towards the polar medium due to H-bonding with $\text{H}_2\text{O/MeOH}$. As a result, sheets were folded to nanospheres whose exterior were decorated with amide groups. The presence of π - π stacking in **HG** was supported by PXRD which showed peak at $2\theta = 24.5^\circ$, corresponding to the d -spacing value of 3.6 \AA (Figure 3). Comparison of FTIR spectra of **HG** xerogel with **L**, did not exhibit significant change in -N-H and -C=O

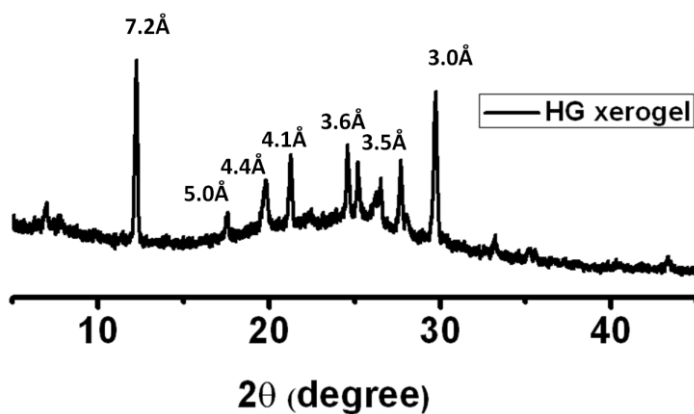


Figure 3. PXRD pattern of **HG** xerogel.

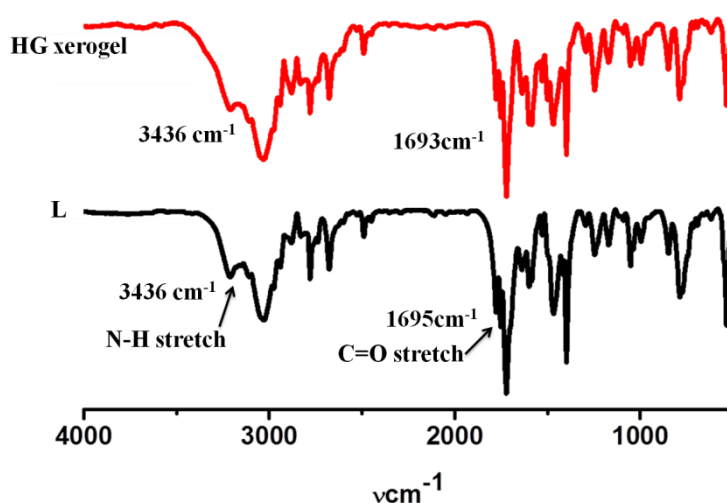


Figure 4. FTIR spectra of **L** (black) and **HG** xerogel (red).

stretching frequency which indicated no H-bonding interaction between **L** and gelation was driven by only π - π stacking/hydrophobic interaction between tmb and tpy groups (Figure 4). UV-Vis spectrum of **HG** xerogel exhibited maxima at 290 nm and a broad shoulder at 410 nm which could be attributed to the interligand CT transition between π -stacked tmb (π -donor) and tpy groups (π -acceptor) (Figure 5a). Similar Ar \rightarrow tpy intraligand charge transfer (ILCT) transition is reported for many Zn^{II} complexes of Ar-tpy derivatives.¹⁰ Upon exciting at 290 nm **HG** xerogel showed cyan emission with maxima at $\lambda = 478$ nm (Figure 5b). Moreover, the intensity of the emission maxima increased upon excitation at 400 nm, further indicating CT based emission in **HG** (Figure 5c). Excitation spectra showed presence of ground state interaction, thus ruling out the possibility of excited state exciplex formation (Figure 5d).¹¹ To further confirm the CT interaction, the absorption and emission spectra of **L** in MeOH/H₂O mixture was recorded by gradually adding H₂O in the MeOH solution of **L**. With incremental addition of H₂O,

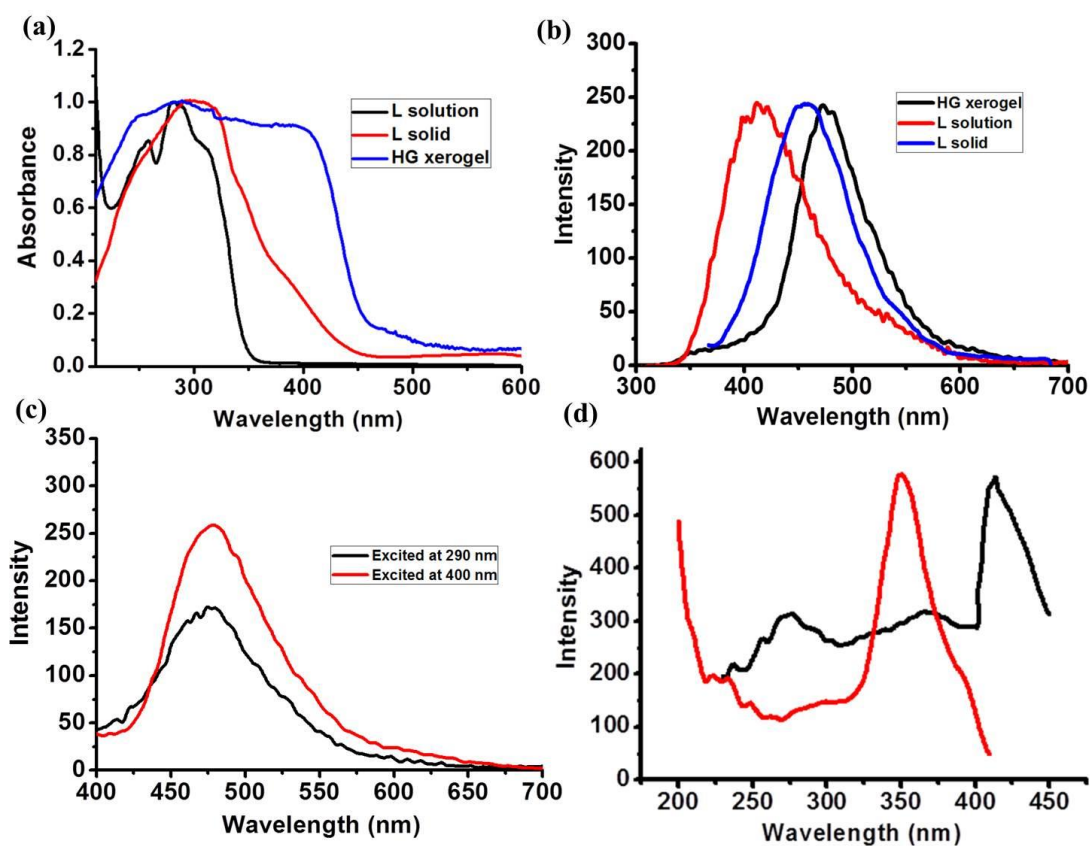


Figure 5. (a) UV-Vis spectra of methanolic solution of **L** (10^{-5} M, Black), solid **L** (Red) and **HG** xerogel (Blue), (b) Emission spectra of methanolic solution of **L** (10^{-5} M, Red), solid **L** (Blue) and **HG** xerogel (Black), (c) Emission spectra of **HG** xerogel when excited at 290 nm (black) and 400 nm (red), (d) Comparison of excitation spectra of **L** (red) and **HG** xerogel (black).

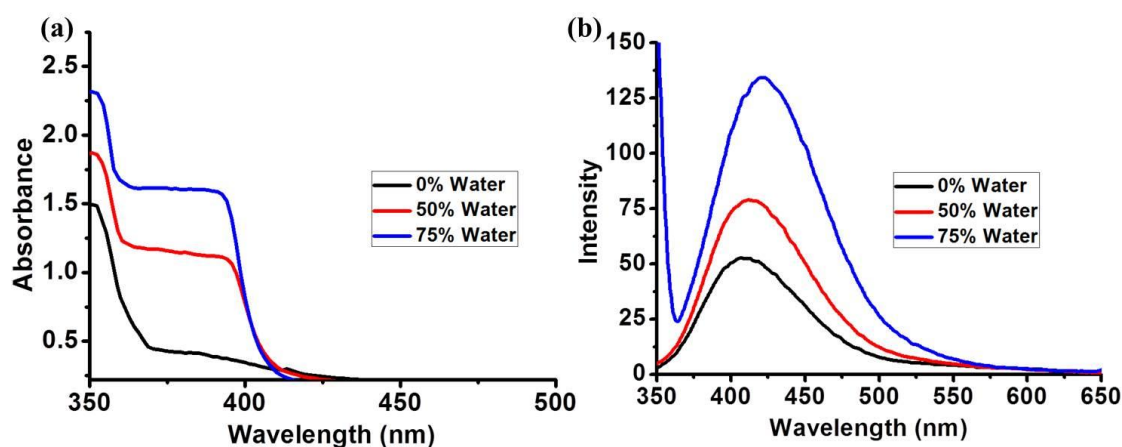


Figure 6. (a) Change in absorption spectra of methanolic solution of **L** with incremental addition of water, (b) Change in emission spectra of methanolic solution of **L** with incremental addition of water.

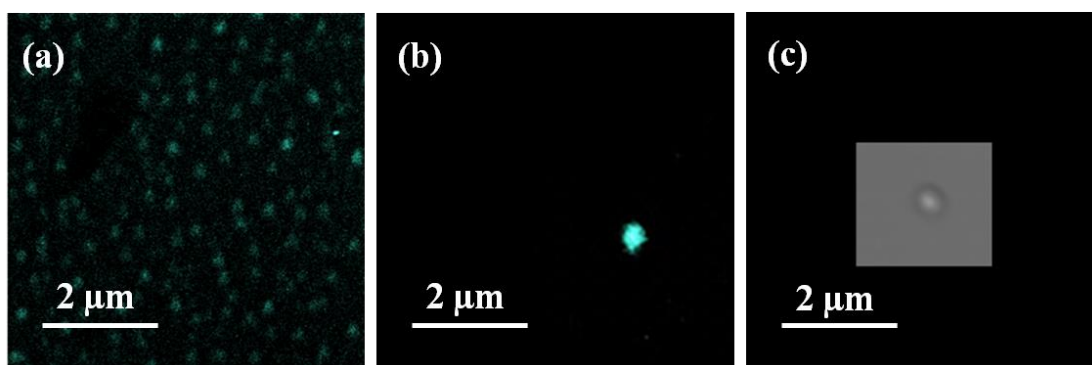


Figure 7. Confocal fluorescence microscopy images of **HG** xerogel showing presence of cyan emissive nano-spheres.

the absorption spectra of **L** showed appearance of a new peak at 410 nm, suggesting intermolecular CT interaction of aggregated **L** in mixed solvent (Figure 6a). The corresponding emission spectrum ($\lambda_{\text{ex}} = 400$ nm) of the solution exhibited red shifted emission with enhanced intensity, confirming CT emission of aggregated **L** in mixed solvent (Figure 6b). Comparison of absorption spectra of **HG** xerogel with solid **L**, showed that the CT band at 410 nm becomes more prominent in **HG** (Figure 5a). This result indicated that the CT interaction between the π - π stacked tmb and tpy groups became prominent in the ordered assembly of **HG**. Confocal fluorescence microscopy images of **HG** xerogel confirmed the formation of cyan emissive nanospheres with an average diameter of 600 ± 100 nm (Figure 7).

3A.3.3 Characterization of organogel (OG)

Heating solution of **L** (8 mg/ml) in CHCl_3/THF mixture followed by cooling resulted in an opaque organogel (**OG**) (Figure 8a). FESEM and TEM images of **OG** xerogel revealed the typical fibrous morphology (Figure 8b-c). Nanofibers were several micrometer long with an average diameter of 80-100 nm. The presence of nanorings was also observed which are formed by coiling of nanofibers. In CHCl_3/THF mixture, self-assembly of **L** was driven by complementary H-bonding interaction between amide groups and π - π stacking between tmb core of neighbouring **L** and results in 1D fibril (Figure 8d). These fibrils upon aggregation formed fibers which further entangled to form fibrous gel architecture. The presence of H-bonding and π - π stacking in **OG** was supported by PXRD and FTIR studies (Figure 9). Comparison of FTIR spectra of **L** and **OG** xerogel exhibited decrease in $-\text{C}=\text{O}$ and $-\text{N}-\text{H}$ stretching frequencies from 1693 cm^{-1} to 1688 cm^{-1} and from 3436 cm^{-1} to 3420 cm^{-1} , respectively, indicating the presence of

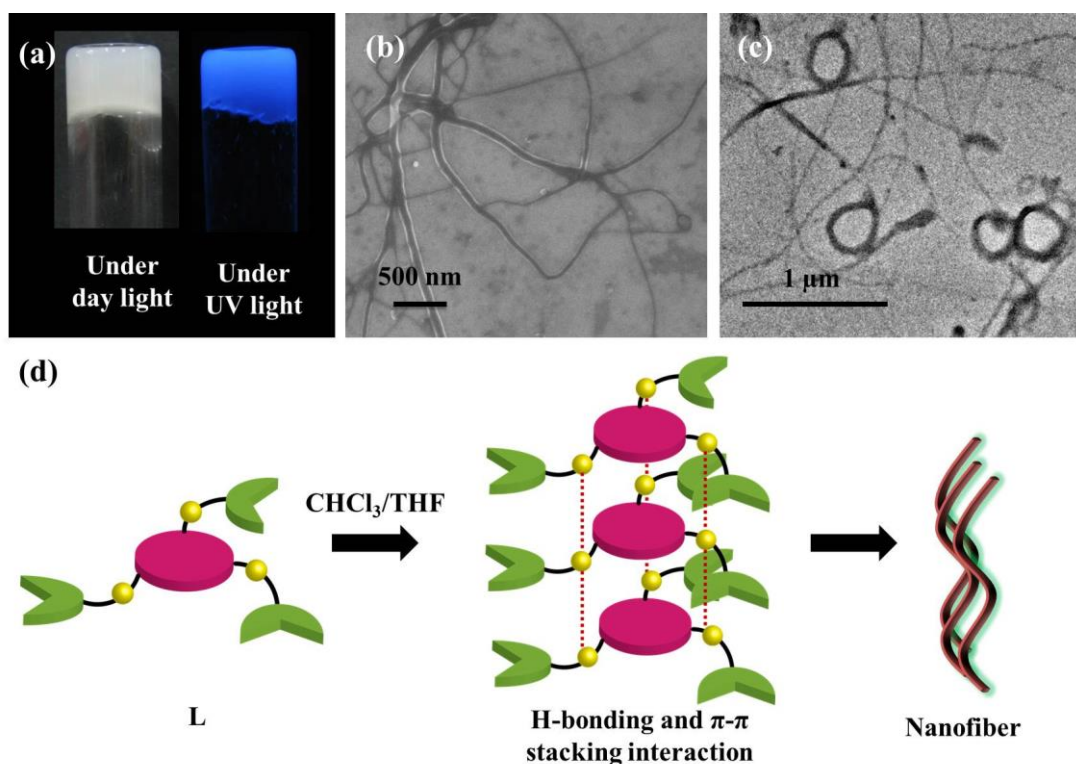


Figure 8. (a) Photograph of **OG** organogel under day light and UV-light, (b) FESEM image of **OG** xerogel, (c) TEM image of **OG** xerogel, (d) The mechanism of self-assembly of **L** in **OG** is driven by the H-bonding and π - π stacking interactions.

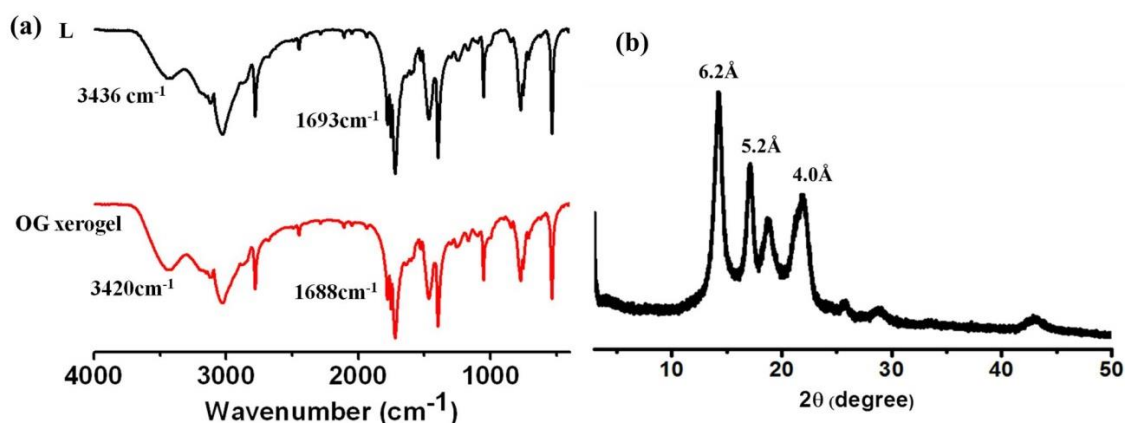


Figure 9. (a) FTIR spectra of **L** (black) and **OG** xerogel (red), (b) PXRD of **OG** xerogel.

intermolecular H-bonding between the amide groups of **L** (Figure 9a). PXRD analysis of **OG** xerogel exhibited broad peak at $2\theta = 21.7^\circ$, corresponding to $d = 4.0 \text{ \AA}$ which indicated the presence of π - π stacking in **OG** (Figure 9b). Absorption spectrum of **OG** xerogel showed maxima around 290 nm. The xerogel exhibited a blue emission with a maxima at 430 nm ($\lambda_{\text{ex}} = 290 \text{ nm}$), originating from both tmb and tpy, similar to the

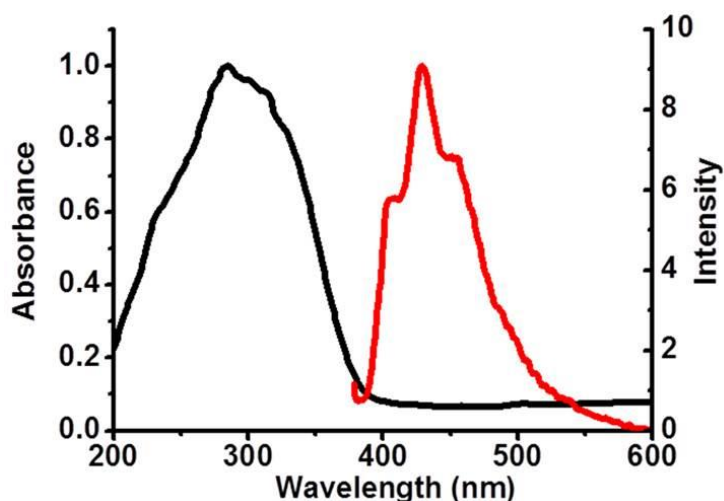


Figure 10. UV-Vis and emission spectra of OG xerogel.

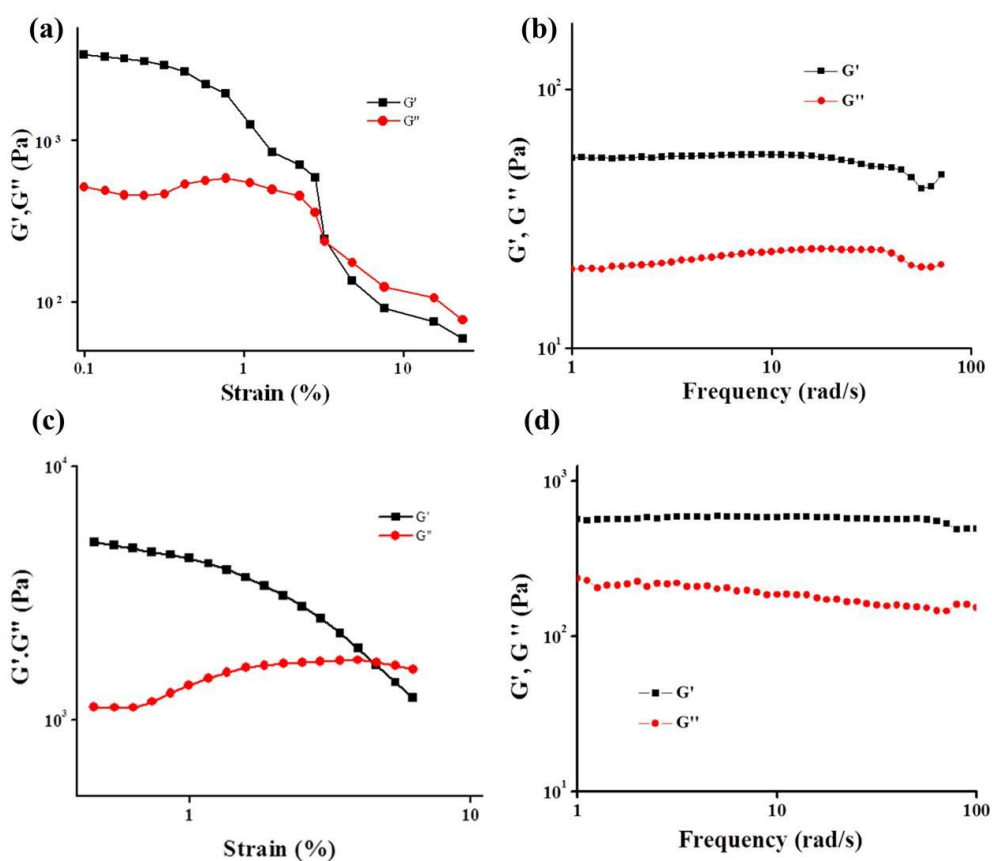


Figure 11. (a) Oscillatory strain measurements (frequency = 1.0 rad/s) and (b) Oscillatory frequency sweep measurements (strain = 0.01%) of **HG**, the squares (black) and circles (red) indicate storage (G') and loss modulus (G'') respectively, (c) Oscillatory strain sweep measurements (frequency = 1.0 rad/s) and (d) Oscillatory frequency sweep measurements (strain = 0.01%) of **OG**, the squares (black) and circles (red) indicate storage (G') and loss modulus (G''), respectively.

methanolic solution of **L** (Figure 10). This also suggested that self-assembly of **L** was different in **HG** and **OG**. Oscillatory strain and frequency sweep measurements on **HG** and **OG** showed that storage modulus (G') was higher than the loss modulus (G'') over a long range of strain (%) indicating viscoelastic nature of the gels (Figure 11). Interestingly, the G' value of **OG** was two-fold higher than the G' value of **HG** indicating greater mechanical strength of **OG** compared to **HG**.

3A.3.4 Catalytic activity of the hydrogel nanospheres

The presence of free amide group on the exterior of nanosphere of **HG** xerogel prompted us to study its catalytic activity towards the Knoevenagel condensation of aldehydes and active methylene compounds. In a typical condensation reaction *p*-nitrobenzaldehyde (1 equiv), malononitrile (1 equiv), and **HG** xerogel (1 mol %) were taken in dry THF and stirred at 40°C under inert conditions. Formation of the product was confirmed by $^1\text{H-NMR}$ and GC-MS analysis (Figure 12 and Figure 13). The quantitative analysis of the product conversion was monitored by a GC-MS analyser at regular intervals of times. The reaction kinetics showed a sharp increase in conversion (69%) in 20 minutes, after 2 h 90% conversion of product was observed and after 4 h almost all

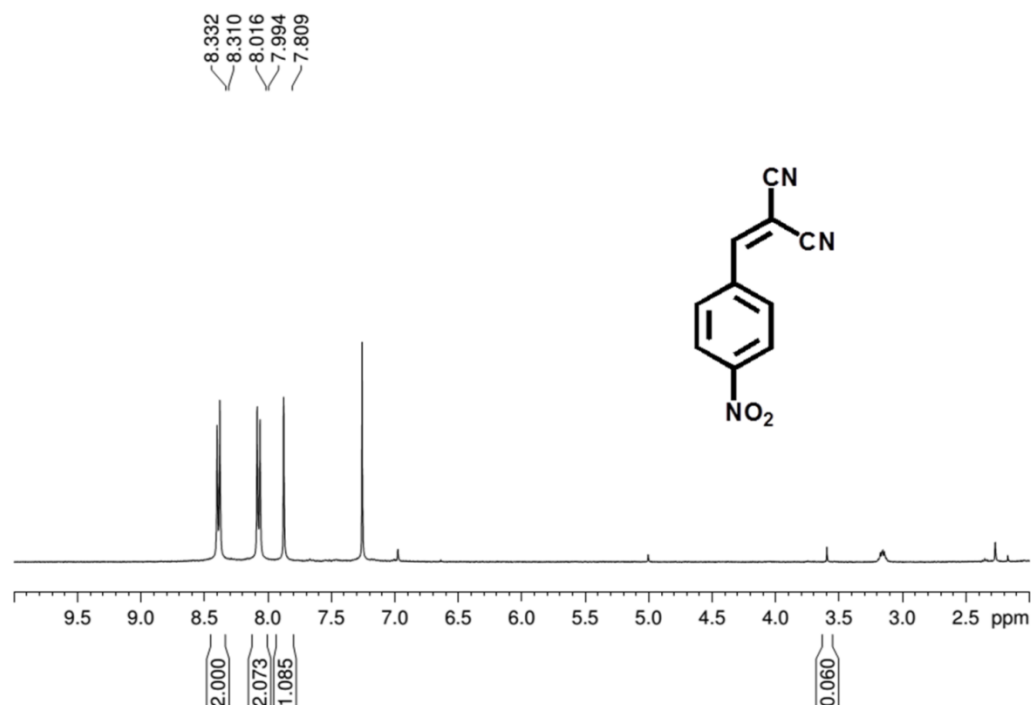


Figure 12. $^1\text{H-NMR}$ spectra (in CDCl_3) of 2-(4-nitrobenzylidene)malononitrile formed by the condensation of malononitrile and 4-nitrobenzaldehyde using **HG** xerogel as catalyst.

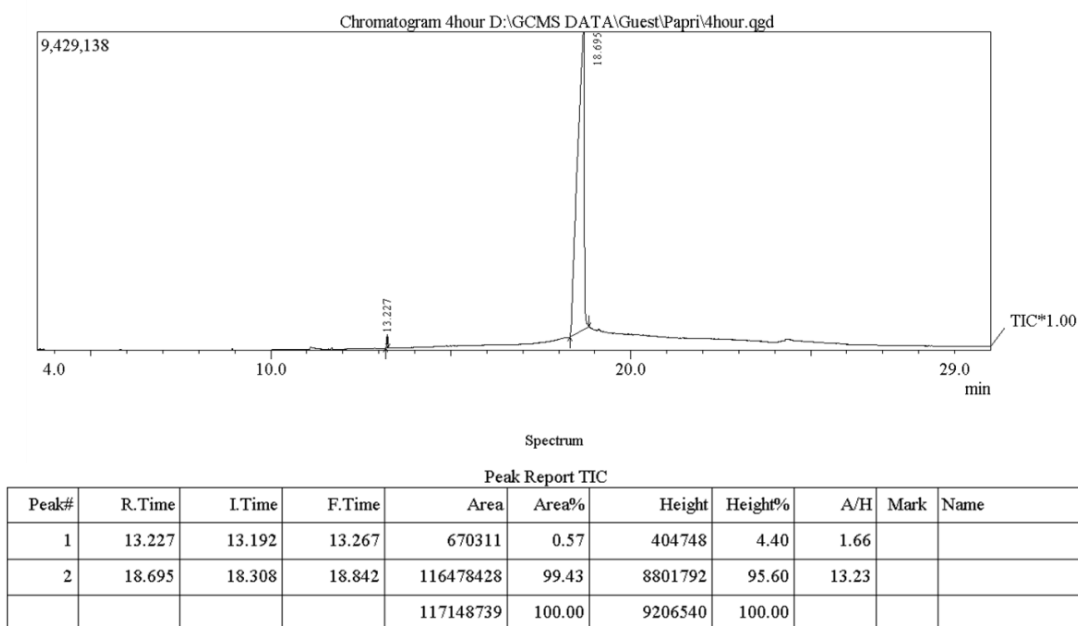


Figure 13. GC-MS of 2-(4-nitrobenzylidene)malononitrile formed by the condensation of malononitrile and 4-nitrobenzaldehyde after 4 hours using **HG** xerogel as catalyst.

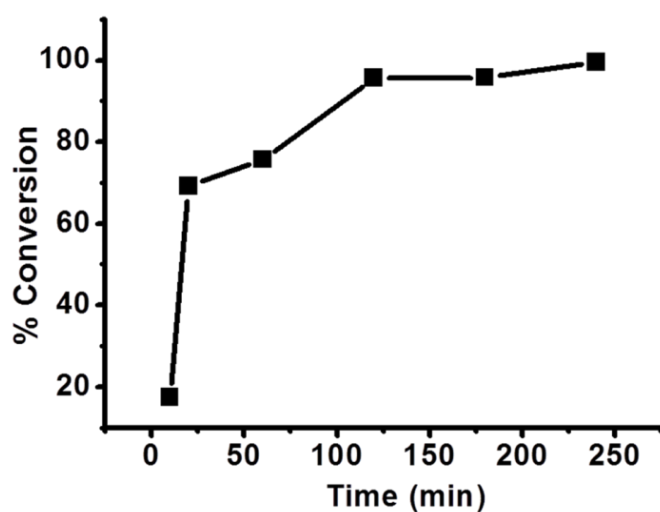


Figure 14. Conversion [%] versus time [min] for Knoevenagel condensation reaction of 4-nitrobenzaldehyde and malononitrile at 40 °C in THF.

aldehyde was converted to product (99%) (Figure 14). However, no detectable amount of product was obtained, when **L** was used as catalyst under the similar reaction condition. This suggested that the direct contacts of the substrate with the amide groups present on the surface of nano-spheres were essential for catalytic activities. The catalytic activities of **HG** xerogel towards different *p*-substituted benzaldehyde ($X = -H, -NO_2, -Cl, -CH_3$ and $-OCH_3$) were studied and the obtained products were analysed by 1H -NMR and

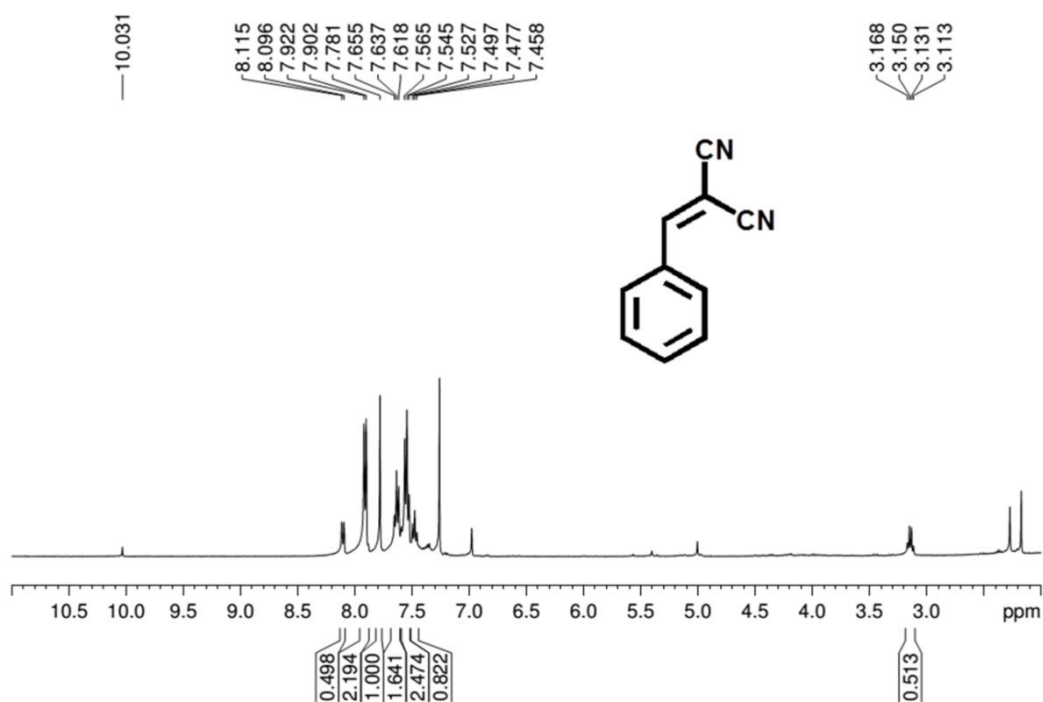


Figure 15. ¹H-NMR spectra (in CDCl_3) of 2-benzylidenemalononitrile formed by the condensation of malononitrile and benzaldehyde using **HG** xerogel as catalyst.

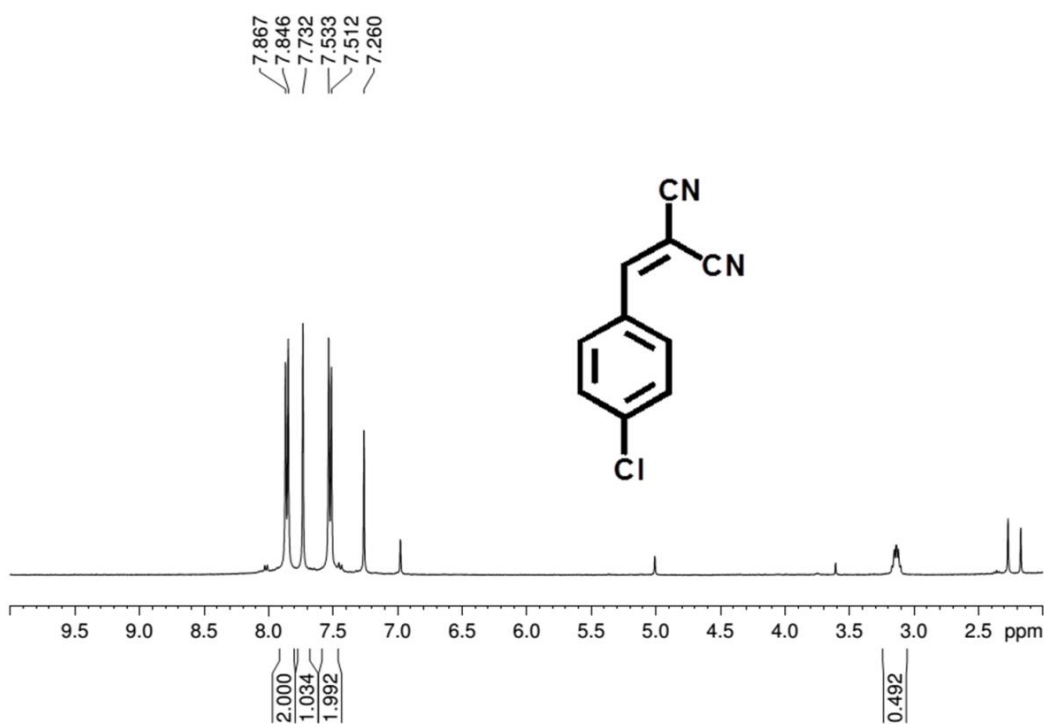


Figure 16. ¹H-NMR spectra (in CDCl_3) of 2-(4-chlorobenzylidene)malononitrile formed by the condensation of malononitrile and 4-chlorobenzaldehyde using **HG** xerogel as catalyst.

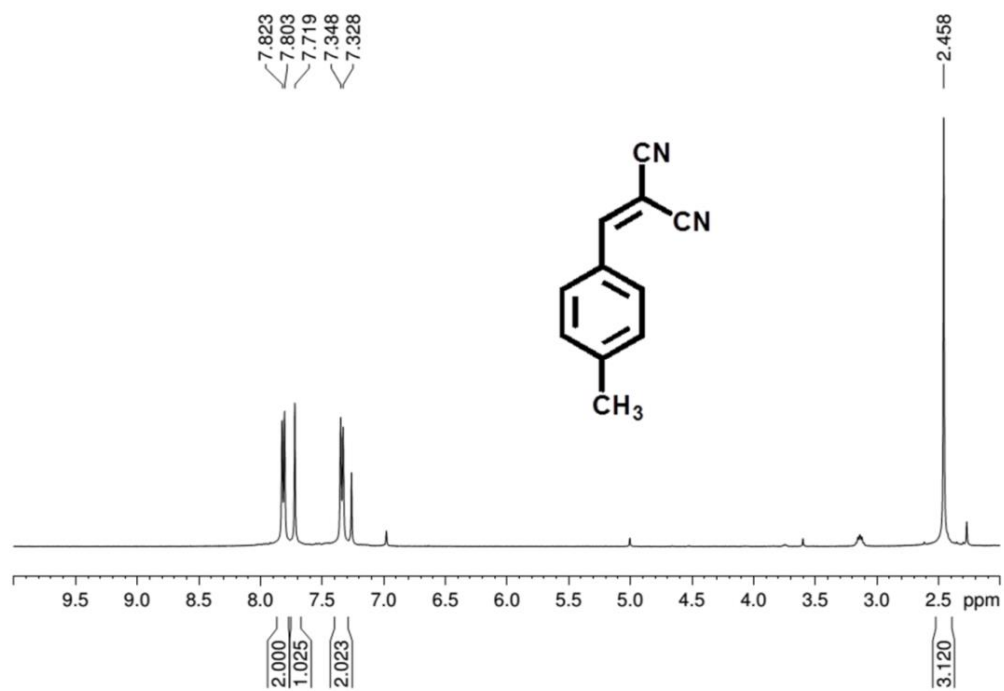


Figure 17. ¹H-NMR spectra (in CDCl₃) of 2-(4-methylbenzylidene)malononitrile formed by the condensation of malononitrile and p-tolualdehyde using **HG** xerogel as catalyst.

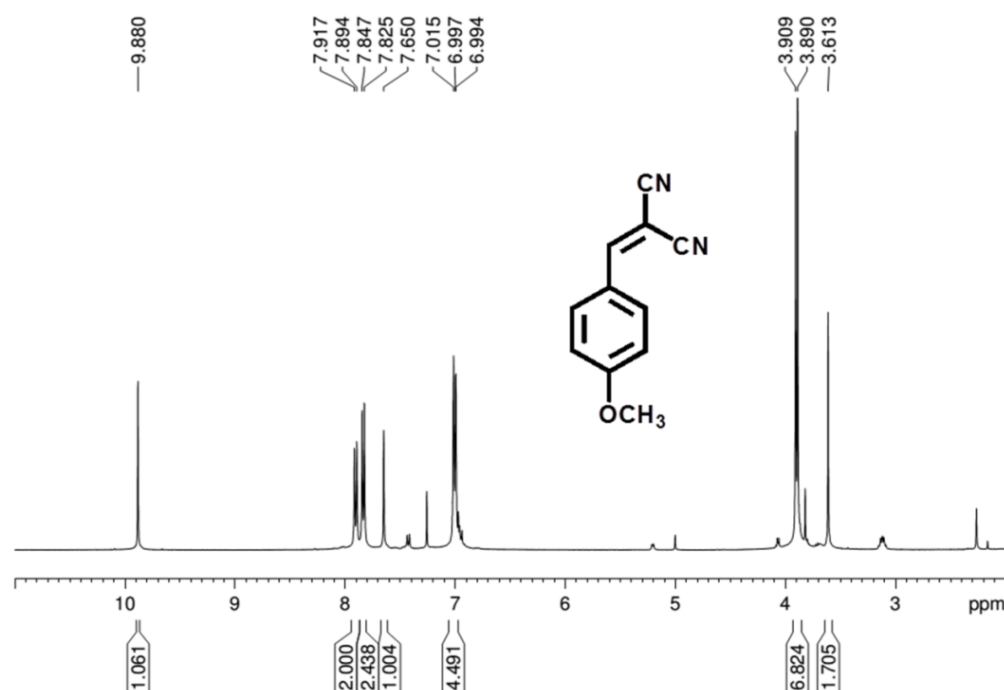
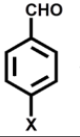
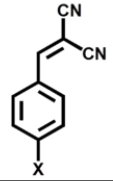
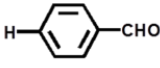
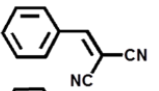
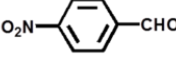
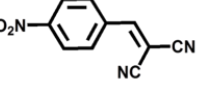
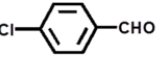
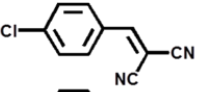
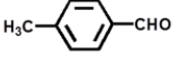
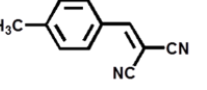
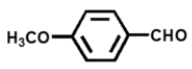
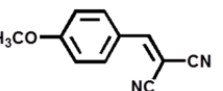


Figure 18. ¹H-NMR spectra (in CDCl₃) of 2-(4-methoxybenzylidene)malononitrile formed by the condensation of malononitrile and p-anisaldehyde using **HG** xerogel as catalyst.

Table 1. The catalytic reactions and the results with varying substituent on the aldehydes.

Reactant	Product	Time [h]	Conversion (%)
			
$\xrightarrow[\text{Dry THF, } 40^\circ\text{C}]{\text{HG xerogel}}$			
		4	90
		4	99
		4	85
		6	63
		6	57

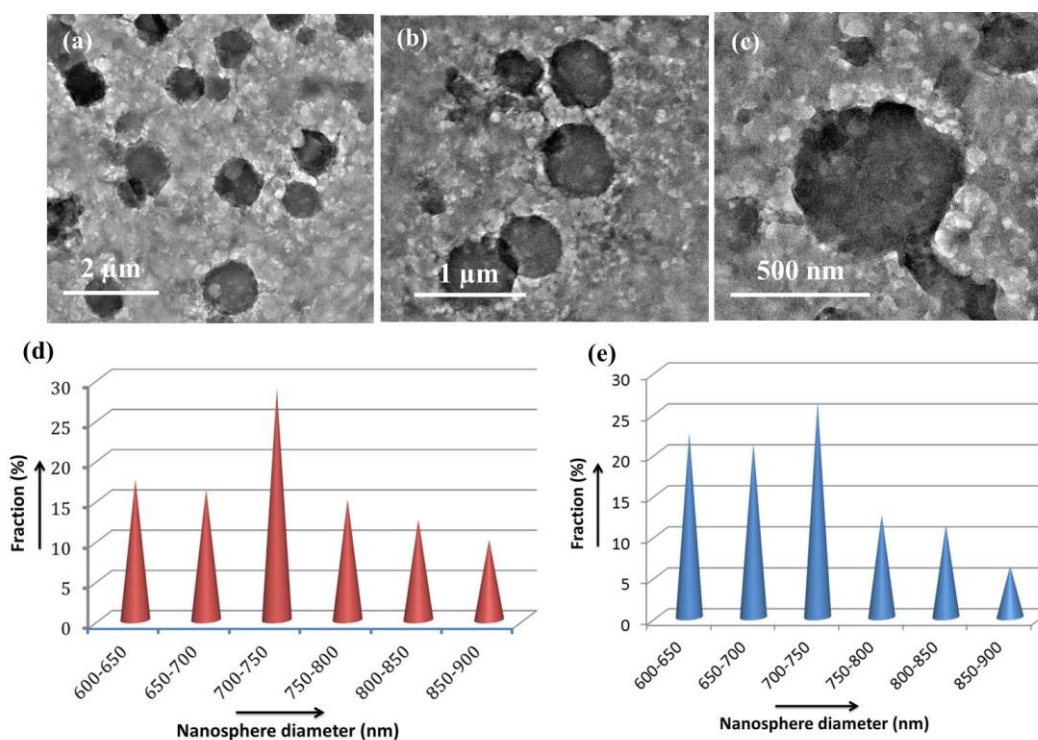


Figure 19. (a), (b), (c) TEM images of **HG** xerogel after 4th cycle of catalytic reaction, (d) Size distribution histogram plot of **HG** xerogel before catalytic reaction, (e) Size distribution histogram plot of **HG** xerogel-catalyst, recovered after 4th cycle of catalytic reaction.

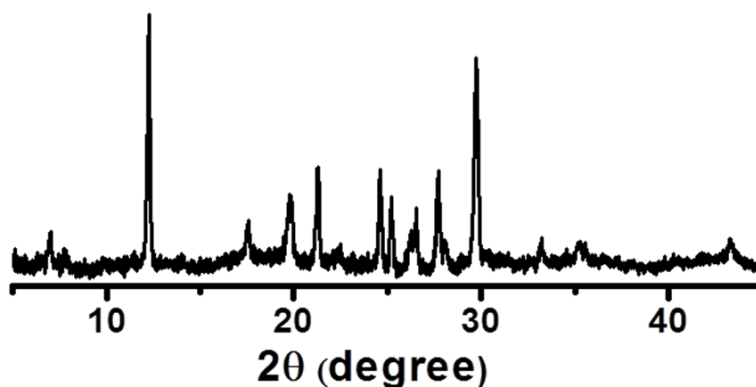


Figure 20. PXRD pattern of **HG** xerogel (**HG@THF**) after immersed in THF for 6 hours at 40°C.

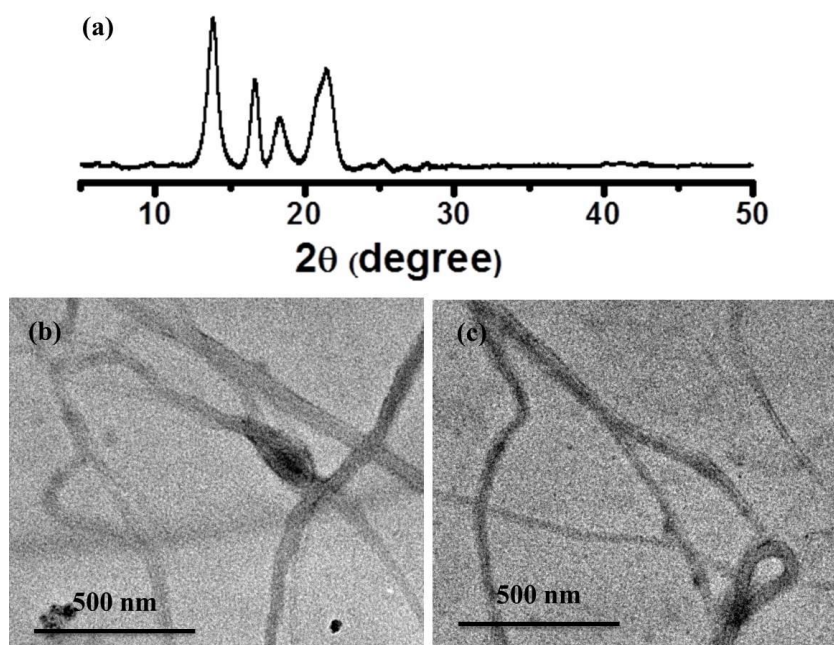


Figure 21. (a) PXRD pattern of **OG** xerogel (**OG@THF**) after immersed in THF for 6 hours at 40°C, (b), (c) TEM images of **OG** xerogel after it was immersed in THF for 6 hours at 40°C.

GCMS (Figure 12 and Figure 15-18). The conversion results were summarized in Table 1. Although the conversion of product was significant for X = -H, -NO₂ and -Cl, the yield was reduced for X = -CH₃, -OCH₃. This suggested that electron withdrawing group (-NO₂, -Cl) at the *para*-position of benzaldehyde enhanced the electrophilicity of the carbonyl carbon and thereby increased its reactivity.¹² However, the electron donating group (-OCH₃, -CH₃) reduced the electrophilicity of the carbonyl carbon and therefore exhibited lesser yield. The catalyst could be reused for at least 4 cycles. TEM images of

the catalyst after 4th cycle showed that the nano-sphere morphology was still retained (Figure 19a-c). The size distribution histogram plots of **HG** xerogel before and after the catalytic reaction also indicated that the sizes of nanosphere were unchanged after reaction (Figure 19d-e). The PXRD of **HG** xerogel did not change after immersing it in THF at 40 °C (**HG@THF**), thus confirming its stability (Figure 20). To further prove that the surface exposed amide groups are essential for the catalytic activity, we have performed same catalytic reactions with nanofiber **OG** xerogel. Interestingly, no conversion of product was observed even after 12 hours. This suggested that **OG** xerogel cannot catalyze the reaction. Stability of **OG** xerogel in THF at 40 °C (**OG@THF**) was confirmed by PXRD and TEM (Figure 21a-c). Since the amide groups were not exposed on the surface of nano-fiber, the reactants could not access the catalytic sites and therefore reaction did not occur. This further supported our conjecture of different self-assembly of **L** in two different solvent systems as discussed earlier.

3A.4 SUMMARY

The preceding results demonstrated design of a LMWG which could self-assemble in both aqueous and organic medium resulting into hydrogel and organogel, respectively. Hydrogel showed unique spherical morphology and CT emission. However, the organogel showed typical fibrous morphology. The nanosphere of hydrogel was utilized for catalysing Knoevenagel condensation reaction, whereas the nano-fibers of organogel failed to show catalytic activity due to inaccessibility of free amide groups. This work would open up a new perspective to rationally design LMWG that can form both organogel and hydrogel and explore their catalytic applications. Furthermore, the effect of metal ion coordination on self-assembly of this LMWG and their properties could be explored.

3A.5 REFERENCES

1. (a) J. W. Steed, *Chem. Soc. Rev.*, 2010, **39**, 3686-3699; (b) N. M. Sangeetha and U. Maitra, *Chem. Soc. Rev.*, 2005, **34**, 821-836; (c) M. D. Segarra-Maset, V. J. Nebot, J. F. Miravet and B. Escuder, *Chem. Soc. Rev.*, 2013, **42**, 7086-7098; (d) M.-O. M. Piepenbrock, N. Clarke, J. A. Foster and J. W. Steed, *Chem. Commun.*, 2011, **47**, 2095-2097; (e) C. Tomasini and N. Castellucci, *Chem. Soc. Rev.*, 2013, **42**, 156-172.
2. (a) S. S. Babu, V. K. Praveen and A. Ajayaghosh, *Chem. Rev.*, 2014, **114**, 1973-2129; (b) H.-Q. Peng, L.-Y. Niu, Y.-Z. Chen, L.-Z. Wu, C.-H. Tung and Q.-Z. Yang,

- Chem. Rev.*, 2015, **115**, 7502-7542; (c) B. O. Okesola and D. K. Smith, *Chem. Soc. Rev.*, 2016, **45**, 4226-4251; (d) P. Sutar and T. K. Maji, *Chem. Commun.*, 2016, **52**, 8055-8074; I P. Sutar, V. M. Suresh and T. K. Maji, *Chem. Commun.*, 2015, **51**, 9876-9879; (f) X. Du, J. Zhou, J. Shi and B. Xu, *Chem. Rev.*, 2015, **115**, 13165-13307; (g) J. Li, L. Mo, C.-H. Lu, T. Fu, H.-H. Yang and W. Tan, *Chem. Soc. Rev.*, 2016, **45**, 1410-1431; (h) M. Martínez-Calvo, O. Kotova, M. E. Möbius, A. P. Bell, T. McCabe, J. J. Boland and T. Gunnlaugsson, *J. Am. Chem. Soc.*, 2015, **137**, 1983-1992; (i) Z. Yu, J. Zhang, R. J. Coulston, R. M. Parker, F. Biedermann, X. Liu, O. A. Scherman and C. Abell, *Chem. Sci.* 2015, **6**, 4929-4933.
3. (a) L. Gao, D. Xu and B. Zheng, *Chem. Commun.*, 2014, **50**, 12142-12145; (b) P. K. Vemula and G. John, *Chem. Commun.*, 2006, 2218-2220; (c) N. Minakuchi, K. Hoe, D. Yamaki, S. Ten-no, K. Nakashima, M. Goto, M. Mizuhata and T. Maruyama, *Langmuir.*, 2012, **28**, 9259-9266; (d) T. Kar, S. K. Mandal and P. K. Das, *Chem. – Eur. J.*, 2011, **17**, 14952-14961; € N. Yan, G. He, H. Zhang, L. Ding and Y. Fang, *Langmuir.*, 2010, **26**, 5909-5917.
4. (a) K. Jalani, M. Kumar and S. J. George, *Chem. Commun.*, 2013, **49**, 5174-5176; (b) A. Das and S. Ghosh, *Chem. Commun.* 2011, **47**, 8922-8924; (c) L. Zhang, X. Wang, T. Wang and M. Liu, *Small*, 2015, **11**, 1024-1024; (d) E. Busseron, Y. Ruff, E. Moulin and N. Giuseppone, *Nanoscale.* 2013, **5**, 7098-7140; € C. Liu, Q. Jin, K. Lv, L. Zhang and M. Liu, *Chem. Commun.* 2014, **50**, 3702-3705.
5. (a) K. V. Rao, K. Jayaramulu, T. K. Maji and S. J. George, *Angew. Chem. Int. Ed.*, 2010, **49**, 4218-4222; (b) S. Basak, S. Bhattacharya, A. Datta and A. Banerjee, *Chem. – Eur. J.* 2014, **20**, 5721-5726; (c) V. M Agranovich, Y. N. Gartstein and M. Litinskaya, *Chem. Rev.*, 2011, **9**, 5179-5214; (d) M. Kumar, K. V. Rao and S. J. George, *Chem. Commun.*, 2014, **16**, 1300-1313; € Y. Liu, N. Zheng, H. Li and B. Yin, *Soft Matter.*, 2013, **9**, 5261-5269; (f) S. Bhattacharjee, B. Maiti and S. Bhattacharya, *Nanoscale.*, 2016, **8**, 11224-11233; (g) S. Bhattacharjee and S. Bhattacharya, *Chem. Asian. J.*, 2015, **10**, 572-580.
6. (a) E. M. Schneider, M. Zeltner, N. Kranzlin, R. N. Grass and W. J. Stark, *Chem. Commun.* 2015, **51**, 10695-10698; (b) S. D. Walker, C. J. Borths, E. DiVirgilio, L. Huang, P. Liu, H. Morrison, K. Sugi, M. Tanaka, J. C. S. Woo and M. M. Faul, *Org. Process Res. Dev.*, 2011, **15**, 570; (c) L. R. Madivada, R. R. Anumala, G. Gilla, S. Alla, K. Charagondla, M. Kagga, A. Bhattacharya and R. Bandichhor, *Org. Process*

Res. Dev., 2009, **13**, 1190-1194; (d) E. Knoevenagel, *Ber. Dtsch. Chem. Ges.*, 1898, **31**, 2596.

7. (a) V. M. Suresh, S. Bonakala, H. S. Atreya, S. Balasubramanian and T. K. Maji, *ACS. Appl. Mater. Interfaces.*, 2014, **6**, 4630-4637; (b) S. Hasegawa, S. Horike, R. Matsuda, S. Furukawa, K. Mochizuki, Y. Kinoshita and S. Kitagawa, *J. Am. Chem. Soc.*, 2007, **129**, 2607-2614; (c) R. Haldar, S. K. Reddy, V. M. Suresh, S. Mohapatra, S. Balasubramanian and T. K. Maji, *Chem. – Eur. J.*, 2014, **20**, 4347-4356; (d) J. Park, J.-R. Li, Y.-P. Chen, J. Yu, A. A. Yakovenko, Z. U. Wang, L.-B. Sun, P. B. Balbuena and H.-C. Zhou, *Chem. Commun.*, 2012, **48**, 9995-9997; € Y. K. Hwang, D.-Y. Hong, J.-S. Chang, S. H. Jung, Y.-K. Seo, J. Kim, A. Vimont, M. Daturi, C. Serre and G. Férey, *Angew. Chem. Int. Ed.*, 2008, **47**, 4144-4148.

8. (a) M. Maity and U. Maitra, *J. Mater. Chem. A.*, 2014, **2**, 18952-18958; (b) F. Rodriguez-Llansola, J. F. Miravet and B. Escuder, *Chem. Commun.*, 2009, 7303-7305. (c) F. Hapiot, S. Menuel and E. Monflier, *ACS Catal.*, 2013, **3**, 1006-1010; (d) K. R. Reddy, K. Rajgopal, C. U. Maheswari and M. Lakshmi Kantam, *New. J. Chem.*, 2006, **30**, 1549-1552.

9. B. G. Bag and S. S. Dash, *Langmuir*, 2015, **31**, 13664-13672.

10. (a) J. F. Michalec, S. A. Bejune, D. G. Cuttell, G. C. Summerton, J. A. Gertenbach, J. S. Field, R. J. Haines and D. R. McMillin, *Inorg. Chem.*, 2001, **40**, 2193-2200; (b) Y. H. Lee, N. V. Nghia, M. J. Go, J. Lee, S. U. Lee and M. H. Lee, *Organometallics.*, 2014, **33**, 753-762.

11. R. Haldar, R. Matsuda, S. Kitagawa, S. J. George and T. K. Maji, *Angew. Chem. Int. Ed.*, 2014, **126**, 11966-11971.

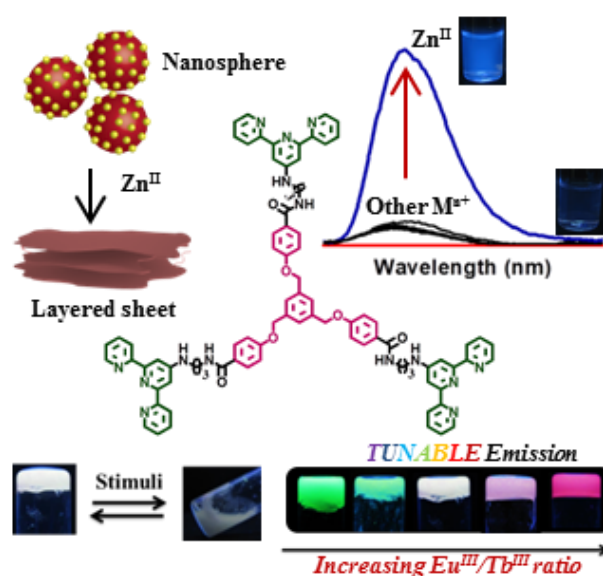
12. A. Chakraborty, S. Bhattacharyya, A. Hazra, A. C. Ghosh and T. K. Maji, *Chem. Commun.*, 2016, **52**, 2831-2834.

Chapter 3B

**Coordination Polymer Gels with Modular
Nano-morphologies, Tunable Emissions
and Stimuli-responsive Behaviour Based
on an Amphiphilic Tripodal Gelator**

Abstract

The recent upsurge in research on coordination polymer gels (CPGs) stems from their synthetic modularity, nanoscale processability and versatile functionalities. This chapter reports the self-assembly of an amphiphilic, tripodal low molecular weight gelator (**L**), consists of 4,4',4-[1,3,5-phenyl-tri(methoxy)]-tris-benzene core and 2,2':6',2''-terpyridyl termini, with different metal ions toward the formation of CPGs which show controllable nanomorphologies, tunable emission and stimuli-responsive behaviours. **L** also acts as a selective chemosensor for Zn^{II} with very low limit of detection (0.18 ppm) in aqueous medium. Coordination driven self-assembly **L** with Zn^{II} in $\text{H}_2\text{O}/\text{MeOH}$ solvent mixture results in a coordination polymer hydrogel (**ZnL**) which exhibits sheet-like morphology. The **ZnL** xerogel shows charge-transfer emission. On the other hand, coordination of **L** with Tb^{III} and Eu^{III} in CHCl_3/THF solvent mixture results in green and red emissive CPGs, respectively with nanotubular morphology. Moreover, precise stoichiometric control of **L**: Eu^{III} : Tb^{III} ratio leads to the formation of bimetallic CPGs which show tunable emissions over a broad spectral range, including white-light-emission. The multi-stimuli responsive properties of the white-light-emitting CPG are also studied by exploiting the dynamics of Ln^{III} -tpy coordination.



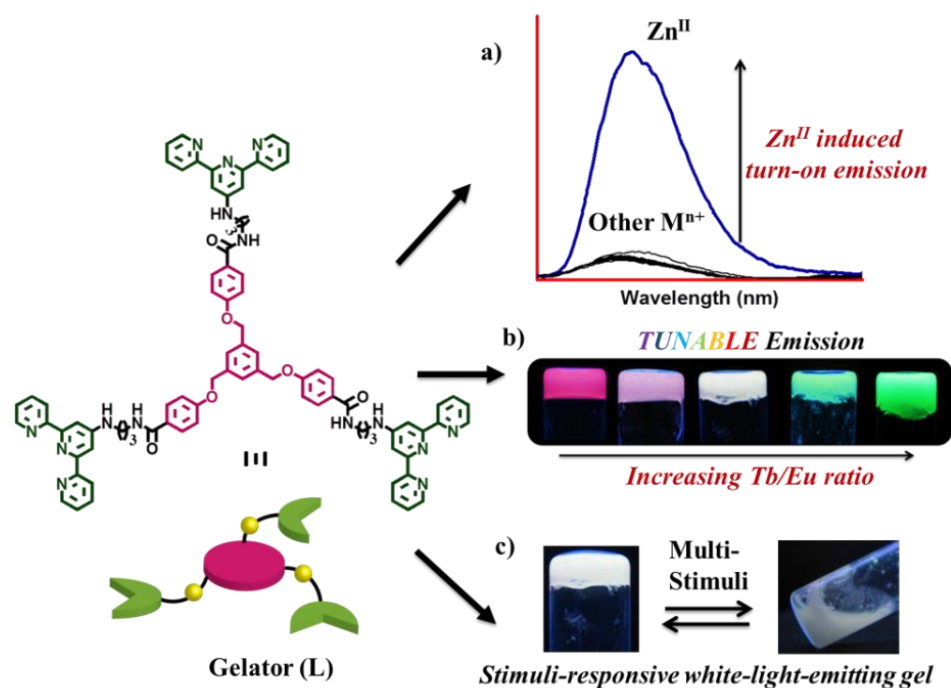
Paper published based on this work:

P. Sutar, and T. K. Maji, *Inorg. Chem.*, 2017, **56**, 9417–9425.

3B.1 INTRODUCTION

Recently, enormous attention has been focused on the development of multi-functional CPGs, achieved by the self-assembly of metal ions and low molecular weight gelators (LMWGs).¹ CPGs are highly promising soft-hybrid materials as the presence of metal ions endows them with unique redox, optical, electronic and catalytic properties.² Also, the metal-LMWG interactions allow the controlled growth of different nanostructures, such as fibers, tubes, rings, ribbons and vesicles in CPGs.^{3,4} Many novel functionalities such as tunable emission, catalysis, proton conductivity, sensing and gas storage have been explored in CPGs, which arise due to the synergistic combination of inorganic and organic components.⁵ Among many divergent classes of LMWGs reported to-date, the amphiphilic gelator containing donor and acceptor π -chromophores connected by a flexible alkylamide chain is intriguing.⁶ This is because dynamic self-assembly of such LMWGs in aqueous or organic solvents results in hydrogel or organogel with different nanostructures and properties.⁷ The previous chapter reports the self-assembly of such flexible, amphiphilic LMWG (**L**) having 4,4',4''-[1,3,5-phenyl-tri(methoxy)]-tris-benzene (tmb) core and 2,2':6',2''-terpyridyl (tpy) termini to hydrogel (HG) and organogel (OG) with nanosphere and nanofiber morphologies, respectively.^{7a} Different spatial organization of tmb (donor) and tpy (acceptor) moieties of **L** resulted in charge transfer (CT) emission in **HG** and LMWG-based emission in **OG**. It was envisioned that the coordination of specific metal ions to the tpy units of **L** could further drive the self-assembly in different way and resulted in CPGs with added complexity and functionality. Moreover, metal binding could provide fluorescence readout signal which could be useful for specific recognition process. Example of LMWG which can act as a chemosensor for a metal ion and form CPG with the same metal ion is very rare.^{1c} In this regard, designing of LMWG for selective detection of Zn^{II} from water is important as it is the second most abundant metal ion in the human body. Zn^{II} is an important structural cofactor in many biological processes.⁸ However, it is also a significant metal pollutant present in drinking water which causes several diseases including alzheimer, epilepsy and ischemic stroke.⁹ Long-term exposure to high levels of Zn^{II} could also induce liver and kidney damage. Hence, detection of Zn^{II} from drinking water is essential. Among various detection procedures, chelation enhanced fluorescence (CHEF) is highly effective as it provide fluorescence enhancement with or without any spectral shifts after chelation with specific metal ions.¹⁰ Hence the presence of metal ion could be easily detected by naked eye. One

important feature of the gel materials is stimuli-responsive behaviour. In this regard, significant amount of work has been done on pH-, mechano-, photo-responsive behaviour of organogels or hydrogels, synthesized from purely organic systems.¹¹ In spite of such overwhelming progress, there are still very few reports on stimuli-responsive CPGs. In this respect, lanthanide (Ln^{III})-based coordination polymer gels (Ln^{III} -CPG) could be a potential platform for studying stimuli-responsive sol-gel transition and corresponding emission change.^{5c} This is because Ln^{III} -based materials exhibit narrow band emissions (red: Eu^{III} , Pr^{III} , Sm^{III} ; green: Tb^{III} , Er^{III} ; blue: Tm^{III} , Ce^{III}) with high quantum yields when coordinate to suitable π -chromophoric chelator, such as terpyridine (NANAN). Recently, many Ln^{III} -based materials, including Ln^{III} -CPGs with unique emission properties, stemming from sensitized f-f electronic transition have been exploited for sensing and solid state lighting applications.¹² However, little attention has been given on fabricating processable white-light-emitting CPG and exploiting their stimuli-responsive behaviours. In this respect, Ln^{III} -CPGs having weak Ln^{III} -NANAN interactions (hard acid-soft base) is interesting as they could be explored for the mechanistic understanding of stimuli-responsive reversible sol-gel transition and corresponding emission dynamics.^{5c}



Scheme 1. Schematic showing the structure of L, a) L acts as a chemosensor for Zn^{II} ion, b) Coordination of L with Tb^{III} / Eu^{III} (in different ratios) results in CPGs with tunable emission property, including white-light-emission, c) The white-light-emitting CPG shows multi-stimuli responsive behaviours.

This chapter reports the chemo-sensing property of **L**, coordination driven self-assembly of **L** to CPGs and multi-stimuli responsive behaviours of the CPGs. The gelator **L** could detect Zn^{II} in ppm level from aqueous solution based on fluorescence turn-on response. Furthermore, the coordination driven self-assembly of **L** with Zn^{II} in $\text{H}_2\text{O}/\text{MeOH}$ solvent mixture led to the formation of a coordination polymer hydrogel (**ZnL**) which exhibited sheet-like morphology. The **ZnL** showed CT emission similar to the previously reported **HG**. Moreover, coordination of **L** with Tb^{III} and Eu^{III} in CHCl_3/THF solvent mixture led to the formation of CPGs (**TbL** and **EuL**) which exhibited green and red emissions, respectively. By controlling the stoichiometry of **L** : Eu^{III} : Tb^{III} , bimetallic CPGs were prepared which showed tunable emission over a broad spectral range, including white-light-emission. Moreover, the multi stimuli-responsive behaviours of the bimetallic CPGs were explored based on the Ln^{III} -tpy coordination dynamics (Scheme 1).

3B.2 EXPERIMENTAL SECTION

3B.2.1 Materials

1,3,5-tris(bromomethyl)benzene, methyl-4-hydroxybenzoate, 4'-chloro-2,2':6',2''-terpyridine, 1,3-diaminopropane, triphenylphosphine (PPh_3), trichloroisocyanuric acid (TCIC) were purchased from Sigma-Aldrich chemical Co. Ltd. All solvents were purchased from Spectrochem Pvt. Ltd. All the metal salts $\text{Zn}(\text{NO}_3)_2 \cdot 6\text{H}_2\text{O}$, $\text{Tb}(\text{NO}_3)_3 \cdot 6\text{H}_2\text{O}$ and $\text{Eu}(\text{NO}_3)_3 \cdot 6\text{H}_2\text{O}$ were purchased from Alfa Aesar. All the other chemicals were purchased from Spectrochem Pvt. Ltd. All solvents were pre-dried using standard procedures before using. For UV-Vis experiments spectroscopic grade solvents were purchased from Spectrochem Pvt. Ltd.

3B.2.2 Physical measurements

$^1\text{H-NMR}$ was recorded on a Bruker AV-400 spectrometer with chemical shifts recorded as ppm and all spectra were calibrated against TMS. High resolution mass spectra (HRMS) was recorded on Agilent 6538 Ultra High Definition (UHD) Accurate-Mass Q-TOF-LC/MS system using electrospray ionization (ESI) modes. Elemental analysis was performed on a Thermo Fisher Flash 2000 Elemental Analyser. UV-Vis spectra were recorded on a Perkin-Elmer lamda 900 spectrometer. Fluorescence studies were accomplished using Perkin Elmer Ls55 Luminescence spectrometer. Fourier transform infrared spectroscopy (FTIR) studies were carried out by making samples with

KBr pellets using Bruker FTIR spectrometer. Morphology studies were carried out using Lica-S440I field emission scanning electron microscopy (FESEM). The xerogel samples were dispersed in ethanol and drop-casted on silicon wafer. The FESEM images were taken under high vacuum using accelerating voltage of 10 kV. Elemental mapping was also performed in the same instrument. Energy dispersive X-ray spectroscopy (EDXS) analysis was performed with an EDAX genesis instrument attached to the FESEM column. Transmission electron microscopy (TEM) analysis was performed using JEOL JEM-3010 with accelerating voltage of 300 kV. For this analysis the xerogel was dispersed in ethanol and then drop casted on a carbon coated copper grid. Inductively Coupled Plasma Atomic Emission Spectroscopy (ICP-AES) measurements were performed on Perkin Elmer Optima 7000dv ICP-AES.

3B.2.3 Synthesis

Synthesis of ZnL hydrogel: 9 mg **L** was dissolved in 600 μl MeOH. 1.9 mg $\text{Zn}(\text{NO}_3)_3 \cdot 6\text{H}_2\text{O}$ was dissolved in 400 μl water. The solution of Zn^{II} was slowly added into the methanolic solution of **L**. The mixture was sonicated for 2-3 minutes. The mixture immediately converted to opaque **ZnL** gel. The formation of gel was confirmed by inversion-test method. Selected FTIR data (KBr, cm^{-1}): For **ZnL** xerogel: 3215 (m), 3063 (b), 2978- 2749 (m), 2673 (sh), 2493 (s), 1705 (sh), 1601 (m), 1470 (sh), 1397 (sh), 1245 (m), 1168 (s), 1055 (m), 848 (s), 788 (sh), 531 (sh).

Synthesis of TbL and EuL gels: 500 μl solution of **L** (1×10^{-3} M) in CHCl_3/THF (2:1) was mixed with 500 μl solution of $\text{Tb}(\text{NO}_3)_3 \cdot 6\text{H}_2\text{O}$ (1×10^{-3} M, in THF). The mixture was heated at 90 $^\circ\text{C}$ for 2-3 minutes to prepare a viscous solution which eventually resulted in stable opaque **TbL** gel upon cooling. Similarly **EuL** gel was also prepared. 500 μl solution of **L** (1×10^{-3} M) in CHCl_3/THF (2:1) was mixed with 500 μl solution of $\text{Eu}(\text{NO}_3)_3 \cdot 6\text{H}_2\text{O}$ (1×10^{-3} M, in THF). The mixture was heated at 90 $^\circ\text{C}$ for 2-3 minutes to prepare a viscous solution which converted to opaque **EuL** gel upon cooling. In both case, the formation of gels were confirmed by inversion-test method. Selected FTIR data (KBr, cm^{-1}) for **TbL** xerogel: 3426 (b), 2973- 2829 (m), 1640 (m), 1457 (s), 1384 (sh), 1168 (s), 997 (s), 973 (s), 840 (s), 808 (s). Selected FTIR data (KBr, cm^{-1}) for **EuL** xerogel: 3419 (b), 2426 (s), 1637 (sh), 1469 (s), 1382 (sh), 1041 (s), 975 (s), 746 (s).

Synthesis of bimetallic CPGs: First (1×10^{-3} M) and (1×10^{-3} M) solutions of $\text{Tb}(\text{NO}_3)_3 \cdot 6\text{H}_2\text{O}$ and $\text{Eu}(\text{NO}_3)_3 \cdot 6\text{H}_2\text{O}$ are prepared by dissolving the metal salts in THF. After that 250 μl solution of $\text{Tb}(\text{NO}_3)_3 \cdot 6\text{H}_2\text{O}$ and 250 μl solution of $\text{Eu}(\text{NO}_3)_3 \cdot 6\text{H}_2\text{O}$ are

added into 500 μl solution of **L** (1×10^{-3} M). The mixture is heated at 90 $^{\circ}\text{C}$ for few minutes to form viscous solution which is eventually converted to stable gel (**CPG1**) after cooling. Similarly **CPG2** was prepared by using (1×10^{-3} M) and (2×10^{-3} M) of $\text{Tb}(\text{NO}_3)_3 \cdot 6\text{H}_2\text{O}$ and $\text{Eu}(\text{NO}_3)_3 \cdot 6\text{H}_2\text{O}$ in THF, respectively. The **CPG3** was prepared by using (1×10^{-3} M) and (2.2×10^{-3} M) solutions of $\text{Tb}(\text{NO}_3)_3 \cdot 6\text{H}_2\text{O}$ and $\text{Eu}(\text{NO}_3)_3 \cdot 6\text{H}_2\text{O}$ in THF, respectively. Selected FTIR data (KBr, cm^{-1}): For **CPG1** xerogel: 3420 (b), 2940-2824 (m), 1635 (sh), 1457 (s), 1382 (sh), 1155 (s), 997 (s), 746 (s). For **CPG2** xerogel: 3421 (b), 2938-2827 (m), 1632 (sh), 1455 (s), 1384 (sh), 1157 (s), 980 (s), 743 (s). For **CPG3** xerogel: 3417 (b), 2941-2824 (m), 1630 (sh), 1457 (s), 1390 (sh), 1163 (s), 987 (s), 739 (s).

3B.3 RESULTS AND DISCUSSION

3B.3.1 Metal ion sensing

The solution of **L** (10^{-4} M) in methanol showed a broad absorption band at 250-320 nm, attributed to the π - π^* transition of the tmb and tpy moieties.^{7a} Since terpyridine is a well-known metal chelating group, the interactions of **L** with different metal ions ($\text{M}^{\text{n}+} = \text{Cu}^{\text{II}}, \text{Al}^{\text{III}}, \text{Ca}^{\text{II}}, \text{Cd}^{\text{II}}, \text{Co}^{\text{II}}, \text{Fe}^{\text{III}}, \text{Mg}^{\text{II}}, \text{Mn}^{\text{II}}, \text{Ni}^{\text{II}}, \text{Pb}^{\text{II}}, \text{Hg}^{\text{II}}, \text{Zn}^{\text{II}}, \text{Cu}^{\text{I}}, \text{Ag}^{\text{I}}$) were studied by gradually adding $\text{M}^{\text{n}+}$ solution (10^{-4} M) to the solution of **L** (10^{-5} M). Absorption spectrum of **L** did not show any spectral shift after addition of 3 equivalents of $\text{Cu}^{\text{II}}, \text{Al}^{\text{III}}, \text{Ca}^{\text{II}}, \text{Cd}^{\text{II}}, \text{Co}^{\text{II}}, \text{Fe}^{\text{III}}, \text{Mg}^{\text{II}}, \text{Mn}^{\text{II}}, \text{Ni}^{\text{II}}, \text{Pb}^{\text{II}}, \text{Hg}^{\text{II}}, \text{Ag}^{\text{I}}, \text{Cu}^{\text{I}}$. However, a significant change in absorption spectrum was observed after addition of Zn^{II} (Figure 1a). With incremental addition of Zn^{II} , absorption maximum of **L** at 280 nm shifted to 297 nm and a broad shoulder appeared at 318 nm which suggested complexation of Zn^{II} to tpy groups of **L** (Figure 1a). The titration curve saturated after reaching **L**: $\text{Zn}^{\text{II}} = 2:3$ which suggested the formation of coordination polymer with octahedral geometry of Zn^{II} . The fluorescence response of **L** in titration with different metal ions has shown in Figure 1b. For this experiment, 10^{-5} M solution of **L** in methanol was mixed with different metal ions and the final concentration of the metal ions was fixed at 1.5×10^{-5} M. A remarkable enhancement (10 folds) in fluorescence intensity at 420 nm was observed only after addition of Zn^{II} (Figure 1c). The change in fluorescence intensity could also be observed by bare eye under UV light (Figure 1d). Such enhancement in fluorescence was probably attributed to chelation enhanced fluorescence (CHEF) effect.¹³ As a control experiment, the fluorescence response of a model compound, 2,2':6',2''-terpyridin-4-yl-propane-1,3-

diamine in presence of different metal ions under similar condition was studied. Enhancement of fluorescence after addition of Zn^{II} , Cd^{II} , Al^{III} and Fe^{III} was observed, among which Zn^{II} showed highest enhancement. Also, slight diminution of fluorescence was observed in some cases (Cu^{II} , Co^{II} , Ni^{II}) (Figure 2). This suggested that the model compound did not show selectivity. The enhancement in fluorescence occurred due to the spatial reorganization of the terpyridine moieties of **L** after complexation with Zn^{II} which was also evident from the UV-Vis titration studies. No significant fluorescent enhancement was observed when metal ions that prefer N-donors, such as Ag^{I} and Cu^{I} were added to the solution of **L**. Above observations indicated that **L** could be used as chemosensor for Zn^{II} . Since methanol is a bio-hazardous solvent and detection of Zn^{II} from water is more important, we carried out the sensing experiment using solution of **L** (10^{-5} M) in $\text{H}_2\text{O}/\text{DMSO}$ (99.9: 0.1) solvent mixture and aqueous solution of Zn^{II} (10^{-5} M).

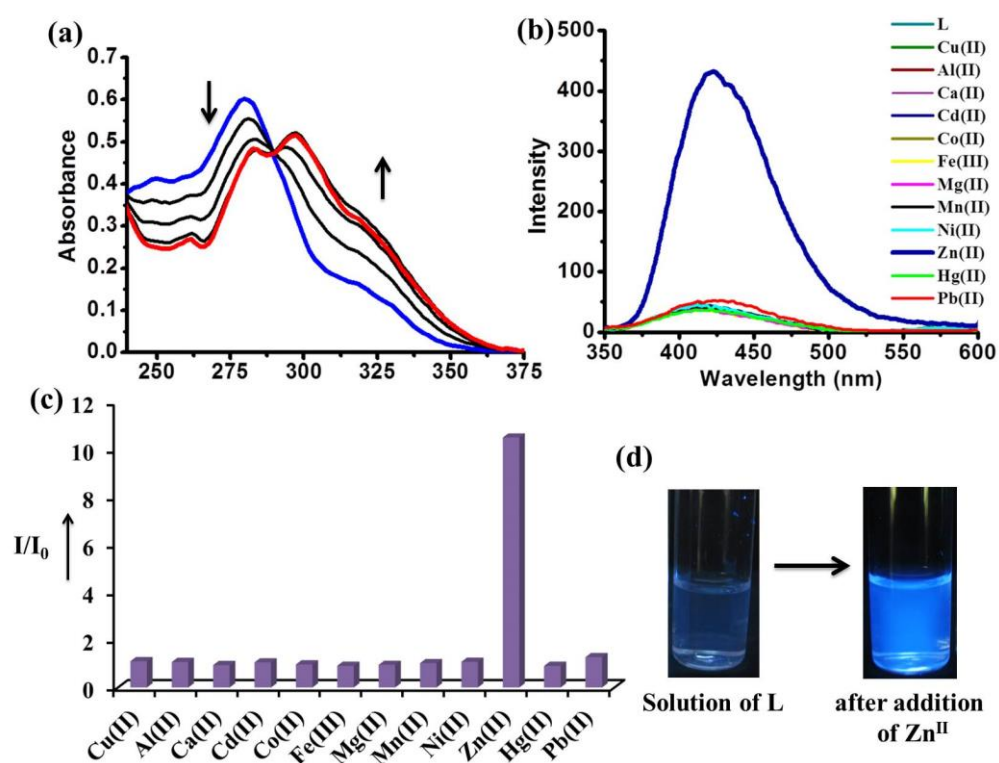


Figure 1. (a) Change in absorption spectra of methanolic solution of **L** after addition of different equivalents of Zn^{II} , (b) Change in emission spectra of methanolic solution of **L** after addition of different metal ions. Turn-on emission is observed after addition of Zn^{II} , (c) Relative fluorescence intensity of **L** in MeOH after addition of different metal ion solution, (d) Photograph of methanolic solution of **L** and after addition of Zn^{II} under UV light.

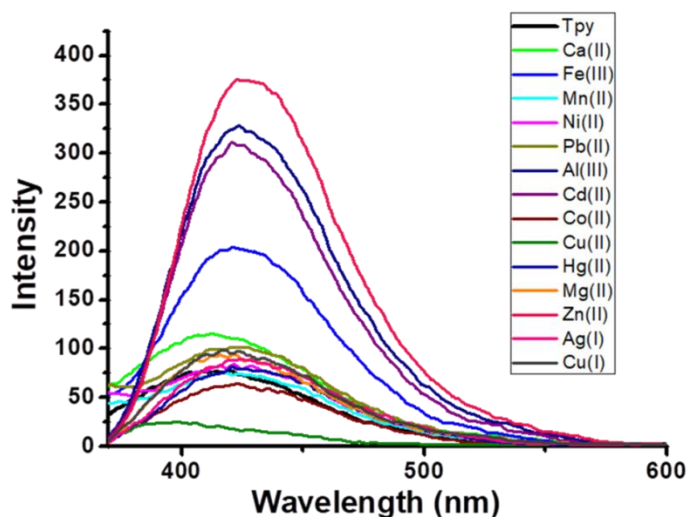


Figure 2 Change in emission spectra of methanolic solution of 2,2':6',2''-terpyridin-4-yl-propane-1,3-diamine (10^{-5} M) after addition of methanolic solution of different metal ions. The final concentration of metal ions in the mixture is 1.5×10^{-5} M in all cases.

Similar turn-on fluorescence response was observed after gradual addition of Zn^{II} to **L** (Figure 3a). In order to prove the selectivity of **L** towards Zn^{II} , the calculation of limit of detection (LOD) was performed through standard deviation and linear fitting. By plotting the relative fluorescence intensity (I/I_0) change as a function of concentration of Zn^{II} the LOD was calculated to be 6.25×10^{-7} M (0.18 ppm) (Figure 3b). According to World Health Organization (WHO) the acceptable limit for Zn^{II} in drinking water is 5 ppm. Hence **L** could act as good chemosensor for the detection of Zn^{II} from water.

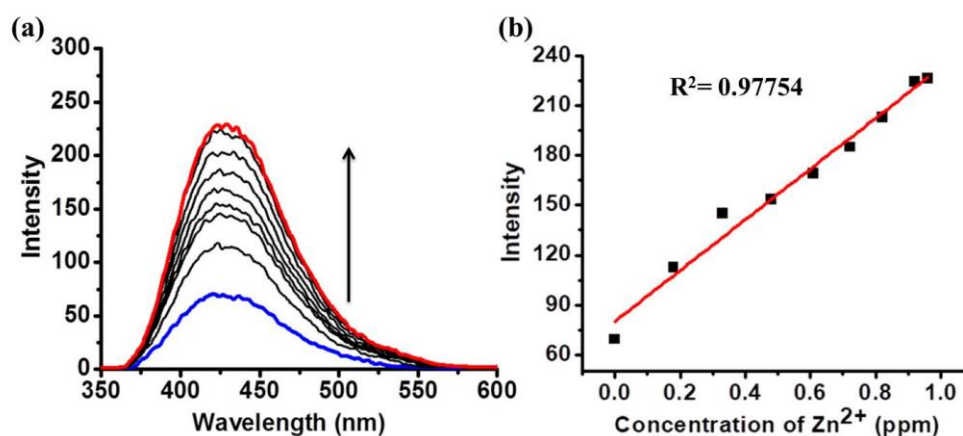


Figure 3. (a) Fluorescence spectra of **L** in $\text{H}_2\text{O}/\text{DMSO}$ (99.9: 0.1) upon addition of aqueous solution of Zn^{II} in ppm scale, (b) Plot of fluorescence intensity of **L** at 420 nm vs concentration of Zn^{II} .

3B.3.2 Synthesis and characterization of charge transfer CPG

The previous chapter reports how self-assembly of **L** in water/MeOH and CHCl_3/THF solvent mixtures resulted in hydrogel (**HG**) and organogel (**OG**) with nanosphere and nanofiber morphology, respectively.^{7c} To know how coordination of metal ions influence the gel nanostructure and corresponding emission properties, the gelation propensity of **L** in presence of Zn^{II} and $\text{Tb}^{\text{III}}/\text{Eu}^{\text{III}}$ was studied. 400 μl aqueous solution of $\text{Zn}(\text{NO}_3)_2 \cdot 6\text{H}_2\text{O}$ ($6.4 \times 10^{-3} \text{ M}$) was added to the 600 μl methanolic solution of **L** ($6.5 \times 10^{-3} \text{ M}$) and the mixture was kept undisturbed at room temperature. The mixture converted to gel (**ZnL**) within 2-3 minutes. The formation of gel was confirmed by inversion test method (Figure 4a). However, when >1 equivalent of Zn^{II} was added, instead of gelation, precipitation was observed. The precipitate was crystalline in nature. Insight into the morphology of **ZnL** was obtained by recording FESEM and TEM images of the corresponding xerogel (Figure 4b-f). The FESEM and TEM images of **ZnL** xerogel revealed the formation of micron sized sheets (Figure 4b-c). High resolution TEM images showed that sheets were stacked upon one another (Figure 4b-c). Formation of sheet-like

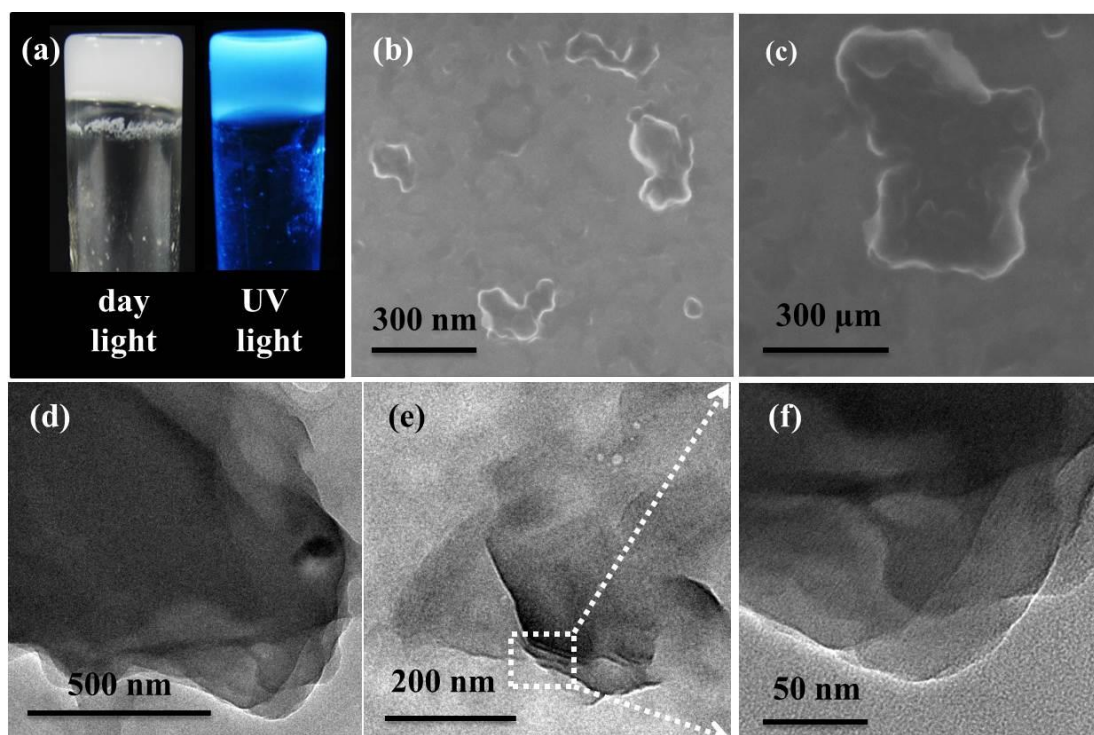
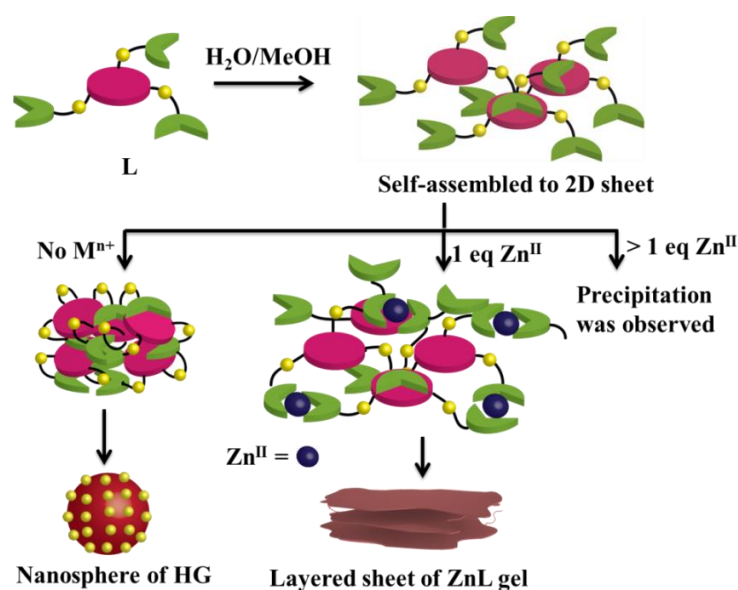


Figure 4. (a) Photograph of **ZnL** CPG under day light and UV-light, (b), (c) FESEM image of **ZnL** xerogel showing the presence of sheet-like morphology, (d), (e) TEM images of **ZnL** xerogel showing sheet-like morphology, (f) High resolution TEM image of **ZnL** xerogel showing layering of sheets.



Scheme 2. Schematic showing the self-assembly of **L** in $\text{H}_2\text{O}/\text{MeOH}$ leads to the formation of hydrogel (**HG**) with nanosphere morphology. In presence of 1 equivalent of Zn^{II} , the coordination polymer gel (**ZnL**) with sheet-like morphology is formed. Addition of >1 equivalent of Zn^{II} leads to the formation of precipitate.

morphology could be explained based on the coordination driven self-assembly of **L** as shown in Scheme 2. First, in polar solvent **L** was assembled through intermolecular π - π stacking between the tmb and tpy moieties.^{7c} In absence of metal ions, like Zn^{II} , the π -stacked tmb and tpy groups tried to minimize their contact with $\text{H}_2\text{O}/\text{MeOH}$ due to the hydrophobic effect. However, the hydrophilic amide groups tried to be exposed towards the polar solvent medium due to H-bonding interaction with $\text{H}_2\text{O}/\text{MeOH}$. As a result, the initial π -stacked nanostructures were folded into nanospheres whose exteriors were decorated with amide groups.^{7c} When Zn^{II} ions were added into the solution of **L** (**L**: Zn^{II} = 1: 1), tpy groups of **L** coordinated with Zn^{II} and reduced the flexibility of the initially formed π -stacked nanostructures. Hence, after coordination with Zn^{II} further folding of the 2D-assembly to nanospheres could not happen. Rather, the coordination of Zn^{II} propagated the self-assembly of **L** in 2D plane and resulted in 2D sheet morphology of **ZnL** (Scheme 2). The presence of Zn^{II} in **ZnL** xerogel was confirmed by energy dispersive X-ray spectroscopy (EDXS) analysis (Figure 5a). The elemental mapping of **ZnL** xerogel showed uniform distribution of C, N, O and Zn^{II} throughout the 2D sheet of **ZnL** (Figure 5b-e). The loading of Zn^{II} in **ZnL** xerogel was measured by ICP-AES analysis, which showed 39 mg Zn^{II} per gram of **ZnL**. This indicates **L** : Zn^{II} = 1 : 0.85 in the **ZnL** xerogel. The XPS of **ZnL** showed the binding energy of Zn 2p at 1029 eV

(Figure 6). These results clearly suggested that coordination of Zn^{II} to **L** has propagated the self-assembly of **L** to **ZnL** gel. However, it could be noted that some of the tpy groups remain uncoordinated in the **ZnL** hydrogel as two tpy groups of **L** participated in coordination at $\text{L} : \text{Zn}^{\text{II}} = 1 : 1$ ratio (Scheme 2). The UV-Vis spectrum of **ZnL** xerogel exhibited a broad absorption with maxima at 410 nm which was attributed to the interligand CT transition between π -stacked tmb (π -donor) and tpy groups (π -acceptor) (Figure 7a). Similar CT transition was also observed in **HG** xerogel.^{7c} Upon exciting at 400 nm **ZnL** xerogel showed cyan emission with maxima at $\lambda = 490$ nm (Figure 7a). Such red shifted emission in **ZnL** xerogel compared to **L** solution originated due to CT interaction.¹⁴ Moreover, excitation spectrum of **ZnL** xerogel showed the presence of ground state interaction, thus ruling out the possibility of excited state exciplex formation (Figure 7b).

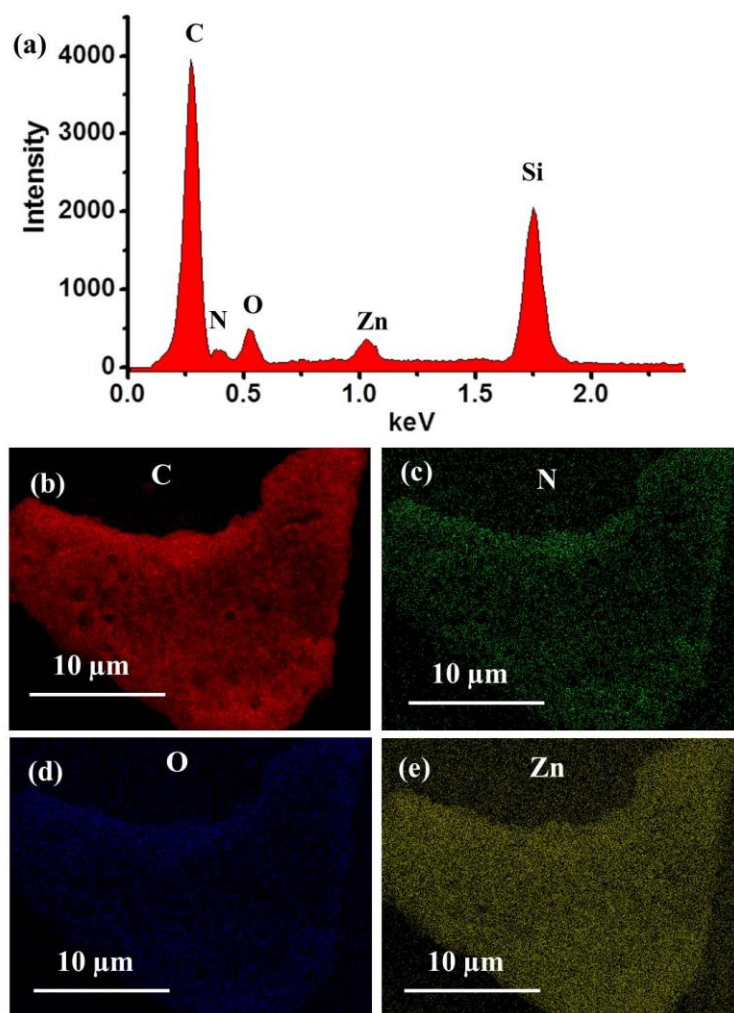


Figure 5. Top: (a) EDXS analysis of **ZnL** xerogel showing the presence of Zn^{II} ions in xerogel, Bottom: Elemental mapping of **ZnL** xerogel for (b) C, (c) N, (d) O, (e) Zn^{II} showing uniform distribution of all the elements throughout the xerogel matrix.

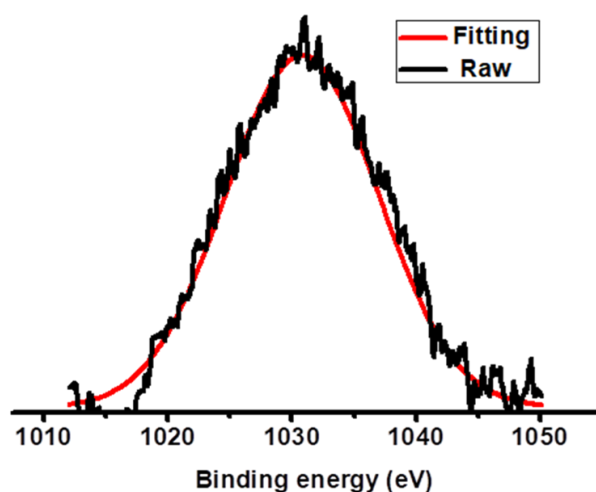


Figure 6. Zn 2p core level XPS spectrum for ZnL.

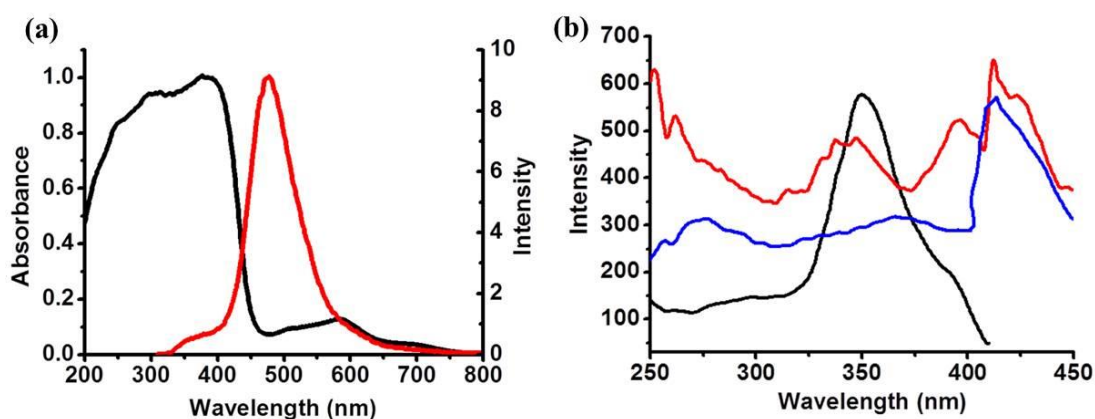


Figure 7. (a) Absorption spectra of ZnL xerogel, (b) Emission spectra of ZnL xerogel after excitation at 400 nm.

3B.3.3 Synthesis, characterization and emission properties of TbL and EuL organogels

Next, the gelation propensity of **L** in presence of different lanthanide ions was investigated. Heating the solution of **L** and $\text{Tb}(\text{NO}_3)_3 \cdot 6\text{H}_2\text{O}$ (molar ratio= 1:1) in CHCl_3/THF (2:1) solvent mixture followed by cooling, resulted in stable CPG (**TbL**) (Figure 8a). Likewise, the Eu^{III} -based CPG (**EuL**) was also prepared by heating and cooling the mixture of **L** and $\text{Eu}(\text{NO}_3)_3 \cdot 6\text{H}_2\text{O}$ (1: 1) in the aforementioned solvent mixture (Figure 8a). To gain insight into the mode of packing, **TbL** xerogel was analyzed by FESEM and TEM images. FESEM images of **TbL** showed the presence of uniformly distributed 1D-nanostructures with length in micrometer range (Figure 8b-c). However,

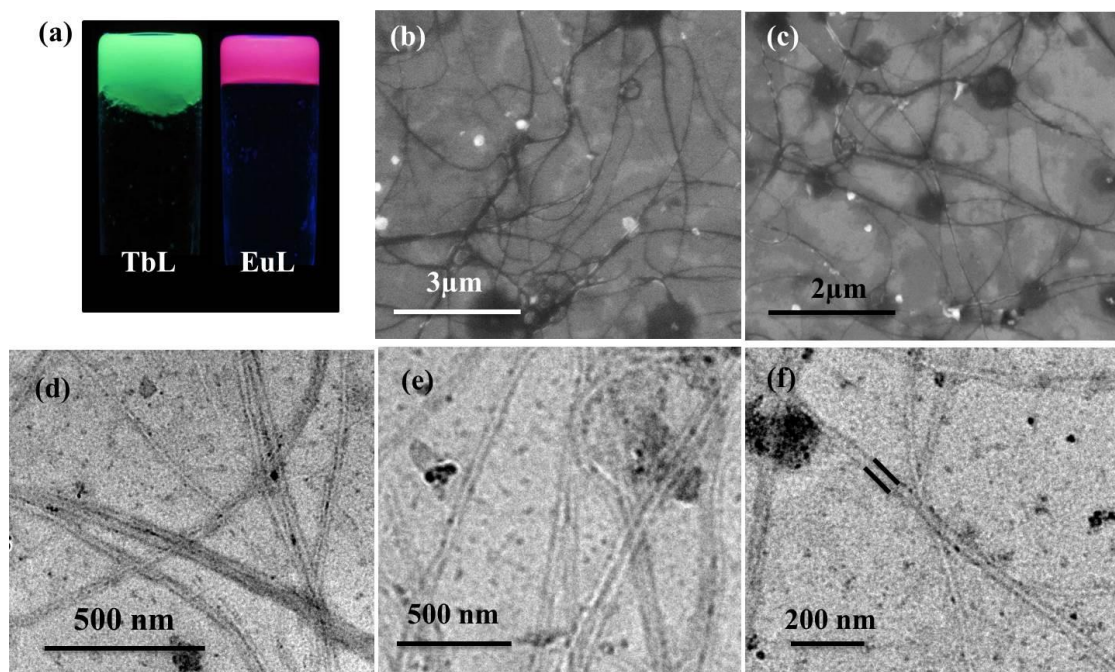


Figure 8. (a) Picture of **TbL** and **EuL** under UV-light, (b), (c) FESEM images of **TbL** xerogel, (d), (e) TEM images of **TbL** xerogel, (f) High resolution TEM image of **TbL** xerogel showing the formation of nanotubes.

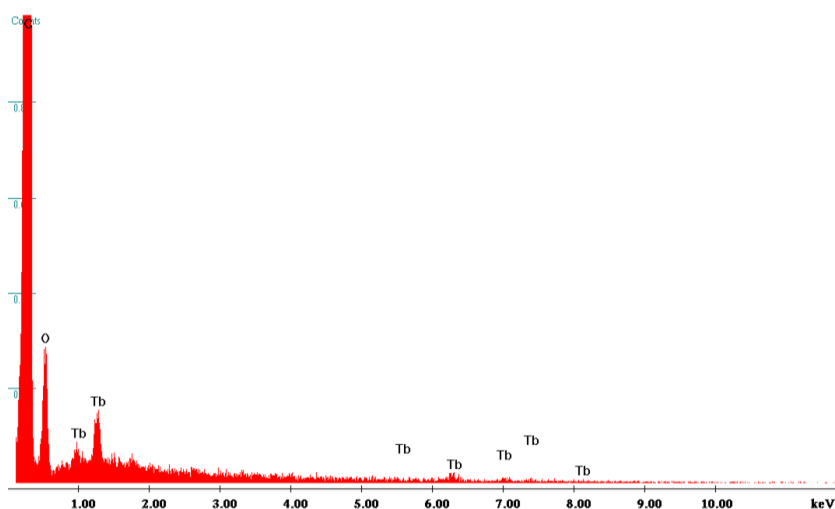


Figure 9. EDAX of **TbL** showing the presence of Tb^{III} .

high resolution TEM images of **TbL** xerogel revealed that the 1D-nanostructures were actually nanotubes with uniformly spaced dark lines separated by bright core (Figure 8d-f). Nanotubes were several micrometers long with an approximate diameter in 90-110 nm range. The presence Tb^{III} on the nanotubes of **TbL** xerogel was confirmed by EDXS analysis (Figure 9). The elemental mapping of **TbL** xerogel revealed uniform distribution

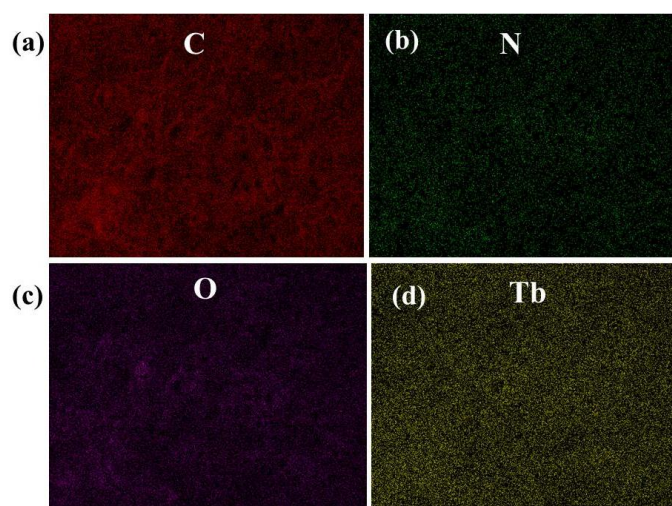


Figure 10. Elemental mapping of **TbL** xerogel showing uniform distribution of (a) C, (b) N, (c) O and (d) Tb^{III} throughout the gel-matrix.

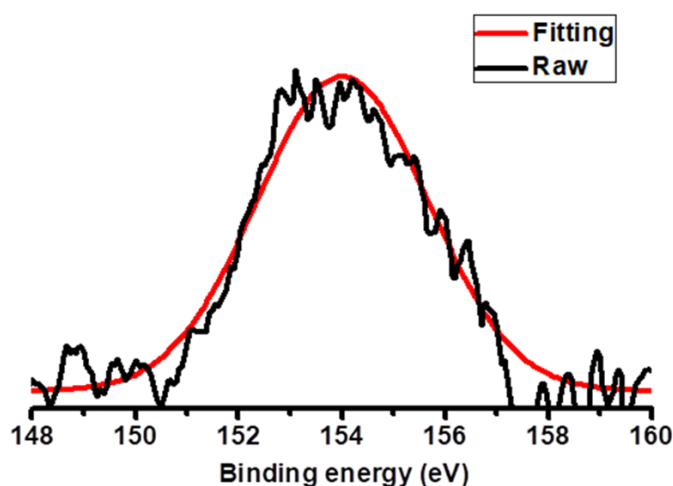


Figure 11. Tb 4d level XPS spectrum for **TbL**.

of Tb^{III} ions throughout the xerogel matrix (Figure 10). The XPS data revealed coordination of Tb^{III} to tpy group of **L** (Figure 11). These results confirmed that self-assembly of **L** in **TbL** has been propagated by coordination of Tb^{III} to **L**. The formation of nanotubes in **TbL** xerogel could be explained based on coordination driven self-assembly of **L** as shown in Figure 12. Initially, **L** self-assembled in CHCl_3/THF solvent mixture by complementary H-bonding between amide groups and π - π stacking between tmb cores of neighboring **L** and formed the nanofiber. When Tb^{III} was added to the solution of **L** in CHCl_3/THF solvent mixture, the pendent tpy groups present on the outer surface of the 1D-assembly coordinated with the Tb^{III} and further extended the assembly. The coordinated tpy units present around Tb^{III} ions oriented them orthogonally in

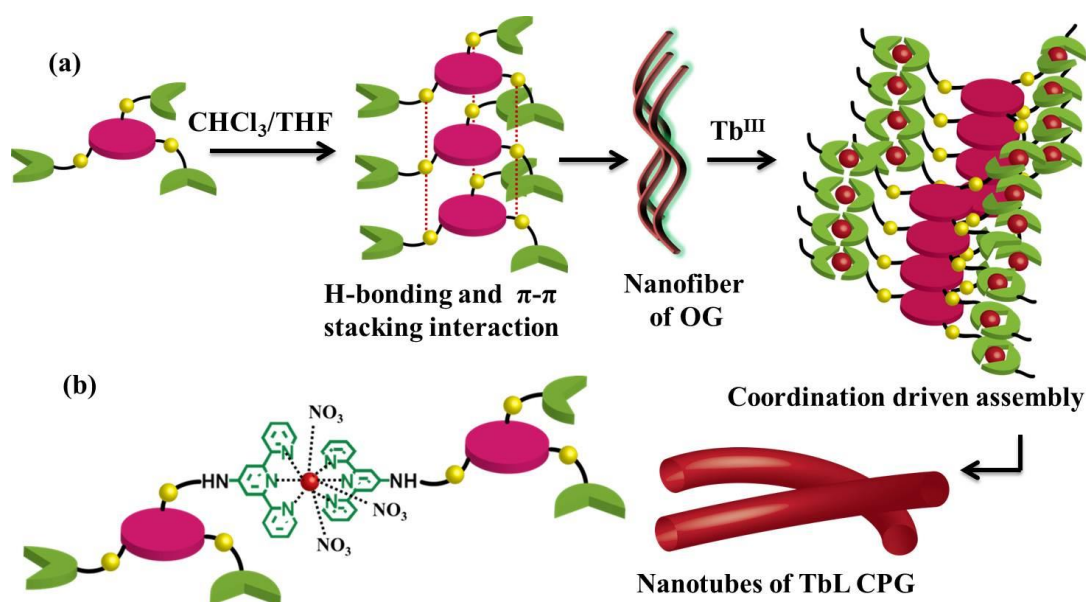


Figure 12. (a) Schematic showing the self-assembly for the formation of **TbL** nanotubes, (b) Probable coordination environment around Tb^{III} in **TbL** which leads to the formation of nanotube morphology.

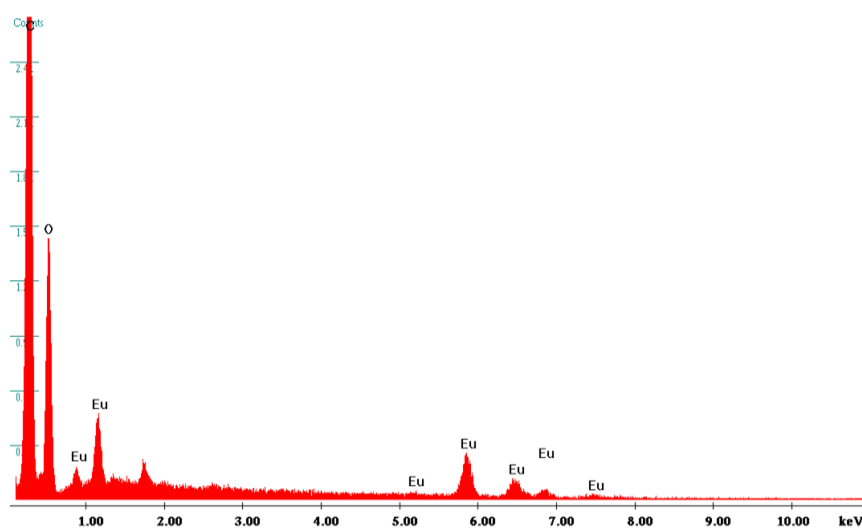


Figure 13. EDAX of **EuL** showing the presence of Eu^{III} .

order to reduce the steric repulsion and thus facilitated bending of primary 1D nanostructures into nanotubes.¹² Similarly, the presence of Eu^{III} in the **EuL** xerogels was confirmed by EDXS analysis (Figure 13). The elemental mapping of **EuL** xerogel showed even distribution of Eu^{III} ions throughout the xerogel network of **EuL** (Figure 14). The ICP-AES analysis of **TbL** exhibited 130.75 mg loading of Tb^{III} per gram of **TbL** xerogel. This indicated $\text{L} : \text{Tb}^{\text{III}} = 1 : 1.02$ in **TbL**. Similarly, ICP-AES analysis of **EuL**

showed 66.8 mg loading of Eu^{III} per gram of **EuL**. This indicated $\text{L} : \text{Eu}^{\text{III}} = 1 : 0.7$ in **EuL**. The XPS showed coordination of Eu^{III} to tpy group of **L** (Figure 14e). The UV-Vis spectra of **TbL** and **EuL** xerogels showed broad absorption with maxima at 340 nm (Figure 15a-b). Upon exciting at 330 nm emission spectrum of **TbL** xerogel displayed peaks at 488 nm, 543 nm, 584 nm and 620 nm which could be attributed to the $^5\text{D}_4-^7\text{F}_j$ ($J=6-3$) transitions of Tb^{III} (Figure 16a). Moreover, **L**-centred peak at 440 nm was also observed in the emission spectrum of **TbL**. Upon exciting at 330nm emission spectrum of **EuL** showed characteristics peaks for $^5\text{D}_0-^5\text{F}_j$ ($J=1-3$) transition of Eu^{III} at 592 nm, 615 nm and 687 nm respectively along with **L**-centred peak at 440 nm (Figure 16b). Under UV-light **TbL** and **EuL** CPG showed intense green and red emission respectively (insets of Figure 16a and 16b). The **TbL**

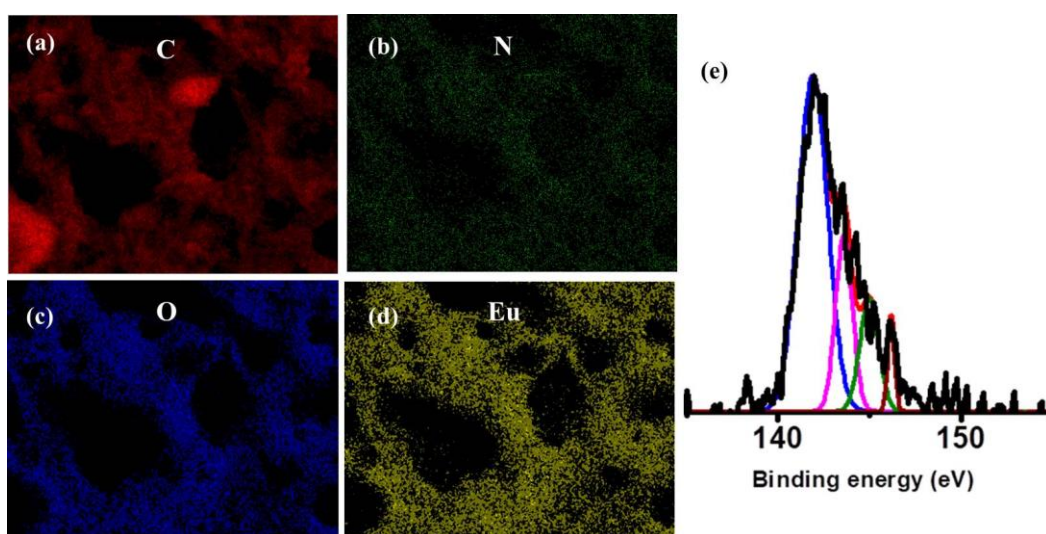


Figure 14. Elemental mapping of **EuL** xerogel showing the uniform distribution of (a) C, (b) N, (c) O and (d) Eu^{III} throughout the gel-matrix, (e) Eu 4d level XPS spectrum for **EuL**.

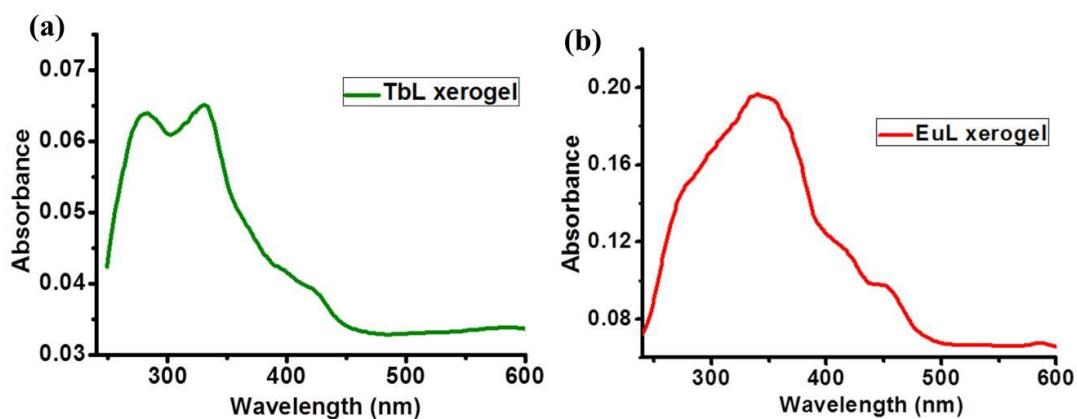


Figure 15. (a), (b) Absorption spectrum of **TbL** and **EuL** xerogel, respectively.

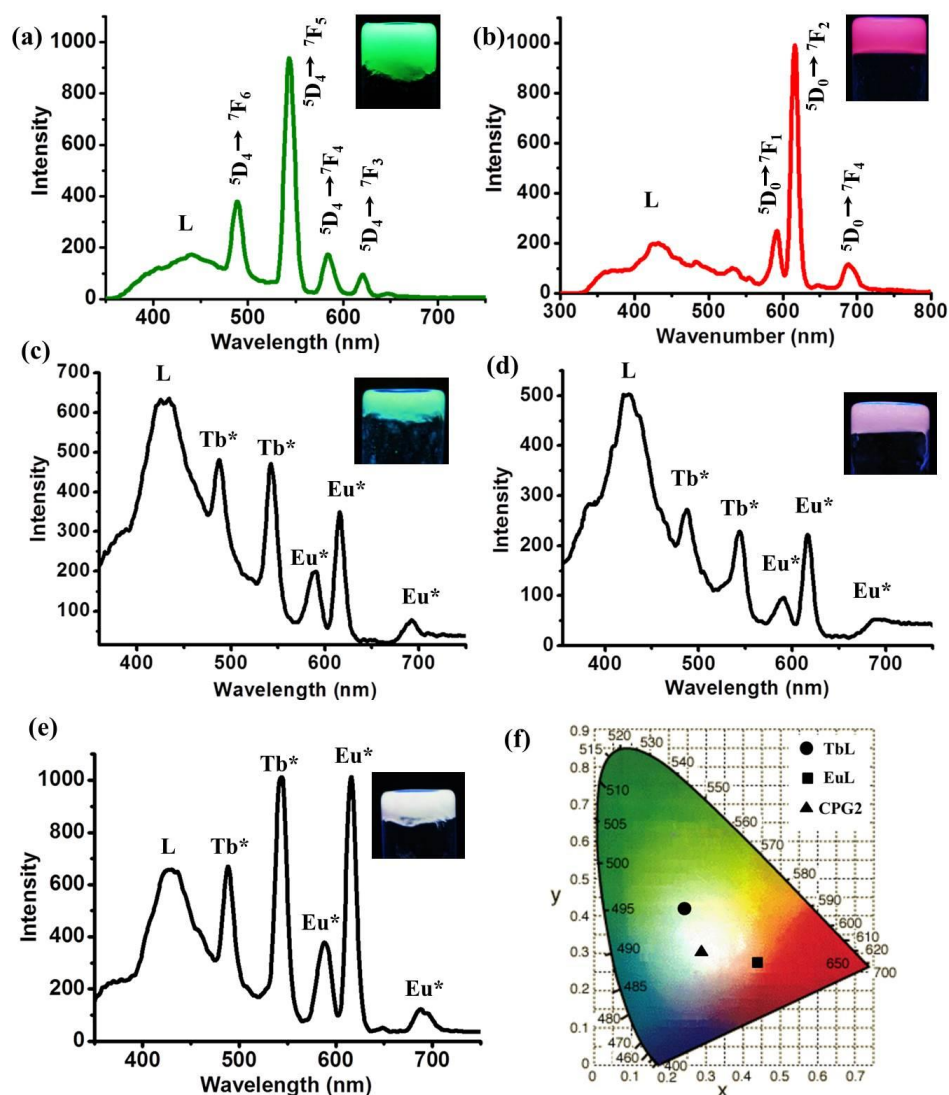


Figure 16. Emission spectra of a) TbL, b) EuL, c) CPG1, d) CPG3 and e) CPG2 ($\lambda_{\text{ex}} = 280$ nm). Insets showing photographs of gels showing green, red, cyan, pink and white emissions under UV-light, f) CIE chromatography of TbL (circle), EuL (square), CPG2 (triangle).

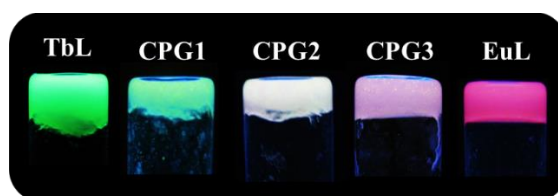


Figure 17. Photograph of TbL, CPG1, CPG2, CPG3, EuL gels under UV light showing green, cyan, white, pink and red emission, respectively.

and EuL exhibited long emission lifetime of 303 μs and 1 ms when monitored at 543 nm and 616 nm, respectively. We also investigated how the emission property of CPGs could

be tuned by modulating the stoichiometry of two lanthanide ions (Tb^{III} and Eu^{III}) and **L**. A series of bimetallic CPGs (**CPG1**, **CPG2**, **CPG3**) were prepared by simultaneously adding different ratios of Tb^{III} and Eu^{III} metal ions into the solution of **L** during gelation (Figure 17). The emission spectra of the bimetallic CPGs revealed that the intensity of the green band at 543 nm decreased and the intensity of the red band at 615 nm increased gradually with increasing Eu^{III} concentration (Figure 16c-e). At 1:1 and 1:2.2 Tb^{III} : Eu^{III} ratios the cyan and pink emitting CPGs (**CPG1** and **CPG3**) were formed. The emission spectra of **CPG1** and **CPG3** showed the characteristic peaks of both Tb^{III} and Eu^{III} when excited at 330 nm (Figure 16c and 16d). Interestingly, a white-light-emitting gel (**CPG2**) was formed by using Tb^{III} : Eu^{III} = 1:2 during the gelation. The emission spectrum of **CPG2** displayed bands corresponding to **L**, Tb^{III} and Eu^{III} in which the **L**-centered emission at 440 nm (blue), Tb^{III} -centered emission at 545 nm (green) and Eu^{III} -centered emission at 615 nm (red) have comparable intensities (Figure 16e). The CIE (Commission International de L'Eclairage) coordinates of **CPG2** was calculated to be (0.29, 0.29) which is quite near to the CIE of pure white light (0.33, 0.33) (Figure 16f). The emission colour of CPGs were tuned over a broad spectrum by using a simple strategy which led to the formation of red, pink, white, cyan and green light-emitting

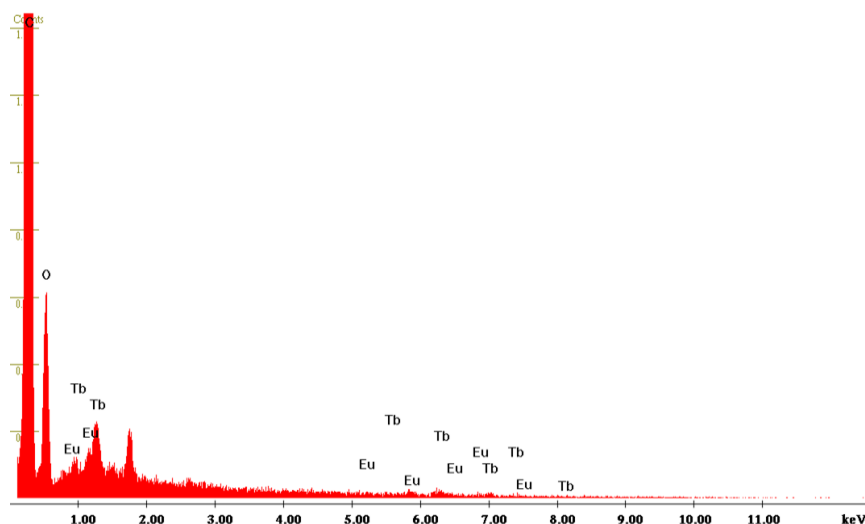


Figure 18. EDAX of **CPG1** showing the presence of both Tb^{III} and Eu^{III} .

CPGs (Figure 17). The presence of both Tb^{III} and Eu^{III} in bimetallic CPGs has been confirmed by EDXS analysis (Figure 18). The elemental mapping of **CPG2** showed even distribution of both Tb^{III} and Eu^{III} ions throughout the gel matrix (Figure 19a-b). ICP-AES analysis was performed to confirm the ratio of Tb^{III} and Eu^{III} loading in **CPG1**,

CPG2 and **CPG3**. This showed $\text{Tb}^{\text{III}} : \text{Eu}^{\text{III}} = 1 : 0.88, 1 : 1.53, 1 : 2.2$ in **CPG1**, **CPG2** and **CPG3**, respectively. The XPS of **CPG2** showed coordination of both Tb^{III} and Eu^{III} to tpy groups of **L** (Figure 19c-d). The emission lifetime of **CPG1**, **CPG2** and **CPG3** at 543 nm were found to be 205 μs , 165 μs and 150 μs , respectively. The absolute quantum yield (QY) values upon excitation at 365 nm were 45.3%, 18.4%, 7.6%, 21.7% and 7.6% for **TbL**, **EuL**, **CPG1**, **CPG2** and **CPG3**, respectively. These values were comparable with reported values of the $\text{Tb}^{\text{III}}/\text{Eu}^{\text{III}}$ based metallogel and coordination polymers.^{12j, l, p}

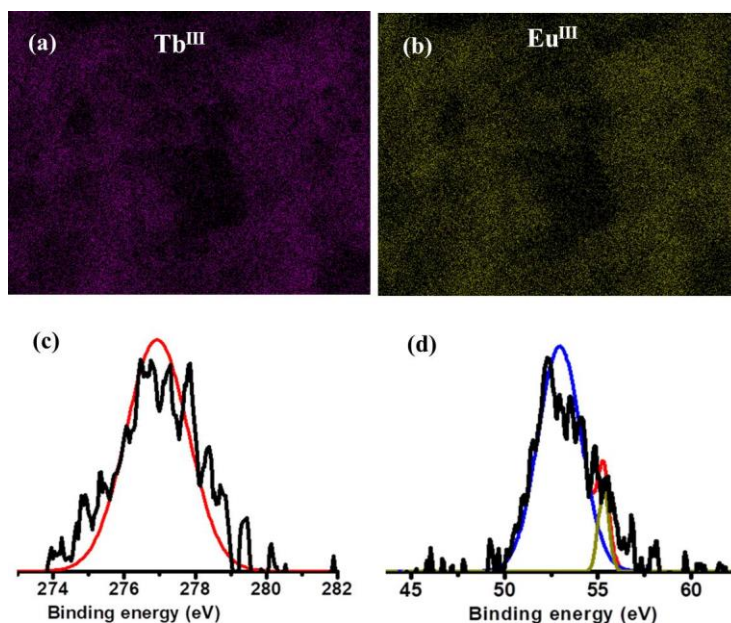


Figure 19. Elemental mapping of **CPG2** xerogel showing uniform distribution of (a) Tb^{III} and (b) Eu^{III} throughout the gel-network, (c) Tb 4d level XPS spectrum for **CPG2**, (d) Eu 5s level XPS spectrum for **CPG2**.

3B.3.4 Stimuli-responsive behaviours of **TbL**, **EuL** and **Tb/Eu** white-light-emitting CPGs

Furthermore, mechano-, thermo- and chemo-responsive behaviours of green (**TbL**), red (**EuL**) and white-light-emitting (**CPG2**) gels were investigated. When **CPG2** was exposed to sonication for 5 min, a gradual gel to sol transition was observed (Figure 20a). In contrast to the intense white luminescence of **CPG2** gel, the sol displayed low intense bluish white emission under UV-light (Figure 20a). The emission spectrum of mechanically induced sol showed a broad band around 420 nm, similar to the emission maxima of free **L** (Figure 20b). This indicated that sonication induced the cleavage of Ln-N_{tpy} coordination bonds which hampered not only the emission colour but also the

stability of gel network. However, due to incomplete cleavage of all Ln-N_{tpy} bonds, the sol showed partial retention of Tb^{III} and Eu^{III} centred peaks. The sol converted back to gel upon resting at room temperature and recovered the white-light-emission. Such sonication induced reversible gel-sol transition and corresponding change in emission colour happened due to the dynamic nature of the Ln-N_{tpy} coordination bonds.¹⁵ Comparative studies with **TbL** and **EuL** showed similar gel to sol transformation (Figure 21). The **TbL** and **EuL** sols exhibited low intense blue and bluish pink emissions respectively under UV-light. The emission spectra of **TbL** and **EuL** sols showed broad L-centered emission at 400 nm and very low intense Tb^{III} and Eu^{III} centered peaks, respectively (Figure 21). To prove that the gel to sol transition was not happening due to the presence

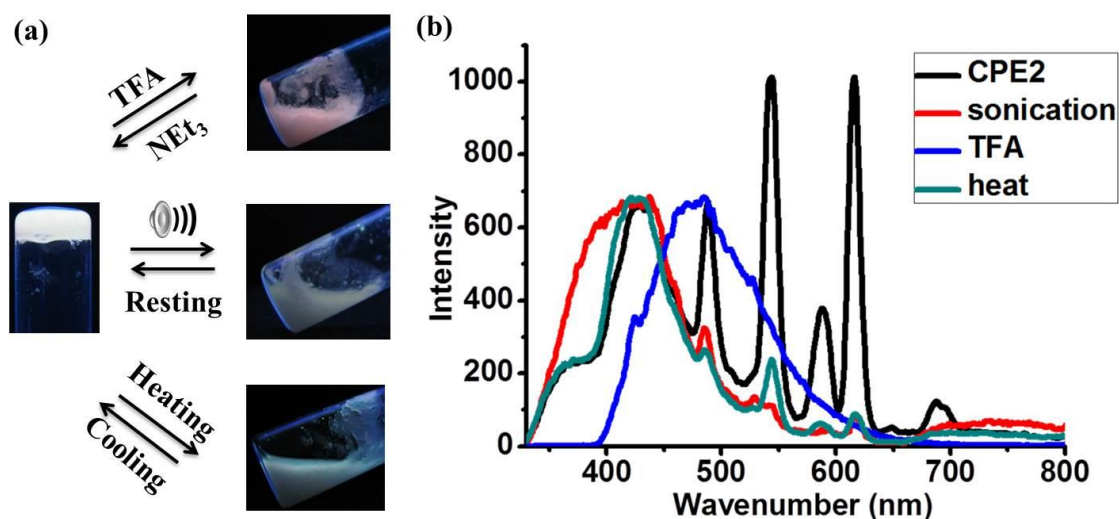


Figure 20. (a) Multi-stimuli responsive properties of white-light-emitting **CPG2**, (b) comparison of emission spectra of sols obtained after sonication (red), addition of TFA (blue) and heating (green) with the xerogel of **CPG2** (black).

of water, 1 ml water was layered on the top of **TbL** gel. No gel to sol transition was observed even after 6 hours. The **CPG2** also exhibited reversible thermo-responsive gel-sol transition (Figure 8a). The emission spectrum of the sol showed a broad L-centered emission at 420 nm and weak Tb^{III} and Eu^{III}-centered peaks (Figure 8b). Furthermore, when **CPG2** was exposed to the vapor of trifluoroacetic acid (TFA) the gel to sol conversion was observed, along with the change in emission colour (Figure 8a). Emission spectrum of the sol showed a broad emission at 440 nm, attributed to the free L (Figure 20b). Diffusion of TFA vapour in the **CPG2** gel matrix resulted in the protonation of the N_{tpy} atoms.¹⁶ The protonated terpyridine (tpyH⁺) showed a lower affinity for the Ln^{III} ions

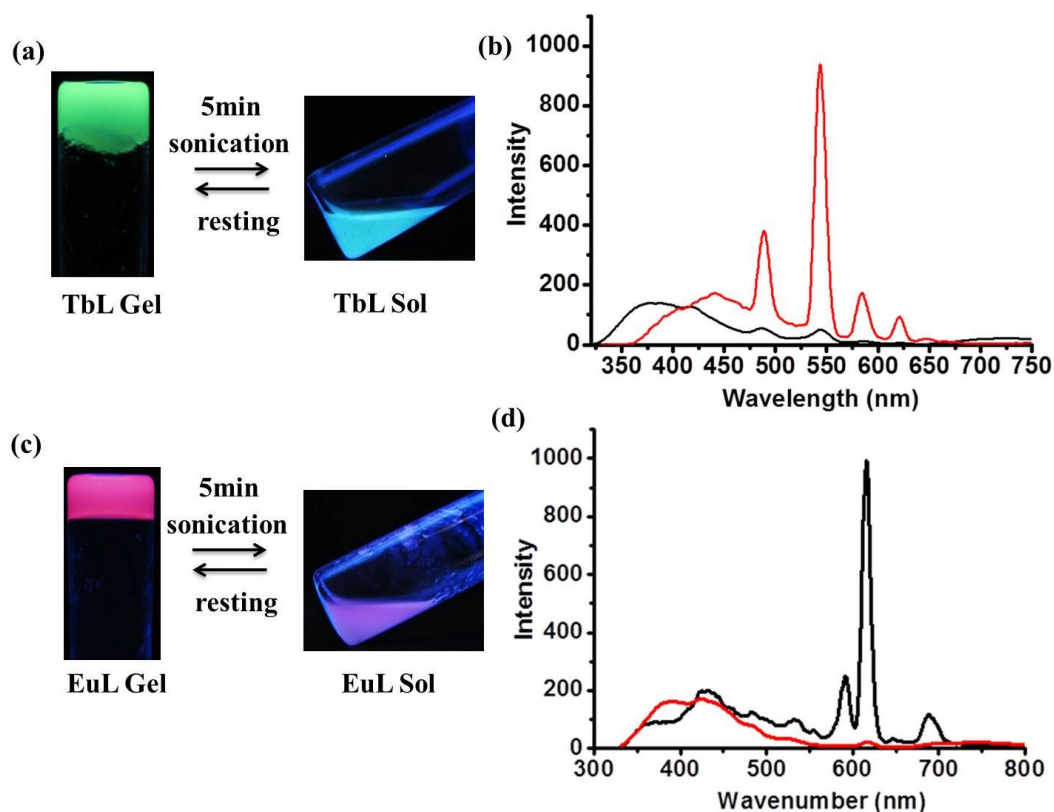


Figure 21. (a) Sonication induced reversible gel to sol transition of **TbL**. The **TbL** gel showing green emission and **TbL** sol is showing blue emission under UV light, (b) Emission spectra of **TbL** gel (red) and **TbL** sol (black), (c) Sonication induced reversible gel to sol transition of **EuL**. The **EuL** gel showing red emission and **EuL** sol is showing bluish pink emission under UV light, (d) Emission spectra of **EuL** gel (red) and **EuL** sol (black).

due to increased electrostatic repulsion. Hence Ln-N_{tpy} coordination bonds break and gel converted to sol. However, after exposing the sol to the vapour of triethylamine (NEt_3) it converted back to gel. This was because NEt_3 deprotonated the tpyH^+ and reformed the Ln-N_{tpy} coordination bonds.

3B.4 SUMMARY

In conclusion, the preceding results demonstrate that designing an amphiphilic, tripodal LMWG could be apposite for synthesizing CPGs with modular nano-morphologies and versatile functionalities. The LMWG not only acted as a chemosensor for Zn^{II} , but also formed **ZnL** coordination polymer hydrogel which exhibited layered sheet morphology. The **ZnL** CPG showed a CT emission. On the other hand, coordination driven self-assembly of **L** with Tb^{III} / Eu^{III} resulted in bright green/red

luminescent CPGs. Furthermore, coordination of both Tb^{III} and Eu^{III} to **L** resulted in bimetallic CPGs whose emissions were tuned over a broad spectral range by simply tuning **L**: Tb^{III}: Eu^{III} ratios. By taking advantage of Ln-N_{tpy} bond dynamics, the reversible mechano-, thermo- and chemo-responsive behaviours of luminescent CPGs were explored. Our strategy of exploiting a flexible, amphiphilic LMWG for synthesizing a series of monometallic and bimetallic CPGs could open-up a new platform for developing multifunctional CPGs from a single LMWG.

3B.5 REFERENCES

1. (a) P. Sutar, T. K. Maji, *Chem. Commun.* 2016, **52**, 8055–8074; (b) J. H. Jung, J. H. Lee, J. R. Silverman, G. John, *Chem. Soc. Rev.*, 2013, **42**, 924–936; (c) A. Y.-Y. Tam, V. W.-W. Yam, *Chem. Soc. Rev.*, 2013, **42**, 1540–1567; (d) M.-O. M. Piepenbrock, G. O. Lloyd, N. Clarke, J. W. Steed, *Chem. Rev.*, 2010, **110**, 1960–2004; (e) K. Nath, A. Husain, P. Dastidar, *Cryst. Growth Des.*, 2015, **15**, 4635–4645.
2. (a) T. Tu, W. Fang, X. Bao, X. Li and K. H. Dötz, *Angew. Chem., Int. Ed.*, 2011, **50**, 6601–6605; (b) M. Maity, U. Maitra, *J. Mater. Chem. A* 2014, **2**, 18952–18958; (b) Mehdi, H.; Pang, H.; Gong, W.; Dhinakaran, M. K.; Wajahat, A.; Kuang, X.; Ning, G., *Org. Biomol. Chem.* 2016, **14**, 5956–5964; (c) Peveler, W. J.; Bear, J. C.; Southern, P.; Parkin, I. P., *Chem. Commun.* 2014, **50**, 14418–14420; (d) Xie, Z.; Wang, F.; Liu, C.-y. Organic–Inorganic Hybrid Functional Carbon Dot Gel Glasses. *Adv. Mater.* 2012, **24**, 1716–1721.
3. Jung, J. H.; Ono, Y.; Shinkai, S. *Angew. Chem., Int. Ed.* 2000, **39**, 1862–1865.
4. Suresh, V. M.; De, A.; Maji, T. K. *Chem. Commun.*, 2015, **51**, 14678–14681.
5. (a) Sutar, P.; Suresh, V. M.; Maji, T. K., *Chem. Commun.* 2015, **51**, 9876–9879; (b) Aiyappa, H. B.; Saha, S.; Wadge, P.; Banerjee, R.; Kurungot, S. *Chem. Sci.* 2015, **6**, 603–607; (c) Chen, P.; Li, Q.; Grindy, S.; Andersen, N. H. *J. Am. Chem. Soc.* 2015, **137**, 11590–11593; (d) Calvo, M. M.; Kotova, O.; Mobius, M. E.; Bell, A. P.; McCabe, T.; Boland, J. J.; Gunnlaugsson, T., *J. Am. Chem. Soc.* 2015, **137**, 1983–1992; (e) Lee, H.; Jung, S. H.; Han, W. S.; Moon, J. H.; Kang, S.; Lee, J. Y.; Jung, J. H.; Shinkai, S. *Chem. – Eur. J.*, 2011, **17**, 2823; (f) Barman, S.; Garg, J. A.; Blacque, O.; Venkatesan, K.; Berke, H. *Chem. Commun.*, 2012, **48**, 11127–11129; (g) Xing, B.; Choi, M.-F.; Xu, B. *Chem. Eur. J.*, 2002, **8**, 5028–5032; (h) Ye, Y.-X.; Liu, W.-L.; Ye, B.-H. *Catal. Commun.* 2017, **89**, 100–105; (i) Lee, J. H.; Kang, S.; Lee, J. Y.; Jung, J. H. *Soft Matter*. 2012, **8**, 6557–6563; (j) Feldner, T.; Häring, M.; Saha, S.; Esquena, J.; Banerjee, R.; Díaz, D. D.

- Chem. Mater.*, 2016, **28**, 3210-3217; (k) Sarkar, S.; Dutta, S.; Bairi, P.; Pal, T. *Langmuir*. 2014, **30**, 7833-7841; (l) Lohe, M. R.; Rose, M.; Kaskel, S., *Chem. Commun.* 2009, 6056–6058.
6. Das, U. K.; Dastidar, P. *Chem. Eur. J.* 2012, **18**, 13079 – 13090.
7. (a) Sutar, P.; Maji, T. K. *Chem. Commun.* 2016, **52**, 13136-13139; (b) Zhang, L.; Wang, X.; Wang, T.; Liu, M. *Small*. 2015, **11**, 1025-1038; (c) Busseron, E.; Ruff, Y.; Moulin, E.; Giuseppone, N., *Nanoscale*. 2013, **5**, 7098–7140; (d) Liu, C.; Jin, Q.; Lv, K.; Zhang, L.; Liu, M., *Chem. Commun.* 2014, **50**, 3702–3705;
8. Frederickson, C. J.; Koh, J. Y.; Bush, A. I., *Nat. Rev. Neurosci.* 2005, **6**, 449–462.
9. (a) Chang, M.; McBroom, M. W.; Scott-Beasley, R. *J. Environ. Manage.* 2004, **73**, 307-315; (b) Reddad, Z.; Gerente, C.; Andresand, Y.; LeCloirec, P. *Environ. Sci. Technol.* 2002, **36**, 2067–2073; (c) Zhang, Y.; Wang, Y.; Yu, R.; Zhang, S.; Wu, Z., *Front. Biol. China*. 2008, **3**, 50; (d) Bush, A. I.; Pettingell, W. H.; Multhaup, G.; Paradis, M. d.; Vonsattel, J.-P.; Gusella, J. F.; Beyreuther, K.; Masters, C. L.; Tanzi, R. E. *Science*. 1994, **265**, 1464–1467; (e) Lee, J.-Y.; Cole, T. B.; Palmiter, R. D.; Suh, S. W.; Koh, J.-Y. *Proc. Natl. Acad. Sci. U. S. A.* 2002, **99**, 7705–7710; (f) Suh, S. W.; Jensen, K. B.; Jensen, M. S.; Silva, D. S.; Kesslak, P. J.; Danscher, G.; Frederickson, C. J., *Brain Res.* 2000, **852**, 274–278; (g) Koh, J.-Y.; Suh, S. W.; Gwag, B. J.; He, Y. Y.; Hsu, C. Y.; Choi, D. W., *Science*. 1996, **272**, 1013–1016.
10. (a) Nugent, J. W.; Lee, H.; Lee, H.-S.; Reibenspies, J. H.; Hancock, R. D. *Chem. Commun.* 2013, **49**, 9749-9751; (b) Chae, M.-Y.; Yoon, J.; Czarnik, A. W., *J. Mol. Recognit.* 1996, **9**, 297-303; (c) Guo, L. E.; Liu, X. Y.; Wang, H.; Chen, Q. L.; Wang, G. K.; Luo, K.; Mi, Q. L.; Zhou, Y.; Zhang, J. F., *Chem. Asian J.* 2015, **10**, 1898-1902; (d) Akkaya, E. U.; Huston, M. E.; Czarnik, A. W. *J. Am. Chem. Soc.* 1990, **112**, 3590- 3593; (e) Zhang, X.; Li, H.; Liu, G.; Pu, S., *J. Photochem. Photobiol. A Chem.* 2016, **330**, 22-29.
11. (a) Fages, F. *Top. Curr. Chem.* 2005, **256**, 283; (b) van Esch, J. H.; Feringa, B. L., *Angew. Chem., Int. Ed.* 2000, **39**, 2263- 2266; (c) Yagai, S.; Nakajima, T.; Kishikawa, K.; Kohmoto, S.; Karatsu, T.; Kitamura, A.; *J. Am. Chem. Soc.* 2005, **127**, 11134; (d) Ahn, S.-K.; Kasi, R. M.; Kim, S.-C.; Sharma, N.; Zhou, Y., *Soft Matter*. 2008, **4**, 1151-1157; (e) Grove, T. Z.; Osuji, C. O.; Forster, J. D.; Dufresne, E. R.; Regan, L. *J. Am. Chem. Soc.*, 2010, **132**, 14024-14026; (f) Ninawe, P. R.; Parulekar, S., *J. Ind. Eng. Chem. Res.* 2012, **51**, 1741–1755.

12. (a) Kotova, O.; Daly, R.; dos Santos, C. M. G.; Boese, M.; Kruger, P. E.; Boland, J. J.; Gunnlaugsson, T. *Angew. Chem., Int. Ed.*, 2012, **51**, 7208–7212; (b) Bhowmik, S.; Banerjee, S.; Maitra, U. *Chem. Commun.*, 2010, **46**, 8642–8644; (c) Roy, S.; Chakraborty, A.; Maji, T. K. *Coord. Chem. Rev.* 2014, **273–274**, 139–164; (d) Liu, Y.; Tu, D.; Zhu, H.; Chen, X. *Chem. Soc. Rev.* 2013, **42**, 6924–6958; (e) Meyer, L. V.; Schönfelda, F.; Müller-Buschbaum, K. *Chem. Commun.*, 2014, **50**, 8093–8108; (f) Dannenbauer, N.; Matthes, P. R.; Scheller, T. P.; Nitsch, J.; Zottnick, S. H.; Gernert, M. S.; Steffen, A.; Lambert, C.; Müller-Buschbaum, K. *Inorg. Chem.* 2016, **55**, 7396–7406; (g) Dechnik, J.; Mühlbach, F.; Dietrich, D.; Wehner, T.; Gutmann, M.; Lühmann, T.; Meinel, L.; Janiak, C.; Müller-Buschbaum, K. *Eur. J. Inorg. Chem.* 2016, **27**, 4408–4415; (h) Surender, E. M.; Comby, S.; Martyn, S.; Cavanagh, B.; Lee, T. C.; Brougham, D. F.; Gunnlaugsson, T. *Chem. Commun.* 2016, **52**, 10858–10861; (i) Barry, D. E.; Caffrey, D. F.; Gunnlaugsson, T. *Chem. Soc. Rev.* 2016, **45**, 3244 – 3274; (j) Mohapatra, S.; Adhikari, S.; Rijju, H.; Maji, T. K., *Inorg. Chem.* 2012, **51**, 4891–4893; (k) Bhattacharyya, S.; Chakraborty, A.; Jayaramulu, K.; Hazra, A.; Maji, T. K. *Chem. Commun.* 2014, **50**, 13567–13570; (l) McCarney, E. P.; Byrne, J. P.; Twamley, B.; Martínez-Calvo, M.; Ryan, G.; Möbius, M. E.; Gunnlaugsson, T. *Chem. Commun.*, 2015, **51**, 14123–14126; (m) Bradberry, S. J.; Savyasachi, A. J.; Peacock, R. D.; Gunnlaugsson, T. *Faraday Discuss.* 2015, **185**, 413 – 431; (n) Kotova, O.; Daly, R.; dos Santos, C. M. G.; Kruger, P. E.; Boland, J. J.; Gunnlaugsson, T. *Inorg. Chem.* 2015, **54**, 7735–7741; (o) Daly, R.; Kotova, O.; Boese, M.; Gunnlaugsson, T.; Boland, J. J. *ACS Nano*, 2013, **7**, 4838–4845; (p) Feng, W.-X.; Yin, S. -Y.; Pan, M.; Wang, H.-P.; Fan, Y. -N.; Lü, X. -Q.; Sua, C. -Y. *J. Mater. Chem. C*, 2017, **5**, 1742–1750; (q) Pan, M.; Du, B. -B.; Zhu, Y. -X.; Yue, M. -Q.; Wei, Z. -W.; Su, C. -Y. *Chem. Eur. J.* 2016, **22**, 2440 – 2451; (r) Yang, Q. -Y.; Pan, M.; Wei, S. -C.; Li, K.; Du, B. -B.; Su, C. -Y., *Inorg. Chem.*, 2015, **54**, 5707–5716.
13. (a) Singha, D.; Gupta, N.; Singh, A. K. *RSC Adv.* 2015, **5**, 65731–65735; (b) Shyamal, M.; Mazumdar, P.; Maity, S.; Samanta, S.; Sahoo, G. P.; Misra, A. *ACS. Sens.*, 2016, **1**, 739–747; (c) Hancock, R. D. *Chem. Soc. Rev.* 2013, **42**, 1500–1524.
14. (a) Michalec, J. F.; Bejuneand, S. A.; Cuttell, D. G.; Summerton, G. C.; Gertenbach, J. A.; Field, J. S.; Haines, R. J.; McMillin, D. R. *Inorg. Chem.*, 2001, **40**, 2193–2200; (b) Lee, Y. H.; Nghia, N. V.; Go, M. J.; Lee, J.; Lee, S. U.; Lee, M. H., *Organometallics*, 2014, **33**, 753–762.
15. (a) Balkenende, D. W. R.; Coulibaly, S.; Balog, S.; Simon, Y. C.; Fiore, G. L.; Weder, C. *J. Am. Chem. Soc.* 2014, **136**, 10493–10498; (b) Burnworth, M.; Tang, L.; Kumpfer,

J. R.; Duncan, A. J.; Beyer, F. L.; Fiore, G. L.; Rowan, S. J.; Weder, C. *Nature.*, 2011, **472**, 334–337.

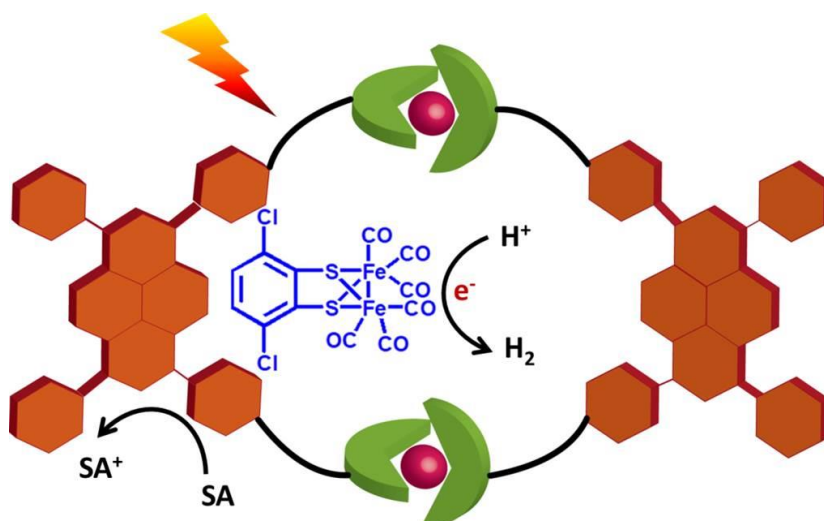
16. (a) Cao, D.-K.; Hu, J. -S.; Li, M. -Q.; Gong, D. -P.; Li, X. -X.; Ward, M. D. *Dalton. Trans.*, 2015, **44**, 21008-21015; (b) Alam, P.; Kaur, G.; Chakraborty, S.; Choudhury, A. R.; Laskar, I. R. *Dalton. Trans.*, 2015, **44**, 6581-6592.

Chapter 4

Ruthenium Based Coordination Polymer Gels as a Photosensitizer for Biomimetic Hydrogen Evolution

Abstract

This chapter reports synthesis and supramolecular self-assembly of two C_4 -symmetric low molecular weight gelators (LMWG) having pyrene core and terminal terpyridine groups. Self-assembly of the LMWGs results in organogels which show nanofiber morphology. However, coordination driven self-assembly in presence of ruthenium ions (Ru^{II}) results in coordination polymer gels (CPGs) that exhibit excellent metal-to-ligand charge transfer transition (MLCT) and nano-sphere morphology. The CPGs show photocatalytic hydrogen evolution and good recyclability under visible light irradiation. Moreover, the photocatalytic activities of the CPGs are improved by many folds after encapsulating an earth-abundant transition metal co-catalyst, $[FeFe](bcbdt)(CO)_6$ that resemble to the active site of $[FeFe]$ -hydrogenases.



Paper based on this work:

P. Sutar, M. Ghosh, P. Kumar, D. Samanta and T. K. Maji, *manuscript under preparation*.

4.1 INTRODUCTION

The increasing energy demand and drastic depletion of fossil fuel have accelerated the search for sustainable, clean and renewable energy sources. Among different alternative energy, photocatalytic water splitting using a semiconductor is the most cost effective and greener route that convert solar energy into hydrogen fuel.¹ In last few decades, extensive research has been focused on the development of various inorganic, organic and inorganic-organic hybrid semiconductors which integrate light-harvesting, electron transport and catalytic functions and hence acts as efficient photocatalyst.² Recently, soft materials, such as π -conjugated hydrogels which facilitate optimum co-localization of light harvesting nanostructures and co-catalyst have emerged as a new type of photocatalyst for water splitting.³ Till now, only pyrene based hydrogels, having strong visible light absorbance and n-type semiconductor properties, are successfully used for photocatalytic hydrogen evolution.^{3b} In all cases platinum or other noble metals serve as heterogeneous co-catalysts for hydrogen evolution. Although design principals of these hydrogels are inspiring, the low chemical stability under harsh photocatalytic reaction condition limits the recyclability of these photocatalysts. Moreover, the limited earth abundance and high cost of Pt co-catalyst limits practical application of the hydrogel photocatalysts. In this regards, designing coordination polymer gels (CPGs) which are more stable and rigid compared to hydrogel/organogel, for photocatalytic hydrogen evolution would be both interesting and challenging task. Moreover, stabilization of earth abundant transition metal co-catalyst inside the CPG matrix would give an opportunity to enhance the photocatalytic activity. Among different earth abundant co-catalyst, organometallic Fe_2 complex that bears structural resemblance to the active site of natural [FeFe]-hydrogenases is an important one.⁴

Coordination polymer gels (CPGs) are an important class of soft-hybrid materials which have potential applications in diverse fields, including biomedicine, optoelectronics and catalysis.⁵ The coordination of metal ions to the suitably crafted LMWGs results in the cross-linked network of CPGs. To date, divergent classes of LMWG have been employed to design wide varieties of CPGs. However, careful design of pyrene-based CPGs is still unexplored. Different pyrene-derivatives are well-known to exhibit strong absorption cross-section, excellent emission property, long excited-state lifetime and high charge-carrier mobility due to the fused-ring aromatic structure. Moreover, optical properties (such as band gap) of pyrene-derivative could be tune by

introducing π -conjugated substituents. Such unique properties of pyrene-based materials make them excellent candidate for photocatalytic hydrogen evolution. To date, many of transition and lanthanide ions have been employed for designing a wide variety of CPGs.⁶ In spite of such overwhelming progress, there are still very few reports on ruthenium (Ru^{II}) based CPGs.⁷ The Ru^{II} complexes typically exhibit metal-to-ligand charge transfer transition (MLCT) in low energy region along with the normal π - π^* transition from organic ligand in UV region. Such unique broad absorption feature of Ru^{II} -complexes covering both UV and visible region, makes them potential photoactive materials which show application in solar cell, opto-electronics and photocatalysis. To date many Ru^{II} -based materials are exploited as photosensitizer in photocatalytic water-splitting because their high excited state life-time is appropriate for the intermolecular electron transfer processes.⁸ We envisioned that by designing a pyrene-based LMWG which on coordination with Ru^{II} results CPGs, we could able to integrate all the necessary component for photocatalytic water splitting. Moreover, the encapsulation of Fe_2 complex inside the CPG matrix would further increase the rate of hydrogen evolution. Furthermore, high rigidity of the Ru^{II} -CPGs could increase recyclability of the gel-catalyst. Designing a Ru^{II} based CPGs for the exploration of photocatalytic hydrogen evolution is still to be demonstrated. Herein, we design two C_4 -symmetrical LMWGs, **G1** and **G2** with 1,3,6,8-Tetrakis(benzoate)pyrene and 4,4',4'',4'''-(pyrene-1,3,6,8-tetra-yltetrakis(ethyne-2,1-diyl))tetra-benzoate core, respectively which are connected to four 2,2':6',2''-terpyridyl (tpy) moieties through flexible alkylamide chains (Figure 1a and 1b). The self-assembly of **G1** and **G2** in organic solvents results in organogels (**OG1** and **OG2**, respectively) with nanofiber morphologies. Coordination of Ru^{II} to the terminal terpyridine groups of **G1/G2** results in CPGs (**Rugel1** and **Rugel2**) that show nanosphere morphologies. The strong MLCT transition of **Rugel1** and **Rugel2** encouraged us to employ them for photocatalytic hydrogen evolution under visible light irradiation (Scheme 1). Both the CPGs show moderate activity and appreciable recyclability without any co-catalyst. Moreover, when a Fe_2 complex as co-catalyst was incorporated inside the CPGs, the photocatalytic activity is increased by many folds.

4.2 EXPERIMENTAL SECTION

4.2.1 Materials

1,3,6,8-tetrabromopyrene, (4-(methoxycarbonyl)phenyl)boronic acid, palladium tetrakis(triphenylphosphine), methyl-4-ethynylbenzoate, copper iodide, 4'-chloro-

2,2':6',2''-terpyridine, 1,3-diaminopropane, trichloroisocyanuric acid (TCIC) and triphenylphosphine (PPh₃) were purchased from Sigma-Aldrich chemical Co. Ltd. Potassium carbonate, sodium hydroxide and all solvents were purchased from Spectrochem. All solvents were pre-dried using standard procedures before using.

4.2.2 Physical measurements

¹H-NMR is recorded on a Bruker AV-400 spectrometer with chemical shifts recorded as ppm and all spectra were calibrated against TMS. High resolution mass spectra (HRMS) were recorded using Agilent QTOF 7200 spectrometer. UV-Vis spectra were recorded in a Perkin-Elmer lamda 900 spectrometer. Fluorescence studies were accomplished using Perkin Elmer Ls 55 luminescence spectrometer. Fourier transform infrared (FTIR) spectral studies were carried out by making samples with KBr pellets using Bruker FTIR spectrometer. The elemental analyses were carried out using a Thermo Scientific Flash 2000 CHN analyzer. Morphology studies were carried out using Lica-S440I field emission scanning electron microscopy (FESEM) by placing samples on silicon wafer under vacuum with accelerating voltage of 10 kV. Transmission electron microscopy (TEM) analysis was performed using JEOL JEM-3010 with accelerating voltage of 300 kV. For this analysis the xerogel was dispersed in ethanol and then drop casted on a carbon coated copper grid.

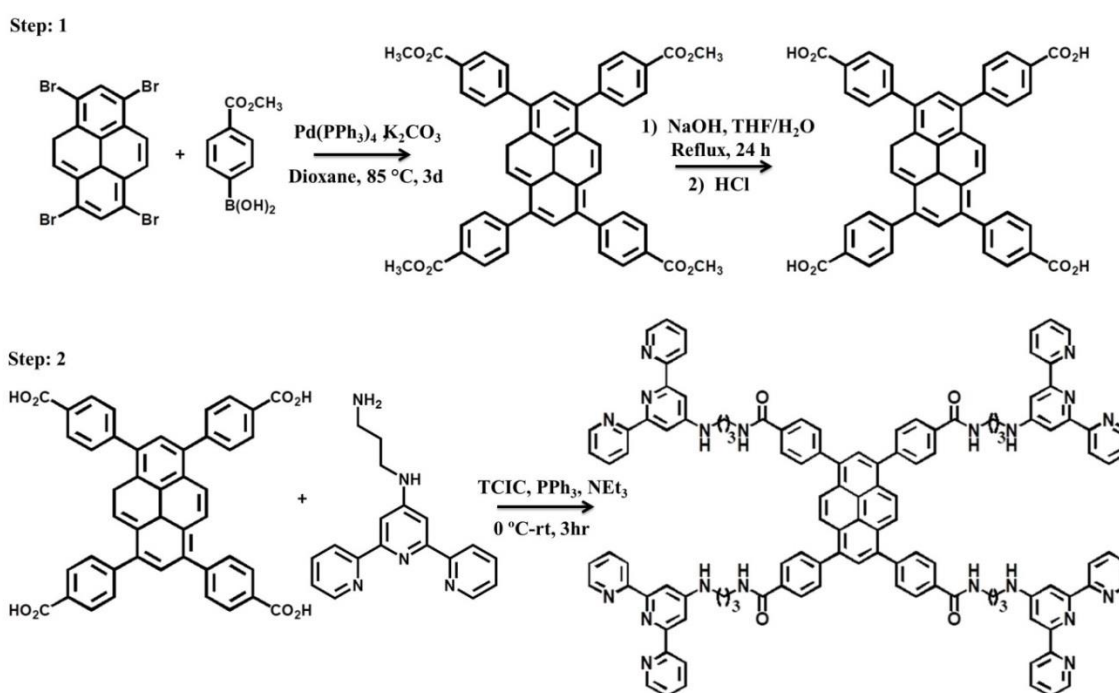
4.2.3 Synthesis

Synthesis of 1,3,6,8-Tetrakis(benzoic acid)pyrene: 4-(Methoxycarbonyl)phenylboronic acid (4.35 g, 24.15 mmol), 1,3,6,8-tetrabromopyrene (2.5 g, 4.83 mmol), K₂CO₃ (5.34 g, 38.64 mmol) and tetrakis(triphenylphosphin)palladium(0) (0.09 g, 0.08 mmol) were suspended in dioxane under Ar-atmosphere. The yellow suspension was continuously heated under stirring condition at 85 °C for 72 h. The neon-yellow suspension formed was allowed to cool to ambient temperature and the solvents were removed in vacuum. The residue was taken up in 50 ml of water and extracted with copious amounts of CHCl₃. The organic phase was dried over anhydrous MgSO₄ and the solvent was removed in vacuum. The neon-yellow residue was suspended in THF and refluxed for 2 h. After that the reaction mixture was cooled down to ambient temperature and the neon-yellow precipitate was collected and dried under suction. Yield: 2.6 g (3.5 mmol, 72.9 %). ¹H-NMR (200 MHz, CDCl₃): δ = 8.23 (d, 8H), 8.15 (s, 4H), 8.01 (s, 2H), 7.75 (d, 8H), 3.99 (s, 12H). The product (1.0 g,

1.35 mmol) was suspended in a solution of 3.0 g (75 mmol) NaOH in 200 ml THF/H₂O (1:1) and then refluxed for 24 h. The solvents were removed and water was added to the residue to give a yellow solution. After acidification to pH < 2 the yellow precipitate was isolated and dried in vacuum. Yield: 1.09 g (1.6 mmol, 80 %). ¹H NMR (200 MHz, DMSO-*d*⁶): δ = 13.08 (s, 4H), 8.19 (d, 8H), 8.14 (s, 4H), 8.06 (s, 2H), 7.84 (d, 4H).

Synthesis of 2,2':6',2''-terpyridin-4'-yl-propane-1,3-diamine: The detail synthetic procedure of 2,2':6',2''-terpyridin-4'-yl-propane-1,3-diamine was discussed in Chapter 2. The ¹H-NMR, FTIR and CHN analysis of 2,2':6',2''-terpyridin-4'-yl-propane-1,3-diamine were also discussed in Chapter 2.

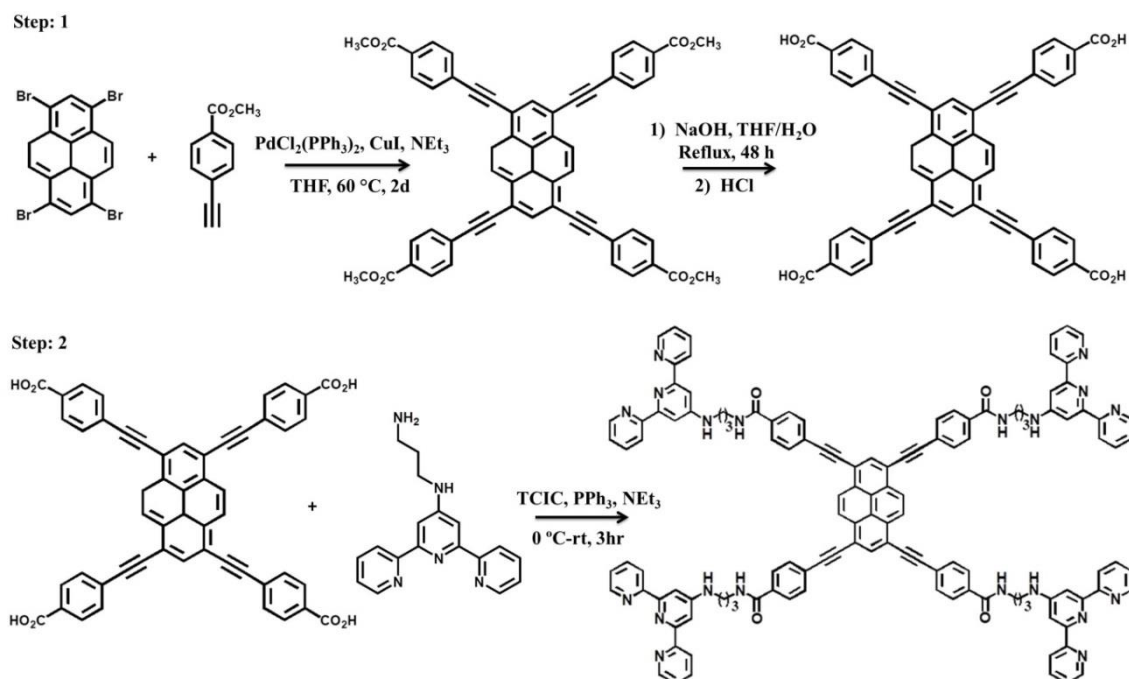
Synthesis of G1: 1,3,6,8-Tetrakis(benzoic acid)pyrene (200 mg, 0.293 mmol) was dissolved in anhydrous THF (30 mL). TCIC (272 mg, 1.172 mmol) and PPh₃ (307.3 mg, 1.172 mmol) were added into the reaction mixture and stirred at 0 °C for 1 hour under inert condition. 2,2':6',2''-terpyridin-4'-yl-propane-1,3-diamine (358 mg, 1.172 mmol) was dissolved in anhydrous THF (20 ml) and Et₃N (330 μl, 2.346 mmol) was added into it. This reaction mixture was drop-wise added into 1,3,6,8-Tetrakis(benzoic acid)pyrene / TCIC/ PPh₃ solution at 0 °C and stirred for 1 hours. After that the reaction mixture was stirred at room temperature for 6 hrs. Precipitate was collected by filtration and washed several times with CHCl₃ and dried under vacuum. Yield: 75%. ¹H-NMR (400 MHz, DMSO-*d*⁶) δ: 8.89 (t, 3H, ArH), 8.15



Scheme 1. Synthetic scheme for G1.

(m, 7H, ArH), 7.79 (m, 3H, ArH), 7.66 (d, 2H, ArH), 5.53 (m, 2H, CONHCH₂), 2.99 (m, 2H, CH₂), 2.02 (m, 2H, CH₂NH). HRMS (ESI, m/z): [M+4H]⁴⁺ calculated for C₁₁₆H₉₆N₂₀O₄, 459.1980; found: 458.9533 (z = 4). [M+2H]²⁺ calculated for C₁₁₆H₉₆N₂₀O₄, 917.3961; found: 916.8993 (z = 2).

Synthesis of 4,4',4'',4'''-(pyrene-1,3,6,8-tetra-yltetrakis(ethyne-2,1-diyl))tetra-benzoic acid: A mixture of 1,3,6,8-tetrabromopyrene (0.594 g, 1.14 mmol), methyl-4-ethynylbenzoate (1.0 g, 5.74 mmol), CuI (20 mg, 0.10 mmol) and PdCl₂(PPh₃)₂ (70 mg, 0.10 mmol) in 70 ml of THF/NEt₃ (1:1) were heated under Ar-atmosphere at 60 °C. After 48 h the orange suspension was allowed to cool down to ambient temperature and then 35 ml of water was added. This mixture was filtrated and the residue was washed with water and CHCl₃ and dried under suction. Yield: 0.75 g (0.84 mmol, 73.4 %). ¹H-NMR (200 MHz, dMSO-d⁶): δ = 8.75 (s, 4H), 8.47 (s, 2H), 8.11 (d, 8H), 7.78 (d, 8H), 3.98 (s, 12H). The product (0.75 g, 0.84 mmol) was suspended in a solution of 3.0 g (75 mmol) NaOH in 200 ml THF/H₂O (1:1) and then refluxed for 24 h. The solvents were removed and water was added to the residue to give an orange solution. After acidification to pH < 2 the yellow precipitate was isolated and dried in vacuum. Yield: 0.45 g (0.58 mmol, 70 %). ¹H-NMR (200 MHz, dMSO-d⁶): δ = 13.18 (s, 4H, -COOH), 8.56 – 7.69 (m, 22H, ArH).



Scheme 2. Synthetic scheme for **G2**.

Synthesis of G2: 4,4',4'',4'''-(pyrene-1,3,6,8-tetra-yltetrakis(ethyne-2,1-diyl))tetra-benzoic acid (225 mg, 0.289 mmol) was dissolved in anhydrous THF (40 mL).

TCIC (275 mg, 1.186 mmol) and PPh₃ (310 mg, 1.186 mmol) were added into the reaction mixture and stirred at 0 °C for 1 hour under inert condition. 2,2':6',2''-terpyridin-4'-yl-propane-1,3-diamine (353 mg, 1.156 mmol) was dissolved in anhydrous THF (20 ml) and Et₃N (240 μl, 1.734 mmol) was added into it. This reaction mixture was drop-wise added into 4,4',4'',4'''-(pyrene-1,3,6,8-tetrayltetrakis(ethyne-2,1-diyl))tetra-benzoic acid / TCIC/ PPh₃ solution at 0 °C and stirred for 1.5 hours. After that the reaction mixture was stirred at room temperature for 8 hrs. Precipitate was collected by filtration and washed several times with CHCl₃ and dried under vacuum. Yield: 70%. ¹H-NMR (400 MHz, DMSO-d₆) δ: 8.89 (t, 3H, ArH), 8.15 (m, 7H, ArH), 7.79 (m, 3H, ArH), 7.66 (d, 2H, ArH), 5.53 (m, 2H, CONHCH₂), 2.99 (m, 2H, CH₂), 2.02 (m, 2H, CH₂NH). HRMS (ESI, m/z): [M+H]⁺ calculated for C₁₁₆H₉₆N₂₀O₄, 1929.7957; found: 1929.8310.

Synthesis of [FeFe](1,4-Dichlorobenzene-2,3-dithiolate)(CO)₆ complex [FeFe](bcbdt)(CO)₆: 3,6-dichlorobenzene-1,2-dithiol (0.225 g, 1.06 mmol) and triiron-dodecacarbonyl (1.2 g, 2.38 mmol) were dissolved in 20 ml dry THF taken in a 100 ml schlenk tube and stirred at room temperature for half an hour. Then the reaction mixture was refluxed at 60 °C for 4 hours under inert atmosphere. The mixture was cooled to RT and the solvent was removed under reduced pressure. Compound was purified by column chromatography by eluting hexane to get brick-red coloured solid compound. Yield: 41%.

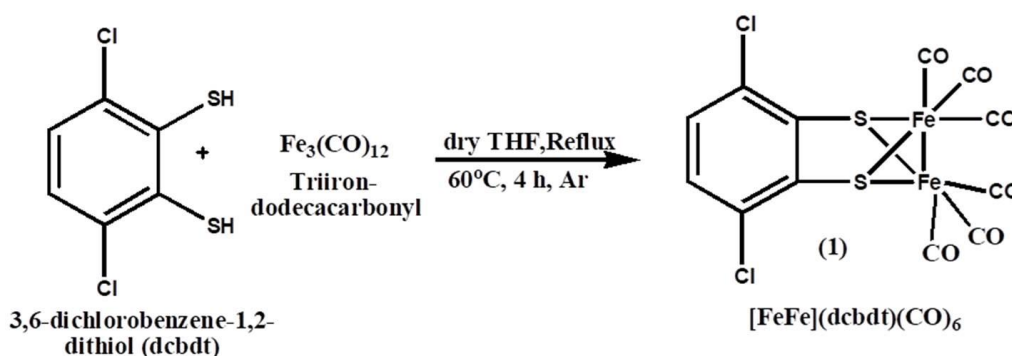


Figure 3. Synthesis of [FeFe](bcbdt)(CO)₆.

Synthesis of OG1: 5 mg of **G1** was dissolved in 300 μl DMF. 400 μl methanol was added into the mixture and sonicated for 5 minutes. The homogeneous mixture was heated at 60 °C until it becomes transparent solution which was later kept at room temperature. The gel was formed after 4-5 hours. The formation of gel was confirmed by inversion test method. The **OG1** xerogel was prepared by drying the gel in vacuum oven at 60 °C.

Synthesis of OG2: 5 mg of **G2** was dispersed in 1:2 mixture of DMF/water by sonication. The homogeneous mixture was heated at 60 °C until it becomes a transparent solution which was later kept at room temperature. The gel is formed after 1 hour. The formation of gel is confirmed by the inversion test method.

Synthesis of Rugel1: 5 mg (2.7×10^{-3} mmol) of **G1** was mixed with 300 μ l DMF and 400 μ l MeOH and sonicated to make a homogeneous mixture. The mixture was heated at 60 °C until it became transparent solution. After that 200 μ l solution of Ru(DMSO)₄Cl₂ (2.5 mg, 5.1×10^{-3} mmol) was added and the reaction mixture was heated until the total volume of the solution reduced to half and the colour turned dark red. At this stage, 200 μ l of water was added and the mixture was heated for 2-3 minutes. The mixture was kept at room temperature for overnight to form gel. The formation of gel was confirmed by inversion test method.

Synthesis of Rugel2: 5 mg (2.6×10^{-3} mmol) of **G1** was mixed with 300 μ l DMF and 400 μ l MeOH and sonicated to make a homogeneous mixture. The mixture was heated at 60 °C until it became transparent solution. After that 200 μ l solution of Ru(DMSO)₄Cl₂ (2.5 mg, 5.1×10^{-3} mmol) was added and the reaction mixture was heated until the total volume of the solution reduced to half and the colour turned dark red. At this stage, 200 μ l of water was added and the mixture was heated for 2-3 minutes. The mixture was kept at room temperature for overnight to form gel. The formation of gel was confirmed by inversion test method.

4.2.4 Photocatalytic hydrogen evolution experiment

Photocatalytic H₂ evolution experiments were carried out in a 80 ml stoppered flask. The flask was charged with 5 mg **Rugel1** / **Rugel2** xerogel and 40 ml aqueous solution of triethylamine (10 vol%). The suspension was ultrasonicated to make a homogeneous dispersion which was later purged with N₂ for 30 minutes to remove all the dissolved gases. The reaction mixture was irradiated with 290 W Xe lamp (Newport) fitted with 12 cm path length of water filter for removal of IR radiation. A visible-bandpass filter (400 nm-800 nm) was used to block the UV-light. The evolved gas was analysed by Agilent CN15343150 Gas Chromatography which use a thermal conductivity detector referencing against a standard (H₂/N₂) gas mixture with a known concentration of hydrogen. No hydrogen evolution was observed for a mixture of water/methanol/trimethylamine under $\lambda > 290$ nm irradiation in absence of a photocatalyst.

4.3 RESULTS AND DISCUSSION

4.3.1 Characterization of $[\text{FeFe}](\text{bcbdt})(\text{CO})_6$

$[\text{FeFe}](\text{bcbdt})(\text{CO})_6$ is a brick-red complex and was prepared by the reaction of 3,6-dichlorobenzene dithiol with triiron dodecacarbonyl (Figure 3). The product was characterized by FTIR and HRMS. FTIR of $[\text{FeFe}](\text{bcbdt})(\text{CO})_6$ showed three prominent C=O stretching vibration bands at 2080, 2048 and 1995 cm^{-1} corresponded to three different C=O attached to Fe^{II} metal ion. Metal-carbonyl Fe-CO vibrations were observed at 619, 577 and 550 cm^{-1} . Also, the aromatic C=C stretching peak was observed at 1424 cm^{-1} (Figure 4). HRMS analysis also proved the formation of $[\text{FeFe}](\text{bcbdt})(\text{CO})_6$ (Figure 5). HRMS (+ESI): m/z calculated for $\text{C}_{12}\text{Fe}_2\text{S}_2\text{C}_{12}\text{O}_6$: 488.8751, found: 495.9055 $[\text{M}+\text{H}]^+$.

4.3.2 Characterization of G1 and G2

G1 and **G2** were synthesized by amide coupling reaction between 2,2':6',2''-terpyridin-4'-yl-propane-1,3-diamine, 1,3,6,8-Tetrakis(benzoic acid)pyrene and 4,4',4'',4'''-(pyrene-1,3,6,8-tetra-yltetrakis(ethyne-2,1-diyl))tetra-benzoic acid respectively. The purity of **G1** and **G2** was confirmed by $^1\text{H-NMR}$, HR-MS, FTIR and elemental analysis. The solution of **G1** (10^{-5} M) in DMSO exhibited two absorption bands. The absorption maxima at 285 nm was attributed to the π - π^* transition of terminal terpyridine moieties, whereas the band at 398 nm was considered as the π - π^* transition of 1,3,6,8-Tetrakis(benzoate)pyrene core (Figure 6a). Similarly, the solution of **G2** (10^{-5} M) in

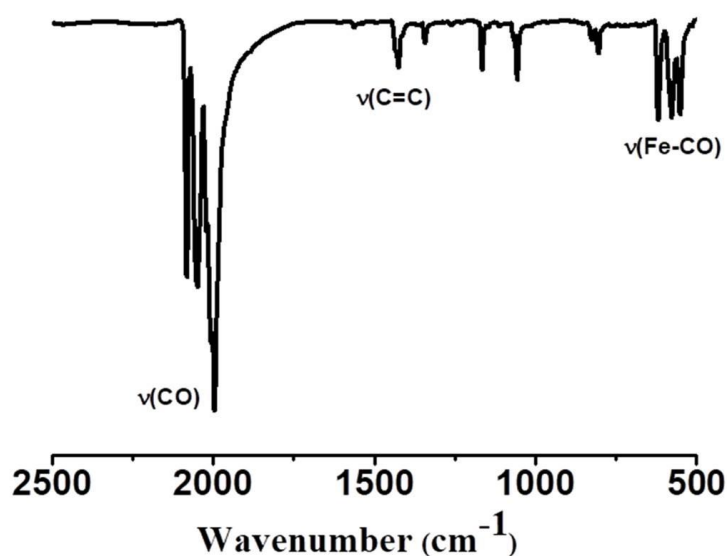


Figure 4. FTIR spectra for $[\text{FeFe}](\text{dcbdt})(\text{CO})_6$.

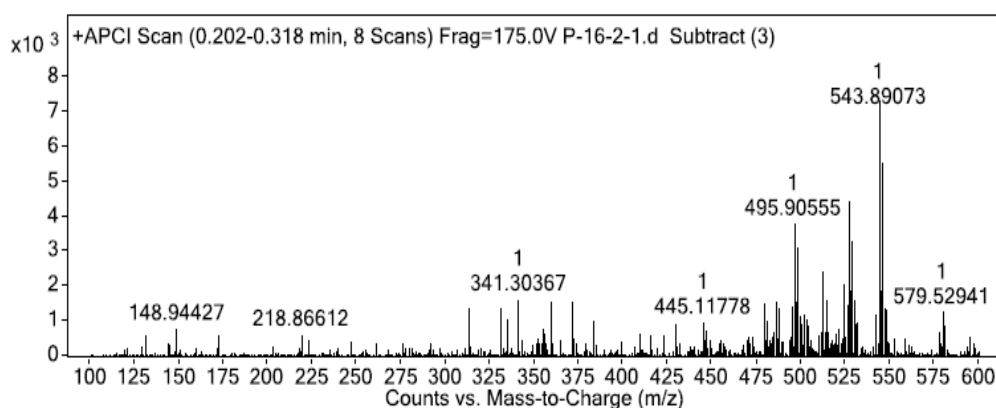


Figure 5. HRMS analysis $[\text{FeFe}](\text{bClbdt})(\text{CO})_6$

DMSO showed the absorption maxima at 285 nm and a band at 432 nm, assigned to the π - π^* transition of the terpyridine and 4,4',4'',4'''-(pyrene-1,3,6,8-tetrayltetrakis(ethyne-2,1-diyl))tetra-benzoate, respectively (Figure 7a). Such red-shifted absorption of **G2** was attributed to the extended conjugation, causing due to the incorporation of triple bond in pyrene core. When excited at 390 nm, **G1** (10^{-5} M) exhibited intense emission at 450 nm (Figure 6b). However the intensity of the emission maxima decreased after exciting at 330 nm which indicated major contribution of 1,3,6,8-Tetrakis(benzoate)pyrene core in the emission of **G1** (Figure 8a). Similar observation was found in case of **G2** (10^{-5} M) (Figure 8b). However, **G2** (10^{-5} M) exhibited red-shifted emission compared to **G1** with maxima at 496 nm. Such red shifted emission was originating from highly conjugated 4,4',4'',4'''-(pyrene-1,3,6,8-tetrayltetrakis(ethyne-2,1-diyl))tetra-benzoate core of **G2** (Figure 7b).

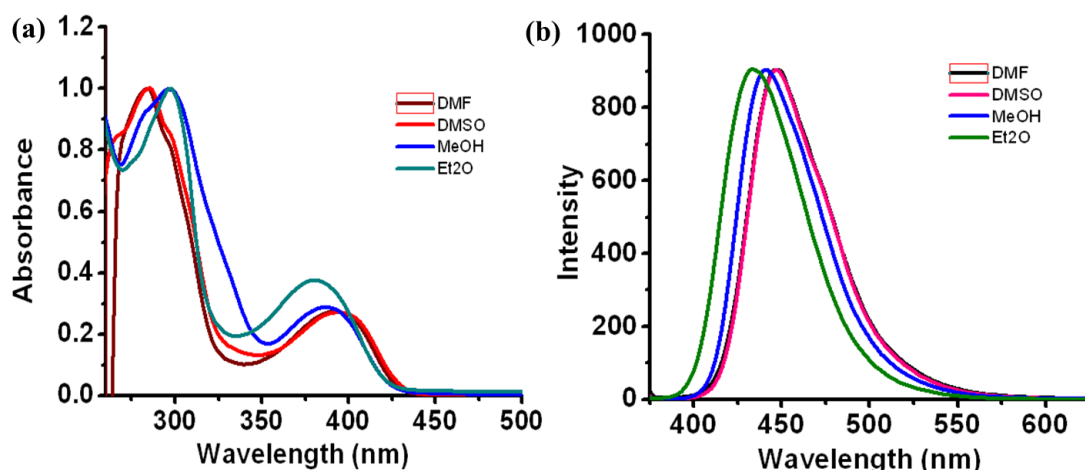


Figure 6: (a) Absorption spectra and (b) emission spectra ($\lambda_{\text{ex}} = 360$ nm) of **G1** (10^{-5} M) in DMF (Black), DMSO (Red), Methanol (Blue) and diethyl ether (Green).

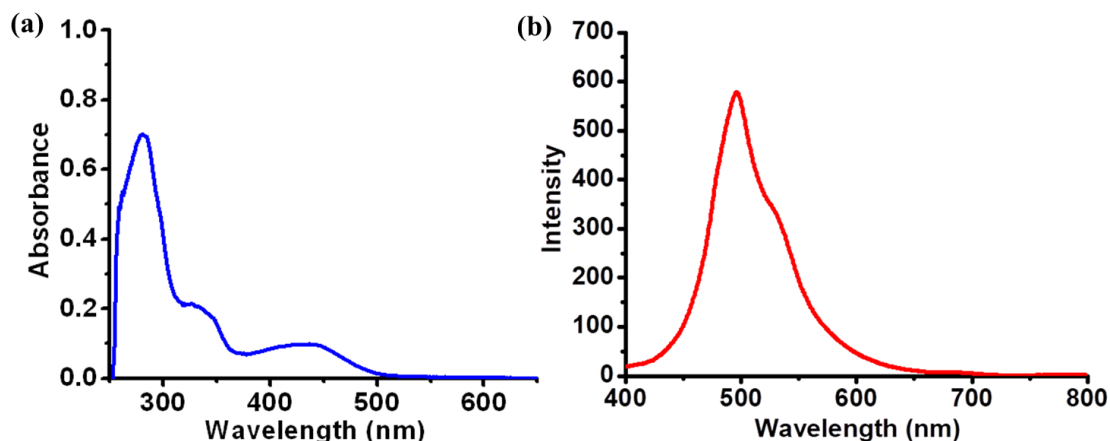


Figure 7: (a) Absorption spectrum and (b) emission spectrum ($\lambda_{\text{ex}} = 360$ nm) of **G2** (10^{-5} M) in DMSO.

4.3.3 Characterization of organogels

The gelation propensity of **G1** and **G2** was checked in a number of solvents. Heating the solution of **G1** in DMF/MeOH (1:2) followed by cooling resulted in a translucent gel, **OG1** (Figure 9a). **G2** did not show gelation in the same solvent mixture. However, heating and cooling the solution of **G2** in DMF/water (2:1) mixture resulted in a stable gel, **OG2**. The formation of gels was confirmed by inversion test method. The FESEM images of **OG1** and **OG2** xerogels revealed the formation of entangled fibrous networks in both (Figure 9b-c and Figure 10a-b). The TEM images of **OG1** xerogel showed that length of the nanofibers varies from 100 nm to 1 μm and the diameter is in 40 - 50 nm range (Figure 9d-f). TEM images of **OG2** xerogel revealed that nanofibers of

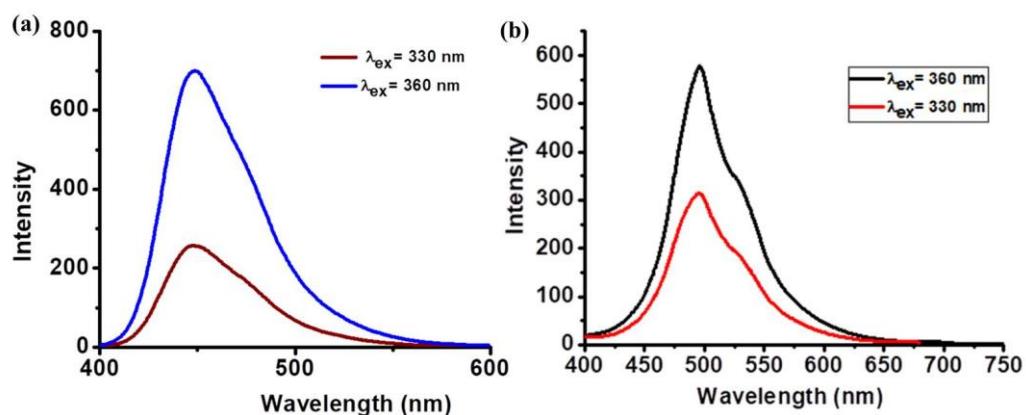


Figure 8: (a) Emission spectra of **G1** (10^{-5} M) in DMSO after exciting at 330 nm (red) and 360 nm (blue), (b) Emission spectra of **G2** (10^{-5} M) in DMSO after exciting at 330 nm (red) and 390 nm (blue).

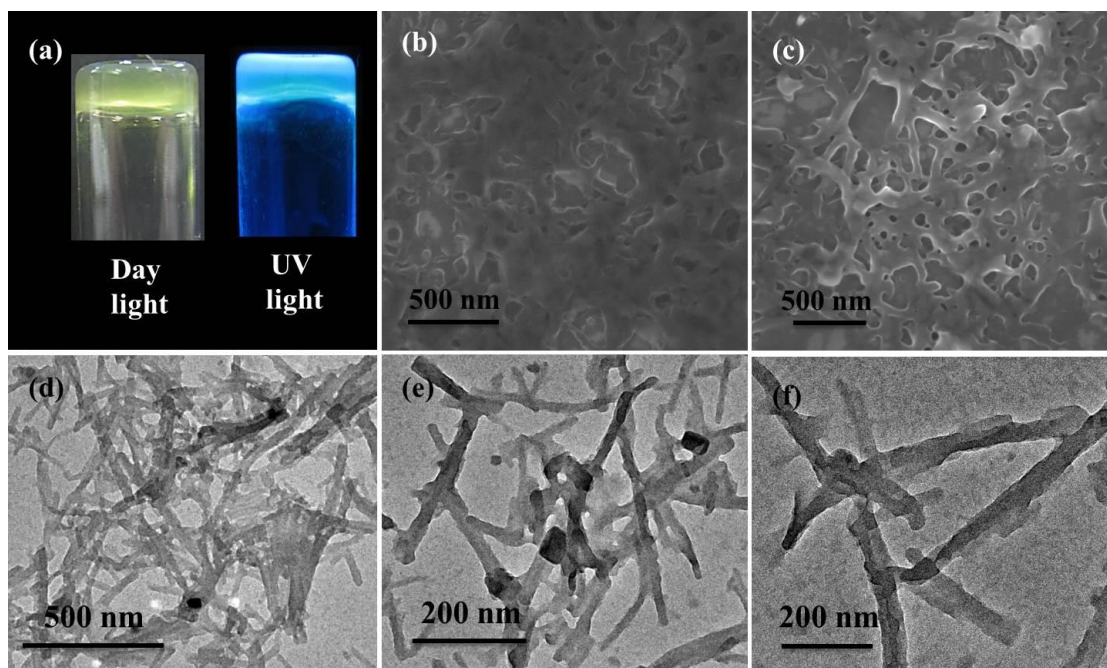


Figure 9. (a) Picture of **OG1** under day light and UV light, (b), (c) FESEM images of **OG1**, (d), (e), (f) TEM images of **OG2**.

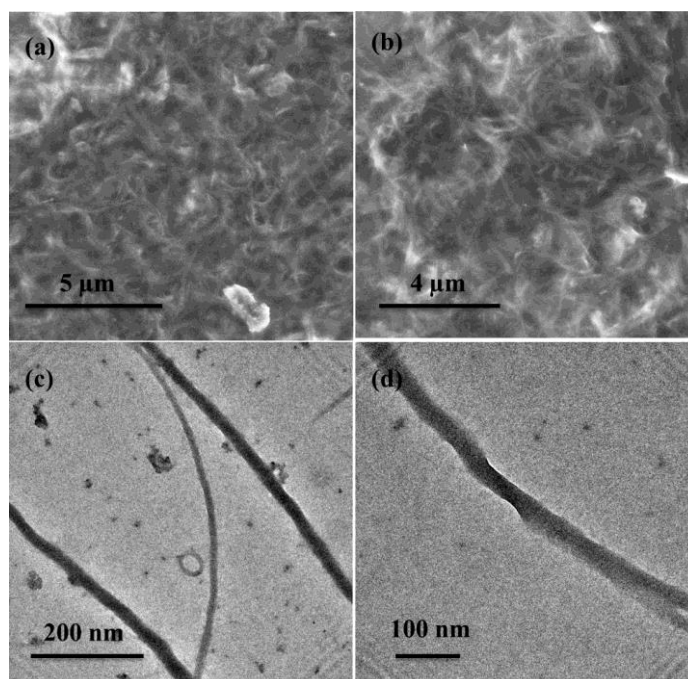


Figure 10: (a), (b) FESEM images of **OG2** xerogel showing the formation of fibrous network, (c), (d) TEM images of **OG2**.

OG2 were longer than the nanofibers of **OG1** xerogel. The nanofibers of **OG2** xerogel were several micrometres long ($\sim 10 \mu\text{m}$) with diameters in 90-110 nm range (Figure 10c-d). The UV-Vis spectrum of **OG1** xerogel showed a broad band at 380-443 nm which

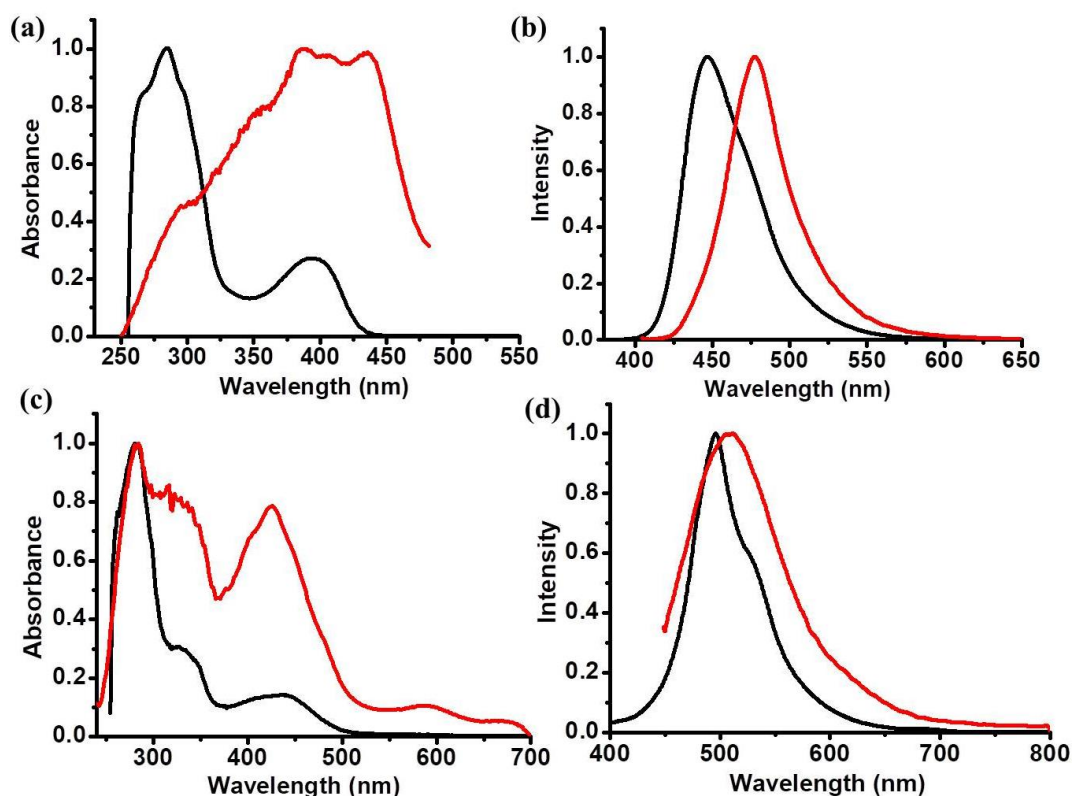


Figure 11: Comparison of the (a) absorption and (b) emission spectrum of **G1** solution (10^{-5} M in DMSO) (black) and **OG1** (red), Comparison of the (c) absorption and (d) emission spectrum of **G2** solution (10^{-5} M in DMSO) (black) and **OG2** (red)

was highly red-shifted compared to the original **G1** (Figure 11a). Corresponding emission spectrum of **OG1** (480 nm, $\lambda_{\text{ex}}=400$ nm) also exhibited a ~ 30 nm red-shift compared to **G1** (Figure 11b). The fast rotation of phenyl groups around C-C single bonds in **G1** was restricted in **OG1** due to the aggregation which increased extend of π -conjugation and thus caused red-shifted absorption and emission in **OG1**. The UV-Vis spectrum of **OG2** xerogel displayed almost identical λ_{max} (285 nm and 430 nm) to that of **G2** (Figure 11c). The corresponding emission spectrum of **OG2** xerogel showed green emission with maxima at 511 nm ($\lambda_{\text{em}}=426$ nm) which was ~ 5 nm red-shifted compared to the **G2** (Figure 11d). The four triple bonds which connect the pyrene core with four phenyl ring enhance the rigidity of **G2** which did not exhibit any change in electronic structure or conjugation, before and after gelation.

4.3.4 Characterization of CPGs

Since Ru^{II} was well known to form stable bis-terpyridine complex, we studied gelation propensity of **G1** and **G2** in presence of Ru^{II} . Initially, the interaction of **G1** with

Ru^{II} was studied by gradually adding Ru^{II} solution into **G1** solution. With increasing amount of Ru^{II} , the absorption peaks at 294 nm and 387 nm showed hypochromic shift and a weak band appeared at 445 nm which became more prominent after heating the mixture at 60 °C for 2-3 minutes. This new peak at 445 nm represented the Ru^{II} MLCT transition. Next, the Ru^{II} -coordinated CPGs (**Rugel1**, **Rugel2**) were prepared. Heating the mixture of **G1** and $\text{Ru}(\text{DMSO})_4\text{Cl}_2$ (molar ratio = 1 : 1) in DMF/MeOH/water solvent mixture, followed by cooling resulted in stable coordination polymer gel (**Rugel1**) (Figure 12a inset). Likewise, **Rugel2** was prepared by using 1:1 molar ratios of **G2** and $\text{Ru}(\text{DMSO})_4\text{Cl}_2$ (Figure 12b inset). Both the CPGs were dark red in colour which indicated MLCT transition of coordinated Ru^{II} . The presence of coordinated Ru^{II} in **Rugel1** and **Rugel2** was confirmed by EDXS analysis. Furthermore, electrochemical behaviours of **Rugel1** and **Rugel2** were investigated in acetonitrile solution containing TBAPF_6 as supporting electrolyte under N_2 atmosphere. The cyclic voltammetry (CV) curves of **Rugel1** and **Rugel2** showed irreversible oxidation peak at 0.79 mV and 0.78 mV vs. $\text{Cp}_2\text{Fe}^+/\text{Cp}_2\text{Fe}$, respectively which were attributed to the Ru^{II} – centred oxidation

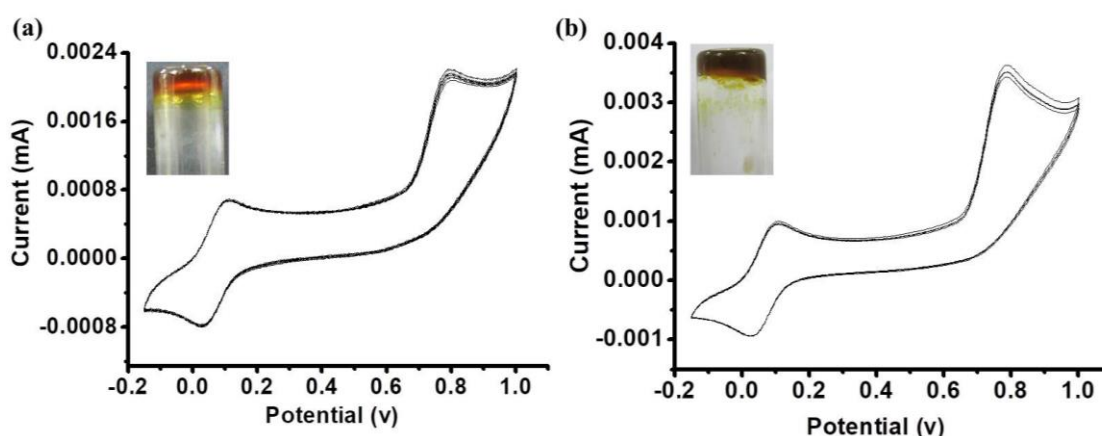


Figure 12: (a) CV curve of **Rugel1** (in MeCN, 10⁻⁴ M) in presence of $\text{Cp}_2\text{Fe}^+/\text{Cp}_2\text{Fe}$, (b) CV curve of **Rugel2** (in MeCN, 10⁻⁴ M) in presence of $\text{Cp}_2\text{Fe}^+/\text{Cp}_2\text{Fe}$.

process (Figure 12a and 12b). In both cases, the oxidation peak intensity decreased with increasing number of cycle which further supported that Ru^{II} centres were irreversibly converting to Ru^{III} . To gain insight into the mode of packing the **Rugel1** and **Rugel2** xerogels were analysed by FESEM and TEM images. The FESEM images of **Rugel1** and **Rugel2** revealed the formation of evenly distributed nanospheres (Figure 13a-c). TEM images of **Rugel1** show that the nanospheres are very small (15- 20 nm diameter) and degrade fast under the electron beam (Figure 13d-f). The nanospheres of **Rugel2** had

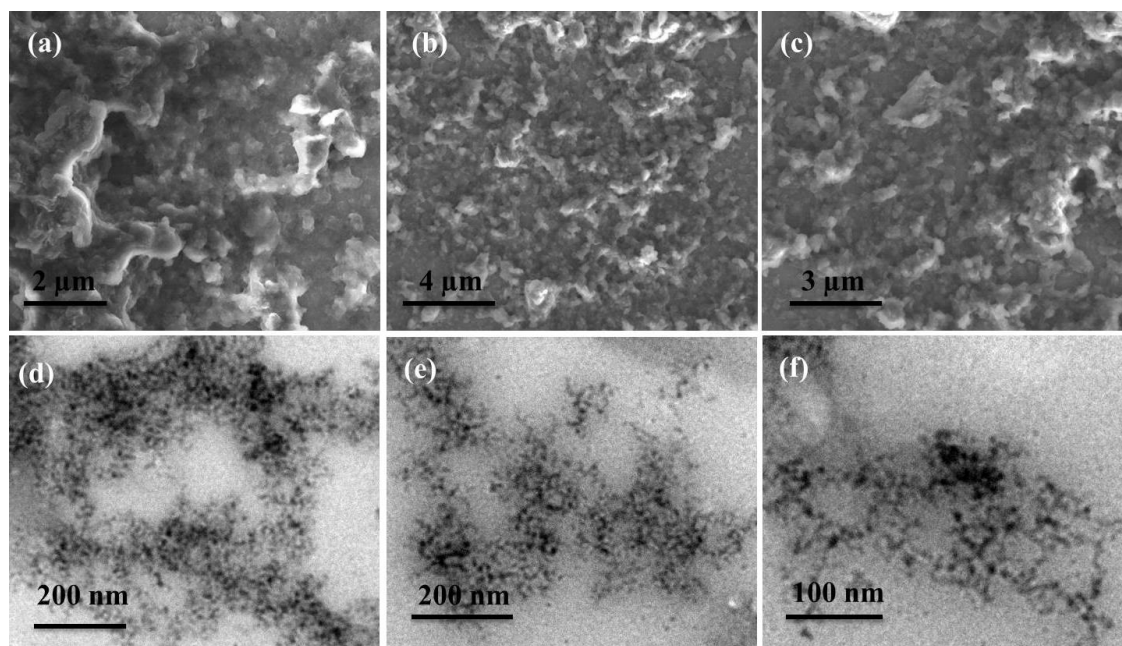


Figure 13: (a), (b), (c) FESEM images of **Rugel1** xerogel, (d), (e), (f) TEM images of **Rugel1** xerogel.

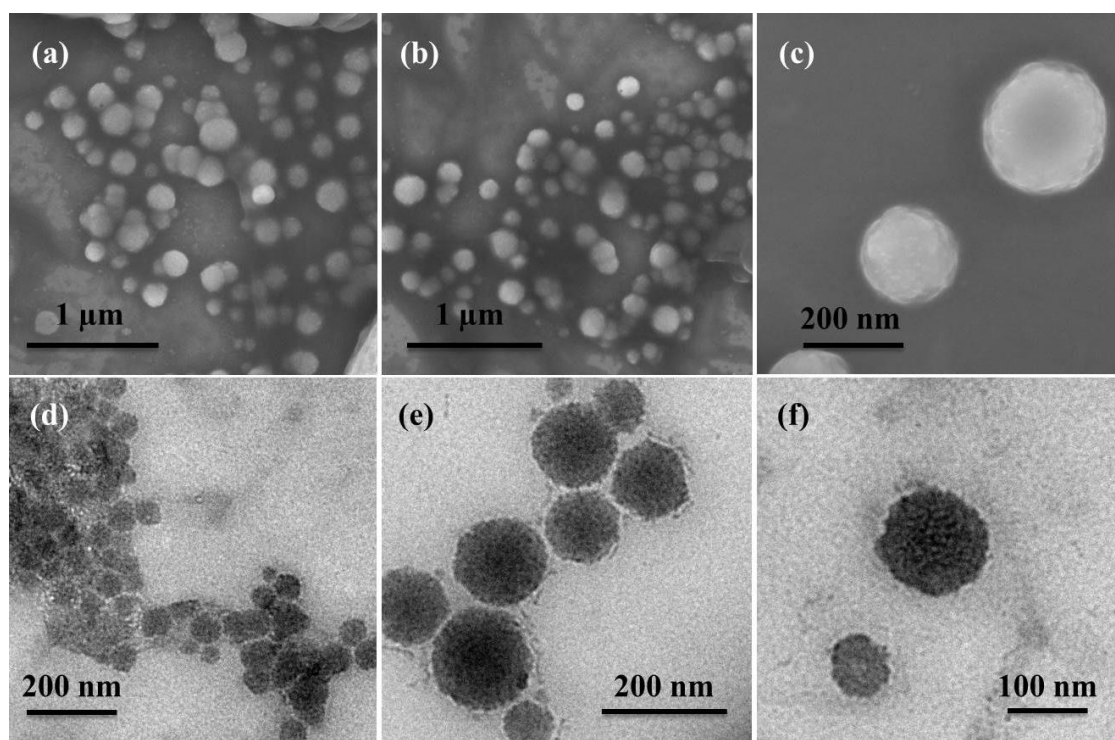


Figure 14: (a), (b), (c) FESEM images of **Rugel2** xerogel, (d), (e), (f) TEM images of **Rugel2** xerogel.

140±30 nm diameter which was evident from FESEM and TEM images (Figure 14a-f). Similar nanosphere morphology of metallogels was previously reported in literature. The

coordination of Ru^{II} drove kinetically controlled self-assembly of **G1/G2** which probably led to the formation of nanospheres.⁹ The UV-Vis spectrum of **Rugel1** exhibited a maximum at 400 nm and a broad shoulder around 550 nm, which was attributed to the MLCT transition of coordinated Ru^{II} (Figure 15a). **Rugel2** also exhibited broad absorption with maxima at 527 nm, however the MLCT transition was not distinguishable in this case as it merges with the π - π^* transition of **G2** (Figure 15b) The **Rugel1** xerogel showed weak emission at 480 nm when excited at 385 nm, originating from pyrene core of **G1** (Figure 15c). However, upon exciting at 550 nm, the **Rugel1** xerogel showed Ru^{II} based MLCT emission at 665 nm (Figure 15d). On the contrary, The **Rugel2** was found to be completely non-emissive. The optical band gaps of **Rugel1** and **Rugel2** were 2.8 and 2.3 eV as calculated by Kubelka-Munk plots.

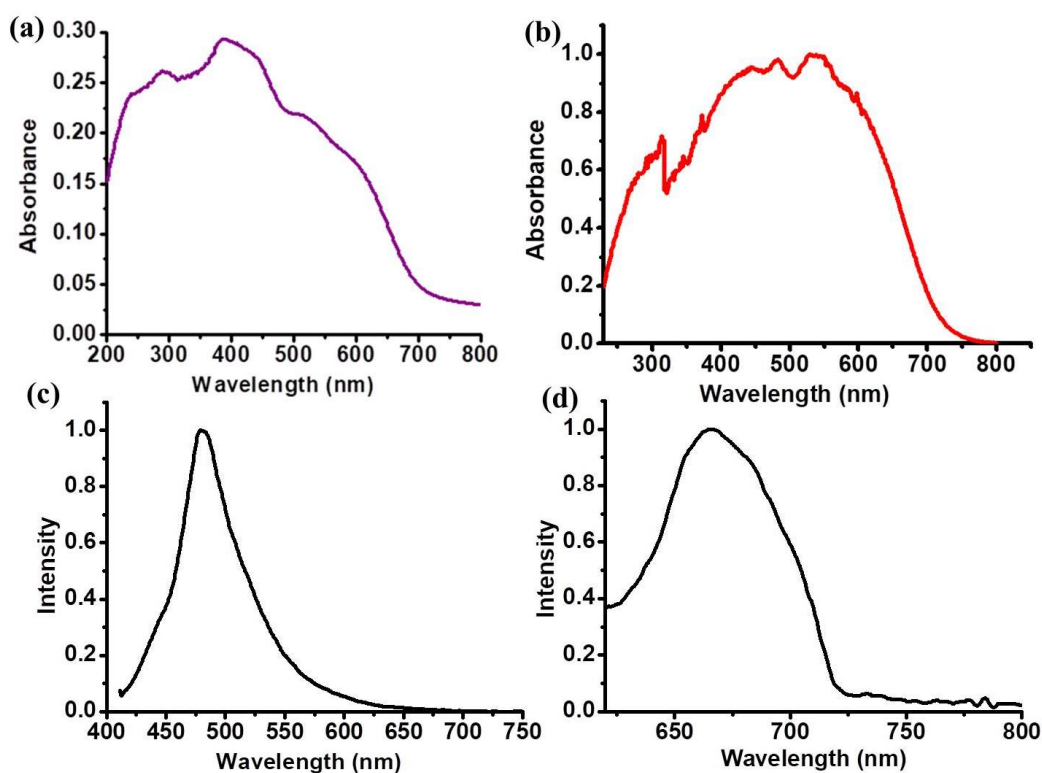


Figure 15: Absorption spectra of (a) **Rugel1** and (b) **Rugel2**, Normalized emission spectra of **Rugel1** after excitation (c) at 385 nm and (d) at 490 nm.

4.3.5 Photocatalytic hydrogen evolution

The low band gap and high visible light absorbance of **Rugel1** and **Rugel2** encouraged us to look into the photocatalytic activity. First, the photocatalytic hydrogen evolution abilities of CPGs were investigated in presence of different sacrificial electron donors. Both the CPG xerogels showed highest photocatalytic activity in presence of 5%

triethylamine (TEA) as sacrificial electron donor (Figure 16a). In a typical experiment, 5 mg CPGs were dispersed in 40 ml water containing 5% TEA. The homogeneous dispersion was taken into a 80 ml photocatalytic reactor and purged with N_2 for 30 minutes to remove the dissolved oxygen. The system was irradiated (290 W xenon arc lamp) under stirring condition to ensure uniform irradiation of the dispersion. The time course of hydrogen evolution was monitored by gas chromatography. Both the CPGs exhibited hydrogen production under illumination of visible light ($\lambda > 400$ nm) (Figure 16b). The rate of hydrogen evolution was found to be 3.45 and 2.5 $\mu\text{mol g}^{-1} \text{h}^{-1}$ for **Rugel1** and **Rugel2** xerogel, respectively (Figure 16c). Furthermore, the stability of **Rugel1** was studied by carrying out the “repeated runs” H_2 evolution experiment under visible-irradiation for total 15 hours (Figure 16d). The reaction was stopped and degasses after every 5 hours. As shown in Figure 16d, the photocatalytic performance of **Rugel1** xerogel was consistent and stable even after three consecutive cycles. **Rugel1** did not

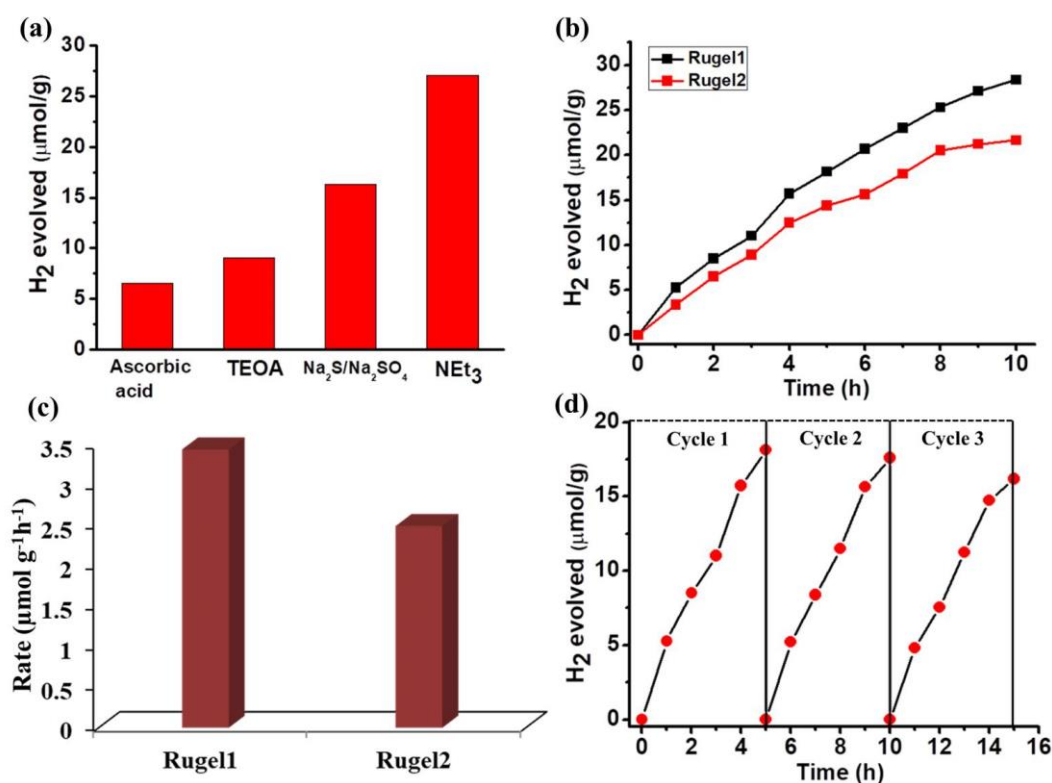


Figure 16. (a) Amount of hydrogen evolved from **RuGel1** in presence of different sacrificial electron donor, (b) The time course of hydrogen evolution of **Rugel1** (black) and **Rugel2** (red) xerogels under visible light irradiation, (c) Rate of hydrogen evolution in presence of **Rugel1** and **Rugel2** xerogel as photocatalyst, (d) The **Rugel1** xerogel shows photocatalytic activity even after three consecutive cycles.

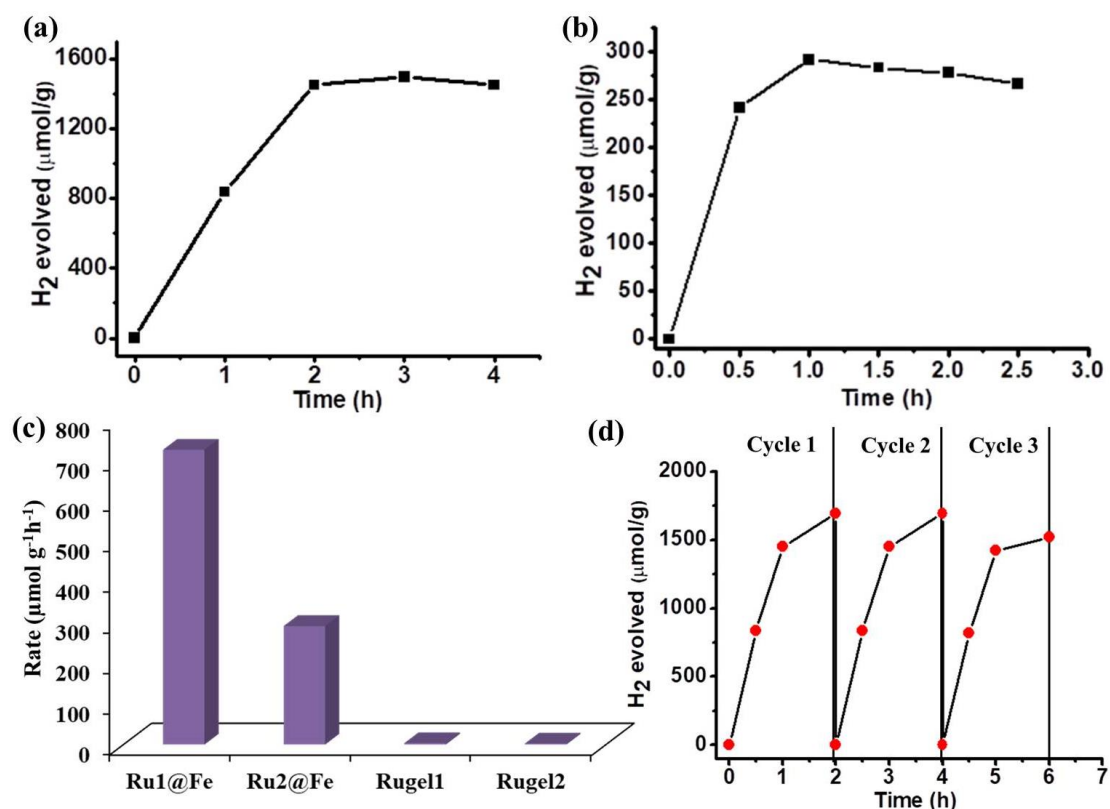


Figure 17. (a) The time course of hydrogen evolution of **Rugel1@Fe-C** under visible light irradiation, (b) The time course of hydrogen evolution of **Rugel2@Fe-C** under visible light irradiation, (c) Comparison of rate of hydrogen evolution of **Rugel1**, **Rugel2**, **Rugel1@Fe** and **Rugel2@Fe**., (d) The **Rugel1@Fe** xerogel shows photocatalytic activity even after three consecutive cycles.

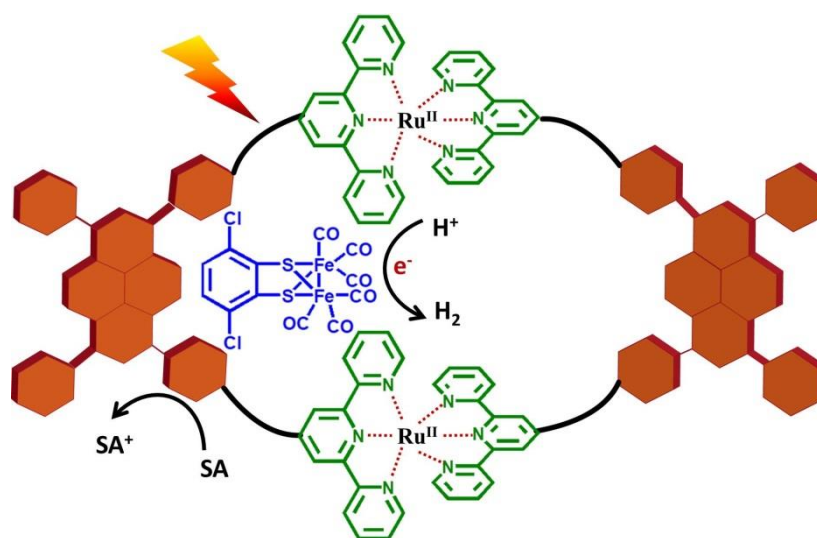


Figure 18. Schematic representation of hydrogen evolution under visible light from **Rugel1@Fe** xerogel.

show any significant changes in absorption, and FT-IR spectra after 15 hours of irradiation ($\lambda > 400$ nm), indicating high stability and structural integrity of the xerogel. No H₂ evolution was detected when the same reaction was performed under dark, indicating irradiation of visible light played the most important role in the H₂ evolution. Moreover, when a blank solution (without catalyst) containing 5% TEA in water was irradiated by visible-light no H₂ evolution was observed. These results confirm that evolution hydrogen is occurred by reduction of proton via an electron transfer process, and not simply by decomposition of the hydrogen bearing donor or CPGs. Next, to improve the photocatalytic activity of the CPGs we incorporate an organometallic Fe₂ complex that bears structural resemblance to the active site of [FeFe] hydrogenase into the CPGs. [FeFe](bcbdt)(CO)₆ (bcbdt = 3,6-Dichloro-1,2-benzenedithiol) was synthesized by following a literature report. 0.01M solution of [FeFe](bcbdt)(CO)₆ was prepared in de-oxygenated methanol and added slowly into the solution of **G1** and Ru(DMSO)₄Cl₂ during gelation to prepare a hybrid gel **Rugel1@Fe**. Similarly, [FeFe](bcbdt)(CO)₆ was also incorporated into the **Rugel2** to form a hybrid gel **Rugel2@Fe**. Both **Rugel1@Fe** and **Rugel2@Fe** xerogels were investigated for photocatalytic hydrogen evolution in aqueous solution of 5% TEA. They showed improved photocatalytic activity compared to the parent CPGs (Figure 17a-b). The rate of hydrogen evolution to calculated to be 725.45 and 291.6 $\mu\text{mol g}^{-1} \text{h}^{-1}$ for **Rugel1@Fe** and **Rugel2@Fe** respectively (Figure 17c). The turn over number (TON) was found to be 2.44 and 0.48 with respect to the mole of [FeFe](bcbdt)(CO)₆ for **Rugel1@Fe** and **Rugel2@Fe** respectively. The photocatalytic activity of **Rugel1@Fe** was retained even after three cycles of reaction, indicating the stability of the Fe-cluster catalyst inside the hydrophobic gel-matrix (Figure 17d). The mechanism of photocatalysis was explained in Figure 18. Initially, upon visible light irradiation the photosensitive Ru^{II}-CPGs get excited and generate photoelectrons which are possibly transferred to the encapsulated [FeFe](bcbdt)(CO)₆ co-catalyst. [FeFe](bcbdt)(CO)₆ molecules then subsequently reduced water to hydrogen. The encapsulated [FeFe](bcbdt)(CO)₆ molecules increase the lifetime of the photogenerated electrons and decrease the chances of the electron-hole recombination and hence increase the rate of hydrogen evolution.

4.3.6 DFT calculation

In order to understand the difference in catalytic performance between **Rugel1** and **Rugel2**, we have performed DFT computations to evaluate energy difference between

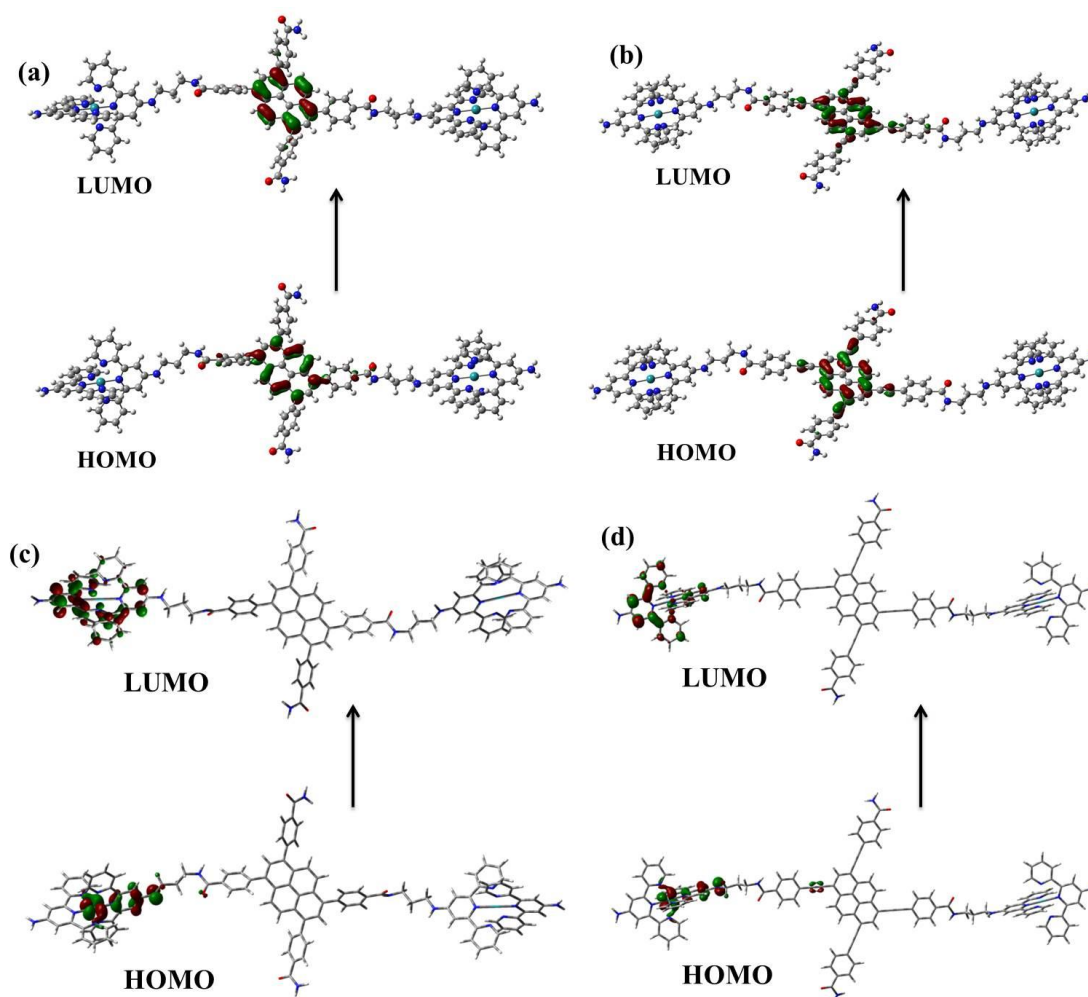


Figure 19. (a), (b) HOMO and LUMO on the pyrene centres of **Rugel1** and **Rugel2** as model-1 and model-2, respectively, (c) and (d) HOMO and LUMO on the Ru^{II}-terpyridine parts of **Rugel1** and **Rugel2** resulting due to MLCT.

highest occupied and lowest unoccupied orbital located on both pyrene and Ru^{II}-terpyridine chromophore. For this purpose, we have considered two different model systems, namely model-1 and model-2 for **Rugel1** and **Rugel2**, respectively (Figure 19a-b). The only difference was that model-2 contains four ethynyl groups connected to pyrene unit whereas model-1 has no ethynyl groups. HSEH1PBE method in conjunction with 6-31+G* basis set was utilized for the computations as the method was known to simulate more accurate orbital energy.^{10a} LANL2DZ was used for basis set and ECP of ruthenium.^{10b} All calculations were performed using Gaussian09 program package.^{10c} In model 1, the energy difference between highest occupied and lowest unoccupied molecular orbital on pyrene chromophore was only 2.72 eV whereas the value was 2.79 eV on Ru^{II}-terpyridine complex (Figure 19a and 19c). Strikingly, in model 2, the energy

difference on pyrene chromophore has dropped down to 2.00 eV due to the presence of four ethynyl groups that provide additional stabilization by extended conjugation (Figure 19b). The energy difference on Ru^{II}-terpyridine part was 2.84 eV which remained similar as in model-2 (Figure 19c). In the catalytic process, pyrene chromophore and the MLCT of Ru^{II}-terpyridine part acted as a sensitizer i.e. it absorbed light energy and generated photoelectrons which were eventually transferred to the encapsulated Fe-cluster where water got reduced to hydrogen. In case of **Rugel2** the low band gap induced the fast electron-hole recombination and hence the photo-catalytic activity decreased.

4.4 SUMMARY

In summary, we have synthesized two LMWGs containing four terminal terpyridine groups which self-assemble in organic solvent to form organogels with nanofiber morphology. The coordination driven self-assembly of LMWGs in presence of Ru^{II} leads to the formation of CPGs that show nanosphere morphology. The CPGs exhibits broad absorption in visible region due to the Ru^{II} centred metal to ligand charge transfer transition which make them a unique photoactive material for hydrogen evolution reaction. Both the CPGs exhibit good photocatalytic activity under visible light irradiation. Moreover, the rate of hydrogen evolution enhances by many folds when an organometallic Fe₂ complex was encapsulated in the CPG matrixes. This study will open up a new perspective for generating hydrogen from coordination polymer gels.

4.5 REFERENCES

- (a) C. Acar, I. Dincer and G. F. Naterer, *Int. J. Energy Res.*, 2016, **40**, 1449–1473; (b) A. Kudo and Y. Miseki, *Chem. Soc. Rev.*, 2009, **38**, 253-278.
- (a) F. E. Osterloh, *Chem. Soc. Rev.*, 2013, **42**, 2294-2320; (b) J. Ran, J. Zhang, J. Yu, M. Jaroniec and S. Z. Qiao, *Chem. Soc. Rev.*, 2014, **43**, 7787-7812; (c) K. Maeda and K. Domen, *J. Phys. Chem. Lett.*, 2010, **1**, 2655-2661; (d) R. S. Sprick, J.-X. Jiang, B. Bonillo, S. Ren, T. Ratvijitvech, P. Guiglion, M. A. Zwijnenburg, D. J. Adams and A. I. Cooper, *J. Am. Chem. Soc.*, 2015, **137**, 3265-3270; (e) R. S. Sprick, B. Bonillo, M. Sachs, R. Clowes, J. R. Durrant, D. J. Adams and A. I. Cooper, *Chem. Commun.*, 2016, **52**, 10008-10011; (f) X. Sun, Q. Yu, F. Zhang, J. Wei and P. Yang, *Catal. Sci. Technol.*, 2016, **6**, 3840-3844; (g) T. Song, L. Zhang, P. Zhang, J. Zeng, T. Wang, A. Ali and H. Zeng, *J. Mater. Chem. A.*, 2017, **5**, 6013-6018; (h) T. Hisatomi, J. Kubota and K. Domen, *Chem. Soc. Rev.*, 2014, **43**, 7520-7535; (h) C. Jiang, S. J. A. Moniz, A. Wang, T. Zhang

- and J. Tang, *Chem. Soc. Rev.*, 2017, **46**, 4645-4660; (i) K. Takanahe, *ACS Catal.*, 2017, **7**, 8006-8022.
3. (a) A. S. Weingarten, R. V. Kazantsev, L. C. Palmer, D. J. Fairfield, A. R. Koltonow and S. I. Stupp, *J. Am. Chem. Soc.*, 2015, **137**, 15241-15246; (b) M. C. Nolan, J. J. Walsh, L. L. E. Mears, E. R. Draper, M. Wallace, M. Barrow, B. Dietrich, S. M. King, A. J. Cowan and D. J. Adams, *J. Mater. Chem. A.*, 2017, **5**, 7555-7563; (c) A. S. Weingarten, R. V. Kazantsev, L. C. Palmer, M. McClendon, A. R. Koltonow, P. S. SamuelAmanda, D. J. Kiebalala, M. R. Wasielewski and S. I. Stupp, *Nat. Chem.*, 2014, **6**, 964-970.
4. (a) W. Lubitz, H. Ogata, O. Rüdiger and E. Reijerse, *Chem. Rev.*, 2014, **114**, 4081-4148; (b) S. Pullen, H. Fei, A. Orthaber, S. M. Cohen and S. Ott, *J. Am. Chem. Soc.*, 2013, **135**, 16997-17003; (c) C. Tard, C. J. Pickett, *Chem. Rev.*, 2009, **109**, 2245-2274; (d) R. Lomoth, S. Ott, *Dalton Trans.*, 2009, **0**, 9952-9959; (e) G. A. N. Felton, A. K. Vannucci, J. Chen, L. T. Lockett, N. Okumura, B. J. Petro, U. I. Zakai, D. H. Evans, R. S. Glass and D. L. Lichtenberger, *J. Am. Chem. Soc.*, 2007, **129**, 12521. (f) D. Streich, Y. Astuti, M. Orlandi, L. Schwartz, R. Lomoth and L. Hammarstrom, S. Ott, *Chem.-Eur. J.*, 2010, **16**, 60.
5. (a) P. Sutar, V. M. Suresh and T. K. Maji, *Chem. Commun.* 2015, **51**, 9876-9879; (b) J. H. Jung, J. H. Lee, J. R. Silverman and G. John, *Chem. Soc. Rev.*, 2013, **42**, 924-936; (c) M.-O. M. Piepenbrock, G. O. Lloyd, N. Clarke and J. W. Steed, *Chem. Rev.*, 2009, **110**, 1960-2004; (d) A. Y.-Y. Tam and V. W.-W. Yam, *Chem. Soc. Rev.*, 2013, **42**, 1540-1567; (e) X. Yan, T. R. Cook, J. B. Pollock, P. Wei, Y. Zhang, Y. Yu, F. Huang and P. J. Stang, *J. Am. Chem. Soc.*, 2014, **136**, 4460-4463; (f) G. M. Peters, L. P. Skala, T. N. Plank, B. J. Hyman, G. N. Manjunatha Reddy, A. Marsh, S. P. Brown and J. T. Davis, *J. Am. Chem. Soc.*, 2014, **136**, 12596-12599; (g) P. Sutar and T. K. Maji, *Chem. Commun.*, 2016, **52**, 8055-8074; (h) P. Sutar and T. K. Maji, *Inorg. Chem.*, 2017, **56**, 9417-9425.
6. (a) V. M. Suresh, A. De, T. K. Maji, *Chem. Commun.*, 2015, **51**, 14678-14681; (b) P. Sutar and T. K. Maji, *Inorg. Chem.*, 2017, **56**, 9417-9425; (c) H. B. Aiyappa, S. Saha, P. Wadge, R. Banerjee, S. Kurungot, *Chem. Sci.*, 2015, **6**, 603-607.
7. (a) J. P. Byrne, J. A. Kitchen, O. Kotova, V. Leigh, A. P. Bell, J. J. Boland, M. Albrecht and T. Gunnlaugsson, *Dalton Trans.*, 2014, **43**, 196-209; (b) O. Kotova, R. Daly, C. M. G. dos Santos, P. E. Kruger, J. J. Boland and T. Gunnlaugsson, *Inorg. Chem.*, 2015, **54**, 7735-7741.

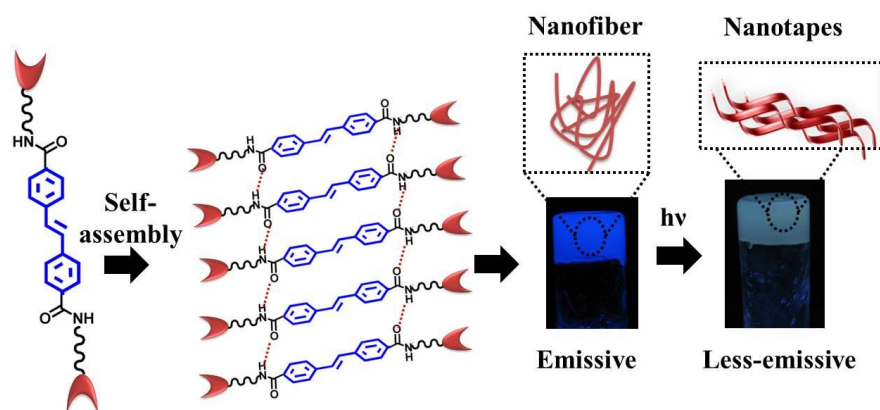
8. (a) A. G. Walden and A. J. M. Miller, *Chem. Sc.*, 2015, **6**, 2405-2410; (b) L.-Y. Zhang, S.-Y. Yin, M. Pan, W.-M. Liao, J.-H. Zhang, H.-P. Wang and C.-Y. Su, *J. Mater. Chem. A*, 2017, **5**, 9807-9814.
9. Y. Wang, R. Huang, W. Qi, Z. Wu, R. Su and Z. He, *Nanotechnology*, 2013, **24**, 465603.
10. (a) T. M. Henderson, A. F. Izmaylov, G. Scalmani, and G. E. Scuseria, *J. Chem. Phys.*, 2009, **131**, 044108; (b) P. J. Hay and W. R. Wadt, *J. Chem. Phys.*, 1985, **82**, 299; (c) M. J. Frisch, et. al. Gaussian 09, revision A.1; Gaussian, Inc.: Wallingford, CT, 2009.

Chapter 5

**Photo-responsive Gel: Tuning of
Morphology and Optical Property by
[2+2] Cyclo-addition Reaction**

Abstract

This chapter reports design and synthesis of two photo-responsive gelators (**L1** and **L2**), one containing stilbene core (**L1**) and another having azobenzene core (**L2**) which are connected to two 2,2':6',2''-terpyridyl (tpy) moieties through flexible alkylamide chains. Self-assembly of **L1** results in organogel (**OG1**) which shows nanofiber morphology. However, **L2** fails to form gel in either aqueous or organic solvent medium. Coordination driven self-assembly of **L1** in presence of Zn^{II} results in coordination polymer gels (**ZnL1**) which exhibits nanofiber morphology. Both **OG1** and **ZnL1** show blue emission which is quenched considerably after irradiation with UV light ($\lambda=365$ nm) indicating photochemical change of gelators in **OG1** and **ZnL1** gels. The 1H -NMR studies indicated that the self-assembled **L1** undergo [2+2] cyclo addition during photo-irradiation and leads to the formation of tetraphenyl cyclobutane derivatives. Moreover, the photo-irradiation also modulate the morphology of **OG1** and **ZnL1** from nano-fibers to nanotapes.



Paper based on this work:

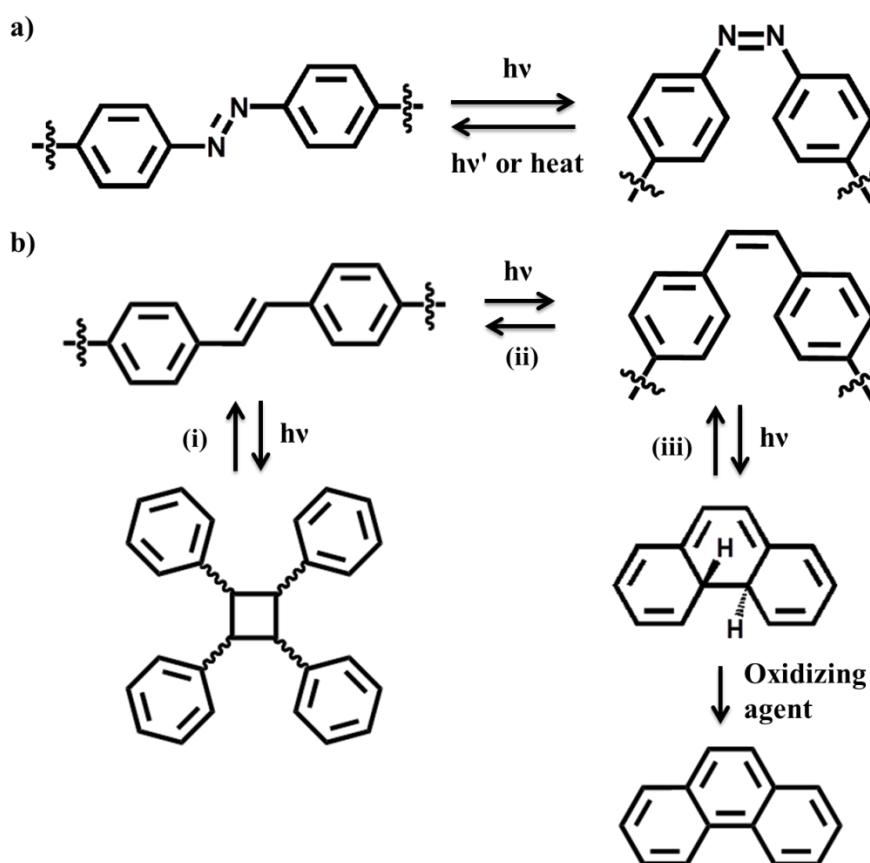
P. Sutar and T. K. Maji, *manuscript under preparation.*

5.1 INTRODUCTION

Development of supramolecular gels by the self-assembly of low molecular weight gelators (LMWGs) have gained enormous attention in last few decades.¹ Easy solution processability and dynamic nature of these soft materials hold great promise for applications in diverse fields, including biomedicine, nanoelectronics and catalysis.² One important class of supramolecular gel which has been emerged very recently is known as coordination polymer gels (CPGs).³ The coordination of metal ions to a suitably designed LMWG results in supramolecular self-assembled networks of CPGs. The CPGs are highly promising soft-hybrid materials, as the presence of metal ions endows them with unique redox, optical, electronic, and catalytic properties.⁴ Also, the metal–LMWG interactions allow the controlled growth of different nanostructures, such as fibers, tubes, rings, ribbons, and vesicles in CPGs.⁵ Many novel functionalities such as tunable emission, catalysis, proton conductivity, sensing, and gas storage have been explored in CPGs, which arise due to the synergistic combination of inorganic and organic components.⁶ Another important property that has been exploited recently in supramolecular gels/CPGs, is the stimuli-responsive behaviours.⁷ The stimuli-responsive supramolecular gels/CPGs generally exhibit multifarious changes in their properties by the application of various physicochemical stimuli, e.g., pH^{8a-c}, temperature^{8d-e}, redox^{8f-j}, mechanical force^{8k-l} and in the presence of small molecules and biomolecules^{8m-o}. They usually exhibit reversible sol–gel transformations, hydrophilic–hydrophobic transitions, shape and volume changes, or assembly–disassembly ordering in presence of these external stimuli. Such intelligent soft-materials have found many applications in the fields of biology, medicine and can be used as sensors and biosensors, for controlled and triggered drug delivery, environmental remediation, chemo-mechanical actuators, and for many other applications.⁹ Among different stimuli exploited to date, light is the most cost effective and non-hazardous external stimulus.^{10a-d} However, there are very few examples of photo-responsive CPGs^{10e}.

Over past few years, development of photo-responsive materials has gained significant research attentions. In this regard, substantial advancement has been done in the field of crystalline porous coordination polymers (PCPs)/ metal-organic frameworks (MOFs), where light is used as a tool to post-synthetically modulate the porosity, magnetic property and polarity of pore.¹¹ The photo-chemical reactions which are exploited to develop such photo-responsive material include polymerization of

diacetylenes to PDA, dimerization of anthracene, [2+2] cycloaddition of alkenes, *cis-trans* isomerization of azobenzene etc. Stilbene and azobenzene derivatives are the most examined systems for developing photo-responsive materials as their photochemistry are well-explored in literature. The only possible photochemical pathway of azobenzene is the *cis-trans* isomerization which is extremely rapid, occurring on picosecond timescales (Scheme 1).¹² However, there are three possible photochemical pathways for stilbene. i) dimerization by [2+2] cyclo-addition, first discovered by Ciamician and Silber^{13a}; ii) the *E/Z*-isomerization, first described by Störmer^{13b}; and iii) the photocyclization via oxidative dehydrogenation of dihydrophenanthrene, found by Smakula^{13c} (Scheme 1). [2+2] cycloaddition occurs between the first excited singlet state S_1 of an *E*-stilbene and ground state of a second *E*-stilbene and results in cyclobutane ring. It is noteworthy that photochemical cycloaddition only occurs when the compounds satisfy Schmidt's [2+2] cycloaddition criteria which tells that i) the two olefinic bond should be parallel to each



Scheme 1. Schematic showing a) Photo-isomerization of azobenzene, b) Three possible photochemical pathways for stilbene (i) dimerization by [2+2] cyclo-addition, (ii) *E/Z*-isomerization and (iii) the photocyclization via oxidative dehydrogenation of dihydrophenanthrene.

other and ii) the distance between them should be $<4.2 \text{ \AA}$.^{13d,e} In most of the photo-responsive gels reported to date azobenzene derivative are used as gelators, however development of stilbene-based gelators for preparing photo-responsive gels is still underexplored.¹⁴ This chapter reports design and synthesis of two photo-responsive gelators (**L1** and **L2**), one containing stilbene core (**L1**) and another having azobenzene core (**L2**) which are connected to two 2,2':6',2''-terpyridyl (tpy) moieties through flexible alkylamide chains. Self-assembly of **L1** results in organogel (**OG1**) which shows nanofiber morphology. **L2** fails to form gel in either aqueous or organic solvent medium. Self-assembly of **L1** in presence of Zn^{II} results in CPGs (**ZnL1**) which exhibits similar nanofiber morphology. Both **OG1** and **ZnL1** show blue emission which is considerably quenched after irradiation with UV light ($\lambda=365 \text{ nm}$), indicating photochemical change of gelators in **OG1** and **ZnL1** gels. The gelator molecules undergo [2+2] cyclo-addition during photo-irradiation as confirmed by $^1\text{H-NMR}$ study which shows the formation of tetraphenyl cyclobutane. Also after photo-irradiation the morphologies of organogel and CPG is changed from nano-fibers to nano-tapes.

5.2 EXPERIMENTAL SECTION

5.2.1 Materials

4,4'-stilbenedicarboxylic acid, 4-nitrobenzoic acid, 4'-chloro-2,2':6',2''-terpyridine, 1,3-diaminopropane, trichloroisocyanuric acid (TCIC) and triphenylphosphine (PPh_3) were purchased from Sigma-Aldrich chemical Co. Ltd. Sodium hydroxide, glucose, sodium chloride and triethylamine were purchased from Spectrochem Pvt. Ltd. All the solvents were purchased from Spectrochem and were pre-dried using standard procedures before using.

5.2.2 Physical measurements

$^1\text{H-NMR}$ was recorded on a Bruker AV-400 spectrometer with chemical shifts recorded as ppm and all spectra were calibrated against TMS. High resolution mass spectra (HRMS) were recorded using Agilent QTOF 7200 spectrometer. UV-Vis spectra were recorded in a Perkin-Elmer lamda 900 spectrometer. Fluorescence studies were accomplished using Perkin Elmer Ls 55 luminescence spectrometer. Fourier transform infrared (FTIR) spectral studies were carried out by making samples with KBr pellets using Bruker FT-IR spectrometer. The elemental analyses were carried out using a Thermo Scientific Flash 2000 CHN analyzer. Morphology studies were carried out using

Lica-S440I field emission scanning electron microscopy (FESEM) by placing samples on silicon wafer under vacuum with accelerating voltage of 10 kV. Transmission electron microscopy (TEM) analysis was performed using JEOL JEM-3010 with accelerating voltage of 300 kV. For this analysis the xerogel was dispersed in ethanol and then drop casted on a carbon coated copper grid.

5.2.3 Synthesis

Synthesis of 2,2':6',2''-terpyridin-4'-yl-propane-1,3-diamine: The detail synthetic procedure of 2,2':6',2''-terpyridin-4'-yl-propane-1,3-diamine was discussed in Chapter 2. The $^1\text{H-NMR}$, FTIR and CHN analysis of 2,2';6',2''-terpyridin-4'-yl-propane-1,3-diamine were also discussed in Chapter 2.

Synthesis of 4,4'-stilbenedi-{[3-(2,2':6',2'')terpyridin-4'-ylamino)-propyl]-amide} (L1): A mixture of 4,4'-stilbenedicarboxylic (300 mg, 1.11 mmol) and trichloroisocyanuric acid (545 mg, 2.34 mmol) was dissolved in anhydrous THF (30 ml). PPh_3 (616 mg, 2.35 mmol) was added into the reaction mixture and stirred at 0 °C for 2 h under inert condition. 2,2':6',2''-terpyridin-4'-yl-propane-1,3-diamine (717 mg, 2.35 mmol) was dissolved in anhydrous THF (20 ml) and Et_3N (624 μl , 4.47 mmol) was added into it. This reaction mixture was drop-wise added into 4,4'-stilbenedicarboxylic acid /TCIC/ PPh_3 solution at 0 °C and stirred for 1 h. After that the reaction mixture was stirred at room temperature for 6 h. Precipitate was collected by filtration and washed several times with CHCl_3 and dried under vacuum. The

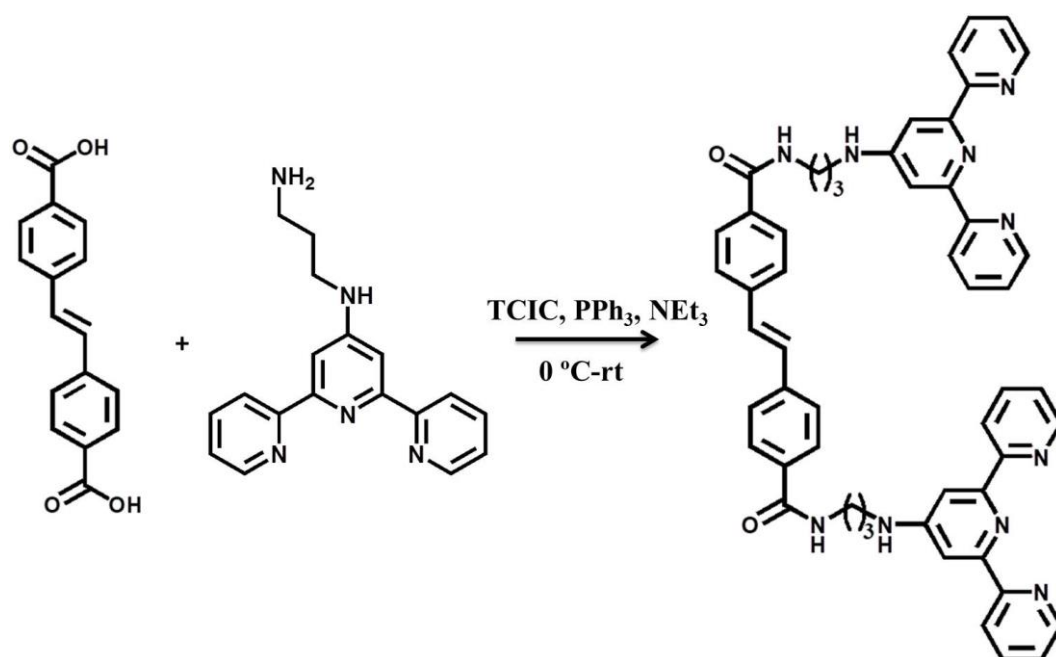


Figure 1. Synthetic scheme for L1.

product was refluxed in methanol for 30 min to remove unreacted 4,4'-stilbenedicarboxylic acid. The mixture was filtered under hot condition and washed repeatedly with methanol. The filtrate was evaporated under reduced pressure to get the pure product. Yield: 80%. $^1\text{H-NMR}$ (400 MHz, DMSO-d^6) δ : 8.70 (s, 2H, ArH), 8.54 (t, 2H, ArH), 7.96 (d, 2H, ArH), 7.89 (d, 2H, ArH), 7.76 (d, 1H, ArH), 7.7 (d, 3H, ArH), 7.48 (m, 2H, ArH), 3.43 (m, 3H, NHCH_2), 1.92 (t, 2H, CH_2). Selected FTIR data (KBr, cm^{-1}): 3429 (b), 3027 (m), 2779 (m), 1723 (sh), 1469 (m), 1398 (sh), 1053 (s), 774 (m), 534 (m). CHN analysis for $\text{C}_{52}\text{H}_{46}\text{N}_{10}\text{O}_2$ Calc.: C, 74.07; H, 5.50; N, 16.62%. Expt.: C, 74.16; H, 5.40; N, 16.55%. HRMS (+ESI): m/z calculated for $\text{C}_{52}\text{H}_{46}\text{N}_{10}\text{O}_2$: 843.3839, found: 843.3879 $[\text{M}+\text{H}]^+$.

Synthesis of 4,4'-dicarboxyazobenzene: 4-nitrobenzoic acid (1 g, 5.98 mmol) and NaOH (3.4 g, 85 mmol) were mixed in a round bottom flux. 15 ml water was added and the mixture was heated until the solid was dissolved completely. The hot aqueous solution of glucose (6 g in 10 ml water) was added drop-wise into the above reaction mixture. The temperature was maintained at 50 °C while adding glucose solution. After that the reaction mixture was cooled down to room temperature and continued to stir for 8 h. The brown coloured compound was formed. The reaction mixture was filtered and the product was washed thoroughly with saturated NaCl solution. The product was dissolved in water and carefully acidified by acetic acid to form pink precipitate. The mixture was filtered and the product was washed repeatedly with water and dried under vacuum. Yield: 90%. $^1\text{H-NMR}$ (400 MHz, DMSO-d^6) δ : 8.15 (d, 4H, ArH), 8.00 (d, 4H, ArH). Selected FTIR data (KBr, cm^{-1}): 2671 (s), 2554 (s), 1685 (sh), 1604 (m), 1427 (sh), 1294 (sh), 943 (m), 871 (m), 781 (m), 698 (m), 539 (s).

Synthesis of 4,4'-azobenedi- $\{[3-([2,2':6',2'']\text{terpyridin-4'-ylamino})\text{-propyl}\}$ -amide} (L2): A mixture of 4,4'-dicarboxyazobenzene (300 mg, 1.11 mmol) and trichloroisocyanuric acid (566 mg, 2.44 mmol) was dissolved in anhydrous THF (30 mL). PPh_3 (639 mg, 2.44 mmol) was added into the reaction mixture and stirred at 0 °C for 2 h under inert condition. Next, 2,2':6',2''-terpyridin-4'-yl-propane-1,3-diamine (711 mg, 2.33 mmol) was dissolved in anhydrous THF (20 ml) and Et_3N (650 μl , 4.66 mmol) was added into it. This reaction mixture was drop-wise added into 4,4'-stilbenedicarboxylic acid / TCIC/ PPh_3 solution at 0 °C and stirred for 1 h. After that the reaction mixture was stirred at room temperature for 6 h. Precipitate was collected by filtration and washed several times with CHCl_3 and dried under vacuum. The product was refluxed in methanol for 30 min to remove unreacted 4,4'-

dicarboxyazobenzene. The mixture was filtered under hot condition and washed repeatedly with methanol. The filtrate was evaporated under reduced pressure to get the pure product. Yield: 73%. $^1\text{H-NMR}$ (400 MHz, DMSO-d^6) δ : 8.88 (s, 2H, ArH), 8.25 (s, 2H, ArH), 8.16 (s, 4H, ArH), 8.01 (d, 2H, ArH), 7.85 (s, 2H, ArH), 7.71 (s, 2H, ArH), 3.69 (s, 2H, NHCH_2), 2.99 (s, 2H, NHCH_2), 2.00 (s, 2H, CH_2). Selected FTIR data (KBr, cm^{-1}): 3422 (b), 3233 (s), 3053 (b), 1690 (m), 1585 (m), 1467 (m), 1295 (sh), 1160 (s), 994 (sh), 871 (m), 792 (sh), 697 (s), 620 (s). CHN analysis for $\text{C}_{50}\text{H}_{44}\text{N}_{12}\text{O}_2$ Calc.: C, 71.05; H, 5.25; N, 19.90%. Expt.: C, 71.10; H, 5.22; N, 19.11%. HRMS (+ESI): m/z calculated for $\text{C}_{52}\text{H}_{46}\text{N}_{10}\text{O}_2$: 845.3744, found: 845.3800 $[\text{M}+\text{H}]^+$.

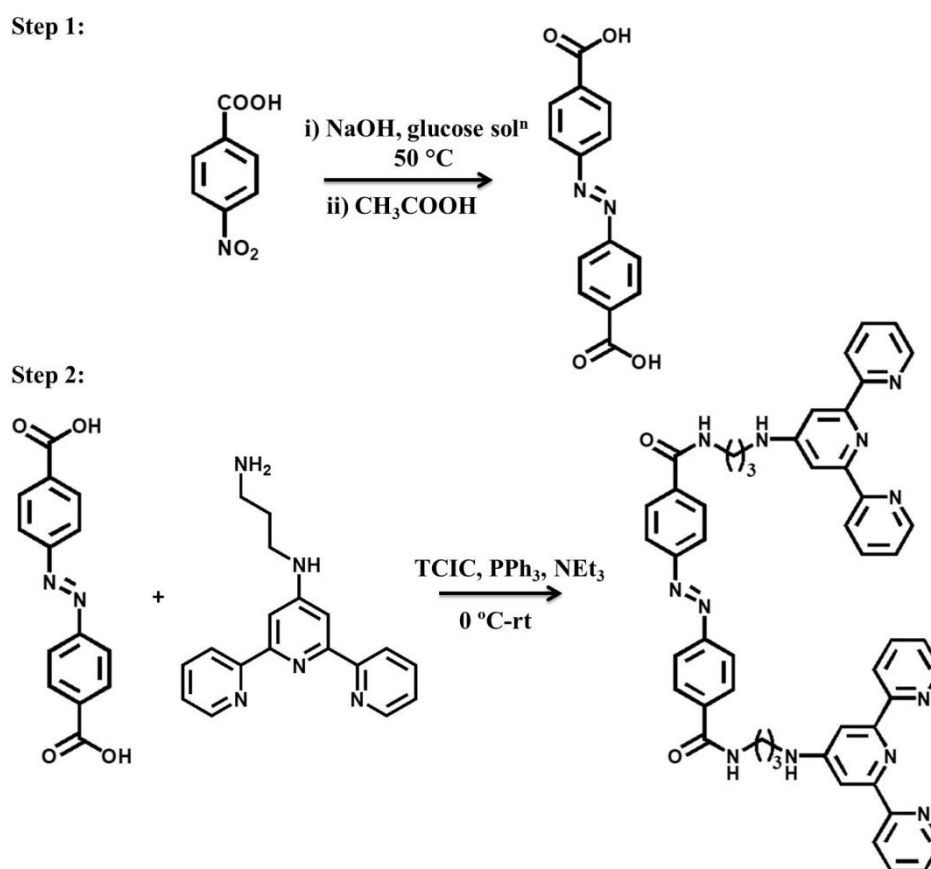


Figure 2. Synthetic scheme for **L2**.

Synthesis of OG1 gel: 2.1×10^{-3} M solution of **L1** in 1:1 CHCl_3/THF mixture was heated at $80\text{ }^\circ\text{C}$ for few minutes to form a viscous liquid which on cooling resulted in opaque gel. The formation of gel was confirmed by inversion test method. Selected FTIR data (KBr, cm^{-1}): 3434 (b), 2964-2859 (b), 1719 (sh), 1617 (m), 1463 (sh), 1168 (m), 1099 (s), 997 (sh), 806 (m), 557 (s).

Synthesis of ZnL1 CPG: Solution of **L1** (2.1×10^{-3} M) in CHCl_3/THF (1:1) was mixed with solution of $\text{Zn}(\text{NO}_3)_2 \cdot 6\text{H}_2\text{O}$ (1.5×10^{-3} M, in THF) in 1:1 volumetric ratio.

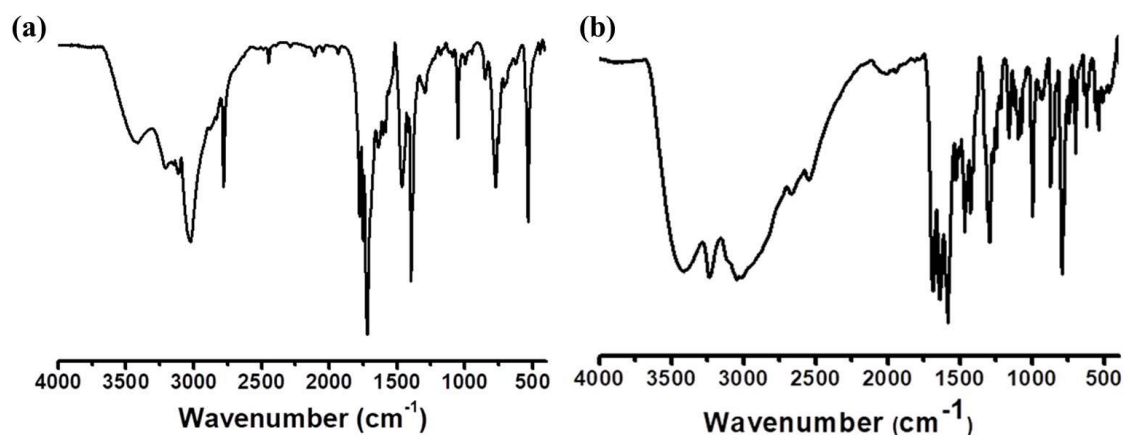


Figure 3. (a) FTIR spectrum of **L1**, (b) FTIR spectrum of **L2**.

The mixture was heated at 80 °C for 3 min to prepare a viscous solution which eventually resulted in stable opaque gel upon cooling. The formation of gel was confirmed by inversion test method Selected FTIR data (KBr, cm^{-1}): 3424 (b), 2960-2855 (b), 1720 (sh), 1618 (m), 1465 (sh), 1178 (m), 1098 (s), 995 (sh), 808 (m), 547 (s).

5.3 RESULTS AND DISCUSSION

5.3.1 Characterization of **L1** and **L2**

Synthesis of **L1** was carried out *via* amide coupling between 4,4'-stilbenedicarboxylic and 2,2':6',2''-terpyridin-4'-yl-propane-1,3-diamine (Figure 1). Similarly **L2** was prepared by amide coupling between 4,4'-dicarboxyazobenzene and 2,2':6',2''-terpyridin-4'-yl-propane-1,3-diamine (Figure 2). The formation of **L1** and **L2** was confirmed by $^1\text{H-NMR}$, HRMS and FTIR spectra. The $^1\text{H-NMR}$ spectrum of **L1** showed peaks corresponding to terminal 2,2':6',2''-terpyridine groups at $\delta = 8.68, 8.54, 7.70$ and 7.43 ppm and the peaks corresponding to 4,4'-stilbenedicarboxylate core appeared at $\delta = 7.94, 7.87$ and 7.76 ppm. Similarly, $^1\text{H-NMR}$ spectrum of **L2** showed peaks corresponding to the aromatic protons of terminal 2,2':6',2''-terpyridine and central 4,4'-dicarboxyazobenzoate at $\delta = 8.8, 8.25, 8.16, 8.01, 7.85$ and 7.71 ppm. In both cases the peaks corresponding to the aliphatic protons of flexible alkylamide chain appeared in 3.7-2.0 ppm range. The formation of **L1** and **L2** was also confirmed by HRMS which showed signals at $m/z = 843.3879$ and 845.3800 , corresponding to $[\text{L1}+\text{H}]^+$ and $[\text{L2}+\text{H}]^+$, respectively. The formation of amide bond in **L1** was confirmed by the FTIR spectra which displayed band at 3429 and 1722 cm^{-1} corresponding to the N-H and C=O stretching of amide, respectively (Figure 3a). Similarly, the FTIR spectrum of **L2** showed

peaks corresponding to N-H and C=O stretching of amide at 3406 and 1698 cm^{-1} , respectively (Figure 3b). The elemental analysis of **L1** and **L2** also confirmed their purity.

5.3.2 Photophysical properties of **L1** and **L2**

The solution of **L1** (10^{-5} M) in DMSO showed a broad absorption with a maxima at 284 nm, corresponding to the π - π^* transition of terminal terpyridine groups, as previously observed by other terpyridine-based LMWG (Figure 4a)¹⁵. Another broad absorption band appeared around 333 nm which was attributed to the π - π^* transition of stilbene core. Upon exciting at 333 nm, the solution of **L1** showed blue emission with maxima at 385 nm which could be considered as the combine emission from terpyridine groups and stilbene core (Figure 4b). Similarly, the solution of **L2** (10^{-5} M) in DMSO showed the absorption maxima at 284 nm and a broad band at 330 nm, assigned to the π - π^* transition of terpyridine and azobenzene core, respectively (Figure 5b). However, **L2** did not show any emission probably due the presence of azo group.

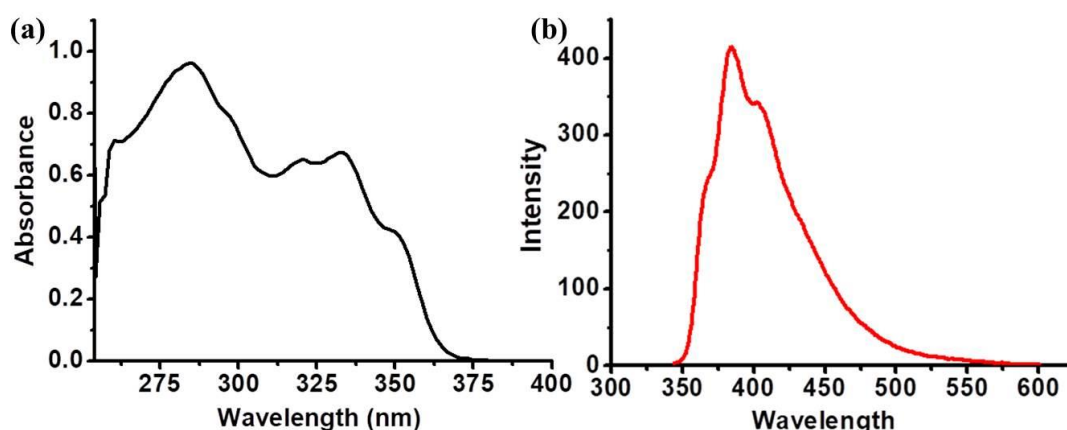


Figure 4. (a) Absorption spectrum of solution of **L1** (10^{-5} M) in DMSO, (b) Emission spectrum of the solution of **L1** (10^{-5} M) in DMSO.

Next the photophysical properties of **L1** and **L2** were studied after photo-irradiation with UV light ($\lambda=365$ nm). When solution of **L1** in DMSO (10^{-5} M) was irradiated with UV light, the absorption spectrum showed significant hypochromic shift at 333 nm and appearance of a new band at 265 nm, indicating photo-isomerization of *trans*-**L1** to *cis*-**L1** (Figure 5a). Similarly, after irradiating the solution of **L2** (10^{-5} M in DMSO) with UV light the absorption spectrum showed a drastic change (Figure 5b). The absorption peak at 330 nm, assigned to the *trans*-conformation of azobenzene core showed sudden decrease in absorbance after 2 min of irradiation. This indicated fast conversion of *trans*-**L2** to *cis*-**L2** in DMSO solution. The photo-isomerization of **L1** in DMSO-*d*⁶ solution was also

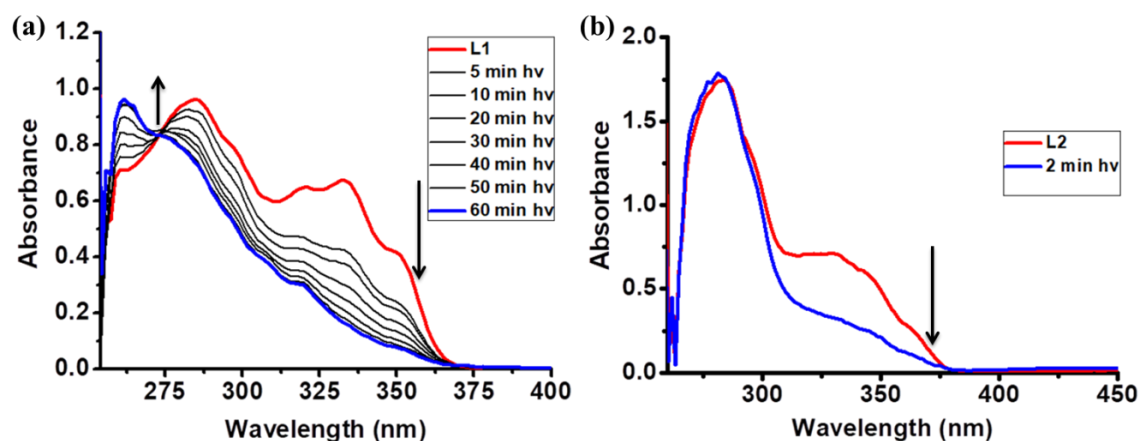


Figure 5. (a) Change in absorption spectrum of **L1** (10^{-5} M, in DMSO) after irradiation with UV light, (b) Change in absorption spectrum of **L2** (10^{-5} M, in DMSO) after irradiation with UV light.

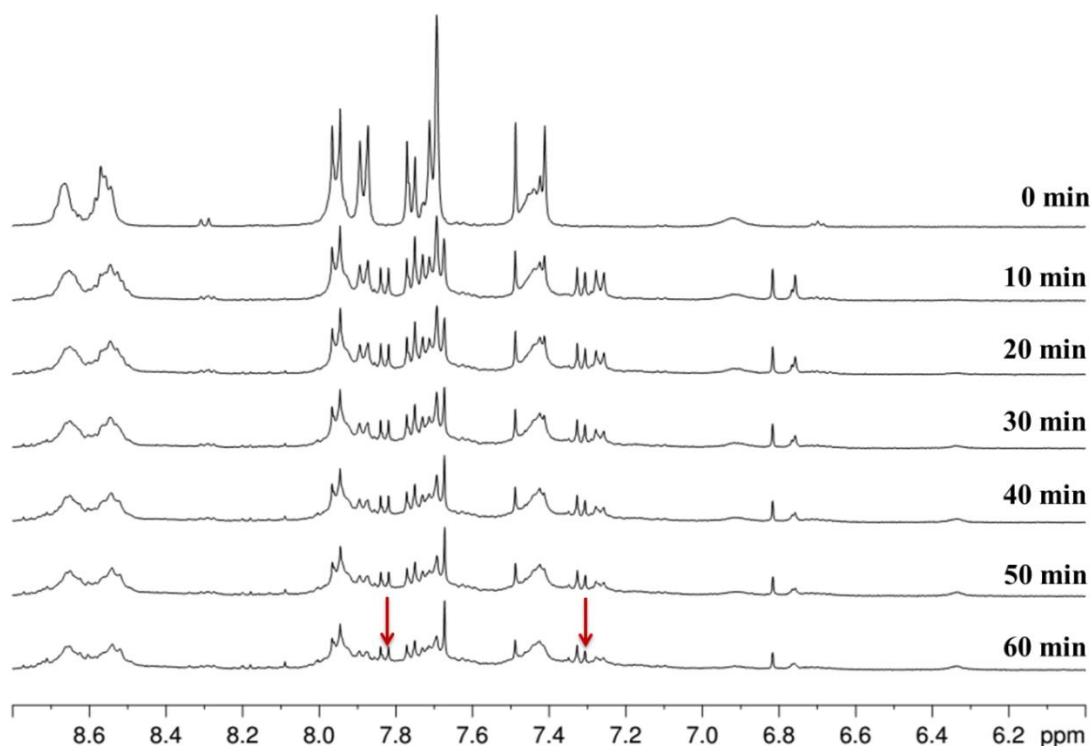


Figure 6. Change in ¹H-NMR spectra of **L1** in DMSO-d₆ after irradiation with UV light for one hour. The red arrows indicate the appearance of new peaks, attributed to the *cis*-conformation of stilbene core.

confirmed by recording time-dependent ¹H-NMR spectrum. The **L1** solution in DMSO-d₆ was irradiated with UV light and ¹H-NMR spectra were recorded after every 10 minutes of photo-irradiation. The solution was irradiated for total 1 h. With increasing irradiation

time the peaks at $\delta = 7.87$ and 7.74 ppm, assigned to the aromatic protons of *trans*-stilbene core weakened slowly and new peaks appeared at $\delta = 7.82$ and 7.30 ppm (Figure 6). These new peaks were attributed to the aromatic protons of *cis*-stilbene core. Since the first excited singlet state (S_1) lifetime of *trans*-stilbene core is very low it couldn't find the dimerization partner through diffusion in dilute solution, hence *trans*-to-*cis* isomerization was observed instead of cycloaddition.

5.3.3 Titration of L1 and L2 with Zn^{II}

Interaction of **L1** and **L2** with Zn^{II} was studied in DMSO solution by gradually adding the solution of Zn^{II} (10^{-4} M) to the solution of **L1** and **L2** (10^{-5} M in DMSO). With incremental addition of Zn^{II} the absorption maxima of **L1** at 284 nm showed a hypochromic shift and a new band appeared around 310 nm which suggested complexation of Zn^{II} to terpyridine groups of **L1** (Figure 7a). However, no significant change was observed at 333 nm which indicated that stilbene core was not interacting

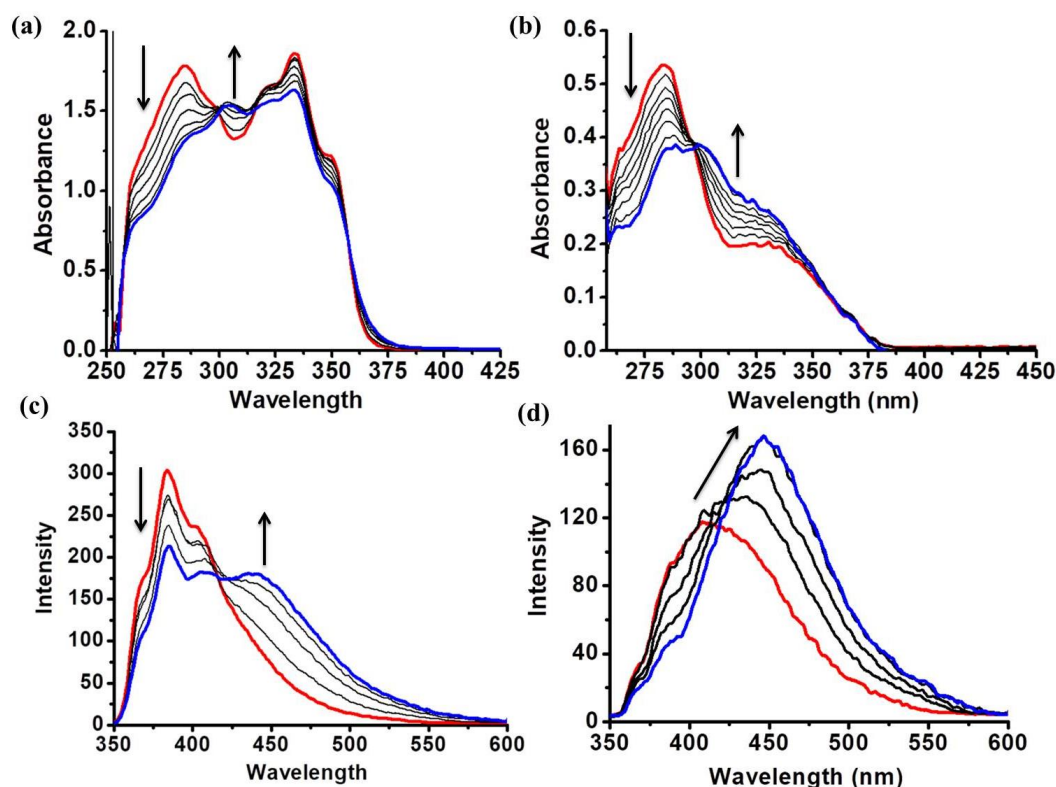


Figure 7. (a) Change in absorption spectrum of **L1** after gradual addition of Zn^{II} ions to the solution of **L1** (10^{-5} M, in DMSO), (b) Change in absorption spectrum of **L2** after gradual addition of Zn^{II} ions to the solution of **L2** (10^{-5} M, in DMSO), (c) Change in emission spectrum of **L1** ($\lambda_{ex} = 285$ nm) during titration with Zn^{II} ions, (d) Change in emission spectrum of **L1** ($\lambda_{ex} = 330$ nm) during titration with Zn^{II} ions.

with metal ions. Similar changes were observed when the solution of **L2** (10^{-5} M in DMSO) was titrated with Zn^{II} (10^{-4} M in DMSO) solution (Figure 7b). Upon gradual addition of Zn^{II} to the solution of **L2**, the absorption maxima at 283 nm displayed hypochromic shift and a broad shoulder appeared around 310 nm, indicating complexation of Zn^{II} to the terpyridine group of **L2**. The change in emission spectrum was also monitored while titrating the solution of **L1** with Zn^{II} . The emission spectrum of the solution showed decrease in intensity of 385 nm ($\lambda_{\text{ex}} = 285$ nm) (Figure 7c). Surprisingly a new peak appeared at around 440 nm and the intensity of this peak increased with incremental addition of Zn^{II} ions. Such bathochromic shift became more prominent when the titrating solution was excited at 330 nm (Figure 7d). Such change in emission spectra of **L1** probably occurred because Zn^{II} coordination induced the formation of excimer.

5.3.4 Characterization of OG1 organogel

Next, we checked the gelation propensity of **L1** and **L2** in different solvents and mixture of solvents. Gelation of **L1** was achieved in CHCl_3/THF solvent mixture. Heating the solution of **L1** (2.1×10^{-3} M) in CHCl_3/THF (2:1), followed by cooling at room temperature resulted in an opaque gel (**OG1**) (Figure 8a). The formation of gel was confirmed by inversion test method. Insight into the morphology of **OG1** was obtained by recording the FESEM and TEM images. FESEM showed the presence of nanofibers which were entangled to each other and formed the typical fibrous morphology of **OG1** (Figure 8b and 8c). Nanofibers were several micrometers long with diameters in 70- 80 nm range. The Scheme 2a explained the probable mechanism of self-assembly of **L1**. In the binary solvent mixture, the self-assembly of **L1** was driven by H-bonding between

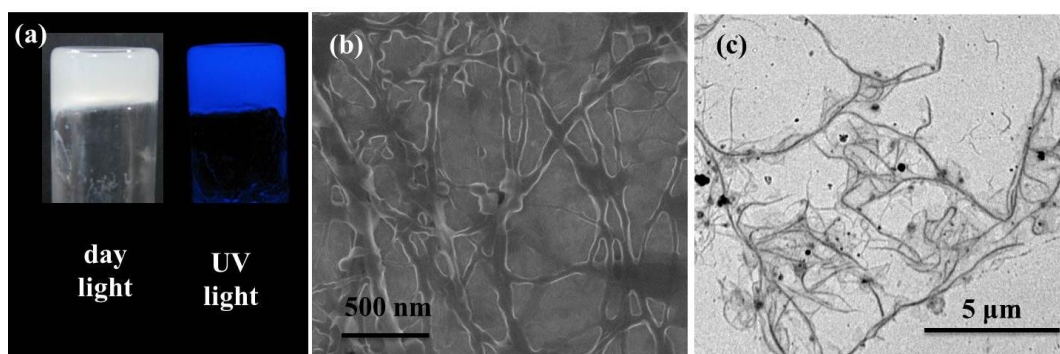
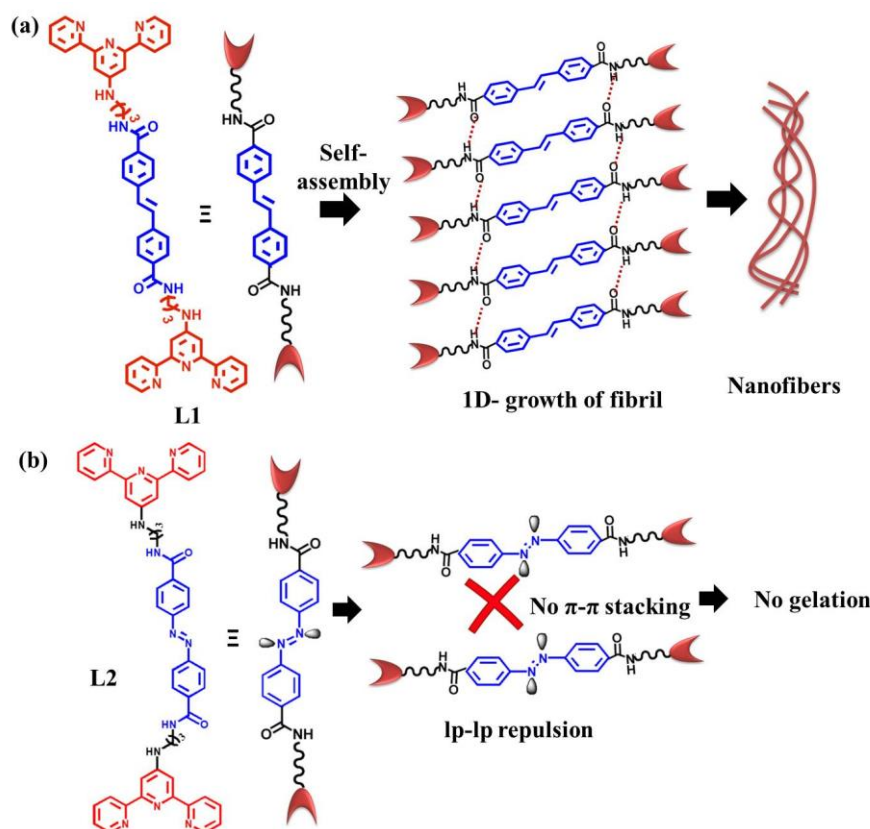


Figure 8. (a) Picture of **OG1** gel under day light and UV light, (b) FESEM and (c) TEM images of **OG1** xerogel showing nanofiber morphology.



Scheme 2. (a) Schematic showing self-assembly of **L1** through H-bonding and π - π stacking interactions, (b) **L2** does not undergo self-assembly due to lone pair-lone pair repulsion.

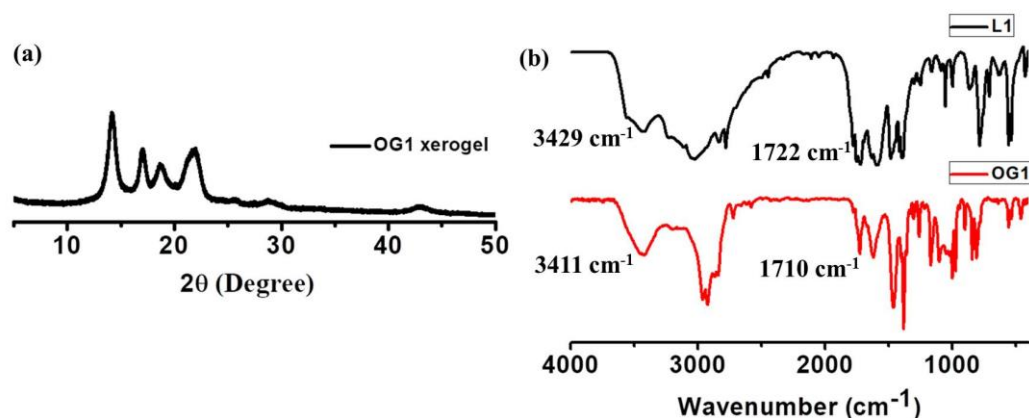


Figure 9. (a) PXRD pattern of **OG1** xerogel, (b) Comparison of FTIR of **L1** and **OG1** xerogel.

amide groups and π - π stacking between the stilbene cores of adjacent **L1** molecules. Such self-assembly process resulted in fibriles which aggregated and formed fibers as shown in figure 8d. The presence of H-bonding and π - π stacking in **OG1** were supported by PXRD and FTIR analysis (Figure 9). PXRD of the xerogel showed broad peak at $2\theta = 21.8^\circ$,

corresponding to the d -spacing value of 4.0 Å which supported the presence of π - π stacking in **OG1** gel (Figure 9a). Comparison of the FTIR spectra of **L1** and **OG1** xerogel exhibited a decrease in C=O and N-H stretching frequency from 1722 cm^{-1} to 1710 cm^{-1} and 3429 to 3411 cm^{-1} , indicating the presence of intermolecular H-bonding in this assembly (Figure 9b). However, **L2** did not form gel in any solvents, probably because the lone pair-lone pair repulsion between the azo groups inhibited the π - π stacking interaction of **L2** (Scheme 2b). The UV-Vis spectrum of **OG1** xerogel showed broad absorption with maxima at around 333 nm (Figure 10a). Upon exciting at 333 nm, the **OG1** xerogel showed blue emission with maxima at 430 nm which was red shifted compared to the monomer **L2** (Figure 10b). Such red shifted emission in **OG1** could be attributed to the excimer emission. The PXRD analysis suggested that the nanofibers of **OG1** gel were formed by the π - π stacking interaction between the stilbene cores of **L1** and the distance between two π -stacked stilbene cores was 4.0 Å. Therefore, **OG1** followed Schmidt's photochemical [2+2] cyclo-addition criteria which stated that the distance between two olefinic bonds should be below 4.2 Å. This motivated us to irradiate

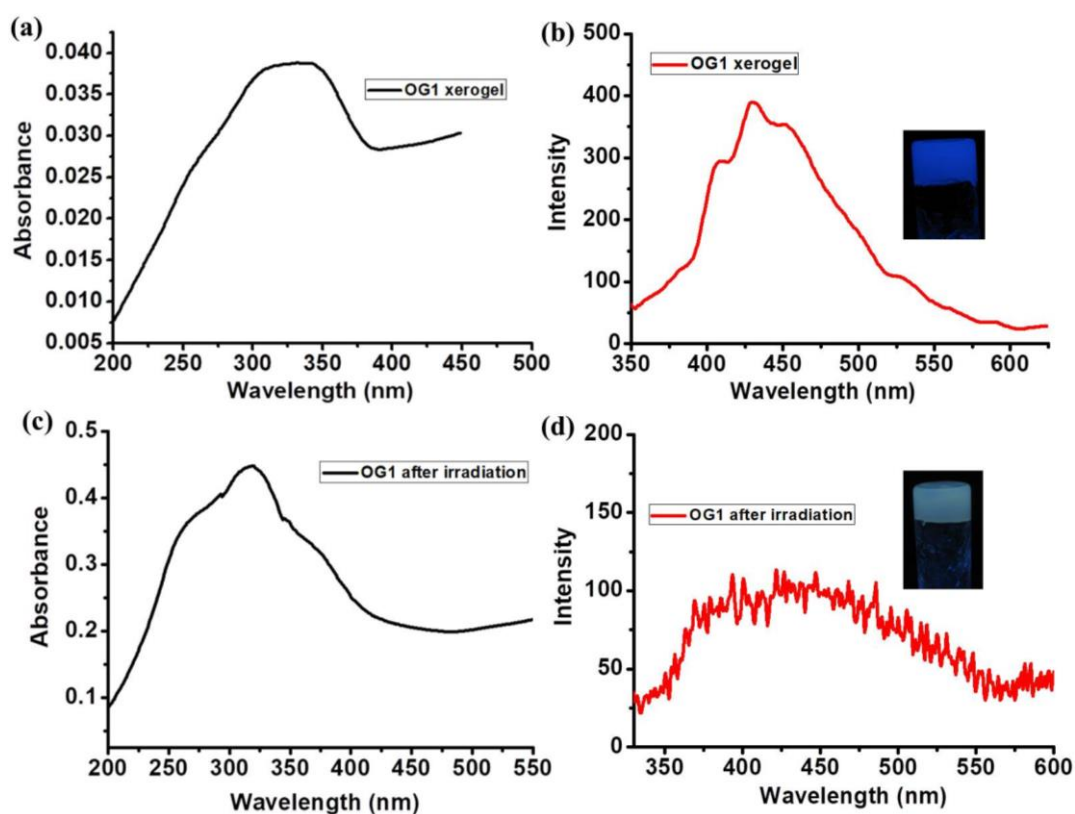


Figure 10. (a) Absorption spectrum of **OG1** xerogel, (b) Emission spectrum of **OG1** xerogel ($\lambda_{\text{ex}} = 333$ nm), (c) Absorption spectrum of **OG1** xerogel after irradiating with UV light for an hour, (d) Emission spectrum of **OG1** xerogel after irradiating with UV light ($\lambda_{\text{ex}} = 333$ nm).

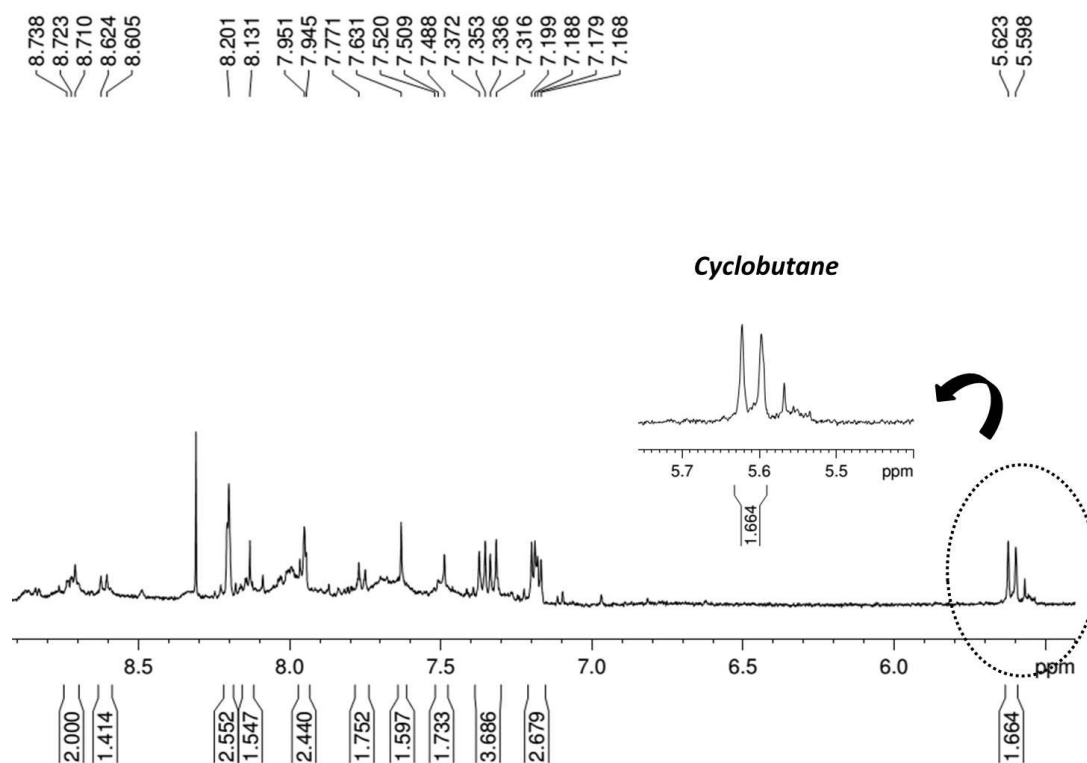


Figure 11. ^1H NMR spectrum of **OG1_{hv}** gel showing the presence of cyclobutane protons at $\delta = 5.62$ ppm.

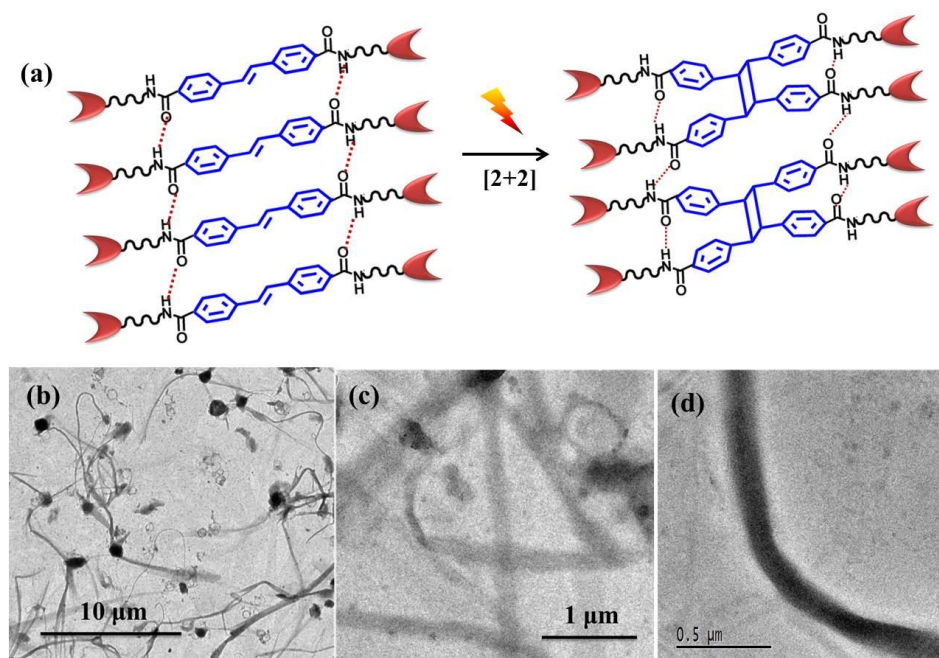


Figure 12. (a) Schematic showing photochemical [2+2] cyclo-addition of stilbene core of **L2** leads to the formation of tetraphenylcyclobutane, (b), (c) and (d) TEM images of **OG1_{hv}** xerogel showing the formation of nanotapes.

the **OG1** xerogel with UV-light which could drive photo-cyclization of stilbene cores of **L1**. Such photo-cyclization could modulate the nanostructure and properties of the **OG1** gel. While irradiating the **OG1** gel with 365 nm UV-light (22.5 W) the blue emission of **OG1** quenched slowly and after an hour the organogel (**OG1_hv**) became considerably less-emissive, as observed under UV light (Figure 10d, inset). The absorption spectrum of **OG1_hv** xerogel showed hypsochromic shift (Figure 10c). Moreover, when **OG1_hv** xerogel was excited at 333 nm, low emission was observed (Figure 10d). This indicated that the π -stacked stilbene cores of **OG1** probably underwent [2+2] cyclo-addition and formed the tetraphenylcyclobutane which is non-emissive due to the loss of conjugation. To further support the formation of cyclobutane ring, $^1\text{H-NMR}$ spectrum of the **OG1** xerogel was recorded. $^1\text{H-NMR}$ spectrum showed the peak at $\delta = 5.62$ ppm, corresponding to the protons of cyclobutane ring (Figure 11). These results confirmed the formation of the tetraphenylcyclobutane core in **OG1_hv** through the [2+2] cyclo-addition of stilbene cores. The figure 12a showed how the π -stacked stilbene cores underwent [2+2] cyclo-addition and formed tetraphenylcyclobutane derivative. The percentage of conversion was calculated to be 40%. However, cyclo-addition was not observed when solution of **L1** was irradiated with UV-light. Interestingly, the TEM images of **OG1_hv** showed the presence of nanotapes which were several micrometers long with the diameters in the 170-180 nm range (Figure 12b-d). Such nanofiber to nanotape morphology transformation probably occurred due to [2+2] cyclo-addition of stilbene cores of **L1**. No significant change was observed in PXRD pattern of **OG1_hv** (Figure 13).

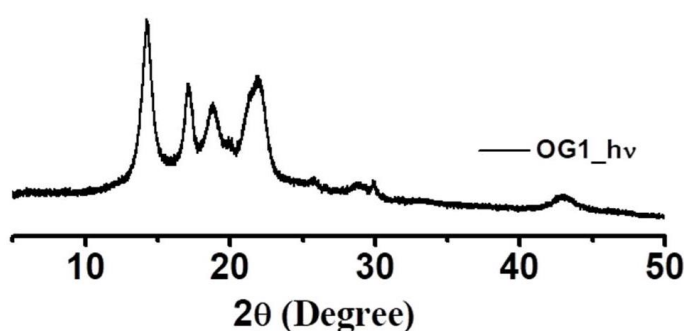


Figure 13. PXRD pattern of the **OG1_hv** xerogel.

5.3.5 Characterization of **ZnL1** coordination polymer gel

Next, the gelation propensity of **L1** in presence of Zn^{II} ions was checked. Heating the solution of **L1** and $\text{Zn}(\text{NO}_3)_2 \cdot 6\text{H}_2\text{O}$ in the aforementioned CHCl_3/THF (1:1) solvent mixture followed by cooling resulted in stable coordination polymer gels (**ZnL1**) (Figure

14a). The formation of gel was confirmed by inversion test method. Insight into the morphology of **ZnL1** xerogel was obtained by recording FESEM and TEM images. The FESEM and TEM images revealed the formation of nanofibers which were several micrometer long and the diameter in 100-110 nm range (Figure 14b-d). However, the nanofibers of **ZnL1** xerogel had greater diameter than the **OG1** nanofibers. The formation of such higher dimensional nanofibers in **ZnL1** xerogel could be explained by coordination driven self-assembly of **L1**. Initially, **L1** self-assembled in CHCl_3/THF solvent mixture by complementary H-bonding between amide groups and π - π stacking between stilbene core of neighbouring **L1** and form the primary 1D self-assembled structures with pendent terpyridine groups on the outer surface. These pendent terpyridine groups coordinated with Zn^{II} ions and formed the higher dimensional nanostructures. The presence of Zn^{II} in **ZnL1** xerogel was confirmed by EDXS analysis. The PXRD of **ZnL1** xerogel showed similar pattern as **OG1** xerogel which indicated that the primary self-assembled π - π stacked structure was retained in **ZnL1** (Figure 14e). However, **ZnL1** showed additional low angle peaks at $2\theta = 4.3^\circ$ (d -spacing = 20.4 Å), indicating the formation of higher order assembly in **ZnL1** upon metal coordination with terpyridine.

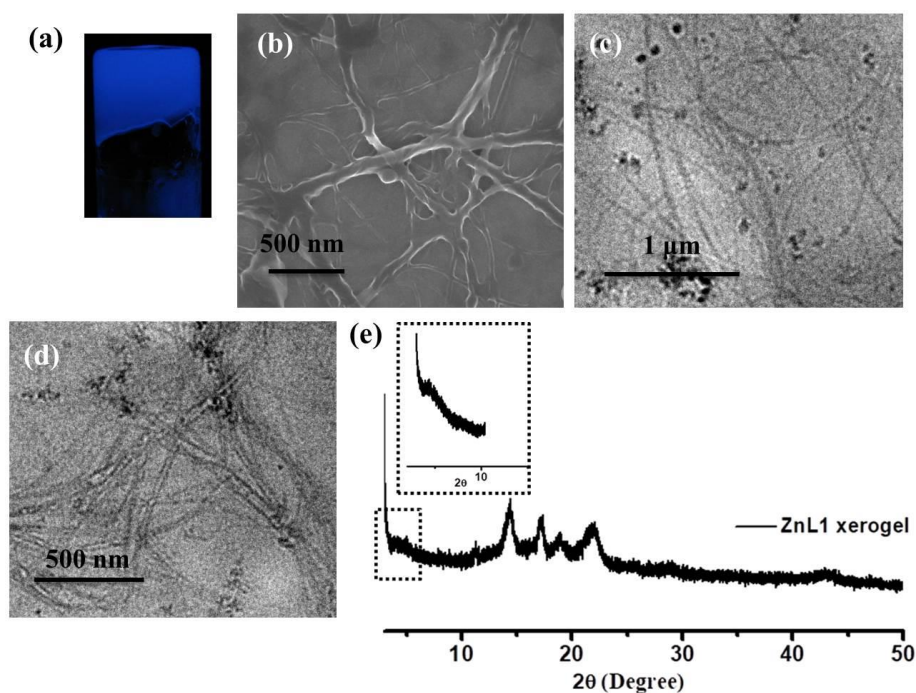


Figure 14. (a) Picture of **ZnL1** coordination polymer gel under UV light, (b) FESEM image of the **ZnL1** xerogel, (b) and (c) TEM images of **ZnL1** xerogel showing the formation of nanofibers, (e) PXRD pattern of **ZnL1** xerogel, inset highlight the low angle peak.

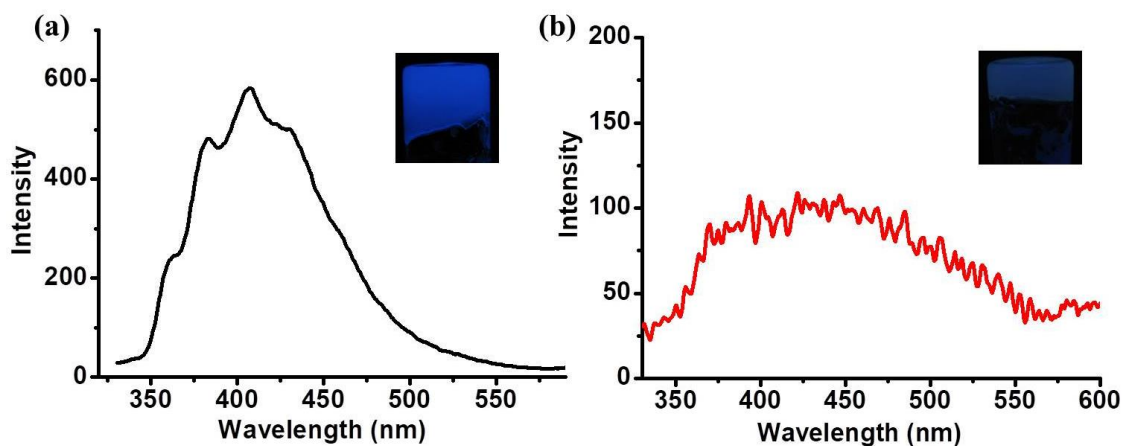


Figure 15. (a) Emission spectrum of **ZnL1** xerogel, (b) Emission spectrum of the **ZnL1_{hv}** xerogel. Inset showing the picture of **ZnL1** and **ZnL1_{hv}** under UV-light.

The absorption spectrum of **ZnL1** xerogel showed maxima at 335 nm. Upon exciting at 333 nm the emission spectrum of **ZnL1** xerogel exhibited blue emission with maxima at 420 nm (Figure 15a). Later, we studied how irradiation of UV-light affected the nano-morphology and properties of the **ZnL1** coordination polymer gel. When the **ZnL1** gel was irradiated with 365 nm UV-light, the blue emission was quenched slowly and after one hour of irradiation the CPG (**ZnL1_{hv}**) became considerably less-emissive, as observed under UV light (Figure 15b, inset). The emission spectrum of **ZnL1_{hv}** xerogel ($\lambda_{\text{ex}} = 333$ nm) did not show any peak, indicating non-emissive nature of **ZnL1_{hv}** (Figure 15b). This indicated that the π -stacked stilbene cores of **ZnL1** underwent [2+2] cyclo-addition and resulted in the non-emissive tetraphenylcyclobutane. The TEM images of **ZnL1_{hv}** xerogel also showed the formation of nanotapes with diameter in 220-240 nm range (Figure 16). Such nanofiber to nanotape morphology transformation probably occurs due to [2+2] cyclo-addition of stilbene cores in **ZnL1**. The PXRD of **ZnL1_{hv}** did not show significant change (Figure 17).

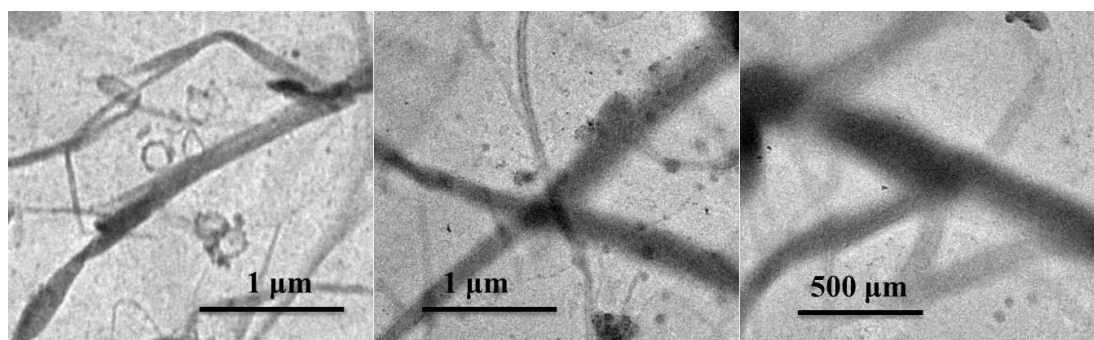


Figure 16. TEM images of **ZnL1_{hv}** xerogel showing the formation of nanotape.

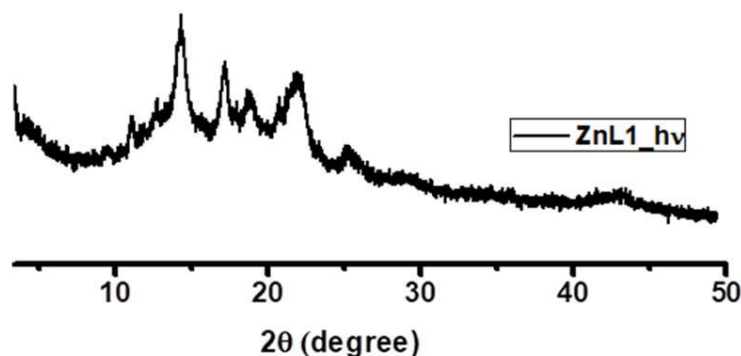


Figure 17. PXRD pattern of **ZnL1_hv** xerogel.

5.4 SUMMARY

In Summary we have synthesized two LMWG, one having stilbene core (**L1**) and another having azobenzene core (**L2**) which is connected to terpyridine moiety through flexible alkylamide chains. Self-assembly of **L1** in organic solvent is driven through the H-bonding and π - π stacking interaction and results in nanofiber morphology in **OG1** gel. However, **L2** falls to show gelation in any solvent probably because the lone pair-lone pair repulsion between two adjacent azobenzene core inhibits the self-assembly of **L2** through π - π stacking. The π -stacked stilbene cores in **OG1** provide the right environment for [2+2] cyclo-addition to occur. Hence, on irradiating the **OG1** gel with UV-light the blue emissive gel become less-emissive due to the formation of tetraphenylcyclobutane ring which is proven by studying $^1\text{H-NMR}$. Moreover, the cyclo-addition leads to the morphology transformation from nanofiber to nanotapes. Coordination driven self-assembly of **L1** in presence of Zn^{II} results in **ZnL1** CPG which also undergoes [2+2] cycloaddition upon irradiation with UV-light.

5.5 REFERENCES

- (a) J. W. Steed, *Chem. Soc. Rev.*, 2010, **39**, 3686–3699; (b) N. M. Sangeetha and U. Maitra, *Chem. Soc. Rev.*, 2005, **34**, 821–836; (c) M. D. Segarra- Maset, V. J. Nebot, J. F. Miravet and B. Escuder, *Chem. Soc. Rev.*, 2013, **42**, 7086–7098; (d) M.-O. M. Piepenbrock, N. Clarke, J. A. Foster and J. W. Steed, *Chem. Commun.*, 2011, **47**, 2095–2097; (e) C. Tomasini and N. Castellucci, *Chem. Soc. Rev.*, 2013, **42**, 156–172.
- (a) D. Diaz Diaz, D. Kuhbeck and R. J. Koopmans, *Chem. Soc. Rev.*, 2011, **40**, 427–448; (b) T. Vermonden, R. Censi and W. E. Hennink, *Chem. Rev.*, 2012, **112**, 2853–2888; (c) S. Zhang, M. A. Greenfield, A. Mata, L. C. Palmer, R. Bitton, J. R. Mantei, C.

Aparicio, M. O. de la Cruz and S. I. Stupp, *Nat. Mater.*, 2010, **9**, 594–601; (d) L. E. Buerkle and S. J. Rowan, *Chem. Soc. Rev.*, 2012, **41**, 6089–6102; (e) R. Parveen, P. Dastidar, *Chem. Eur. J.*, 2016, **22**, 9257.

3. (a) J. H. Jung, J. H. Lee, J. R. Silverman and G. John, *Chem. Soc. Rev.*, 2013, **42**, 924–936; (b) M.-O. M. Piepenbrock, G. O. Lloyd, N. Clarke and J. W. Steed, *Chem. Rev.*, 2009, **110**, 1960–2004; (c) A. Y.-Y. Tam and V. W.-W. Yam, *Chem. Soc. Rev.*, 2013, **42**, 1540–1567; (d) X. Yan, T. R. Cook, J. B. Pollock, P. Wei, Y. Zhang, Y. Yu, F. Huang and P. J. Stang, *J. Am. Chem. Soc.*, 2014, **136**, 4460–4463; (e) G. M. Peters, L. P. Skala, T. N. Plank, B. J. Hyman, G. N. Manjunatha Reddy, A. Marsh, S. P. Brown and J. T. Davis, *J. Am. Chem. Soc.*, 2014, **136**, 12596–12599; (f) P. Sutar and T. K. Maji, *Chem. Commun.*, 2016, **52**, 8055–8074.

4. (a) T. Tu, W. Fang, X. Bao, X. Li and K. H. Dötz, *Angew. Chem., Int. Ed.*, 2011, **50**, 6601–6605; (b) C. Po, Z. Ke, A. Y.-Y. Tam, H.-F. Chow and V. W.-W. Yam, *Chem. – Eur. J.*, 2013, **19**, 15735–15744; (c) S. Sarkar, S. Dutta, S. Chakrabarti, P. Bairi and T. Pal, *ACS Appl. Mater. Interfaces*, 2014, **6**, 6308–6316; (d) M. Maity and U. Maitra, *J. Mater. Chem. A*, 2014, **2**, 18952–18958; (e) W. Fang, C. Liu, Z. Lu, Z. Sun and T. Tu, *Chem. Commun.*, 2014, **50**, 10118–10121; (f) S. Bhattacharjee and S. Bhattacharya, *Chem. Commun.*, 2014, **50**, 11690–11693; (g) I. U. Arachchige and S. L. Brock, *J. Am. Chem. Soc.*, 2007, **129**, 1840–1841; (h) W. J. Peveler, J. C. Bear, P. Southern and I. P. Parkin, *Chem. Commun.*, 2014, **50**, 14418–14420; (i) Z. Xie, F. Wang and C.-y. Liu, *Adv. Mater.*, 2012, **24**, 1716–1721.

5. (a) J. H. Jung, Y. Ono, S. Shinkai, *Angew. Chem., Int. Ed.*, 2000, **39**, 1862–1865; (b) V. M. Suresh, A. De, T. K. Maji, *Chem. Commun.*, 2015, **51**, 14678–14681; (c) P. Sutar, T. K. Maji, *Inorg. Chem.*, 2017, **56**, 9417–9425.

6. (a) P. Sutar, V. M. Suresh, T. K. Maji, *Chem. Commun.*, 2015, **51**, 9876–9879; (b) H. B. Aiyappa, S. Saha, P. Wadge, R. Banerjee, S. Kurungot, *Chem. Sci.*, 2015, **6**, 603–607; (c) P. Chen, Q. Li, S. Grindy, N. Holten-Andersen, *J. Am. Chem. Soc.*, 2015, **137**, 11590–11593; (d) M. Martinez-Calvo, O. Kotova, M. E. Mobius, A. P. Bell, T. McCabe, J. J. Boland, T. Gunnlaugsson, *J. Am. Chem. Soc.*, 2015, **137**, 1983–1992; (e) H. Lee, S. H. Jung, W. S. Han, J. H. Moon, S. Kang, J. Y. Lee, J. H. Jung and S. Shinkai, *Chem. – Eur. J.*, 2011, **17**, 2823; (d) S. Barman, J. Anand Garg, O. Blacque, K. Venkatesan, H. Berke, *Chem. Commun.*, 2012, **48**, 11127–11129; (e) B. Xing, M.-F. Choi, B. Xu, *Chem. – Eur. J.* 2002, **8**, 5028–5032; (f) Y.-X. Ye, W.-L. Liu, B.-H. Ye, *Catal. Commun.* 2017, **89**, 100–105; (g) J. H. Lee, S. Kang, J. Y. Lee, J. H. Jung, *Soft Matter.*, 2012, **8**,

6557–6563; (h) T. Feldner, M. Häring, S. Saha, J. Esquena, R. Banerjee, D. D. Díaz, *Chem. Mater.* 2016, **28**, 3210–3217; (i) S. Sarkar, S. Dutta, P. Bairi, T. Pal, *Langmuir.*, 2014, **30**, 7833–7841; (j) M. R. Lohe, M. Rose, S. Kaskel, *Chem. Commun.*, 2009, 6056–6058.

7. (a) A. J. R. Amaral and G. Pasparakis, *Polym. Chem.*, 2017, **8**, 6464–6484; (b) S. Ahn, R. M. Kasi, S. –C. Kim, N. Sharma and Y. Zhou, *Soft Matter*, 2008, **4**, 1151–1157; (c) S. Ganta, H. Devalapally, A. Shahiwala and M. Amiji, *J. Control. Release.*, 2008, **126**, 187–204; (d) M. A. C. Stuart, W. T. S. Huck, J. Genzer, M. Müller, C. Ober, M. Stamm, G. B. Sukhorukov, I. Szleifer, V. V. Tsukruk, M. Urban, F. Winnik, S. Zauscher, I. Luzinov and S. Minko, *Nat. Mater.*, 2010, **9**, 101; (e) A. V. Goponenko and Y. A. Dzenis, *Polymer*, 2016, **101**, 415–449.

8. (a) S. Zhang, A. M. Bellinger, D. L. Gletting, R. Barman, Y.-A. L. Lee, J. Zhu, C. Cleveland, V. A. Montgomery, L. Gu, L. D. Nash, D. J. Maitland, R. Langer and G. Traverso, *Nat. Materials.*, 2015, **14**, 1065–1071; (b) P. Gupta, K. Vermani and S. Garg, *Drug Discov Today.*, 2002, **7**, 569–579; (c) A. A. Martens, G. Portale, M. W. T. Werten, R. J. de Vries, G. Eggink, M. A. Cohen Stuart and F. A. de Wolf, *Macromolecules.*, 2009, **42**, 1002–1009; (d) W. Ha, J. Yu, X.-y. Song, J. Chen and Y.-p. Shi, *ACS Appl. Mater. Interfaces.*, 2014, **6**, 10623–10630; (e) J. Wang, L. Wang and X. Shi, *Soft Matter.*, 2018, DOI: 10.1039/C8SM00220G; (f) C. Wang, D. Q. Zhang and D. B. Zhu, *J. Am. Chem. Soc.*, 2005, **127**, 16372–16373; (g) C. Wang, F. Sun, D. Q. Zhang, G. X. Zhang and D. B. Zhu, *Chin. J. Chem.*, 2010, **28**, 622–626; (h) J. O. Jeppesen, J. Perkins, J. Becher and J. F. Stoddart, *Angew. Chem., Int. Ed.*, 2001, **40**, 1216; (i) V. Balzani, A. Credi, G. Mattersteig, O. A. Matthews, F. M. Raymo, J. F. Stoddart, M. Venturi, A. J. P. White and D. J. Williams, *J. Org. Chem.*, 2000, **65**, 1924–1936; (j) R. E. Gillard, F. M. Raymo and J. F. Stoddart, *Chem.–Eur. J.*, 1997, **3**, 1933–1940; (k) A. K. Chaudhari and J.-C. Tan, *Chem. Commun.*, 2017, **53**, 8502–8505; (l) A. Dawn, T. Shiraki, H. Ichikawa, A. Takada, Y. Takahashi, Y. Tsuchiya, L. T. N. Lien and S. Shinkai, *J. Am. Chem. Soc.*, 2012, **134**, 2161–2171; (m) M. L. Ma, Y. Kuang, Y. Gao, Y. Zhang, P. Gao and B. Xu, *J. Am. Chem. Soc.*, 2010, **132**, 2719–2728; (n) Y. Gao, Y. Kuang, Z. F. Guo, Z. H. Guo, I. J. Krauss and B. Xu, *J. Am. Chem. Soc.*, 2009, **131**, 13576; (o) Z. M. Yang, K. M. Xu, Z. F. Guo, Z. H. Guo and B. Xu, *Adv. Mater.*, 2007, **19**, 3152.

9. (a) X. Yang, G. Zhang and D. Zhang, *J. Mater. Chem.*, 2012, **22**, 38–50.

10. (a) K. Murata, M. Aoki, T. Suzuki, T. Harada, H. Kawabata, T. Komori, F. Ohseto, K. Ueda and S. Shinkai, *J. Am. Chem. Soc.*, 1994, **116**, 6664–6676; (b) N. Koumura, M.

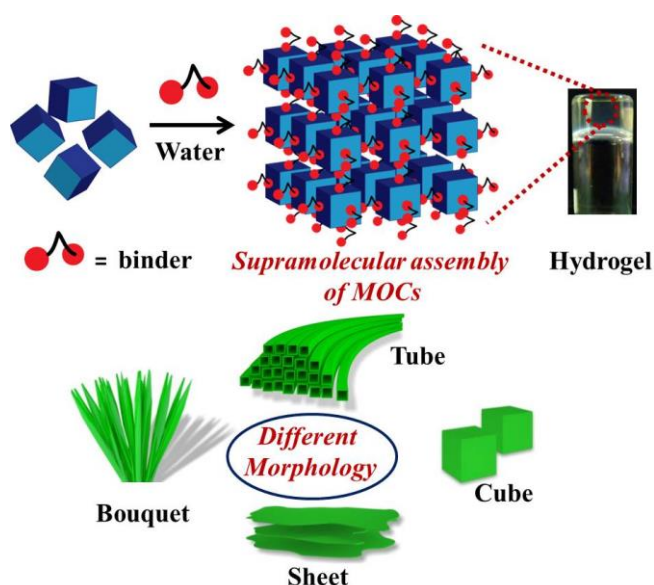
- Kudo and N. Tamaoki, *Langmuir*, 2004, **20**, 9897–9900; (c) S. Yagai, T. Iwashima, K. Kishikawa, S. Nakahara, T. Karatsu and A. Kitamura, *Chem.–Eur. J.*, 2006, **12**, 3984–3994; (d) S. Yagai, T. Nakajima, K. Kishikawa, S. Kohmoto, T. Karatsu and A. Kitamura, *J. Am. Chem. Soc.*, 2005, **127**, 11134–11139; (e) R. D. Mukhopadhyay, V. K. Praveen, A. Hazra, T. K. Maji and A. Ajayaghosh, *Chem. Sci.*, 2015, **6**, 6583–6591.
11. (a) S. Horike, S. Shimomura, S. Kitagawa, *Nat. Chem.*, 2009, **1**, 695; (b) X. Lin, I. Telepeni, A. J. Blake, A. Dailly, C. M. Brown, J. M. Simmons, M. Zoppi, G. S. Walker, K. M. Thomas, T. J. Mays, P. Hubberstey, N. R. Champness, M. Schröder, *J. Am. Chem. Soc.*, 2009, **131**, 2159; (c) S. Xiang, W. Zhou, Z. Zhang, M. A. Green, Y. Liu, B. Chen, *Angew. Chem. Int. Ed.*, 2010, **49**, 4615; (d) Z. Zhang, Z. Yao, S. Xiang, B. Chen, *Energy Environ. Sci.*, 2014, **7**, 2868; (e) C. Song, Y. He, B. Li, Y. Ling, H. Wang, Y. Feng, R. Krishna, B. Chen, *Chem. Commun.*, 2014, **50**, 12105; (f) A. Hazra, S. Bonakala, K. K. Bejagam, S. Balasubramanian and T. K. Maji, *Chem. Eur. J.* 2016, **22**, 7792–7799.
12. H. M. D. Bandara and S. C. Burdette, *Chem. Soc. Rev.*, 2012, **41**, 1809–1825.
13. (a) G. Ciamician, P. Silber, *Chem. Ber.* 1902, **35**, 4128; (b) R. Störmer, *Ber. Dtsch. Chem. Ges.*, 1909, **42**, 4865; (c) A. Smakula, *Z. Phys. Chem. Abt. B.*, 1934, **25**, 90; (d) M. D. Cohen, G. M. J. Schmidt and F. I. Sonntag, *J. Chem. Soc.*, 1964, 2000; (e) D. Liu, Z.-G. Ren, H.-X. Li, J.-P. Lang, N.-Y. Li and B. F. Abrahams, *Angew. Chem. Int. Ed.*, 2010, **49**, 4767; *Angew. Chem.* 2010, **122**, 4877.
14. (a) R. Balamurugan, W. K.-Ming, C.-C. Chien and J. H. Liu, *Soft Matter*, 2014, **10**, 8963–8970; (b) C. Wang, Q. Chen, F. Sun, D. Zhang, G. Zhang, Y. Huang, R. Zhao, and D. Zhu, *J. Am. Chem. Soc.*, 2010, **132**, 3092–3096; (c) S. Miljanić, L. Frkanec, Z. Meić, and M. Žinić, *Eur. J. Org. Chem.*, 2006, 1323–1334.
15. P. Sutar, V. M. Suresh and T. K. Maji, *Chem. Commun.*, 2015, **51**, 9876–9879.

Chapter 6A

Binder Driven Self-assembly of Metal-Organic Cubes towards Functional Hydrogels

Abstract

The process of assembling astutely designed well defined metal-organic cube (MOC) into hydrogel by using a suitable molecular binder is a promising method for preparing processable functional soft materials. This chapter reports the synthesis of a water soluble anionic MOC $\{[\text{Ga}_8(\text{ImDC})_{12}]^{12-}\}$ and its self-assembly to hydrogels in presence of different molecular binders. The charge-assisted H-bonding interactions between the anionic MOCs and cationic molecular binders such as, ammonium ion (NH_4^+), N-(2-aminoethyl)-1,3-propanediamine, guanidine hydrochloride, and β -alanine, drive the self-assembly to hydrogels. Depending upon the structure and geometry of the molecular binders, the hydrogels show different morphologies. The hydrogel prepared with ammonium cations exhibits nanotubular morphology with negatively charged surface and is explored for gel-chromatographic separation of cationic species from anionic counterparts. The hydrogels also show pH-responsive behaviour.



Paper based on this work:

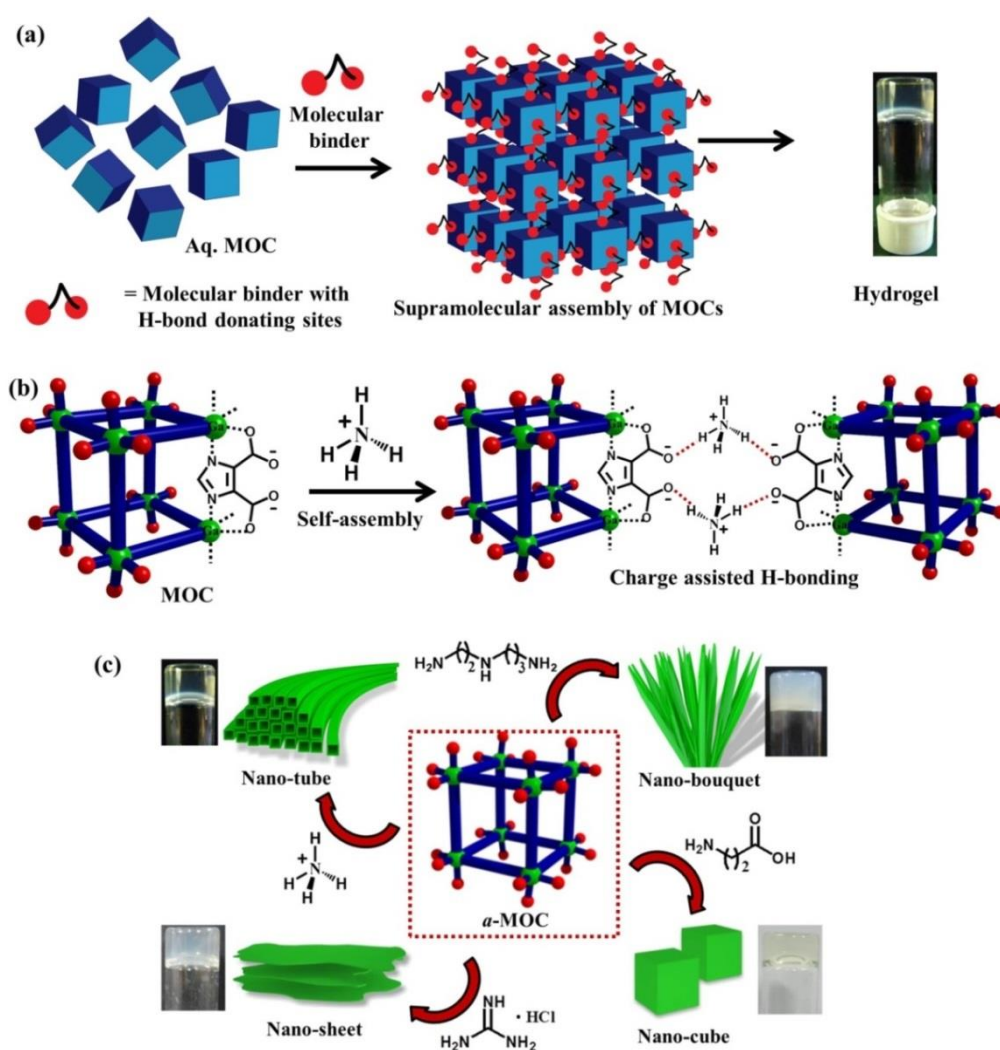
P. Sutar, V. M Suresh, K. Jayaramulu, A. Hazra and T. K. Maji, *manuscript under revision*.

6A.1 INTRODUCTION

Charge-assisted hydrogen bond (CAHB) is a type of non-covalent interaction ($X-H^{(+)}\cdots Y^{(-)}$) that plays an important role in the structure-property correlation of bio-macromolecules and in various biological molecular recognition processes.¹ CAHB is also widely employed in the construction of discrete organic cages, extended crystalline metal-organic architectures² and soft supramolecular gels.³ The reason behind such versatility of CAHB is essentially its intrinsic strength (stronger than neutral $X-H\cdots Y$ bond) and directionality, that result in wide range of materials with an array of exciting and complementary properties.⁴ In this regard, CAHB driven self-assembly of pre-designed metal-organic polyhedrals (MOPs)⁵ which are discrete metal-organic cages with confined cavities and large number of connecting sites, into soft supramolecular hydrogel is unprecedented.

Among different classes of MOPs, metal organic cubes (MOCs) with a general formula $[M_8L_{12}]^x$ ($x=0, n^-$), comprising metal ions ($M^n = Ni^{II}, Zn^{II}, In^{III}, Cr^{III}$) as vertices and imidazoledicarboxylate (L) as edges of a cube have been well explored.⁶ Aesthetic appeal, structural modularity and robustness pertaining to the MOCs showed great promise for diverse applications.⁷ MOCs are neutral ($x=0$) or anionic ($x=n^-$, **a-MOC**) depending upon the charge balance between M^n and L.⁸ MOCs are exploited as molecular building blocks by connecting the peripheral free carboxylate oxygens with metal ions or with H-bond donor molecules and the resulting extended structures showed potential applications in gas storage/ separation and proton-conductivity.⁹ Since exteriors of **a-MOCs** are decorated with free polar carboxylate groups, they could be soluble in polar solvents, like water.¹⁰ We envisioned that interaction of soluble **a-MOCs** with the positively charged or neutral, H-bond donor molecular binders through CAHB interaction could result in extended, supramolecular network.¹¹ In aqueous solution, such supramolecular assembly between **a-MOC** and different molecular binders could result in hydrogels. Aida *et al.* have shown that CAHB interaction between anionic clay nanosheets and dendritic molecular binders containing multiple guanidinium ions facilitated the cross-linking of the clay nanosheets and formed hydrogels.¹² Recently, Johnson *et al.* and Nitschke *et al.* have reported metal-organic cage based hydrogels.¹³ However, in their method, soluble polymers with appropriate functional groups were reacted with metal ions to yield gels that consist of cages linked together by polymers.

Although their approach is inspiring, use of a water soluble *a*-MOC as a platform to study self-assembly in the presence of different molecular binders is yet to be accounted.



Scheme 1: (a) Schematic showing interaction of **MOC** with small molecular binders results in hydrogel, (b) Schematic showing charge assisted H-bonding between **MOC** and NH_4^+ induces the self-assembly of **MOCs**, (c) Self-assembly of **MOC** with different molecular binders resulting in hydrogels with different morphologies.

It was envisioned that introduction of different molecular binders would tune the properties and nano-morphologies of the resulting MOC-hydrogels. For example, the surface charge of the hydrogel-nanostructure could be altered by choosing appropriate cationic/anionic binders, making the hydrogel useful for gel-chromatographic separation of oppositely charged species. Moreover, suitably designed chromophoric molecular binder would result in a processable soft luminescent hybrid hydrogel.

This chapter reports the synthesis of a new MOC-based supramolecular framework, $\{(\text{Me}_2\text{NH}_2)_{12}[\text{Ga}_8(\text{ImDC})_{12}] \cdot \text{DMF} \cdot 29\text{H}_2\text{O}\}$ (**1**), which was formed by the CAHB interaction between the anionic $[\text{Ga}_8(\text{ImDC})_{12}]^{12-}$ (**MOC**) and Me_2NH_2^+ (DMA) cations. Compound **1** was highly soluble in water. In aqueous solution though the extended networks broke, the discrete **MOCs** remained intact. This particular phenomenon was exploited to crosslink the dissolved **MOCs** with a wide range of molecular binders that led to the formation of charge-assisted hydrogels. Different molecular binders were assembled with **MOC** and the resulting hydrogels showed different morphologies and properties. When ammonium cation (NH_4^+) was used as molecular binder, the resulting hydrogel showed tubular nanostructures with negatively charged surface. This hydrogel was exploited for gel chromatographic separation of positively charged species.

6A.2 EXPERIMENTAL SECTION

6A.2.1 Materials

4, 5-Imidazoleedicarboxylic acid (4, 5-ImDC), $\text{Ga}(\text{NO}_3)_3 \cdot 6\text{H}_2\text{O}$, N-(2-aminoethyl)-1,3-propanediamine, β -alanine and guanidine hydrochloride were purchased from Sigma-Aldrich chemical Co. Ltd. All the dyes, sulforhodamine G, Nile blue, rhodamine B, methylene blue, acridine orange were purchased from Sigma-Aldrich chemical Co. Ltd. Ammonia solution was purchased from SDFCL. All solvents and triethylamine (NEt_3) were obtained from Spectrochem. For UV-Vis experiments, spectroscopic grade solvents were purchased from Spectrochem Pvt. Ltd. (Mumbai, India).

6A.2.2 Physical measurements

$^1\text{H-NMR}$ was recorded on a Bruker AV-400 spectrometer with chemical shifts recorded as ppm and all spectra were calibrated against TMS. UV-Vis spectra were recorded in a Perkin-Elmer Lambda 900 spectrometer. Fluorescence studies were accomplished using Perkin Elmer LS 55 Luminescence spectrometer. Fourier transform infrared (FTIR) spectral studies were carried out by making samples with KBr pellets using Bruker FTIR spectrometer. Powder X-ray diffraction (PXRD) studies were recorded on a Bruker D8 Discover instrument using $\text{Cu-K}\alpha$ radiation. Thermal stability was analysed using Mettler Toledo TGA 850 instrument under inert atmosphere in the temperature range of 25–800°C at the heating rate of 3°C per min. Morphology studies were carried out using Lica-S440I field emission scanning electron microscopy (FESEM) by placing samples on silicon wafer under vacuum with accelerating voltage of 10 kV.

Energy dispersive X-ray spectroscopy (EDXS) analysis was performed with an EDAX genesis instrument attached to the FESEM column. Transmission electron microscopy (TEM) analysis was performed using JEOL JEM-3010 with accelerating voltage of 300 kV. For this analysis the samples were dispersed in ethanol and then drop casted on a carbon coated copper grid. Rheological measurement was performed using a Physical interfacial rheology system (IRS).

6A.2.3 Adsorption measurements

Porosity measurements were carried out using QUANTACHROME QUADRASORD-SI analyser at 77 K for N₂ and 195 K for CO₂. In the sample tube the adsorbent sample (~100-150 mg) was placed and degassed at 160 °C under 1×10⁻¹ Pa vacuum for about 10 h prior to the isotherm measurement. Helium gas (99.999 % purity) was introduced in the gas chamber at a certain pressure and allowed to diffuse into the sample tube by opening the valve. The amount of gas adsorbed was calculated from the pressure difference (P_{cal} – P_e), where P_{cal} was the calculated pressure with no gas adsorbed and P_e was the observed equilibrium pressure. All operations were computer-controlled.

6A.2.4 Single-crystal X-ray diffraction

X-ray single-crystal structural data of **1** was collected on a Bruker Smart-CCD diffractometer equipped with a normal focus, 2.4 kW sealed tube X-ray source with graphite monochromated Mo–K α radiation ($\lambda = 0.71073 \text{ \AA}$) operating at 50 kV and 30 mA. The program SAINT^{14a} was used for integration of diffraction profiles and absorption correction was made with SADABS^{14b} program. All the structures were solved by SIR 92^{14c} and refined by full matrix least square method using SHELXL-97.^{14d} All the non-hydrogen atoms were refined anisotropically and the hydrogen atoms were fixed by HFIX and placed in ideal positions. All calculations were carried out using SHELXL 97, PLATON^{14e} and WinGX system, Ver 1.70.01.^{14f} All crystallographic and structure refinement data of **1** are summarized in Table 1. Selected bond lengths and angles are displayed in Tables 2.

6A.2.5 Synthesis

Synthesis of $\{(\text{Me}_2\text{NH}_2)_{12}[\text{Ga}_8(\text{ImDC})_{12}]\cdot\text{DMF}\cdot 29\text{H}_2\text{O}\}$ (1**):** 4, 5-ImDC (0.5 mmol, 78 mg), Ga(NO₃)₃·H₂O (0.5 mmol, 128 mg) and 10 ml DMF were mixed in a 20

ml Teflon container and stirred for 30 minutes at room temperature. 15 μl NEt_3 was added into the reaction mixture and stirred for additional 30 minute. After that the Teflon container was kept inside a stainless steel autoclave which was heated at 120 $^\circ\text{C}$ for 24 hours. After the reaction was over, the autoclave was slowly cooled down to room temperature. The white product formed was centrifuged and washed repeatedly by methanol and dried in air. The air dried powder was dissolved in 10 ml water and kept for recrystallization at room temperature. Within 4 days colourless, block shaped crystals were formed. The crystal structure determination reveals the molecular formula of the compound as $\{(\text{Me}_2\text{NH}_2)_{12}[\text{Ga}_8(\text{ImDC})_{12}]\cdot\text{DMF}\cdot 29\text{H}_2\text{O}\}$. Selected FTIR data (KBr, cm^{-1}): 3447 (b), 3086 (m), 2775 (m), 1676 (s), 1473 (s), 1363 (s), 1100 (s), 857 (m), 660 (m), 550 (m). Anal. Calcd for $\text{C}_{60}\text{H}_{12}\text{Ga}_8\text{N}_{24}\text{O}_{48}$: C, 30.15; H, 0.50; N, 14.07. Found: C, 30.14; H, 0.55; N, 14.76. The phase purity of the powder sample was checked by comparing PXRD of the bulk powder sample with the simulated data from single crystal.

Preparation of MOC-G1 hydrogel: 15 mg **1** was dissolved in 1 ml water. 100 μl aq. NH_3 solution was added in the solution and sonicated for few minutes. The mixture was kept at room temperature. After 8 hours the solution formed transparent hydrogel. Formation of gel was confirmed by inversion test method. The hydrogel was found to be stable over several months. The xerogel was prepared by air-drying the **MOC-G1** hydrogel. Selected FTIR data of **MOC-G1** xerogel (KBr, cm^{-1}): 3436 (b), 3120 (m), 1663 (s), 1471 (m), 1357 (s), 1102 (s), 844 (m), 658 (m), 492 (m).

Preparation of MOC-G2 hydrogel: 80 μl N-(2-aminoethyl)-1,3-propanediamine was dissolved in 5 ml water to make 0.126 M solution of N-(2-aminoethyl)-1,3-propanediamine. 20 mg **1** was dissolved in 500 μl water. 500 μl N-(2-aminoethyl)-1,3-propanediamine solution (0.126 M) was added dropwise and the mixture was sonicated for few minutes. The mixture was kept undisturbed at room temperature. The mixture became viscous after 4-5 hours and formed **MOC-G2** hydrogel after one day. The formation of hydrogel was confirm by inversion test method. The xerogel was prepared by air-drying the **MOC-G2** hydrogel. Selected FTIR data of **MOC-G2** xerogel (KBr, cm^{-1}): 3438 (b), 3110 (m), 1763 (s), 1471 (m), 1355 (s), 1102 (s), 844 (m), 658 (m), 492 (m).

Preparation of MOC-G3 hydrogel: 0.1 M solution of guanidine hydrochloride was prepared by dissolving 24 mg guanidine hydrochloride in 2.5 ml water. 20 mg **1** was dissolved in 300 μl water. 600 μl solution of guanidine hydrochloride was added into the solution of **1** and the mixture was sonicated for few minutes. The mixture was kept

undisturbed at room temperature. Transparent hydrogel was formed after 1 day. The formation of hydrogel was confirmed by inversion test method. The xerogel was prepared by air-drying the **MOC-G3** hydrogel. Selected FTIR data of **MOC-G3** xerogel (KBr, cm^{-1}): 3400 (b), 3166 (m), 2781 (m), 1666 (sh), 1473 (sh), 1357 (sh), 1232 (s), 1103 (sh), 1022 (m), 855 (m), 828 (s), 655 (s), 550 (s).

Preparation of MOC-G4 hydrogel: 0.1 M solution of β -alanine was prepared by dissolving 22 mg β -alanine in 2.5 ml water. 20 mg **1** was dissolved in 500 μl water. 500 μl solution of β -alanine was added into the solution of **1** and the mixture was sonicated for few minutes. The mixture was kept undisturbed at room temperature. Transparent hydrogel was formed after 1 day. The formation of hydrogel was confirmed by inversion test method. The xerogel was prepared by air-drying the **MOC-G4** hydrogel. Selected FTIR data of **MOC-G4** xerogel (KBr, cm^{-1}): 3436 (b), 3220 (m), 1673 (s), 1471 (m), 1367 (s), 1102 (s), 844 (m), 658 (m), 492 (m).

Table 1. Cell parameters and structure refinement parameters for **1**

Parameter	1
Empirical formula	$\text{C}_{60} \text{H}_{12} \text{Ga}_8 \text{N}_{24} \text{O}_{48}$
Formula weight	3556.46
Crystal system	trigonal
Space group	$R\bar{3}$ (No.148)
a , Å	26.96000
b , Å	26.96000
c , Å	22.676(5)
γ , deg	120
V , Å ³	14274(4)
Z	3
T, K	295
μ , mm^{-1}	1.205
D_{calcd} , g/cm^3	1.241
F (000)	5401
reflections [$I > 2\sigma(I)$]	3358
unique reflections	6281
measured reflections	109182
R_{int}	0.110
GOF on F^2	1.11
$^aR_1[I > 2\sigma(I)]$	0.0667

$R_w[I > 2\sigma(I)]$	0.2640
-----------------------	--------

$${}^a R_I = \frac{\sum ||F_o| - |F_c||}{\sum |F_o|}; {}^b R_w = \left[\frac{\sum \{w(F_o^2 - F_c^2)^2\}}{\sum \{w(F_o^2)^2\}} \right]^{1/2}$$

Table 2. Selected bond distances (Å) and bond angles (°) for **1**.

Ga1-O1	1.980(5)	Ga2-O2	1.970(5)
Ga1-O5	1.980(5)	Ga2-N2	2.023(6)
Ga1-N1	2.024(5)	Ga2-O2_a	1.969(6)
Ga1-N3	2.030(5)	Ga2-N2_a	2.023(6)
Ga1-O8_e	1.976(8)	Ga2-O2_b	1.970(5)
Ga1-N4_e	2.034(5)	Ga2-N2_b	2.023(6)
O1-Ga1-O5	89.8(2)	O2_a-Ga2-N2	168.5(2)
O1-Ga1-N1	80.4(2)	N2-Ga2-N2_a	95.0(2)
O1-Ga1-N3	169.23(19)	O2_b-Ga2-N2	96.0(3)
O1-Ga1-O8_e	89.6(2)	N2-Ga2-N2_b	95.0(3)
O1-Ga1-N4_e	95.4(2)	O2_a-Ga2-N2_a	80.8(2)
O5-Ga1-N1	96.5(2)	O2_a-Ga2-O2_b	89.0(3)
O5-Ga1-N3	81.2(2)	O2_a-Ga2-N2_b	96.0(3)
O5-Ga1-O8_e	88.9(2)	O2_b-Ga2-N2_a	168.5(3)
O5-Ga1-N4_e	168.4(2)	N2_a-Ga2-N2_b	95.0(2)
N1-Ga1-N3	94.8(2)	O2_b-Ga2-N2_b	80.8(2)
O8_e-Ga1-N1	168.6(2)	Ga1-O1-C4	118.0(5)
N1-Ga1-N4_e	94.7(2)	Ga2-O2-C5	117.7(4)
O8_e-Ga1-N3	96.0(2)	Ga1-O5-C9	117.1(5)
N3-Ga1-N4_e	94.6(2)	Ga1_d-O8-C10	117.2(4)
O8_e-Ga1-N4_e	80.8(3)	Ga1-N1-C1	140.7(4)
O2-Ga2-N2	80.7(2)	Ga1-N1-C3	112.4(5)
O2-Ga2-O2_a	89.0(2)	Ga2-N2-C1	141.9(5)
O2-Ga2-N2_a	96.0(2)	Ga2-N2-C2	112.1(4)
O2-Ga2-O2_b	89.0(2)	Ga1-N3-C6	142.1(4)
O2-Ga2-N2_b	168.5(2)	Ga1-N3-C7	111.2(4)

6A.3 RESULTS AND DISCUSSION

6A.3.1 Characterization of $\{(\text{Me}_2\text{NH}_2)_{12}[\text{Ga}_8(\text{ImDC})_{12}]\cdot\text{DMF}\cdot 29\text{H}_2\text{O}\}$ (1)

Solvothermal reaction of $\text{Ga}(\text{NO}_3)_3\cdot 6\text{H}_2\text{O}$ and 4,5-imidazoledicarboxylic acid (ImDC) in *N,N'*-dimethylformamide (DMF) in presence of triethylamine (Et_3N) at $120\text{ }^\circ\text{C}$ afforded a pale yellow powder. Aqueous solution of the powder on slow evaporation yielded block-shaped single crystals of **1**. The asymmetric unit of **1** contained two Ga^{III} (Ga1, Ga2) centers, two ImDC^{3-} , two dimethyl ammonium cations (Me_2NH_2^+ , DMA) and

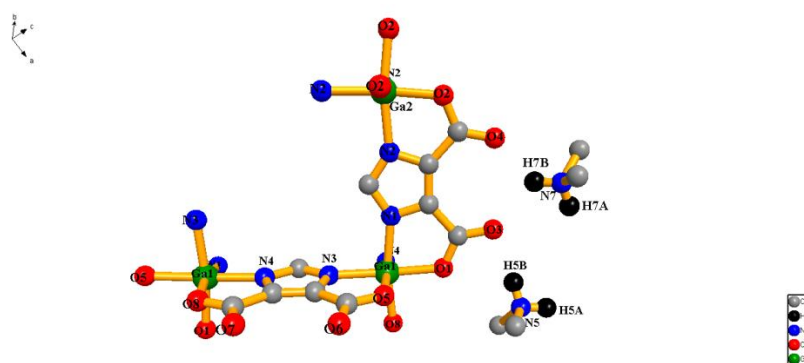


Figure 1. Asymmetric unit of **1** containing two Ga^{III} (Ga1, Ga2) centres, two ImDC^{3-} , two dimethyl ammonium cations (Me_2NH_2^+ , DMA). Guest water molecules are deleted for clarity.

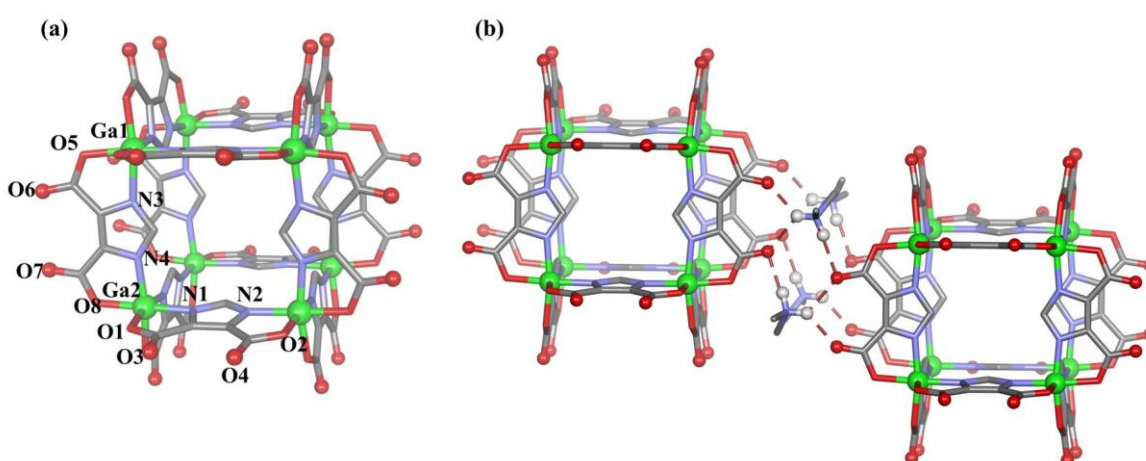


Figure 2. (a) Structure of $[\text{Ga}_8(\text{ImDC})_{12}]^{12-}$ cube, (b) two $[\text{Ga}_8(\text{ImDC})_{12}]^{12-}$ cube are connected to each other via intermolecular H-bonding with four DMA cations.

eight guest water and one DMF molecules (Figure 1). The DMA cations were formed *in situ* from DMF under solvothermal condition.¹⁵ Each ImDC^{3-} (ImDC_a or ImDC_b) linker chelated two Ga^{III} (Ga1 \cdots Ga2 or Ga1 \cdots Ga1) centres in a bis(bidentate) fashion

through two imidazole nitrogen atoms (N1, N2 or N3, N4) and two carboxylate oxygen atoms (O1,O2 or O5, O8), while other two oxygen atoms (O3,O4 or O7, O6) remained free (Figure 2a). Twelve ImDC^{3-} alternatively connected eight Ga^{III} centres to form an anionic metal-organic cube, $[\text{Ga}_8(\text{ImDC})_{12}]^{12-}$ (**MOC**), where $\text{Ga1}\cdots\text{Ga2}$ and $\text{Ga1}\cdots\text{Ga1}$ distances were 6.232 Å and 6.244 Å, respectively and $\text{Ga1}\cdots\text{Ga2}\cdots\text{Ga1}$, $\text{Ga1}\cdots\text{Ga1}\cdots\text{Ga2}$, $\text{Ga1}\cdots\text{Ga1}\cdots\text{Ga1}$ angles were 90.11°, 90.00°, 89.89°, respectively (Table 2). In the $[\text{Ga}_8(\text{ImDC})_{12}]^{12-}$ cube eight Ga^{III} ions occupied the vertices and twelve ImDC^{3-} occupied the edges (Figure 2a). The negative charge from 12 carboxylate group of each cube was neutralized by twelve surrounding DMA cations. Two DMA cations (N5 and N7) played an important role in the extending of **MOCs** as they connected two adjacent cubes through N-H \cdots O H-bonding interaction with pendent carboxylate oxygen atoms (O3, O4 and O7, O6) (Figure 2b). The N-H \cdots O H-bond distances and N-H \cdots O H-bond angles were in the range of 1.992-2.127 Å and 127-166°, respectively which

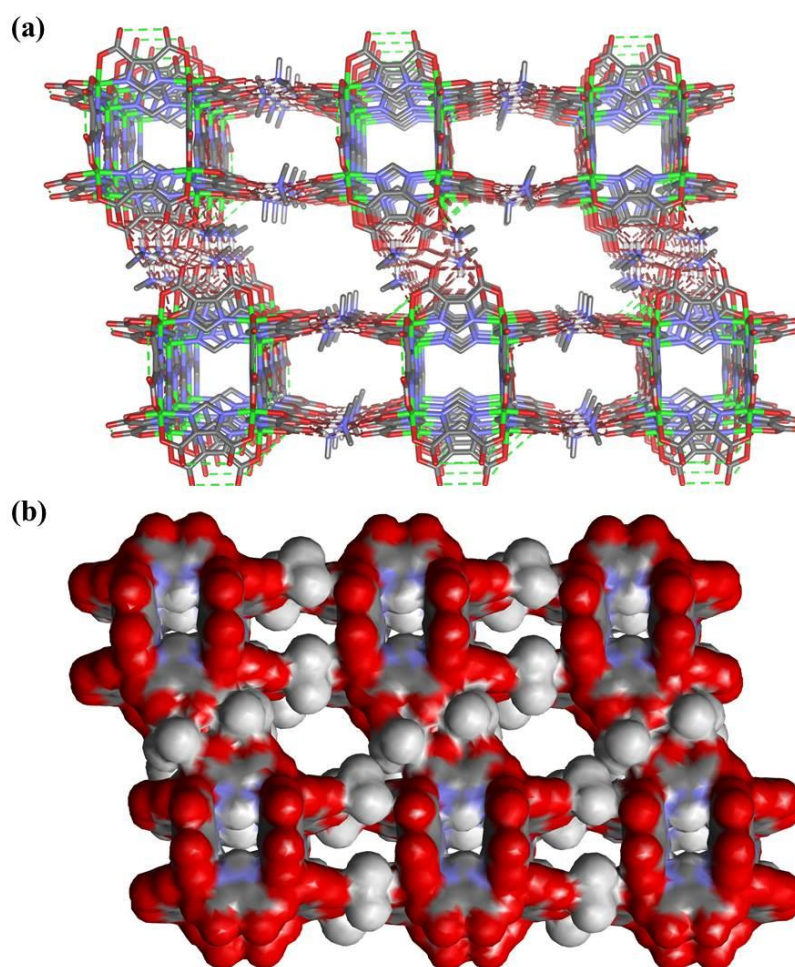


Figure 3. (a) 3D supramolecular packing of the cubes in **1**, (b) Space filling model of **1** showing the bimodal channels.

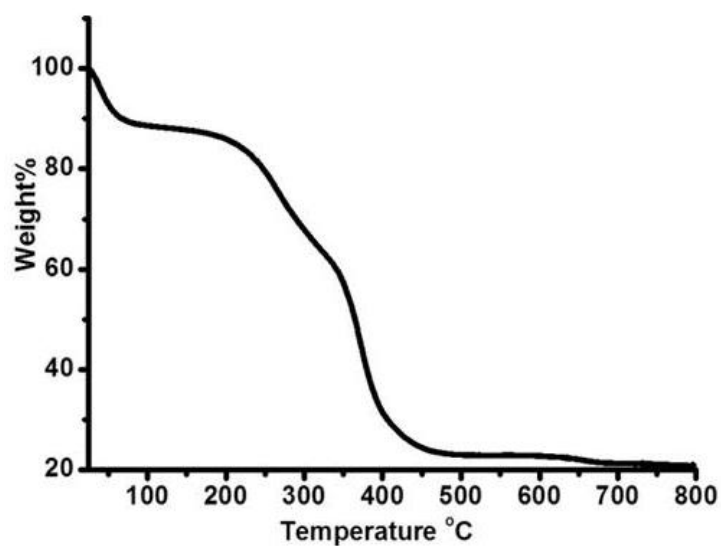


Figure 4. TGA profile of **1** in temperature range 25°C – 800°C under N₂ atmosphere.

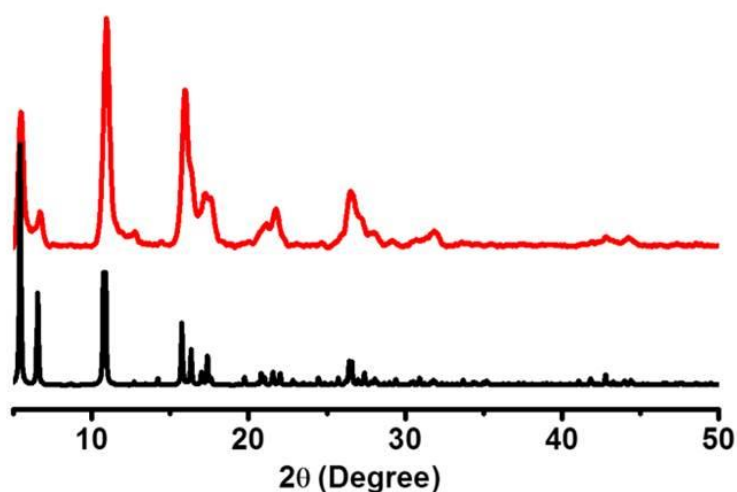


Figure 5. PXRD patterns of **1** simulated (black) and as-synthesized (red).

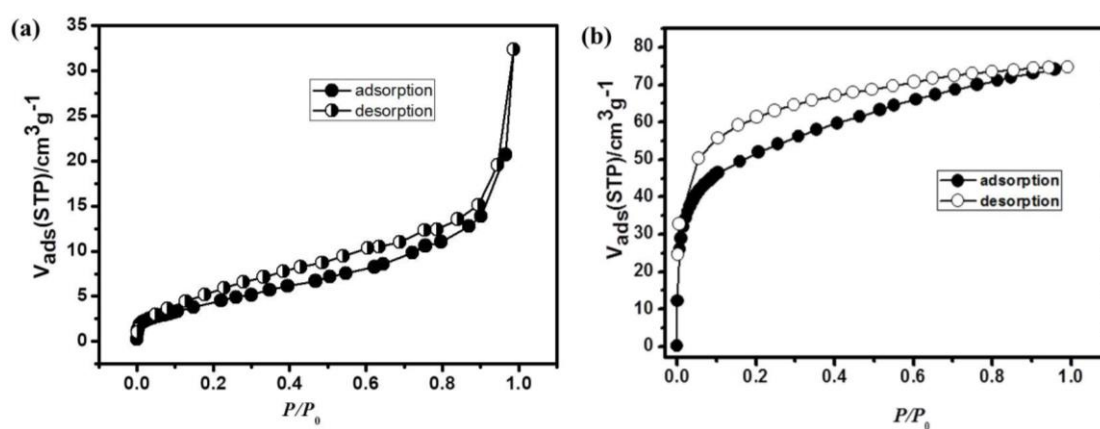


Figure 6. (a) N₂ adsorption profile of **1** at 77 K, (b) CO₂ adsorption profile of **1** at 195 K.

indicated strong charge-assisted intermolecular H-bonding interaction (Table 2). The minimum distance between two adjacent cube ($O3 \cdots O7$) was 3.429 Å. Each cube was concomitantly connected to six neighbouring ones through H-bonding with DMA cations and forming 3D extended structure (Figure 3a). The periodic arrangement of cubes generated an open framework which exhibited two types of alternative 3D channels with an approximate window size of ($8.14 \times 5.95 \text{ \AA}^2$) and ($7.66 \times 4.9 \text{ \AA}^2$), respectively (Figure 3b). TGA of as-synthesized **1** showed an initial weight-loss of 15 % at 200 °C that corresponds to a loss of guest molecules (Figure 4). The similar PXRD pattern of the as-synthesized powder and the simulated one indicates purity of the compound (Figure 5). N_2 adsorption isotherm of desolvated **1** (**1'**) at 77 K shows a type-II profile indicating surface adsorption (Figure 6a). However, CO_2 adsorption isotherm of **1'** at 195 K shows type-I behaviour with the total uptake of $\sim 75 \text{ mL g}^{-1}$ suggesting microporous nature of the extended framework of **1** (Figure 6b).

6A.3.2 Characterization of MOC-G1 hydrogel

1 was highly soluble in water (Figure 7a-b). HRMS analysis of the aqueous solution showed presence of discrete anionic cubes ($m/z = 1234.2459$, $z = 2$) suggesting high stability of $[Ga_8(ImDC)_{12}]^{12-}$ in water (Figure 7c). Moreover, 1H -NMR spectrum of **1** in D_2O showed the presence DMA cations (Figure 8). Addition of 3.5% aq. NH_3 into the aqueous solution of **1** resulted in stable, transparent hydrogel (**MOC-G1**) after 8 hours at room temperature (critical gelation concentration = 15 mg mL^{-1}) (Figure 9a). **MOC-G1** did not show any visible weakening over a month. The sol-gel transition was completely reversible after multiple shaking - resting cycles, indicating its thixotropic behaviour. **MOC-G1** was also pH responsive; it (intrinsic pH=11) formed a precipitate on addition of 0.1 M HCl (pH= 4 - 5) and reformed gel on adding aq. NH_3 (pH= 12) (Figure 9b). This indeed suggested the interaction of NH_4^+ with **MOC** was crucial for hydrogelation and it was feasibly driven through charge-assisted H-bonding between NH_4^+ and peripheral carboxylate oxygens of **MOC**. PXRD of **1** and xerogel showed no significant change, which suggested **MOCs** were intact in the gel state (Figure 10). Rheology studies of **MOC-G1** revealed that storage modulus (G') was higher than the loss modulus (G'') and both of them (G' and G'') were independent of angular frequency (ω) over a large range of strain (%) indicating viscoelastic nature of the hydrogel (Figure 11). The FESEM images of **MOC-G1** xerogel showed micrometer ($3 \mu\text{m} - 8 \mu\text{m}$) long tubular nanostructures with rectangular cross-section (Figure 12a-c). The wall thickness of the nanotubes was found

to be 9-10 nm from TEM analysis (Figure 12d-f). To get an insight into the growth mechanism of these nanotubes, FESEM images of MOC/aq.NH₃ solution were recorded at various stages of hydrogel formation (Figure 13a-i). Initially, MOCs self-assembled to

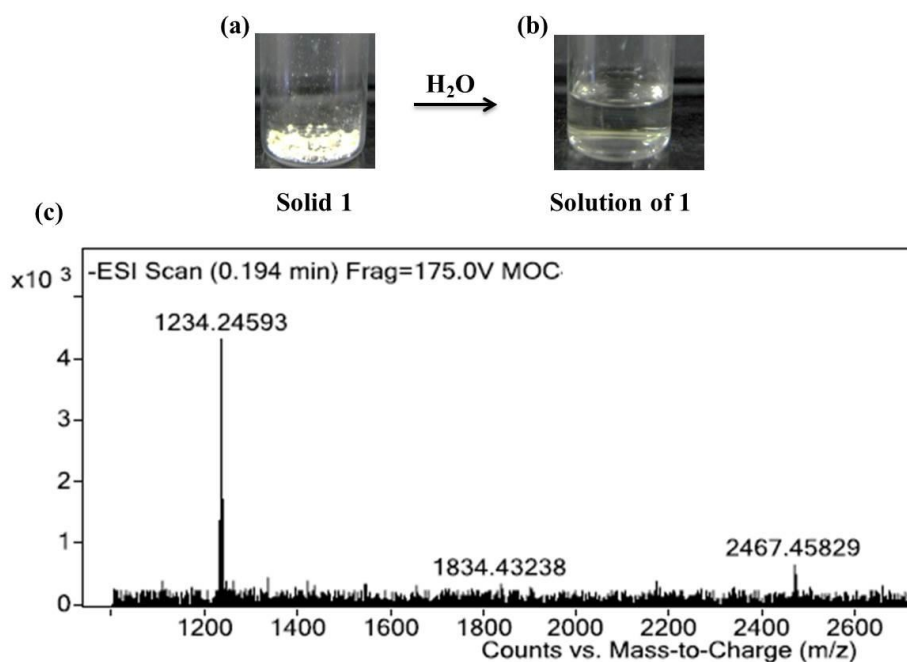


Figure 7. (a) The solid powder of **1**, (b) The aqueous solution of **1**.

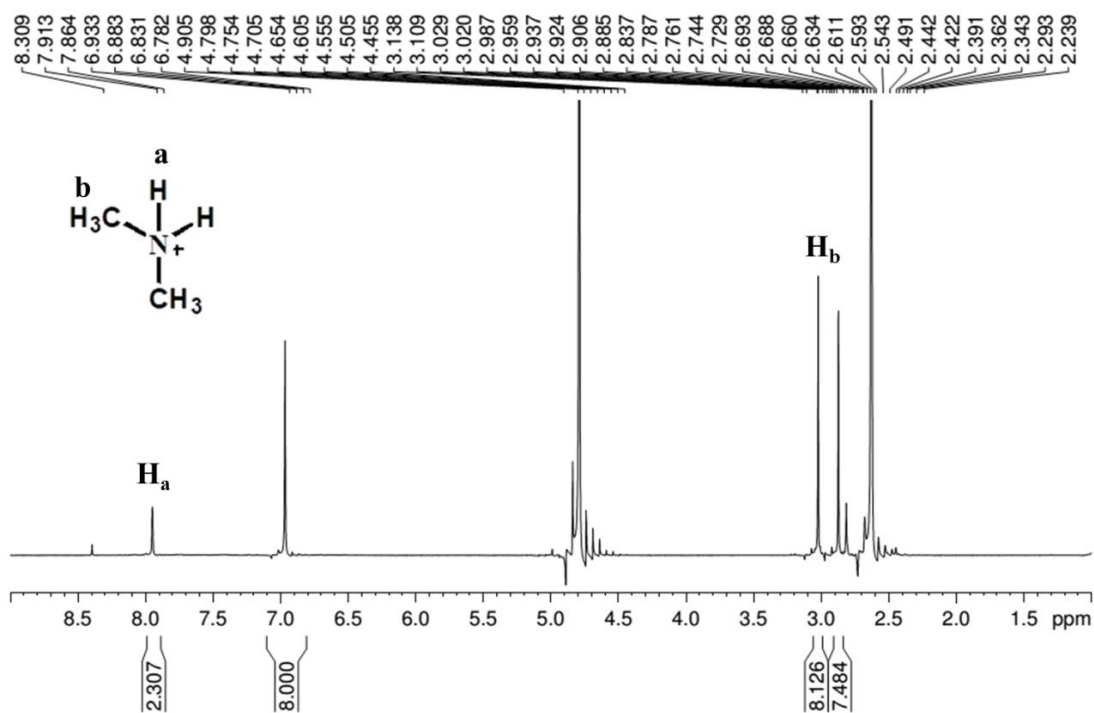


Figure 8. ¹H-NMR spectrum of **1** after dissolving in D₂O.

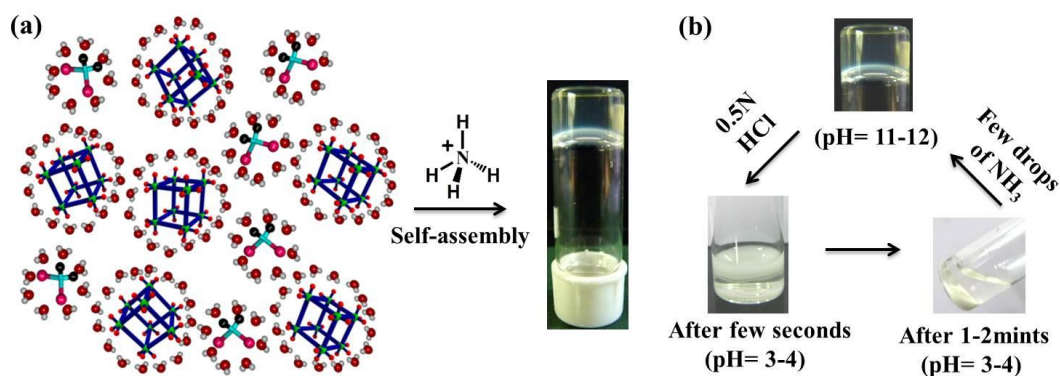


Figure 9. (a) The process of hydrogelation in presence of ammonium cations, (b) pH responsive behaviour of the MOC-G1 hydrogel.

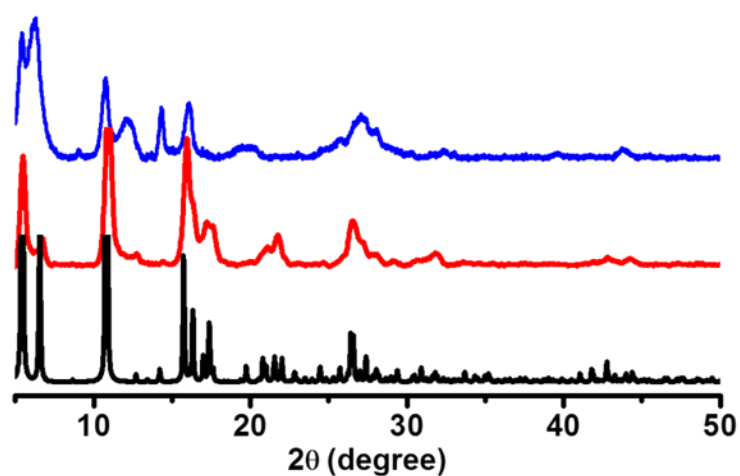


Figure 10. Comparison of PXRD pattern of simulated 1 (black), as-synthesized 1 (red) and MOC-G1 xerogel (blue).

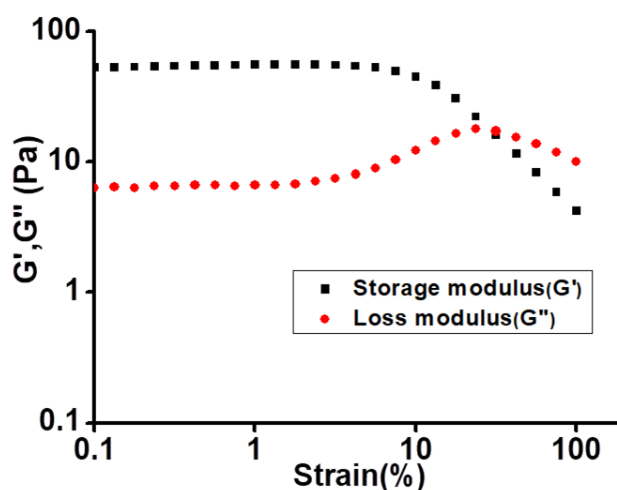


Figure 11. Oscillatory strain measurements (frequency = 1.0 rad/s) of MOC-G1, the squares (black) and circles (red) indicate storage (G') and loss modulus (G''), respectively.

form cubic seeds. Higher concentration of NH_4^+ at the early stage of gelation led to fast aggregation of seeds and resulted in irregular crumpled sheets, as observed from FESEM images after 2 h (Figure 13a-c). Each crumpled sheet acted as a nodal point for further anisotropic growth towards the closely spaced 1D tapes which were observed in FESEM images after 4 h (Figure 13d-f). Such anisotropic growth to 1D tape was probably governed by the competitive binding of DMA and NH_4^+ cations.¹⁶ As the reaction proceeds, these 1D tapes further assembled to form partially-grown nanotubes in which three sides of nanotubes were formed, as seen from FESEM after 6 h (Figure 13g-i). It was interesting to note that the solution converted to viscous liquid at this stage. After 8 h stable transparent gel was formed and FESEM images showed complete formation of nanotubes (Figure 12). The above analysis indicates that DMA cations might have a critical role in the formation of nanotube and the growth mechanism involved nucleation, followed by aggregation of particle seed, fusion, growth and finally annealing processes¹⁶ (Figure 14).

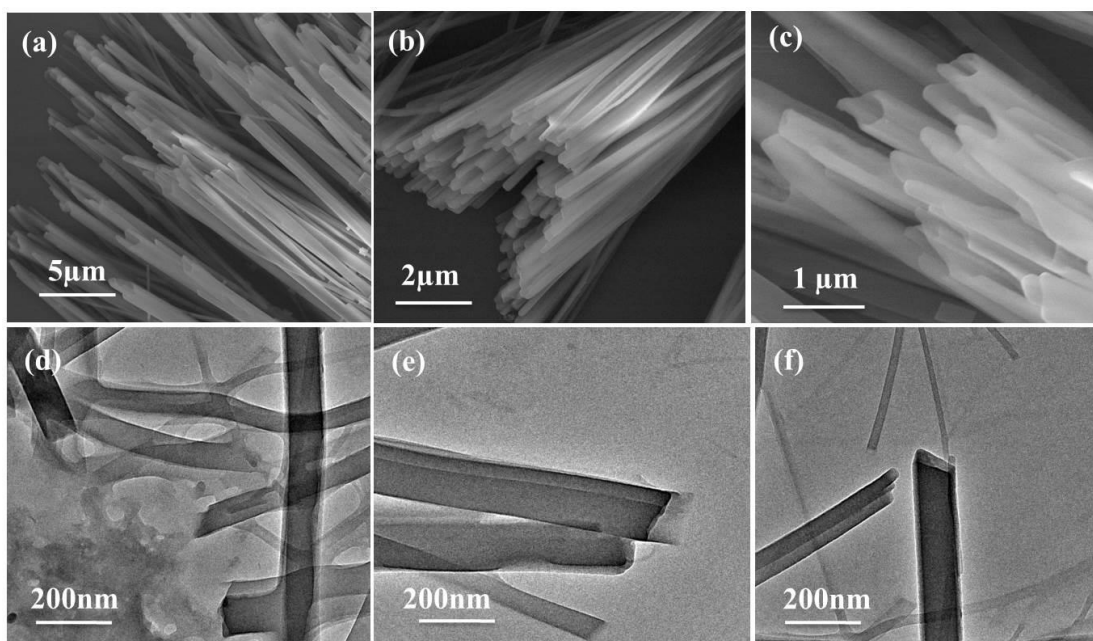


Figure 12. (a), (b), (c) FESEM images of **MOC-G1** xerogel, (d), (e), (f) TEM images of **MOC-G1** xerogel showing the formation of nanotubes.

6A.3.3 Characterization of other hydrogels

To generalize the hypothesis that externally added cationic molecular binder with H-donor sites were facilitating the self-assembly of **MOCs**, the gelation propensity of **MOCs** in presence of various aliphatic amines and amino acids, such as

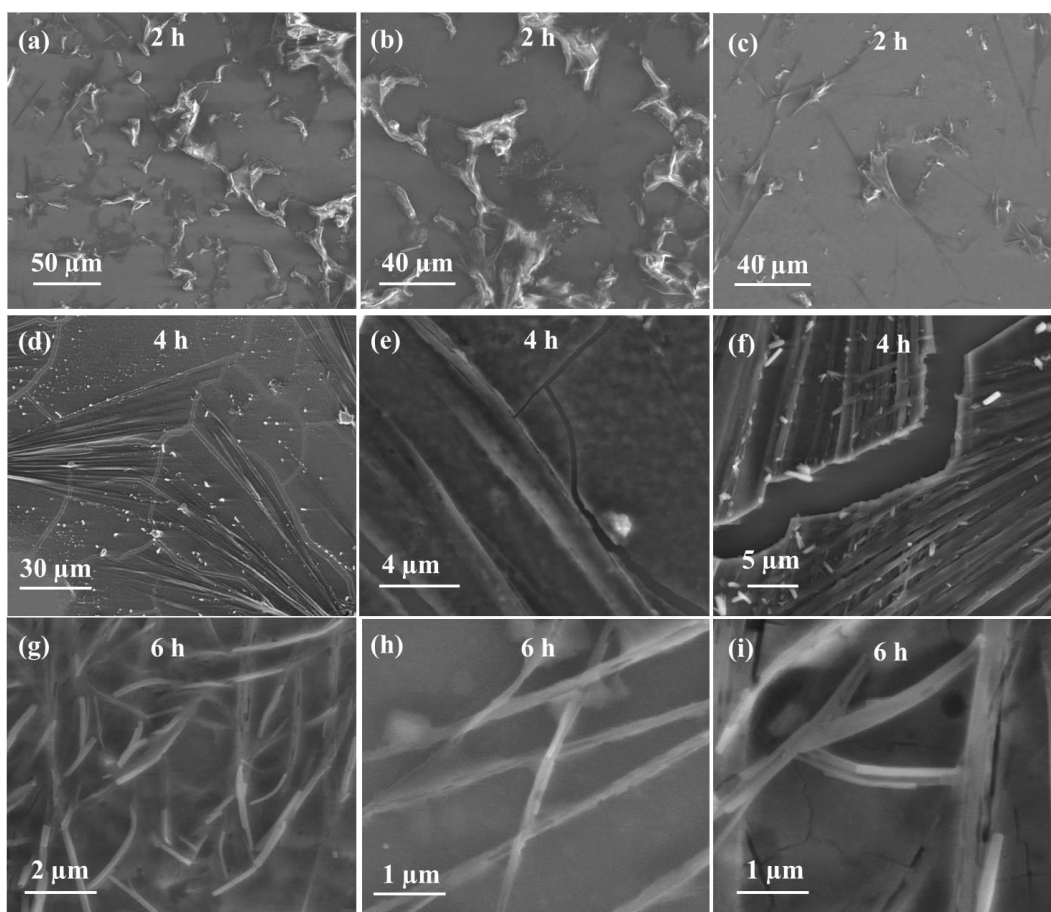


Figure 13. (a), (b), (c) FESEM images of **MOC/aq.NH₃** solution at 2 h, (d), (e), (f) at 4 h and (g), (h), (i) at 6 h.

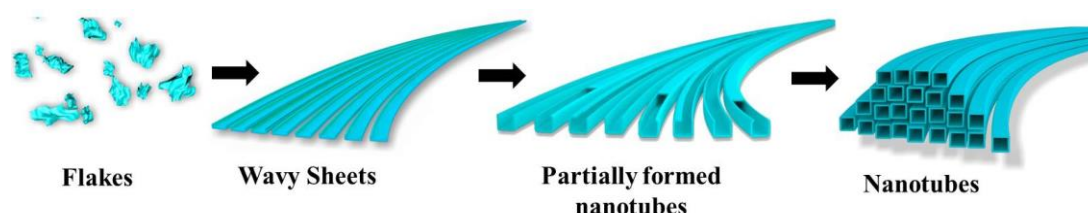


Figure 14. Schematic showing time dependent change in morphology from flakes to wavy sheets to half-folded tubes to full tubes.

N-(2-aminoethyl)-1,3- propanediamine (AEPD), guanidine hydrochloride (gua.HCl), and β -alanine (β -ala), were checked (Figure 15a). When certain concentration of aq. AEPD, aq. gua.HCl and aq. β -ala were added to the aqueous solution of **MOC**, within one day the mixtures transformed into stable **MOC-G2**, **MOC-G3** and **MOC-G4** hydrogels, respectively (Figure 15a). FESEM and TEM images of **MOC-G2** xerogel showed bouquet-like morphology in which individual needles were several micrometer long with an approximate diameter of 200-300 nm (Figure 15b-c and Figure 16 and 17). FESEM

and TEM images of **MOC-G3** xerogel revealed sheet-like nanostructure (Figure 18). Similar analysis with **MOC-G4** xerogel revealed nanocube morphologies with dimension in 200-250 nm range (Figure 19). The above observations indicated that structure, geometry and number of H-bonding donor sites of molecular binders had immense impact on the morphology of hydrogel nanostructures.

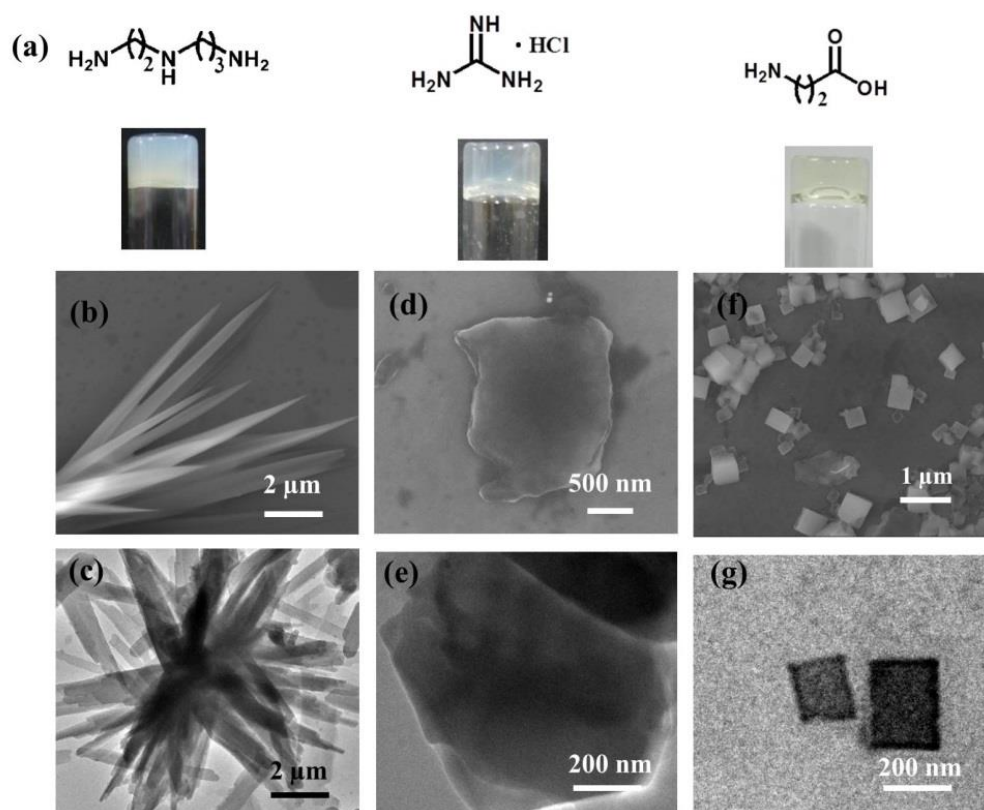


Figure 15. (a) Structure of molecular binders, N-(2-aminoethyl)-1,3-propanediamine, guanidine hydrochloride, β -alanine, and their respective hydrogels, (b) and (c) FESEM and TEM images of **MOC-G2** xerogel, (d) and (e) FESEM and TEM images of **MOC-G3** xerogel, (f) and (g) FESEM and TEM images of **MOC-G4** xerogel.

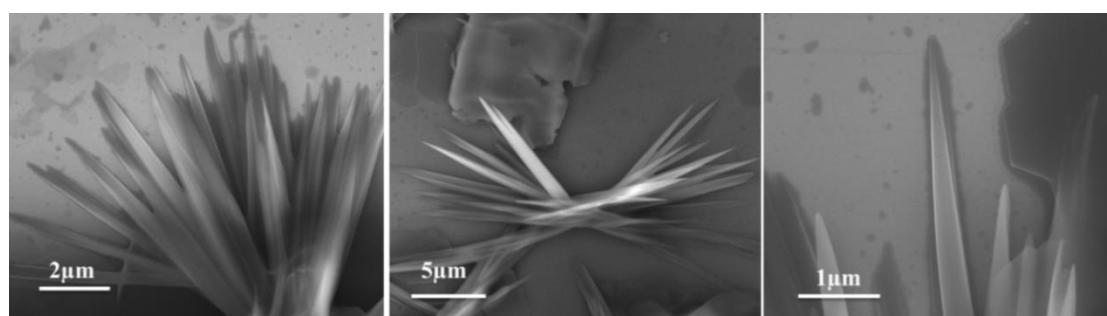


Figure 16. FESEM images of **MOC-G2** xerogel showing the formation of bouquet-like nanostructures.

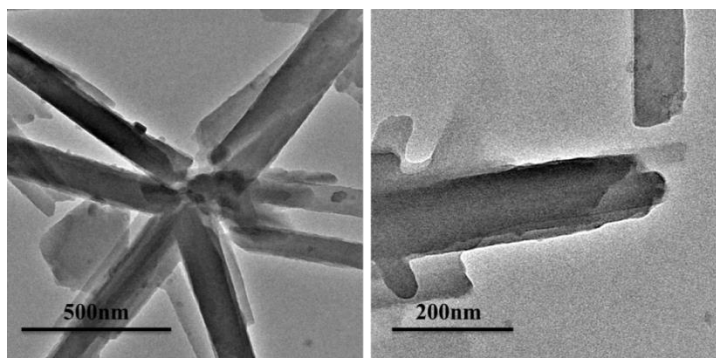


Figure 17. TEM images of **MOC-G2** xerogel.

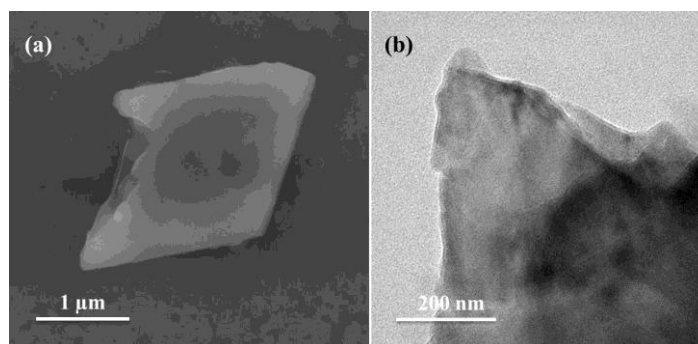


Figure 18. (a) FESEM and (b) TEM images of **MOC-G3** xerogel showing the formation of sheet-like morphology.

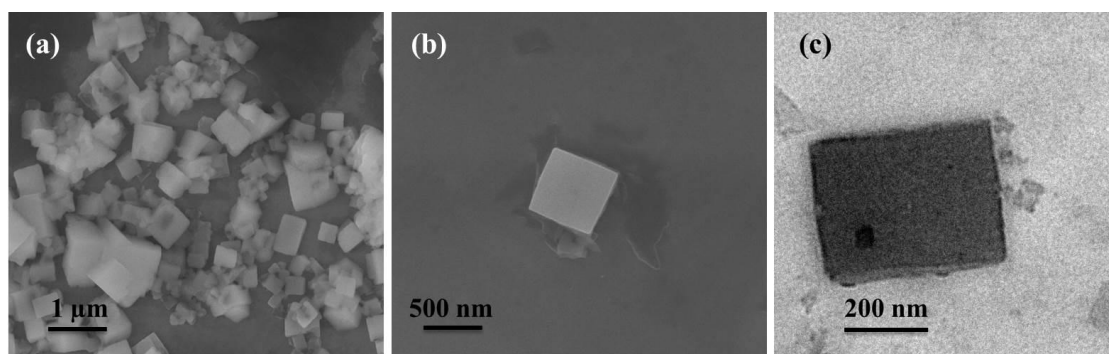


Figure 19. (a), (b) FESEM and (c) TEM images of **MOC-G4** xerogel, showing the formation of nanocubes.

6A.3.4 Gel-column chromatographic separation

Zeta potential **MOC-G1** xerogel was found to be -22 mV which indicated surfaces of the nanotube was negatively charged (Figure 20). The negatively charged surface of one dimensionally aligned nanotubes prompted us to use **MOC-G1** for gel chromatographic separation of oppositely charged species from their mixture. For this study, anionic (sulforhodamine G, **SHG**) and cationic (nile blue, **NB** and acridine orange,

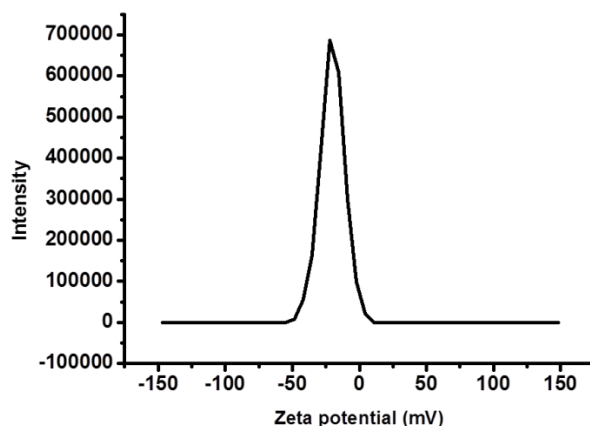


Figure 20. Zeta potential of MOC-G1 xerogel (dispersed in MeOH) indicating the value -22 mV.

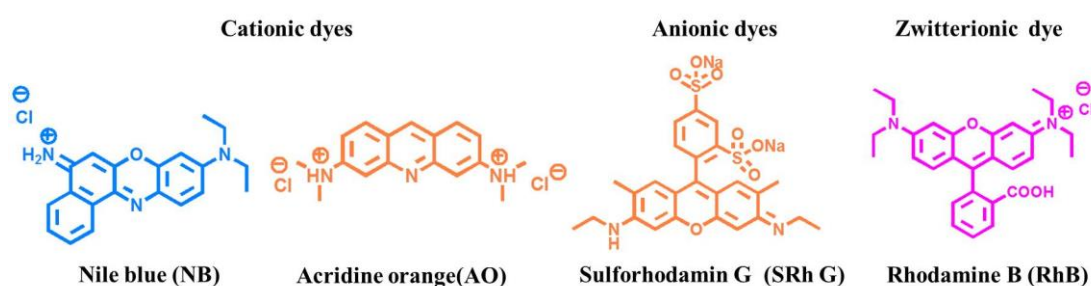


Figure 21. The molecular structures of cationic (nile blue, acridine orange), anionic (sulforhodamin G) and zwitterionic (rhodamine B) dyes.

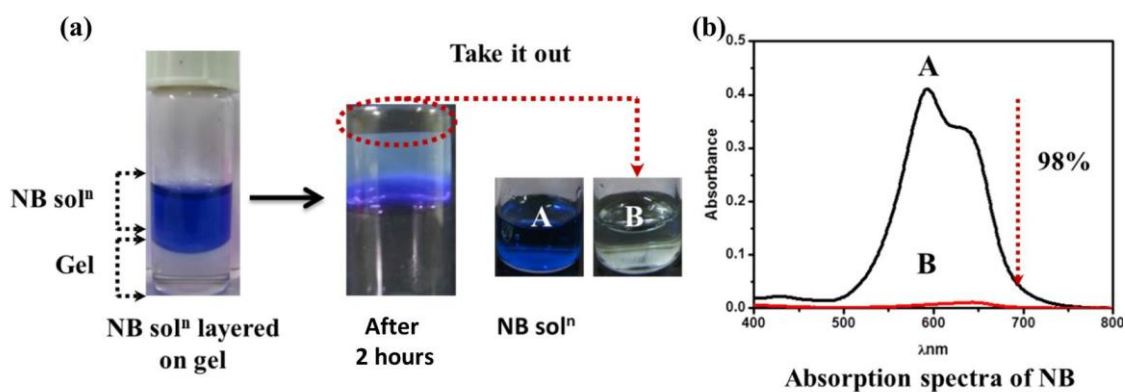


Figure 22. (a) 10^{-5} M aqueous solution of nile blue (NB) was layered on the MOC-G1 gel. After few hours most of the nile blue gets absorbed in the gel. **A** is the 10^{-5} M nile blue solution. **B** is the clear solution collected below the gel after few hours. This solution was taken out by using a syringe. (b) Absorption spectra of 10^{-5} M nile blue solution (black) and the clear solution (red) collected below the hydrogel.

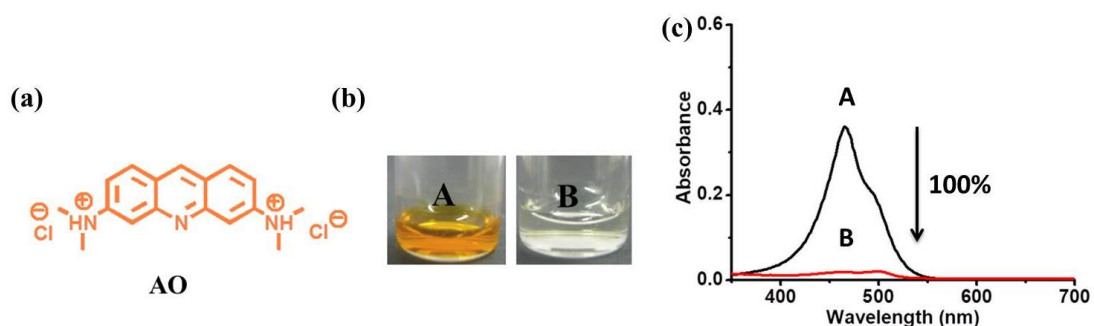


Figure 23. (a) The molecular structure of acridine orange (**AO**). (b) **A** is the 10^{-5} M acridine orange solution. **B** is the clear solution collected below the gel after few hours. (c) Absorption spectra of 10^{-5} M acridine orange solution (black) and the clear solution (red) collected below the hydrogel.

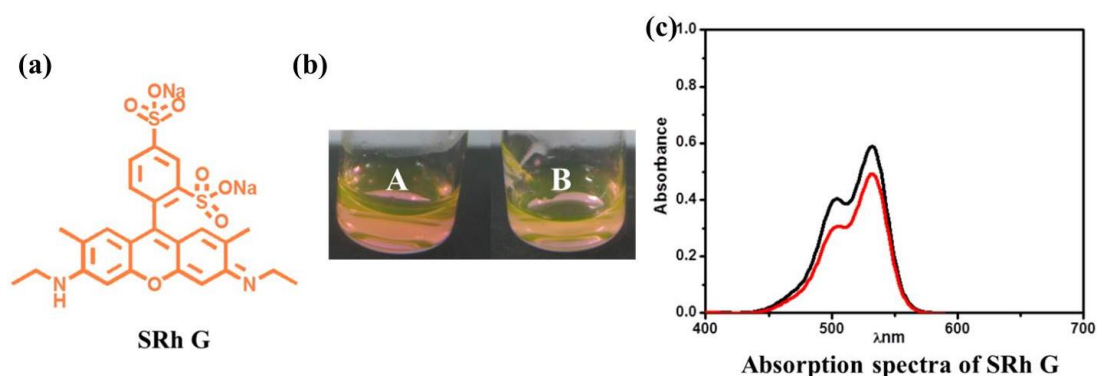


Figure 24. (a) The molecular structure of sulforhodamin G (**SRh G**). (b) **A** is the 10^{-5} M sulforhodamin G solution. **B** is the solution collected below the gel after few hours. (c) Absorption spectra of 10^{-5} M sulforhodamin G solution (black) and the solution (red) collected below the hydrogel.

AO) dye molecules were used, since they would give better visual demonstration (Figure 21). Initial studies showed that the hydrogel could fully adsorb ($\sim 100\%$) the cationic dyes (10^{-5} M solution) but not the anionic dyes (10^{-5} M solution) as observed from UV-Vis spectra (Figure 22, 23 and 24). For demonstrating separation of dyes from their mixture, a chromatographic column (2.5 cm long) was packed with hydrogel (stationary phase) and eluted with mixture of **NB** (1×10^{-6} M) and **SHG** (1×10^{-6} M) in methanol (Figure 25). On passing the feed solution the column first became orange because **SHG** eluted rapidly through the column due to electrostatic repulsion with nanotubes (Figure 25b). Gradually, all **SHG** molecules passed through the column and at that point the column turned completely blue indicating the presence of **NB** in hydrogel (Figure 25b)

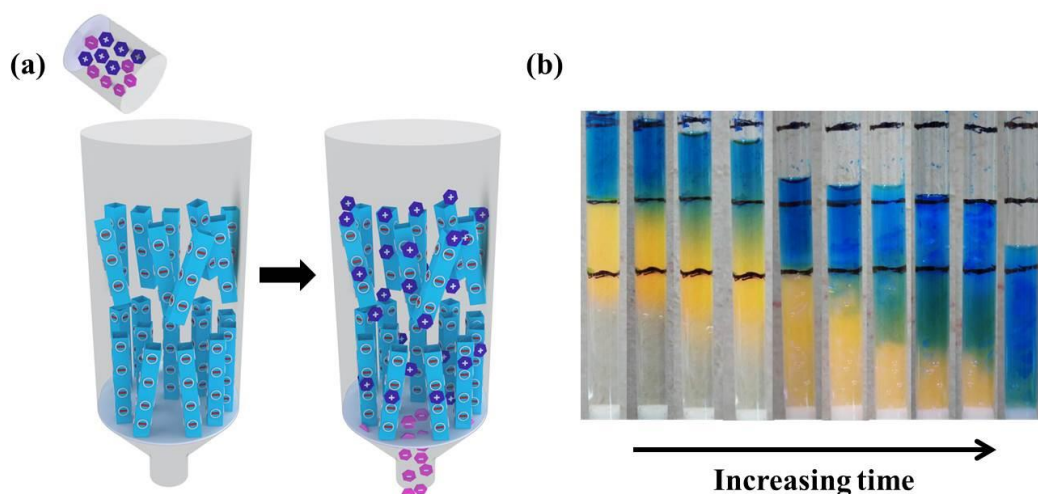


Figure 25. (a) The schematic of chromatographic separation of dye molecules, (b) change in gel-column with time indicating separation of **SHG** from **NB**.

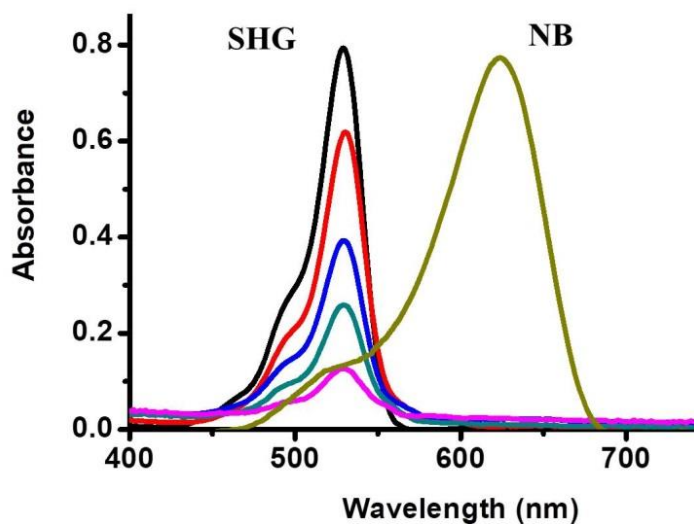


Figure 26. comparison of absorption spectra of eluent indicating gradual separation of **SHG** from **NB**. With increasing time, more **SHG** molecules come out of the column which is evident from increase in absorbance of 530 nm band. After all **SHG** has come out, the gel-column is converted to precipitate and washed with methanol to remove **NB**.

and Figure 26). Such selective adsorption of **NB** in **MOC-G1** was resulting due to the electrostatic interaction of the cationic dye onto the surface of anionic nanotubes. However, the as-synthesized **1**, which also has negatively charged surface as confirmed by zeta potential, showed minimal adsorption (29%) of **NB** (Figure 27). This observation indicated that not only the negative surface but also the entangled nanotube morphology and the entrapped water molecules between them were helping the selective adsorption of

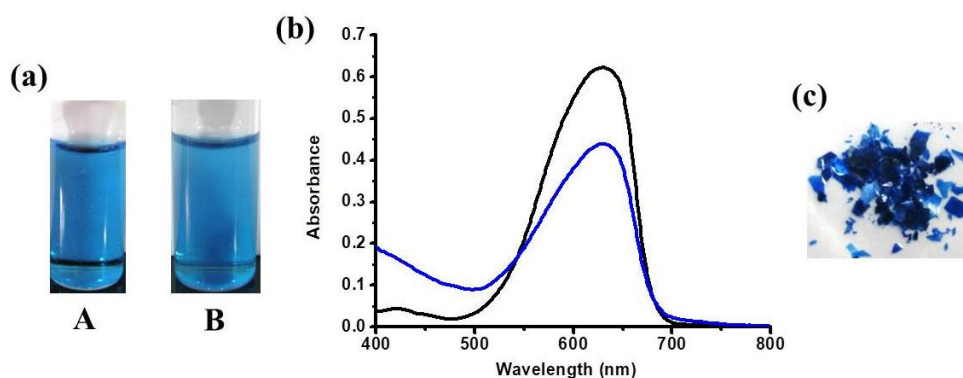


Figure 27. (a) A is the 10^{-5} M methanolic solution of Nile Blue. B is the solution of Nile Blue after soaking the crystals of **1** into it for 2 days, (b) Absorption spectra of 10^{-5} M Nile Blue solution (black) and the solution (blue) obtained after soaking the crystals of **1**, (c) The picture of the crystals of **1** after soaking it in the Nile Blue solution for 2 days and washing repeatedly by methanol.

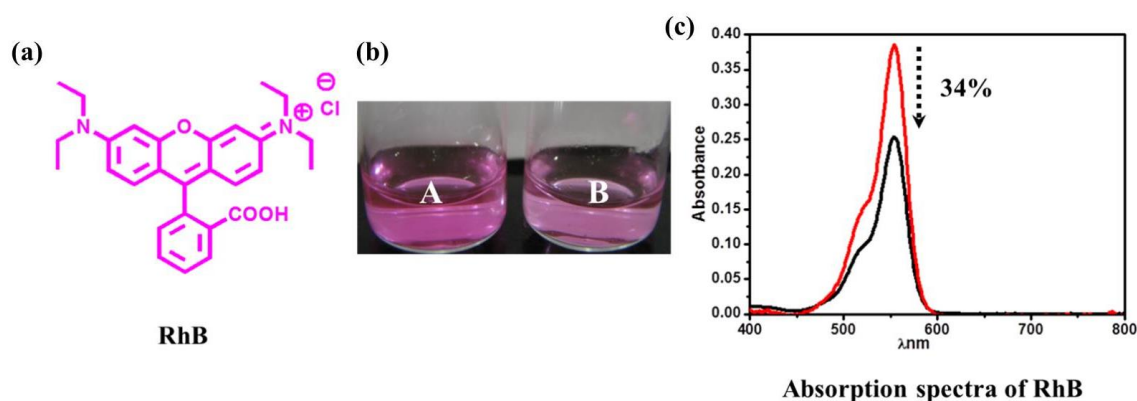


Figure 28. (a) The molecular structure of Rhodamine B (**RhB**), (b) A is the 10^{-5} M Rhodamine B solution. B is the solution collected below the gel after few hours, (c) Absorption spectra of 10^{-5} M Rhodamine B solution (red) and the solution (black) collected below the hydrogel.

cationic dyes in gel and the fast removal of anionic dyes through gel. To the best of our knowledge, this was the first example of hydrogel utilized for the column-chromatographic separation of oppositely charged species. Next, Rhodamine B (**RhB**) dye was selected which has a cationic group $[=N(Et)_2^+]$ and the easily deprotonable carboxylic acid group ($-COOH$). The hydrogel adsorbed only 34% **RhB** (Figure 28). Since the hydrogel was basic (pH=11) the $-COOH$ group of **RhB** got deprotonated easily while passing through the gel and hence was repelled by the surface of anionic nanotubes. On the other hand, the cationic part of **RhB** $[=N(Et)_2^+]$ forced the molecule to be

attached with the gel matrix. Because of such two opposite forces, only 34% dye was absorbed by **MOC-G1**. Moreover, the hydrogel column was recyclable as it could be easily converted to precipitate by adding HCl (pH=4 - 5), which was washed by methanol to remove adsorbed dyes and the recovered **MOC** could be converted to hydrogel by adding aq. NH_3 .

6A.3.5 pH responsive behaviour

A pyrene-based molecular binder was synthesized, 1,8-bis (1-methylpyrenyl)-1,4,8-triazaheptane which is well-known to exhibit pH dependent emission. Conformations of 1,8-bis-(1-methylpyrenyl)-1,4,8-triazaheptane are pH dependant (Figure 29a) . Under acidic condition, owing to the electrostatic repulsion of protonated nitrogen atoms, 1,8-bis-(1-methylpyrenyl)-1,4,8-triazaheptane remained in unstacked condition. Therefore, at lower pH it exhibited monomer emission at 377-435 nm which arose from locally excited pyrene chromophores (Figure 29b). However, in basic pH the molecule existed in a stacked conformation owing to π - π interaction and showed a broad emission at 470 nm (Figure 29d). Under neutral condition (pH 7) the aqueous solution of 1,8-bis-(1-methylpyrenyl)-1,4,8-triazaheptane showed presence of both monomer and excimer which was clear from the emission spectra (Figure 29c). When aqueous solution

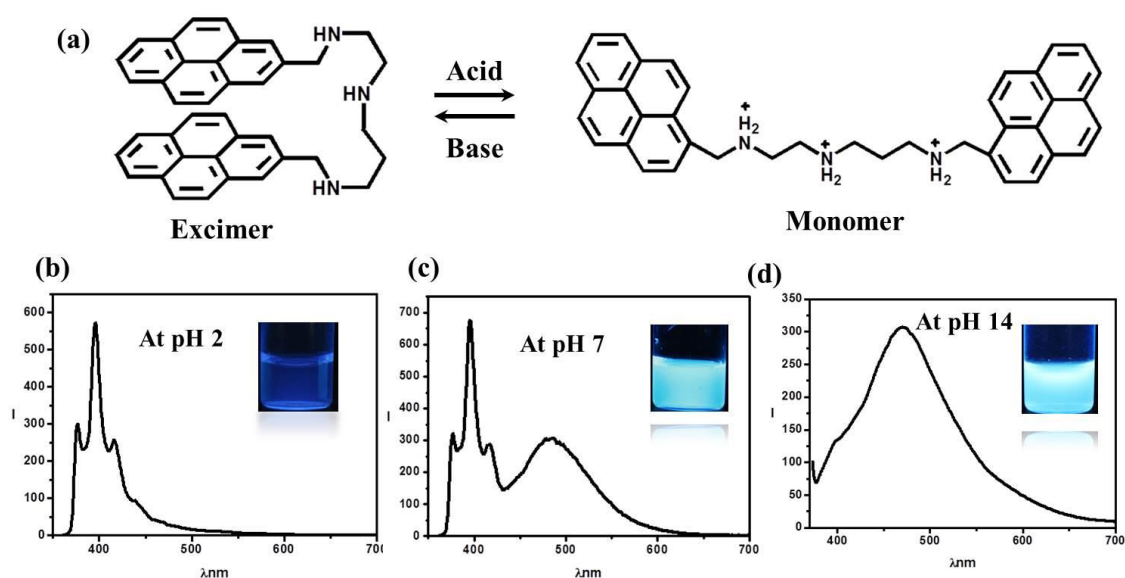


Figure 29: (a) Two different pH-dependent conformations of 1,8-bis-(1-methylpyrenyl)-1,4,8-triazaheptane, (b), (c) and (d) Emission spectra of the aqueous solution of 1,8-bis-(1-methylpyrenyl)-1,4,8-triazaheptane at pH=2, 7 and 14, respectively. Inset shows the picture of the corresponding solutions under UV-light.

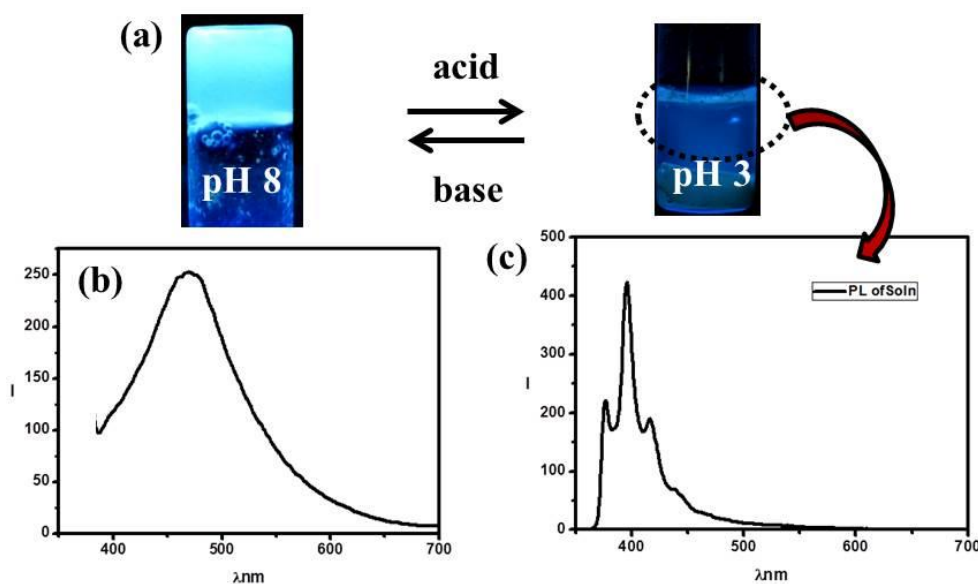


Figure 30: (a) The picture of **MOC-G5** and the sol formed after addition of acid, (b) Emission spectrum of **MOC-G5** hydrogel, (c) emission spectrum of sol formed after addition of acid.

of **MOC** was mixed with aqueous solution of 1,8-bis-(1-methylpyrenyl)-1,4,8-triazaheptane (2×10^{-3} M) the mixture converted to opaque hydrogel (**MOC-G5**) after 24 hours (Figure 30a). Upon mechanical shaking the hydrogel easily converted into sol. Emission spectra of the sol exhibited contribution from both monomer and excimer and displayed blue emission under UV light. However, the hydrogel was cyan emissive under UV light and showed only excimer emission at 470nm (figure 30b). Gelation *via* the H-bonding interaction reinforced the pyrene molecule to come closer and form the excimer. The hydrogel was pH responsive. At low pH the hydrogel network disrupted and formed the precipitate and the solution showed monomer emission (Figure 30a, c). However on increasing pH the hydrogel reformed and the emission of the pyrene excimer was regained.

6A.4 SUMMARY

In summary, we have prepared a water soluble **MOC** which self-assembled to hydrogel in presence of different molecular binders. Depending upon shape and geometry of the molecular binders, the hydrogels showed different morphologies, such as nanotube, nano- bouquet, nanosheet and nanocube. Moreover, the properties of the hydrogels were tuned by selecting the suitable binders. The surface negative charge of the nanotubes of **MOC-G1** was exploited for gel-chromatographic separation of cationic dyes from anionic dye. We believe that **MOC** hydrogels would provide a new platform to realize

novel properties, like high temperature proton conductivity or supercapacitive behaviour after integrating with 2D materials like graphene oxide.

6A.5 REFERENCES

1. (a) G. A. Jeffrey, W. Saenger, Hydrogen Bonding in Biological Structures. *Springer-Verlag: New York*, 1991; (b) W. Saenger, Principles of Nucleic Acid Structure. *Springer-Verlag: New York*, 1984; (c) G. E. Schulz, R. H. Schirmer, Principles of Protein Structure. *Springer-Verlag: New York*, 1979; (d) J. S. Redinha, A. J. Lopes Jesus, Molecular Recognition and Crystal Growth. In *Molecular Recognition: Biotechnology, Chemical Engineering and Materials Applications*. Ed.; *Nova Publishers: New York*, 2011.
2. (a) C. Mottillo and T. Friscic, *Chem. Commun.*, 2015, **51**, 8924-8927; (b) A. Hazra, K. L. Gurunatha and T. K. Maji, *Cryst. Growth Des.*, 2013, **13**, 4824-4836.
3. P. Dastidar, U. K. Das, T. K. Adalder, J. Majumder and R. Roy, in *Hydrogen Bonded Supramolecular Materials*, edited by Zhan-Ting Li and Li-Zhu Wu (Springer Berlin Heidelberg, Berlin, Heidelberg, 2015), pp. 101-131.
4. G. R. Desiraju, *Acc. Chem. Res.*, 2002, **35**, 565-573.
5. (a) J. J. Perry Iv, J. A. Perman and M. J. Zaworotko, *Chem. Soc. Rev.*, 2009, **38**, 1400-1417; (b) D. J. Tranchemontagne, Z. Ni, M. O'Keeffe and O. M. Yaghi, *Angew. Chem. Int. Ed.*, 2008, **47**, 5136-5147; (c) M. J. Prakash and M. S. Lah, *Chem. Commun.*, 2009, 3326-3341; (d) Q.-F. Sun, J. Iwasa, D. Ogawa, Y. Ishido, S. Sato, T. Ozeki, Y. Sei, K. Yamaguchi, and M. Fujita, *Science.*, 2010, **328**, 1144-1147; (e) A. Mallick, B. Garai, D. D. Díaz, and R. Banerjee, *Angew. Chem. Int. Ed.*, 2013, **52**, 13755-13759; (f) Y. Yan, X. Lin, S. Yang, A. J. Blake, A. Dailly, N. R. Champness, P. Hubberstey, and M. Schroder, *Chem. Commun.*, 2009, 1025-1027; (g) I. A. Riddell, M. M. J. Smulders, J. K. Clegg and J. R. Nitschke, *Chem. Commun.*, 2011, **47**, 457-459; (h) W. Lu, D. Yuan, A. Yakovenko and H.-C. Zhou, *Chem. Commun.*, 2011, **47**, 4968-4970; (i) H.-N. Wang, X. Meng, G.-S. Yang, X.-L. Wang, K.-Z. Shao, Z.-M. Su and C.-G. Wang, *Chem. Commun.*, 2011, **47**, 7128-7130; (j) S. Hong, M. Oh, M. Park, J. W. Yoon, J.-S. Chang, and M. S. Lah, *Chem. Commun.*, 2009, 5397-5399; (k) D. Zhao, S. Tan, D. Yuan, W. Lu, Y. H. Rezenom, H. Jiang, L.-Q. Wang and H.-C. Zhou, *Adv. Mater.*, 2011, **23**, 90-93; (l) D. Tian, Q. Chen, Y. Li, Y.-H. Zhang, Z. Chang and X.-H. Bu, *Angew. Chem. Int. Ed.*, 2014, **53**, 837-841; (m) M. Jung, H. Kim, K. Baek and K. Kim, *Angew. Chem. Int. Ed.*, 2008, **47**, 5755-5757; (n) J. Park, L.-B. Sun, Y.-P. Chen, Z. Perry, and H.-C. Zhou, *Angew. Chem. Int. Ed.*, 2014, **53**, 5842-5846; (o) S.-T. Zheng, T. Wu, B. Irfanoglu, F. Zuo, P. Feng and X. Bu, *Angew.*

- Chem. Int. Ed.*, 2011, **50**, 8034-8037; (p) H. Furukawa, J. Kim, K. E. Plass and O. M. Yaghi, *J. Am. Chem. Soc.*, 2006, **128**, 8398-8399; (q) S. P. Argent, A. Greenaway, M. d. C. Gimenez-Lopez, W. Lewis, H. Nowell, A. N. Khlobystov, A. J. Blake, N. R. Champness and M. Schröder, *J. Am. Chem. Soc.*, 2012, **134**, 55-58; (r) I. A. Riddell, Y. R. Hristova, J. K. Clegg, C. S. Wood, B. Breiner and J. R. Nitschke, *J. Am. Chem. Soc.*, 2013, **135**, 2723-2733; (s) J. Park, Y.-P. Chen, Z. Perry, J.-R. Li and H.-C. Zhou, *J. Am. Chem. Soc.*, 2014, **136**, 16895-16901; (t) L.-B. Sun, J.-R. Li, W. Lu, Z.-Y. Gu, Z. Luo and H.-C. Zhou, *J. Am. Chem. Soc.*, 2012, **134**, 15923-15928; (u) T.-F. Liu, Y.-P. Chen, A. A. Yakovenko and H.-C. Zhou, *J. Am. Chem. Soc.*, 2012, **134**, 17358-17361.
6. Y. Liu, V. Kravtsov, R. D. Walsh, P. Poddar, H. Srikanth and M. Eddaoudi, *Chem. Commun.*, 2004, **24**, 2806-2807.
7. Q.-G. Zhai, C. Mao, X. Zhao, Q. Lin, F. Bu, X. Chen, X. Bu and P. Feng, *Angew. Chem. Int. Ed.*, 2015, **54**, 7886-7890 ().
8. M. H. Alkordi, J. L. Belof, E. Rivera, L. Wojtas and M. Eddaoudi, *Chem. Sci.*, 2011, **2**, 1695-1705.
9. (a) M. H. Alkordi, J. A. Brant, L. Wojtas, V. C. Kravtsov, A. J. Cairns and M. Eddaoudi, *J. Am. Chem. Soc.* **131**, 17753-17755 (2009); (b) D. F. Sava, V. C. Kravtsov, J. Eckert, J. F. Eubank, F. Nouar and M. Eddaoudi, *J. Am. Chem. Soc.*, 2009, **131**, 10394-10396; (c) S. S. Mondal, A. Bhunia, A. Kelling, U. Schilde, C. Janiak and H.-J. Holdt, *Chem. Commun.*, 2014, **50**, 5441-5443.
10. R. W. Larsen, *J. Am. Chem. Soc.*, 2008, **130**, 11246-11247.
11. (a) Y. Li, D. Zhang, F. Gai, X. Zhu, Y.-n. Guo, T. Ma, Y. Liu and Q. Huo, *Chem. Commun.*, 2012, **48**, 7946-7948; (b) T. D. Hamilton, G. S. Papaefstathiou, T. Frišćić, D.-K. Bučar and L. R. MacGillivray, *J. Am. Chem. Soc.*, 2008, **130**, 14366-14367.
12. Q. Wang, J. L. Mynar, M. Yoshida, E. Lee, M. Lee, K. Okuro, K. Kinbara and T. Aida, *Nature.*, 2010, **463**, 339-343.
13. (a) J. A. Foster, R. M. Parker, A. M. Belenguer, N. Kishi, S. Sutton, C. Abell and J. R. Nitschke, *J. Am. Chem. Soc.*, 2015, **137**, 9722-9729; (b) A. B. Grommet, J. L. Bolliger, C. Browne and J. R. Nitschke, *Angew. Chem. Int. Ed.*, 2015, **50**, 15100-15104; (c) A. V. Zhukhovitskiy, M. Zhong, E. G. Keeler, V. K. Michaelis, J. E. P. Sun, M. J. A. Hore, D. J. Pochan, R. G. Griffin, A. P. Willard and J. A. Johnson, *Nat. Chem.*, 2016, **8**, 33-41.
14. (a) SMART (V 5.628), SAINT (V 6.45a), XPREP, SHELXTL; Bruker AXS Inc. Madison, Wisconsin, USA, 2004; (b) G. M. Sheldrick, Siemens Area Detector Absorption Correction Program, University of Göttingen, Göttingen, Germany, 1994; (c)

- A. Altomare, G. Cascarano, C. Giacovazzo, A. Gualaradi, *J. Appl. Cryst.*, 1993, **26**, 343;
- (d) G. M. Sheldrick, SHELXL-97, Program for Crystal Structure Solution and Refinement; University of Göttingen, Göttingen, Germany, 1997; (e) A. L. Spek, *J. Appl. Cryst.*, 2003, **36**, 7; (f) L. J. Farrugia, WinGX—A Windows Program for Crystal Structure Analysis, *J. Appl. Crystallogr.*, 1999, **32**, 837.
15. (a) A. Chakraborty, S. Bhattacharyya, A. Hazra, A. C. Ghosh, and T. K. Maji, *Chem. Commun.*, 2016, **52**, 2831-2834; (b) S. Bhattacharyya, A. Chakraborty, K. Jayaramulu, A. Hazra and T. K. Maji, *Chem. Commun.*, 2014, **50**, 13567-13570.
16. (a) T. Tsuruoka, S. Furukawa, Y. Takashima, K. Yoshida, S. Isoda, and S. Kitagawa, *Angew. Chem. Int. Ed.*, 2009, **48**, 4739-4743; (b) W. Cho, H. J. Lee and M. Oh, *J. Am. Chem. Soc.*, 2008, **130**, 16943-16946; (c) A. Umemura, S. Diring, S. Furukawa, H. Uehara, T. Tsuruoka and S. Kitagawa, *J. Am. Chem. Soc.*, 2011, **133**, 15506-15513.

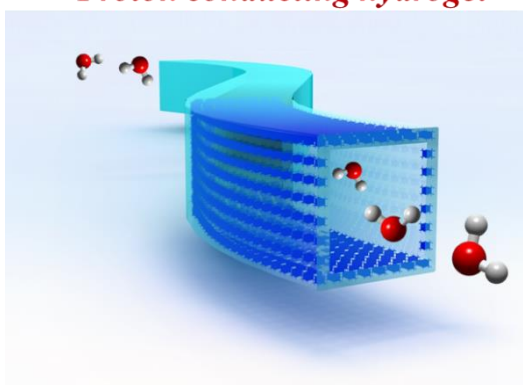
Chapter 6B

Proton Conductivity in Metal-Organic Cube Based Framework and derived Hydrogels

Abstract

This chapter reports the proton conductivity of a metal-organic cube (MOC)-based supramolecular porous framework (**1**) and MOC-based hydrogels. **1** was formed by the charge-assisted intermolecular H-bonding between anionic MOC $\{[\text{Ga}_8(\text{ImDC})_{12}]^{12-}\}$ and dimethyl ammonium cations. The proton conductivity of **1** increases with increasing relative humidity and follow the Grotthuss mechanism. Under ambient condition (25 °C and 40% RH) the proton conductivity of **1** was found to be $5.6 \times 10^{-5} \text{ S cm}^{-1}$, which increased to $1.4 \times 10^{-3} \text{ S cm}^{-1}$ at 98% RH and 25 °C. However, a drastic drop in proton conductivity of **1** was observed under anhydrous condition. This indicates that the extended H-bonded framework involving guest water molecules have an important role in facilitating the proton conductivity of **1**. Proton conductivity of two MOC-based hydrogels, **MOC-G1** and **MOC-G2**, prepared by using ammonium cations and guanidium cations as molecular binders, respectively, were also studied. The H-bonded nanostructures and the presence of additional proton carriers (ammonium cations and guanidium cations) facilitated the proton conductivity of **MOC-G1** and **MOC-G2** xerogels. Among all the three materials, the **MOC-G1** having tubular nanostructures exhibited highest proton conductivity $\sigma = 1.8 \times 10^{-2} \text{ S cm}^{-1}$ (at 25°C and 98 % RH) which is comparable with the highest reported values.

Proton conducting hydrogel



Paper based on this work:

P. Sutar and T. K. Maji, *manuscript under preparation*

6B.1 INTRODUCTION

The development of renewable clean energy has been the subject of recent attention. Among various energy storage and conversion systems, fuel cell is a promising one as it delivers energy density that are greater than conventional batteries and capacitors.¹ The proton conducting membrane is the integral part of fuel cell. Over the years, researchers have developed many organic and inorganic materials, such as sulfonated polyether ketone, oxo acid, ceramic oxides hydroxides, apatites etc. as promising candidates for proton conduction.² However, low mechanical strength and chemical stability at high temperature limits wide-spread application of these materials in proton exchange membrane fuel cell (PEMFC). The commercially used proton exchange membrane, Nafion shows appreciable proton conductivity at low temperature and high humidity.³ However, the conductivity decreases drastically with increasing temperature and decreasing humidity. Therefore, developing new proton conducting materials which operates at wide temperature and humidity range, without compromising the chemical stability and mechanical strength, is of utmost importance.⁴ Recently, porous materials such as, coordination polymers (CPs) or metal–organic frameworks (MOFs) and porous organic materials (POM) have emerged as a promising proton conducting materials.⁵ The high crystallinity, open framework architecture and high structural stability make them better candidates for studying proton conductivity and understanding its mechanisms.⁶ The reported strategies for improving the proton conductivity of these materials focused on increasing the concentration of proton carriers by controlling framework or extra-framework compositions as well as on improving proton mobility by constructing materials with desired H-bonded networks.⁷ However, synthesis of these materials usually requires greater degree of ligand deprotonation which sometimes reduces the concentration of proton carriers. For this reason, researchers have recently showed that discrete metal–organic cages which are formed through partial deprotonation of ligands, represent a superior materials for improved proton conductivity.⁸ The finite structures of metal-organic cages provide an opportunity to decorate their external surface with free functional groups (such as, carboxylate, sulfonate, imidazolate etc.) which eventually helps in fast mobility of proton carriers. Moreover, the extensive hydrogen bonding between the cage and the surrounding guest molecules also offer an efficient pathway for proton conduction. Nevertheless, low processability of solid, crystalline MOFs or cages sometimes inhibits easy fabrication of membrane which is practically used in PEMFC.

The above discussions indicate that there is no single best proton conducting material and still ample opportunities are there to improve the conductivity by designing new materials. It was envisioned that soft-hybrid materials containing self-assembled metal-organic cages inside the gel matrix could be a new promising candidate for proton conductivity as it would blend the goodness of metal organic cage (structural regularity and surface functionality) and gel (high processibility) together.

In last few years, there has been a growing interest to develop a new type of hybrid-gel by the integration of rigid metal-organic cages into the elastic polymer matrix.⁹ The metal-organic cages served as the cross-linked junction of the soft-hybrid whose mechanical properties and functionalities had been extensively tuned by choosing right combination of suitably designed polymers and metal ions.⁹ In the previous chapter it was reported that predesigned, water soluble metal-organic cubes (MOCs) whose exteriors were decorated with free carboxylate groups could also self-assemble to hydrogel in presence of positively charged, H-bond donating molecular binders.¹⁰ The self-assembly was driven by the charge-assisted H-bonding interaction between MOCs and molecular binders. The nanostructures and intrinsic properties of the hydrogel were readily tuned by selecting wide varieties of molecular binders. An important property of such MOC-based hydrogels would be their ability to conduct protons exploiting the inherent H-bonded nanostructures. To date, limited gel systems are exploited for proton conductivity and MOC-based hydrogel systems are yet to be explored for this purpose.

In this chapter, proton conductivity of a MOC-based supramolecular porous framework and MOC-based hydrogels were reported. The MOCs, $\{[\text{Ga}_8(\text{ImDC})_{12}]^{12-}$ were connected to each other by charge assisted H-bonding interaction with dimethyl ammonium cations (Me_2NH_2^+) and form supramolecular open framework $\{(\text{Me}_2\text{NH}_2)_{12}[\text{Ga}_8(\text{ImDC})_{12}] \cdot \text{DMF} \cdot 29\text{H}_2\text{O}\}$ (**1**). Abundant free carboxylate groups on the surface of each cube (24 oxide groups per cube), the guest water molecules, together with the extensive hydrogen bonds between guest water and DMA cations around the cube contributed to the high proton conductivity of **1**. Self-assembly of MOCs in presence of molecular binders such as, ammonium cation, guanidine hydrochloride, resulted in hydrogels with nanotube and nanosheet morphologies which exhibited higher proton conductivity than parent framework **1** due to high loading of proton carrier.

6B.2 EXPERIMENTAL SECTION

6B.2.1 Materials

4,5-Imidazolecarboxylic acid (4,5-ImDC), $\text{Ga}(\text{NO}_3)_3 \cdot 6\text{H}_2\text{O}$, and guanidine hydrochloride were purchased from Sigma-Aldrich chemical Co. Ltd. Ammonia solution was purchased from SDFCL. N,N-dimethylformamide and triethylamine (NEt_3) were obtained from Spectrochem. For preparing saturated salt solution NaCl, KCl and K_2SO_4 were purchased from Spectrochem.

6B.2.2 Physical measurements

Fourier transform infrared (FTIR) spectral studies were carried out by making samples with KBr pellets using Bruker FTIR spectrometer. Powder X-ray diffraction (PXRD) studies were recorded on a Bruker D8 discover instrument using $\text{Cu-K}\alpha$ radiation. Thermal stability was analysed using Mettler Toledo TGA 850 instrument under inert atmosphere in the temperature range of 25-800°C at the heating rate of 3°C per min. Morphology studies were carried out using Lica-S440I field emission scanning electron microscopy (FESEM) by placing samples on silicon wafer under vacuum with accelerating voltage of 10 kV. Energy dispersive X-ray spectroscopy (EDXS) analysis was performed with an EDAX genesis instrument attached to the FESEM column. Transmission electron microscopy (TEM) analysis was performed using JEOL JEM-3010 with accelerating voltage of 300 kV. For this analysis the samples were dispersed in ethanol and then drop casted on a carbon coated copper grid.

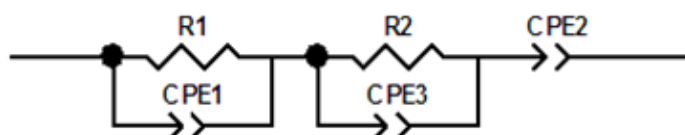
6B.2.3 Proton conductivity measurement

The ac impedance spectroscopy measurements were performed on Multi-autolab M204 and the obtained data were analysed using NOVA 2.1 software. The temperature variation ($T = 25\text{ }^\circ\text{C}$ to $35\text{ }^\circ\text{C}$) proton conductivity measurements at different relative humidity (RH) were performed inside a glass chamber containing saturated salt solution (saturated aq. solution of NaCl= 75% RH; saturated aq. solution of KCl= 85% RH; saturated aq. solution of K_2SO_4 = 98% RH). The measurements under humid conditions were performed up to a temperature of $35\text{ }^\circ\text{C}$ to maintain the humidified condition. The proton conductivity measurements under inert (Ar) atmosphere were performed after removing the guest water molecules from the material by evacuating the sample pellet for 8 hours at $100\text{ }^\circ\text{C}$. The high temperature proton conductivities of the materials were performed inside an oven in the temperature range of $30\text{ }^\circ\text{C}$ - $100\text{ }^\circ\text{C}$, without maintaining

any humidity. The proton conductivities of all the materials were estimated from the intercept of the low frequency spike with the real axis as obtained from the impedance measurements. The reproducibility of the data and the compound stability were checked by collecting the data for a single set of heating-cooling cycle on the same pellet. The equivalent circuit used for the analysis of the impedance plots is shown in Scheme 1. The data were fitted to a series combination of two resistances which were parallel with constant phase elements (CPE), using the NOVA 2.1 software. The proton conductivity (σ) at a particular humidity and temperature was finally calculated using the following equation

$$\sigma = \frac{1}{R} \times \frac{L}{A}$$

where L and A are the thickness (cm) and cross-sectional area (cm²) of the pellet respectively, and R is the bulk resistivity of the sample.



Scheme 1: Equivalent circuit used for analysing the impedance plots of **1**, **MOC-G1** and **MOC-G2**. Here, R1 and R2 correspond to the bulk and grain-boundary resistances respectively and CPE1, CPE2 and CPE3 are constant phase elements.

6B.3 RESULTS AND DISCUSSION

6B.3.1 Synthesis and structure description

Detailed synthesis and structural characterization of $\{(\text{Me}_2\text{NH}_2)_{12}[\text{Ga}_8(\text{ImDC})_{12}] \cdot \text{DMF} \cdot 29\text{H}_2\text{O}\}$ (**1**) were given in Chapter 6A. Compound **1** was synthesized from $\text{Ga}(\text{NO}_3)_3 \cdot 6\text{H}_2\text{O}$ and 4,5-imidazoledicarboxylic acid (ImDC) under solvothermal condition. The 3D supramolecular structure of compound **1** consisted of anionic metal-organic cubes, $[\text{Ga}_8(\text{ImDC})_{12}]^{12-}$ (**MOC**) which contained eight Ga^{III} ions at the vertices and twelve ImDC^{3-} at the edges of the cube (Figure 1a). The negative charges of each cube were neutralized by the surrounding dimethyl ammonium (Me_2NH_2^+ , DMA) cations which played an important role in the extending the supramolecular structure. Two DMA cations connect two adjacent cubes through

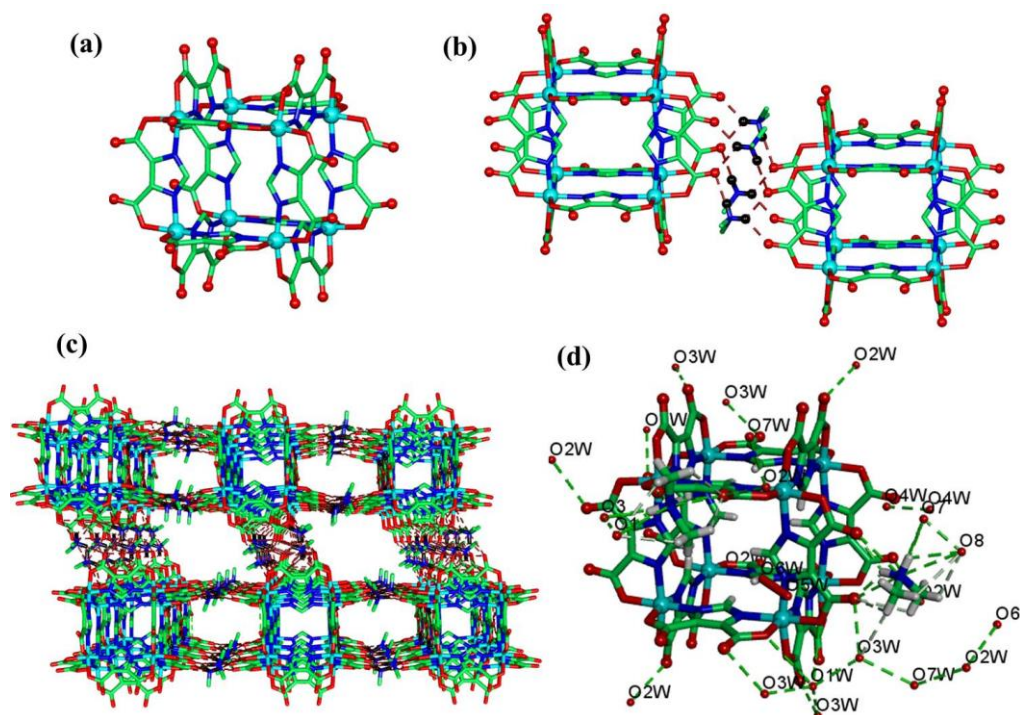


Figure 1. (a) Structure of $[\text{Ga}_8(\text{ImDC})_{12}]^{12-}$ cube, (b) two cubes are connected to each other via intermolecular H-bonding with four dimethyl ammonium cations, (c) 3D supramolecular packing of $[\text{Ga}_8(\text{ImDC})_{12}]^{12-}$ cubes in **1**, (d) The H-bonding interaction $[\text{Ga}_8(\text{ImDC})_{12}]^{12-}$ with surrounded water molecules.

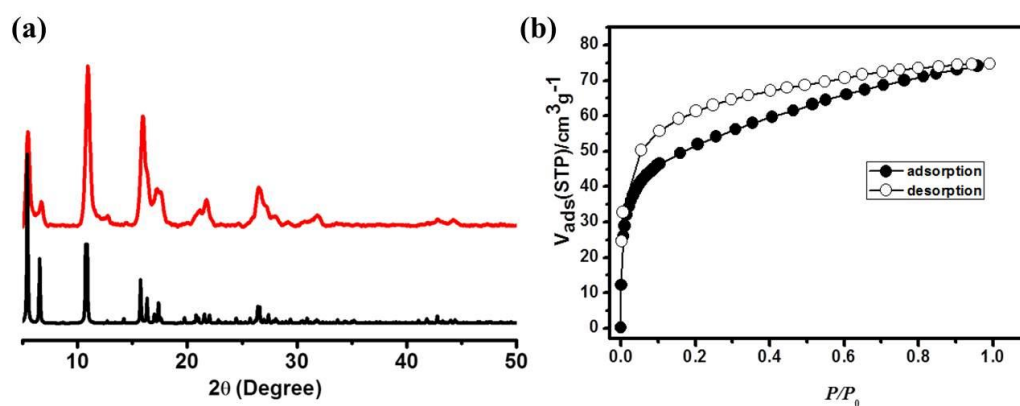


Figure 2. (a) PXRD pattern of as-synthesized **1** (red) and simulated pattern (black), (b) CO_2 adsorption isotherm de-solvated **1** at 195K.

N-H \cdots O H-bonding interaction with pendent carboxylate oxygen atoms of $[\text{Ga}_8(\text{ImDC})_{12}]^{12-}$ (Figure 1b). Each cube was concomitantly connected to six neighbouring ones through H-bonding with DMA cations and form the 3D extended structure (Figure 1c). The guest water molecules were also H-bonded with the free carboxylates of $[\text{Ga}_8(\text{ImDC})_{12}]^{12-}$ and DMA cations (Figure 1d). The phase purity of the bulk compound **1** was confirmed by matching the PXRD pattern of the as-synthesized

powder with the simulated pattern (Figure 2a). The microporosity of compound **1** was confirmed by the CO₂ adsorption isotherm at 195K which showed type I profile (Figure 2b). Such hydrogen-bonded open framework of compound **1** containing abundant protons from carboxylic acids, DMA cations and guest water molecules could provide efficient pathway for proton conduction.

6B.3.2 Characterization of MOC-G1 hydrogels

Compound **1** was highly soluble in water. In aqueous solution the anionic cubes [Ga₈(ImDC)₁₂]¹²⁻ remain stable and solvated as confirmed by HRMS and ¹HNMR analysis (discussed in Chapter 6a). The **MOC-G1** hydrogel was synthesized by adding aq. NH₃ solution into the aqueous solution of **1**. The gelation was driven by charge-assisted H-bonding interaction between peripheral carboxylate groups of **MOC** and ammonium cations. Comparison of the FTIR spectra of **1** and **MOC-G1** xerogel exhibited a decrease in COO⁻ asymmetric and symmetric stretching frequency from 1678 cm⁻¹ to 1660 cm⁻¹ and 1474 cm⁻¹ to 1472 cm⁻¹, respectively (Figure 3a). The difference between asymmetric and symmetric stretch (Δv_{a-s}) was found to be 204 cm⁻¹ and 188 cm⁻¹ for **1** and **MOC-G1** xerogel, respectively. Such significant decrease in Δv_{a-s} indicated the presence of strong intermolecular H-bonding between the carboxylate oxygen of **MOC** and ammonium cations in **MOC-G1** assembly. The PXRD of **1** and **MOC-G1** xerogel showed no significant change suggesting the structure of **MOCs** was intact **MOC-G1** (Figure 3b). FESEM and TEM images of **MOC-G1** xerogel showed the formation of

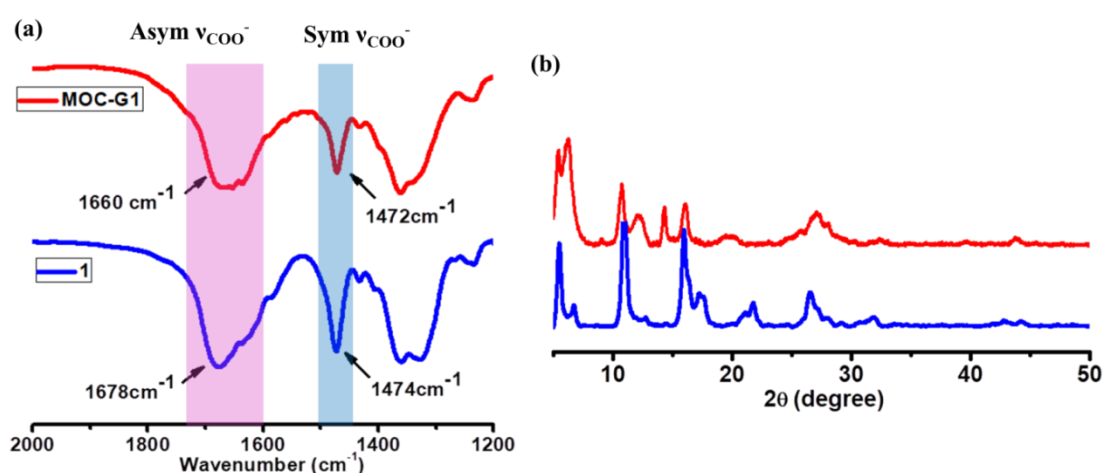


Figure 3. (a) Comparison of the FTIR spectra of **1** (blue) and **MOC-G1** (red) highlighting the asymmetric and symmetric COO⁻ stretching frequency, (b) Comparison of the PXRD pattern of **1** (blue) and **MOC-G1** (red).

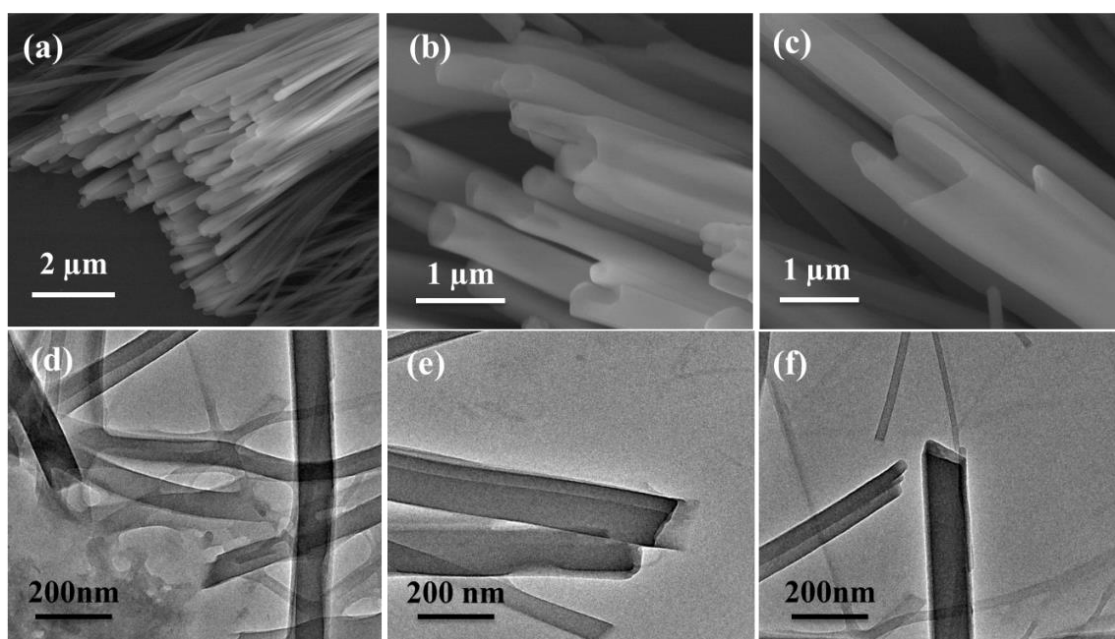


Figure 4. (a), (b), (c) FESEM images **MOC-G1** showing the formation of nanotubes, (d), (e), (f) TEM images **MOC-G1**.

nanotubes which were several micrometer ($3\ \mu\text{m} - 8\ \mu\text{m}$) long with diameters in 500-600 nm range (Figure 4). Interestingly, the TEM and FESEM images indicated rectangular cross-section of the nanotubes (Figure 4c and 4f). The wall thickness of the nanotubes was in 9-10 nm range.

6B.3.3 Characterization of MOC-G2 hydrogels

Next, **MOC-G2** hydrogel was prepared by adding aq. solution of guanidine hydrochloride (0.1 M) into the aq. solution of **1**. Comparison of the FTIR spectra of **1** and **MOC-G2** xerogel showed a decrease in COO^- asymmetric and symmetric stretching frequency from $1678\ \text{cm}^{-1}$ to $1665\ \text{cm}^{-1}$ and $1474\ \text{cm}^{-1}$ to $1472\ \text{cm}^{-1}$, respectively (Figure 5a). $\Delta\nu_{\text{a-s}}$ value was found to be $118\ \text{cm}^{-1}$ for **MOC-G2** xerogel. Such decrease in $\Delta\nu_{\text{a-s}}$ value in **MOC-G2** xerogel indicated intermolecular H-bonding between the carboxylate oxygen of **MOC** and guanidium cations drove the self-assembly in **MOC-G2** hydrogel. The PXRD pattern of **MOC-G2** xerogel showed similar diffraction peaks as that of as-synthesized **1** indicating structural integrity of **MOCs** in **MOC-G2** hydrogel (Figure 5b). However, the change in peak intensity and appearance of some new peaks in **MOC-G2** suggested different packing of **MOCs** after binding with guanidium ions. FESEM and TEM images of **MOC-G2** xerogel show the formation of uniformly distributed micron size nanosheets (Figure 6).

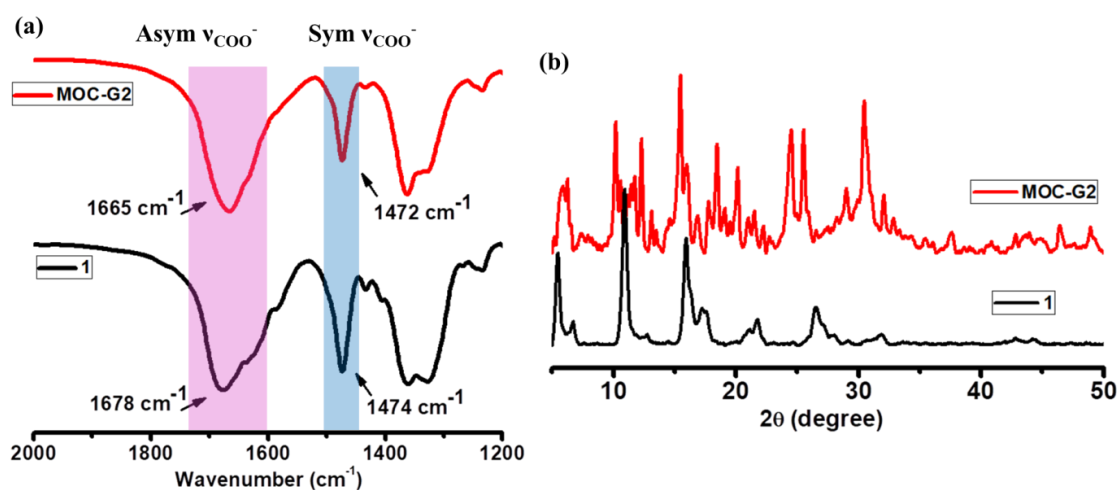


Figure 5. (a) Comparison of the FTIR spectra of **1** (black) and **MOC-G2** (red) highlighting the asymmetric and symmetric COO⁻ stretching frequency, (b) Comparison of the PXRD pattern of **1** (black) and **MOC-G2** (red).

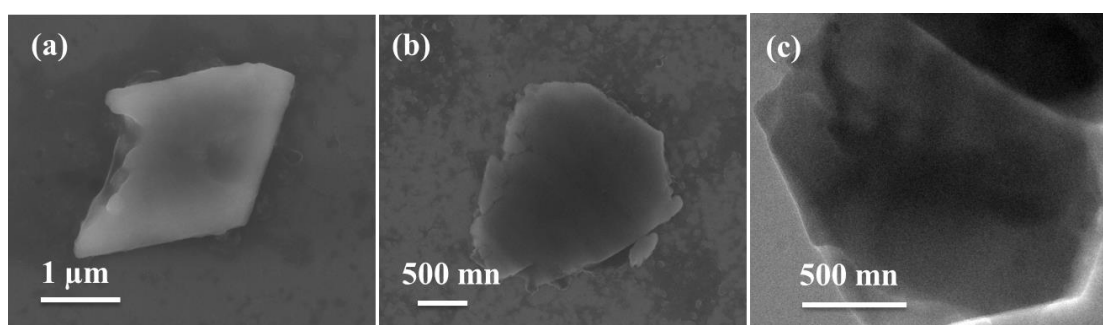


Figure 6. (a), (b) FESEM images and (c) TEM image of **MOC-G2** xerogel.

6B.3.4 Proton conductivity of **1**

It was envisioned that the extended H-bonded structure of **1** involving carboxylate groups, DMA cations and water molecules could provide efficient pathways for proton conduction. The proton conductivity of **1** was measured using the AC impedance spectroscopy. First, the pelletized sample was sandwiched between two gold-coated stainless steel electrodes and kept inside a closed glass chamber. The electrodes were then connected to electrochemical work station (Figure 7). The pellet was scanned in the frequency range of 10⁻² to 10⁶ Hz to get the Nyquist plots which were later fitted to the equivalent circuit to obtain the proton conductivity values. The Nyquist plot of the as-synthesized **1** under ambient condition (40% RH and T= 25 °C) is shown in Figure 8a. The semi-circle in the high frequency region indicated bulk and grain boundary resistance, whereas the tail at low frequency corresponded to the mobile ions that are

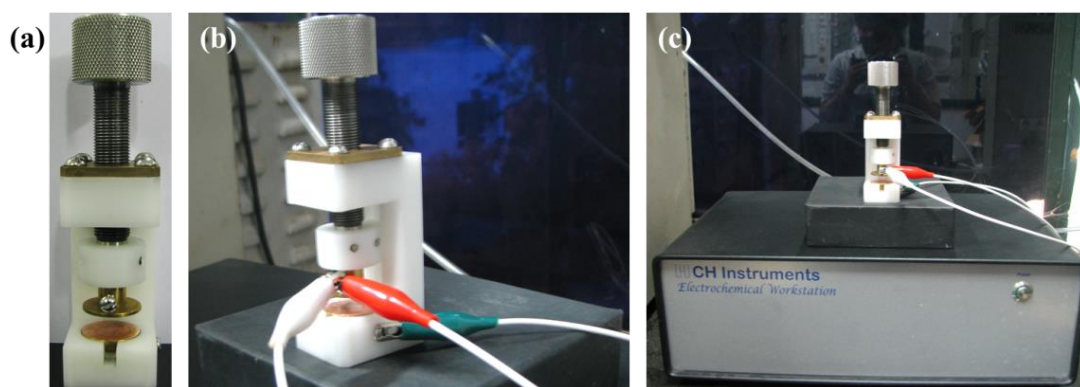


Figure 7. (a) The picture of gold-coated stainless steel electrode used for measuring proton conductivity, (b) One electrode is connected to working electrode connector (green) and other electrode is connected to reference (red) and counter (white) electrode connector, (c) the whole proton conductivity set-up.

blocked by electrode-electrolyte interface. The proton conductivity of the as-synthesized **1** was found to be $2.3 \times 10^{-5} \text{ S cm}^{-1}$ under ambient condition. Upon increasing the temperature from $25 \text{ }^\circ\text{C}$ to $100 \text{ }^\circ\text{C}$ (without maintaining any particular RH) the proton conductivity of **1** decreased and the values were found to be 2.7×10^{-6} , 6.1×10^{-7} , 2.9×10^{-7} , 9.9×10^{-8} , 3.6×10^{-8} , 2.5×10^{-8} and 1.0×10^{-8} at $40 \text{ }^\circ\text{C}$, $50 \text{ }^\circ\text{C}$, $60 \text{ }^\circ\text{C}$, $70 \text{ }^\circ\text{C}$, $80 \text{ }^\circ\text{C}$, $90 \text{ }^\circ\text{C}$ and $100 \text{ }^\circ\text{C}$, respectively (Figure 8b). Such decrease in proton conductivity probably resulted because at high temperature the number of H-bonded water molecules present inside the channels of compound **1** decreased. These observation motivated us to measure the proton conductivity of **1** under humid condition (RH=75%, 85% and 98%). The sample pellet was exposed to a particular humidity for 4-5 hours prior to the impedance measurement. Interestingly, the proton conductivity of **1** increased drastically with increasing RH and the values were 5.6×10^{-5} (40% RH), 1.8×10^{-4} (75% RH), 4.6×10^{-4} (85% RH), $1.4 \times 10^{-3} \text{ Scm}^{-1}$ (98% RH) at 25°C (Figure 9). The room temperature (25°C) proton conductivity value of **1** ($1.4 \times 10^{-3} \text{ Scm}^{-1}$) under 98% RH is comparable with some of the highest reported values. No noticeable change in PXRD pattern of **1** was observed before and after the impedance measurement which indicated structural integrity of **1** during the measurement (Figure 10). To obtain a clear insight of the mechanism of proton conductivity under humid condition, temperature-dependent conductivity measurements (both heating and cooling process) were performed in the temperature range of $23\text{--}36 \text{ }^\circ\text{C}$ (Figure 11a-c). On increasing the temperature the conductivity of **1** (under 75%, 85% and 98%) increased linearly and the trend was reversible while

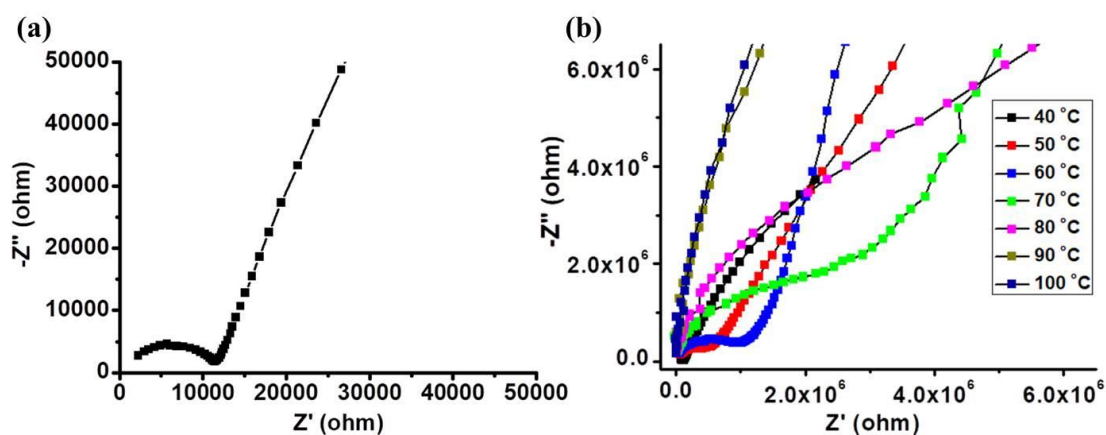


Figure 8. (a) Nyquist plot of **1** at 25 °C and 40 % RH, (b) Nyquist plots of **1** at 40 °C, 50 °C, 60 °C, 70 °C, 80 °C, 90 °C and 100 °C without maintaining any particular RH.

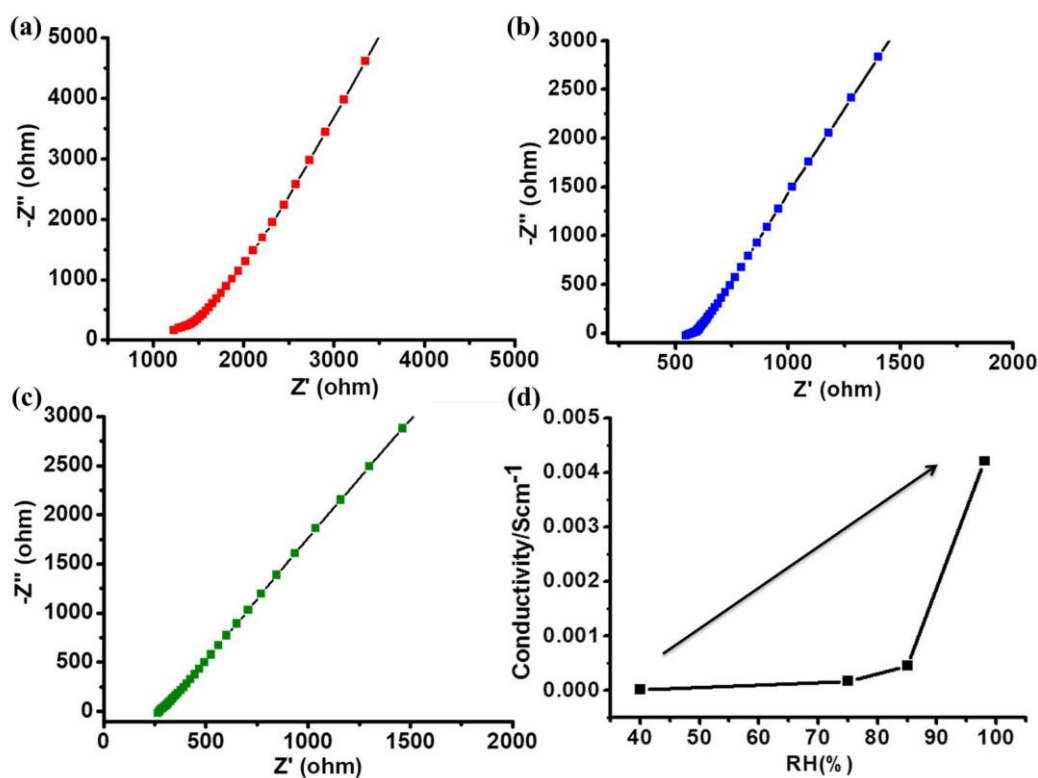


Figure 9. (a), (b) and (c) Nyquist plots of **1** at 75%, 85% and 98% RH, respectively and 25°C, (d) The plot of proton conductivity of **1** vs RH (%).

decreasing the temperature at the same rate. The calculated activation energy values of **1** were 0.26 eV, 0.08 eV and 0.083 eV at 75%, 85% and 98% RH, respectively which were well below the energy threshold (0.5 eV), indicating Grotthuss mechanism of proton conductivity in **1** (Figure 11d- f). Moreover, the decrease in activation energy with rise in RH indicated facile proton conduction at higher RH. To prove the importance of guest

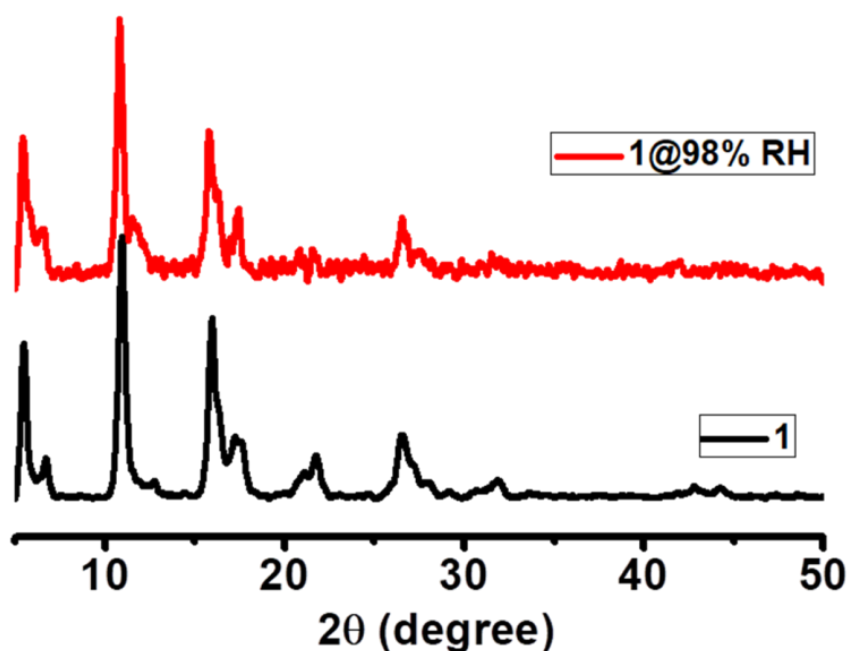


Figure 10. PXRD patterns of as-synthesised **1** before (black) and after (red) the impedance measurement at 98% RH.

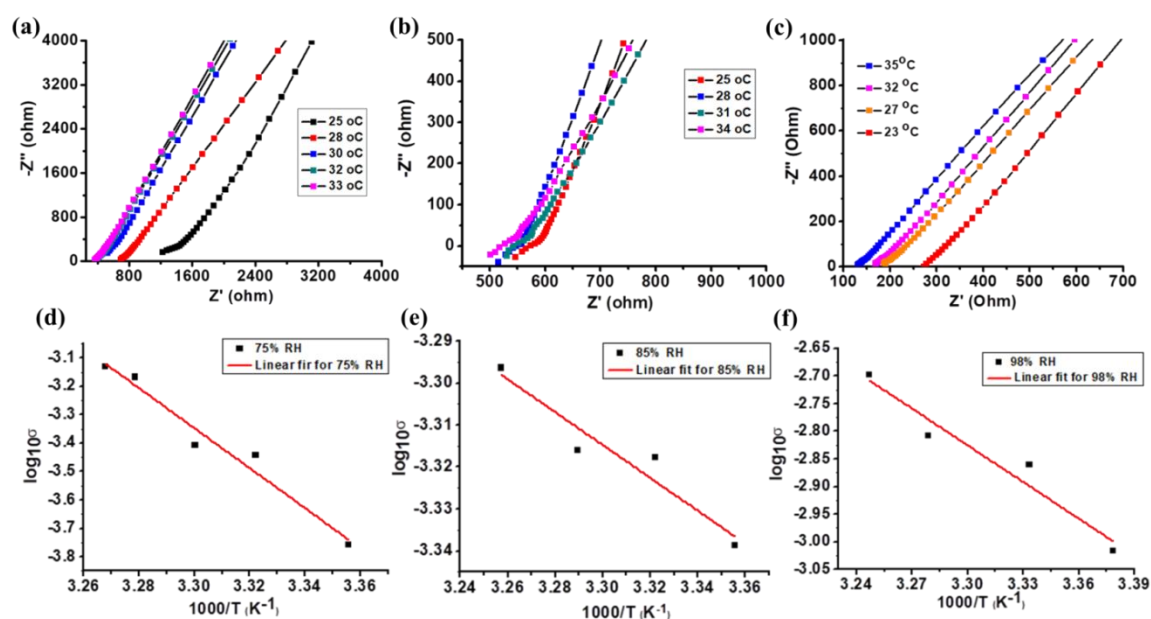


Figure 11. (a) Nyquist plots of **1** in the temperature range of (25–33) °C under 75 % RH, (b), Nyquist plots of **1** in the temperature range of (25–34) °C under 85, (c) Nyquist plots of **1** in the temperature range of (23–35) °C under 98% RH, (d), (e), (f) Arrhenius plots of **1** under 75%, 85% and 98% RH conditions, respectively. Black plots indicate experimental data and red line indicates linear fits of the experimental data.

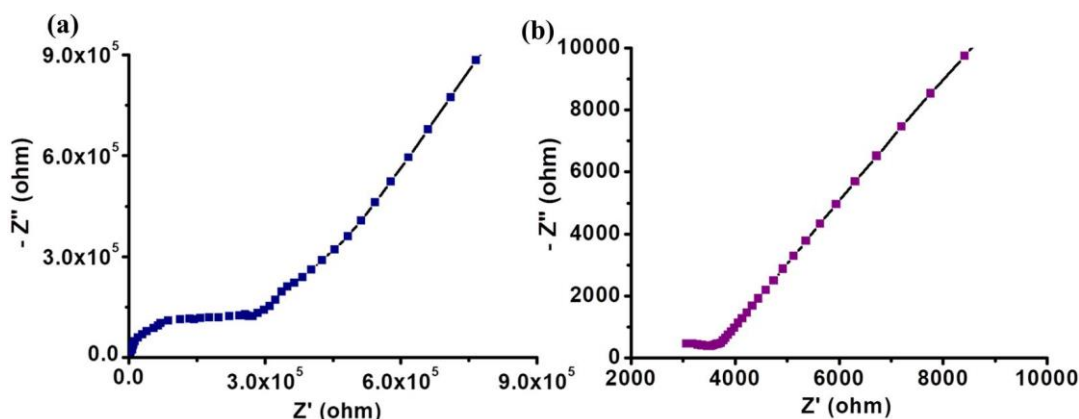


Figure 12. (a) Nyquist plot of **1'** at 25 °C, (b) Nyquist plot of re-hydrated **1'** at 25 °C.

water molecules, the proton conductivity of de-solvated **1** (**1'**) was also measured. First, the sample was evacuated at 100 °C for 6 hours to ensure removal of guest water molecules. Then the pellet was prepared and kept inside an argon chamber for 24 hours. The proton conductivity of **1'** dropped down to $4.0 \times 10^{-7} \text{ S cm}^{-1}$ at 25 °C under inert condition (Figure 12a). However, after exposing the pellet to 40 % RH, it re-gained the conductivity values of $8.7 \times 10^{-5} \text{ S cm}^{-1}$ (Figure 12b). This clearly indicated the role of guest water molecules in the proton conductivity of **1**. From the crystal structure of **1**, it is evident that many guest water molecules were loosely H-bonded with carboxylate groups of **MOCs** and **DMA** cations. These water molecules probably facilitated the proton conduction of **1**. However, activating the pellet under inert atmosphere removed the loosely bounded water molecules and affected the proton conduction pathway.

6B.3.5 Proton conductivity of MOC-G1

Next, the proton conductivities of **MOC-G1** xerogel at different temperature and humidity condition were measured. It was envisioned that the hydrogen bonded nanotubes of **MOC-G1** could exhibit facile proton transport due to the presence of NH_4^+ and **DMA** cations which can act as good proton carrier. The Nyquist plots of the **MOC-G1** xerogel showed the semi-circle in the high-frequency region and a tail in the low-frequency region, as observed in the case of **1**. At 25°C and 40% RH the proton conductivity of **MOC-G1** xerogel was calculated to be $6.0 \times 10^{-5} \text{ Scm}^{-1}$ which was higher than the conductivity of **1** under the similar condition (Figure 13a). The extended H-bonding interaction of **MOC** with ammonium and dimethyl ammonium cations in **MOC-G1** probably facilitated the proton conduction. However, the proton conductivity of the material decreased drastically with increasing temperature. At 40°C, 50 °C, 60°C, 70 °C

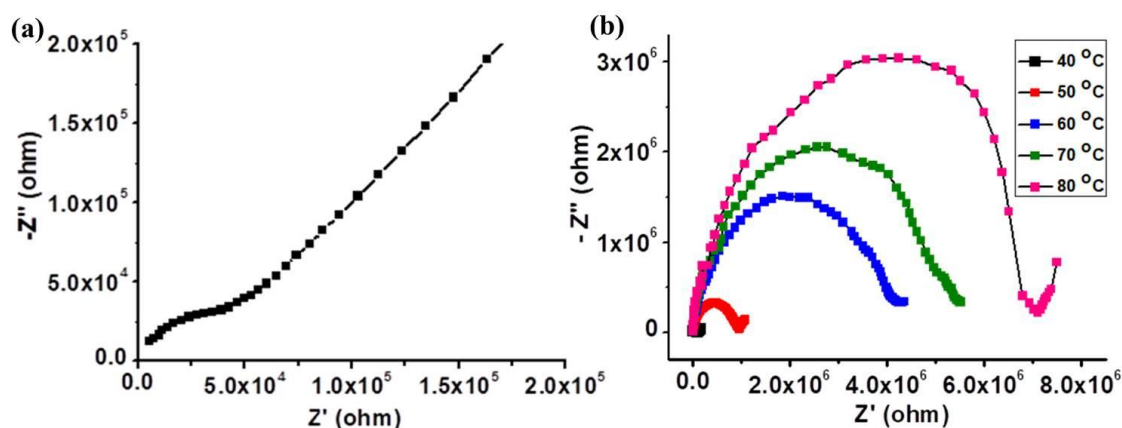


Figure 13. (a) The Nyquist plot of **MOC-G1** xerogel at 40 % RH and 25 °C, (b) The Nyquist plots of **MOC-G1** xerogel at T= 40°C, 50 °C, 60°C, 70 °C and 80°C (without maintaining any particular RH%).

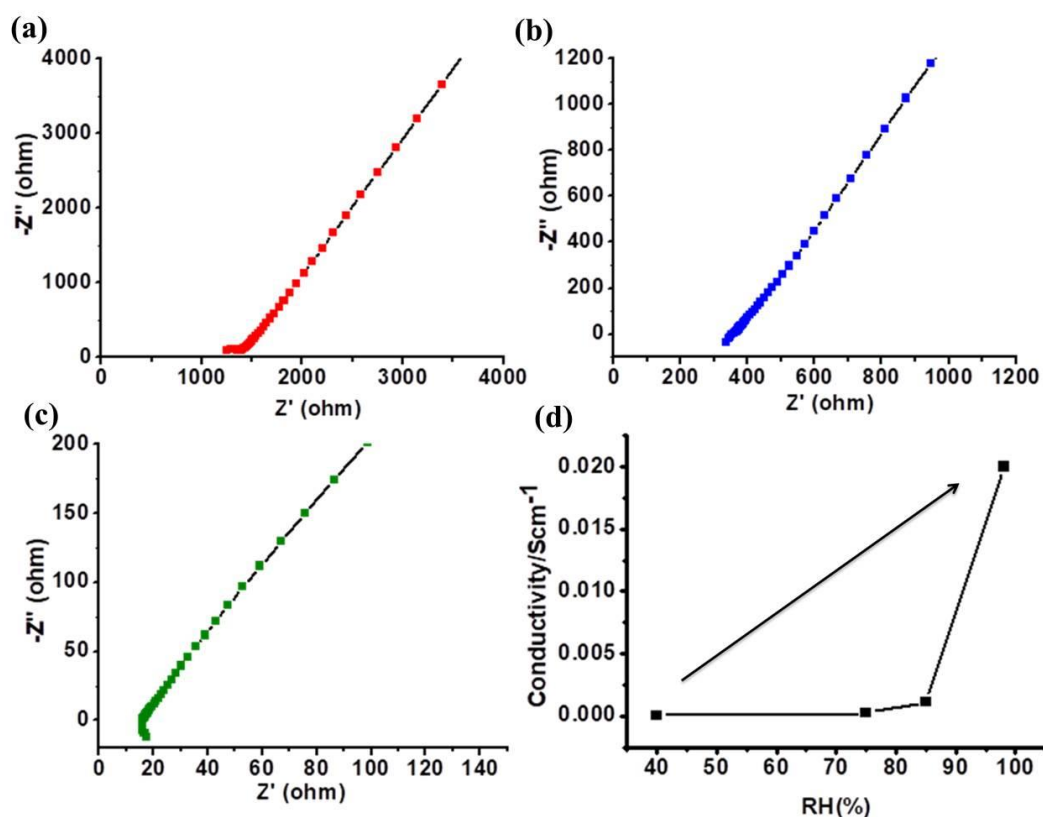


Figure 14 (a), (b) and (c) Nyquist plots of **MOC-G1** at 75%, 85% and 98% RH, respectively and 25 °C and, (d) The plot of proton conductivity of **MOC-G1** vs RH (%).

and 80°C the proton conductivity of **MOC-G1** xerogel was found to be 2.7×10^{-6} , 2.7×10^{-7} , 6.3×10^{-8} , 4.8×10^{-8} and 3.7×10^{-8} S cm⁻¹ (Figure 13b). Such decrease in proton conductivity indicated the importance of H-bonded water molecules inside the nanotubes

in the proton conduction. The proton conductivity of **MOC-G1** was also measured under humid condition by exposing the sample at different RH (75%, 85% and 98%). As expected, with increasing RH% the proton conductivity of **MOC-G1** increased drastically (Figure 14). At 25°C it exhibited the proton conductivity values of 2.0×10^{-4} , 8.1×10^{-4} , $1.8 \times 10^{-2} \text{ S cm}^{-1}$ under 75%, 85% and 98% RH, respectively (Figure 14a-c). The room temperature (25°C) proton conductivity value of **MOC-G1** ($1.8 \times 10^{-2} \text{ Scm}^{-1}$) under 98%

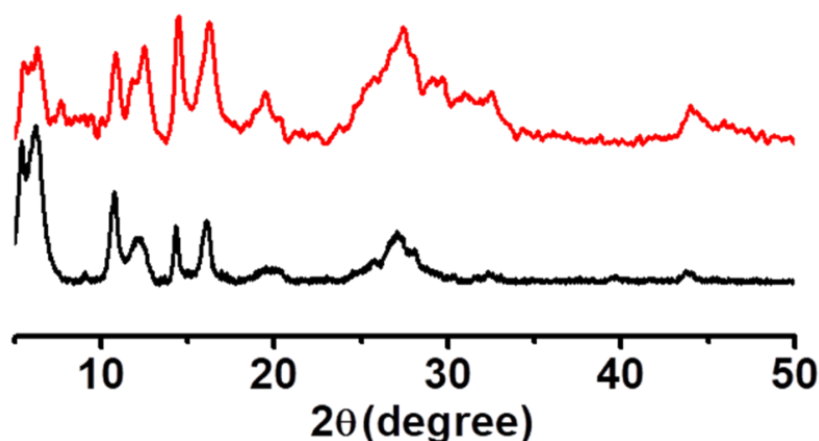


Figure 15. PXRD patterns of as-synthesised **MOC-G1** before (black) and after (red) the impedance measurement at 98% RH.

RH was comparable with some of the highest reported values of metal-organic hybrid materials. Moreover, no noticeable change in PXRD pattern of **MOC-G1** was observed before and after the impedance measurement which indicated structural integrity of **MOC-G1** during the measurement (Figure 15). To obtain a clear insight of the mechanism of proton conductivity under humid condition, the temperature dependent conductivity measurements (both heating and cooling process) were performed in the temperature range of 23–36 °C (Figure 16a-c). On increasing the temperature the conductivity of **MOC-G1** (under RH= 75%, 85% and 98%) increased linearly and the trend was reversible while decreasing the temperature at the same rate (Figure 16d-f). The calculated activation energy values of **MOC-G1** were 0.093 eV, 0.08 eV and 0.037 eV at 75%, 85% and 98% RH, respectively. Such low activation energy indicated that Grotthuss mechanism of proton conductivity was operating in **MOC-G1** xerogel. The decrease in activation energy with rise in RH% indicated facile proton conduction at higher RH%. Interestingly, the activation energy for **MOC-G1** xerogel was lower than that of **1**, indicating facile proton conduction in **MOC-G1** due to the presence of ammonium cations. To prove the importance of guest water molecules, the proton

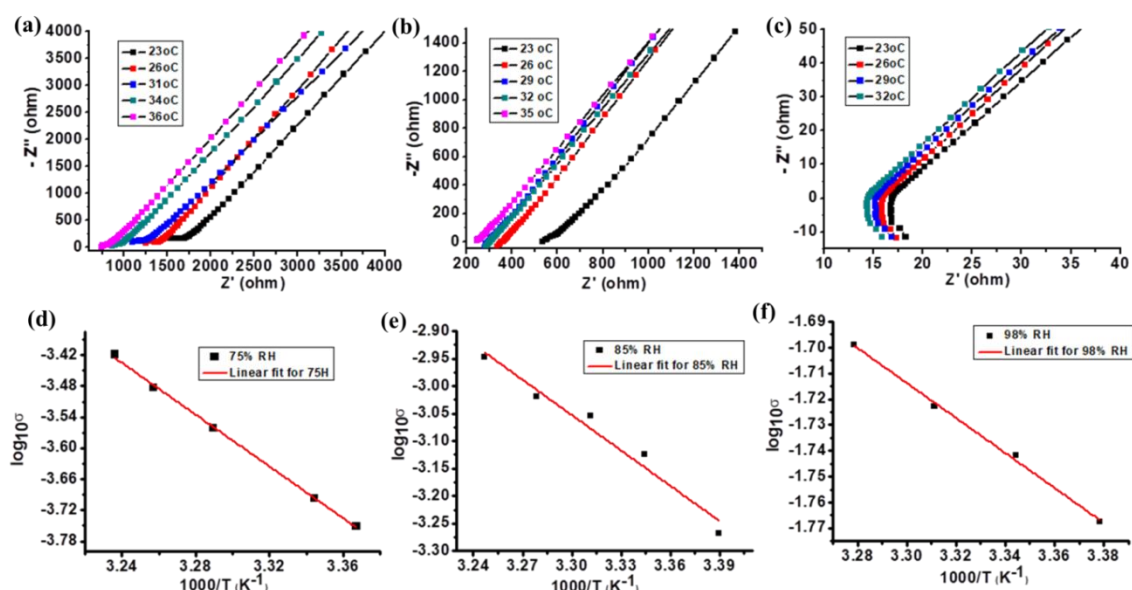


Figure 16. (a) Nyquist plots of **MOC-G1** in the temperature range of (25–33) °C under 75 % RH, (b), Nyquist plots of **MOC-G1** in the temperature range of (25–34) °C under 85, (c) Nyquist plots of **MOC-G1** in the temperature range of (23–35) °C under 98% RH, (d), (e), (f) Arrhenius plots of **MOC-G1** under 75%, 85% and 98% RH conditions, respectively. Black plots indicate experimental data and red line indicates linear fits of the experimental data.

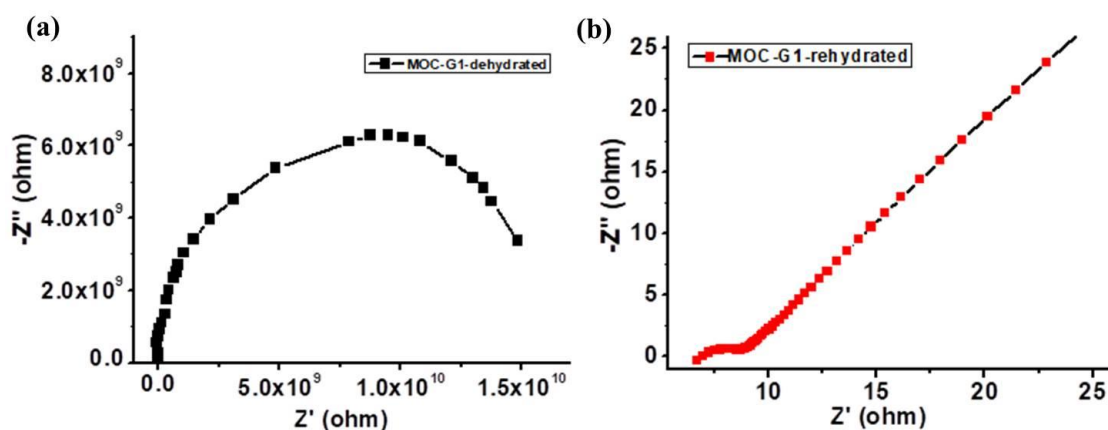


Figure 17. (a) Nyquist plot of **MOC-G1'** at 25 °C, (b) Nyquist plot of re-hydrated **MOC-G1'** at 25 °C.

conductivity of de-solvated **MOC-G1** xerogel (**MOC-G1'**) was measured under argon atmosphere after evacuating the pellet at 100 °C for 6 hours. The proton conductivity of **MOC-G1'** dropped down to $6.5 \times 10^{-11} \text{ S cm}^{-1}$ at 25 °C under inert condition (Figure 17a). However, after exposing the pellet to 85 % RH, it re-gained the conductivity values

of $3.2 \times 10^{-3} \text{ S cm}^{-1}$ (Figure 17b). This clearly indicated the important role of guest water molecules in the proton conductivity of **MOC-G1**.

6B.3.6 Proton conductivity of MOC-G2

Next, the proton conductivity of **MOC-G2** xerogel was measured at different temperature and humidity. We envisioned that the guanidium cations which acted as a molecular binder, could facilitate the proton conductivity in **MOC-G2** xerogel. The Nyquist plots of **MOC-G2** xerogel showed two well-defined semi-circles in higher frequency region and a small tail in the low-frequency region. At 25 °C and 40% RH the proton conductivity of **MOC-G2** xerogel was calculated to be $2.27 \times 10^{-7} \text{ Scm}^{-1}$ (Figure 18a). Surprisingly, the value of proton conductivity was less compared to the as-synthesized **1**. However, we could not perform the proton conductivity measurement at high temperature as the pallet was not stable after 35 °C. The proton conductivity of **MOC-G2** xerogel was measured under different humidity conditions (RH= 75%, 85%). As expected, with increasing relative humidity the proton conductivity increased and the values were found to be $6.57 \times 10^{-5} \text{ S cm}^{-1}$ and $7.76 \times 10^{-3} \text{ S cm}^{-1}$ under RH= 75% and 85%, respectively at 25 °C (Figure 18b,c). However, we could not carry out the measurement at

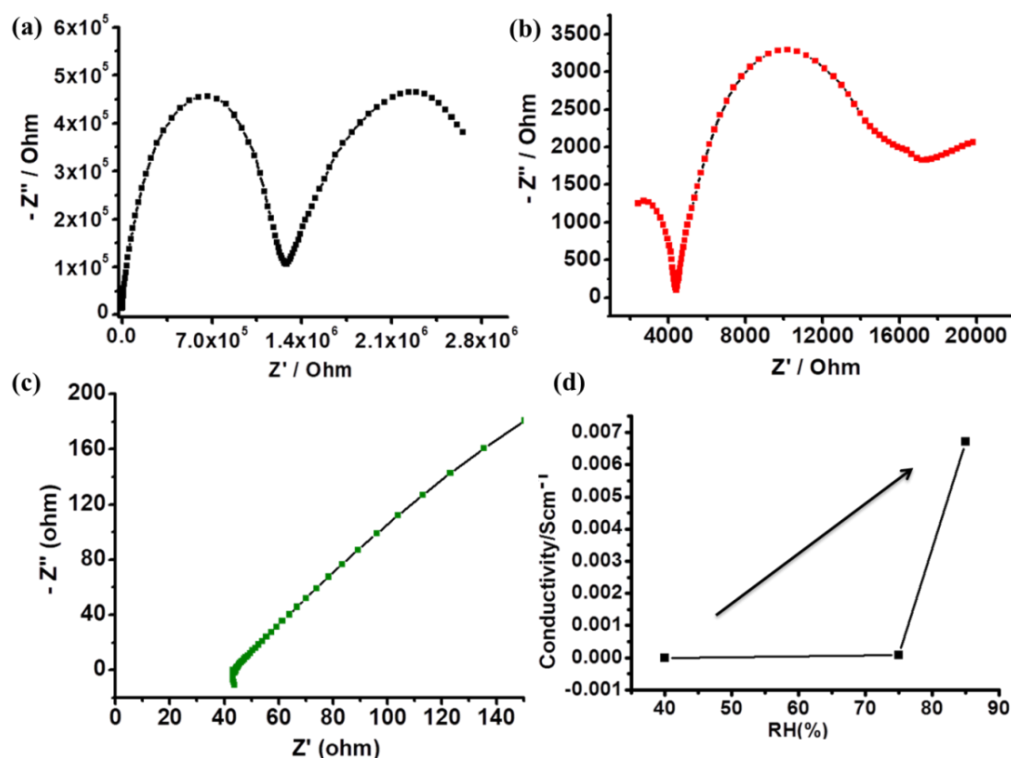


Figure 18. (a), (b) and (c) Nyquist plots of **MOC-G2** at 25 °C and 40%, 75% and 85% RH, respectively, (d) The plot of proton conductivity of **MOC-G2** vs RH (%).

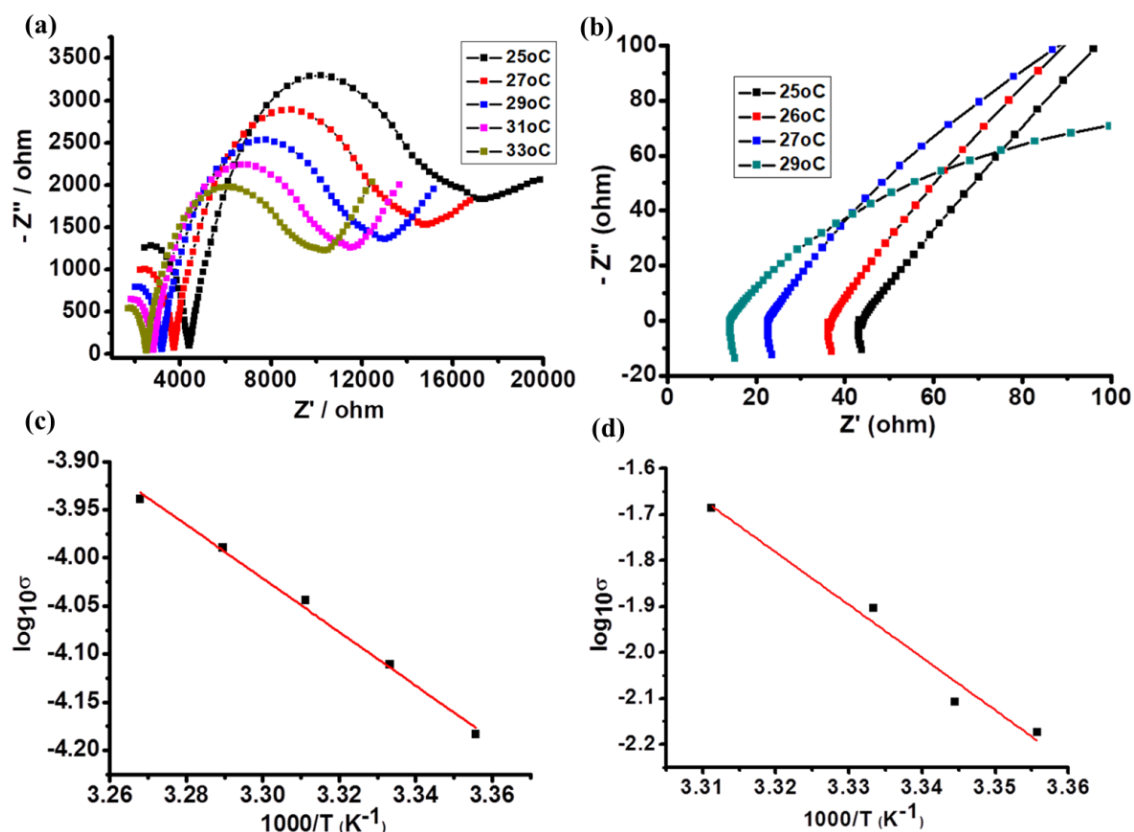


Figure 19. (a) Nyquist plots of **MOC-G2** in the temperature range of (25–33) °C under 75 % RH, (b), Nyquist plots of **MOC-G2** in the temperature range of (25–29) °C under 85% RH, (c) and (d) Arrhenius plots of **MOC-G2** under 75% and 85% and RH conditions, respectively. Black square symbols indicate experimental data and red line indicates linear fits of the experimental data.

98% RH because the pallet was fragile at high humidity. The proton conductivity of **MOC-G2** increased with increasing RH% (Figure 18d). No significant change in PXRD pattern of **MOC-G2** xerogel was observed before and after the impedance measurement, indicating stability of **MOC-G2** xerogel during the measurement. To know the mechanism of proton conductivity in **MOC-G2** under humid condition, temperature dependent conductivity (both heating and cooling process) was measured in the temperature range of 25 °C-33 °C (Figure 19a-b). On increasing the temperature the conductivity of **MOC-G2** (under RH= 75% and 85%) increased linearly and the trend was reversible while decreasing the temperature at the same rate (Figure 19c-d). The activation energy values, calculated from Arrhenius plots were 0.43 eV and 0.24 eV at 75% and 85% RH, respectively. The decrease in activation energy with increase in RH% indicated facile proton conduction at higher RH%.

6B.4 SUMMARY

In summary, we have synthesized a **MOC**-based supramolecular porous framework and **MOC**-based hydrogels which exhibited good proton conductivity at room temperature. The proton conductivity of **1** increased with increasing humidity. The highest value of proton conductivity of **1** was found to be $1.4 \times 10^{-3} \text{ S cm}^{-1}$ at 98 % RH and 25 °C. The presence of H-bonded guest water molecules played important role in facilitating the proton conductivity of **1**. Hence, under anhydrous condition the proton conductivity dropped drastically. Moreover, two **MOC**-based hydrogels, **MOC-G1** and **MOC-G2**, were prepared by using ammonium cations and guanidium cations as molecular binders. The H-bonded nanostructures as well as the presence of additional proton carriers (ammonium cations and guanidium cations) facilitated the proton conductivity of **MOC-G1** and **MOC-G2** xerogels. Among all the three materials, **MOC-G1** having H-bonded tubular nanostructure showed the highest proton conductivity and the value was $1.8 \times 10^{-2} \text{ S cm}^{-1}$ which was comparable with the highest reported values.

6B.5 REFERENCES

- (a) M. Winter and R. J. Brodd, *Chem. Rev.*, 2004, **104**, 4245-4270; (b) C. Laberty-Robert, K. Valle', F. Pereirab and C. Sanchez, *Chem. Soc. Rev.*, 2011, **40**, 961-1005; (c) C. Jiang, J. Ma, G. Corre, S. L. Jaina and J. T. S. Irvine, *Chem. Soc. Rev.*, 2017, **46**, 2889-2912; (d) C. -Y. Wang, *Chem. Rev.* 2004 **104**, 4727-4766; (e) R. Borup, J. Meyers, B. Pivovar, Y. S. Kim, R. Mukundan, N. Garland, D. Myers, M. Wilson, F. Garzon, D. Wood, P. Zelenay, K. More, K. Stroh, T. Zawodzinski, J. Boncella, J. E. McGrath, M. Inaba, K. Miyatake, M. Hori, K. Ota, Z. Ogumi, S. Miyata, A. Nishikata, Z. Siroma, Y. Uchimoto, K. Yasuda, K. Kimijima, and N. Iwashita, *Chem. Rev.*, 2007, **107**, 3904-3951; (f) Shun-Li Li and Qiang Xu, *Energy Environ. Sci.*, 2013, **6**, 1656-1683.
- (a) J. A. Asensio, E. M. Sánchez and P. Gómez-Romero, *Chem. Soc. Rev.*, 2010, **39**, 3210-3239; (b) S. R. Narayanan, S. -P. Yen, L. Liu, and S. G. Greenbaum, *Phys. Chem. B*, 2006, **110**, 3942-3948; (c) "Proton Conductors: Solids, Membranes and Gels-Materials and Devices": P. Colomban in *Chemistry of Solid State Materials*, Vol. 2, Cambridge University Press, Cambridge, 1992; (d) K. D. Kreuer, *Chem. Mater.*, 1996, **8**, 610-641; (e) K. D. Kreuer, S. J. Paddison, E. Spohr and M. Schuster, *Chem. Rev.* 2004, **104**, 4637-4678; (f) S. H. Kim, A. Mehmood, Y. Ahn, H.-S. Kim, H. Y. Ha, D. Kim and O. H. Han, *J. Electroanal. Chem.*, 2016, **782**, 32-35; (g) C. H. Lee, H. B. Park, Y. M. Lee and R. D.

- Lee, *Ind. Eng. Chem. Res.*, 2005, **44**, 7617–7626; (h) Y. –L. Liu, *Polym. Chem.*, 2012, **3**, 1373–1383; (i) S. P. Jiang, *J. Mater. Chem. A*, 2014, **2**, 7637–7655; (i) R. He, Q. Li, G. Xiao and N. J. Bjerrum, *J. Membr. Sci.*, 2003, **226**, 169–184.
3. (a) S. J. Paddison, *Annu. Rev. Mater. Res.*, 2003, **33**, 289 – 319; (b) S. J. Peighambardoust, S. Rowshanzamir, M. Amjadi, *Int. J. Hydrogen Energy.*, 2010, **35**, 9349 – 9384.
4. (a) T. Bayer, B. V. Cunning, R. Selyanchyn, M. Nishihara, S Fujikawa, K. Sasaki and S. M. Lyth, *Chem. Mater.*, 2016, **28**, 4805–4814; (b) V. Nalini, R. Haugrud and T. Norby, *Solid. State. Ion.*, 2010, **181**, 510–516; (c) R. Haugrud and T. Norby, *Solid. State. Ion.*, 2006, **177**, 1129–1135; (d) M. Moradi, A. Moheb, M. Javanbakht and K. Hooshyari, *Int. J. Hydrogen Energy.*, 2016, **41**, 2896–2910.
5. (a) M. Yoon, K. Suh, S. Natarajan and K. Kim, *Angew. Chem. Int. Ed.*, 2013, **52**, 2688 – 2700; (b) S. S. Nagarkar, S. M. Unni, A. Sharma, S. Kurungot, and S. K. Ghosh, *Angew. Chem. Int. Ed.* 2014, **53**, 2638 –2642; (c) P. Ramaswamy, R. Matsuda, W. Kosaka, G. Akiyama, H. J. Jeona and S. Kitagawa, *Chem. Commun.*, 2014, **50**, 1144–1146; (d) P. Ramaswamy, N. E. Wong and G. K. H. Shimizu, *Chem. Soc. Rev.*, 2014, **43**, 5913–5932; (e) V. G. Ponomareva, K. A. Kovalenko, A. P. Chupakhin, D. N. Dybtsev, E. S. Shutova and V. P. Fedin, *J. Am. Chem. Soc.*, 2012, **134**, 15640–15643; (f) D. B. Shinde, H. B. Aiyappa, M. Bhadra, B. P. Biswal, P. Wadge, S. Kandambeth, B. Garai, T. Kundu, S. Kurungot and R. Banerjee, *J. Mater. Chem. A.*, 2016, **4**, 2682–2690; (g) H. Xu, S. Tao and D. Jiang, *Nature Mater.*, 2016, **15**, 722–726; (h) H. Ma, B. Liu, B. Li, L. Zhang, Y.-G. Li, H.-Q. Tan, H.-Y. Zang and G. Zhu, *J. Am. Chem. Soc.*, 2016, **138**, 5897–5903; (i) S. Chandra, T. Kundu, K. Dey, M. Addicoat, T. Heine and R. Banerjee, *Chem. Mater.*, 2016, **28**, 1489–1494; (j) A. Karmakar, R. Illathvalappil, B. Anothumakkool, A. Sen, P. Samanta, A. V. Desai, S. Kurungot, S. K. Ghosh, *Angew. Chem. Int. Ed.*, 2016, **55**, 10667- 10671.
6. (a) X. Meng, H.-N. Wang, S.-Y. Song and H.-J. Zhang, *Chem. Soc. Rev.*, 2017, **46**, 464–480; (b) B. Joarder, J. –B. Lin, Z. Romero and G. K. H. Shimizu, *J. Am. Chem. Soc.*, 2017, **139**, 7176–7179; (c) P. G. M. Mileo, S. Devautour-Vinot, G. Mouchaham, F. Faucher, N. Guillou, A. Vimont, C. Serre, and G. Maurin, *J. Phys. Chem. C.*, 2016, **120**, 24503–24510; (d) Fan Yang, Gang Xu, Yibo Dou, Bin Wang, Heng Zhang, Hui Wu, Wei Zhou, Jian-Rong Li & Banglin Chen, *Nat. Energy.*, 2017, **2**, 877–883; (e) W. J. Phang, W. R. Lee, K. Yoo, D. W. Ryu, B. Kim and C. S. Hong, *Angew. Chem. Int. Ed.*, 2014, **53**, 8383–8387; (f) M. Yoon, K. Suh, S. Natarajan and K. Kim, *Angew. Chem. Int. Ed.*, 2013,

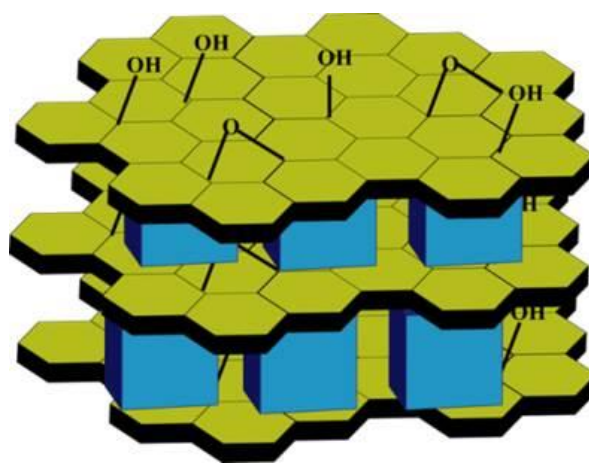
- 52, 2688-2700; (g) J. M. Taylor, K. W. Dawson and G. K. H. Shimizu, *J. Am. Chem. Soc.*, 2013, **135**, 1193–1196.
7. (a) S. Kim, K. W. Dawson, B. S. Gelfand, J. M. Taylor and G. K. H. Shimizu, *J. Am. Chem. Soc.*, 2013, **135**, 963–966; (b) M. Sadakiyo, T. Yamada and H. Kitagawa, *J. Am. Chem. Soc.*, 2009, **131**, 9906–9907; (c) V. G. Ponomareva, K. A. Kovalenko, A. P. Chupakhin, D. N. Dybtsev, E. S. Shutova and V. P. Fedin, *J. Am. Chem. Soc.*, 2012, **134**, 15640–15643; (d) J. A. Hurd, R. Vaidhyanathan, V. Thangadurai, C. I. Ratcliffe, I. L. Moudrakovski and G. K. H. Shimizu, *Nat. Chem.*, 2009, **1**, 705–710; (e) S. Bureekaew, S. Horike, M. Higuchi, M. Mizuno, T. Kawamura, D. Tanaka, N. Yanai and S. Kitagawa, *Nat. Mater.*, 2009, **8**, 831–836; (f) G. K. H. Shimizu, J. M. Taylor and S. Kim, *Nature.*, 2013, **341**, 354-355; (g) N. Sikdar, D. Dutta, R. Haldar, T. Ray, A. Hazra, A. J. Bhattacharyya and T. K. Maji, *J. Phys. Chem. C.*, 2016, **120**, 13622–13629; (h) S. Chandra, T. Kundu, S. Kandambeth, R. BabaRao, Y. Marathe, S. M. Kunjir and R. Banerjee, *J. Am. Chem. Soc.*, 2014, **136**, 6570–6573; (i) C. Dey, T. Kundu and R. Banerjee, *Chem. Commun.*, 2012, **48**, 266-268.
8. (a) Q. –G. Zhai, C. Mao, X. Zhao, Q. Lin, F. Bu, X. Chen, X. Bu and P. Feng, *Angew. Chem. Int. Ed.*, 2015, **54**, 1 – 6; (b) X. Du, R. Fan, L. Qiang, Y. Song, K. Xing, W. Chen, P. Wang and Y. Yang, *Inorg. Chem.*, 2017, **56**, 3429–3439.
9. (a) A. V. Zhukhovitskiy, J. Zhao, M. Zhong, E. G. Keeler, E. A. Alt, P. Teichen, R. G. Griffin, M. J. A. Hore, A. P. Willard and J. A. Johnson, *Macromolecules.*, 2016, **49**, 6896–6902; (b) J. A. Foster, R. M. Parker, A. M. Belenguer, N. Kishi, S. Sutton, C. Abell and J. R. Nitschke, *J. Am. Chem. Soc.*, 2015, **137**, 9722–9729; (c) Y. Wang, M. Zhong, J. V. Park, A. V. Zhukhovitskiy, W. Shi and J. A. Johnson, *J. Am. Chem. Soc.*, 2016, **138**, 10708–10715; (d) Y. Wang, Y. Gu, E. G. Keeler, J. V. Park, R. G. Griffin and J. A. Johnson, *Angew. Chem. Int. Ed.*, 2017, **56**, 188 –192; (e) A. V. Zhukhovitskiy, M. Zhong, E. G. Keeler, V. K. Michaelis, J. E. P. Sun, M. J. A. Hore, D. J. Pochan, R. G. Griffin, A. P. Willard and J. A. Johnson, *Nat. Chem.*, 2016, **8**, 33–41; (f) M. J. MacLeod and J. A. Johnson, *Polym. Chem.*, 2017, **8**, 4488-4493.
10. P. Sutar, V. M Suresh, K. Jayaramulu, A. Hazra and T. K. Maji, *manuscript under revision*.

Chapter 6C

**Layered Heterostructure Hydrogels
Based on Metal-Organic Cube and
GO/MoS₂ as Capacitive Materials**

Abstract

This chapter reports three hydrogel, formed by the supramolecular self-assembly of MOC (metal-organic cube), GO and 1T/2H-MoS₂, which show capacitive behaviour in non-aqueous medium. Self-assembly of anionic MOC and GO is driven by H-bonding interaction between the carboxylate groups of MOC and hydroxyl or epoxy groups of GO, present on the basal plane. Such self-assembly results in **MOC+GO** hydrogel which show layer-by-layer nanostructure. Similarly, self-assembly of MOC and MoS₂ in presence of ammonium cations results in hydrogel (**MOC+MoS₂** hydrogel) which show layered sheet-like morphology. Both of the di-component hydrogels exhibits capacitive behaviour. Next we prepare a tri-component hydrogel by the supramolecular self-assembly of GO, MoS₂ and MOC (**MOC+GO+MoS₂** hydrogel) which exhibits capacitive behaviour and it is superior compared to the di-component hydrogels.

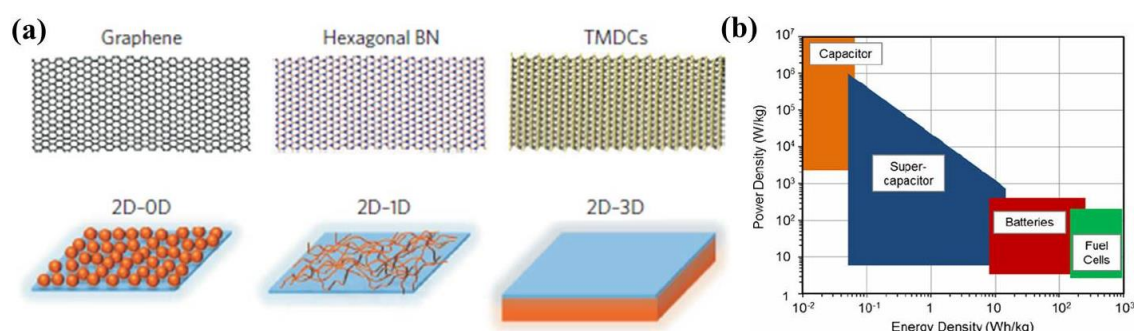


Paper based on this work:

P. Sutar, C. Das and T. K. Maji, *manuscript under preparation*

6C.1 INTRODUCTION

Recently, multi-component layered materials, also known as van der Waals (vdW) heterostructures have emerged as new functional hybrid materials which have potential for various applications.^{1a} They are usually formed by integrating 0D/2D/3D materials into the layers of 2D material via vdW interaction (Scheme 1a). Several combination of 2D materials and 0D/2D/3D materials have been reported to date which exhibit unique properties such as, field-effect tunneling transistor, vertical field-effect transistor, logic transistors, flexible and transparent electronics etc.^{1b-f} Another important application that could be realized from vdW-heterostructure is supercapacitive behaviour. Supercapacitors, also known as electrochemical capacitors or ultracapacitors, have attracted significant attention owing to their high power density, fast charge-discharge rate and long cycle life (>1000000 cycles).² When compare with other energy conversion or storage devices, as shown in the simplified 'Ragone plot', supercapacitors occupy an important part as they have superior power density and relatively large energy density (Scheme 1b).^{2c} This indicates that supercapacitors are promising materials to meet the ever increasing power demands of energy storage systems. Currently, supercapacitors are widely used for many applications, such as electronics, transportation, military, aerospace etc.³ Depending upon the energy storage mechanism, they are classified into two categories: i) electrical double layer capacitors (EDLC) and, ii) *pseudo*-capacitor.⁴ In EDLC, the capacitance originates from the electrical double layer formation at the electrode-electrolyte interface.⁵ However, in *pseudo*-capacitor reversible faradic process takes place due to the presence of electro-active species.⁶ These two mechanisms can function simultaneously depending upon the nature of the electrode material. So far, carbon based materials such as, activated carbon (AC), template carbon, carbide-derived



Scheme 1. (a) The schematic representation of vdWs heterostructure, (b) Ragone plot for energy storage devices. Figures reproduced with permission from ref. 1a.

carbon, carbon nanotube (CNT) and graphene are mostly used as active electrode materials in EDLC.^{2c, 7} High processability, inert electrochemistry, tunable porosity, low cost and easy availability in different form (powder, fibers, aerogels, sheets, tubes etc.) make them suitable materials for EDCL. Among different carbon materials, one ideal electrode material is graphene oxide (GO), which exists as layered sheet.⁸ GO is mainly produced by oxidation of graphite in presence of strong acids and oxidants.⁹ GO has many active edges and oxygen functional groups which in one hand enhance the wettability and capacitance value, and on the other hand provides the opportunity of functionalization by grafting organic/inorganic moieties.¹⁰ Such chemically modified GO having extraordinary electrochemical properties and mechanical stability, found applications in energy storage devices. Recently, a non-carbon based two-dimensional layered material, molybdenum disulphide (MoS_2) nanosheet, has been emerged as efficient supercapacitor material. MoS_2 exists in two possible phase, i) a naturally occurring semiconducting phase (2H- MoS_2) and ii) chemically derived metallic state (1T- MoS_2).¹¹ The 1T- MoS_2 is prepared from bulk MoS_2 either by lithium intercalation or electrochemical exfoliation and is highly conducting (10^7 times higher than the 2H phase).¹² Due to such high conductivity 1T- MoS_2 has found many electrochemical applications, including supercapacitor electrode, catalysts for hydrogen evolution, dye-sensitized solar cell etc.¹³ Chhowalla *et al.* showed that chemically exfoliated nanosheets of MoS_2 , containing high concentration of 1T phase show extraordinarily high capacitance value in different aqueous electrolytes.^{11d} It was envisioned that a self-assembled heterostructure based on 2D nanostructure of GO and MoS_2 with another active component would be a new material to look for supercapacitive application.

Recently, the development of flexible solid-state supercapacitors has drawn significant research attention due to their application in portable and light weight energy storage devices. Generally, flexible supercapacitors are composed of hydrogels or aerogels. The unique inherent properties of the hydrogels make them superior candidates for flexible electrode. The intrinsic 3D nanostructures and water medium of the hydrogels promote easy transportation of charges or ion. The hydrogel supercapacitors reported to date are mainly made of conducting polymers such as, polythiophen, polyaniline and polypyrrole.¹⁴ Hence ample opportunities are there to make new type of hydrogel supercapacitors. This chapter reports preparation of three different hydrogels, by supramolecular self-assembly of **MOC**, GO and MoS_2 , which showed capacitive behaviour in non-aqueous medium. As described in Chapter 6A, **MOC** has a 0D-structure

with molecular formula $[\text{Ga}_8(\text{ImDC})_{12}]^{12-}$. All the three hydrogels showed mixed dimensional 0D-2D-heterostructure where 0D **MOC** component was stabilized on the 2D GO/ MoS₂ layered materials. It should be noted that use of **MOC** as a 0D matrix for designing vdWs heterostructure has not been accounted yet. Self-assembly of anionic **MOC** and GO was driven by H-bonding interaction between the carboxylate groups of **MOC** and hydroxyl or epoxy groups of GO, present on the basal plane. Such self-assembly resulted in **MOC+GO** hydrogel which showed layer-by-layer nanostructure. Similarly, self-assembly of **MOC** and MoS₂ in presence of ammonium cations resulted in hydrogel (**MOC+MoS₂** hydrogel) which showed layered sheet-like morphology. Both of the di-component hydrogels exhibited capacitive behaviour. Moreover, a tri-component hydrogel was prepared by the supramolecular self-assembly of GO, MoS₂ and **MOC** (**MOC+GO+MoS₂** hydrogel) which exhibited superior capacitive behaviour compared to the other two di-component hydrogels.

6C.2 EXPERIMENTAL SECTION

6C.2.1 Materials

4,5-Imidazolecarboxylic acid, $\text{Ga}(\text{NO}_3)_3 \cdot 6\text{H}_2\text{O}$, Graphite and molybdenum sulphide (MoS₂) powder were purchased from Sigma-Aldrich chemical Co. Ltd. Aqueous ammonia solution was purchased from SDFCL. Triethylamine (NEt₃) was obtained from Spectrochem. For electrochemical studies anhydrous acetonitrile, polyvinylidene fluoride (PVDF), N-methyl-2-pyrrolidone (NMP), tetraethylammonium tetrafluoroborate (Et₄NBF₄) and carbon black were purchased from Sigma-Aldrich.

6C.2.2 Physical measurements

Fourier transform infrared (FTIR) spectral studies were carried out by making samples with KBr pellets using Bruker FTIR spectrometer. Raman spectroscopic measurements were carried out using a LabRAM HR Evolution Raman spectrometer with a HeNe laser of wavelength 632.8 nm and 1800 lines/mm grating. The laser power was ~5 mW at the sample. Powder X-ray diffraction (PXRD) patterns were recorded on a Bruker D8 discover instrument using Cu-K α radiation. Thermal stability was analysed using Mettler Toledo TGA 850 instrument under inert atmosphere in the temperature range of 25-800°C at the heating rate of 3°C per min. Morphology studies were carried out using Lica-S440I field emission scanning electron microscopy (FESEM) by placing samples on silicon wafer under vacuum with accelerating voltage of 10 kV. Energy

dispersive X-ray spectroscopy (EDXS) analysis was performed with an EDAX genesis instrument attached to the FESEM column. Transmission electron microscopy (TEM) analysis was performed using JEOL JEM-3010 with accelerating voltage of 300 kV. For this analysis the samples were dispersed in ethanol and then drop casted on a carbon coated copper grid.

6C.2.3 Electrochemical measurement

The supercapacitor measurements were performed on Multi-autolab M204 electrochemical workstation at room temperature in a closed three-electrode system with platinum wire as the reference electrode, platinum mesh as the counter electrode and sample coated stainless steel as working electrode. 1 M solution of tetraethylammonium tetrafluoroborate (Et_4NBF_4) in anhydrous acetonitrile (CH_3CN) was used as non-aqueous electrolyte. The cyclic voltammetry (CV) measurements were conducted at different scan rates (10 to 1000 mV s^{-1}) within the positive and negative potential windows ranging from 0 to 0.8 V and 0 to -0.8 V, respectively. The electrochemical impedance spectroscopy (EIS) was performed in the frequency range of 10^6 Hz to 10^{-2} Hz at the amplitude = 0.01 V with an AC perturbation of 5 mV. The EIS plots were fitted in the equivalent circuit using the Nova 2.1.2 software. The galvanostatic charge–discharge (GCD) measurements were performed at different current densities (0.1 - 5 A g^{-1}). The specific capacitance values were calculated from the CV and GCD curves using the formula (1) and (2), respectively:

$$C_{sp} = \frac{I\Delta t}{m_e\Delta V} \quad (1)$$

$$C_{sp} = \frac{I_d}{\text{slope}} \quad (2)$$

The specific energy density and power density were calculated from the equation (3) and (4), respectively:

$$E_d = \frac{1}{2}C_{sp}(\Delta V)^2 \quad (3)$$

$$P_d = \frac{E_d}{t_d} \quad (4)$$

m_e = mass of the active material, $\frac{\Delta V}{\Delta T}$ = scan rate, I_d = current density, slope = slope for discharge, t_d = discharge time.

6C.2.4 Synthesis

Synthesis of MOC: Detailed synthetic procedure and characterization of MOC were discussed in Chapter 6A.

Preparation of GO: GO was prepared by using a modified Hummers and Offeman method.⁹ In a typical synthesis, 1.5 g of NaNO₃ and 1.5 g graphite powder were slowly added to 75 ml concentrated H₂SO₄ in ice bath and allowed to mix properly under constant stirring for 10 min. 10 g KMnO₄ was added to this uniform mixture and then it was transferred into an oil bath (40 °C) and the reaction was continued under stirring condition for 30 min. Graphite was oxidized and very viscous dark brown product was formed after 30 min. To this mixture 75 ml deionized water was added and the temperature of oil bath was raised to 75 °C. The reactants were stirred at 75 °C for another 15 min. Then 15 ml H₂O₂ (30%) was mixed with 150 ml warm water (at 70 °C) and added to the reaction mixture. Colour of dispersion was changed from brown to yellow. Then product was centrifuged and washed several times with water. Washed product was dispersed in water and dialysed for 24 h. Dialysed product was centrifuged to remove excess water and solid product was freeze dried. The as-synthesized GO was also characterized by PXRD, FTIR, TEM, Raman and absorption spectra. Selected FTIR data (KBr, cm⁻¹): 3413 (b), 1722 (sh), 1621 (sh), 1258 (s), 1078 (s).

Exfoliation of bulk MoS₂: The bulk MoS₂ was exfoliated to 1T/2H-MoS₂ by following a previously reported procedure.¹² 300 mg bulk MoS₂ was taken in round bottom flask and dissolved in 5 ml anhydrous hexane. 2 ml n-butyl lithium (2.5 M) was added into the reaction mixture under inert condition. After that the reaction mixture was refluxed at 80 °C for 72 h. The product was filtered and washed repeatedly with n-hexane to remove excess reactant. The product was dried in vacuum oven at 45 °C and dispersed in water and centrifuged repeatedly to remove LiOH and other impurities. The product obtained was dispersed in water (1 mg in 1 ml) by sonication for 4-5 h and kept under dark. The as-synthesized 1T/2H-MoS₂ was characterized by Raman spectroscopy, PXRD and TEM studies.

Preparation of MOC+GO hydrogel: First, 5 mg GO was taken in 1 ml water and the mixture was sonicated for 4-5 h until a uniform dispersion is formed. 20 mg of MOC was dissolved in 500 µl water and the solution was added into the GO solution. The mixture was sonicated for 10 min and kept at room temperature under undisturbed

condition. The solution turned into stable hydrogel after 2 days. The formation of gel was confirmed by inversion test method. The xerogel was prepared by freeze-drying the hydrogel. Selected FTIR data (KBr, cm^{-1}): 3444 (b), 2787 (s), 1675 (sh), 1473 (sh), 1365 (sh), 1102 (sh), 857 (s), 660 (s), 549 (s).

Preparation of MOC+MoS₂ hydrogel: 5 mg 1T/2H-MoS₂ was taken in 5 ml water and the mixture was sonicated for 4-5 h to make a uniform dispersion. 20 mg MOC was dissolved in 200 μl water and 1 ml dispersion of 1T/2H-MoS₂ was added into it. The mixture was sonicated for 15 min to make a homogeneous dispersion. Into this mixture 100 μl aqueous NH₃ solution was added and the mixture was sonicated for another 2-3 min. The mixture was kept at room temperature in undisturbed condition. The stable hydrogel was formed after 24 h. The formation of gel was confirmed by inversion test method. Selected FTIR data (KBr, cm^{-1}): 3448 (b), 3140 (s), 1668(sh), 1470(sh), 1397(sh), 1111(s), 858(m), 656(s).

Preparation of MOC+GO+MoS₂ hydrogel: 5 mg GO was taken in 2 ml water and the mixture was sonicated for 4-5 h until a homogeneous dispersion is formed. Similarly, 5 mg MoS₂ was taken in 5 ml water and the mixture was sonicated to form a uniform dispersion. 20 mg of MOC was dissolved in 200 μl water and to it 300 μl dispersed solution of MoS₂ and 500 μl dispersed solution of GO were added. The mixture was sonicated for 10-15 min. After that, 100 μl aqueous NH₃ was added and the mixture was sonicated for another 2-3 min. The mixture was kept at room temperature in undisturbed condition. The stable hydrogel was formed after 24 h. The formation of gel was confirmed by inversion test method. Selected FTIR data (KBr, cm^{-1}): 3446 (b), 3170 (s), 1655(sh), 1469(sh), 1357(sh), 1105(sh), 858(m), 656(s).

6C.2.5 Preparation of electrode

The working electrode was prepared by mixing 85% xerogel, 10% carbon black and 5% PVDF binder in a mortar until a homogeneous black powder was obtained. To this mixture few drops of anhydrous NMP solvent were added to make homogeneous paste which was uniformly coated on the stainless steel working electrode ($1 \times 1 \text{ cm}^2$). Prior to coating, the stainless steel electrode was polished and washed thoroughly in ethanol (by sonication) and dried at 120 °C under vacuum. After preparing the working electrode it was kept for drying at 120 °C for 12 h.

6C.3 RESULTS AND DISCUSSION

6C.3.1 Characterization of GO and 1T/2H-MoS₂

GO was synthesized by using a modified Hummers and Offeman method.⁹ The as-synthesized GO was characterized by PXRD, FTIR, TEM, Raman and UV-Vis spectroscopy. The PXRD pattern of GO showed a sharp peak at $2\theta = 11.1^\circ$, corresponding to the d -spacing value of 8.4 \AA (Figure 1a). This confirmed the formation of GO. The FTIR spectrum of GO showed peaks at 3424 , 1736 , 1624 and 1070 cm^{-1} , corresponding to O-H, C=O, C=C and C-O stretching frequencies, respectively (Figure 1b). The presence of oxygen containing functional groups, such as C=O, C-O and O-H confirmed that graphite has been oxidized to GO. The Raman spectrum of GO showed the characteristic defect (D) and graphene (G) band at 1360 and 1613 cm^{-1} , respectively and the I_D/I_G value was found to be 0.99 , indicating the formation of GO (Figure 1c). Moreover, the TEM images showed the formation of randomly oriented GO layers (Figure 1d). The absorption spectrum of dilute solution of GO in water showed two characteristic peaks. The maximum at 243 nm was attributed to the π - π^* transition of aromatic rings and the shoulder at 298 nm was attributed to the n - π^* transition of the C=O groups of GO (Figure 1e). Similarly, the exfoliated MoS₂ was characterized by Raman spectrum, PXRD and TEM analysis. The Raman spectrum of bulk MoS₂ showed

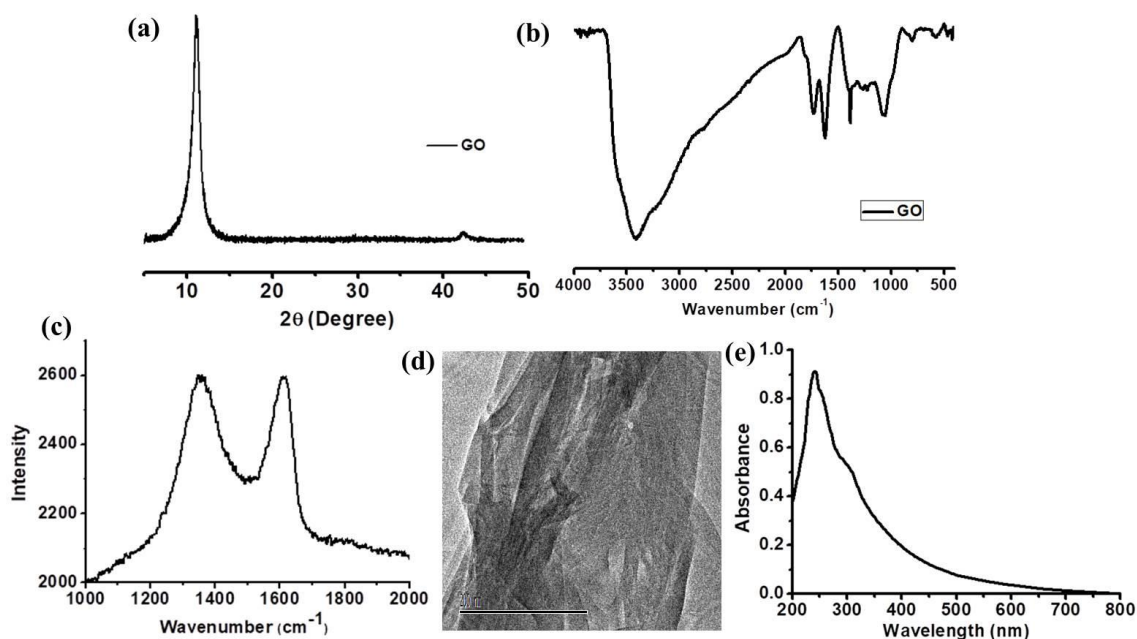


Figure 1. (a) PXRD pattern of GO, (b) FTIR spectrum of GO, (c) Raman spectrum of GO, (d) TEM image of GO, (e) UV-Vis spectrum of GO dispersion in water.

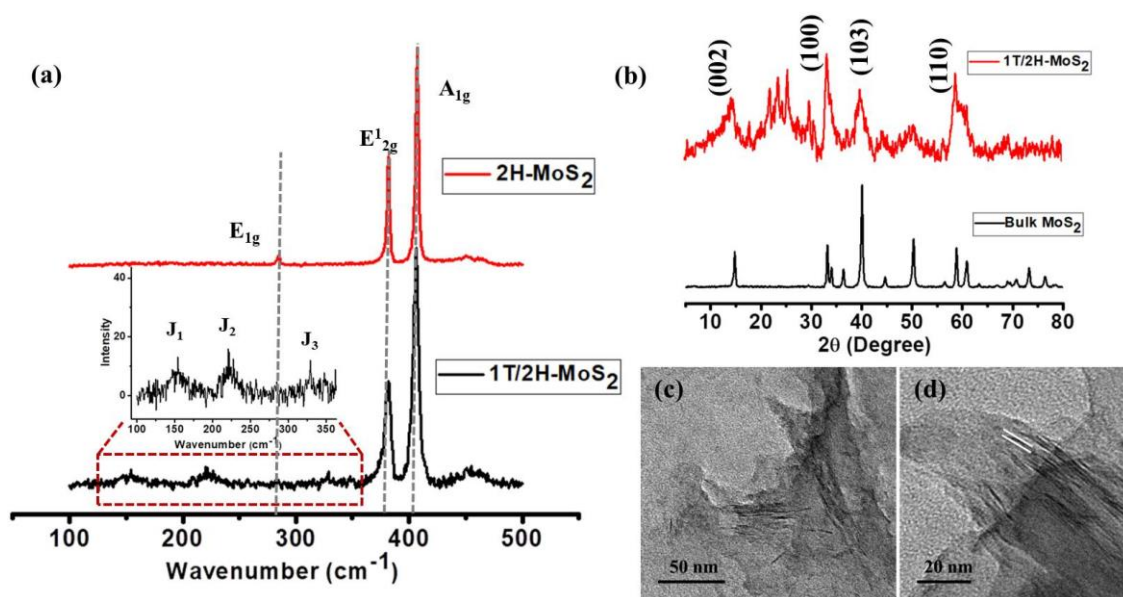


Figure 2. (a) Comparison of Raman spectra of bulk MoS_2 (red) and 1T/2H- MoS_2 (black). Inset shows the J_1 , J_2 and J_3 peaks, correspond to 1T- MoS_2 , (b) Comparison of PXRD pattern of bulk MoS_2 (black) and 1T/2H- MoS_2 (red), (c), (d) TEM images of 1T/2H- MoS_2 .

three peaks at 284.8, 381.7 and 407 cm^{-1} , corresponding to the E_{1g} , E_{2g}^1 and A_{1g} longitudinal acoustic phonon modes of 2H- MoS_2 , respectively (Figure 2a). Interestingly, the exfoliated MoS_2 showed a decrease in intensity and broadening of E_{2g}^1 and A_{1g} peaks which indicated low crystallinity due to less concentration of 2H-phase in exfoliated MoS_2 . Moreover, new peaks appeared at 153.7, 221.3, 328.8 cm^{-1} could be assigned as the J_1 , J_2 and J_3 peaks, corresponding to the phonon modes of 1T- MoS_2 (Figure 2a). This result indicated the co-existence of 1T and 2H-phases in the exfoliated MoS_2 , which was therefore named as 1T/2H- MoS_2 . The comparison of PXRD pattern of bulk MoS_2 and 1T/2H- MoS_2 indicated the broadening of (002) peak which could be deconvoluted into two peaks at 9.7 Å and 14.7 Å (Figure 2b). This indicated interlayer expansion in 1T/2H- MoS_2 due to the formation of 1T-phase. The interlayer distance was calculated to be 9.1 Å, which is $\sim 3\text{Å}$ greater than the interlayer distance of bulk MoS_2 (6.02 Å). This was also supported by TEM images which showed the interlayer distance of $\sim 10\text{Å}$ (Figure 2c-d).

6C.3.2 Characterization of hydrogels

GO is a 2D layered material with hydroxyl or epoxy groups on the basal plane. It was envisioned that these active groups of GO could interact with carboxylate groups of MOC and thus drove the self-assembly towards gel. The gelation study of MOC with GO

was carried out in water at room temperature. Water was chosen as a solvent for gelation study because MOC is highly soluble in water and the GO is highly dispersible in water. In a typical gelation experiment 20 mg MOC was dissolved in 500 μl water and 1 ml homogeneous water dispersed GO solution (5 mg in 2 ml water) was added into it. After 2-3 days formation of stable hydrogel was observed. The formation of gel was confirmed by inversion test method. Probably, the free carboxylate groups of MOC participated in H-bonding with the hydroxyl or epoxy groups of GO and thus MOC was intercalated between two consecutive GO sheet. Such intercalation drive the self-assembly of GO sheets resulted in the **MOC+GO** hydrogel (Figure 3a). Insight into the morphology of the hydrogel was obtained by recording FESEM and TEM images. The cross-sectional FESEM image of **MOC+GO** xerogel showed the formation of stacked layered structure, indicating the formation of ordered 3D stack of layered material (Figure 3b-c). However,

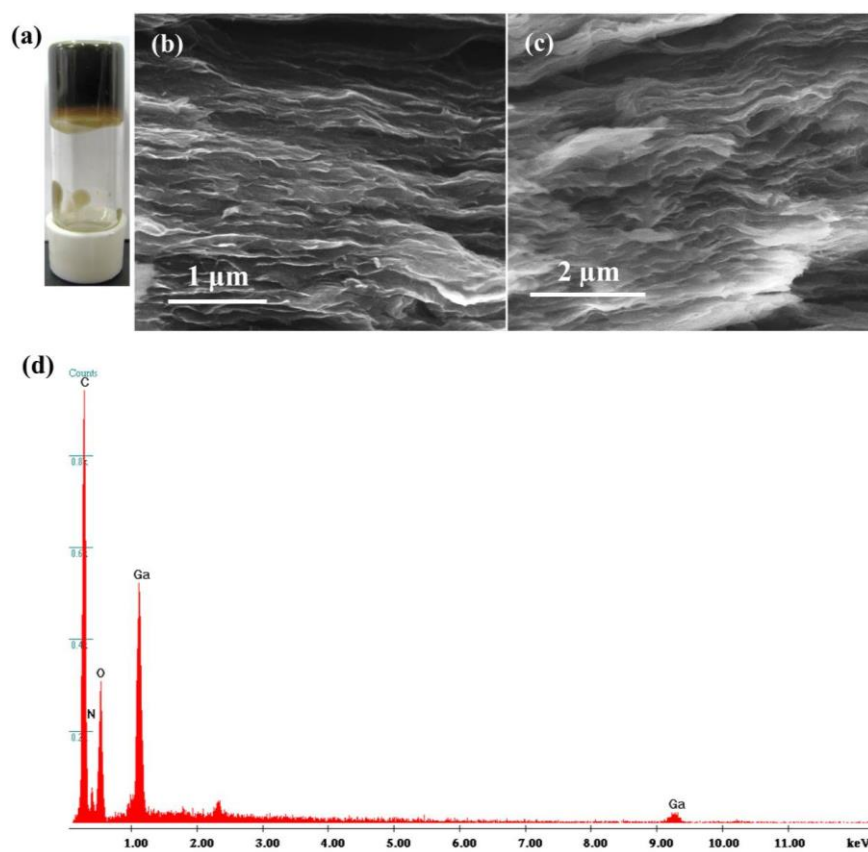


Figure 3. (a) Picture of the **MOC+GO** hydrogel, (b), (c) cross-sectional FESEM images of **MOC+GO** xerogel showing the layered structure based on intercalation of **MOCs** between GO sheets, (d), (e) EDAX spectrum of **MOC+GO** xerogel showing the presence of Ga^{III} .

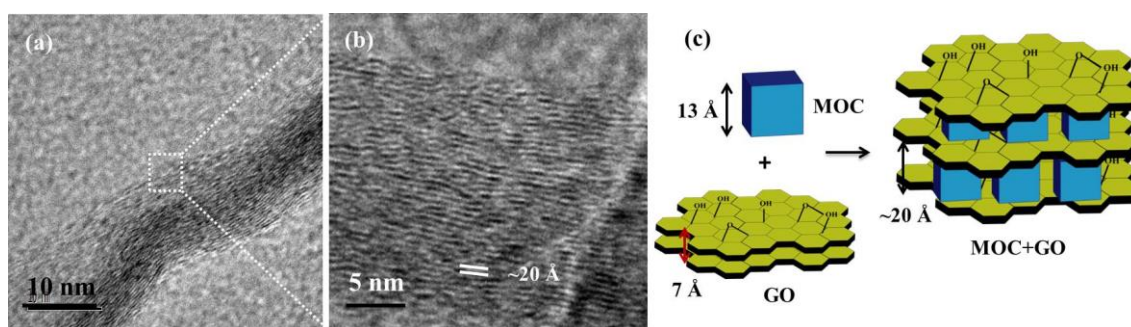


Figure 4. (a), (b) TEM images of **MOC+GO** xerogel, (c) Schematic of layered heterostructures of **MOC+GO** hydrogel.

the as-prepared GO did not show such ordered arrangement, rather randomly oriented GO sheets were observed. Moreover, the point EDAX recorded between two layers shows the presence of Ga^{III} ions (Figure 3d). This indicates that **MOCs** are intercalated between two layers of GO sheet. The TEM images also show the stacked layered structure of **MOC+GO** xerogel and the distance between two layers is found to be 15–20 Å (Figure 4a–b). The PXRD analysis of **MOC+GO** xerogel provided more insight into the self-assembly process of GO and MOC (Figure 5). The PXRD pattern of GO showed sharp peak at $2\theta = 11.15^\circ$, corresponding to the d -spacing values of 7.9 Å. The PXRD pattern of **MOC+GO** xerogel exhibited peaks at $2\theta = 6.3^\circ, 11.0^\circ, 11.7^\circ, 14.2^\circ, 16.1^\circ$ and 27.3° , corresponding to the d -spacing values of 14.3, 15.1, 15.12, 12.4, 11.0, 6.5 Å. The broad peak at $2\theta = 6.3^\circ$ ($d = 14.7$ Å) corresponded to the distance between two consecutive layers of GO which increased by 6.8 Å. The distance between two GO sheets in **MOC+GO** xerogel could be correlated with the size of MOC ($13.5 \times 13.5 \text{ \AA}^2$) (Figure 4c). The other peaks in the PXRD pattern of **MOC+GO** xerogel corresponded to the **MOC**, as they

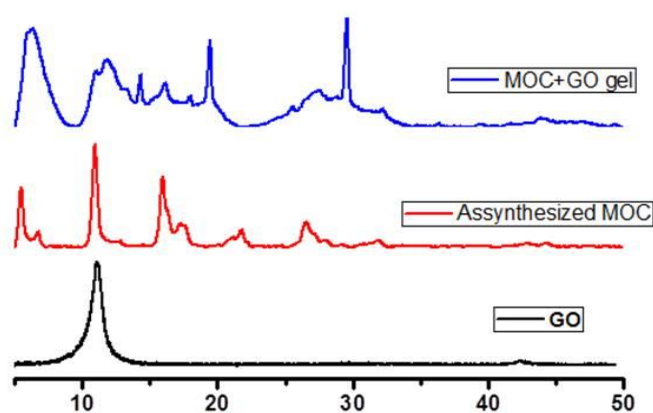


Figure 5. Comparison of PXRD of GO, MOC and **MOC+GO** xerogel.

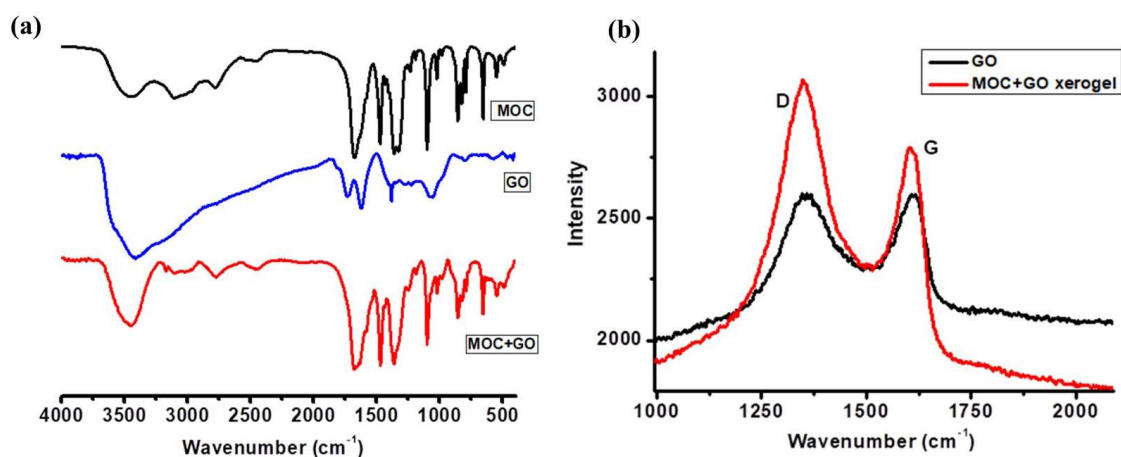


Figure 6. (a) Comparison of FTIR spectra of GO, MOC, **MOC+GO** xerogel, (b) Comparison of Raman spectra of GO and **MOC+GO** xerogel.

were matching with the PXRD pattern of as-synthesised MOC. Next, the FTIR spectra of GO, **MOC** and **MOC+GO** xerogel were compared. FTIR spectrum of GO showed peak corresponding to O-H, C=O, C=C and C-O stretching frequency at 3424, 1736, 1624 and 1070 cm⁻¹ (Figure 6a). The FTIR spectrum of **MOC+GO** xerogel showed peaks corresponding to both MOC and GO, indicating presence of both in the self-assembled material. To further validate the interaction between MOC and GO in the hydrogel, the Raman spectrum of GO and **MOC+GO** xerogel were recorded (Figure 6b). For the as-synthesized GO, the D and G band appeared at 1360 and 1613 cm⁻¹, respectively and the I_D/I_G value for was found to be 0.99. Interestingly, for **MOC+GO** xerogel the D and G bands appeared at 1348 and 1604 cm⁻¹, respectively and the I_D/I_G value was calculated to be 1.09. Such red shift of D and G band and increase of I_D/I_G value in **MOC+GO** xerogel indicated strong coupling between GO sheets and **MOC**. In order to investigate the thermal stability, the thermogravimetric analysis of GO, **MOC** and **MOC+GO** xerogel were performed. The as-synthesized GO exhibited a weight loss of 29.4% between 170 °C to 238 °C which was attributed to the removal of chemical functionalities of GO sheets. The **MOC** showed an initial weight loss of 13 % at 170 °C, corresponding to a loss of guest water and DMF molecules. After that it showed a two-step weight loss of 64% in between 196 °C to 440 °C, indicating decomposition of the extended framework. Interestingly, **MOC+GO** xerogel showed a three step TGA curve. It showed a weight loss of 7.8 % between 130 °C to 216 °C, indicating the removal of chemical functionalities from the stacked GO sheets of **MOC+GO** xerogel. After that, 36.7 % weight loss was observed between 220 °C to 464 °C, indicating the degradation of **MOC**

which were intercalated between two GO sheets. To know the porosity of the material gas adsorption study was carried out. N_2 adsorption isotherm of desolvated MOC at 77 K showed a type-II profile indicating surface adsorption. However, N_2 adsorption isotherm of the composite **MOC+GO** hydrogel showed a type-I profile and the surface area was measured to be $43.88 \text{ m}^2 \text{ g}^{-1}$.

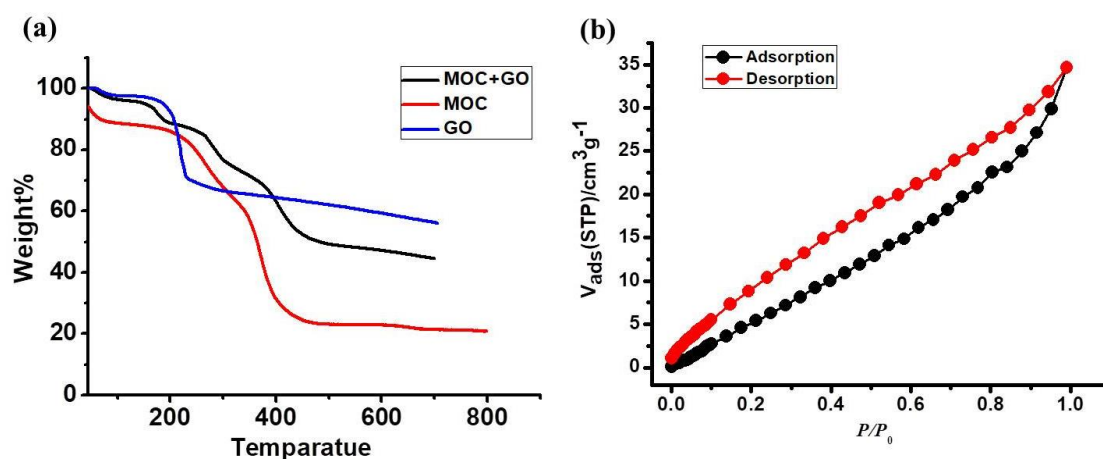


Figure 7. (a) Comparison of TGA curve of GO, MOC and MOC+GO xerogel, (b) N_2 adsorption isotherm of MOC+GO at 77 K showing type-I profile.

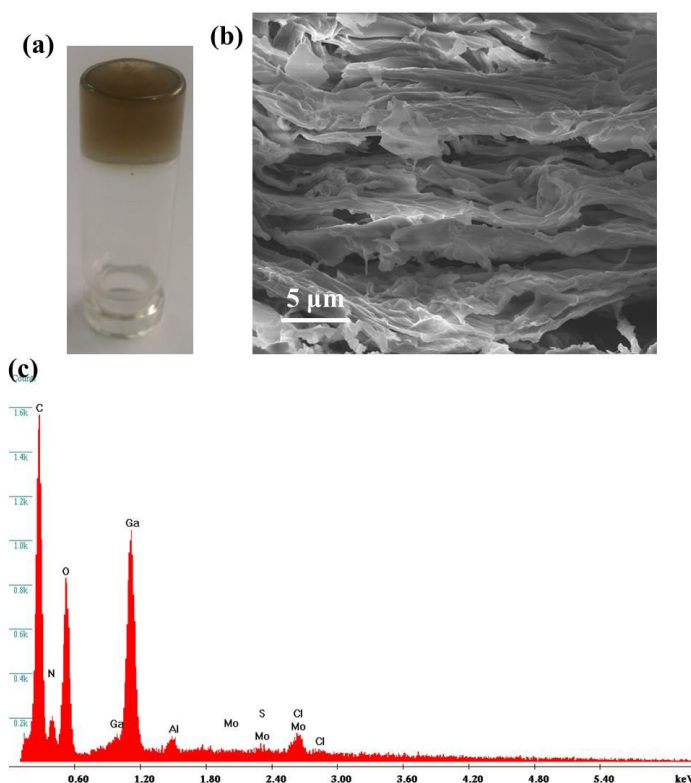


Figure 8. (a) The MOC+MoS₂ hydrogel, (b) The cross-sectional FESEM image of MOC+MoS₂ xerogel, (c) The EDAX spectrum of MOC+MoS₂ xerogel.

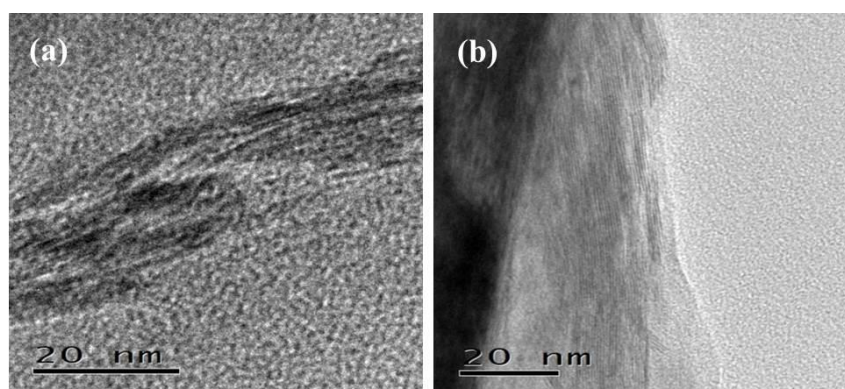


Figure 9. (a), (b) TEM images of **MOC+MoS₂** xerogel.

Next, the self-assembly of **MOC** with 1T/2H-MoS₂ was carried out. The 1T/2H-MoS₂ was prepared by exfoliating the bulk MoS₂ by conventional lithium intercalation technique and dispersed immediately in water (1 mg in 1 ml). The gelation propensity of **MOC** in presence of 1T/2H-MoS₂ was checked. In a typical experiment 20 mg of **MOC** was dissolved in 200 μ l water and 1 ml homogeneous dispersion of 1T/2H-MoS₂ was added into it. After sonication for 10-15 min the mixture was kept undisturbed. The solution did not turn out to gel even after 3-4 days. This was probably because the

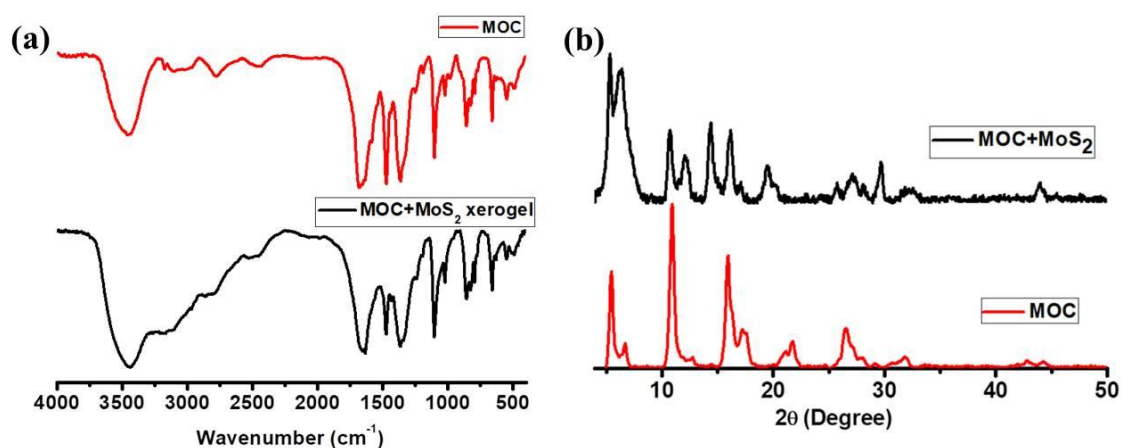


Figure 10. (a) Comparison of FTIR spectra of **MOC** and **MOC+MoS₂** xerogel, (b) FTIR of **MOC+MoS₂** xerogel.

negatively charged surface of 1T/2H-MoS₂ got repealed by the peripheral carboxylate groups of **MOC** and hence self-assembly did not occur. However, when 100 μ l aq. NH₃ solution was added into the mixture, the solution converted to hydrogel after one day. The formation of **MOC+MoS₂** gel was confirmed by inversion test method (Figure 8a). Probably, the ammonium cations facilitated the self-assembly by participating in H-

bonding which connected the **MOC** with MoS_2 nanosheets. The **MOC+MoS₂** hydrogel was characterized by FTIR, PXRD, TGA, Raman, TEM and FESEM analysis. The cross-section FESEM images of the **MOC+MoS₂** xerogel showed the layered nanostructure (Figure 8b). Moreover, the point EDAX showed the presence of Ga^{III} ions which indicated that **MOC** was intercalated between two MoS_2 layers (Figure 8c). Moreover, the TEM images showed the layered nanostructures and the distance between two layers was found to be $\sim 17 \text{ \AA}$ (Figure 9). The FTIR spectrum of The **MOC+MoS₂** xerogel showed peaks corresponding to both **MOC** and 1T/2H- MoS_2 , indicating presence of both in the self-assembled material (Figure 10a). The PXRD of **MOC+MoS₂** showed similar pattern as that of **MOC** indicating the presence of **MOC** in the self-assembled structure (Figure 10b). The Raman spectrum of **MOC+MoS₂** xerogel showed characteristic E_{2g}^1 and A_{1g} peaks of 1T/2H- MoS_2 at 386 and 411 cm^{-1} (Figure 11)

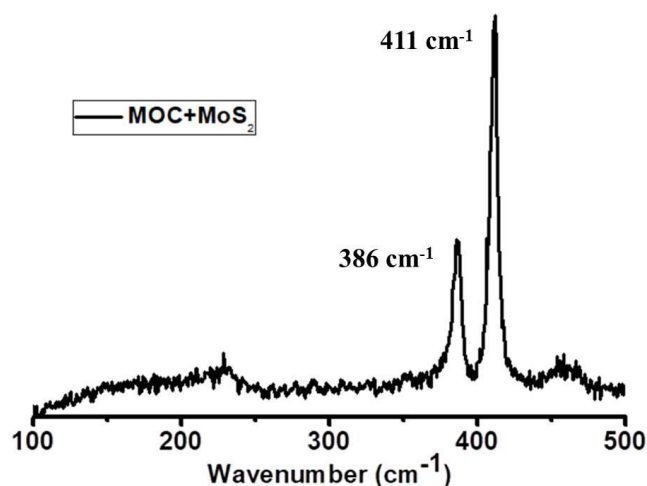


Figure 11. Raman spectrum of **MOC+MoS₂** xerogel.

To know the effect of both GO and 1T/2H- MoS_2 in the structure and properties of **MOC**-based hydrogel a tri-component gel was prepared by the self-assembly of **MOC** with mixture of GO and 1T/2H- MoS_2 in presence of ammonium cation. In a typical gelation experiment 20 mg of **MOC** was dissolved in $200 \mu\text{l}$ water and $300 \mu\text{l}$ of 1T/2H- MoS_2 dispersion and $500 \mu\text{l}$ of GO dispersion was added into the solution. The mixture was sonicated for 10-15 min. After that, $100 \mu\text{l}$ aq. NH_3 was added and the mixture was sonicated for another 2-3 min. The mixture converted to stable hydrogel (**MOC+GO+MoS₂** hydrogel) after 24 hours (Figure 12a). The formation of **MOC+GO+MoS₂** hydrogel was confirmed by inversion test method. In this case also ammonia cation facilitate the self-assembly by connecting **MOC**, GO and 1T/2H- MoS_2 by H-bonding interaction. The **MOC+GO+MoS₂** hydrogel was characterized by FTIR,

PXRD, TGA, FESEM and TEM analysis. The cross-sectional FESEM image of **MOC+GO+MoS₂** xerogel showed the layered nanostructure morphology (Figure 12b). The EDAX analysis indicated the presence of MOC in the xerogel matrix (Figure 12c). The TEM images of **MOC+GO+MoS₂** xerogel also confirmed the formation of layered nanostructures and the distance between two layers was ~ 17 Å (Figure 13a-b). The FTIR spectrum of **MOC+GO+MoS₂** xerogel showed peaks corresponding to GO, **MOC** and 1T/2H-MoS₂, indicating presence of all three in the self-assembled material (Figure 14a). The PXRD **MOC+GO+MoS₂** shows similar pattern as that of **MOC** indicating the presence of **MOC** in the self-assembled structure (Figure 14b). The Raman spectrum of **MOC+GO+MoS₂** xerogel showed characteristic peaks of 1T/2H-MoS₂ at 384 and 408 cm^{-1} , whereas the D and G band of GO came around 1343 and 1591 cm^{-1} , respectively (Figure 15).

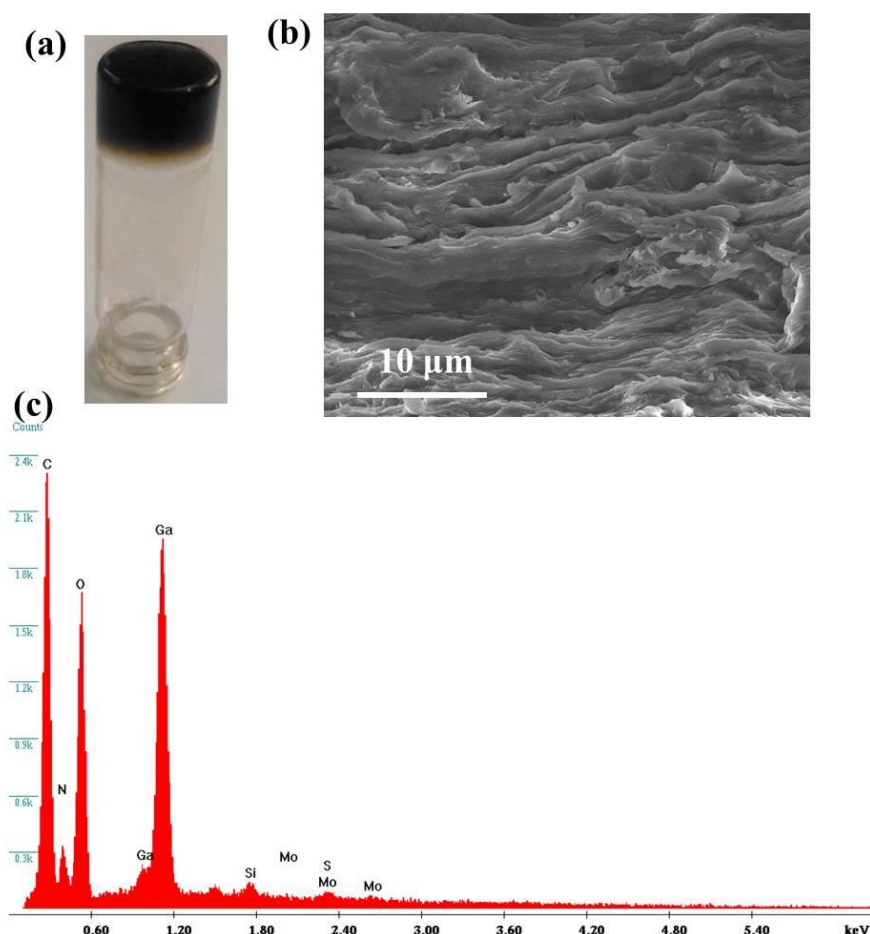


Figure 12. (a) Picture of **MOC+GO+MoS₂** hydrogel, (b) The cross-sectional FESEM image of **MOC+GO+MoS₂** xerogel, (c) The EDAX spectrum of **MOC+GO+MoS₂** xerogel.

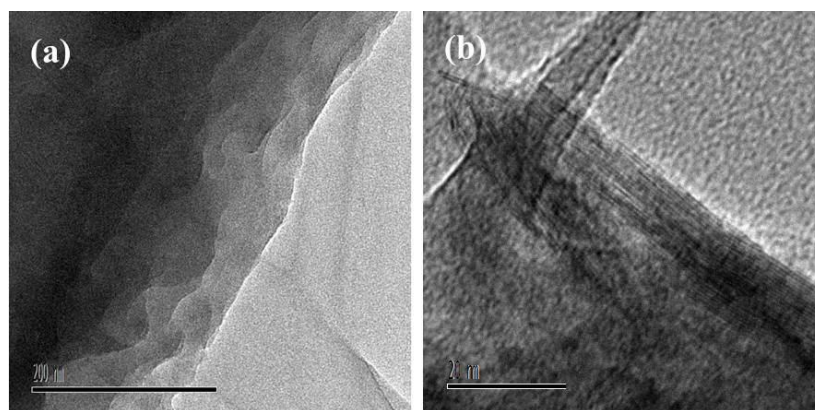


Figure 13. (a), (b) TEM images of **MOC+GO+MoS₂** xerogel.

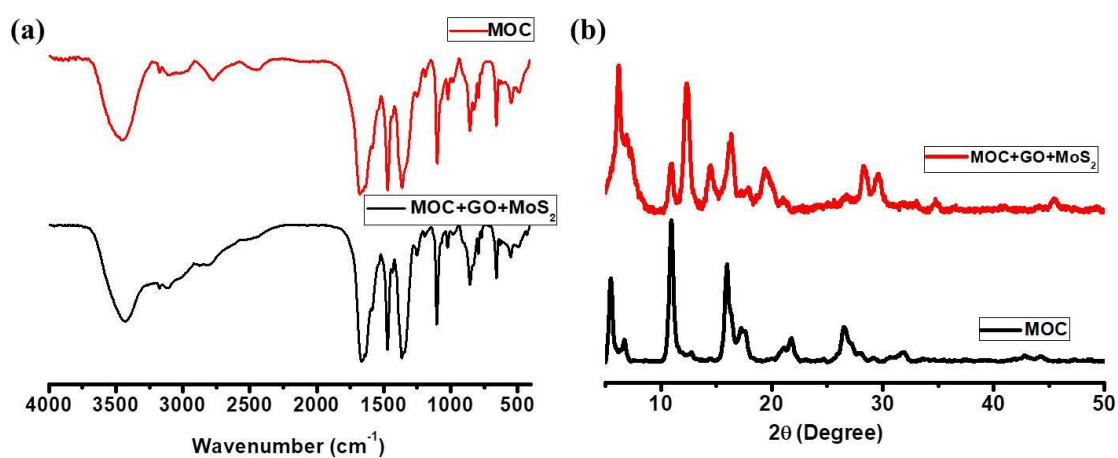


Figure 14. (a) Comparison of FTIR spectra of **MOC** and **MOC+GO+MoS₂** xerogel, (b) FTIR of **MOC+GO+MoS₂** xerogel.

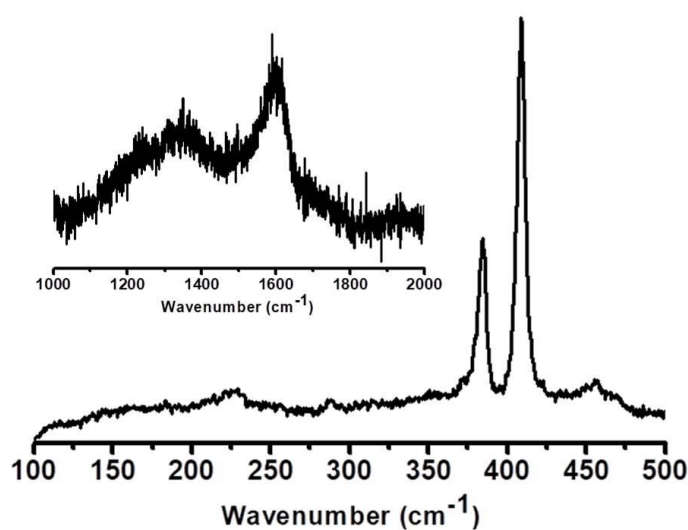


Figure 15. Raman spectrum of **MOC+GO+MoS₂** xerogel showing the characteristic peaks of MoS₂. The inset shows the D and G peaks of GO.

6C.3.3 Electrochemical studies of hydrogels

The supercapacitive behaviour of the binary and the ternary hydrogels were evaluated by cyclic voltammetry (CV), cyclic charge-discharge (CCD) and electrochemical impedance spectroscopy (EIS). GO is a well-known capacitive material which shows charge storage in the positive potential region. Hence, the CV of **MOC+GO** binary hydrogel was recorded in the potential window between 0 and 0.8 V at various scan rates. The CV is devoid of any faradaic peak confirming the electrochemical double layer capacitive behaviour (Figure 16a). The CCD recorded in the same region shows fast charging and discharging which are also very symmetric in nature (Figure 16b). The specific capacitance (C_{sp}) calculated from CV was 1.8 F/g at a scan rate of 50 mV/s. The maximum capacitance calculated from the slope of the discharge plot of CCD was found to be 10 F/g at a current density of 0.1 A/g. From the CV shown in Figure 16c, the calculated C_{sp} of GO and **MOC+GO** was 0.68 and 1.65 F/g respectively. When GO is

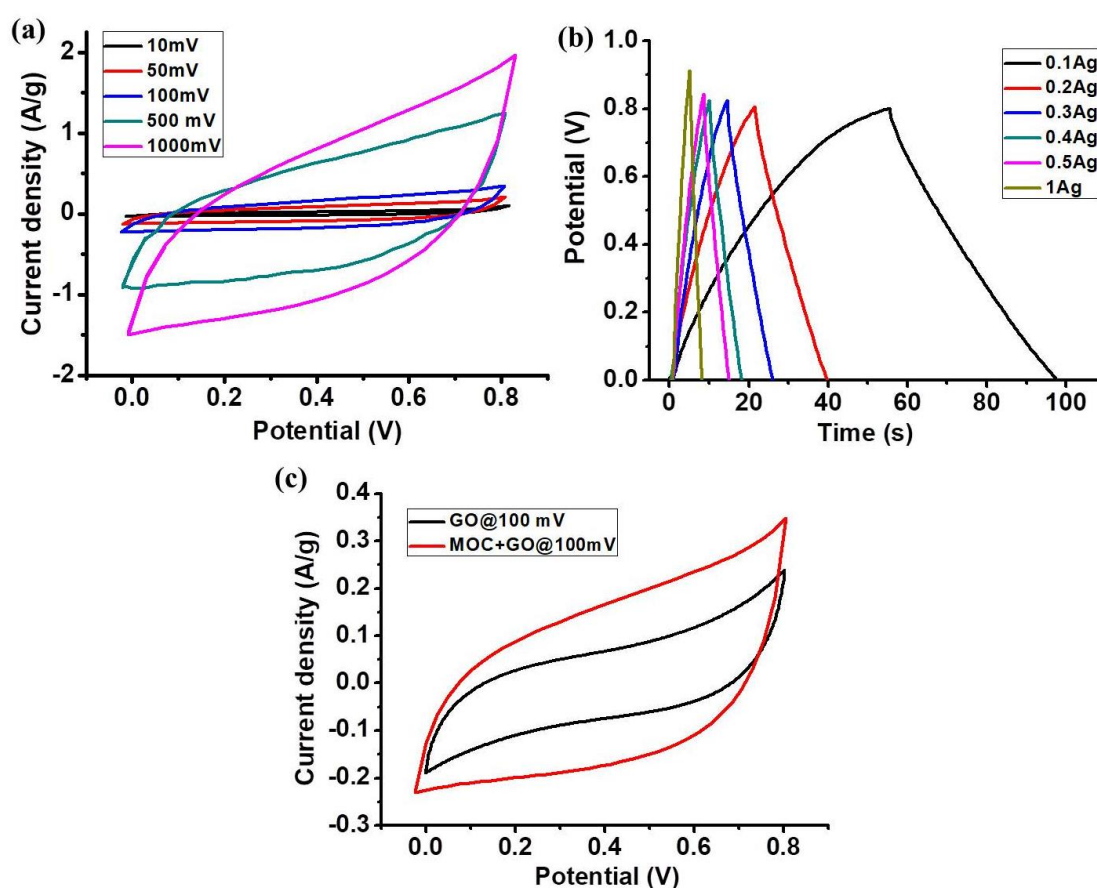


Figure 16. (a) CV of **MOC+GO** xerogel at 10, 50, 100, 500 and 1000 mV scan rate, (b) Galvanostatic charge discharge curve of **MOC+GO** xerogel at the current density of 0.1, 0.2, 0.3, 0.4, 0.5 and 1 A/g, (c) Comparison of CV of GO and **MOC+GO** xerogel.

derived from graphite by Hammer's method, the GO layers exist in a very disordered orientation, which makes the flow of electron tortuous. On gelation with MOC, the GO layers became more ordered consequently providing a smoother electron flow. This is reflected by the increase in the current density in the CV of **MOC+GO** compared to that of the GO (Figure 16c), consequently increasing the capacity of the former. 1T/2H-MoS₂, another layered capacitive material, was also subjected to gelation with MOC, with the same hypothesis of achieving more ordered orientation to improve the capacity. Since MoS₂ showed the capacitive behaviour in the negative region, CV and CCD of **MOC+MoS₂** xerogel was studied between the potential windows of 0 to -0.8 V. The CVs showed no faradaic peak unfolding the double layer nature of the capacitance (Figure 17a). C_{sp} from CV is found out to be 2 F/g at 50 mV/s scan rate. The CCD plots of **MOC+MoS₂** xerogel are symmetrical in nature with same charging and discharging rates (Figure 17b). C_{sp} calculated from the slope of the discharge curve was 1.16 F/g at a current density of 0.1 A/g. Energy density, one of the two most important aspects of energy storage devices, is directly proportional to the potential window between which the device performs. Therefore, a material which can perform in a wide potential range is expected to have an impressive energy density. As seen above, **MOC+GO** shows capacitance in the positive potential window and **MOC+MoS₂** shows capacitance in the negative potential window. It is hypothesized that a material having both GO and MoS₂ would outperform the materials containing any one of the two. Thus, the ternary gel consisting GO and MoS₂ as the capacitive component and MOC as the gelator was

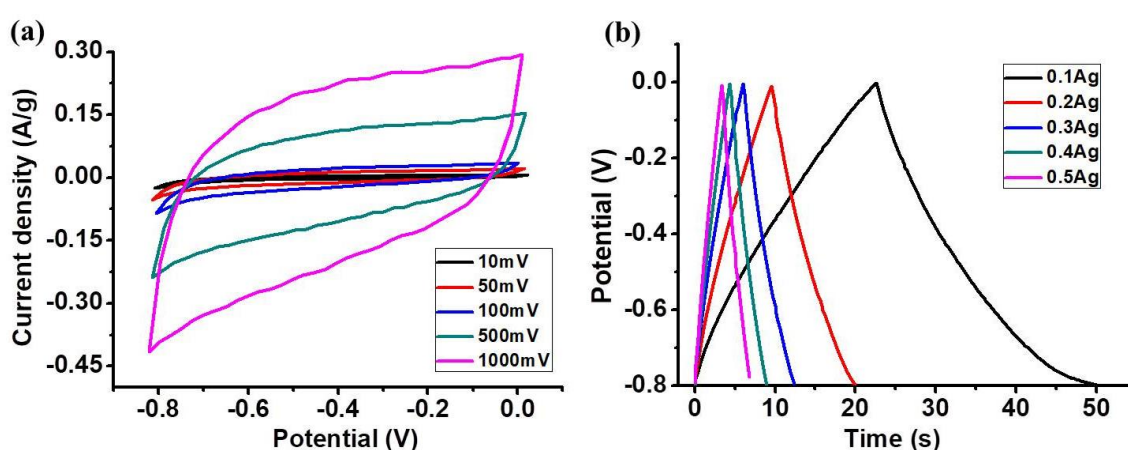


Figure 17. (a) CV of **MOC+MoS₂** xerogel at 10, 50, 100, 500 and 1000 mV scan rate, (b) Galvanostatic charge discharge curve of **MOC+MoS₂** xerogel at the current density of 0.1, 0.2, 0.3, 0.4 and 0.5 A/g.

synthesized. To examine the capacitive behaviour of **MOC+GO+MoS₂**, CVs and CCDs were recorded both in the negative and positive potential windows. The CVs at both the potential windows showed purely capacitive nature without any faradaic electron transfers (Figure 18a and 18c). The calculated C_{sp} was 20 F/g for both positive and negative potential regions. The CCDs recorded at a various current density in the positive potential region shows symmetric charging and discharging with a slight improvement in the C_{sp} (Figure 18b). Importantly, the rate of decrease in the C_{sp} with increasing current density are slowed in Figure 19a-b. In case of **MOC+GO**, the C_{sp} at 0.5 A/g is 66 % lower than that at 0.1 A/g, whereas, in case of **MOC+GO+MoS₂** the decrease is only 40 %. This could be an effect of ordering of the GO and 1T/2H-MoS₂ planes. Similarly, CVs and CCDs of the same material were recorded in the negative potential region (Figure 18c

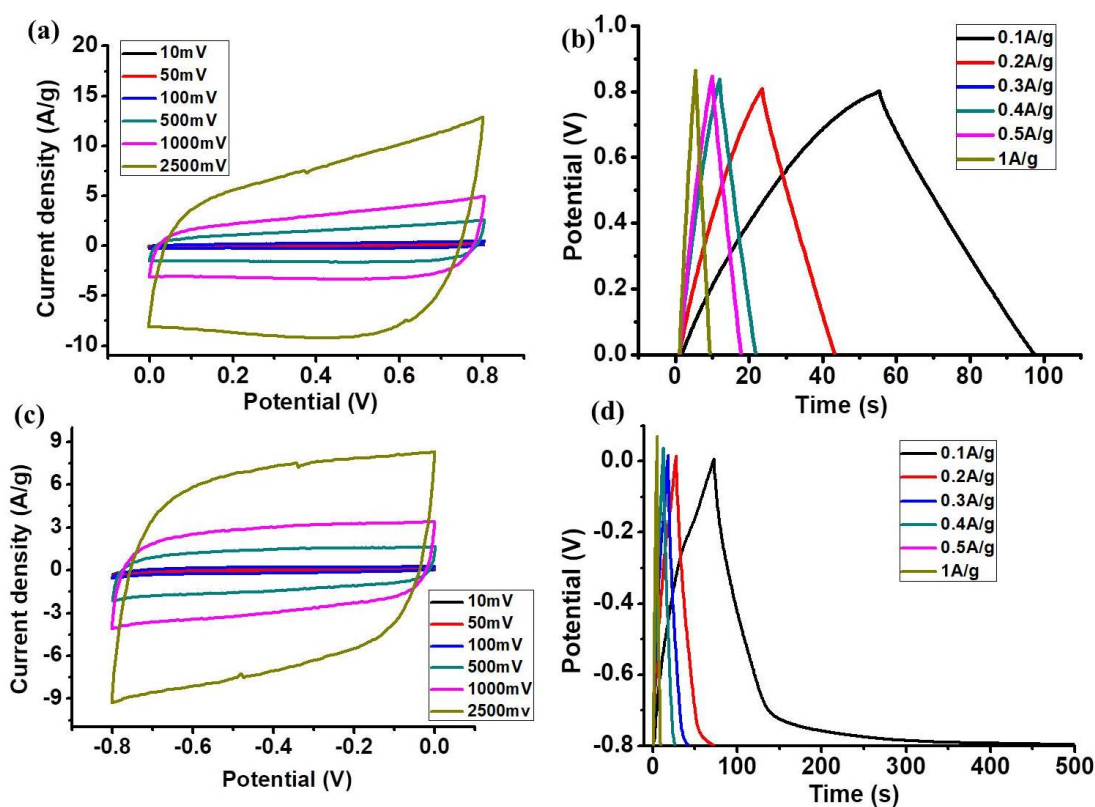


Figure 18. (a) CV of **MOC+GO+MoS₂** xerogel at 10, 50, 100, 500 and 1000 mV scan rate in the positive potential range, (b) CV of **MOC+GO+MoS₂** xerogel at 10, 50, 100, 500 and 1000 mV scan rate in the negative potential range, (c) Galvanostatic charge discharge curve of **MOC+GO+MoS₂** xerogel at the current density of 0.1, 0.2, 0.3, 0.4 and 0.5 A/g in the positive potential range, (d) Galvanostatic charge discharge curve of **MOC+GO+MoS₂** xerogel at the current density of 0.1, 0.2, 0.3, 0.4 and 0.5 A/g in the negative potential range.

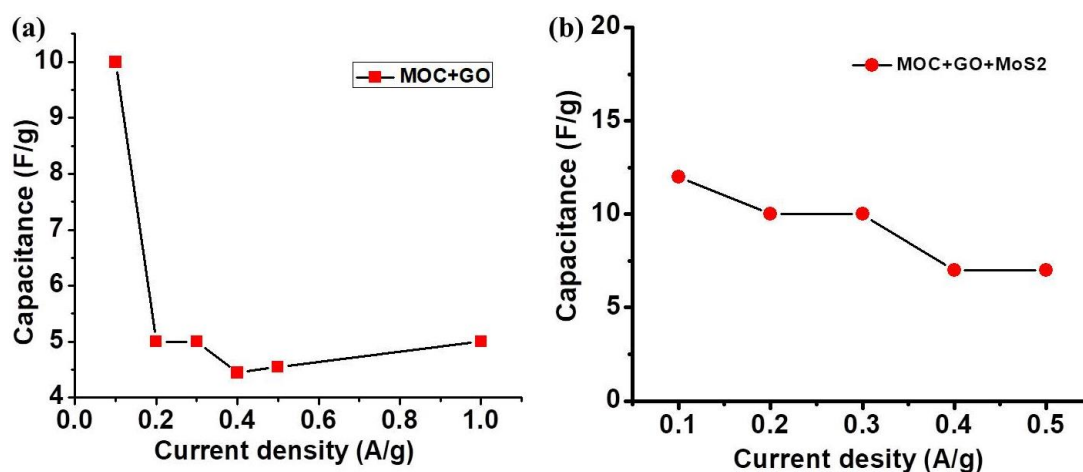


Figure 19. Specific capacitance vs current density plot for (a) **MOC+GO** and (b) **MOC+GO+MoS₂** xerogel.

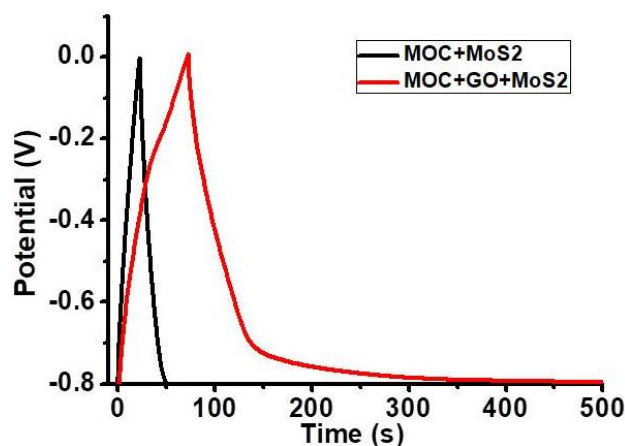


Figure 20. Comparison of CCD plot of **MOC+MoS₂** and **MOC+GO+MoS₂** xerogels at the current density of 0.1 A/g.

and 16d). The CVs at different scan rates revealed purely capacitive nature of the material with a C_{sp} of 20 F/g at 50 mV/s (Figure 18c). The CCDs recorded at different current densities were not symmetrical, implying uneven rates of charging and discharging (Figure 18d). However, drastic improvement in the C_{sp} ($C_{sp} = 56$ F/g at 0.1 A/g) was achieved as compared to the binary **MOC+MoS₂** gel (Figure 20). Having examined the capacitive performance of **MOC+GO+MoS₂** at both positive and negative potential windows, the outcomes prompted to examine the capacitive behaviour in the range of -0.8 to 0.8 V. CVs recorded at various scan rates are shown in Figure 21a. From Figure 21b, the effect of ternary hydrogel operated in the region -0.8 to 0.8 is comprehensible. The CCDs at various current densities show unsymmetrical charging and discharging with

discharge profile having characteristics similar to discharge profiles obtained for the individual regions (Figure 21c). EIS of the electrodes coated with all the hydrogels were also recorded. The high-frequency intercept of the Nyquist plot indicates the equivalent series resistance (ESR) and the vertical plot explains the capacitive behaviour (Figure 21d). ESR for the hydrogels were 4, 3.9 and 3.8 Ω for **MOC+MoS₂**, **MOC+GO** and **MOC+GO+MoS₂** respectively, which are very close to each other. Whereas the vertical region is steeper for the ternary hydrogel portraying its higher capacitive nature compared to the binary hydrogels. At this point, an insight into the energy and power density is both important and interesting. The highest energy density of 6.2 Wh/kg was obtained for the electrode examined in the entire potential range from -0.8 to 0.8 V (Figure 22). Interestingly, the power densities obtained for the electrode performance in the individual regions were 2000 W/kg and it was doubled (4000 Wh/kg) for the same electrode when

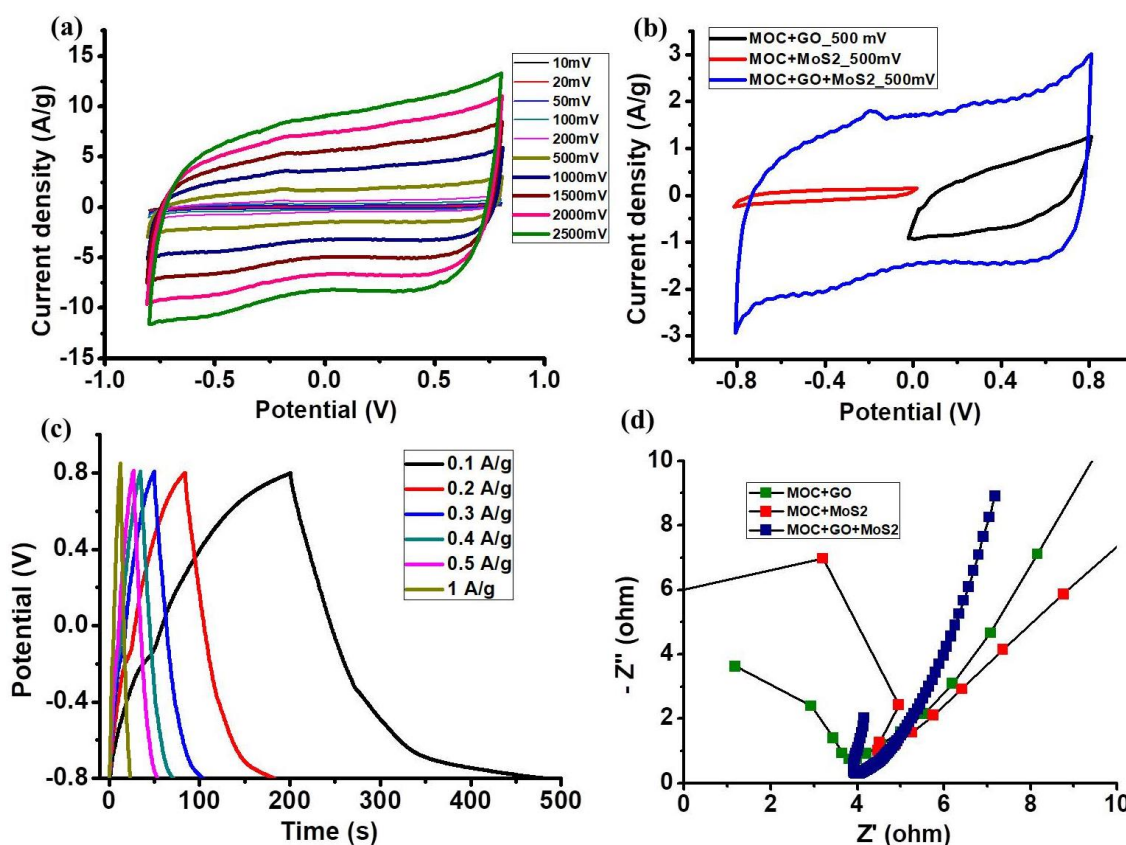


Figure 21. (a) CV of **MOC+GO+MoS₂** xerogel at 10, 20, 50, 100, 200, 500, 1000, 1500, 2000 and 2500 mV scan rate in the full potential range, (b) Comparison of CV of **MOC+GO+MoS₂** (Full range), **MOC+MoS₂** (negative potential range) and **MOC+GO** xerogel (positive potential range), (c) charge discharge of **MOC+GO+MoS₂** using the full potential range, (d) The Impedance spectra of all three xerogels.

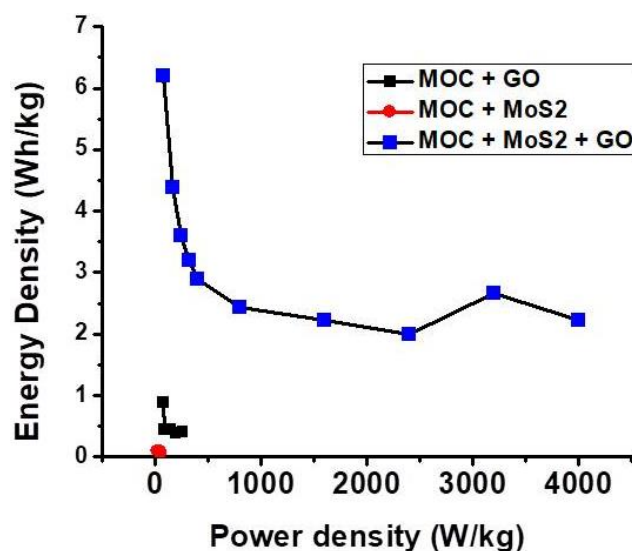


Figure 22. Ragone plot of all three hydrogel.

studied for the whole potential range. Thus, the capacitive behaviour of the binary and the ternary hydrogels were studied. Improved capacitive performance of the ternary hydrogels compared to the binary hydrogels and also the individual components highlights its effectiveness. After achieving elevated performance at the positive and negative potential regions, the performance of the ternary hydrogel between -0.8 to 0.8 V was also examined. Improved performance in terms of C_{sp} and energy density was achieved. Impressively a very high power density of 4000 W/kg was obtained. Thus proving the ternary hydrogel when operated between the potential region of -0.8 to 0.8 V outperforms the binary gels operated separately at the positive and negative potential regions.

6C.4 SUMMARY

In summary, we synthesized three hydrogels by supramolecular self-assembly of **MOC**, **GO** and **1T/2H-MoS₂**, which showed capacitive behaviour in non-aqueous medium. Self-assembly of **MOC** and **GO** was driven by the H-bonding interaction between the carboxylate group of **MOC** and hydroxyl/epoxy group of **GO** and resulted in hydrogel. The **MOC+GO** hydrogel showed layered nanostructures where **MOCs** were intercalated between two consecutive **GO** sheets and formed mixed dimensional heterostructures. Similar soft heterostructures (**MOC+MoS₂**) were prepared by the self-assembly of **MOCs** and **1T/2H-MoS₂**. **MOC+GO** and **MOC+MoS₂** hydrogels showed moderate capacitive behaviour in positive (0 to $+0.8$ V) and negative potential (0 to -0.8),

respectively. Moreover, a ternary hydrogel (**MOC+GO+MoS₂**) was prepared by self-assembly of **MOCs**, **GO** and **1T/2H-MoS₂** which operate over a wide potential range (-0.8 to +0.8 V) and hence showed better capacitive behaviour compared to the bi-component **MOC+GO** and **MOC+MoS₂** hydrogels.

6C.5 REFERENCES

1. (a) D. Jariwala, T. J. Marks and M. C. Hersam, *Nat. Mater.*, 2017, **16**, 170-181; (b) L. Britnell, R. V. Gorbachev, R. Jalil, B. D. Belle, F. Schedin, A. Mishchenko, T. Georgiou, M. I. Katsnelson, L. Eaves, S. V. Morozov, N. M. R. Peres, J. Leist, A. K. Geim, K. S. Novoselov and L. A. Ponomarenko, *Science*, 2012, **335**, 947-950; (c) L. Britnell, *et al. Science.*, 2013, **340**, 1311-1314; (d) T. Georgiou, *et al. Nat. Nanotech.*, 2013, **8**, 100-103; (e) A. Mishchenko, *et al. Nat. Nanotech.*, 2014, **9**, 808-813; (f) W. J. Yu *et al. Nat. Mater.*, 2012, **12**, 246-252; (g) W. J. Yu, *Nat. Nanotech.*, 2013, **8**, 952-958; (g) I. V. Grigorieva, A. K. Geim, *Nature.*, 2013, **499**, 419-425.
2. (a) J. R. Miller and P. Simon, *Science*, 2008, **321**, 651; (b) M. Winter and R. J. Brodd, *Chem. Rev.*, 2004, **104**, 4245; (c) A. Burke, *J. Power Sources*, 2000, **91**, 37; (c) L. L. Zhang and X. S. Zhao, *Chem. Soc. Rev.*, 2009, **38**, 2520-2531; (d) C. Zhong, Y. Deng, W. Hu, J. Qiao, L. Zhang and J. Zhang, *Chem. Soc. Rev.*, 2015, **44**, 7484-7539; (e) M. Winter and R. J. Brodd, *Chem. Rev.*, 2004, **104**, 4245-4270.
3. (a) Y. Wang, Y. Song and Y. Xia, *Chem. Soc. Rev.*, 2016, **45**, 5925-5950; (b) Y. -Z. Zhang, Y. Wang, T. Cheng, W. -Y. Lai, H. Pang and W. Huang, *Chem. Soc. Rev.*, 2015, **44**, 5181-5199; (c) F. Wang, X. Wu, X. Yuan, Z. Liu, Y. Zhang, L. Fu, Y. Zhu, Q. Zhou, Y. Wu and W. Huang, *Chem. Soc. Rev.*, 2017, **46**, 6816- 6854; (d) A. C. Forse, C. Merlet, J. M. Griffin and C. P. Grey, *J. Am. Chem. Soc.*, 2016, **138**, 5731-5744.
4. B. E. Conway, *Electrochemical Supercapacitors: Scientific Fundamentals and Technological Applications*, Kluwer Academic/ Plenum Publisher, New York, 1999.
5. (a) H. V. Helmholtz, *Ann. Phys. (Leipzig)*, 1853, **89**, 21; (b) G. Gouy, *J. Phys.*, 1910, **4**, 457; (c) D. L. Chapman, *Philos. Mag.*, 1913, **6**, 475; (d) R. Burt, G. Birkett and X. S. Zhao, *Phys. Chem. Chem. Phys.*, 2014, **16**, 6519-6538; (e) R. Parsons, *Chem. Rev.*, 1990, **90**, 813-826; (f) C. Lian, K. Liu, K. L. Van Aken, Y. Gogotsi, D. J. Wesolowski, H. L. Liu, D. E. Jiang, and J. Z. Wu, *ACS Energy Lett.*, 2016, **1**, 21-26; (g) W. Schmickler, *Chem. Rev.*, 1996, **96**, 3177-3200; (h) Y. Lauw, M. D. Horne, T. Rodopoulos, A. Nelson and F. A. M. Leermakers, *J. Phys. Chem. B*, 2010, **114**, 11149-11154; (i) C. Largeot, C.

- Portet, J. Chmiola, P. -L. Taberna, Y. Gogotsi, and P. Simon, *J. Am. Chem. Soc.*, 2008, **130**, 2730–2731.
6. (a) M. Zhi, C. Xiang, J. Li, M. Li and N. Wu, *Nanoscale*, 2013, **5**, 72-88; (b) J. H. Jang, S. Han, T. Hyeon and S. M. Oh, *J. Power Sources*, 2003, **123**, 79-85; (c) M. M. Sk, C. Y. Yue, K. Ghosh and R. K. Jena, *J. Power Sources*, 2016, **308**, 121-140; (d) V. Augustyn, P. Simon and B. Dunn, *Energy Environ. Sci.*, 2014, **7**, 1597-1614.
7. (a) A. Borenstein, O. Hanna, R. Attias, S. Luski, T. Brousse and D. Aurbach, *J. Mater. Chem. A*, 2017, **5**, 12653-12672; (b) Y. Zhu, S. Murali, M. D. Stoller, K. J. Ganesh, W. Cai, P. J. Ferreira, A. Pirkle, R. M. Wallace, K. A. Cychosz, M. Thommes, D. Su, E. A. Stach and R. S. Ruoff, *Science*, 2011, **332**, 1537-1541; (c) H. Jiang, P. S. Lee and C. Li, *Energy Environ. Sci.*, 2013, **6**, 41-53; (d) S. Bose, T. Kuila, A. K. Mishra, R. Rajasekar, N. H. Kim and J. H. Lee, *J. Mater. Chem.*, 2012, **22**, 767-784; (e) D. Pech, M. Brunet, H. Durou, P. Huang, V. Mochalin, Y. Gogotsi, P. -L. Taberna and P. Simon, *Nat. Nanotechnol.*, 2010, **5**, 651–654; (f) Y. Wang, Z. Shi, Y. Huang, Y. Ma, C. Wang, M. Chen and Y. Chen, *J. Phys. Chem. C*, 2009, **113**, 13103–13107; (g) E. Frackowiak and F. Béguin, *Carbon*, 2001, **39**, 937-950; (h) Y. Mateyshina, A. Ulihin, A. Samarov, C. Barnakov and N. Uvarov, *Solid State Ionics*, 2013, **251**, 59-61.
8. (a) S. Wang, N. Liu, J. Su, L. Li, F. Long, Z. Zou, X. Jiang and Y. Gao, *ACS Nano.*, 2017, **11**, 2066–2074; (b) Q. Zhang, K. Scraftford, M. Li, Z. Cao, Z. Xia, P. M. Ajayan and B. Wei, *Nano Lett.* 2014, **14**, 1938–1943; (c) J. Chen, K. Sheng, P. Luo, C. Li and G. Shi, *Adv. Mater.*, 2012, **24**, 4569–4573; (d) M. G. Hahm, A. L. M. Reddy, D. P. Cole, M. Rivera, J. A. Vento, J. Nam, H. Y. Jung, Y. L. Kim, N. T. Narayanan, D. P. Hashim, C. Galande, Y. J. Jung, M. Bundy, S. Karna, P. M. Ajayan and R. Vajtai, *Nano Lett.* 2012, **12**, 5616–5621; (e) X. Yang, J. Zhu, L. Qiu and D. Li, *Adv. Mater.*, 2011, **23**, 2833–2838.
9. W. Hummars and R. Offeman, *J. Am. Chem. Soc.*, 1995, **80**, 1339.
10. (a) Z. -L. Wang, D. Xu, J. -J. Xu, L. -L. Zhang and X. -B. Zhang, *Adv. Funct. Mater.* 2012, **22**, 3699–3705; (b) Z. -L. Hu, M. Aizawa, Z.-M. Wang, N. Yoshizawa and H. Hatori, *Langmuir*, 2010, **26**, 6681–6688.
11. (a) H. Li, J. Wu, Z. Yin and H. Zhang, *Acc. Chem. Res.*, 2014, **47**, 1067–1075; (b) X. Li and H. Zhu, *J. Materiomics.*, 2015, **1**, 33-44; (c) A. Ejigu, I. A. Kinloch, E. Prestat and R. A. W. Dryfe, *J. Mater. Chem. A*, 2017, **5**, 11316–11330; (d) M. Acerce, D. Voiry and M. Chhowalla, *Nat. Nanotech.*, 2015, **10**, 313-318.
12. A. Achari, Sahana S. and M. Eswaramoorthy, *Energy Environ. Sci.*, 2016, **9**, 1224-1228.

13. G. Zhang, H. Liu, J. Qua and J. Li, *Energy Environ. Sci.*, 2016, **9**, 1190-1209.
14. (a) B. –S. Yin, S. –W. Zhang, Q. –Q. Ren, C. Liu, K. Ke and Z. –B. Wang, *J. Mater. Chem. A*, 2017, **5**, 24942-24950; (b) Y. Xu, Z. Lin, X. Huang, Y. Liu, Y. Huang, and X. Duan, *ACS Nano.*, 2013, **7**, 4042–4049; (c) K. Yang, K. Cho, D. S. Yoon, and S. Kim, *Sci. Rep.*, 2017, **7**, 40163; (d) X. Wu and M. Lian, *J. Power Sources*, 2017, **362**, 184-191.

Chapter 7

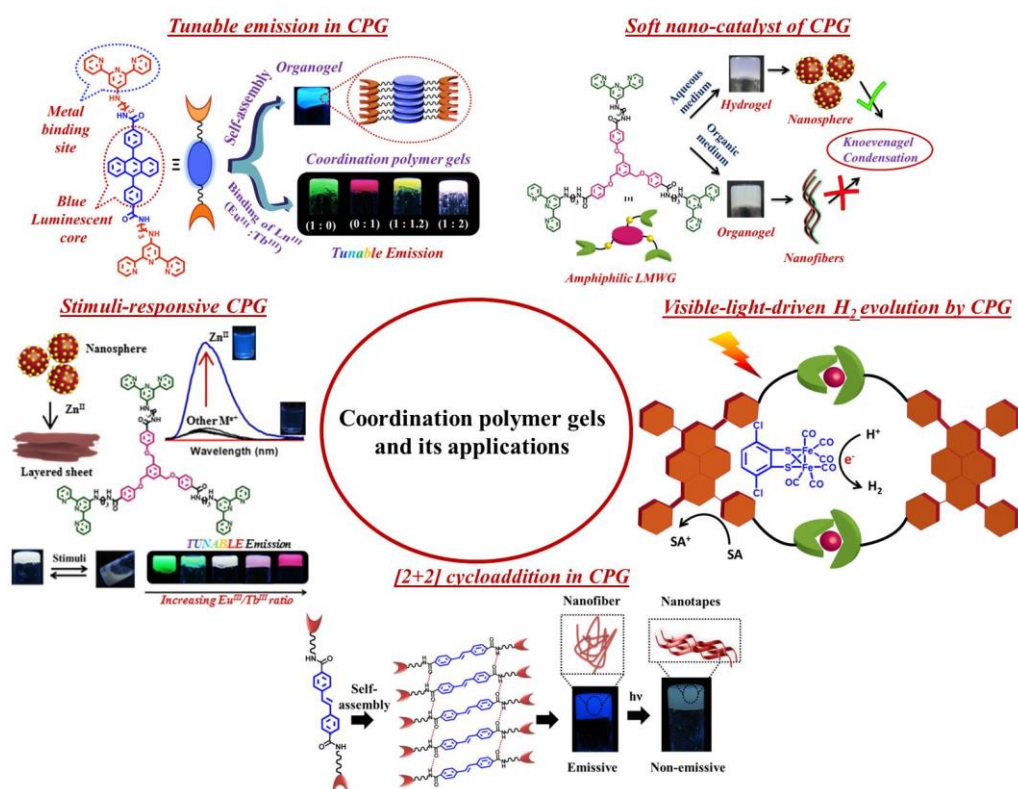
Thesis Summary

Thesis Summary

The thesis work comprises self-assembly of various low molecular weight gelators (LMWG) and metal-organic cubes (MOCs) to supramolecular hydrogel/organogel and inorganic-organic hybrid-gels which are exploited for energy and environmental applications. Before going into the self-assembly study, a series of LMWGs were designed and synthesized. The common design principle adopted to construct the LMWGs involves: i) the π -chromophores as the core, ii) terminal terpyridine groups iii) the core and terpyridines were connected via flexible alkylamide chain. The different π -chromophores used to prepare LMWG were: i) C2 symmetric 9,10-diphenylanthracene, stilbene and azobenzene, ii) C3 symmetric 4,4',4''-[1,3,5-phenyl-tri(methoxy)]-tris-benzene, and iii) C4 symmetric 1,3,6,8-Tetrakis(benzoate)pyrene and 4,4',4'',4'''-(pyrene-1,3,6,8-tetra-yltetrakis(ethyne-2,1-diyl))tetra-benzoate. These cores were specifically chosen by keeping their respective properties in mind. In all cases, the π -cores were connected to terpyridine via alkylamide chain which induced flexibility and drove the self-assembly of LMWGs to hydrogels or organogels. The terpyridine termini of LMWGs involved in the coordination with different metal ions, such as Tb^{III}, Eu^{III}, Zn^{II} and Ru^{II} and drive the self-assembly to CPGs. The synergistic combination of LMWGs and the metal ions induced exciting properties in the CPGs, such as tunable emission, stimuli-responsive properties, catalysis, tunable nano-morphology, photo-responsive behaviour, photo-catalytic properties etc (Scheme 1).

In one approach it was shown that coordination driven self-assembly of a blue emitting LMWG having 9,10-diphenylanthracene in presence of Tb^{III} and Eu^{III} resulted in CPGs with tunable emission, including white-light-emission. The high processability of the white-light-emitting CPG was exploited for coating purpose. On the same line, another white-light-emitting gel was prepared from self-assembly of 4,4',4''-[1,3,5-phenyl-tri(methoxy)]-tris-benzene-based LMWG and Tb^{III}/ Eu^{III} ions. In this case, the white-light-emitting gel showed reversible mechano-, thermo- and chemo-responsive gel-sol transition and change in emission properties by exploiting dynamic nature of Ln^{III}-terpyridine coordination bond. In another study it was shown that the 4,4',4''-[1,3,5-phenyl-tri(methoxy)]-tris-benzene-based LMWG behaved as a amphiphilic gelator and underwent bimodal self-assembly to hydrogel and organogel with nanosphere and nanofiber morphologies, respectively. Due to the different special disposition of the donor and acceptor chromophores, the hydrogels showed charge transfer emission whereas the

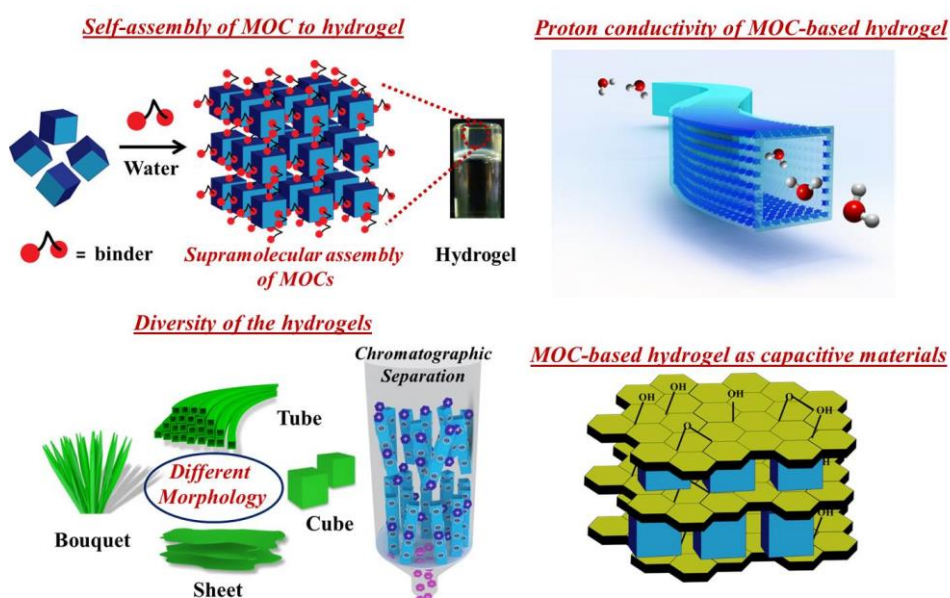
organogel showed LMWG-based emission. Moreover, the nanospheres of the hydrogel having surface exposed amide groups were exploited as nano-catalyst for Knoevenagel condensation reaction. In addition, this gelator showed Zn^{II} sensing properties and the CPG prepared with Zn^{II} showed change in morphology. In another work, photo-responsive behaviours of stilbene and azobenzene-based gelators were studied. Moreover, the photo-chemical [2+2] cyclo-addition was used as a tool to tune morphology and properties of organogels and CPG. The two pyrene-based gelators were self-assembled to organogels and CPGs in presence of Ru^{II} . The broad visible-light absorption of the CPGs resulting due to combined Ru^{II} -terpyridine LMCT and pyrene-centred absorption made them excellent photo-sensitizer. After encapsulating an earth-abundant co-catalyst, $[\text{FeFe}](\text{bcbdt})(\text{CO})_6$ that resemble to the active site of $[\text{FeFe}]$ -hydrogenases inside the CPGs, they showed excellent visible-light-driven catalytic hydrogen evolution.



Scheme 1: Self-assembly of different LMWGs to hydrogel/organogel and coordination polymer gel and their applications.

In another work, synthesis of water soluble metal-organic cube its self-assembly to hydrogels in presence of different H-bond donating molecular binders, such as ammonium ion (NH_4^+), N-(2-aminoethyl)-1,3-propanediamine, guanidine hydrochloride, and β -alanine, were studied. The hydrogels showed different morphologies depending

upon the structure and geometry of the molecular binders. The hydrogel, formed with ammonium cations exhibits nanotubular morphology with negatively charged surface which was utilized for gel–column chromatographic separation of charged species. Moreover, proton conductivity of these MOC-based hydrogels were studied. Due to the presence of ammonium cations as proton carrier and 1D nanotube morphology, the hydrogel with NH_4^+ cation as binder showed high proton conductivity. In another approach MOC was used as 0D material to prepare soft heterostructure materials with graphene oxide/ MoS_2 . These materials also exhibited good charge storage behaviour. In conclusion, MOC was used as a template to prepare hydrogels with various applications (Scheme 2).



Scheme 2: Self-assembly of MOC to hydrogels in presence of different binders and there applications.

Biography



Papri Sutar obtained her B.Sc. degree from Dinabandhu Andrews College, University of Calcutta in 2010. She obtained her master's degree from the Department of Chemistry, Indian Institute of Technology, Kanpur, in 2012. She was awarded with Council of Scientific and Industrial Research (CSIR) fellowship to pursue doctoral research in India after securing an All India Rank of 70 in National Eligibility Test (NET, 2012) in Chemical Science. She secured an All India Rank of 9 in Graduate Aptitude Test Engineering (GATE, 2012) in chemistry. After that she joined Chemistry and Physics of Materials Unit (CPMU), Jawaharlal Nehru Centre for Advanced Scientific Research (JNCASR), Bangalore as a Junior Research Fellow (JRF) in August, 2012. Presently, she is pursuing her Ph.D. under the supervision of Prof. Tapas K. Maji in Molecular Materials Laboratory, JNCASR. Her research work focuses on the development of multi-functional coordination polymer gels for diverse applications. She has also worked upon metal-organic cube based hydrogels and studied their applications.

List of Publications

1. **P. Sutar**, V. M. Suresh and T.K. Maji, Tunable emission in lanthanide coordination polymer gels based on a rationally designed blue emissive gelator, *Chem. Commun.*, **2015**, **51**, 9876-9879.
2. **P. Sutar** and T. K. Maji, Coordination polymer gels: soft metal-organic supramolecular materials and versatile applications, *Chem. Commun.*, **2016**, **52**, 8055-8074.
3. **P. Sutar** and T. K. Maji, Bimodal self-assembly of an amphiphilic gelator into a hydrogel-nanocatalyst and an organogel with different morphologies and photophysical properties, *Chem. Commun.*, **2017**, **52**, 13136- 13139.
4. **P. Sutar** and T. K. Maji, Coordination Polymer Gels with Modular Nano-morphologies, Tunable Emissions and Stimuli-responsive Behaviour Based on an Amphiphilic Tripodal Gelator, *Inorg. Chem.*, **2017**, **56**, 9417-9425.
5. **P. Sutar**, V. M Suresh, K. Jayaramulu, A. Hazra and T. K. Maji, Binder driven self-assembly of metal-organic cubes towards functional hydrogels, *Manuscript under revision in Nat. Commun.*, **2018**.

-
6. V. M. Suresh[#], **P. Sutar**[#], P. Verma and T. K. Maji, Tunable band-gap in donor-acceptor conjugated microporous polymers: efficient photocatalyst for hydrogen generation, *Manuscript under submission*, 2018. [#]These authors contributed equally.
 7. **P. Sutar** and T. K. Maji, Proton conductivity in metal-organic cube based supramolecular framework and derived hydrogels, *Manuscript under preparation*, 2018.
 8. **P. Sutar**, M. Ghosh, P. Kumar, D. Samanta and T. K. Maji, Ruthenium Based Coordination Polymer Gels for Visible-light-driven Hydrogen Evolution, *Manuscript under preparation*, 2018.
 9. **P. Sutar** and T. K. Maji, Photo-responsive Gel: Tuning of Morphology and Optical Property by [2+2] Cyclo-addition Reaction, *Manuscript under preparation*, 2018
 10. **P. Sutar**, C. Das and T. K. Maji, Layered Heterostructure Hydrogels Based on Metal-Organic Cube and GO/MoS₂ as Capacitive Materials, *Manuscript under preparation*, 2018

Book chapter

1. P. Kanoo, R. Haldar, **P. Sutar**, A. Chakraborty and T. K. Maji, in *Functional Supramolecular Materials: From Surfaces to MOFs*, The Royal Society of Chemistry, 2017, pp. 412-453.